

NASA-CR-3845 19850005241

NASA Contractor Report 3845

Experimental Investigation of Shock-Cell Noise Reduction for Single Stream Nozzles in Simulated Flight

FOR REFERENCE
NOT TO BE TAKEN FROM THE BOOKS

K. Yamamoto, J. F. Brausch, T. F. Balsa,
B. A. Janardan, and P. R. Knott

CONTRACT NAS3-22514
DECEMBER 1984



NASA Contractor Report 3845

**Experimental Investigation
of Shock-Cell Noise Reduction
for Single Stream Nozzles
in Simulated Flight**

K. Yamamoto, J. F. Brausch, T. F. Balsa,
B. A. Janardan, and P. R. Knott

*General Electric Company
Cincinnati, Ohio*

Prepared for
Lewis Research Center
under Contract NAS3-22514



National Aeronautics
and Space Administration

Scientific and Technical
Information Branch

1984

TABLE OF CONTENTS

<u>Section</u>	<u>Page</u>
1.0 SUMMARY	1
2.0 INTRODUCTION	3
3.0 TEST FACILITY DESCRIPTION AND DATA REDUCTION PROCEDURES	8
3.1 Jet Noise Test Facility Description	8
3.2 Acoustic Data Acquisition and Reduction Procedures	8
3.3 Diagnostic Test Instrumentation	14
3.3.1 Laser Velocimeter	14
3.3.2 Shadowgraph System	18
4.0 CONFIGURATION DESCRIPTION AND SCOPE OF TESTING	20
4.1 Description of Test Nozzle Configurations	20
4.1.1 Baseline Convergent Circular Nozzle: Model 1	21
4.1.2 Convergent-Divergent Circular Nozzle: Model 2	21
4.1.3 Baseline Contoured Convergent Annular Plug Nozzle: Model 3	25
4.1.4 Baseline Contoured Convergent Annular Plug Nozzle with Shock Screech Tabs: Model 3 with Tabs	25
4.1.5 Convergent-Divergent Annular Plug Nozzle: Model 4	25
4.1.6 20 Chute Annular Plug Suppressor, Convergent Flow Element Terminations: Model 5	31
4.1.7 20 Chute Annular Plug Suppressor, Convergent- Divergent Flow Element Terminations: Model 6	31
4.2 Scope of Testing	37
4.2.1 Acoustic Tests	37
4.2.2 Diagnostic Tests	37
5.0 ACOUSTIC TEST RESULTS	38
5.1 Assessment of Noise Reduction by Convergent-Divergent Termination	38
5.1.1 C-D Effectiveness of Circular Nozzle	40
5.1.2 C-D Effectiveness of Annular Plug Nozzle	57
5.1.3 C-D Effectiveness of Multi-Element Suppressor Plug Nozzle	72

TABLE OF CONTENTS (Concluded)

<u>Section</u>	<u>Page</u>
5.2 Influence of Flight, Jet Temperature and Nozzle Geometry on Shock-Cell Noise	70
5.2.1 Influence of Flight on Shock-Cell Noise	90
5.2.2 Jet Temperature Effects on Shock-Cell Noise	161
5.2.3 Influence of Nozzle Configuration on Shock-Cell Noise	169
5.3 Discussion on Shock Screech	214
5.4 Comparison of Measured Shock-Cell Noise Data With Predictions from Existing Models	233
6.0 DIAGNOSTIC TEST RESULTS	248
6.1 Laser Velocimeter Test Results	248
6.1.1 General Flow Characteristics of Supersonic Jets	249
6.1.2 Mean and Turbulent Flow Properties in Turbulent Shear Layer	262
6.2 Shadowgraph Photo Test Results	283
7.0 PREDICTIVE MODELING	300
7.1 Preliminary Remarks and Perturbation Equations	303
7.2 Solution for the Mean Velocity Field	313
7.3 Solution for the Random Velocity Field	317
7.4 Interaction Between Mean and Random Fields	321
7.5 Acoustic Field	327
7.6 Discussions and Conclusions	331
8.0 CONCLUSIONS AND RECOMMENDATIONS	339
8.1 Conclusions	339
8.2 Recommendations	341
9.0 NOMENCLATURE	342
10.0 REFERENCES	344
APPENDICES	
I - Aerodynamic and Acoustic Test Data	349
II - Aerodynamic Test Matrix for Laser Velocimeter Measurements	374
III - Aerodynamic Test Matrix for Shadowgraph Photo Tests	380

1.0 SUMMARY

This report, along with the companion Comprehensive Data Report, summarizes the experimental and analytical results of a scale-model free-jet acoustic and aerodynamic investigation performed by the General Electric Company under NASA-Lewis Research Center sponsorship on single-stream convergent and convergent-divergent nozzles.

Seven single stream model nozzles were tested for a total of one hundred forty acoustic test points so as to evaluate the effectiveness of Convergent-Divergent (C-D) flowpaths in the reduction of shock-cell noise under static and simulated flight conditions. The test nozzles included a baseline convergent circular nozzle, a C-D circular nozzle, a convergent annular plug nozzle, a C-D annular plug nozzle, a convergent multi-element suppressor plug nozzle and a C-D multi-element suppressor plug nozzle. To better quantify the effectiveness of C-D terminations for shock-cell noise control and to help formulate a proper physical model of the experimentally observed phenomena, diagnostic flow visualization with a shadowgraph and aerodynamic plume measurements with a laser velocimeter were performed with the test nozzles. Most of the tests were conducted at elevated exhaust nozzle temperatures ($T_T \approx 1730^\circ\text{R}$) and nozzle pressure ratios that are typical of mixed conditions of a variable cycle engine (VCE) applicable for advanced supersonic transport (AST). In addition, a theory of shock-cell noise for annular plug nozzles in the vicinity of the plug was developed based on recent theories of shock-turbulence interaction.

Some of the key results of this investigation are:

- Effectiveness of convergent-divergent terminations in the flowpaths of circular, annular and suppressor nozzles in the reduction of front quadrant noise has been demonstrated under both static and simulated flight conditions. At an angle of 50 degrees to the inlet, the perceived noise level (PNL) relative to the baseline convergent circular nozzle is reduced under static and simulated flight conditions, respectively, by a maximum of 7.5 and 11 dB with the C-D circular nozzle, 6 and 8 dB for the C-D annular nozzle

and 9.5 and 10 dB for the C-D multi-element suppressor nozzle. The shock noise benefit of these C-D nozzles is observed over a broad range of pressure ratios in the vicinity of their design conditions.

- For the baseline convergent circular nozzle, eight shock-cells were observed on the nozzle axis while four to five shock-cells were noted along the lip-line. The C-D circular nozzle was noted to be completely shock-free at the design conditions.
- At the C-D design condition, the C-D annular nozzle was found to be free of shock-cells on the plug. However, shock-cells downstream of the plug were noted indicating complete shock-cell noise reduction has not been achieved by the C-D termination on the annular plug nozzle.
- The regions downstream of the plugs of convergent and C-D multi-element suppressor nozzles were identified to be practically shock-free.
- The C-D circular nozzle was identified to be the quietest among the test configurations regarding front-quadrant noise levels.
- Tabs were found to suppress both the discrete and broadband shock noise components for the convergent annular plug nozzle. However, the presence of tabs was found to shift the broadband peak frequency to a higher value.
- Jet temperature does not significantly influence the shock-cell generated noise.

2.0 INTRODUCTION

The General Electric Company under NASA-Lewis Research Center sponsorship has conducted scale model acoustic and diagnostic aerodynamic tests on circular, unsuppressed and mechanically suppressed annular plug nozzles to determine the effectiveness of convergent-divergent terminations in mitigating shock-cell associated noise. This contract report summarizes the major results of this study. A Comprehensive Data Report (Reference 2-1) contains the detailed acoustic and diagnostic test data.

One source of jet noise from non-ideally expanded jets operating at supercritical pressure ratios is the shock-cell associated noise from the jet exhaust. The shock-cell associated noise has been identified as a potentially significant engine noise problem for advanced supersonic cruise aircraft at takeoff. Studies at the General Electric Company suggest that for practical designs, shock-cell associated noise may be in fact the limiting exhaust nozzle noise mechanism which could inhibit the ability to achieve subsonic commercial noise levels for advanced supersonic aircraft. For circular nozzles, References 2-2 and 2-3, as well as others, have demonstrated the use of convergent-divergent (C-D) nozzle passages as one means for achieving shock-cell noise control. Figure 2-1 from Reference 2-4 illustrates typical results obtained from ambient temperature tests. This figure shows that for a relatively large range of nozzle pressure ratios, a circular nozzle with a C-D termination designed for ideal expansion at a Mach Number, M_j , of 1.5 ($\beta = \sqrt{M_j^2 - 1} = 1.1$) radiated significantly less noise than that of a convergent circular nozzle operating at equivalent supercritical pressure ratios.

Recently the General Electric Company, under NASA-Lewis sponsorship (Reference 2-5), has demonstrated the acoustic effectiveness of a convergent-divergent (C-D) termination on an annular plug nozzle with heated jets and under simulated flight conditions. The results from this test, summarized in Figure 2-2, indicated that in the vicinity of the C-D design point ($M_j = 1.44$) up to 9.0 PNdB forward quadrant noise reduction, relative

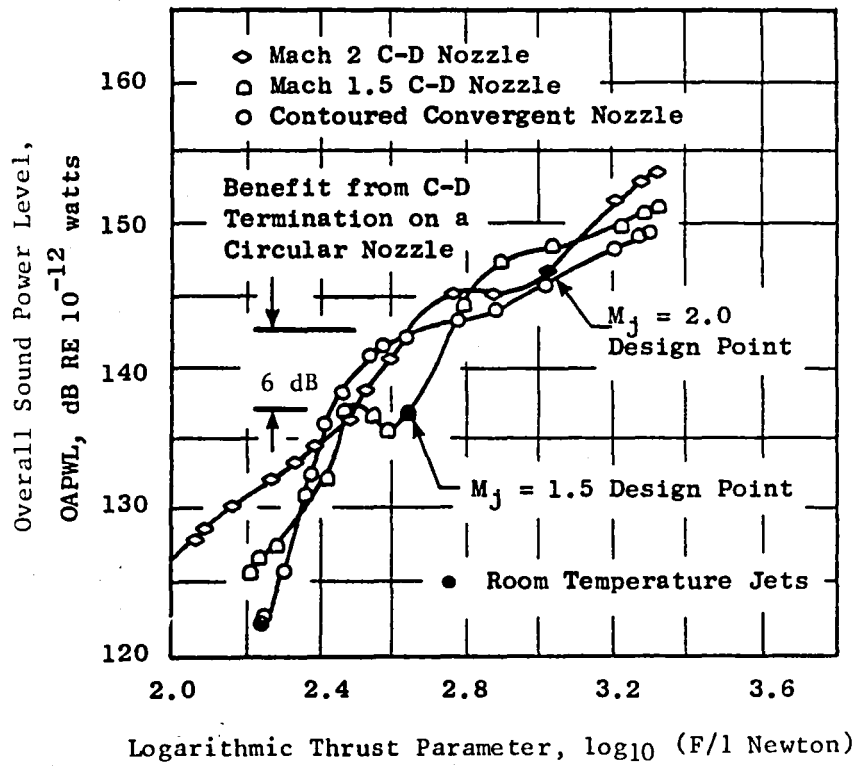
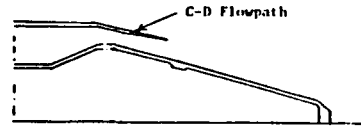
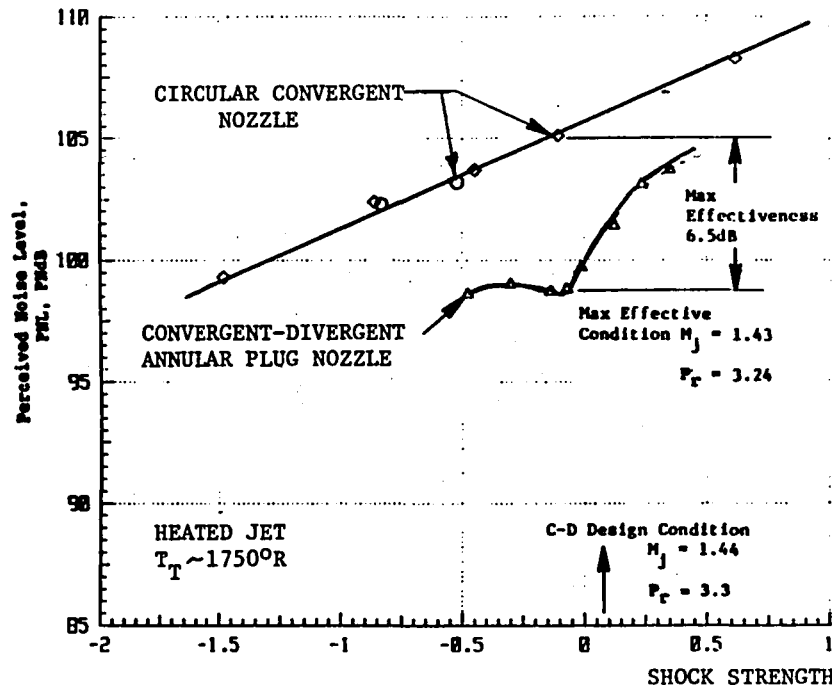


Figure 2-1. Overall Noise Benefit of Convergent-Divergent (C-D) Circular Nozzles (From Reference 2-4).

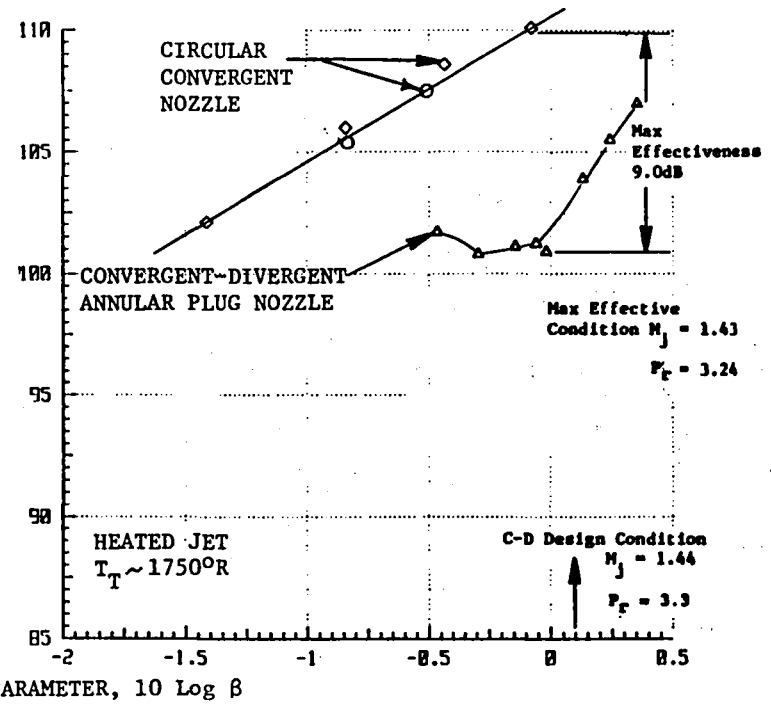


Data Scaled to Product Size: $A^* = 0.903 \text{ m}^2$ (1400 in.²) and
731.5 m (2400 ft) Sideline

5



a) STATIC



b) SIMULATED FLIGHT, $V_{a/c} = 122 \text{ m/sec}$ or
400 f/s

Figure 2-2. Shock-Cell Noise Reduction for a C-D Annular Plug Nozzle Relative to a Circular Convergent Nozzle; Static and Simulated Flight PNL Data at $\theta = 60^\circ$. (From Ref. 2-5)

to a convergent circular nozzle, can be obtained for an advanced supersonic cruise type aircraft engine. The results also showed that the region of sensitivity for C-D effectiveness covered a wide range of operating conditions.

For a more practical range of design jet Mach numbers, ($M_j = 1.3$ to 1.5), the usefulness of C-D nozzles for shock noise control in flight needs to be ascertained. Additionally, the extent and range of validity of existing shock noise theories must be determined. To meet these needs, an experimental investigation of the usefulness of C-D nozzles for circular, annular plug, and multi-element suppressor nozzles in simulated flight was conducted over a wide range of operating conditions during this program.

The overall objective of this program was to determine means by which supersonic jet shock noise can be reduced to acceptable levels for advanced supersonic aircraft. Specifically, the usefulness of C-D passages was investigated and the effect of off-design nozzle pressure ratio was determined statically and in simulated flight. Work efforts of this program consisted of the following major steps:

1. Design and fabrication of convergent-divergent single stream flow passages for circular, annular plug and multi-element suppressor nozzles. The types of seven nozzle configurations investigated are described in Section 4.0.
2. Scale-model acoustic tests in the General Electric's Anechoic Free-Jet Facility. (The facility is described in Section 3.0.) Data were taken statically and at a free-jet velocity typical of a supersonic cruise aircraft at takeoff. One hundred forty acoustic test points were taken over the seven nozzle configurations for a wide range of exhaust nozzle velocity and temperature conditions. The acoustic data are discussed in Section 5.0.
3. Diagnostic flow visualizations with a shadowgraph and aerodynamic plume measurements with a laser velocimeter were carried out on the test configurations. Testing was done both under static

and simulated flight conditions. The General Electric's optical and laser velocimeter equipment was employed so as to quantify the effectiveness of C-D terminations for shock-cell noise control. The diagnostic data are discussed in Section 6.0.

4. In addition to the acoustic and diagnostic studies, development of a theory of shock-cell noise for annular plug nozzles in the vicinity of the plug was carried out based on the Howe and Ffowcs-Williams model (Reference 2-6). This is presented in Section 7.0.

3.0 TEST FACILITY DESCRIPTION AND DATA REDUCTION PROCEDURES

All of the acoustic, laser velocimeter, and shadowgraph tests of this program were conducted in the General Electric Anechoic Free-Jet Facility located in Evendale, Ohio. Brief descriptions of the facility and acoustic data acquisition, reduction, and flight transformation procedures are provided in this section (refer to Reference 2-1 for details).

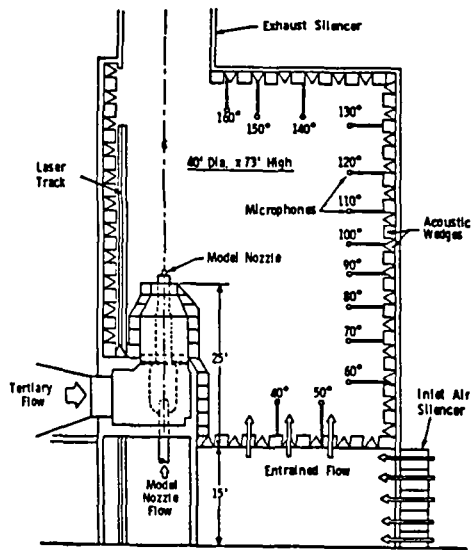
3.1 JET NOISE TEST FACILITY DESCRIPTION

The test facility, schematically shown in Figure 3-1, is a cylindrical chamber having a diameter of 13.1 meters (43 feet) and a height of 21.95 meters (72 feet). The inner surfaces of the chamber are lined with anechoic wedges made of fiberglass to yield a low frequency cutoff below 220 Hz and an absorption coefficient of 0.99 above 220 Hz.

A tertiary duct surrounds the model nozzles with the necessary airflow to simulate a forward flight up to a Mach number of 0.41. The tertiary air passes through a silencer plenum chamber before it is discharged through the 1.22-meter (4-foot) free-jet exhaust. An overhead view of the tertiary exhaust surrounding a test conical nozzle is presented in Figure 3-2.

3.2 ACOUSTIC DATA ACQUISITION AND REDUCTION PROCEDURES

A schematic of the microphone data acquisition system used to obtain the acoustic data during tests in the anechoic chamber is shown on Figure 3-3. This system is optimized for obtaining the acoustic data up through the 80 kHz 1/3-octave center frequency. The microphones used to obtain the data are B&K 4135, 0.64-centimeter (0.25-inch) condenser microphones for far-field measurements. All the tests are conducted with microphone grid caps removed to obtain the best frequency response. The cathode followers are the transistorized B&K 2619 for optimum frequency response and lower inherent system noise characteristics. All systems utilize the B&K 2801 power supply operated in the direct mode.



Angle (Degrees)	Radial Distance	
	m	ft
40	7.92	26.0
50	9.48	31.1
60	9.50	31.18
70	8.76	28.73
80	8.36	27.42
90	8.23	27.00
100	8.36	27.42
110	8.76	28.73
120	9.5	31.18
130	10.74	35.25
140	9.17	30.17
150	8.23	27.0
160	7.92	26.0

Microphone Arrangement

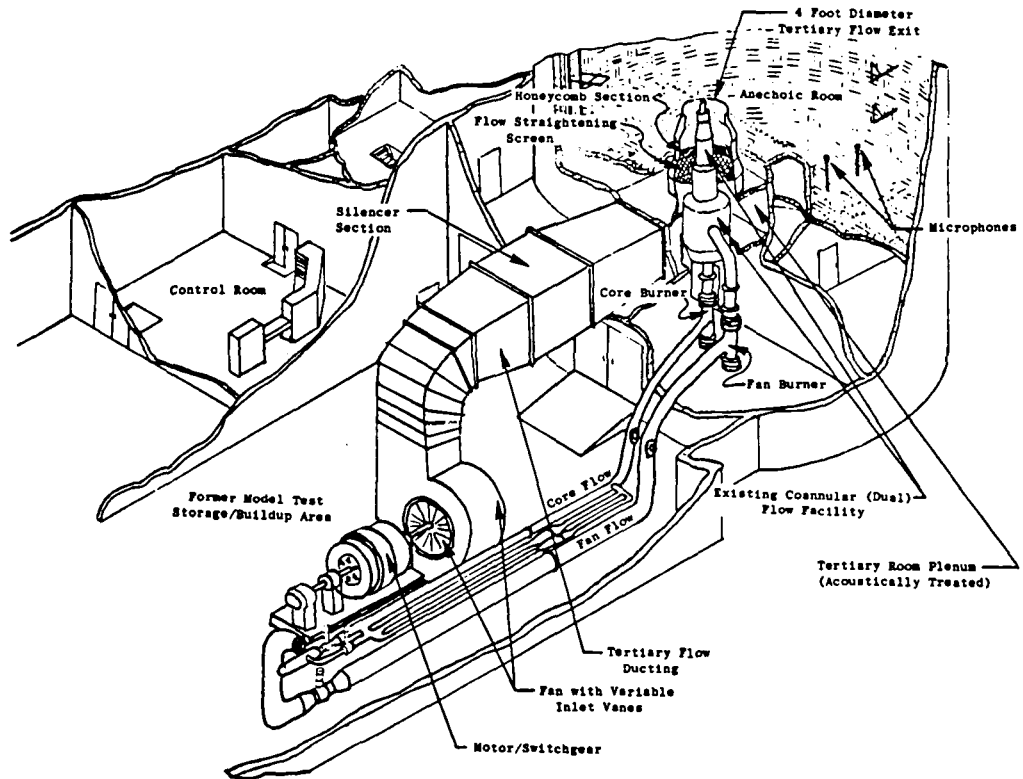


Figure 3-1. Anechoic Free-Jet/Jet Noise Facility Schematic.

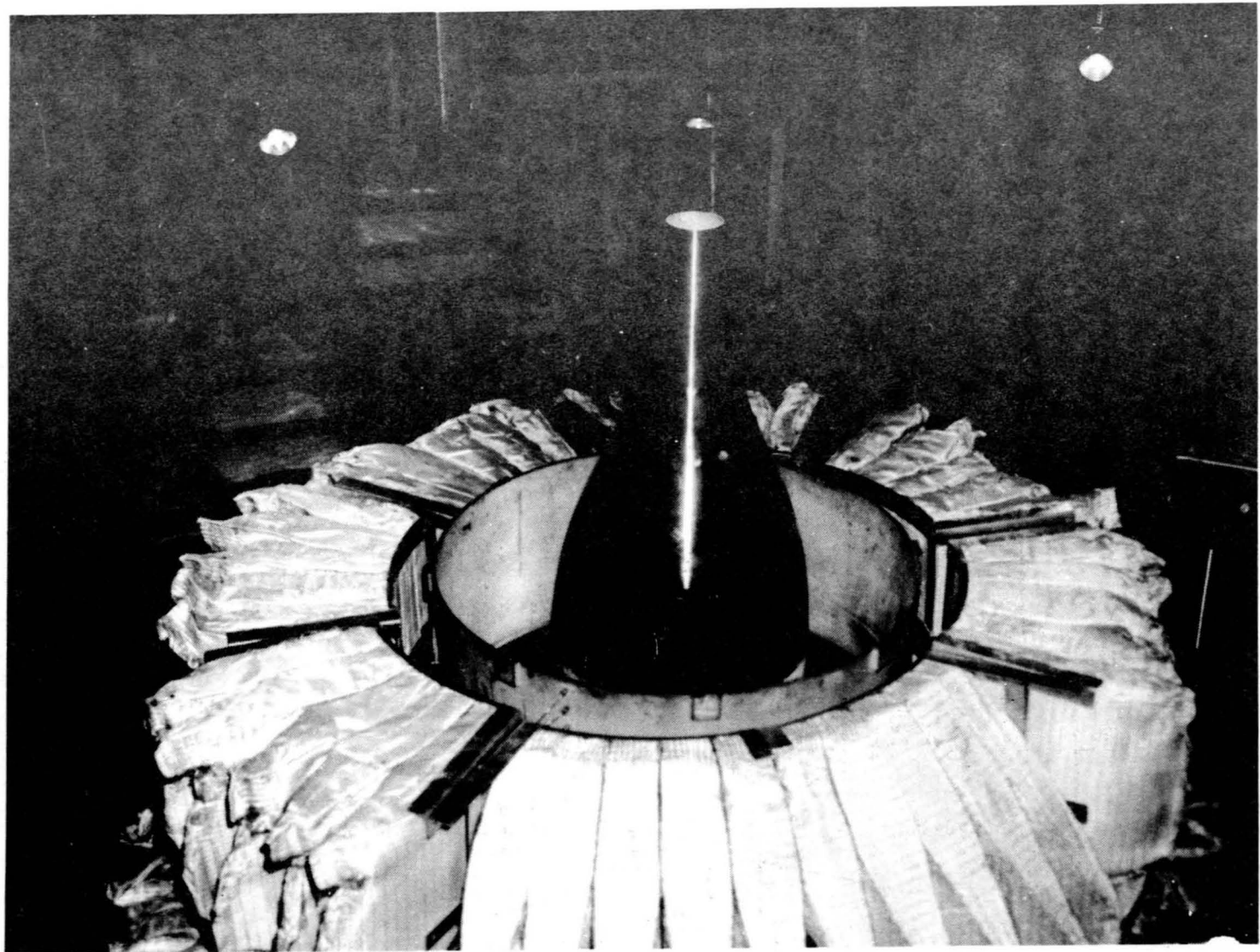


Figure 3-2. Overhead View of the Tertiary Exhaust With a Test Conical Nozzle.

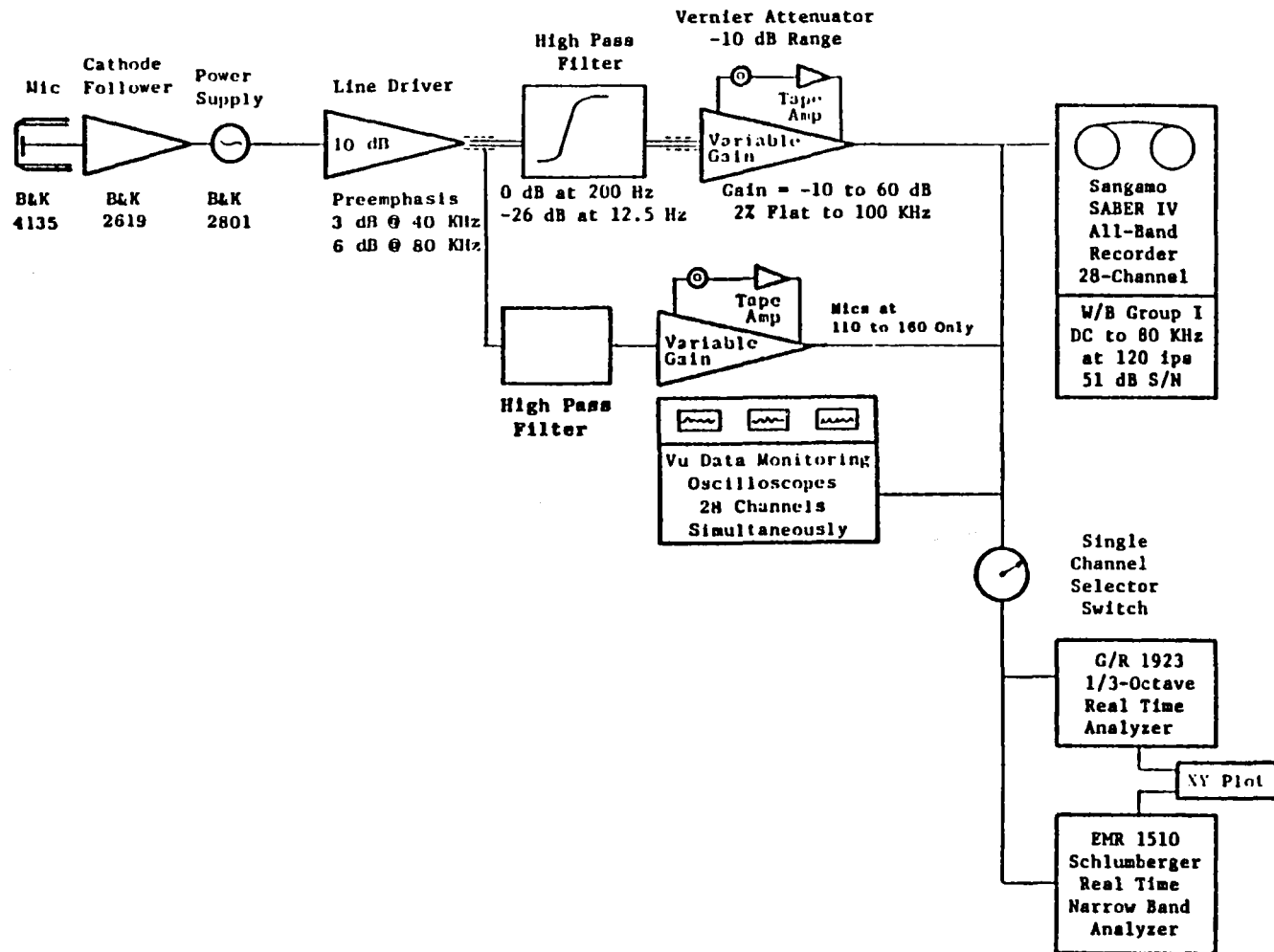


Figure 3-3. Acoustic Data Acquisition System.

The output of the power supply is connected to a line driver adding 10 dB of amplification to the signal as well as adding "preemphasis" to the high frequency portion of the spectrum. The net effect of this amplifier is a 10 dB gain at all frequencies, plus an additional 3 dB at 40 kHz and 6 dB at 80 kHz due to "preemphasis." This procedure improves low amplitude, high frequency data. In order to remove low frequency noise, high-pass filters with attenuations of approximately 26 dB at 12.5 Hz and decreasing to 0 dB at 200 Hz are installed in the system.

The tape recorder amplifiers have a variable gain from -10 dB to +60 dB in 10 dB steps and a gain trim capability for normalizing incoming signals. The prime system used for recording acoustic data is a Sangamo/Sabre IV, 28-track FM recorder. The system is set up for Wideband Group I (intermediate band double extended) at 120 ips tape speed. Operating at this tape speed provides a better dynamic range that is necessary for obtaining the high frequency/low amplitude portion of the acoustic signal. The tape recorder is set up for $\pm 40\%$ carrier deviation with a recording level of 8 volts peak-to-peak. During recording, the signal is displayed on a calibrated master oscilloscope, and the signal gain is adjusted to maximum without exceeding the 8 volt peak-to-peak level.

High-pass filters are incorporated in the acoustic data acquisition systems to enhance the high frequency data of microphones from 110° through 160° ; both the filtered and unfiltered signals are recorded on tape. For data below 20 kHz, the unfiltered signal is used to calculate the sound pressure levels; while for high frequencies, the filtered signal is employed. The entire jet noise spectrum at a given angle is obtained by computationally merging these two spectra.

Standard data reduction is conducted in the General Electric's AEBG Instrumentation and Data Room (IDR). As shown in Figure 3-4, the data tapes are played back on a CBC3700B tape deck with electronics capable of reproducing characteristics within the specifications indicated for Wideband Group I. An automatic shuttling control is incorporated in the system. In normal operation, a tone is inserted on the recorder in the time slot designed for data analysis. Tape control automatically shuttles the tape, initiating an integration start signal to the analyzer at the tone as the tape moves in

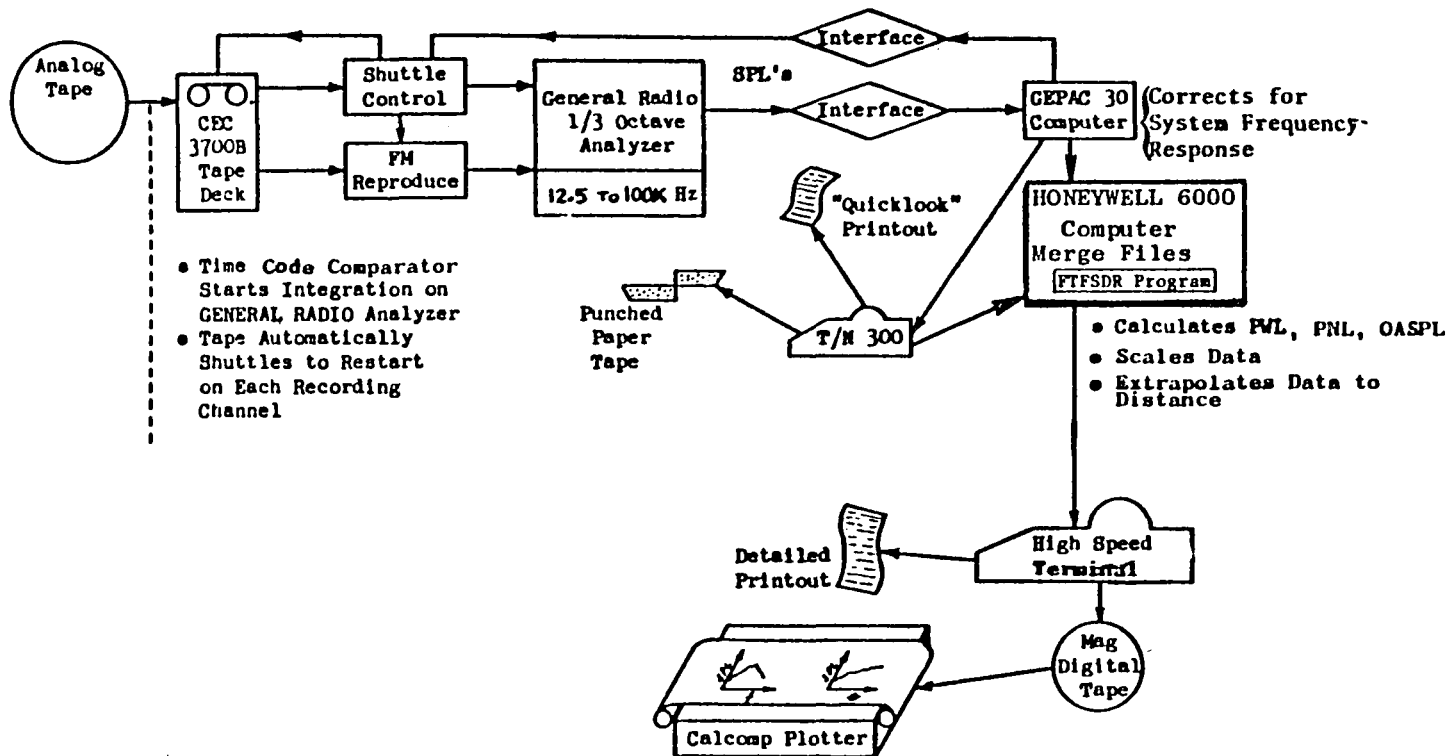


Figure 3-4. Acoustic Data Reduction System.

its forward motion. This motion continues until an "integration complete" signal is received from the analyzer, at which time the tape direction is reversed, and at the tone the tape restarts in the forward direction advancing to the next channel to be analyzed until all the channels have been processed. In addition, a time code generator is utilized to signal tape position as directed by the computer program control.

All 1/3-octave analyses are performed on a General Radio 1921 analyzer. Normal integration time is set for 32 seconds to ensure good integration for the low frequency content. The analyzer has 1/3-octave filter sets from 12.5 Hz to 100 kHz and has a rated accuracy of $\pm 1/4$ dB in each band. Each data channel is passed through an interface to the GEPAC 30 computer where the data are corrected for the frequency response of the microphone and the data acquisition system, corrected to standard day (15°C, 70% RH atmospheric attenuation conditions) as recommended by Shield and Bass (Reference 3-1) and processed to calculate the perceived noise level and OASPL from the spectra. For calculation of the acoustic power, scaling to other nozzle sizes, or extrapolation to different far-field distances, the data are sent to the Honeywell 6000 computer for processing. This is accomplished by transmitting the SPL via direct time share link to the 6000 computer through a 1200 Band Modem. In the 6000 computer the data are processed through the Flight Transformed Full Scale Data Reduction (FTFSDR) Program as per the flow chart shown in Figure 3-5. The data printout is accomplished on a high speed "remote" terminal. In addition, the FTFSDR Program writes a magnetic tape for CALCOMP plotting of the data.

3.3 DIAGNOSTIC TEST INSTRUMENTATION

3.3.1 LASER VELOCIMETER

The basic optical system of the laser velocimeter used in the present program is a differential Doppler, backscatter, single-package arrangement that has the proven feature of ruggedness for the severe environments encountered in high velocity, high temperature jets. Figure 3-6 shows a photograph of the LV system in the General Electric Anechoic Test Facility and a schematic arrangement of the laser package. The laser beams are projected from below the lens, forming an angle that keeps the major axis on the control

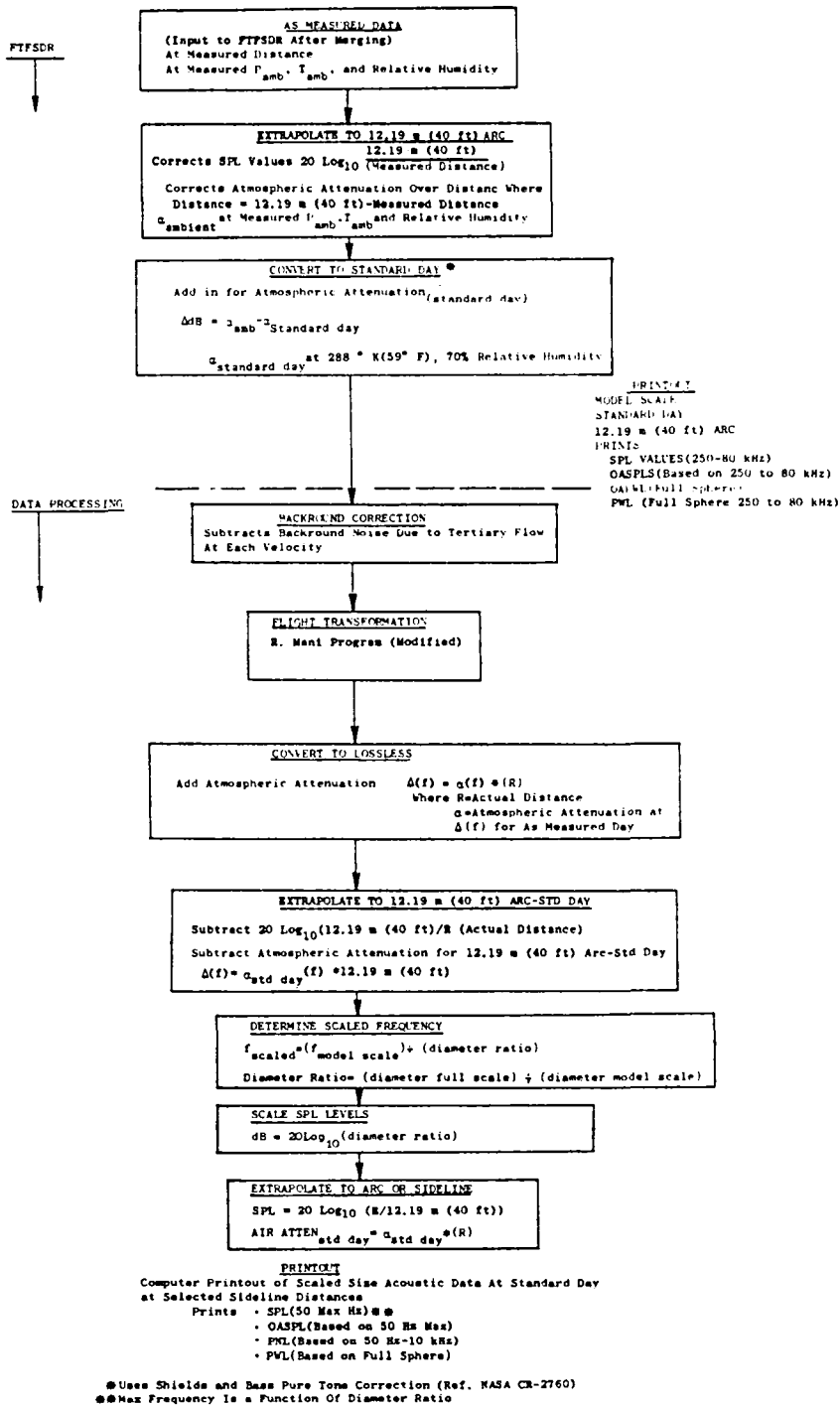
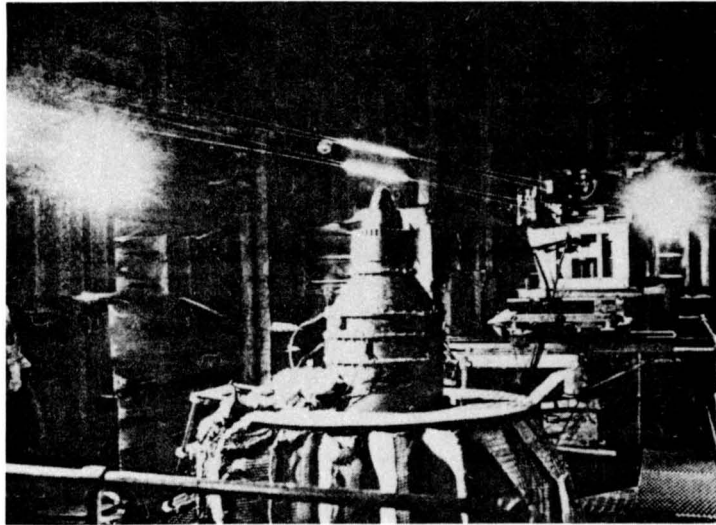
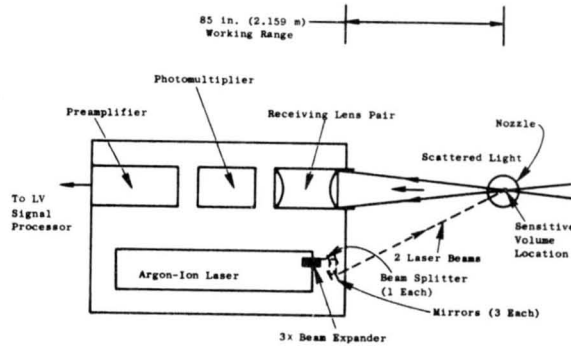


Figure 3-5. Acoustic Data Processing and Scaling Flow Chart.



a. LV System in the GE Anechoic Acoustic Test Facility



b. Schematic of LV Optics Package

Figure 3-6. General Electric Laser Velocimeter.

volume ellipsoid to a minimum. The dimensions of the control volume are 0.535 centimeter (0.25 inch) for the major axis and 0.518 centimeter (0.020 inch) for the minor axis. The range of the LV control volume from the laser hardware is 2.16 meters (85 inches). The three steering mirrors and the beam splitter are mounted on adjustable supports that are made from the same aluminum alloy to eliminate any temperature-oriented alignment problems.

The remotely actuated platform has vertical, horizontal, and axial travel capabilities of 0.813 meter (32 inches), 0.813 meter (32 inches), and 5.79 meters (228 inches), respectively. The resolution is +0.1588 centimeter (0.0625 inch) for each axis except for the last 5.28 meters (208 inches) of axial travel which has a resolution of ± 0.3175 centimeters (0.125 inch).

Seeding is by injection of aluminum oxide (Al_2O_3) powder having a nominal 1-micron diameter into the air supply to the burners and into a region exterior of the test nozzle so as to seed the tertiary air. The powder-feed equipment used is described in Reference 2-3. However, the air supply to the fluidized bed column is heated currently to about 394°K (250°F) to prevent powder aggregation by moisture absorption.

The laser velocimeter signal processor is a direct-counter-(time domain) type similar to that reported in Reference 2-3, but with improvements. These improvements result in a lowered rate of false validations and improved linearity and resolution. Turbulent-velocity probability distributions (histograms) are recorded by a 256-channel, NS633 pulse-height analyzer. The data acquired from the LV are transmitted to a micro-computer system (APPLE-II) for storage on a disk and performance data reduction.

The processing capabilities of the LV system are as follows:

- Velocity range - 10.7 to 1524 mps (35 to 5000 fps).
- Random error for single particle accuracy (error associated with system inaccuracies such as fringe spacing, linearity, stability, burst noise) - 0.75%.

- Bias error for mean velocity - 0.5%.
- False data rejection capability (possibility of accepting bad data) - 0.0002%. The system uses a 16-fringe control volume where all of the 8 center fringes are used in the data acceptance/rejection testing. On an average, 1000 accepted data samples are taken during a histogram.

3.3.2 SHADOWGRAPH SYSTEM

A shadowgraph system was installed in the anechoic free-jet facility to accomplish diagnostic flow visualization tests. To obtain the shadowgraph photos of good resolution, the system was mounted in near proximity of the nozzle. The light source mounted on the optical bench was a steady-state type system. Collimation of the light beam through the test volume was achieved by means of a reflective mirror system of 10 inch diameter. Shadowgraph images were backdropped on a screen that is located at 3.7m (12 feet 2 inches) from the jet nozzle. The steady-state light source, mirror and camera system is mounted on a platform that is remotely controlled so as to position the shadowgraph system over an approximately 0.91m (3 ft) vertical plume study. The schematic arrangement of the shadowgraph setup is shown in Figure 3-7.

19

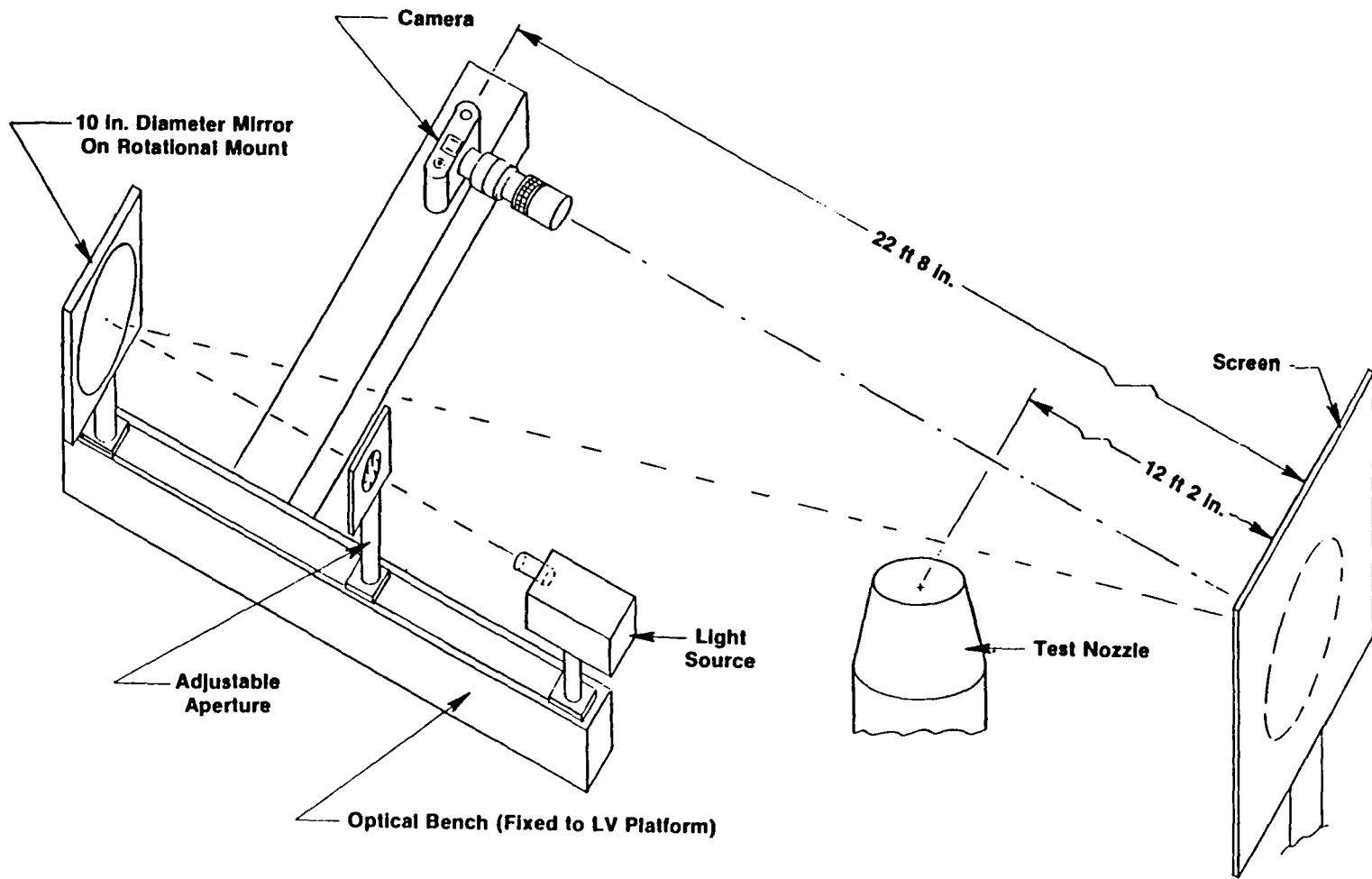


Figure 3-7. Schematic Arrangement of the Shadowgraph Setup in the Anechoic Jet Facility.

4.0 CONFIGURATION DESCRIPTION AND SCOPE OF TESTING

In order to identify the effectiveness of the convergent-divergent termination in the flowpath for shock-cell noise reduction, seven single stream nozzle configurations were tested during this program. In this section an outline of the nozzle configurations and the scope of the acoustic and diagnostic tests are described. Detailed description of the test hardware is given in the Comprehensive Data Report of this contract (Reference 2-1).

4.1 DESCRIPTION OF TEST NOZZLE CONFIGURATIONS

A total of seven single stream nozzle configurations were tested during this program. They were grouped in sets in order to study the impact of convergent-divergent flowpaths on acoustic and aerodynamic properties relative to baseline convergent flowpaths. Three sets were structured around systems of a) circular non-plug (Models 1 and 2), b) annular plug, non-mechanically suppressed (Models 3 and 4), and c) annular plug, mechanically suppressed (Models 5 and 6). The seventh configuration (Model 3 with tabs) was a modification of the convergent annular plug, nonmechanically suppressed system, to evaluate a potential method for shock screech elimination. The configurations are briefly described as follows:

- Model 1 - Baseline Convergent Circular Nozzle
- Model 2 - Convergent-Divergent Circular Nozzle, Design Point at
M = 1.4
- Model 3 - Baseline Contoured Convergent Annular Plug Nozzle
(NonMechanically Suppressed)
- Model 3 w/Tabs - Baseline Contoured Convergent Annular Plug Nozzle
with Shock Screech Tabs (Non-Mechanically Suppressed)
- Model 4 - Convergent-Divergent Annular Plug Nozzle
(NonMechanically Suppressed)

- Model 5 - 20 Chute Annular Plug Suppressor, Convergent Flow Element Terminations

- Model 6 - 20 Chute Annular Plug Suppressor, Convergent-Divergent Flow Element Terminations

Within this section the basic model geometries are described.

Table 4-1 summarizes the significant dimensions of the seven configurations.

4.1.1 BASELINE CONVERGENT CIRCULAR NOZZLE: MODEL 1

The geometric dimensions of this configuration are presented in Figure 4-1, and it is shown installed in the Anechoic Free-Jet Facility in Figure 3-2. The nozzle external flow lines were designed to be compatible with free-jet operation and contoured to eliminate any flow separation upstream of the nozzle exit plane. The nozzle internal flow passage near the 5.094" dia. exit plane ($A_{th} = 20.38 \text{ in}^2$) has a mild convergence angle of 5.3 for a distance of 1.7 throat diameters upstream of the exit plane. The nozzle has a thin trailing lip of thickness equivalent to 1% of the throat diameter. Installed within the 48" dia. free-jet nozzle, it sets a system area ratio of approximately 89 (area free-jet nozzle/area primary nozzle).

4.1.2 CONVERGENT-DIVERGENT CIRCULAR NOZZLE: MODEL 2

The C-D circular nozzle is shown schematically in Figure 4-2. Its throat diameter of 5.1 inch closely matches that of Model 1, the convergent circular nozzle and, therefore, also has a free-jet system area ratio of approximately 89. The exit plane diameter of 5.395 inch, at a distance of 5.525 inch from the throat plane, sets the area ratio, A_{exit}/A_{throat} , at 1.119. The objective of the aerodynamic design for the C-D flowpath (design methodology is given in Reference 4-1) was to obtain isentropic, uniform, and parallel flow at the nozzle exit for the design Mach No. of 1.4, thereby preempting, to a large degree, any shock-cell induced noise.

Table 4-1. Summary of Significant Geometric Characteristics of Test Nozzles.

	Baseline Convergent Circular Nozzle	C-D Circular Nozzle	Baseline Contoured Convergent Annular Plug Nozzle	Baseline Contoured Convergent Annular Plug Nozzle with Shock Screech Tabs	C-D Annular Plug Nozzle	20 Chute Annular Plug Suppressor Convergent Flow Segment Terminations	20 Chute Annular Plug Suppressor, C-D Flow Element Terminations
Model Description	1	2	3	3 W/Tabs	4	5	6
• Convergent/C-D	Converg.	C-D	Converg.	Converg.	C-D	Converg.	C-D
• Throat Area, cm ² (in. ²)	131.5 (20.38)	131.8 (20.43)	163.0 (25.27)	163.0 (25.27)	163.2 (25.3)	131.3 (20.36)	130.5 (20.23)
• Throat Equiv. Dia., cm. (in.)	12.94 (5.09)	12.95 (5.10)	14.4 (5.67)	14.4 (5.67)	14.4 (5.67)	12.93 (5.09)	12.89 (5.08)
• Throat Height, cm. (in.)	- -	- -	2.06 (.811)	2.06 (.811)	2.06 (.811)	- -	- -
• Throat Radius Ratio	-	-	.854	.854	.854	.764	.764
• Exit Area, cm ² (in. ²)	- -	147.5 (22.86)	- -	- -	182.6 (28.3)	- -	147.9 (22.92)
• Exit Equiv. Dia, cm. (in.)	- -	13.70 (5.395)	- -	- -	15.24 (6.00)	- -	13.72 (5.403)
• Exit Height, cm. (in.)	- -	- -	- -	- -	2.63 (1.036)	- -	- -
• Exit Radius Ratio	-	-	-	-	.791	-	.743
• A _e /A _{th}	-	1.119	-	-	1.119	-	1.113
• System Area Ratio	89.0	89.0	71.6	71.6	71.6	89.0	89.0

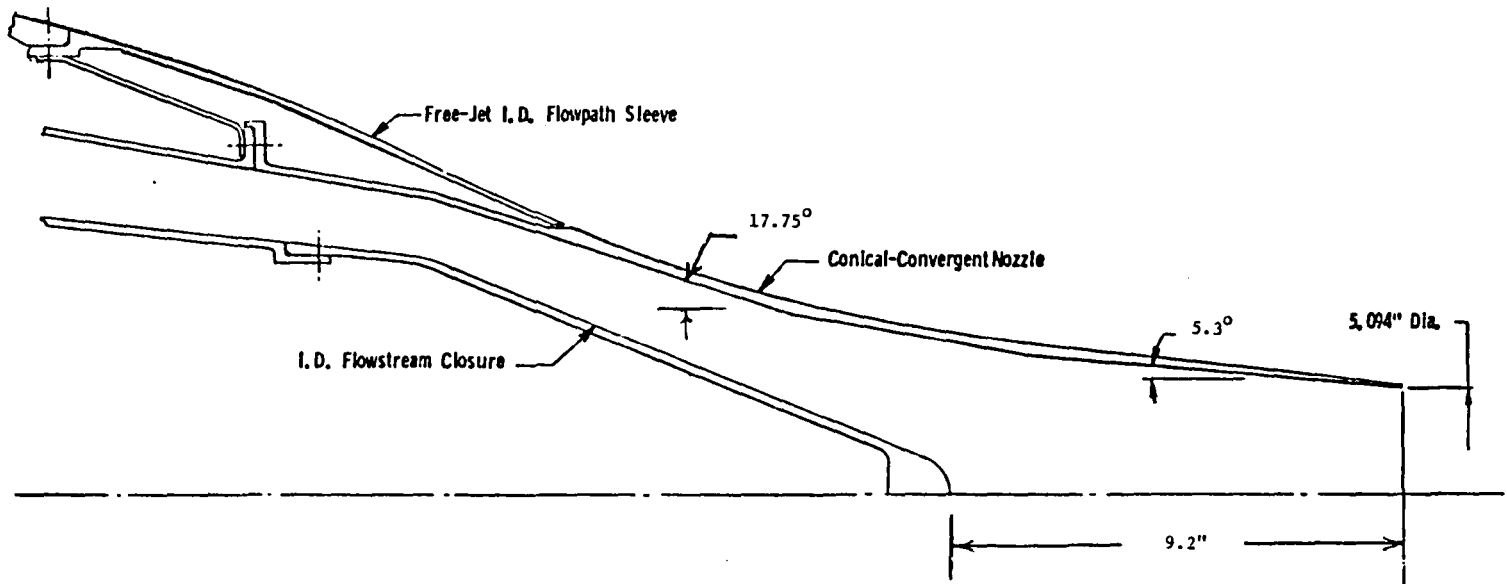


Figure 4-1. Model 1: Baseline Convergent Circular Nozzle.

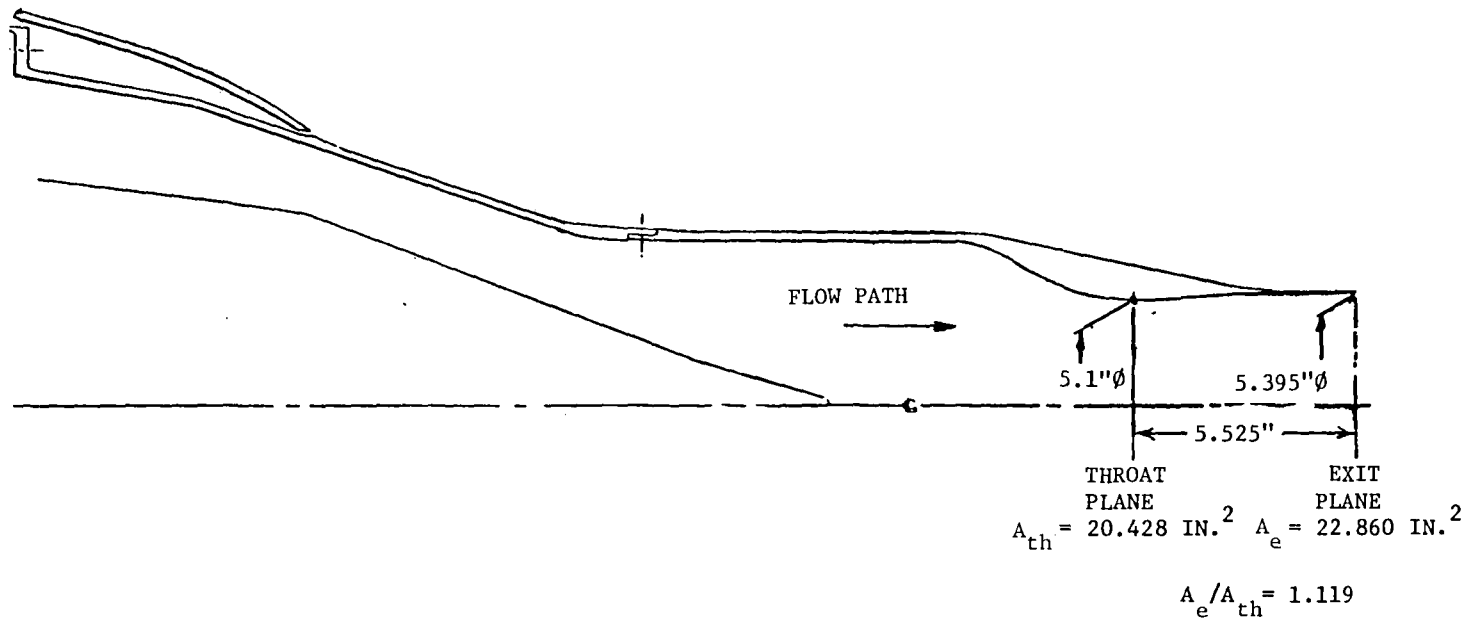


Figure 4-2. Model 2: Convergent-Divergent Circular Nozzle.

The C-D nozzle is shown uninstalled in Figure 4-3a and installed within the Anechoic Free-Jet Facility in Figure 4-3b.

4.1.3 BASELINE CONTOURED CONVERGENT ANNULAR PLUG NOZZLE: MODEL 3

The contoured convergent annular plug nozzle (non-mechanically suppressed) is shown schematically in Figure 4-4. Basic design parameters are summarized in Table 4-1. (See Reference 4-2 for design details.)

4.1.4 BASELINE CONTOURED CONVERGENT ANNULAR PLUG NOZZLE WITH SHOCK SCREECH TABS: MODEL 3 WITH TABS

This model utilized the same hardware items as Model 3. However, 8 shock screech tabs were applied to the annular sleeve at the exit plane lip. The tabs were configured as shown in Figure 4-5. The design was initiated and scaled from Reference 4-3. The tabs were equally spaced around the annular sleeve utilizing nichrome straps. A photo of the application is shown in Figure 4-6.

4.1.5 CONVERGENT-DIVERGENT ANNULAR PLUG NOZZLE: MODEL 4

The C-D annular plug nozzle (non-mechanically suppressed) is shown schematically in Figure 4-7.

Design parameters for the $M = 1.4$ selected case are:

- $A_{th} = 25.3 \text{ in}^2$
- $P_T/P_S = 3.120$
- $A_e = 28.3 \text{ in}^2$
- $T_T = 1760^\circ\text{R}$
- $A_e/A_{th} = 1.119$
- $T_S = 1309^\circ\text{R}$
- $(R_r)_{th} = 0.854$
- $V_j = 2439 \text{ ft/sec}$
- $(R_r)_e = 0.791$
- $\gamma = 1.351$
- $M = 1.4$

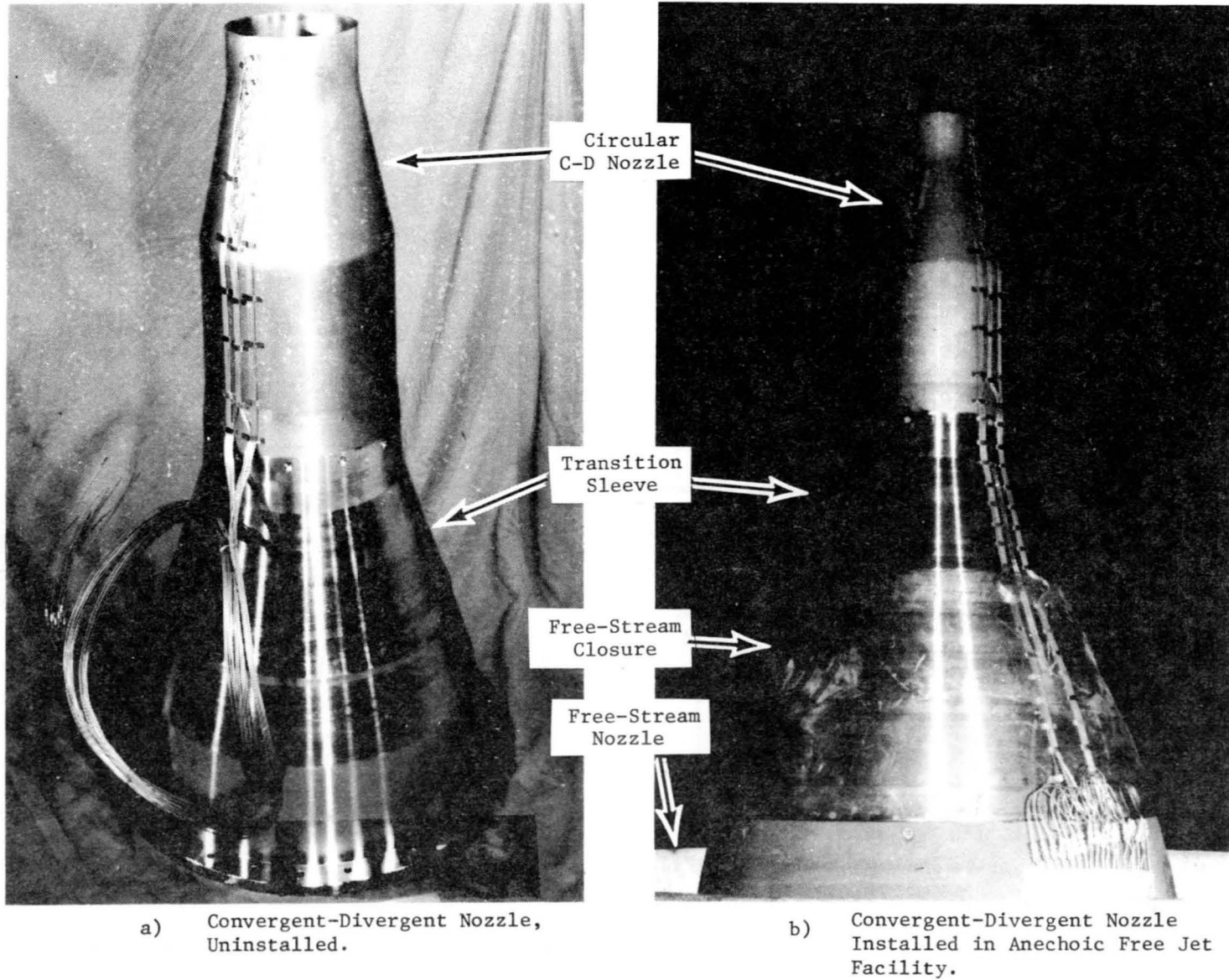


Figure 4-3. Model 2: Convergent-Divergent Circular Nozzle, Uninstalled and Installed.

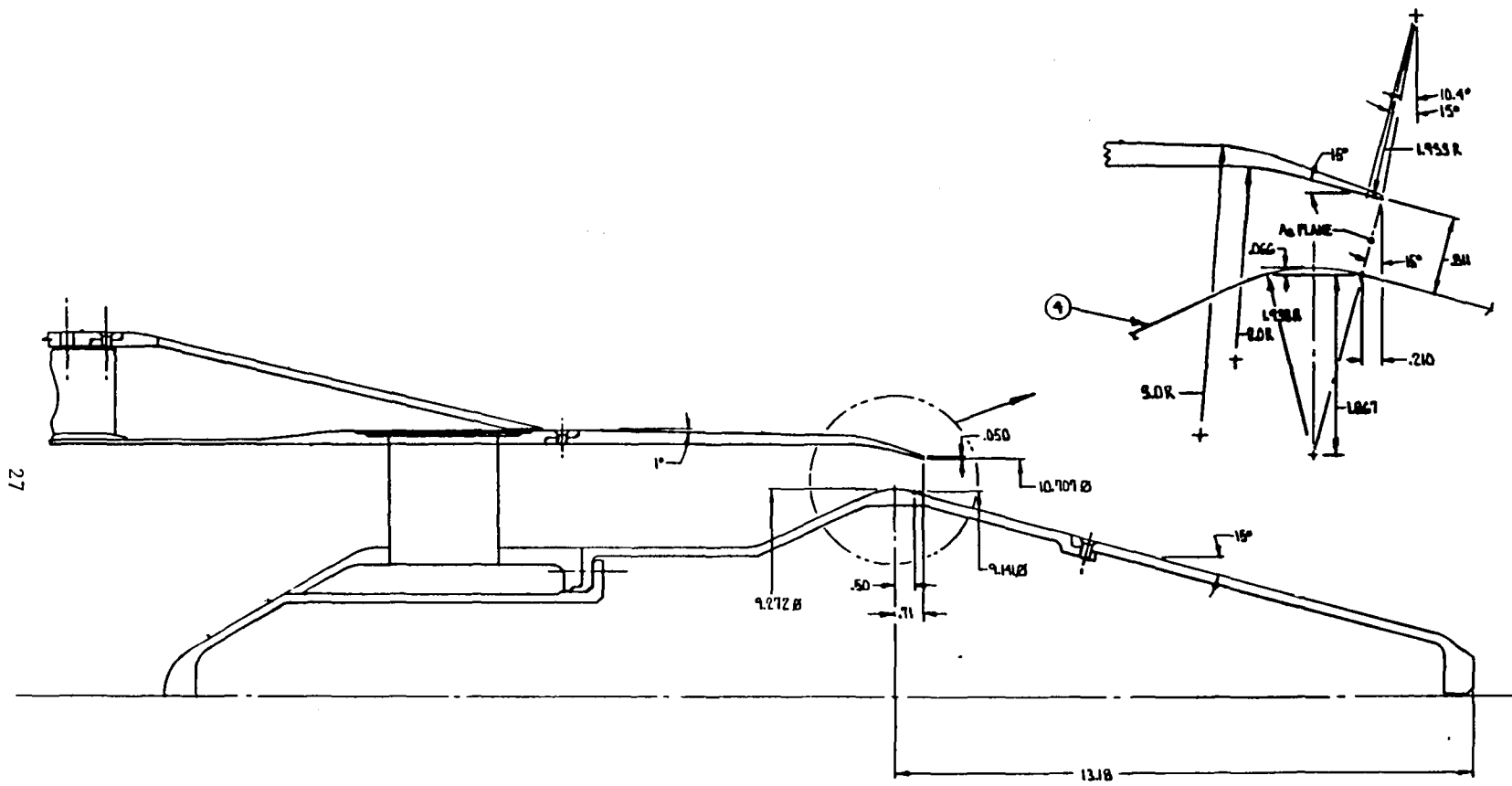


Figure 4-4. Schematic of Model 3: Baseline Contoured Convergent Annular Plug Nozzle.

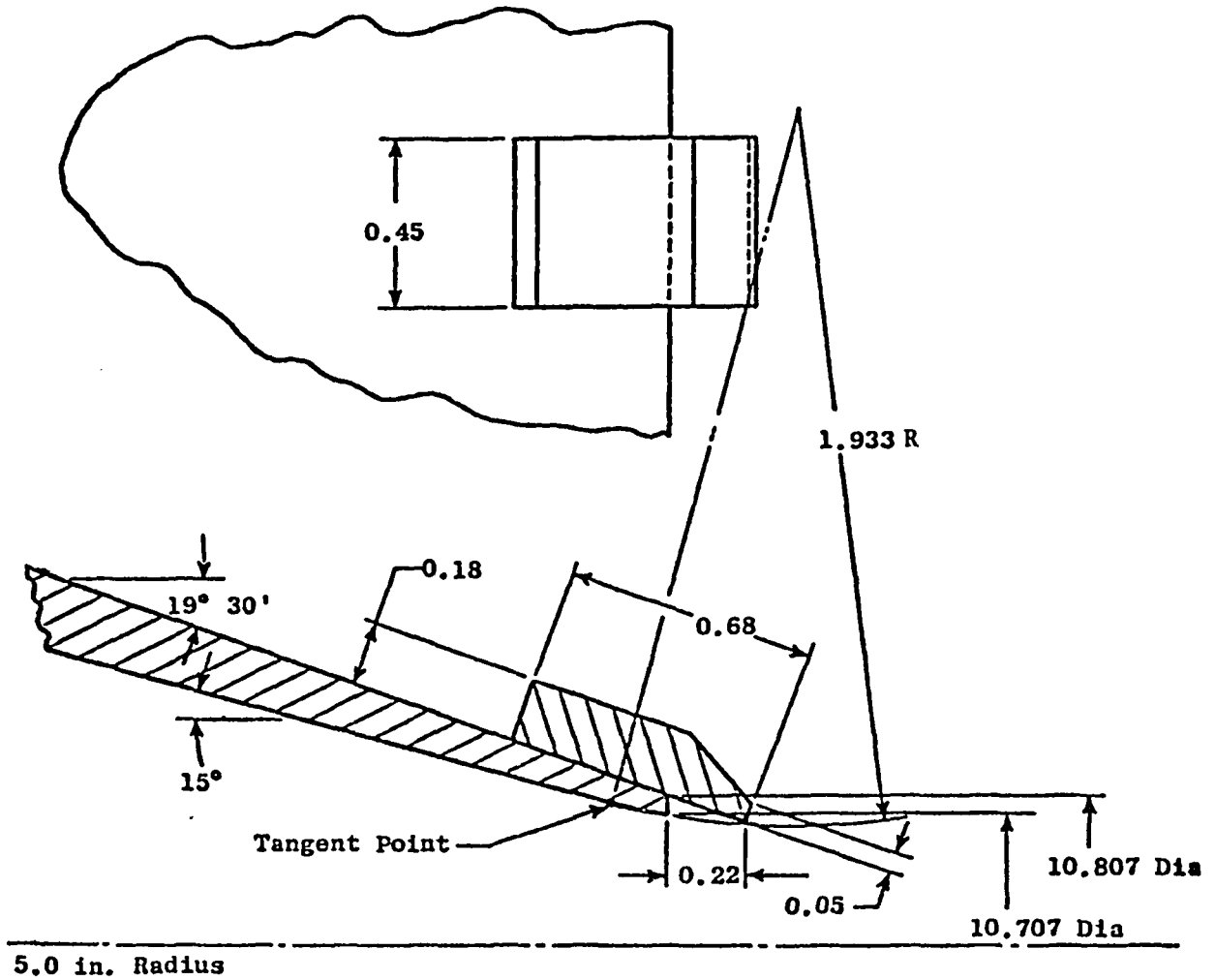


Figure 4-5. Schematic of Screech Tab Application to Model 3, Contoured Convergent Annular Plug Nozzle.

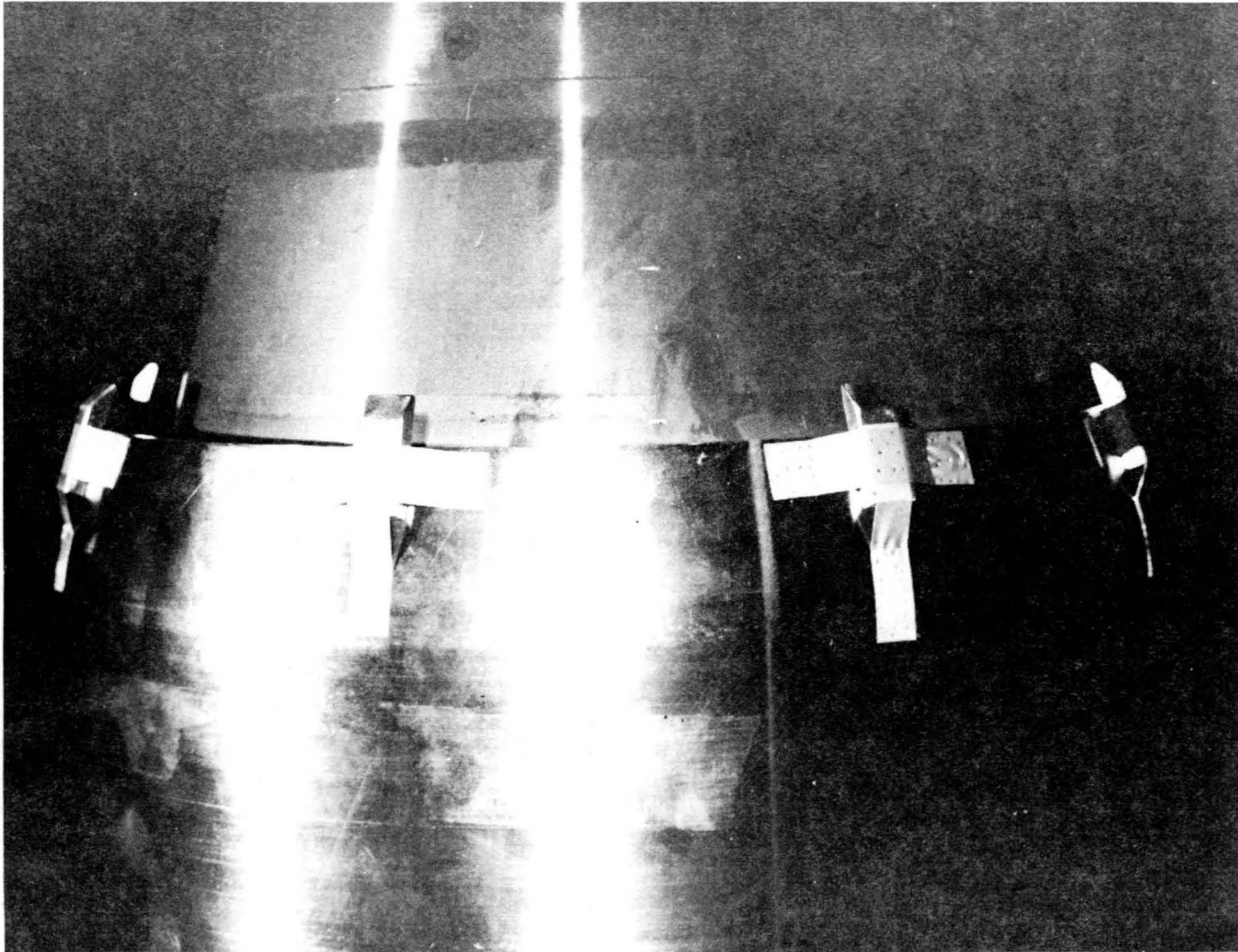


Figure 4-6. Photo of Screech Tab Application to Model 3, Contoured Convergent Annular Plug Nozzle.

30

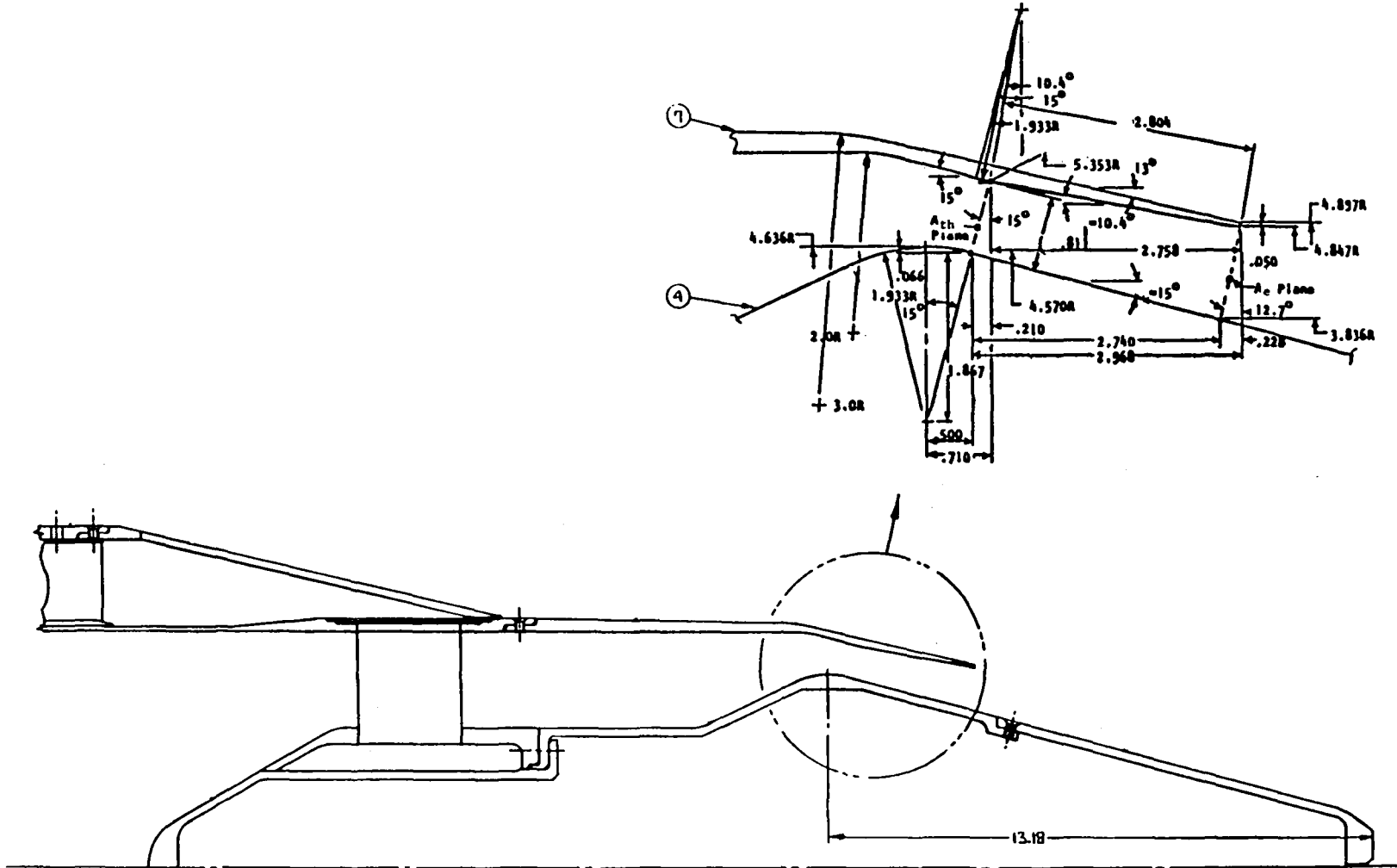


Figure 4-7. Schematic of Model 4: Convergent-Divergent Annular Plug Nozzle.

The internal flowpath of Model 4 is identical to that of Model 3 up to the throat plane. The throat plane for the C-D nozzle is at the tangency point of 15° plug angle to the crown radius. The supersonic flow is expanded to the appropriate area ratio (i.e., exit plane area/throat plane area) of 1.119 as calculated by one-dimensional isentropic formula for the design Mach number of 1.4.

4.1.6 20 CHUTE ANNULAR PLUG SUPPRESSOR, CONVERGENT FLOW ELEMENT
 TERMINATIONS: MODEL 5

The annular plug suppressor system with convergent flow element terminations, Figures 4-8 and 4-9, utilizes the 20-chute mechanical suppressor of Reference 4-4. Within that program it was tested as a dual-flow system with an annular convergent inner flowpath. This nozzle is a scaled model of the YJ101 Test-Bed Engine suppressor configuration under Contract NAS3-20582.

Specifics of the nozzle system are:

- Number of Suppressor Elements	20
- Elemental Planform Shape	Radial
- Suppressor Area Ratio	1.75
- Suppressor Radius Ratio	0.764
- Angle Subtended by Each Chute, degrees	7.714
- Angle Subtended by Each Flow Element, degrees	10.286
- Chute Depth-to-Width Ratio	1.0
- Chute Entrance Design Mach Number	0.7
- Throat Plane Area, in. ² (Design)	20.358
- Equivalent Throat Diameter, in.	5.09
- System Area Ratio	89

4.1.7 20 CHUTE ANNULAR PLUG SUPPRESSOR, CONVERGENT-DIVERGENT FLOW ELEMENT
 TERMINATIONS: MODEL 6

The annular plug 20-chute suppressor system with convergent-divergent flow element terminations is schematically shown in Figure 4-10 with photo

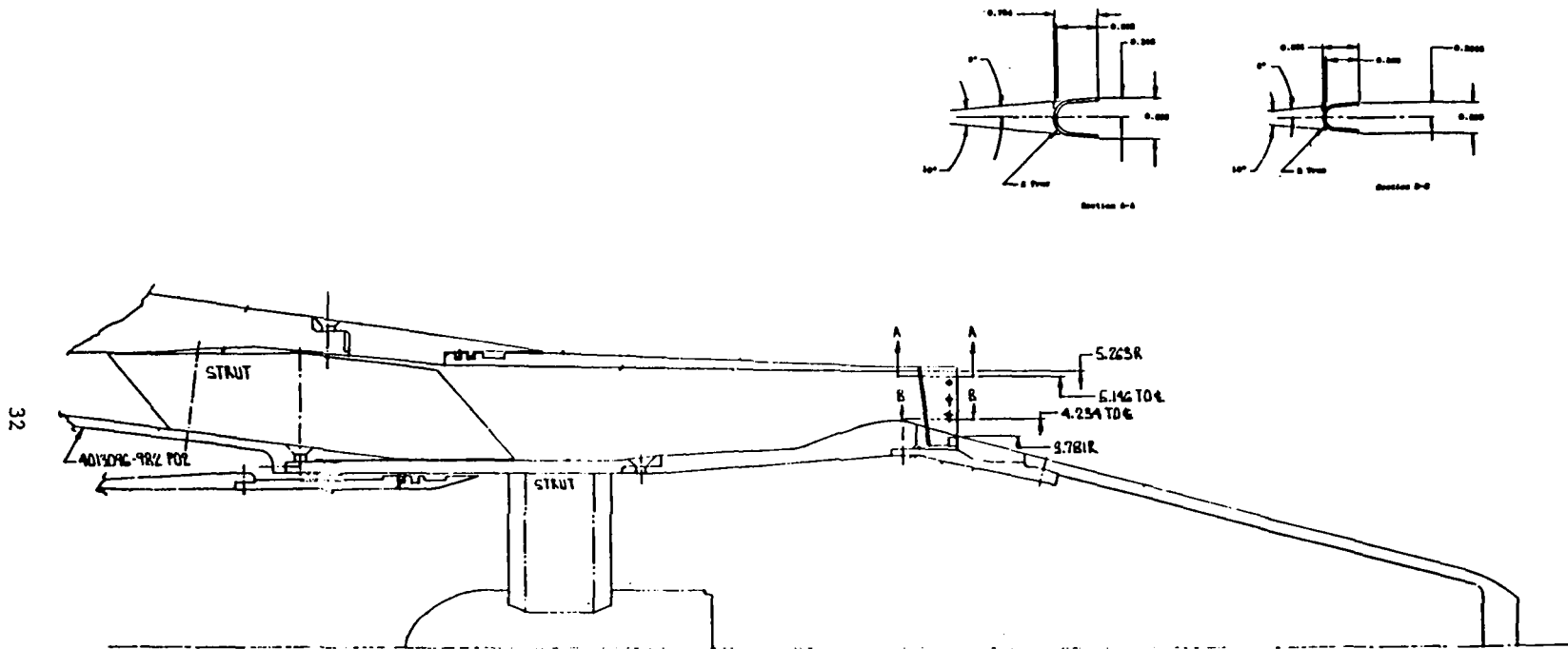


Figure 4-8. Schematic of Model 5: 20 Chute Annular Plug Suppressor, Convergent Flow Element Terminations.

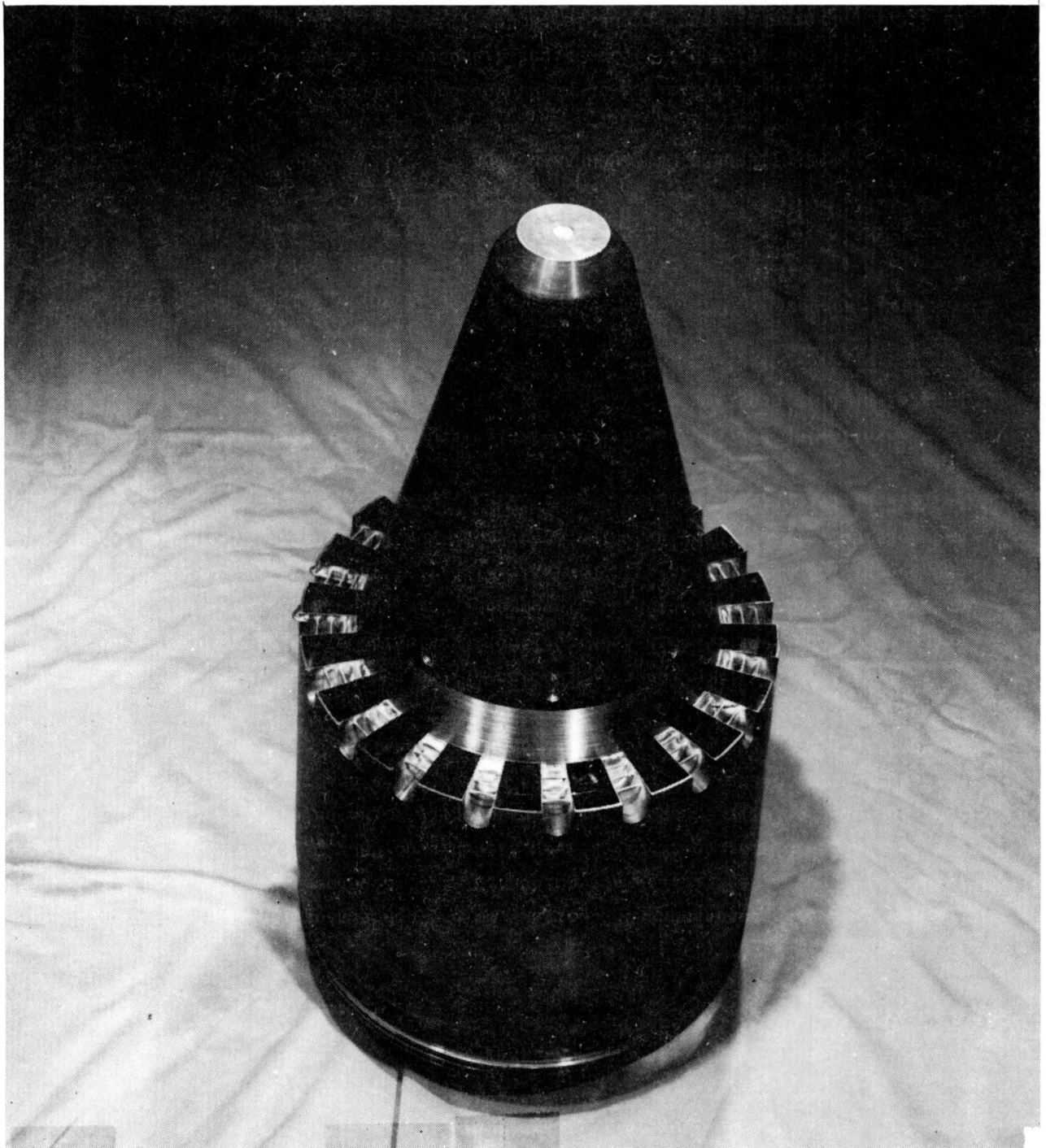


Figure 4-9. Photo of Model 5: 20 Chute Annular Plug Suppressor, Convergent Flow Element Terminations.

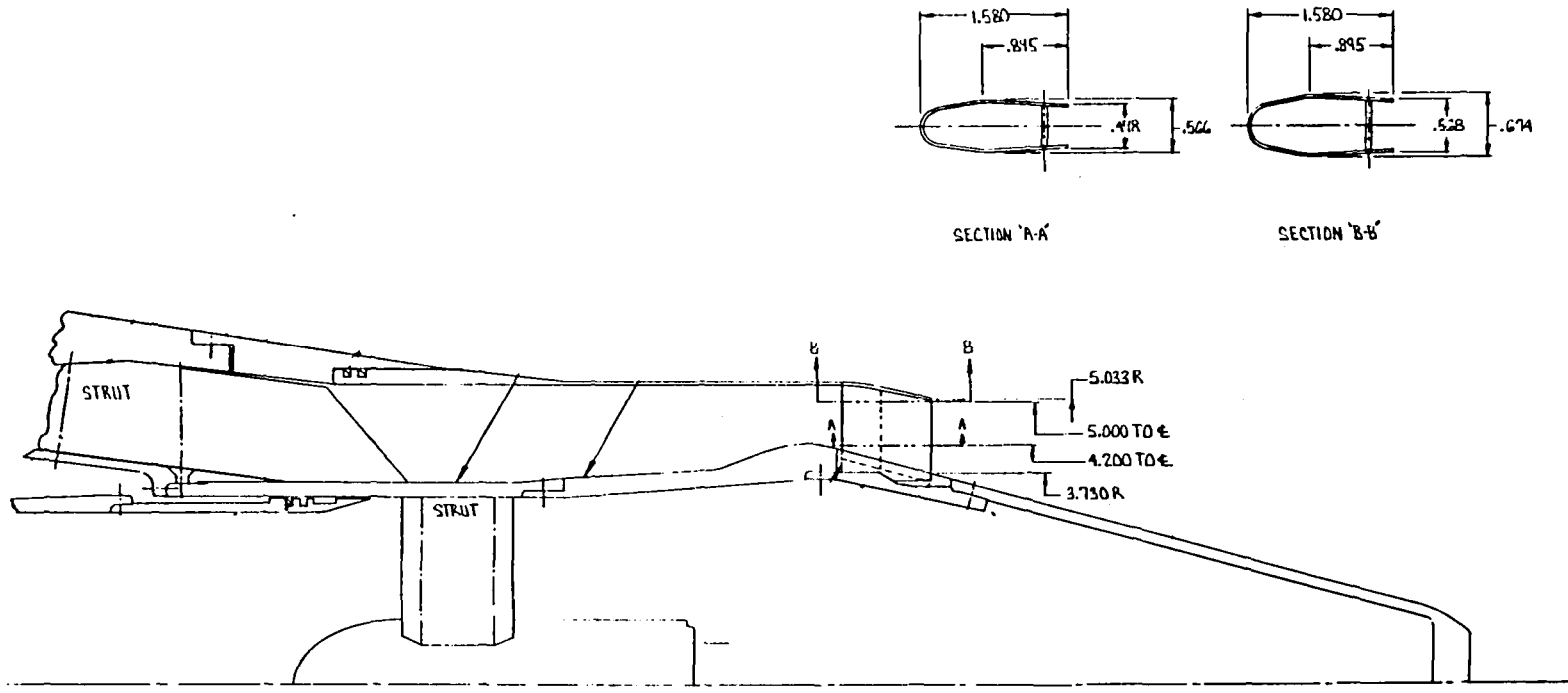


Figure 4-10. Schematic of Model 6: 20 Chute Annular Plug Suppressor, Convergent-Divergent Flow Element Terminations.

presented in Figure 4-11. Design methodology for the C-D elemental flowpaths is documented in the Comprehensive Design Report (Reference 2-1). Specific design values are summarized as follows:

-	Mach No.	1.425
-	P_T/P_{amb}	3.238
-	$T_T, ^\circ R$	1730
-	$T_s, ^\circ R$	1271
-	γ	1.354
-	$V_j, \text{ft/sec}$	2448
-	Number of Suppressor Elements	20
-	Elemental Planform Shape	Radial
-	A_e/A_{th}	1.133

	<u>At Throat</u>	<u>At Exit Plane</u>
● Suppressor Area Ratio	1.752	1.56
● Suppressor Radius Ratio	.764	.743
● Angle Subtended by Each Chute, degrees	7.72	6.44
● Angle Subtended by Each Flow Element, degrees	10.28	11.56
● Flow Area, in. ²	20.227	22.924
● Equivalent Flow Dia, in.	5.075	5.403
● Chute Blockage Area, in. ²	15.20	12.77

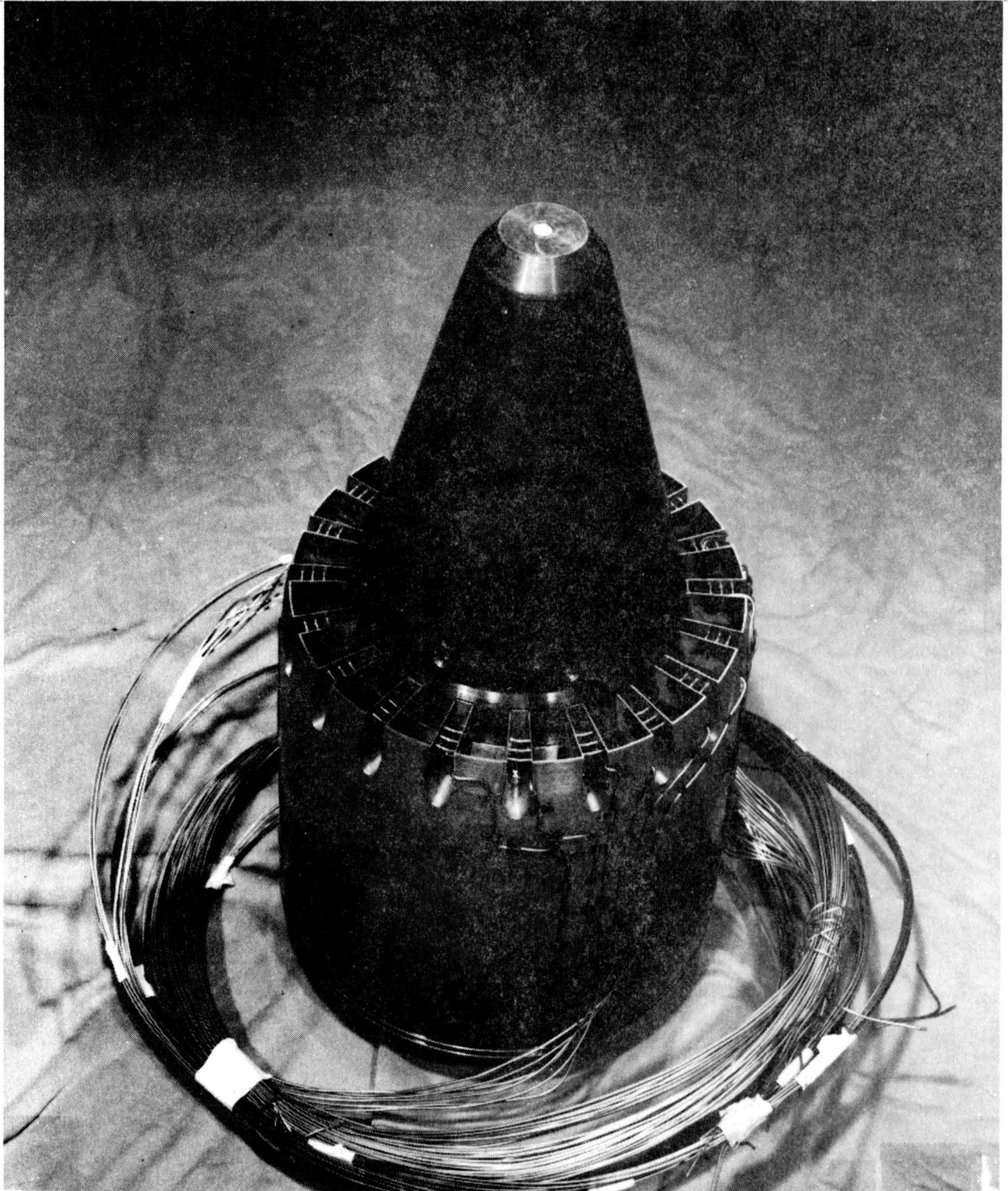


Figure 4-11. Photo of Model 6: 20 Chute Annular Plug Suppressor, Convergent-Divergent Flow Element Terminations, Uninstalled.

4.2 SCOPE OF TESTING

The test points for both acoustic and diagnostic tests were selected to meet the required objectives of the contract effort, i.e., to identify the usefulness of C-D passages and also to determine the effect of off-design nozzle pressure ratio under static and simulated flight conditions.

4.2.1 ACOUSTIC TESTS

The total number of static and flight acoustic tests performed with the seven selected nozzle configurations was 140. Details of the test conditions are given in Appendix I. Detailed acoustic test results are presented in the Comprehensive Data Report (Reference 2-1).

4.2.2 DIAGNOSTIC TESTS

The aerodynamic flow conditions of the LV tests and shadowgraph tests are presented in Appendices II and III respectively.

5.0 ACOUSTIC TEST RESULTS

The analysis of the acoustic test data of the model nozzle configurations described in Section 4.0 are presented in this section.

This section consists of four subsections: Subsection 5.1 contains a discussion of the acoustic effectiveness of the convergent-divergent terminations in the shock-associated jet noise reduction. Discussions on the range of the C-D sensitivity are included also. Subsection 5.2 contains a discussion of the influence of flight, jet plume temperature and the various nozzle configurations on the shock associated noise. Discussions on shock screech are presented in Subsection 5.3. Finally, spectral comparisons of acoustic data with predictions from existing analytical models are made in Subsection 5.4. Unless otherwise stated, the acoustic data presented herein are scaled to a typical supersonic cruise engine size of 1400 in.² at a 2400 foot sideline distance, using the conventional diametric scaling method.

5.1 ASSESSMENT OF NOISE REDUCTION BY CONVERGENT-DIVERGENT TERMINATION

It has been well known for some time that shock noise is a significant entity in supersonic exhaust noise and its suppression is essential to achieve subsonic commercial noise rule levels for advanced supersonic cruise aircraft for commercial aviation. The role of shocks in supersonic exhaust noise generation for imperfectly expanded jet plumes has been extensively studied, both theoretically and experimentally by several investigators (References 5-1 through 5-5). Yet, details of the relationship of shock noise to the dynamics of the turbulence-shock interactions remain unknown.

From the viewpoint of shock noise suppression, a convergent-divergent (C-D) nozzle has been a matter of increasing interest to the jet engine manufacturers. Tanna (Reference 5-6) and Norum and Seiner (Reference 5-7) have reported the effectiveness of using a C-D termination to reduce or eliminate broadband shock-cell noise for circular cold jets. Under a recent GE/NASA program (Reference 2-5), the C-D effectiveness has been demonstrated with annular and coannular plug nozzles. In one case, a simple isentropic expansion area ratio design was used, while in another attempt, a more controlled contour design was evolved. In the former case, effective shock

reduction for the C-D design was not realized; while in the latter case, the effectiveness of a C-D termination in reducing shock broadband noise was demonstrated under both static and simulated flight conditions. These experimental studies have pointed out that a C-D termination can be an effective means for shock noise control for annular and coannular plug nozzles, but sufficient care in design and manufacture of the nozzle flowpaths must be exercised.

A key objective of the present investigation was to systematically assess the value of a convergent-divergent nozzle as a means for shock noise control under VCE/AST operating conditions at both static and simulated flight conditions.

In this subsection, the following plots are presented for both static and simulated flight cases:

1. PNL_{50°} versus 10 log β
2. PNLN_{130°}* versus 10 log V_j/a_{amb}
3. PNL, OASPL versus θ
4. 1/3-octave SPL versus frequency

The radiation angle θ = 50° was selected as a representative forward quadrant radiation angle, while θ = 130° was chosen to represent a typical aft quadrant radiation angle.

In each figure, a comparison is made between a convergent and a C-D nozzle. Since the broadband shock noise is usually dominant in the forward quadrant, the first comparison will indicate effect of the C-D termination on

$$* \text{ PNLN} = \text{PNL} - 10 \log \left(\frac{F}{F_{\text{ref}}} \right) \left(\frac{\rho_j}{\rho_{\text{amb}}} \right)^{(\omega-1)}$$

the level of the broadband shock noise. On the other hand, jet mixing noise is usually predominant in the aft quadrant, and, therefore the effect of the C-D on the jet mixing noise may be revealed by the $PNLN_{130^\circ}$ variation as a function of the fully expanded jet exit velocity. The third correlation between PNL (or OASPL) and the acoustic angle (θ) is used in order to define the C-D effect on the acoustic radiation directionality.

Finally, how the frequency content of the shock associated noise is affected by the C-D flowpath termination is evaluated by means of one-third-octave SPL spectrum comparisons. Throughout this subsection, the directional and spectral comparisons of a C-D nozzle with its convergent counterpart are made exclusively at the C-D design condition* which corresponds to a typical AST/VCE at takeoff.

Following are the nominal C-D design conditions for the three C-D nozzles of this program.

Model	P_r	$T_T(^{\circ}R)$	M_j
2	3.122	1730	1.40
4	3.122	1730	1.40
6	3.222	1730	1.42

5.1.1 C-D EFFECTIVENESS OF CIRCULAR NOZZLE

Overall characteristics of the supersonic jet noise produced by a circular C-D nozzle (Model 2) are first discussed relative to those of the baseline convergent circular nozzle (Model 1).

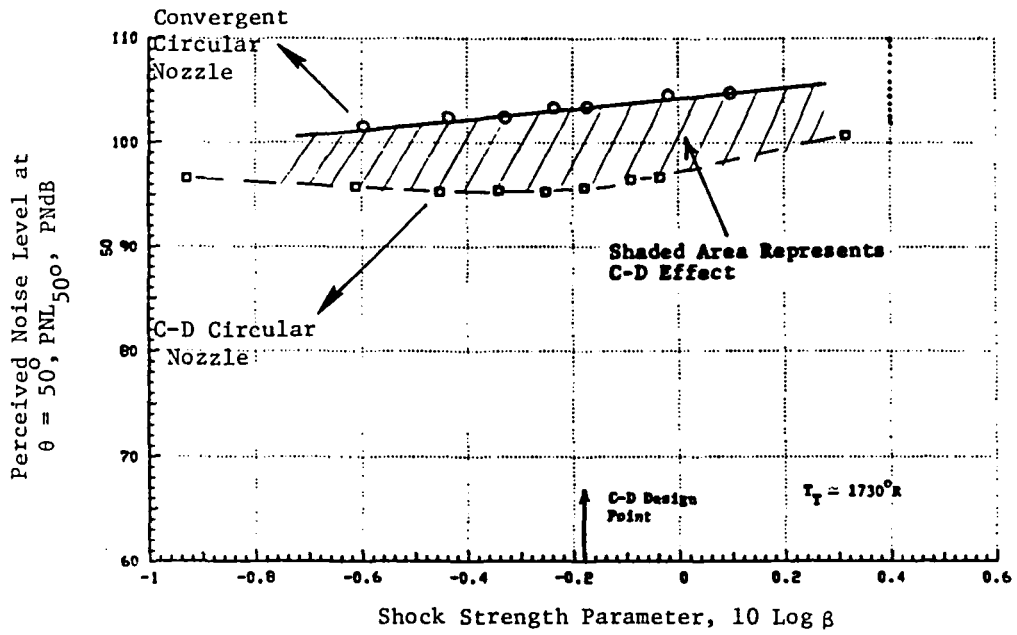
Variation of PNL_{50° with the shock strength parameter $\beta \left(= \sqrt{M_j^2 - 1} \right)$ and variation of $PNLN_{130^\circ}$ with the fully-expanded jet exit velocity (V_j) for circular nozzles, with jet temperature maintained approximately at

*The test point whose last two digits are 13 corresponds to the C-D design point at static condition, while the test point whose last two digits are 14 corresponds to the C-D design point at simulated flight conditions. Examples: Test Point 213 (C-D design point of Model 2 static) and Test Point 414 (C-D design point of Model 4, flight).

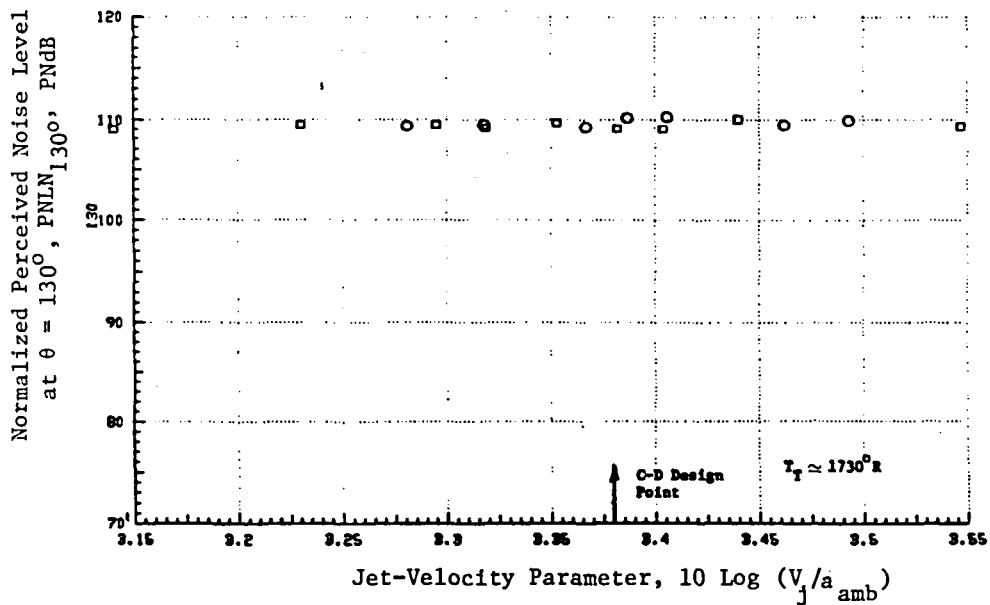
$T_T=1730^\circ R$, are illustrated comparatively in Figure 5-1. Corresponding nozzle pressure ratios cover the typical VCE/AST takeoff conditions. In Figure 5-1(a), we note that PNL_{50° increases with increasing pressure ratio like β^4 for the baseline convergent circular nozzle, while in the case of the C-D circular nozzle, PNL_{50° shows an almost constant value of 95.5 dB near the C-D design point, indicating the C-D effectiveness over a rather broad range of pressure ratios with as much as 7.5 dB reduction in terms of PNL. Since the shock-cell noise is, relatively speaking, dominant over the jet mixing noise in the forward quadrant, this observed reduction in PNL_{50° must be attributed to the significant suppression of the shocks by the C-D termination. As will be discussed in later sections, this viewpoint is evidenced clearly by the diagnostic LV measurement results. Shown in Figure 5-1(b) is the variation of normalized PNL_{130° as a function of the jet exit velocity. No significant difference is observed in the normalized perceived noise level between the two nozzles, indicating that the C-D termination had no effect on the jet mixing noise generation mechanism. Figure 5-2 is presented to illustrate $OASPL_{50^\circ}$ variation with β for the circular convergent and circular C-D nozzles, where the β^4 line is given as a reference.

PNL and PNLN comparisons of the C-D circular nozzle with the baseline convergent circular nozzle for a simulated flight environment, $V_{a/c} = 400$ fps, are presented in Figure 5-3. A front-quadrant reduction in PNL due to the C-D termination to the extent of 11 dB is noted in this figure. Again, no appreciable difference is noted in jet mixing noise level between the convergent and C-D nozzles at simulated flight conditions, as can be seen in Figure 5-3(b).

Next, PNL and OASPL directivities at C-D design condition are presented in Figure 5-4. In this figure, test points 213 and 214 correspond to the C-D design point of the C-D circular nozzle (Model 2), and the acoustic data at the C-D design point are compared with those of the convergent circular nozzle (test points 113 and 114). A relative dominance of shock associated noise over jet mixing noise in the forward quadrant for the convergent nozzle can be observed in Figure 5-4. Larger magnitude of PNL values in the forward quadrant as compared with that for OASPL is also noted, which is indicative of a high frequency content shock noise.



(a) Perceived Noise Level at $\theta = 50^\circ$



(b) Normalized Perceived Noise Level at $\theta = 130^\circ$

Figure 5-1. Comparison of C-D Circular Nozzle Levels with Those of Baseline Convergent Circular Nozzle. (Static)

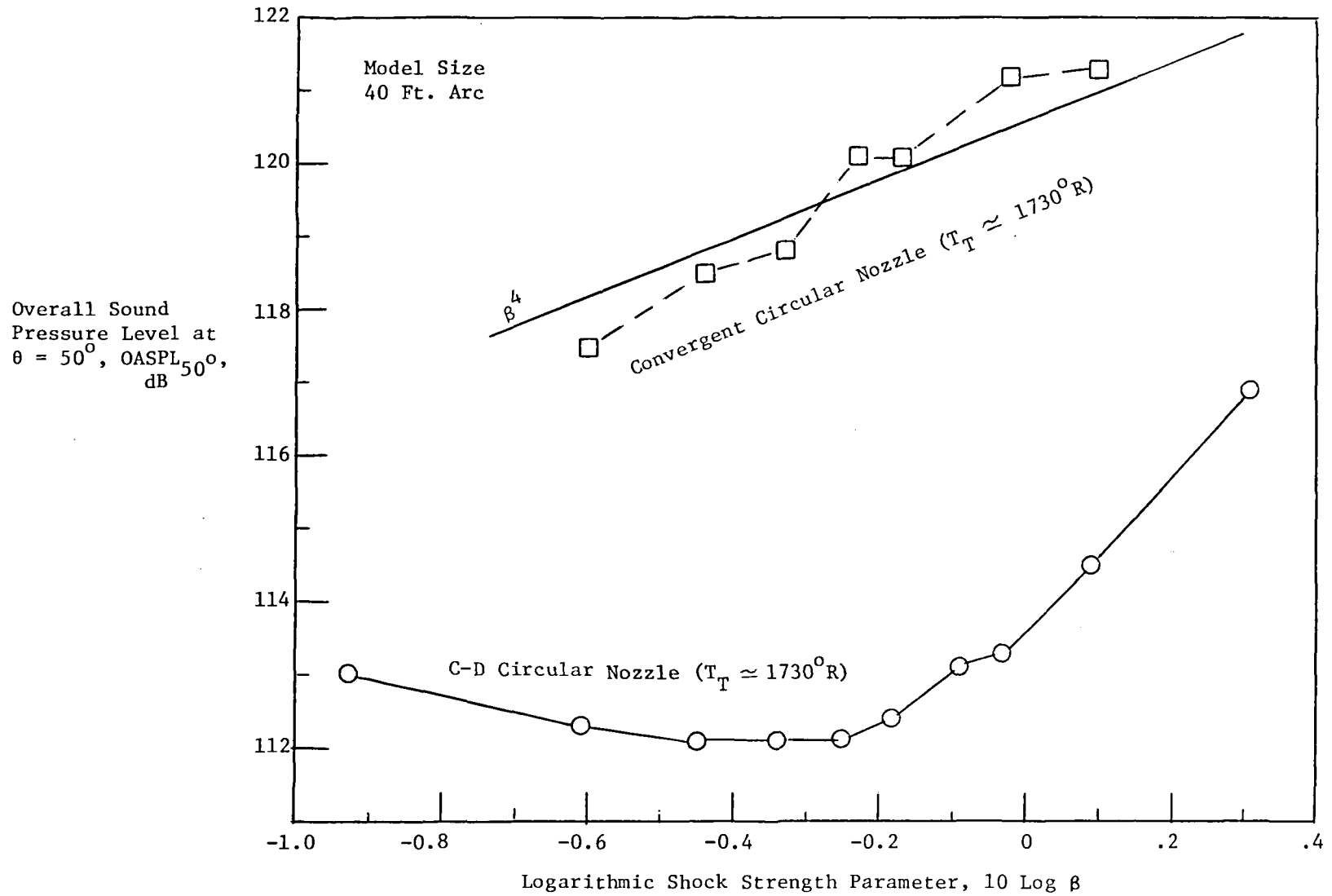
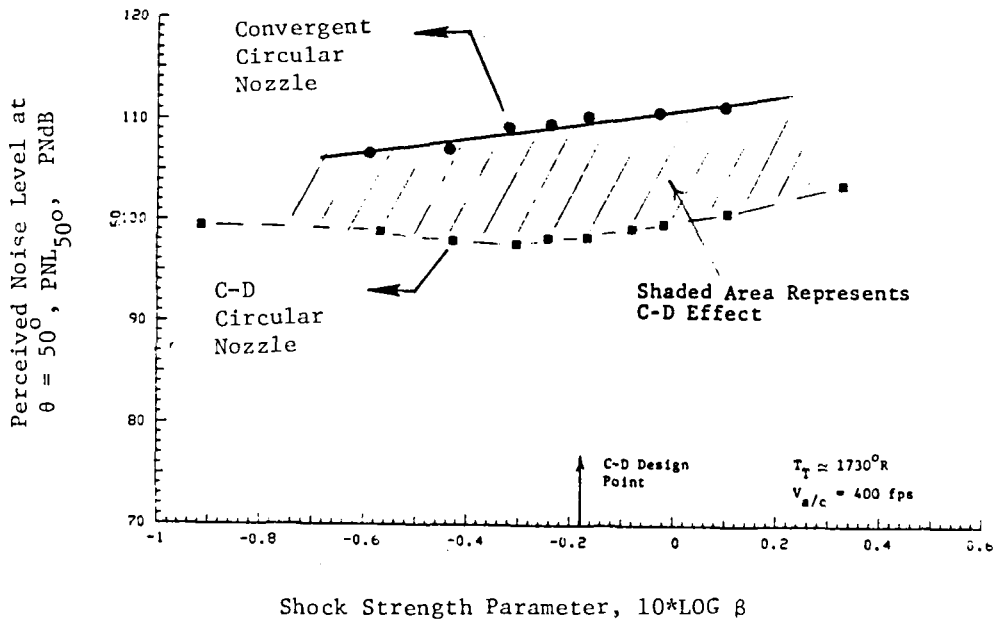
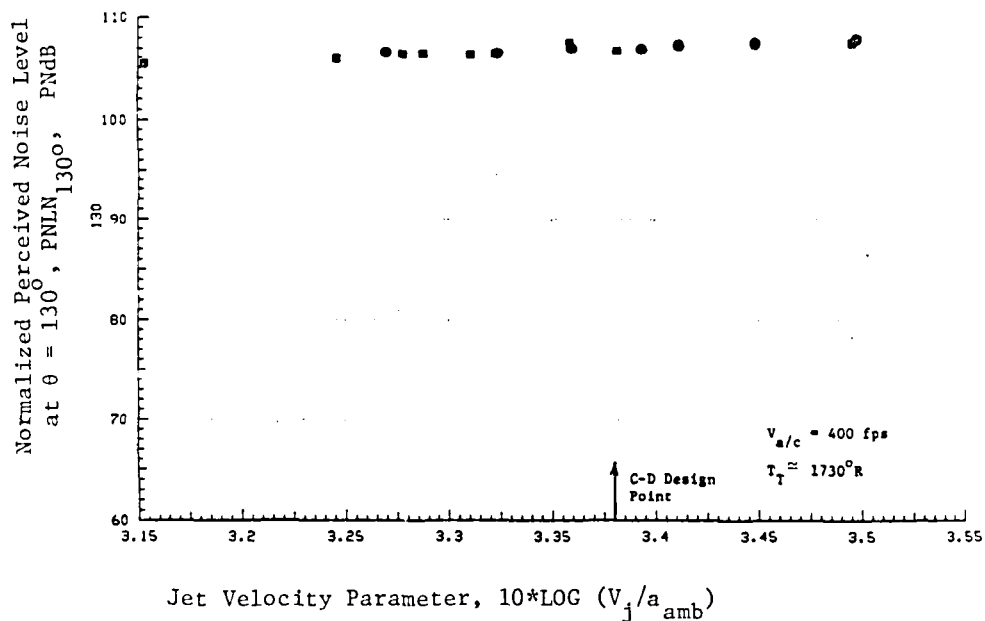


Figure 5-2. OASPL $_{50^\circ}$ as a Function of Shock Strength Parameter for Circular Convergent and Circular Convergent-Divergent Nozzles - Static Data.



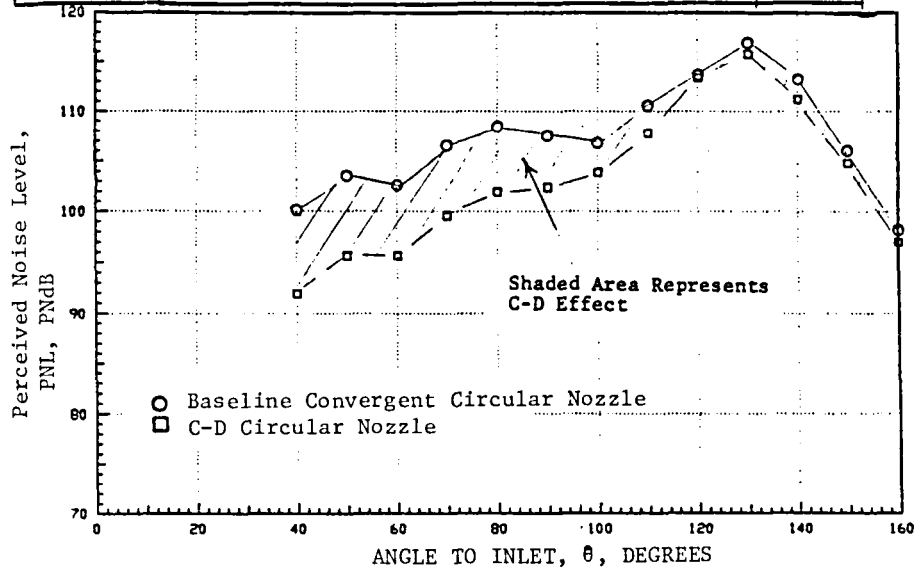
(a) Perceived Noise Level at $\theta = 50^\circ$



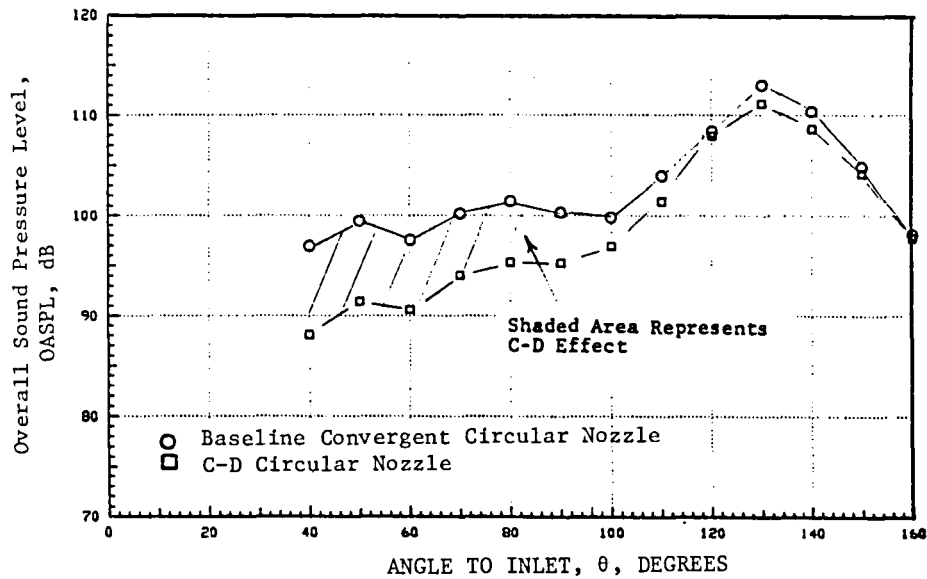
(b) Normalized Perceived Noise Level at $\theta = 130^\circ$

Figure 5-3. Comparison of C-D Circular Nozzle Levels with Those of Baseline Convergent Circular Nozzle. (Flight)

Symbol	Model	Test Point	P_r	T_T , (°R)	V_j (f/s)	$V_{a/c}$ (f/s)
○	1	113	3.12	1707	2403	0
□	2	213	3.12	1728	2417	0



(a) Perceived Noise Level



(b) Overall Sound Pressure Level

Figure 5-4. Comparison of Directivity of C-D Circular Nozzle with That of Baseline Convergent Circular Nozzle. (Static)

An OASPL directivity comparison of scale model jets is illustrated in Figure 5-5, where the acoustic data are extrapolated to 40 foot arc distance. Here the sound radiated by the presence of shocks in a jet flow is observed to be fairly omni-directional. This result is in good agreement with the results obtained by cold jets under similar aerodynamic conditions (References 5-3, 5-6 and 5-7). A rather flat directivity pattern as far as $\theta = 100^\circ$ is noted.

Figure 5-6 illustrates similar directivity comparisons of PNL and OASPL between convergent and C-D circular nozzle jets under simulated flight test conditions. A significant C-D benefit in the forward-quadrant is noted. Several important remarks can be made about the acoustic characteristics of discrete and broadband shock containing jets by comparing Figure 5-6 (flight) with Figure 5-4 (static). First the flight speed is noted to have little affect on the forward quadrant PNL or OASPL for the C-D nozzle jets. This indicates that by the C-D termination, shocks are significantly, if not completely, eliminated from the C-D circular nozzle plume at the given test point, while the shock-cell noise of the baseline convergent circular nozzle undergoes a significant amplification by flight.

Spectral characteristics of shock associated noise is discussed next in conjunction with the C-D effectiveness. Spectral comparisons between the C-D circular nozzle and the baseline convergent nozzle are presented in Figure 5-7 (static) and Figure 5-8 (flight). The aerodynamic conditions are identical to those for Figures 5-4 through 5-6. It can be observed in these figures that the shock noise content of the baseline convergent circular nozzle is primarily associated with the mid to high frequency bands. The peak noted in static data of the convergent configuration at a lower frequency was identified to be the screech fundamental (narrowband indicating the presence of the screech is presented later in Figure 5-69). It is noted that with the use of the C-D flowpath termination, a significant reduction of both shock and discrete noise is achieved. As expected, however, the C-D termination does not affect the mixing noise generation, which is demonstrated by the almost identical spectral profiles observed in the aft quadrant.

Figure 5-8 illustrates spectral comparison between a C-D circular nozzle and the baseline convergent circular nozzle at the simulated flight condition. The fundamental screech tone observed in the spectra shown in Figure 5-7 (static) is now noted to be absent (see Figure 5-69, also). As is

Symbol	Model	Test Point	P_r	T_T , ($^{\circ}R$)	V_j , (f/s)	$V_{a/c}$, (f/s)
	1	113	3.12	1707	2403	0
	2	213	3.12	1728	2417	0

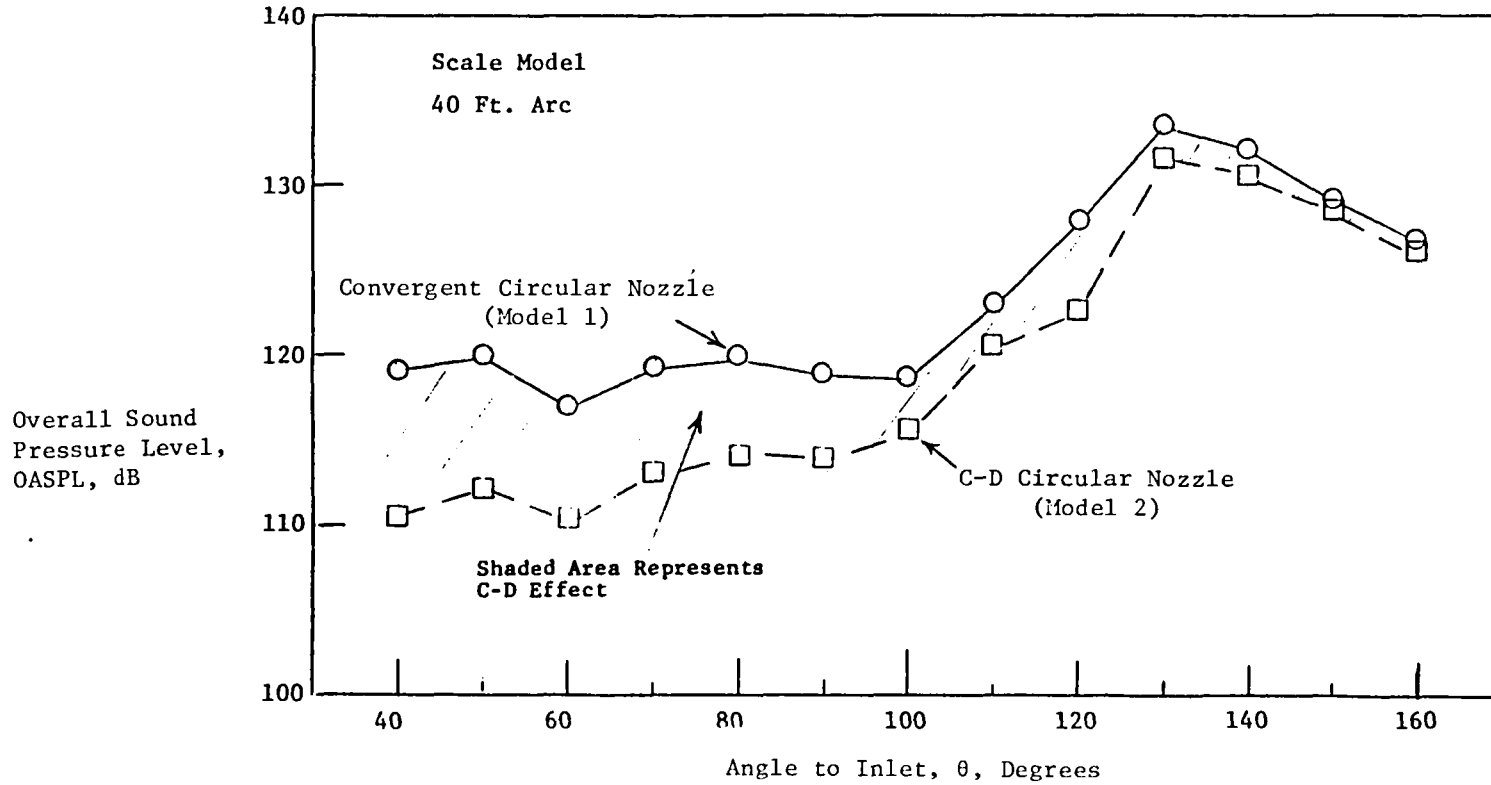


Figure 5-5. OASPL Directivities for Convergent Circular Nozzle and C-D Circular Nozzle, Scale Model Levels on 40 Ft. Arc.

Symbol	Model	Test Point	P_r	T_r , ($^{\circ}R$)	V_j (f/s)	$V_{a/c}$ (f/s)
●	1	114	3.13	1714	2409	400
■	2	214	3.13	1736	2425	400

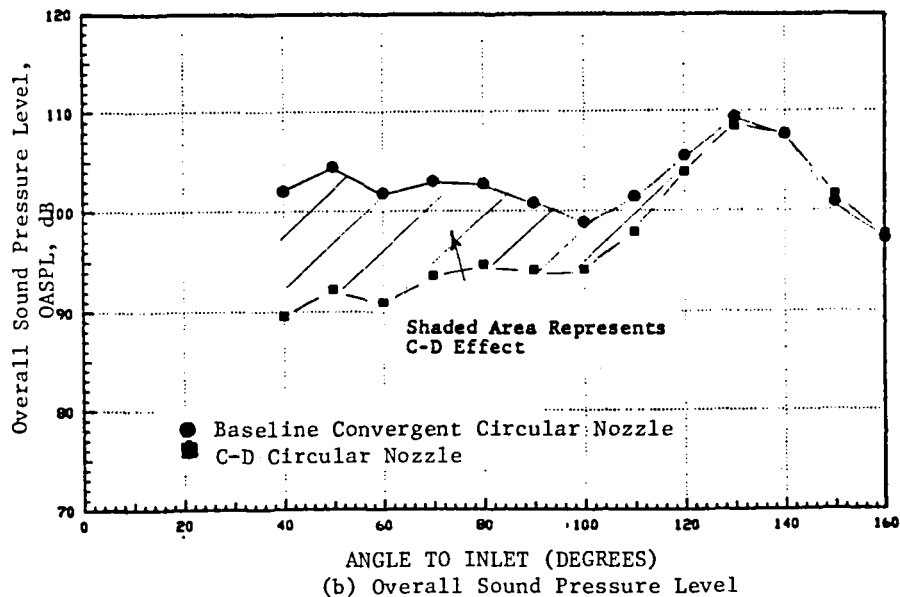
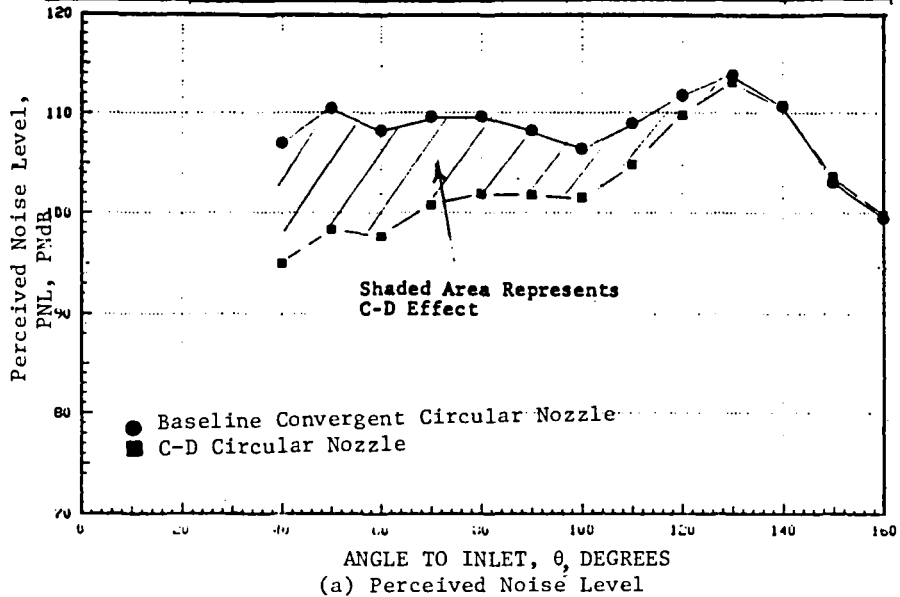


Figure 5-6. Comparison of Directivity of C-D Circular Nozzle With That of Baseline Convergent Circular Nozzle. (Flight)

Symbol	Model	Test Point	P_r	T_T , ($^{\circ}R$)	V_j (f/s)	$V_{a/c}$ (f/s)
○	1	113	3.12	1707	2403	0
□	2	213	3.12	1728	2417	0

○ - Baseline Convergent Circular Nozzle
 □ - C-D Circular Nozzle

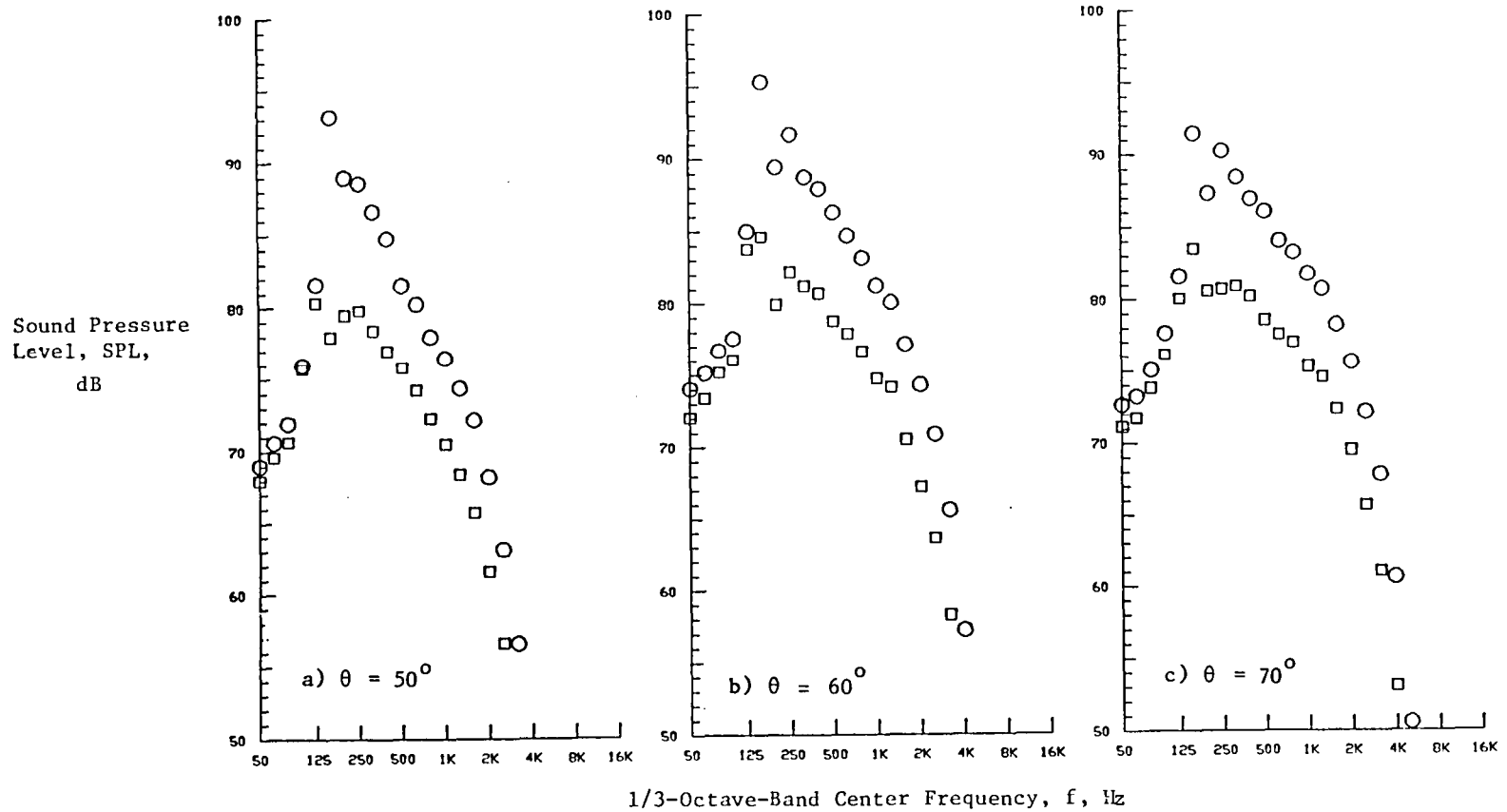


Figure 5-7. Spectral Comparison Between C-D Circular Nozzle and Baseline Convergent Circular Nozzle. (Static)

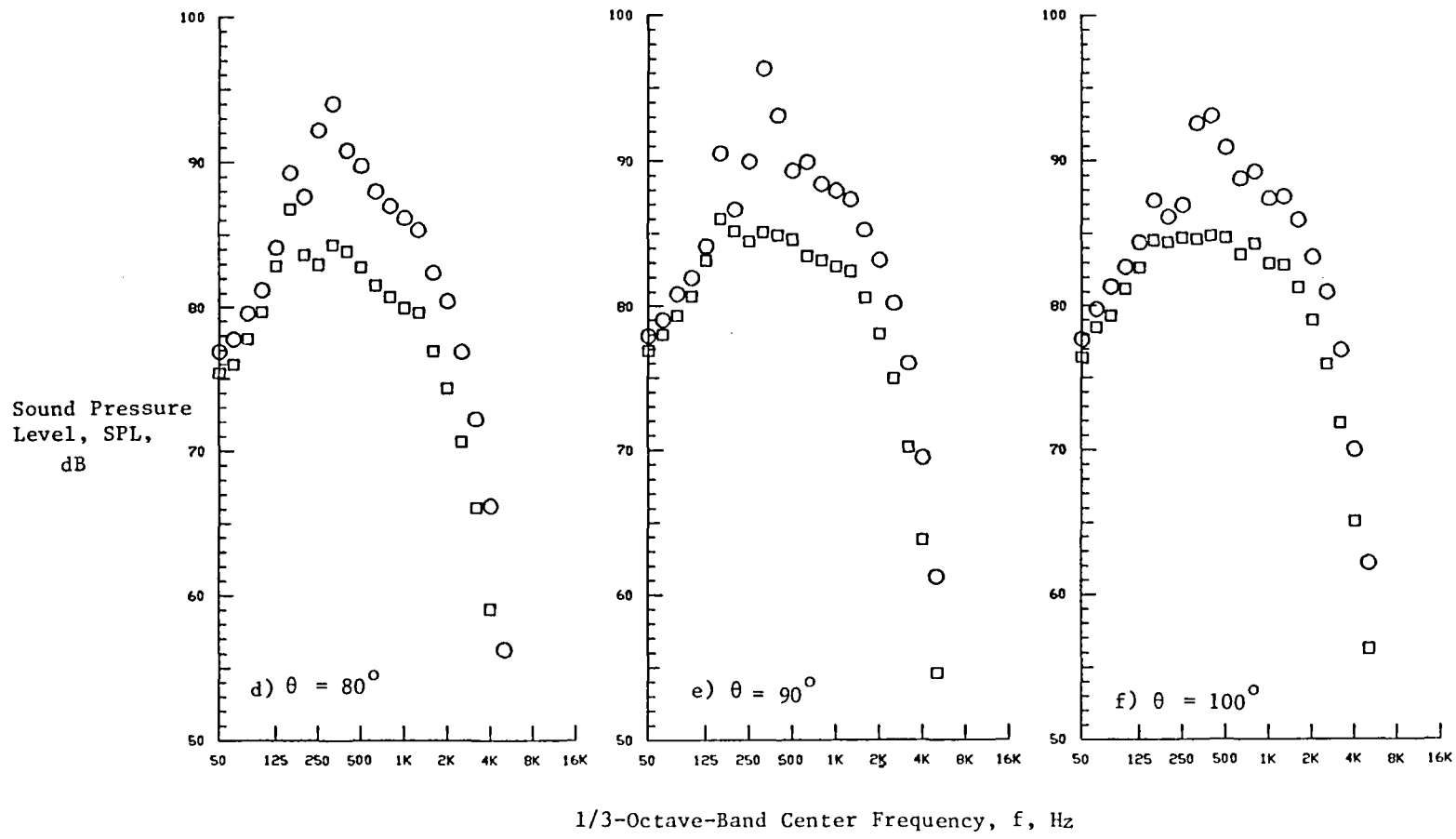


Figure 5-7. (Cont'd). Spectral Comparison Between C-D Circular Nozzle and Baseline Convergent Circular Nozzle. (Static)

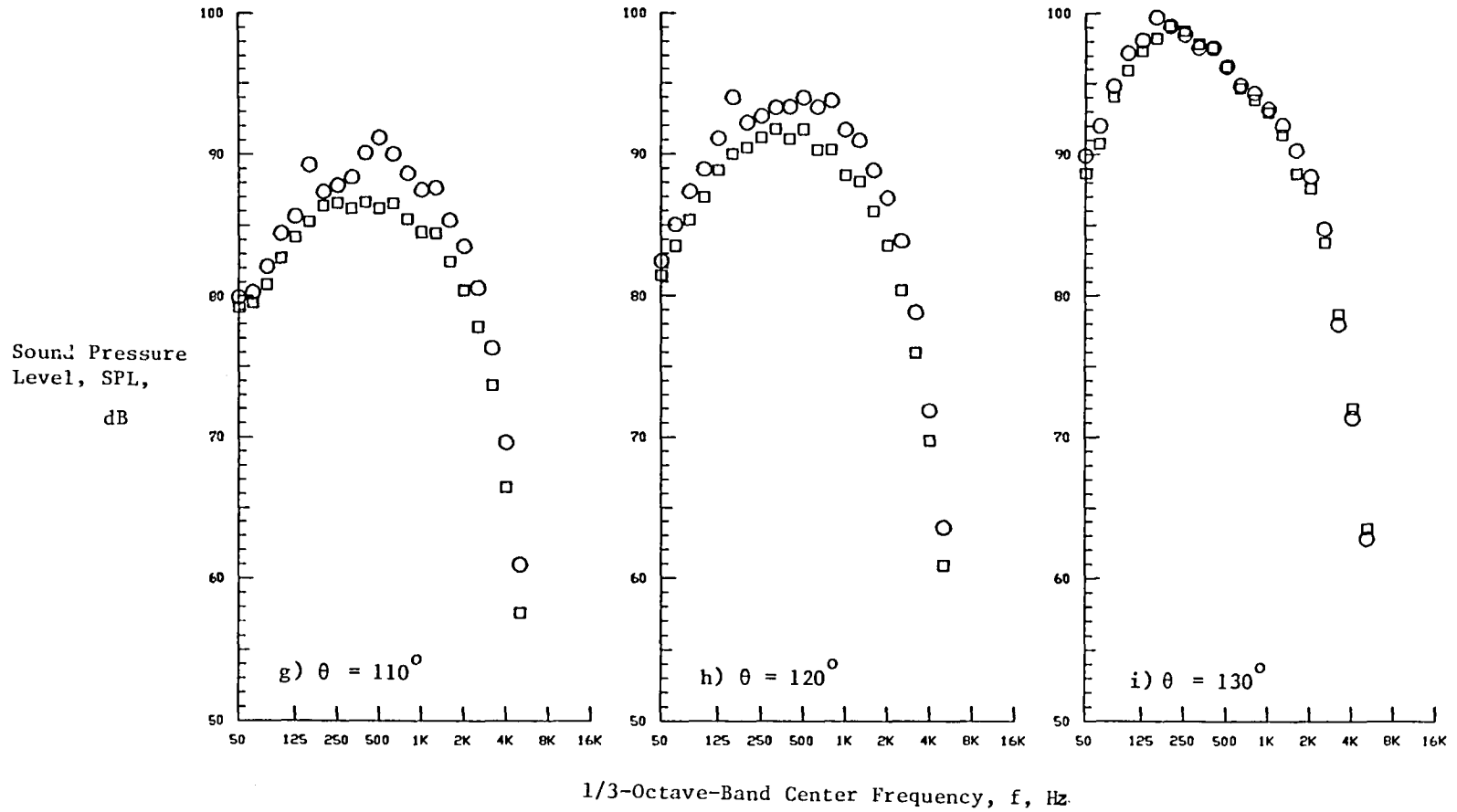


Figure 5-7. (Cont'd). Spectral Comparison Between C-D Circular Nozzle and Baseline Convergent Circular Nozzle. (Static)

Sound Pressure
Level, SPL,
dB

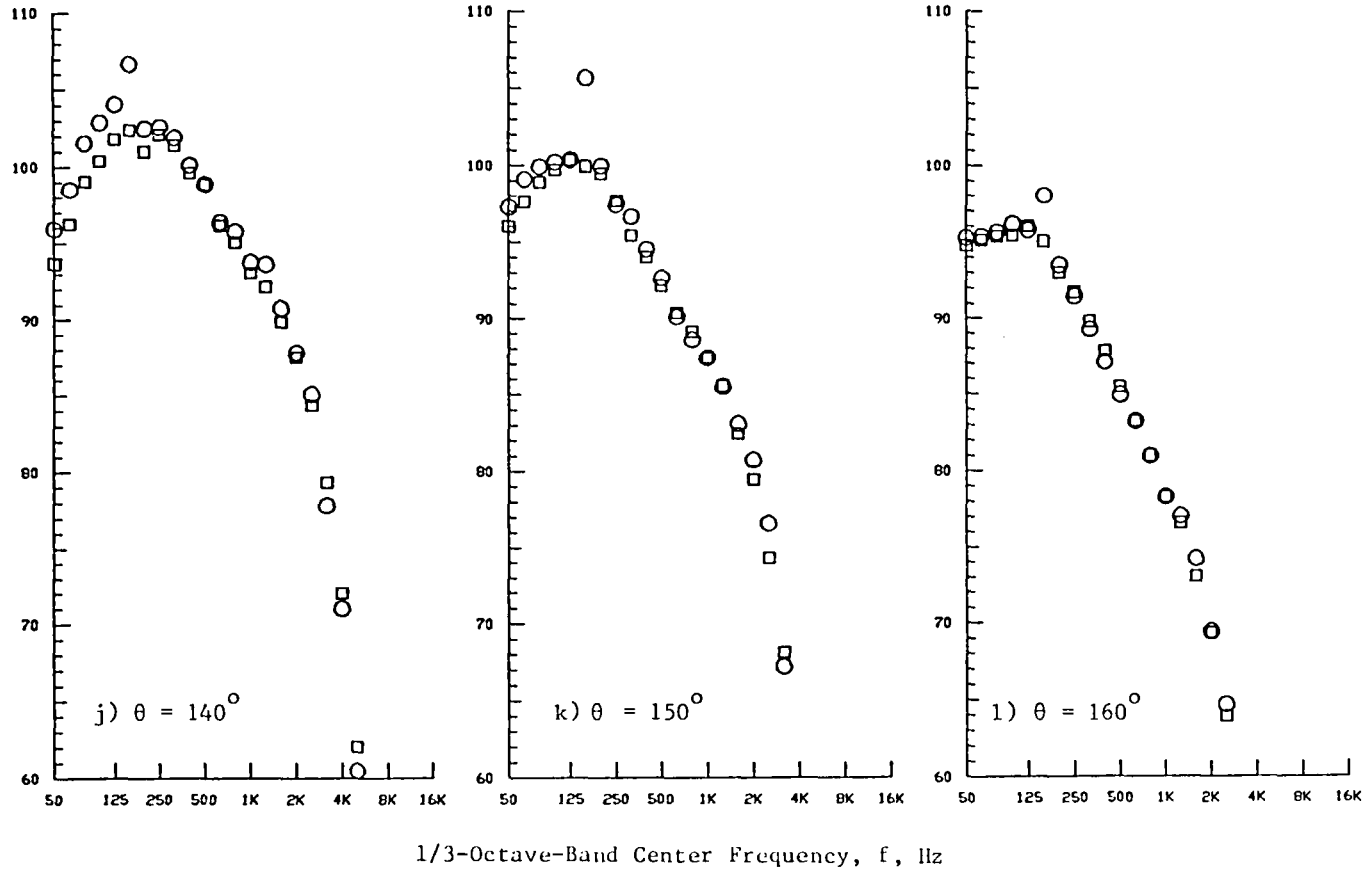


Figure 5-7. (Concluded) Spectral Comparison Between C-D Circular Nozzle and Baseline Convergent Circular Nozzle. (Static)

Symbol	Model	Test Point	P_r	$T_{T'}$ (°R)	V_j (f/s)	$V_{a/c}$ (f/s)
⊙	1	114	3.13	1714	2409	400
⊠	2	214	3.13	1736	2425	400

⊙ - Baseline Convergent Circular Nozzle
 ⊠ - C-D Circular Nozzle

53

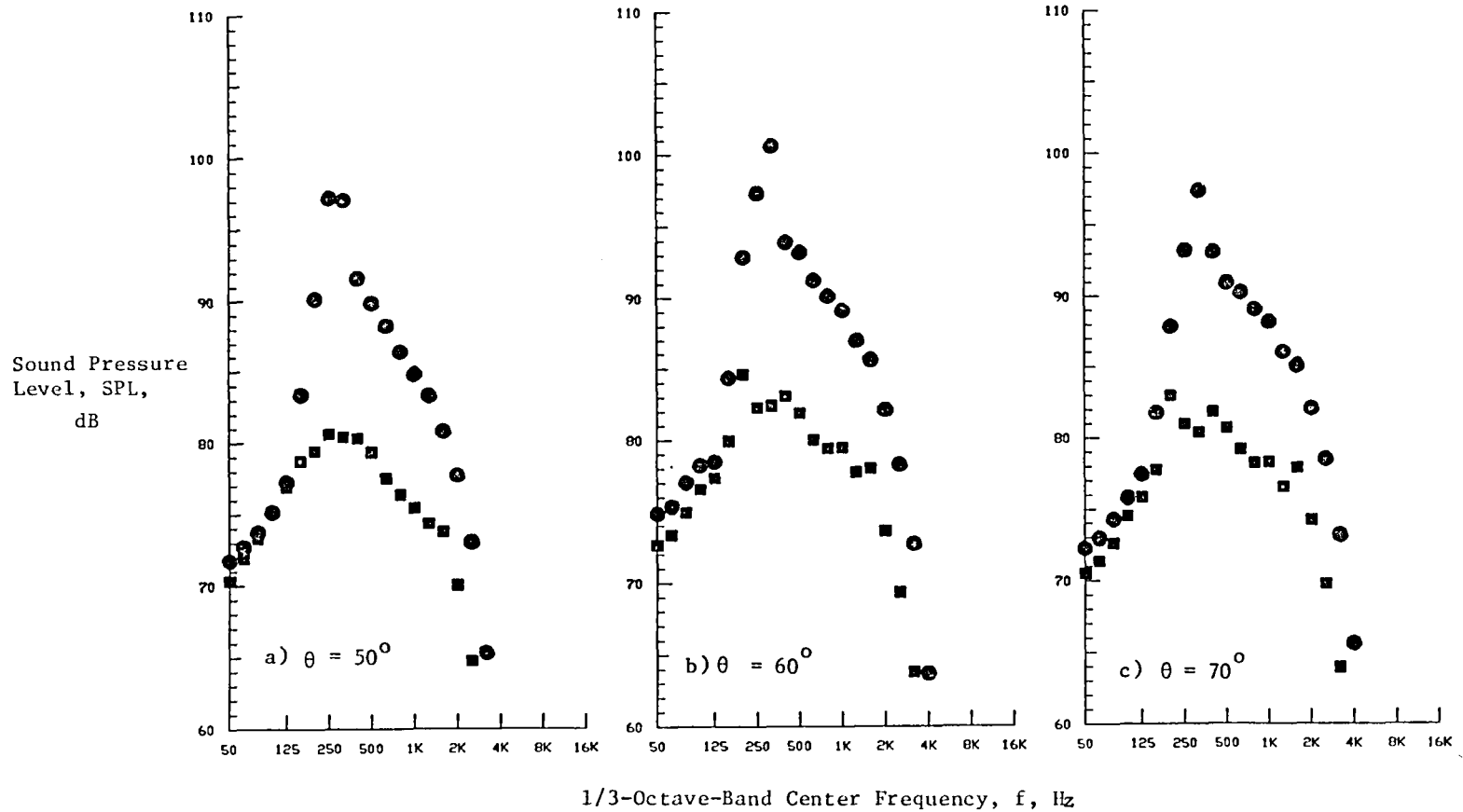


Figure 5-8. Spectral Comparison Between C-D Circular Nozzle and Baseline Convergent Circular Nozzle. (Flight)

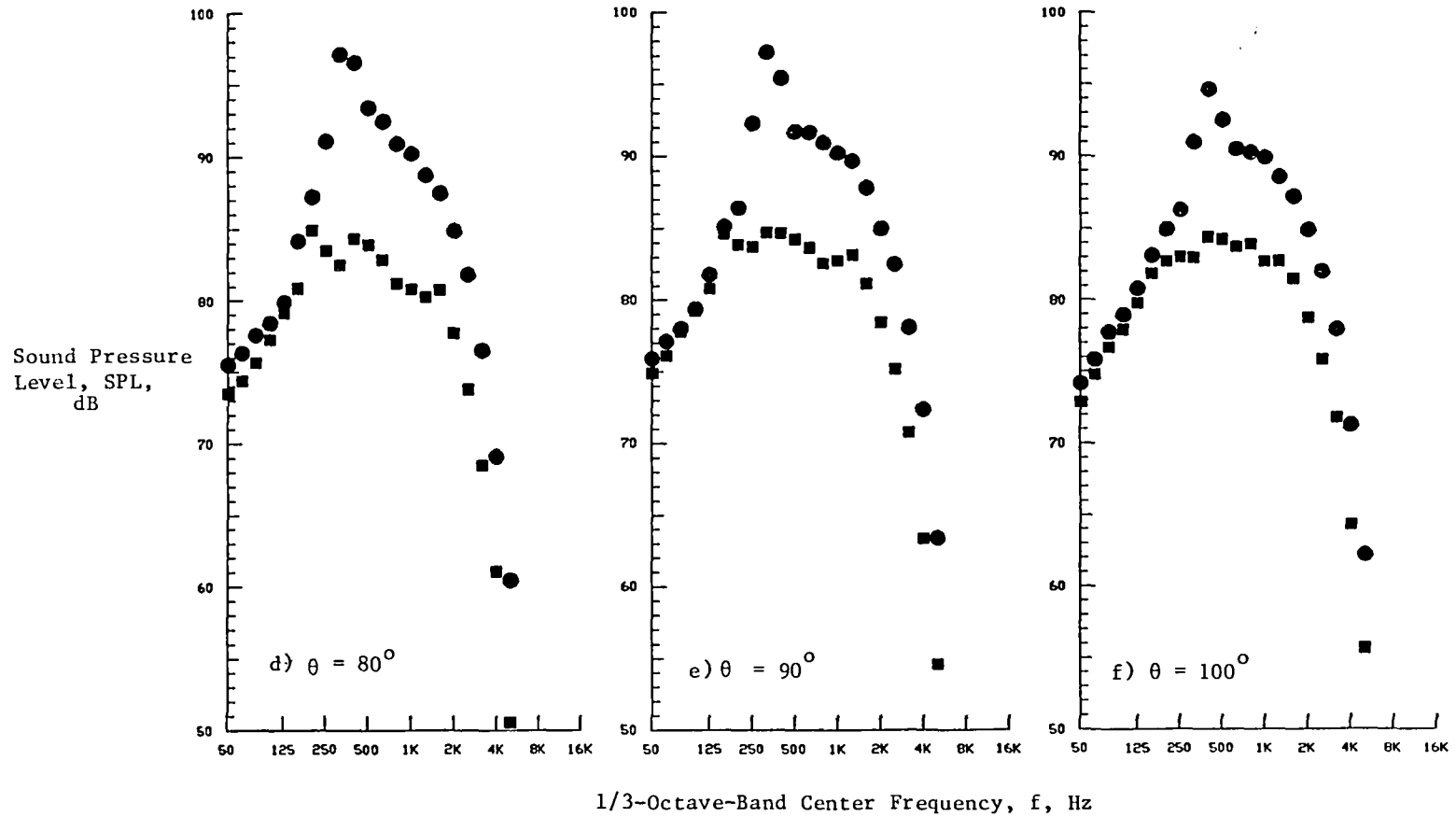


Figure 5-8. (Cont'd). Spectral Comparison Between C-D Circular Nozzle and Baseline Convergent Circular Nozzle. (Flight)

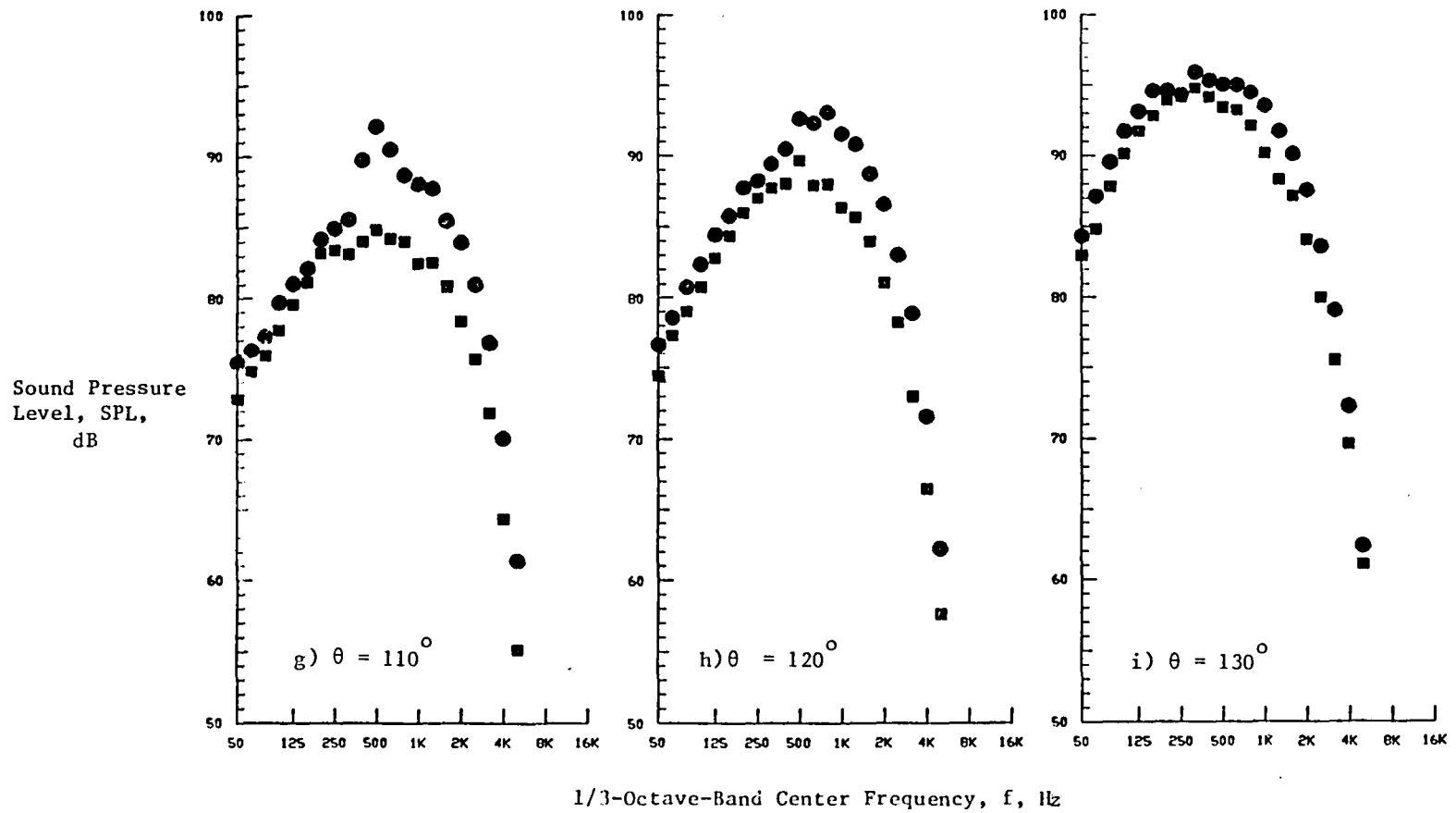


Figure 5-8. (Cont'd). Spectral Comparison Between C-D Circular Nozzle and Baseline Convergent Circular Nozzle. (Flight)

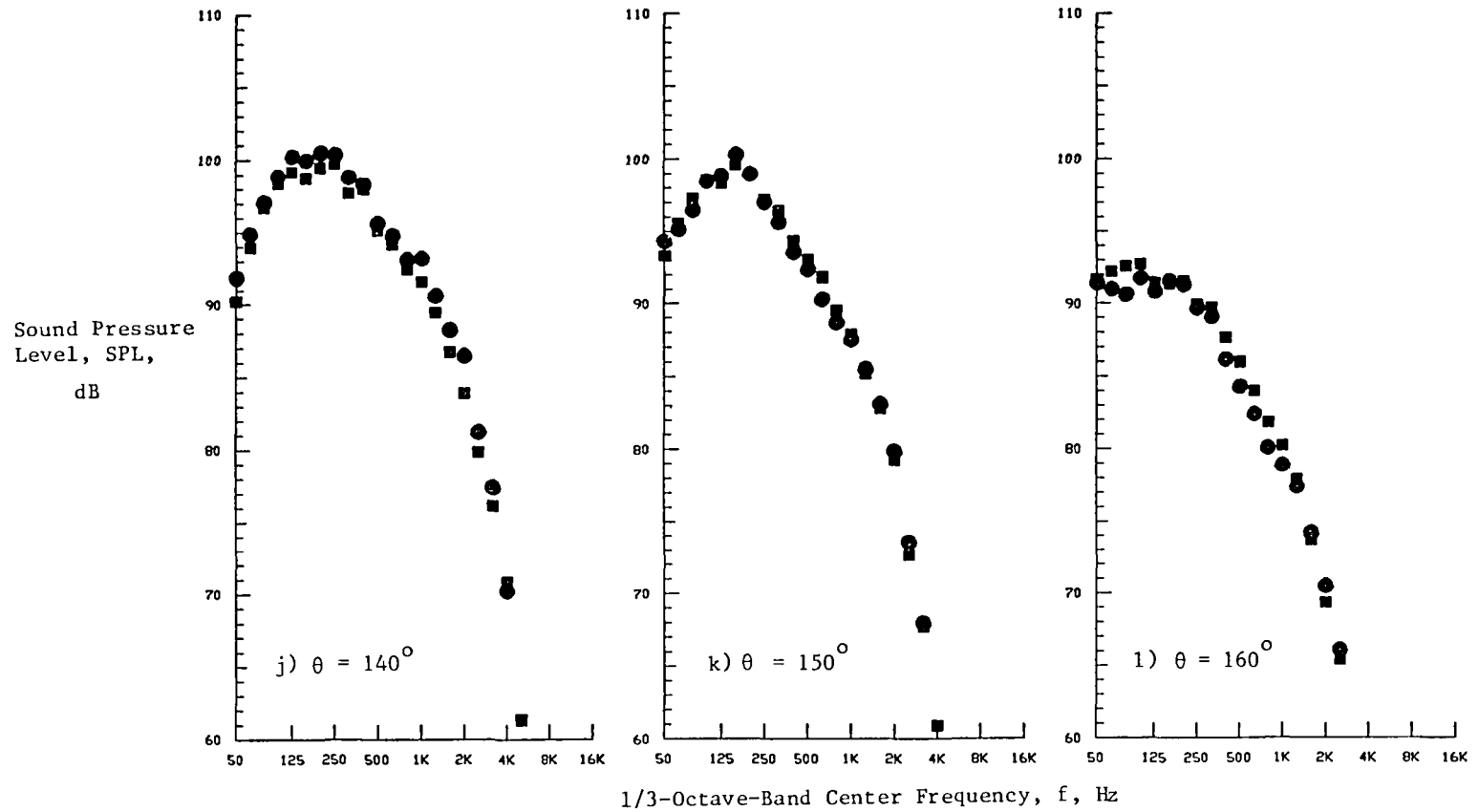


Figure 5-8. (Concluded) Spectral Comparison Between C-D Circular Nozzle and Baseline Convergent Circular Nozzle. (Flight)

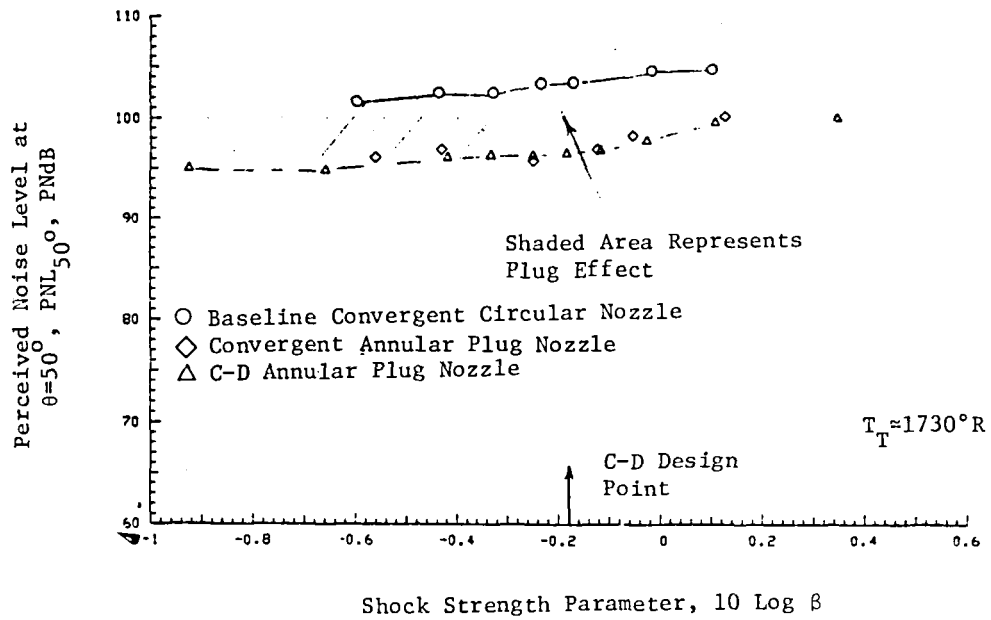
known, the screech is produced by an acoustic feedback mechanism which is extremely sensitive to the externally exerted disturbances. The lack of the discrete screech tone in Figure 5-8 may be attributed to the disturbances caused by the simulated flight environment.*

5.1.2 C-D EFFECTIVENESS OF ANNULAR PLUG NOZZLE

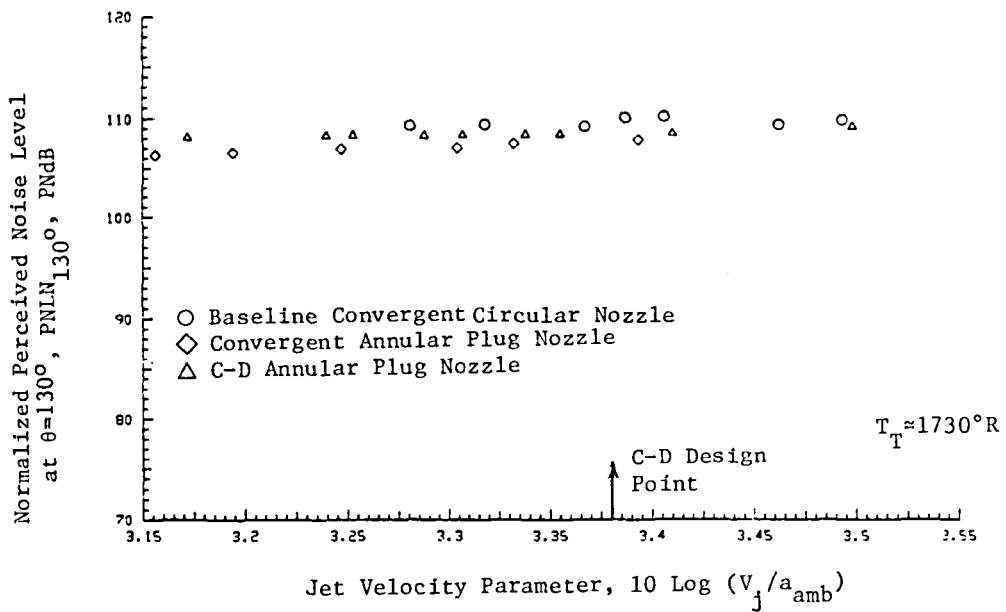
In the present survey two annular plug nozzles were tested, one of which has a convergent termination while the other has a C-D termination in the flowpath. Both nozzles have an identical equivalent diameter of 5.67 inches. The overall and spectral characteristics of the supersonic jet noise generated by the C-D annular plug nozzle (Model 4) compared with those of the convergent annular plug nozzle (Model 3) and the baseline convergent circular nozzle (Model 1) are presented.

Figure 5-9 presents PNL_{50° and $PNLN_{130^\circ}$ variations as a function of the shock strength parameter (β) and the fully expanded jet exit velocity, respectively. The total temperature of the plume was maintained at approximately $T_T \approx 1730^\circ R$ for all the test points shown in the figure. One of the striking observations in Figure 5-9(a) is that the C-D termination in the plug nozzle flowpath does not show any shock-cell noise reduction near the C-D design point as compared with its convergent counterpart. The reason for this is, as the diagnostic LV measurement results show (presented under Section 6.0), near the C-D design point both convergent and C-D plug nozzles have shocks in the region downstream of the nozzle plug, and the shock noise produced there is dominant over the shock noise generated on the plug surface. As LV test results also showed, the plume speed at the plug tip of the C-D plug nozzle is still supersonic when the flow is fully expanded. Consequently, due to the plug curvature, the flow must necessarily experience an expansion in the proximity of the nozzle plug and, thus, a series of expansion/shock waves is formed in the region downstream of the plug which subsequently causes generation of downstream shock-cells.

*Hay and Rose (Reference 5-8) reported that the relative motion of the ambient medium does not always eliminate screech tones. Similar observation has been made during this program, also.



(a) Perceived Noise Level at $\theta=50^\circ$.



(b) Normalized Perceived Noise Level at $\theta=130^\circ$.

Figure 5-9. Comparison of C-D Annular Plug Nozzle Levels with Those of Convergent Annular Plug Nozzle and Baseline Convergent Circular Nozzle. (Static)

A similar situation is observed for the plume of the convergent plug nozzle at the test point corresponding to the C-D design point. Because of its convergent termination, the flow is choked at the nozzle exit and the rapid variation in the mean pressure which must occur at the nozzle exit is accommodated by a system of Mach waves emanating from the nozzle lip. The cell-like structure of the jet arises from the subsequent multiple internal reflections of this system between the plug surface and the boundaries of the jet. It is well known that for a given Mach number and a streamline, generally there exists two shock angles which satisfy the relationships governing oblique shocks. The shock with a larger shock angle is called a strong shock wave, whereas the shock with a smaller shock angle is normally referred to as a weak shock wave. The plume velocity behind the strong shock wave is always subsonic. However, in the case of the weak shock wave, the flow maintains a supersonic speed before and after shock formation except for a certain range of the flow deflection angles. It is not always possible to predict which of these oblique shock waves actually occurs in a given flow. However, a system of weak oblique shock waves is preferably formed in most cases. This is understandable, because nature has a tendency to minimize entropy change in any thermodynamic process. Thus, since the flow still has a supersonic speed at the nozzle plug tip, subsequent formation of a system of compression and expansion waves is not avoidable, as in the case of its C-D counterpart.

To summarize the above argument, based on the aerodynamic flow measurements to be discussed in Section 6, it can be said that both the convergent and the C-D annular plug nozzles have shocks downstream of the plug at the C-D design point and, subsequently, generate shock noise which appears to be dominant over the noise produced by the shocks formed on the plug surface. Even so, it can be observed that over a wide range of pressure ratios, the C-D annular plug nozzle shows about 5 dB PNL_{50} reduction relative to the baseline convergent circular nozzle. At high pressure ratios, shock noise level tends to be saturated as is reported in Reference 5-6 for cold convergent circular nozzle jets.

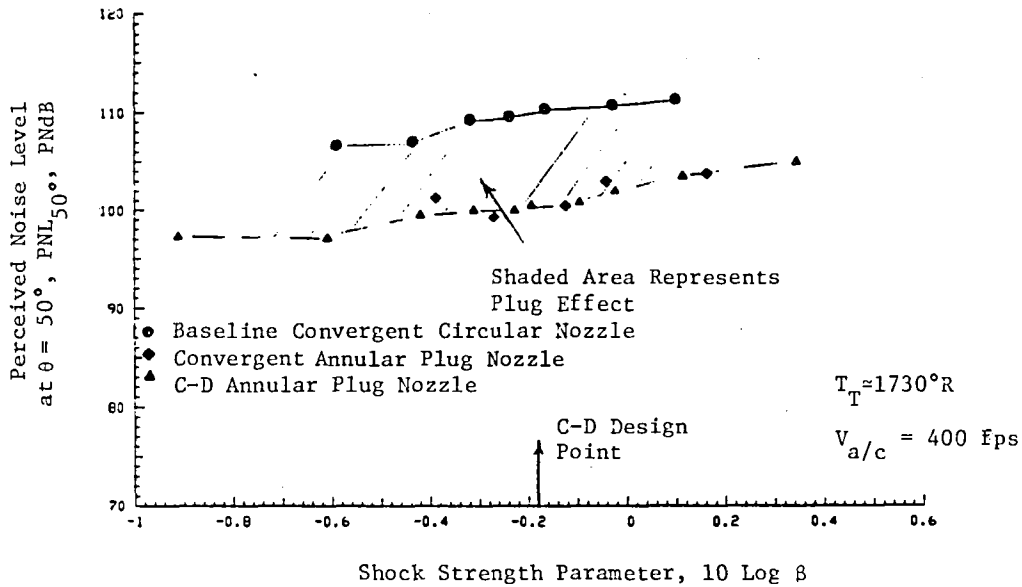
Figure 5-9(b) illustrates a correlation of $PNLN_{130}$ with the ideally expanded jet exit velocity for the baseline convergent circular, convergent annular plug and C-D annular plug nozzles. Here again, we note that the C-D termination appears not to significantly alter the mixing noise.

The corresponding flight data is presented in Figure 5-10. By comparing Figure 5-10(a) with 5-9(a), it is noted that the amount of amplification of shock associated noise by flight appears to be different for different nozzle geometries. More amplification is observed for the convergent circular nozzle than for the convergent annular plug nozzle. Mixing noise attenuation by flight, however, appears to be the same, irrespective of the nozzle geometry. Again, the C-D termination is noted not to affect the jet mixing noise level, though a modest noise reduction due to the central plug is observed (Reference 5-9 and 5-10).

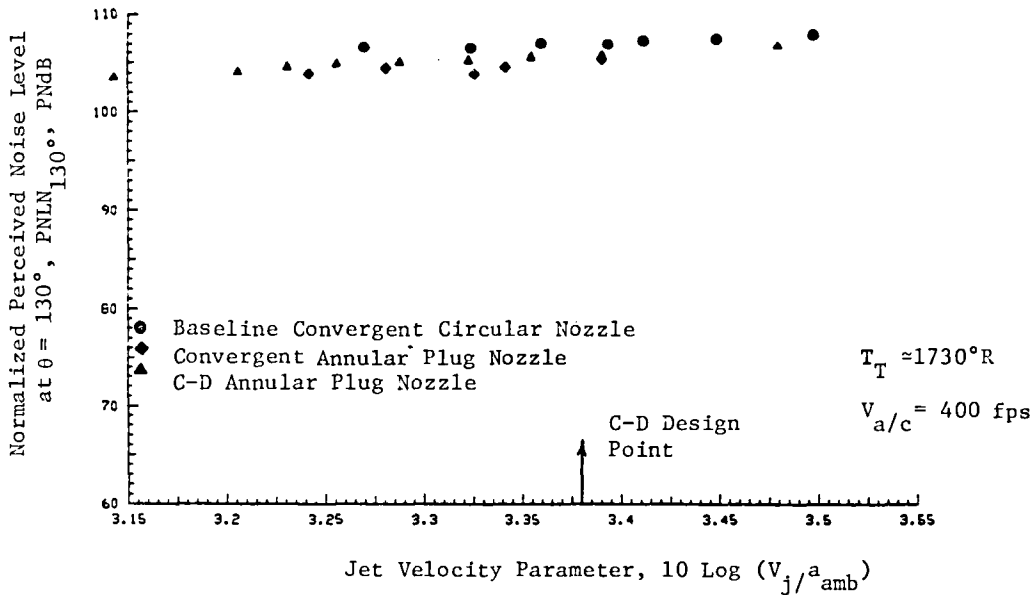
Figure 5-11 shows the OASPL and PNL directivity characteristics for the convergent and the C-D annular plug nozzles, as compared with those of the baseline convergent circular nozzle. Again it can be seen that the C-D termination has very little effect. However, it can be observed from these comparisons that, over the entire radiation angle range, plug nozzles have an edge on convergent circular nozzles as far as noise reduction is concerned. The measurements indicate a 6 PNdB noise reduction, primarily in shock noise, at $\theta = 50^\circ$ and 1.5 to 2 PNdB noise reduction at the peak aft quadrant acoustic angle, due primarily to screech tone reduction but also including some reduction of jet mixing noise, as will be seen in subsequent spectral comparisons.

Corresponding OASPL and PNL directivities in a simulated flight case are presented in Figure 5-12. These results show, comparing with the results for static conditions, that in the aft quadrant the jet mixing noise has been reduced in flight. In the forward quadrant, amplification of the shock associated noise is observed. The measurements indicate 2 to 3 PNdB noise reduction for annular plug nozzles at the peak aft quadrant acoustic angle with a corresponding 8 PNdB reduction in the forward quadrant at $\theta = 50^\circ$, as compared with the baseline convergent circular nozzle.

The spectral acoustic test results for the convergent and the C-D annular plug nozzles are shown in Figure 5-13 (static) and Figure 5-14 (flight), which also include the spectra of the baseline convergent circular nozzle shown as a reference. From an examination of a typical forward quadrant angle ($\theta = 50^\circ$) spectra, it is observed that a significant reduction of high frequency noise components for the annular plug nozzle



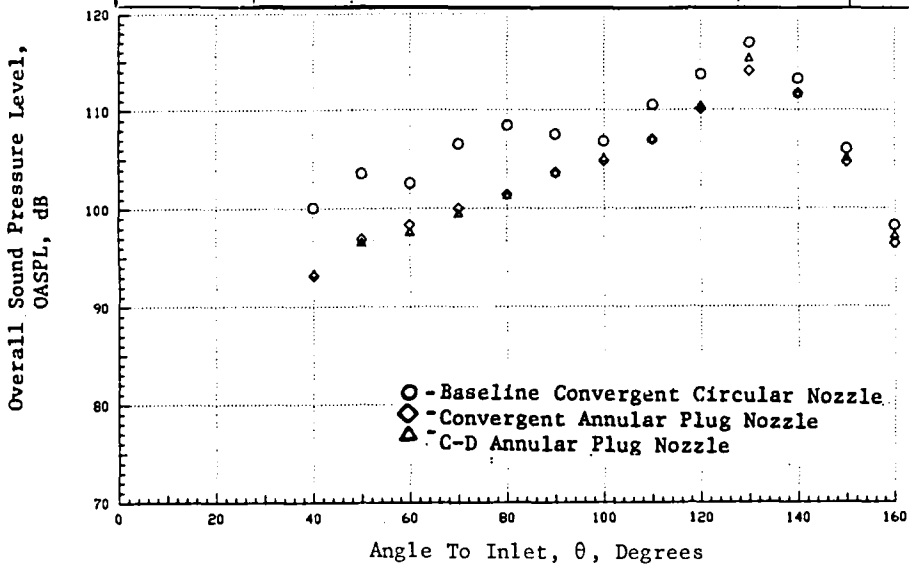
(a) Perceived Noise Level at $\theta=50^\circ$.



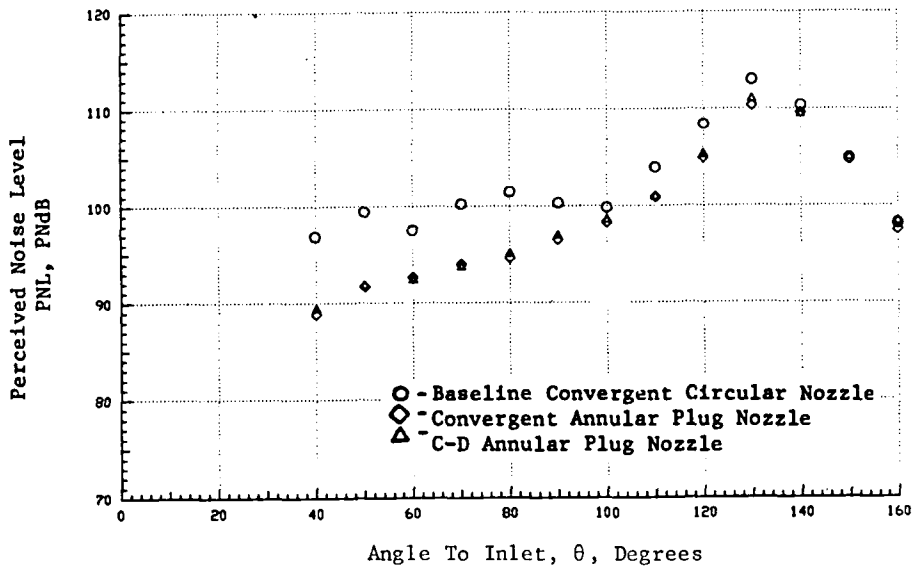
(b) Normalized Perceived Noise Level at $\theta=130^\circ$.

Figure 5-10. Comparison of C-D Annular Plug Nozzle Levels with Those of Convergent Annular Plug Nozzle and Baseline Convergent Circular Nozzle. (Flight)

Symbol	Model	Test Point	P_r	$T_{T,OR}$ ($^{\circ}R$)	V_j (ft/s)	$V_{a/c}$ (ft/s)
○	1	113	3.12	1707	2403	0
◇	3	313	3.16	1741	2436	0
△	4	413	3.12	1731	2418	0



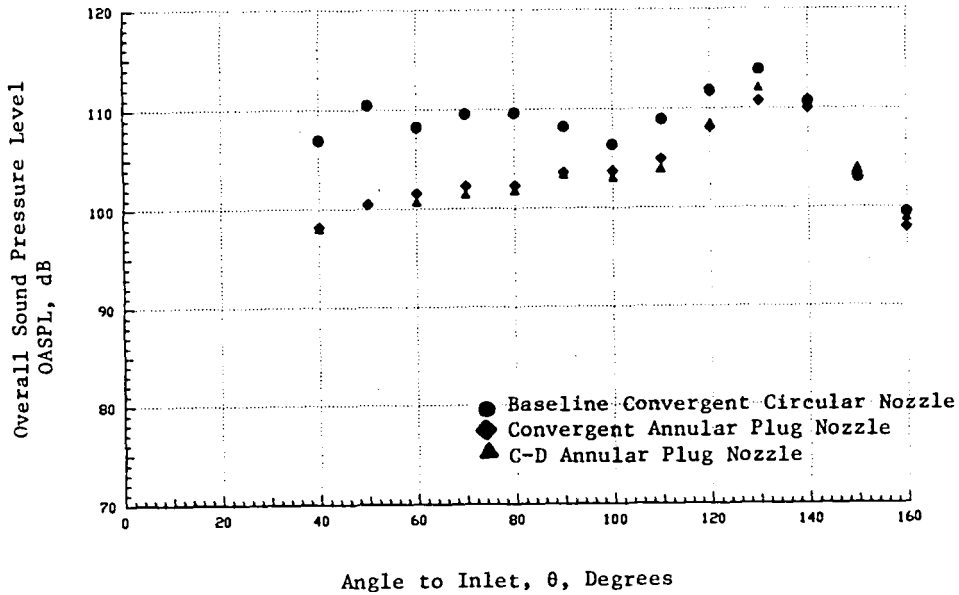
a) Overall Sound Pressure Level



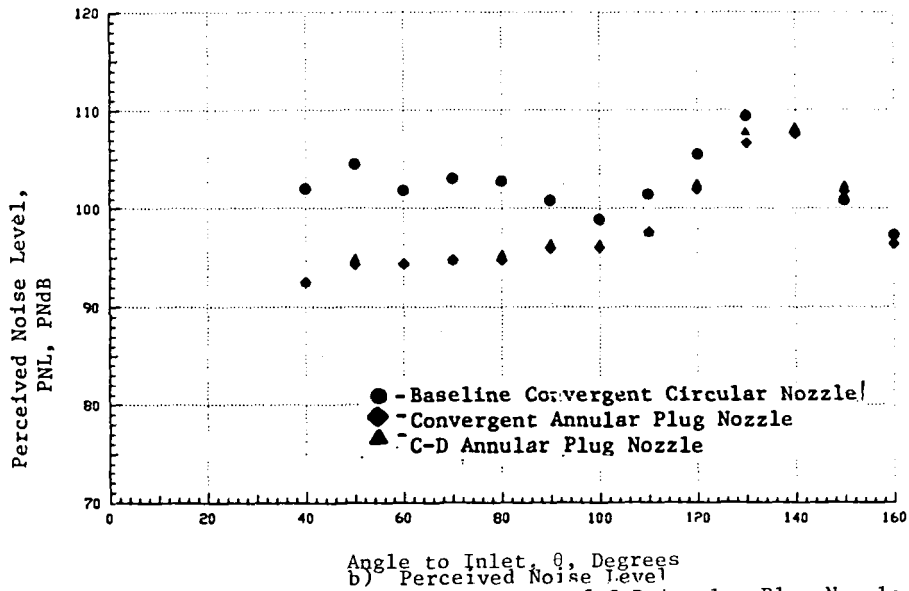
b) Perceived Noise Level

Figure 5.11. Comparison of Directivity of C-D Annular Plug Nozzle with Those of Convergent Annular Plug Nozzle and Baseline Convergent Circular Nozzle. (Static)

Symbol	Model	Test Point	P_r	T_{T^*} ($^{\circ}R$)	V_j (f/s)	$V_{a/c}$ (f/s)
●	1	114	3.13	1714	2409	400
◆	3	314	3.16	1744	2439	400
▲	4	414	3.11	1741	2423	400



a) Overall Sound Pressure Level



b) Perceived Noise Level
Figure 5-12. Comparison of Directivity of C-D Annular Plug Nozzle with Those of Convergent Annular Plug Nozzle and Baseline Convergent Circular Nozzle. (Flight)

Symbol	Model	Test Point	P_r	$T_{T,}$ ($^{\circ}R$)	V_j (f/s)	$V_{a/c}$ (f/s)
○	1	113	3.12	1707	2403	0
◇	3	313	3.16	1741	2436	0
△	4	413	3.12	1731	2418	0

○ - Baseline Convergent Circular Nozzle
◇ - Convergent Annular Plug Nozzle
△ - C-D Annular Plug Nozzle

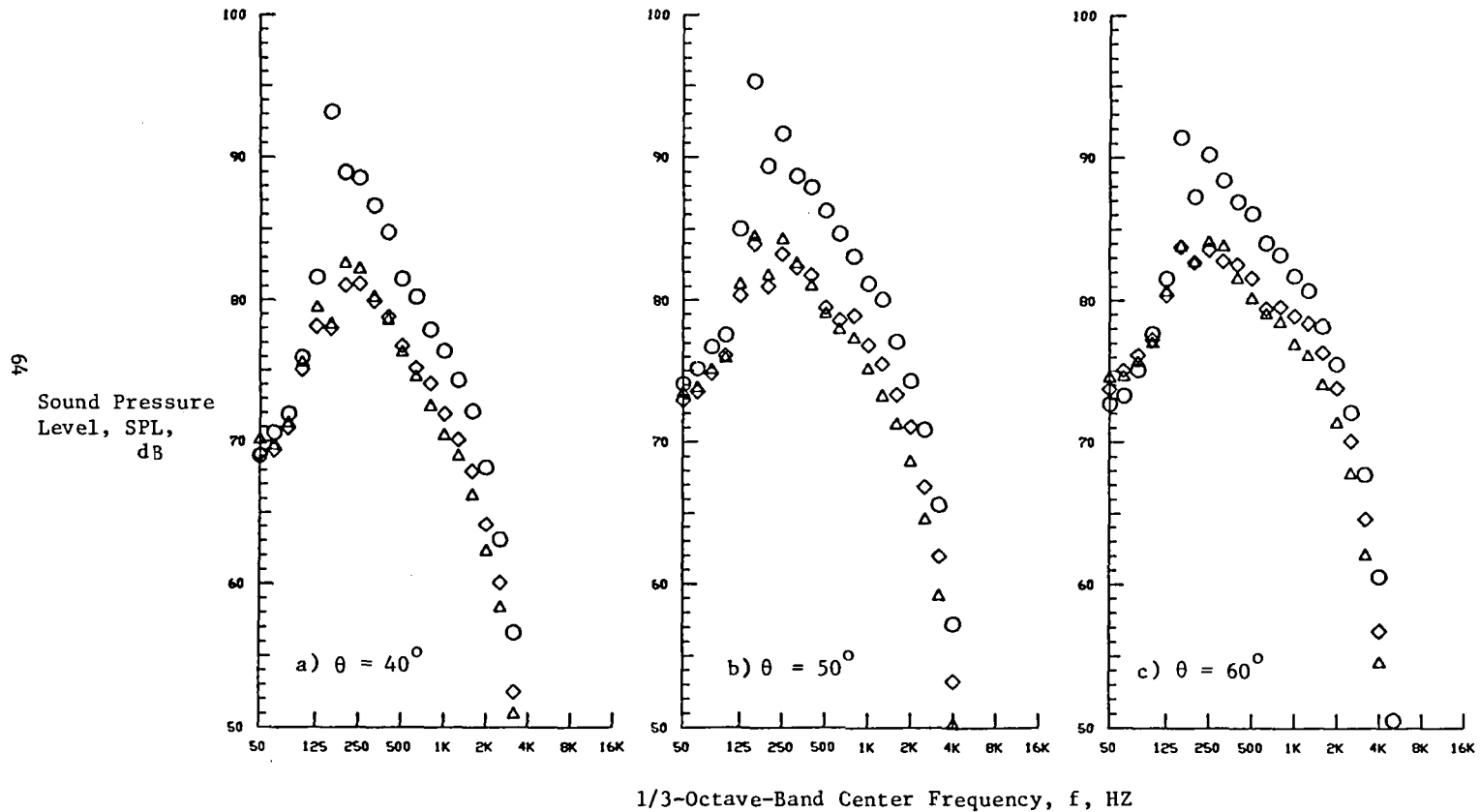


Figure 5-13. Spectral Comparison Between C-D Annular Plug Nozzle, Convergent Annular Plug Nozzle, and Baseline Convergent Circular Nozzle. (Static)

Sound Pressure
Level, SPL,
dB

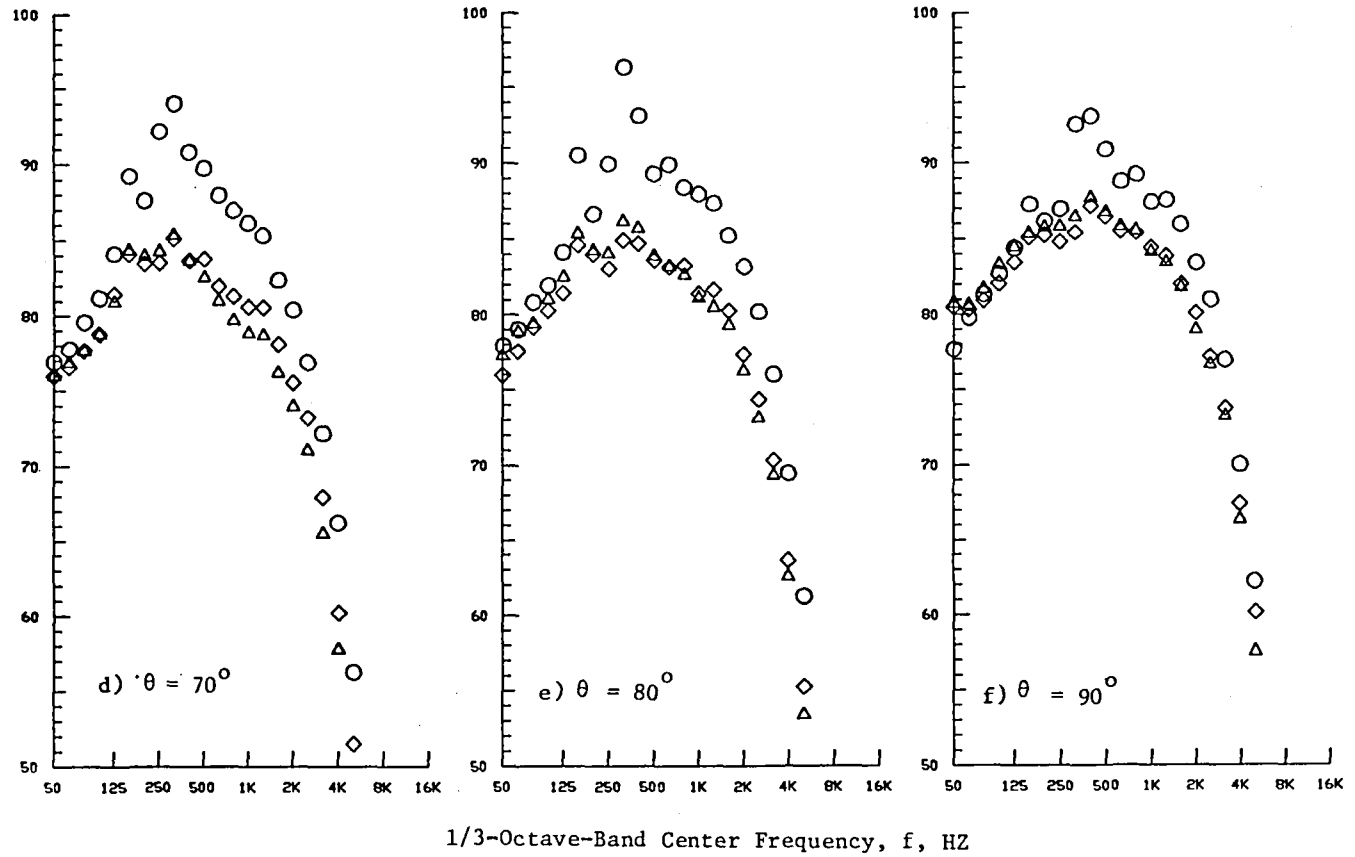


Figure 5-13. (Cont'd). Spectral Comparison Between C-D Annular Plug Nozzle, Convergent Annular Plug Nozzle, and Baseline Convergent Circular Nozzle. (Static)

Sound Pressure
Level, SPL
dB

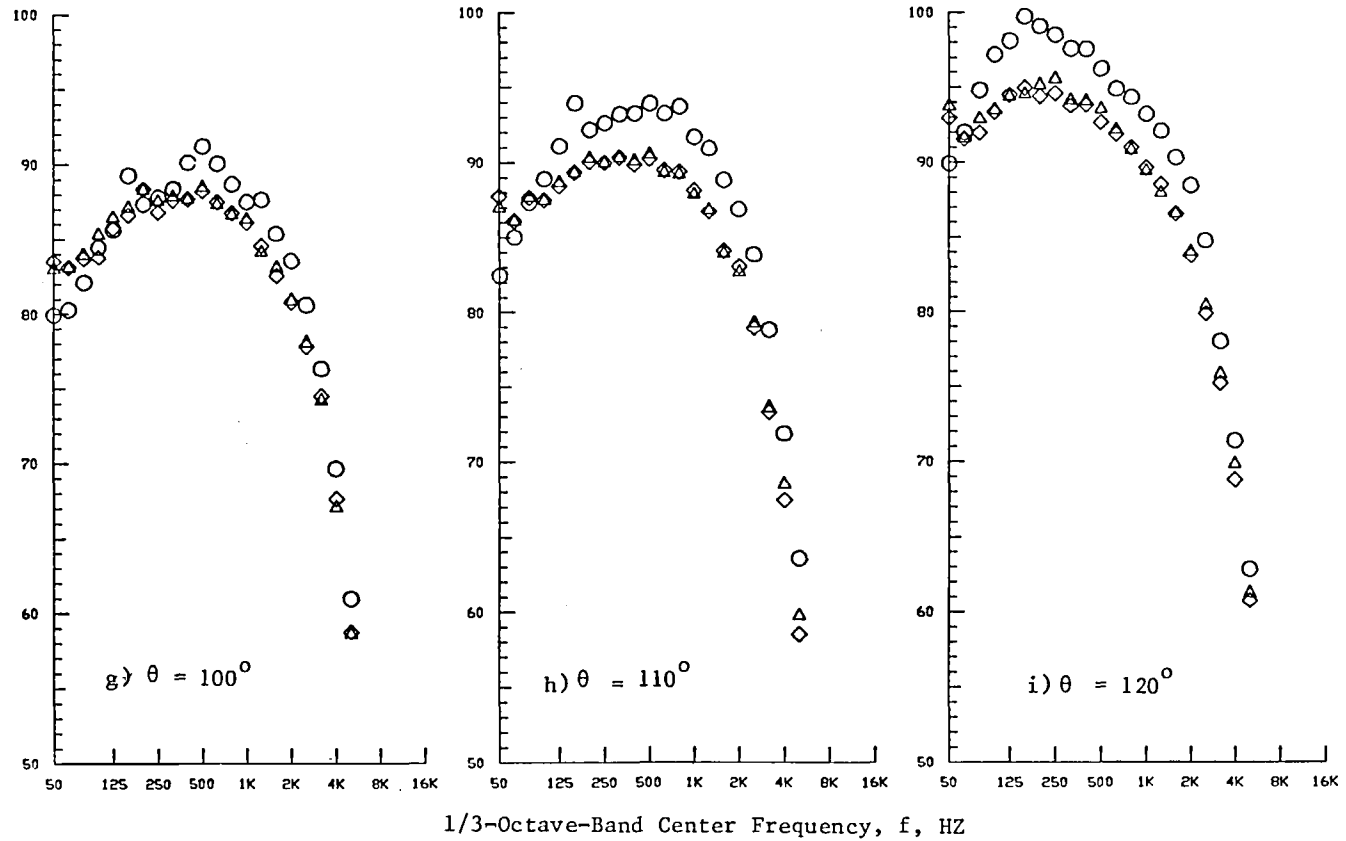


Figure 5-13. (Cont'd). Spectral Comparison Between C-D Annular Plug Nozzle, Convergent Annular Plug Nozzle, and Baseline Convergent Circular Nozzle. (Static)

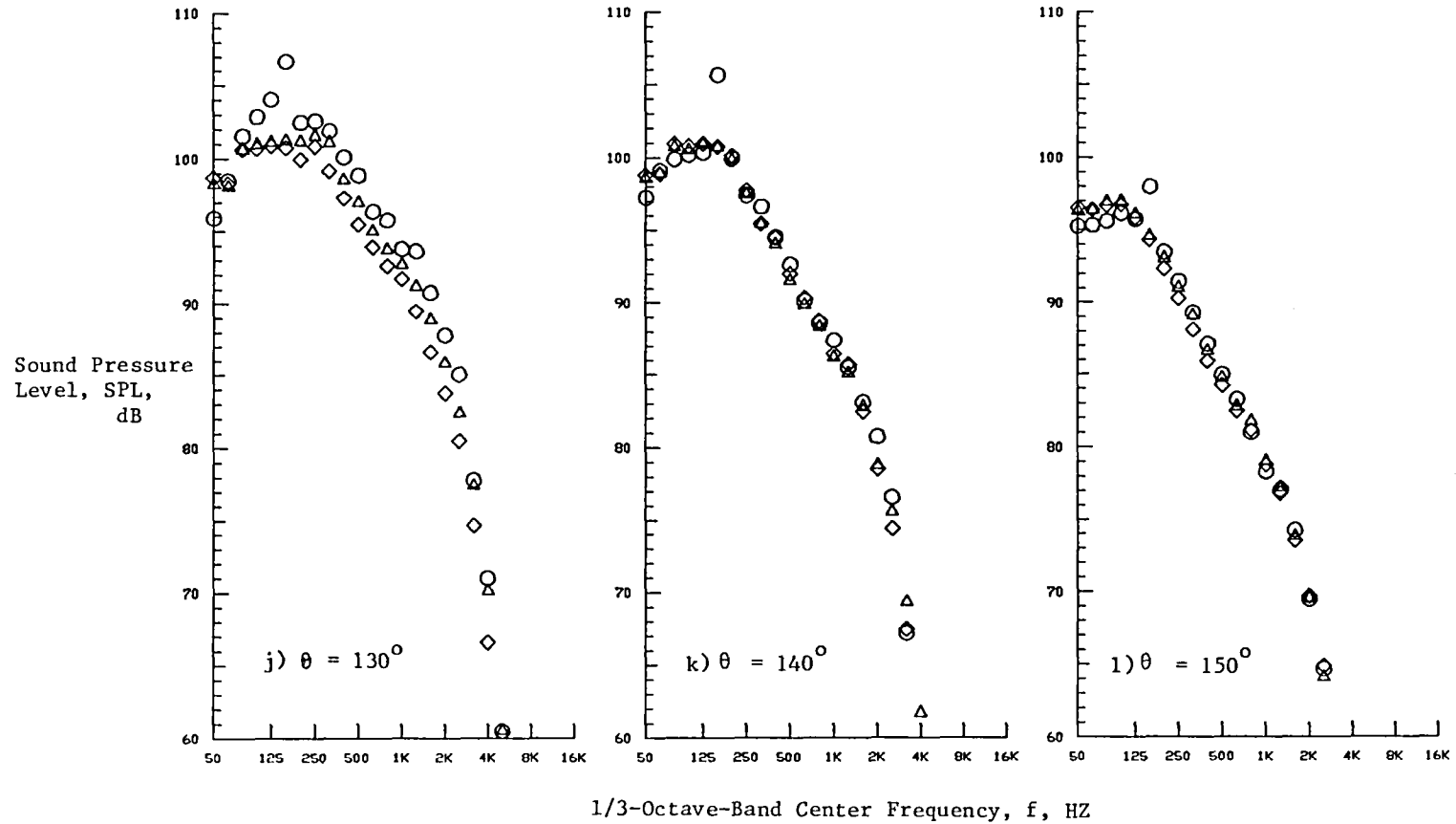


Figure 5-13. (Concluded). Spectral Comparison Between C-D Annular Plug Nozzle, Convergent Annular Plug Nozzle, and Baseline Convergent Circular Nozzle. (Static)

	Model	Test Point	P_r	T_T , ($^{\circ}R$)	V_j (f/s)	$V_{a/c}$ (f/s)
●	1	114	3.13	1714	2409	400
◆	3	314	3.16	1744	2439	400
▲	4	414	3.11	1741	2423	400

- - Baseline Convergent Circular Nozzle
- ◆ - Convergent Annular Plug Nozzle
- ▲ - C-D Annular Plug Nozzle

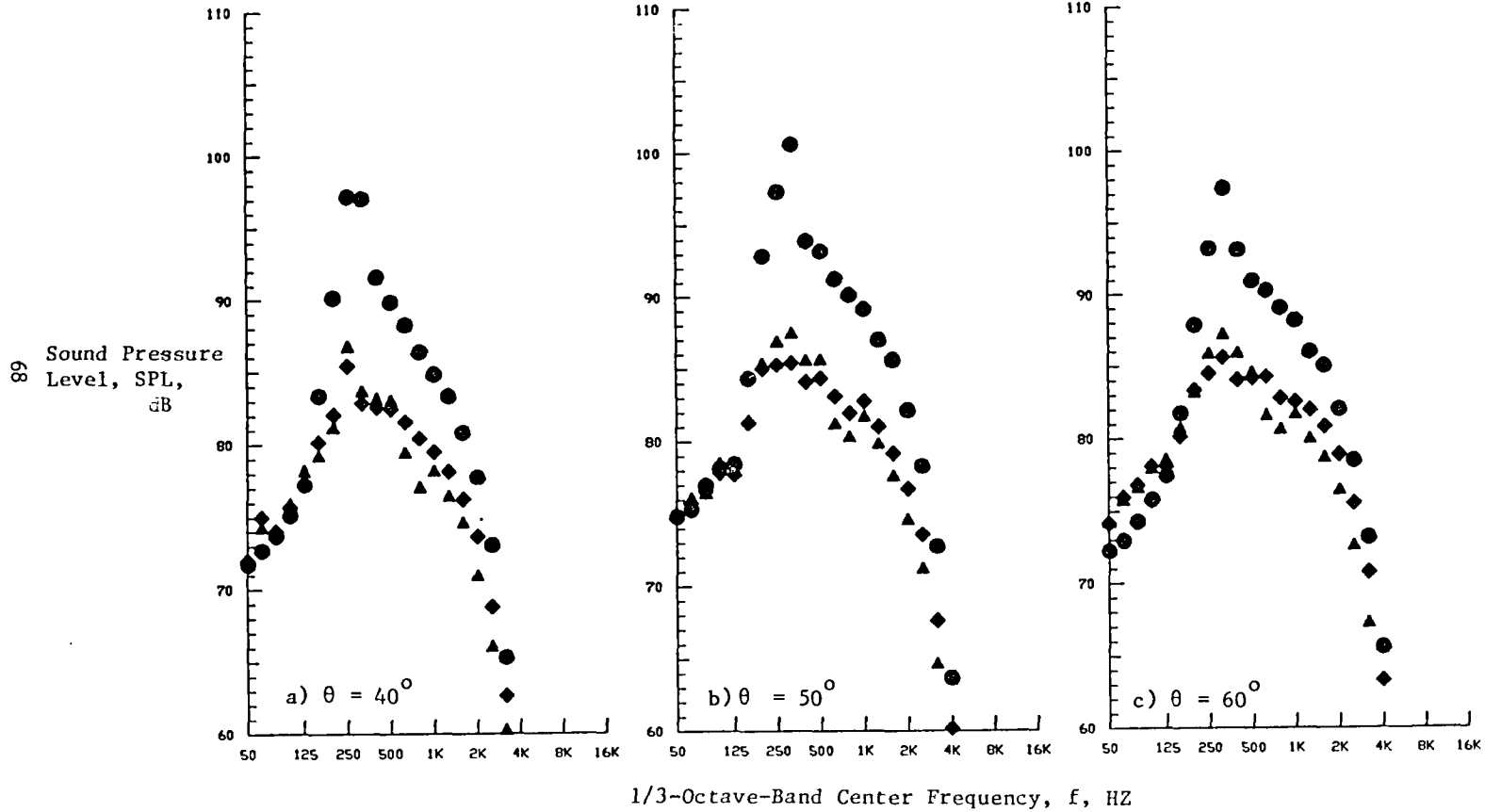


Figure 5-14. Spectral Comparison Between C-D Annular Plug Nozzle, Convergent Annular Plug Nozzle, and Baseline Convergent Circular Nozzle. (Flight)

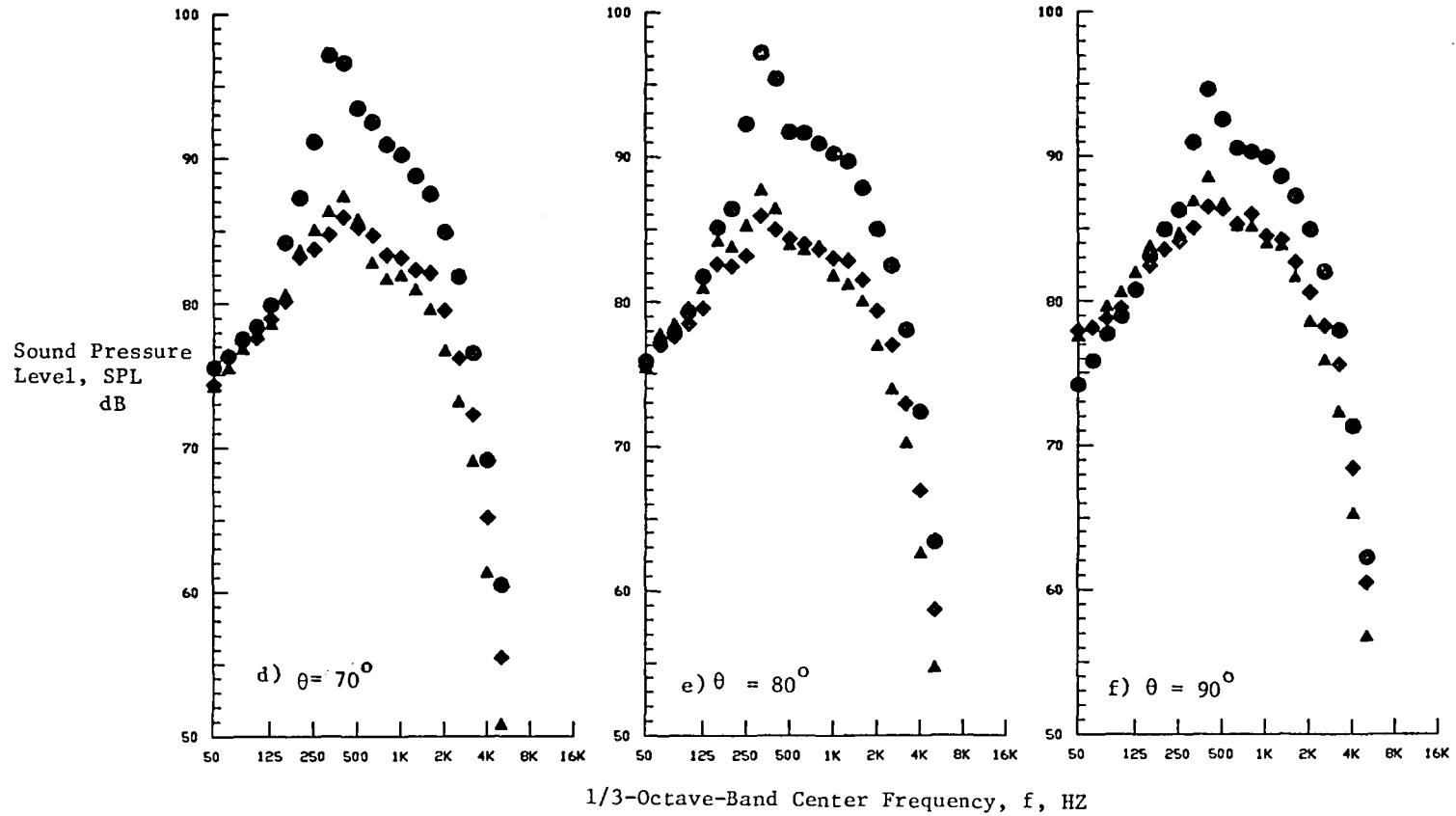


Figure 5-14. (Cont'd). Spectral Comparison Between C-D Annular Plug Nozzle, Convergent Annular Plug Nozzle, and Baseline Convergent Circular Nozzle. (Flight)

70

Sound Pressure
Level, SPL,
dB

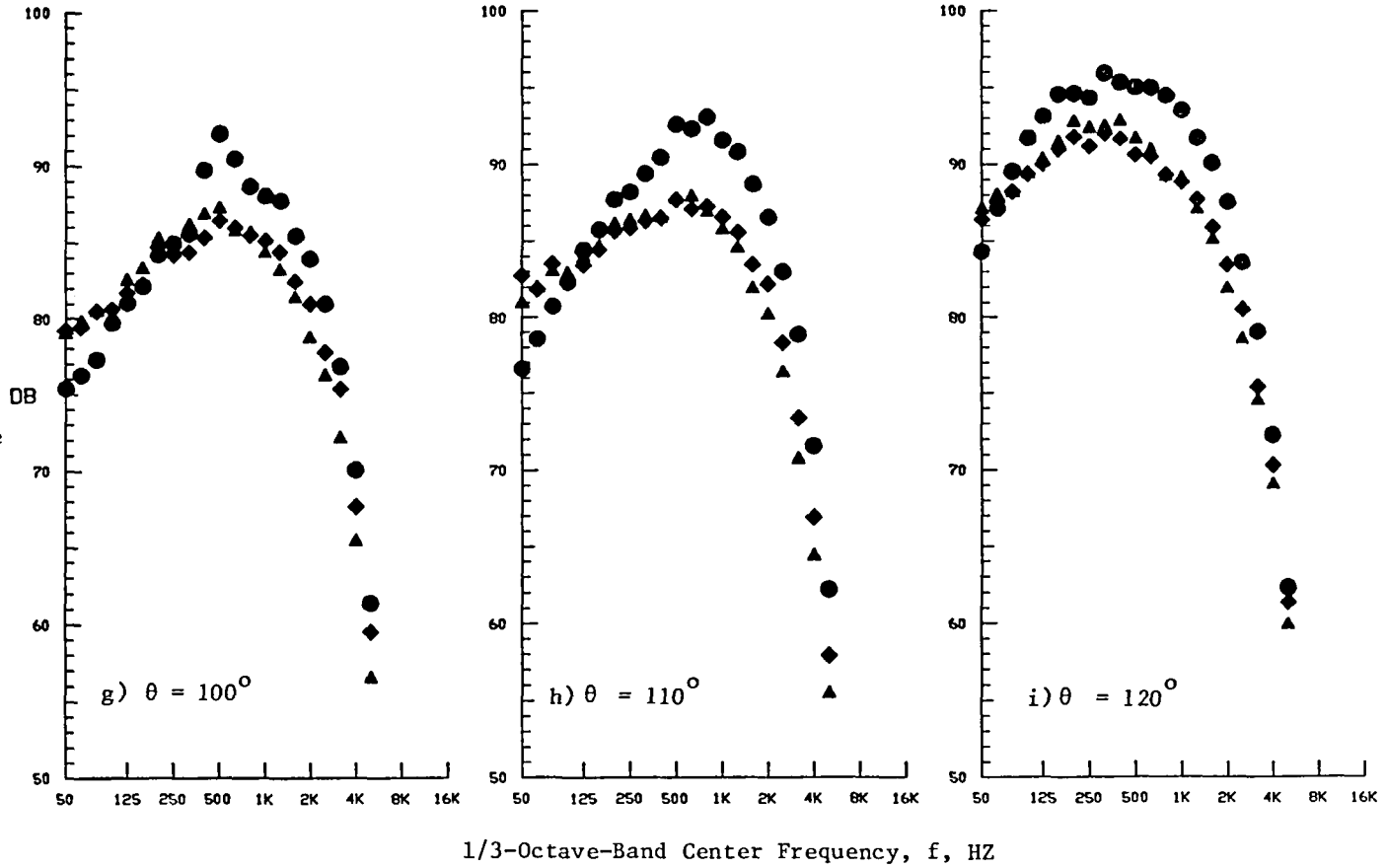


Figure 5-14. (Cont'd). Spectral Comparison Between C-D Annular Plug Nozzle, Convergent Annular Plug Nozzle, and Baseline Convergent Circular Nozzle. (Flight)

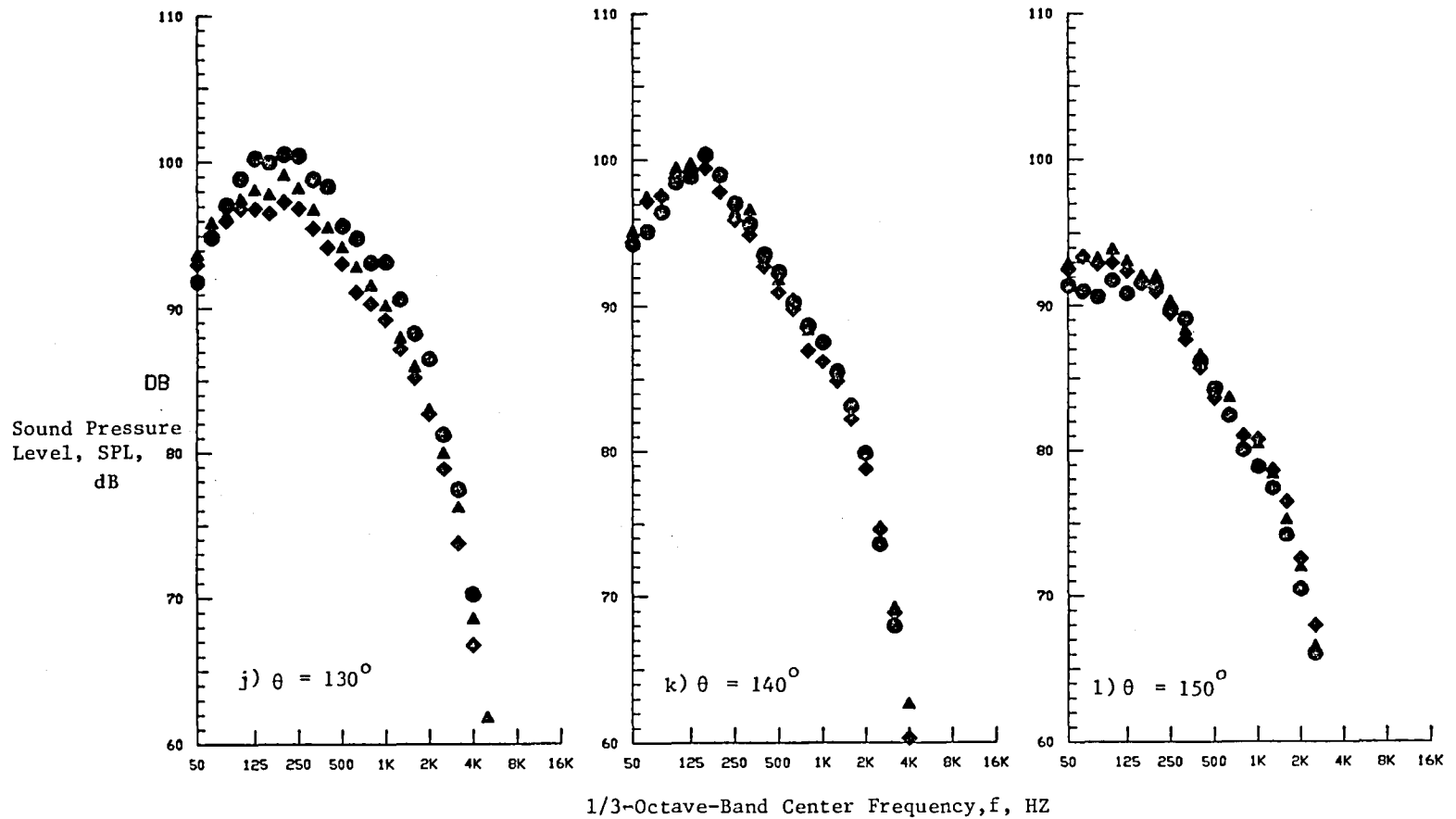


Figure 5-14. (Concluded). Spectral Comparison Between C-D Annular Plug Nozzle, Convergent Annular Plug Nozzle, and Baseline Convergent Circular Nozzle. (Flight)

occurs compared to those of the baseline convergent circular nozzle. A generally observed lower SPL for the C-D nozzle in the high frequency range may be attributed to the lack of the shocks formed on the plug surface. Furthermore, a two-hump spectral profile is noted for the convergent annular plug nozzle indicating two clearly distinguishable shock systems formed in the flow of this nozzle. Further discussions on the spectral characteristics of shock-cell noise from annular plug nozzles will be given in Subsection 5.4, in conjunction with the comparison of spectral data with prediction.

To conclude this subsection, it should be mentioned that in order to further suppress shock broadband noise for the annular plug nozzles, some measures should be taken to mitigate shocks produced in the region downstream of the plug due to the plug curvature. One possible solution would be to use a long plug instead of the conventional truncated plug in order to allow a smooth plume expansion on the plug.*

5.1.3 C-D EFFECTIVENESS OF MULTI-ELEMENT SUPPRESSOR PLUG NOZZLE

In this subsection, the acoustic characteristics of the multi-element suppressor plug nozzles (Model 5 and Model 6) are discussed. The benefits of the convergent-divergent termination in the flowpath on the multi-element suppressor noise relative to its convergent counterpart and the baseline convergent circular nozzle is discussed.

As described in Section 4.0, two multi-element suppressor nozzles were tested during the present shock noise investigation. The 20-chute-annular plug suppressor with convergent flow segment terminations (Model 5) has a suppressor area ratio of 1.75 and an equivalent exit diameter of 5.091 inches. Its C-D counterpart, i.e., 20-chute-annular plug suppressor with convergentdivergent flow element terminations (Model 6), has a suppressor area ratio of 1.752 (at throat) and 1.56 (at exit) and is designed for an exit Mach

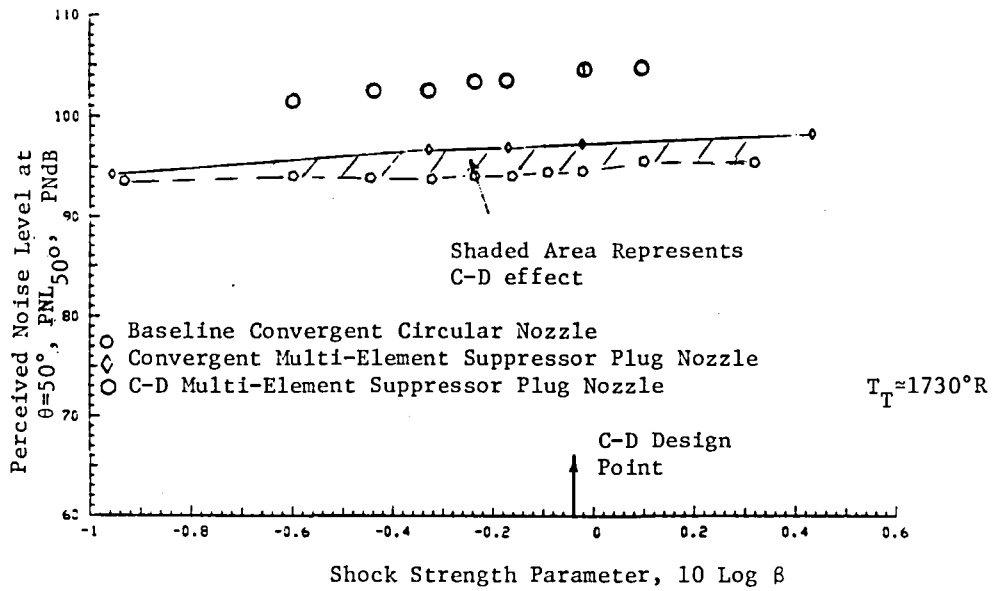
*In the work effort on follow-on contract program, NAS3-23166, "Experimental Investigation of Shock-Cell Noise Reduction For Dual-Stream Nozzles in Simulated Flight," this idea has been explored, and preliminary test results with this type of nozzle have indicated additional reduction in shock noise.

Number of 1.42. The equivalent diameter at the throat is 5.075 inches. Geometrical details of these configurations are presented in Subsection 4.1.

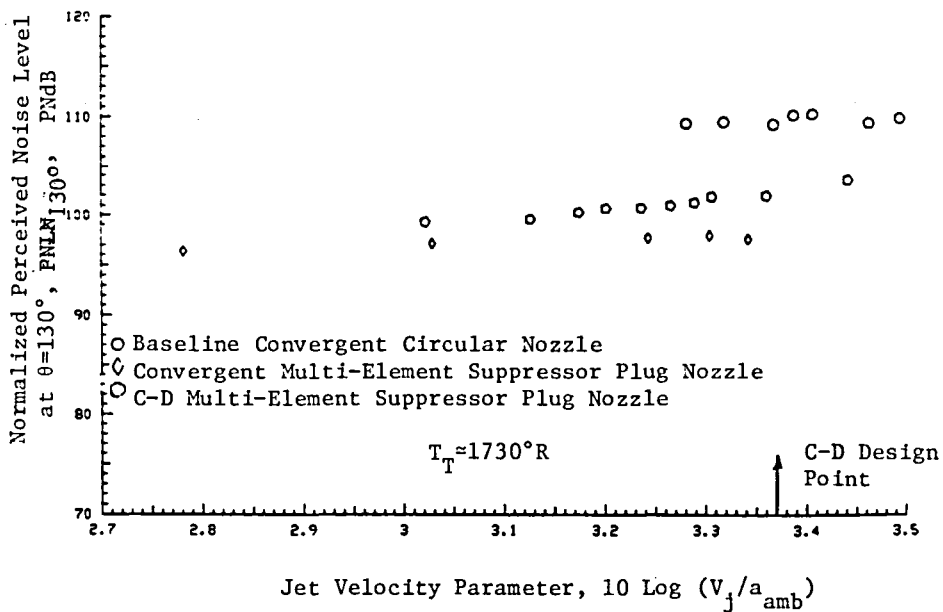
The PNL_{50° and $PNLN_{130^\circ}$ of the C-D suppressor nozzle (Model 6) measured during static and simulated flight tests are summarized in Figures 5-15 and 5-16, respectively. The measured data are compared in each of these figures with the corresponding data of the convergent suppressor nozzle (Model 5) and the baseline convergent circular nozzle (Model 1).

The PNL_{50° data of the C-D suppressor nozzle measured at static conditions and shown in Figure 5-15(a) indicates 2 to 3 PNdB reduction compared to the convergent suppressor nozzle and 9.5 PNdB suppression relative to the baseline convergent circular nozzle near the C-D design point which corresponds to a typical AST takeoff condition. This comparison indicates the effectiveness of the C-D terminations in the flowpath of the chutes of the C-D suppressor nozzle. Corresponding simulated flight data comparisons are made in Figure 5-16(a). An examination of this figure indicates a significant shock associated noise amplification by flight speed for each of the nozzles over the entire range of pressure ratios. It should be noted that the relative magnitude of PNL_{50° among these nozzles remains almost unchanged, indicating an almost equal amount of flight amplification for each of the nozzles. This means that the acoustic data for the C-D suppressor nozzle still contains broadband shock noise components even at the C-D design condition, indicating that the C-D termination in the chute flowpath of the C-D suppressor nozzle is not as effective as that of the C-D circular nozzle. This is made clear by the aerodynamic flow measurement results presented in Section 6.0.

The effects of C-D terminations on the jet mixing noise can be observed in Figures 5-15(b) and 5-16(b). An examination of these figures indicates a significant amount of the mixing noise reduction due to the suppressor (i.e., 20 chutes). As indicated by the LV data presented in Section 6.0, a rather rapid axial mean velocity decay and a consequent lower turbulence level in the jet plume produced by the convergent suppressor nozzle (Model 5) is responsible for lower static $PNLN_{130^\circ}$ magnitude compared to corresponding $PNLN_{130^\circ}$ for the C-D suppressor nozzle (see Figure 6-6). This may indicate

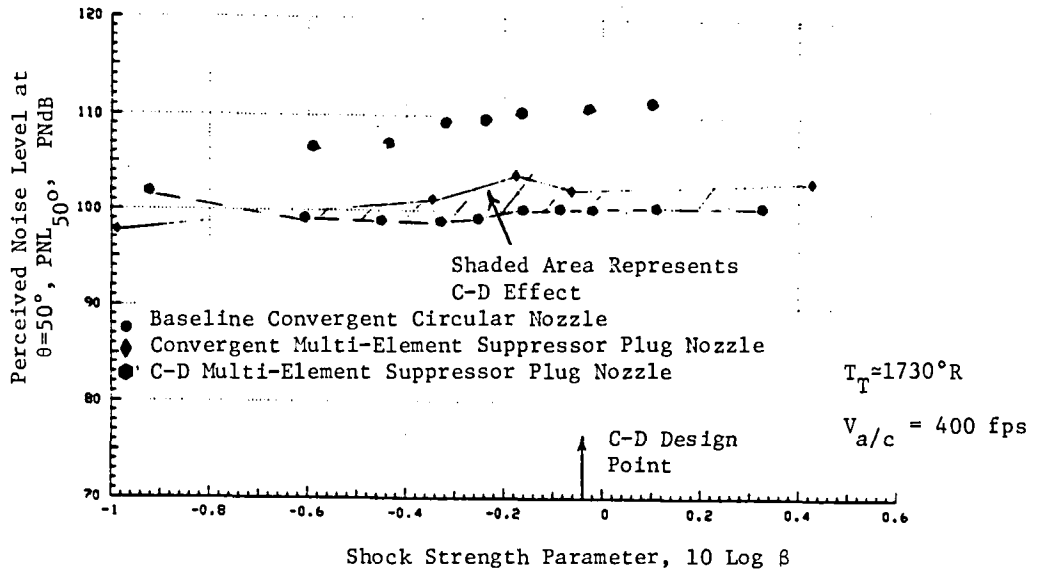


(a) Perceived Noise Level at $\theta=50^\circ$.

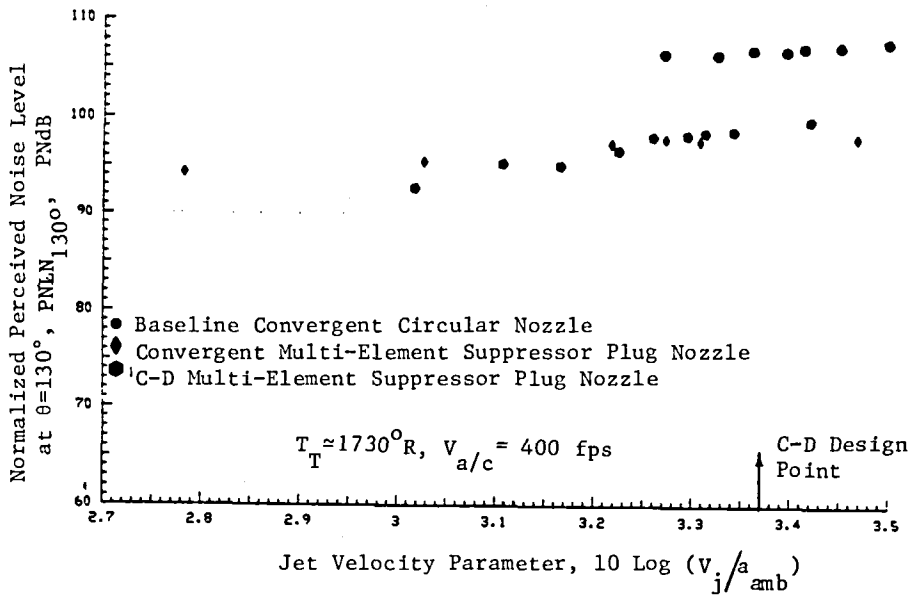


(b) Normalized Perceived Noise Level at $\theta=130^\circ$.

Figure 5-15. Comparison of Baseline Convergent Circular Nozzle Levels with those of Convergent Multi-Element Suppressor Plug Nozzle and C-D Multi-Element Plug Nozzle. (Static)



(a) Perceived Noise Level at $\theta=50^\circ$



(b) Normalized Perceived Noise Level at $\theta=130^\circ$

Figure 5-16. Comparison of Baseline Convergent Circular Nozzle Levels with Those of Convergent Multi-Element Suppressor Plug Nozzle and C-D Multi-Element Suppressor Plug Nozzle. (Flight)

an adverse C-D effect on jet mixing noise caused by the C-D suppressor nozzles. However, the difference of $PNLN_{130^\circ}$ noted for the static data between the convergent and C-D suppressor nozzles apparently disappears in the simulated flight data. The reason for this is not apparent at the present time.

The PNL and OASPL directivities of the C-D suppressor nozzle are compared to those of the baseline convergent circular and convergent suppressor nozzles in Figures 5-17 (static) and 5-18 (flight) at the C-D design condition. The C-D benefits in terms of PNL are evident over the forward quadrant angles, while in the aft quadrant the convergent suppressor appears to be more favorable, as far as mixing noise reduction is concerned, compared to the baseline convergent circular nozzle. Since, as is indicated by the LV test data (see Section 6.1), shocks were formed only in the proximity of the jet exit (i.e., on the surface of the plug) for the suppressor nozzles (Models 5 and 6) at the C-D design condition, the characteristic length scale associated with the broadband shock noise emission should be of the order of chute flowpath dimension. Accordingly, corresponding peak frequency of the shock associated noise falls in a rather high frequency range. As a direct consequence of the high frequency noise which is weighted higher in the standard PNL calculation procedures, different directivity patterns for PNL and OASPL are noted.

Figure 5-18 shows corresponding PNL and OASPL directivities under simulated flight conditions. Once again, a typical forward quadrant flight amplification and aft quadrant flight suppression in terms of both PNL and OASPL are noted. In addition, Figure 5-18(a) indicates that noise suppression due to the C-D effectiveness is only very moderately affected by flight in the forward quadrant. No systematic change, however, is observed in the aft quadrant. Figure 5-18(b) illustrates the OASPL comparison of the C-D suppressor nozzle with the convergent suppressor and the baseline convergent circular nozzles in the flight case. Although not significant, some differences in OASPL are observed in the forward quadrant between the C-D suppressor and the corresponding convergent suppressor nozzles in contrast to the static case.

	Model	Test Point	P_r	$T_{T'}$ (°R)	V_j (f/s)	$V_{a/c}$ (f/s)
○	1	113	3.12	1707	2403	0
◇	5	513	3.13	1718	2412	0
⊙	6	613	3.13	1714	2410	0

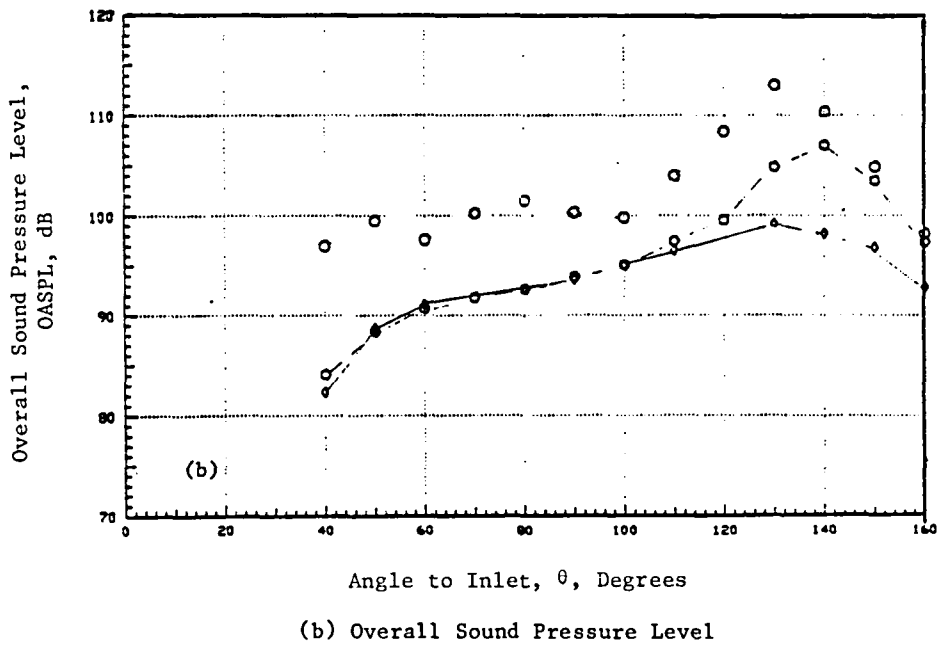
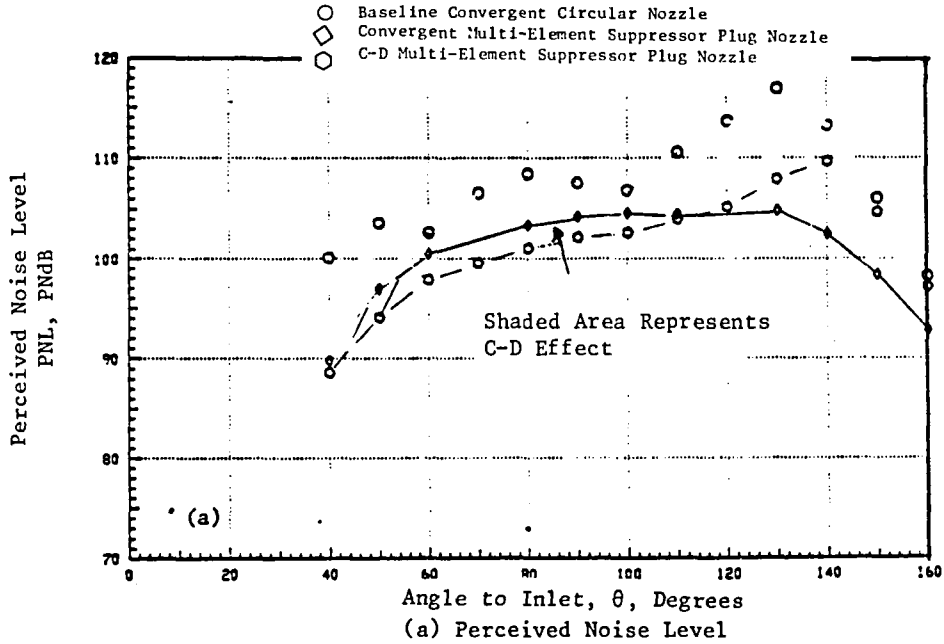


Figure 5-17. Static PNL and OASPL Directivity Comparisons Between Baseline Convergent Circular Nozzle, Convergent Multi-Element Suppressor Plug Nozzle, and C-D Multi-Element Suppressor Nozzle.

	Model	Test Point	P_r	$T_{T'}$ (°R)	V_j (f/s)	$V_{a/c}$ (f/s)
●	1	114	3.13	1715	2410	400
◆	5	514	3.12	1706	2401	400
●	6	614	3.13	1720	2414	400

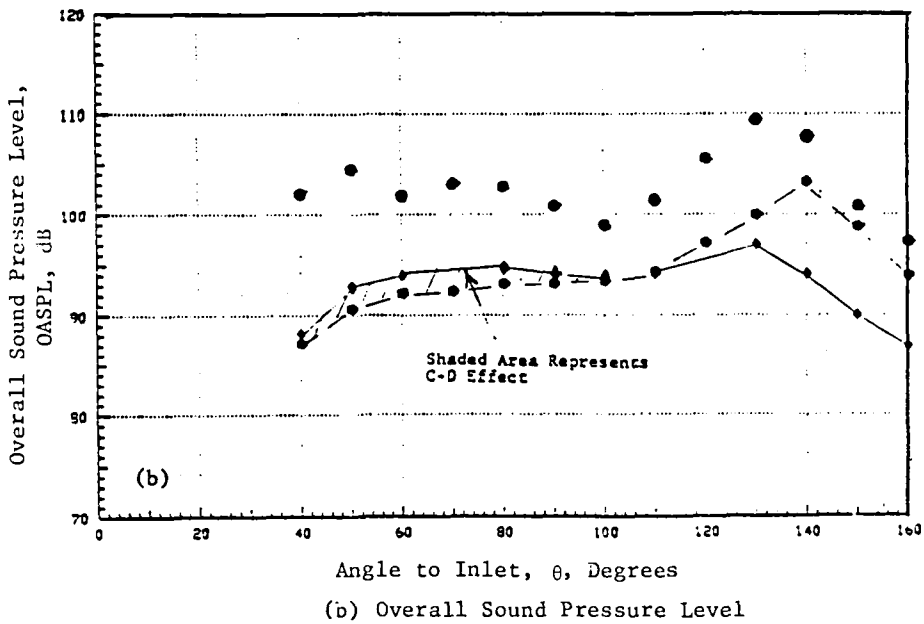
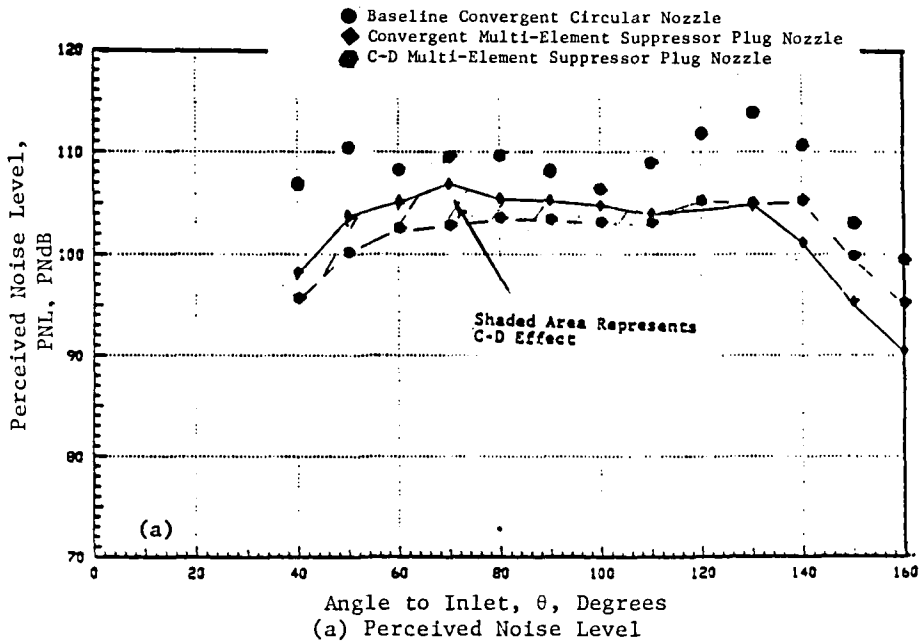


Figure 5.18. Simulated Flight PNL and OASPL Directivity Comparisons Between Baseline Convergent Circular Nozzle, Convergent Multi-Element Suppressor Plug Nozzle, and C-D Multi-Element Suppressor Plug Nozzle.

Typical spectral data corresponding to the flow conditions of Figures 5-17 and 5-18 are provided in Figures 5-19 and 5-20. A significant change in spectral shape is observed for both kinds of suppressor nozzles relative to the rather simple spectra of the baseline convergent circular nozzle.

It may be useful at this point to consider what factors contribute to the complexity of these spectra. When the jet from a suppressor plug nozzle is imperfectly expanded, it can have several mutually independent sound sources located over the wide region of its flow field. Major noise sources would be mixing noise sources (near the jet exit and downstream of the plug), shock screech and broadband shock noise sources (on the plug surface and downstream of the plug), and so-called excess noise sources due to the obstructions (chutes) in the flowpath of the jet. A characteristic length scale is associated with each of these sound sources. This scale is usually determined by the mechanisms which generate the flow irregularities (e.g., turbulence). In this particular case, the width of the mixing layer at any axial station is an appropriate local measure of the scale of the energy-containing eddies which determine the shock and mixing noise emission, and the maximum thickness of the obstruction (chute) may be an appropriate choice for the length scale associated with the excess noise. These length scales along with suitably selected characteristic velocity (or time) scales form Strouhal numbers which determine the corresponding peak emission frequencies. Since the sound emission directivity differs from one type of source (e.g., monopole) to another (e.g., dipole), the location of the peak frequency in a spectrum varies not only with the emission angle but also with the type of source.

An examination of a typical forward quadrant spectrum, say, at $\theta = 50^\circ$, indicates that, compared to the baseline convergent circular nozzle, the C-D suppressor nozzle shows significant noise reduction over the entire frequency range of interest. However, when compared to the convergent suppressor nozzle, the C-D termination appears to have advantages only in the high frequency region. Apparently, the C-D effectiveness is observed in the frequency range above 1 kHz. A rather low sound pressure level observed in the low to mid frequency range for the convergent suppressor nozzle may be attributed, as indicated by the LV test data presented in Section 6.0, to the higher mixing rate and hence higher mean velocity decay rate.

	Model	Test Point	P_r	T_{T_0} (°R)	V_j (ft/s)	$V_{a/c}$ (ft/s)
○	1	113	3.12	1707	2403	0
◇	5	513	3.13	1718	2412	0
○	6	613	3.13	1714	2410	0

- Baseline Convergent Circular Conic Nozzle
- ◇ Convergent Multi-Element Suppressor Plug Nozzle
- C-D Multi-Element Suppressor Plug Nozzle

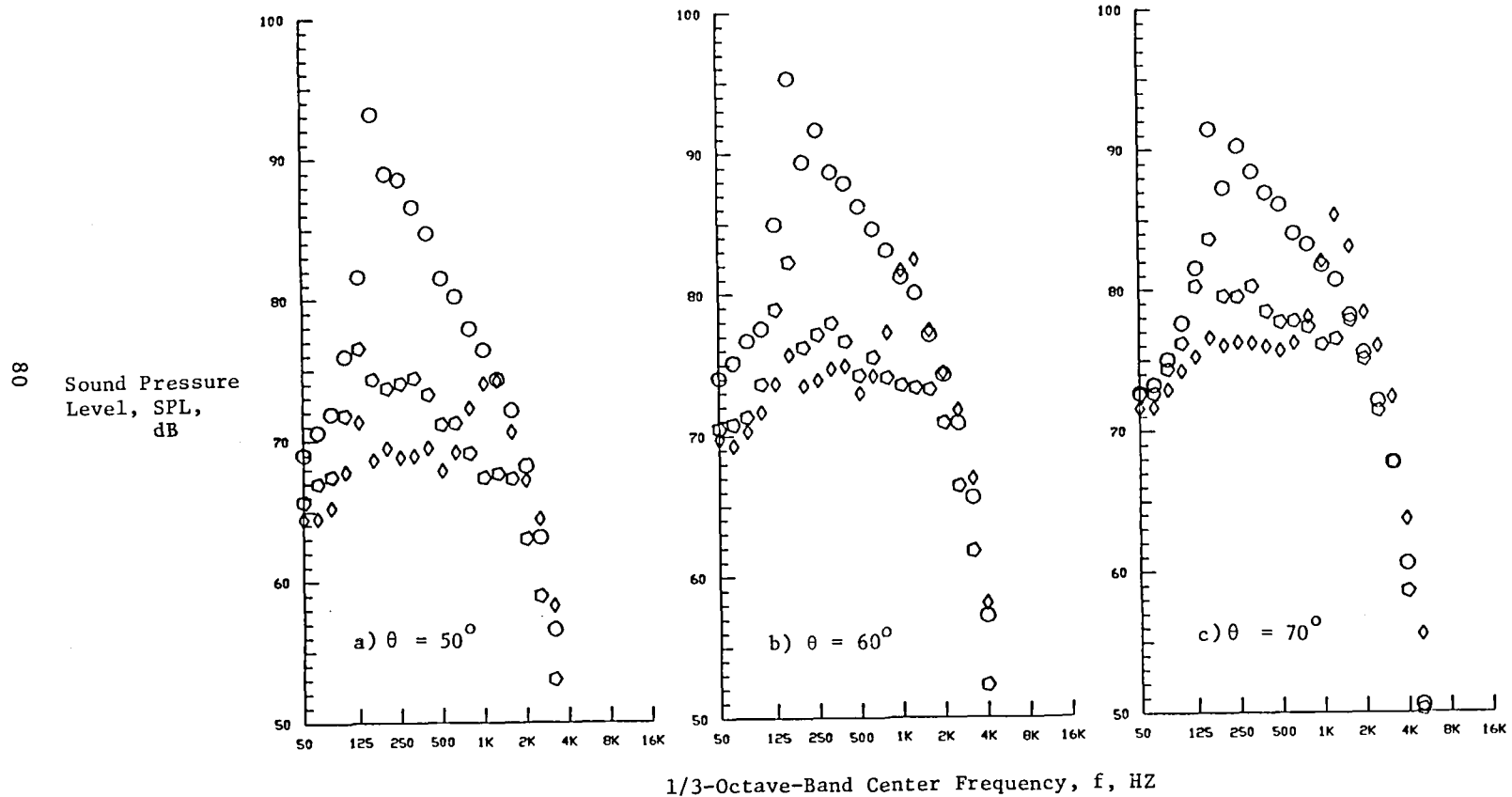


Figure 5-19. Static Spectral Comparison Between Baseline Convergent Circular Nozzle, Convergent Multi-Element Suppressor Plug Nozzle, and C-D Multi-Element Suppressor Plug Nozzle.

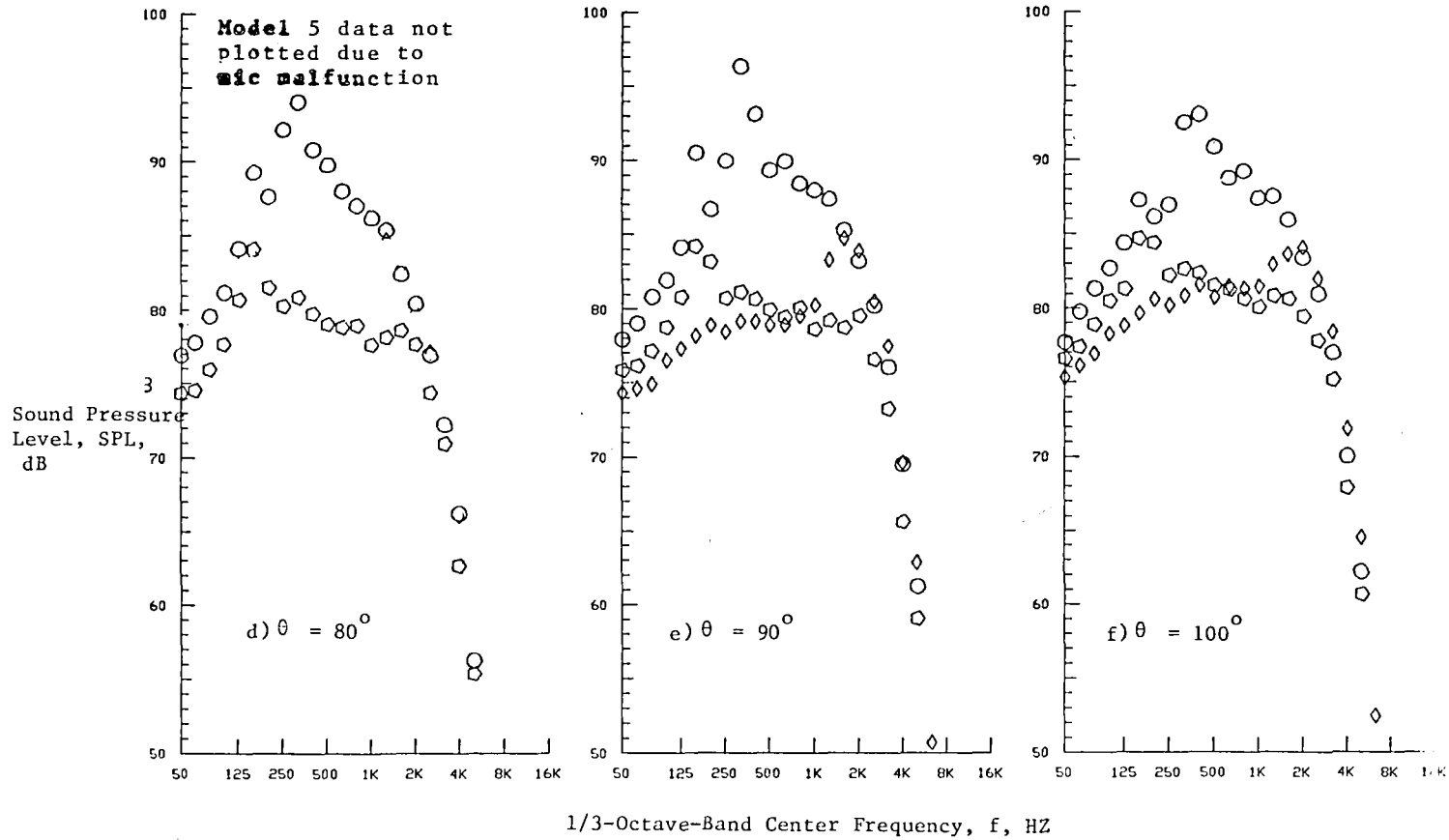


Figure 5-19. (Cont'd). Static Spectral Comparison Between Convergent Circular Nozzle, Convergent Multi-Element Suppressor Plug Nozzle, and C-D Multi-Element Suppressor Plug Nozzle.

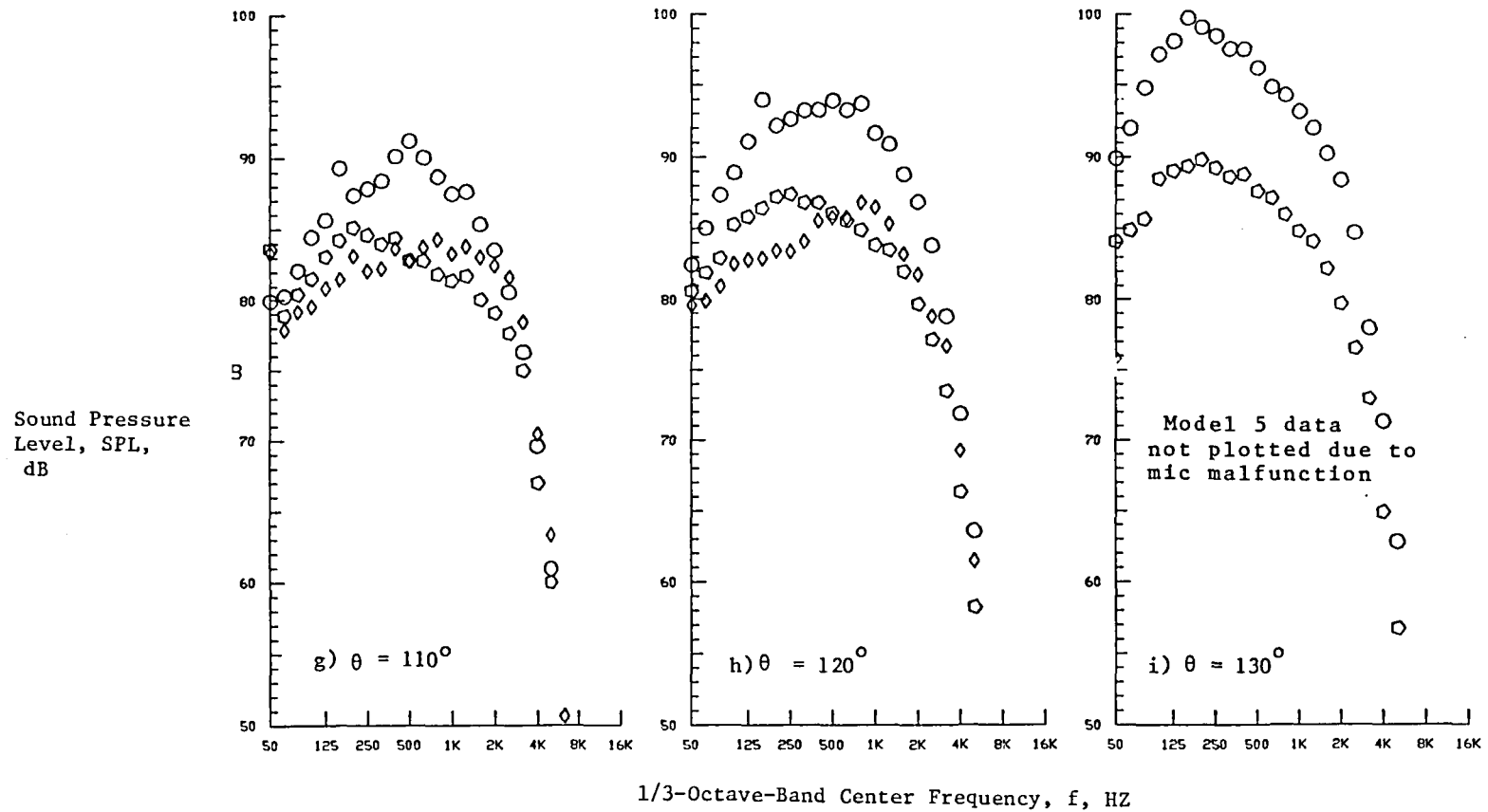


Figure 5-19. (Cont'd). Static Spectral Comparison Between Convergent Circular Nozzle, Convergent Multi-Element Suppressor Plug Nozzle, and C-D Multi-Element Suppressor Plug Nozzle.

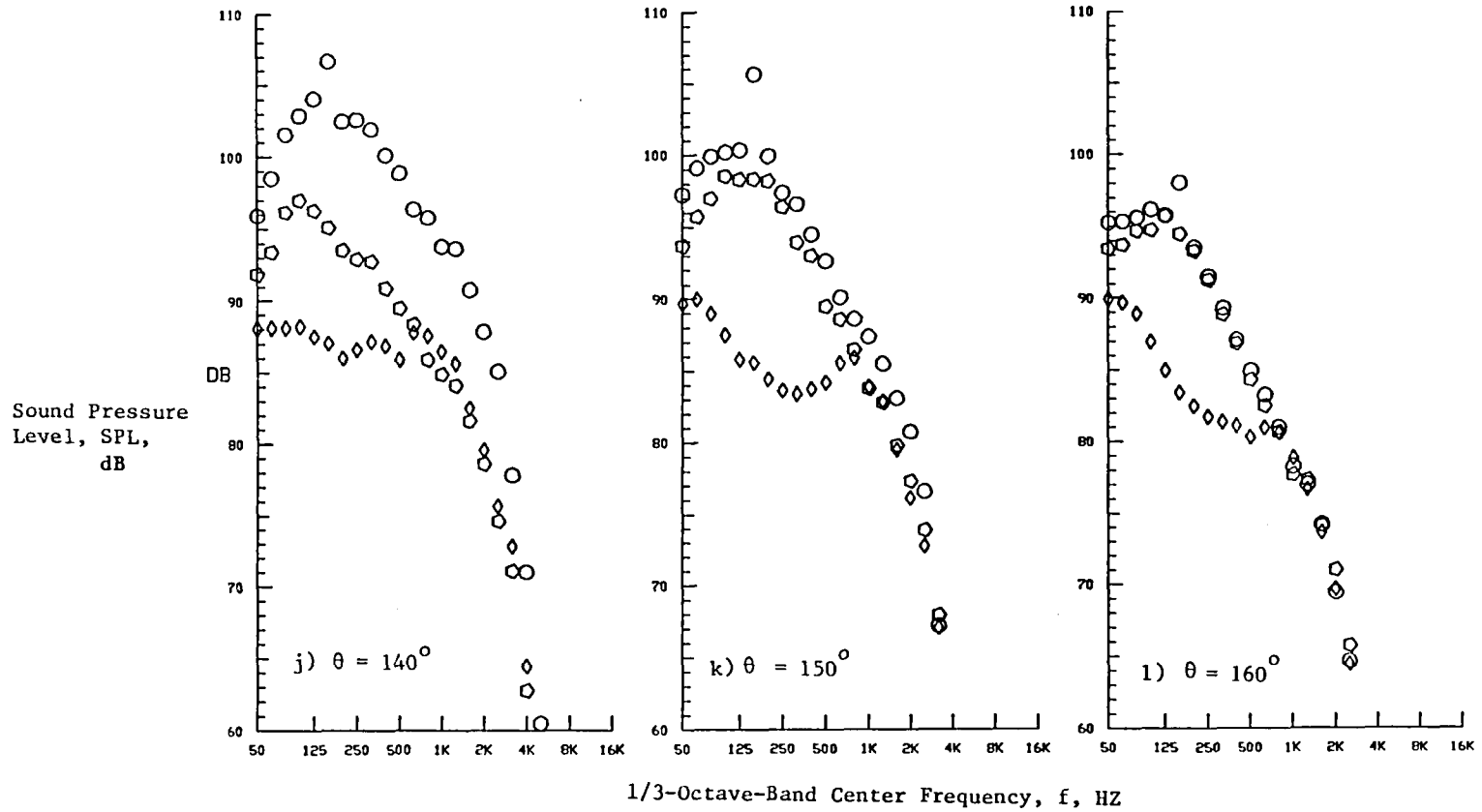


Figure 5-19. (Concluded) Static Spectral Comparison Between Convergent Circular Nozzle, Convergent Multi-Element Suppressor Plug Nozzle, and C-D Multi-Element Suppressor Plug Nozzle.

	Model	Test Point	P_r	T_T ($^{\circ}R$)	V_j (f/s)	$V_{a/c}$ (f/s)
●	1	114	3.13	1715	2410	400
◆	5	514	3.12	1706	2401	400
●	6	614	3.13	1720	2414	400

- Baseline Convergent Circular Conic Nozzle
- ◆ Convergent Multi-Element Suppressor Plug Nozzle
- C-D Multi-Element Suppressor Plug Nozzle

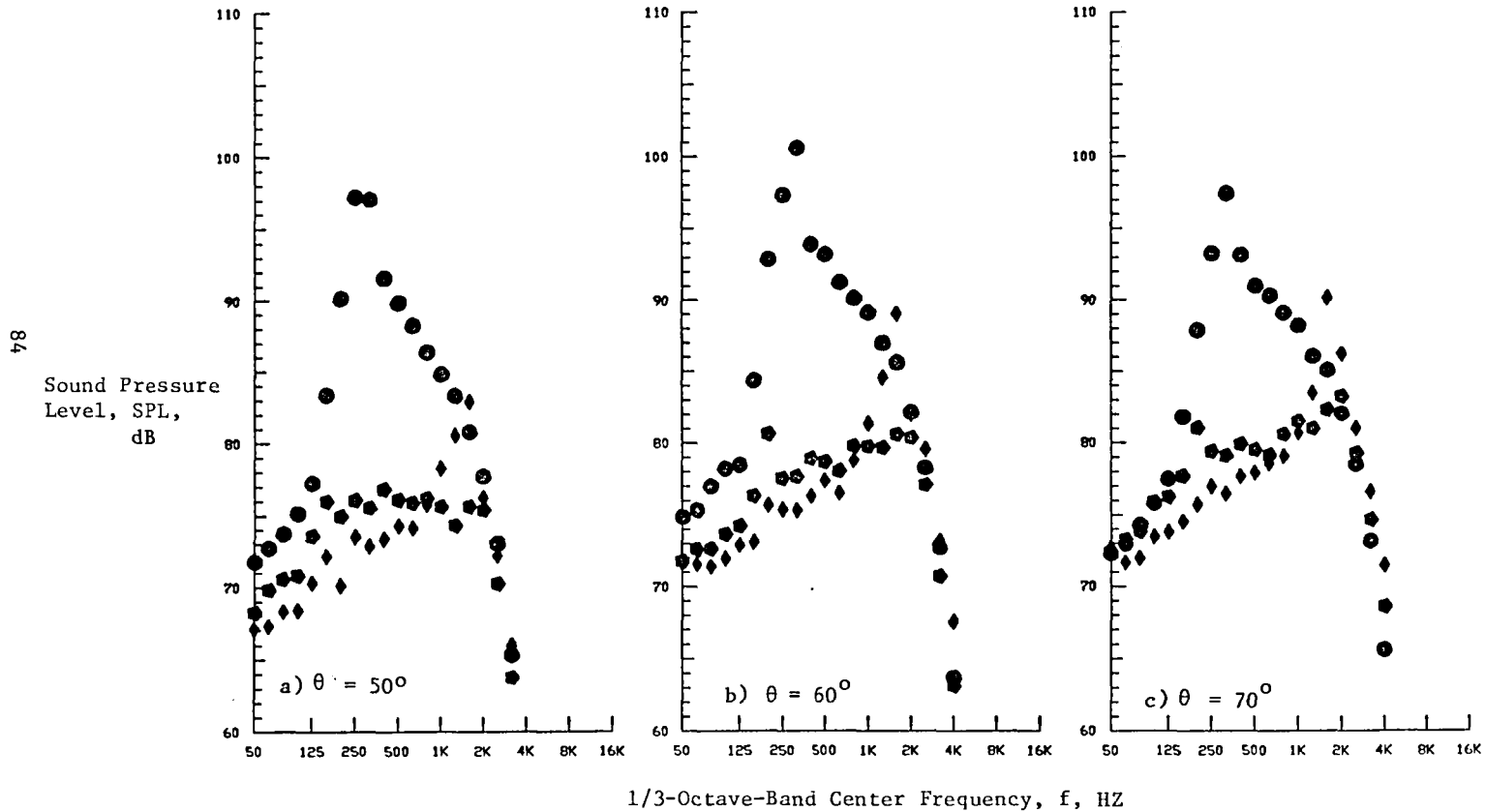


Figure 5-20. Simulated Flight Spectral Comparison Between Baseline Convergent Circular Nozzle, Convergent Multi-Element Suppressor Plug Nozzle, and C-D Multi-Element Suppressor Plug Nozzle.

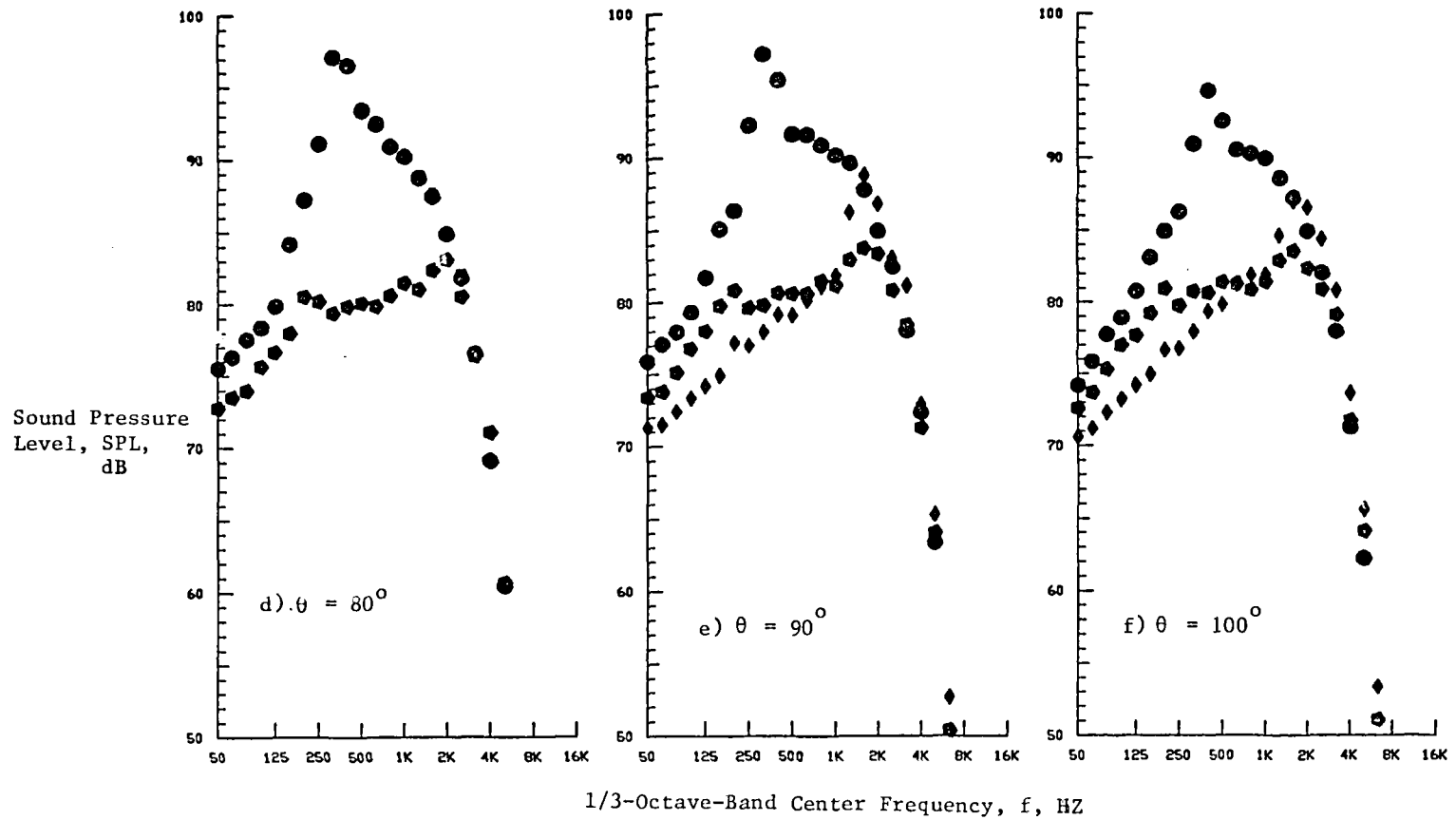


Figure 5-20. (Cont'd). Simulated Flight Spectral Comparison Between Baseline Convergent Circular Nozzle, Convergent Multi-Element Suppressor Plug Nozzle, and C-D Multi-Element Suppressor Plug Nozzle.

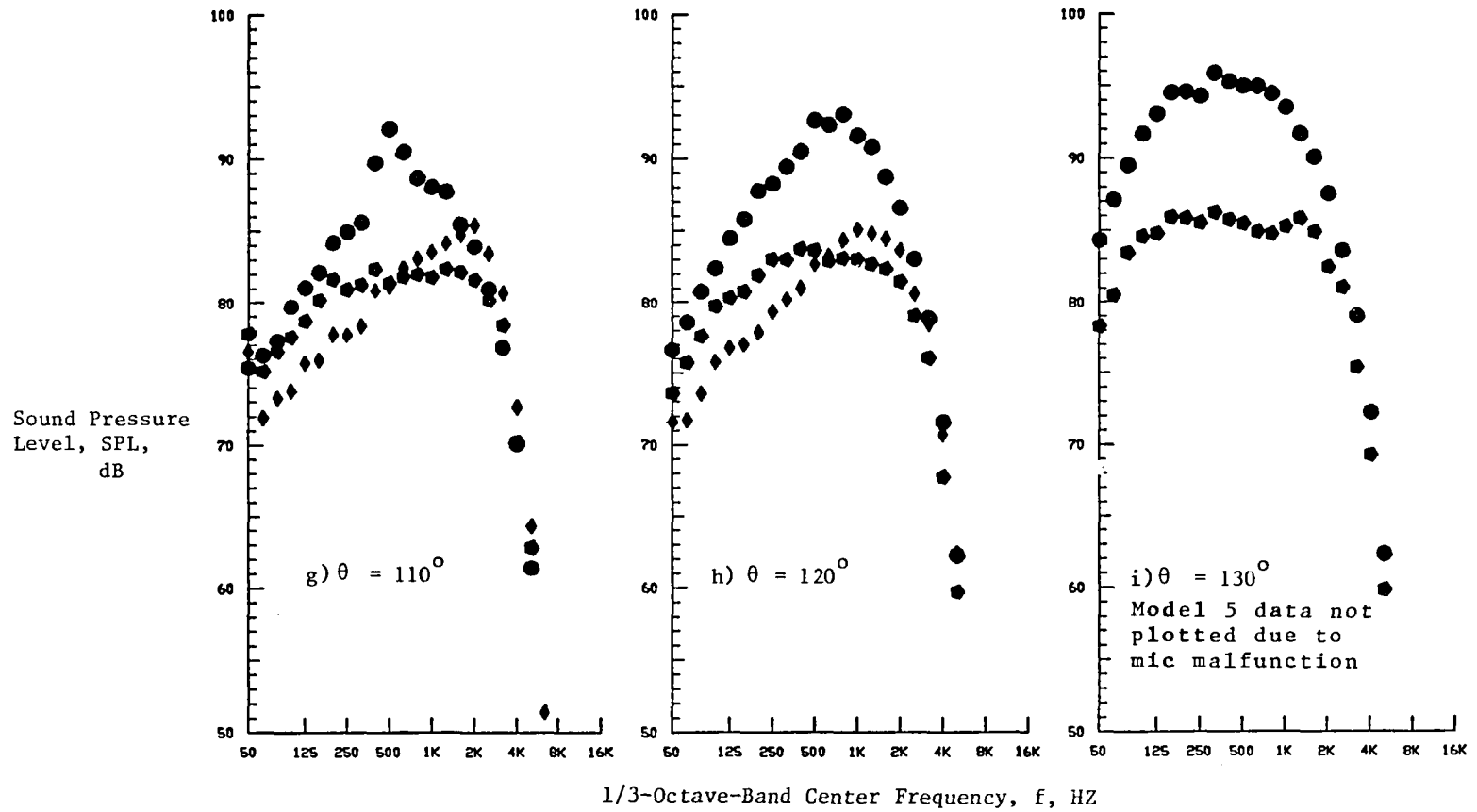


Figure 5-20. (Cont'd). Simulated Flight Spectral Comparison Between Baseline Convergent Circular Nozzle, Convergent Multi-Element Suppressor Plug Nozzle, and C-D Multi-Element Suppressor Plug Nozzle.

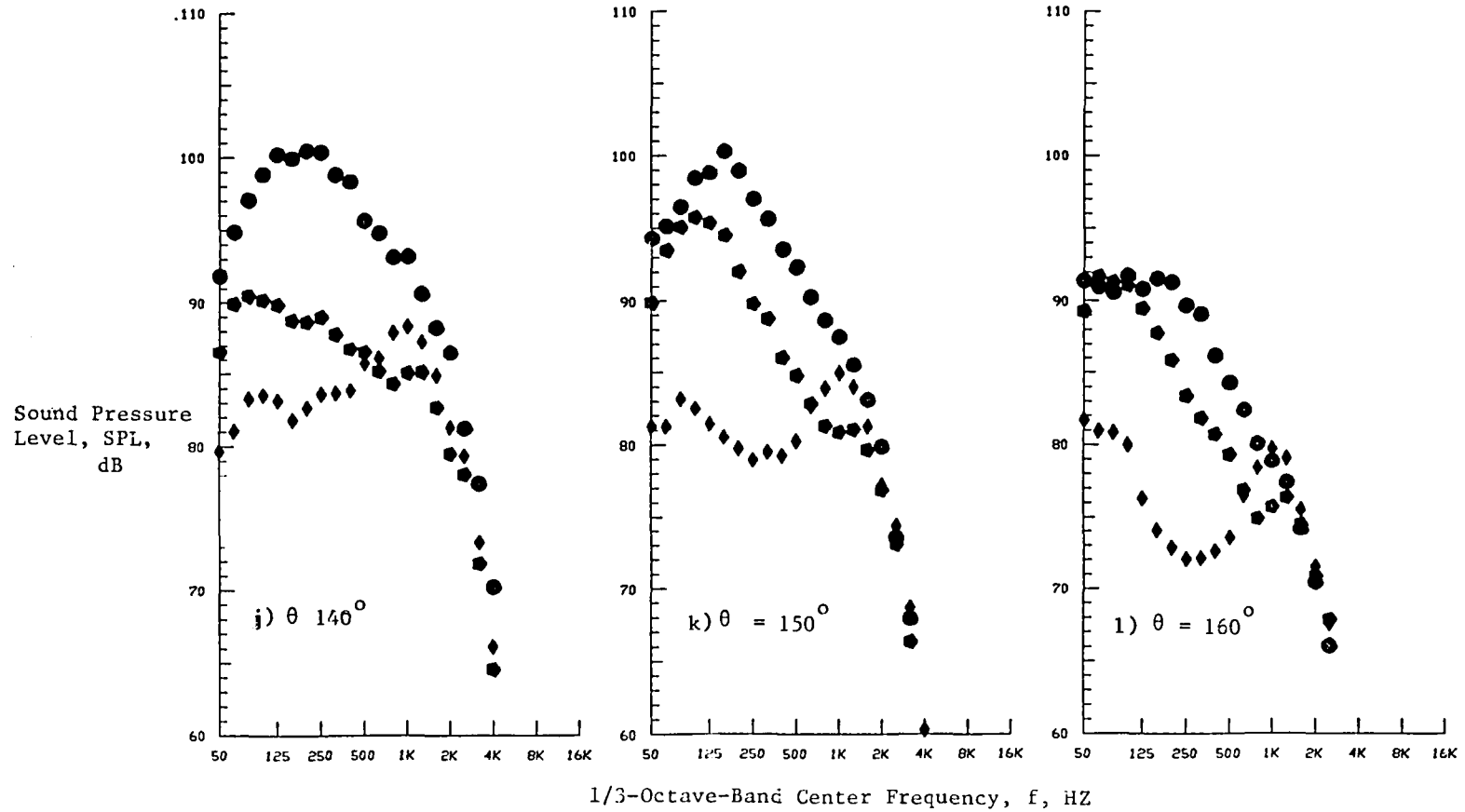


Figure 5-20. (Concluded). Simulated Flight Spectral Comparison Between Baseline Convergent Circular Nozzle, Convergent Multi-Element Suppressor Plug Nozzle, and C-D Multi-Element Suppressor Plug Nozzle.

Corresponding spectra obtained under simulated flight conditions is presented in Figure 5-20. A static-to-flight comparison of the 50° spectra reveals a significant forward quadrant amplification of high frequencies for both suppressor nozzles.

Finally, it may be useful to illustrate the overall acoustic efficiency of the C-D suppressor nozzle in terms of power level. This is presented in Figure 5-21 where corresponding PWL spectra for the baseline convergent circular and the convergent multi-element suppressor plug nozzles are included also. Selected test points are identical to those in Figure 5-18. The comparison indicates that over the wide range of frequencies, suppressor nozzles generate less noise relative to the convergent circular nozzle and the C-D suppressor nozzle has benefits in higher frequencies while the convergent suppressor nozzle radiates significantly less amount of low to mid frequency noise compared to the other two. To conclude the discussions on the assessment of noise reduction by the convergent-divergent termination, significant results from the analyses of this subsection are summarized below:

- Effectiveness of the convergent-divergent termination in the flowpath in reducing front-quadrant noise has been demonstrated with the C-D circular, C-D annular and C-D suppressor nozzles under both static and simulated flight conditions. Maximum reduction in PNL_{50° relative to the baseline convergent circular nozzle was:
 - 7.5 (static) and 11 (flight) PNdB for the C-D circular nozzle at the design condition
 - 6 (static) and 8 (flight) PNdB for the C-D annular nozzle (but essentially no suppression relative to the convergent annular nozzle)
 - 9.5 (static) and 10 (flight) PNdB for the C-D multi-element suppressor nozzle (but only 2 to 3 PNdB reduction relative to the convergent suppressor).

- The C-D benefit on the circular, annular plug and suppressor plug nozzle data is observed over a broad range of pressure ratios in the vicinity of the design condition.

Symbol	Modal	Test Point	P_r	T_{T^*} ($^{\circ}R$)	V_j (ft/s)	$V_{a/c}$ (ft/s)
●	1	113	3.12	1707	2403	0
■	5	513	3.13	1718	2412	0
▲	6	613	3.13	1714	2410	0

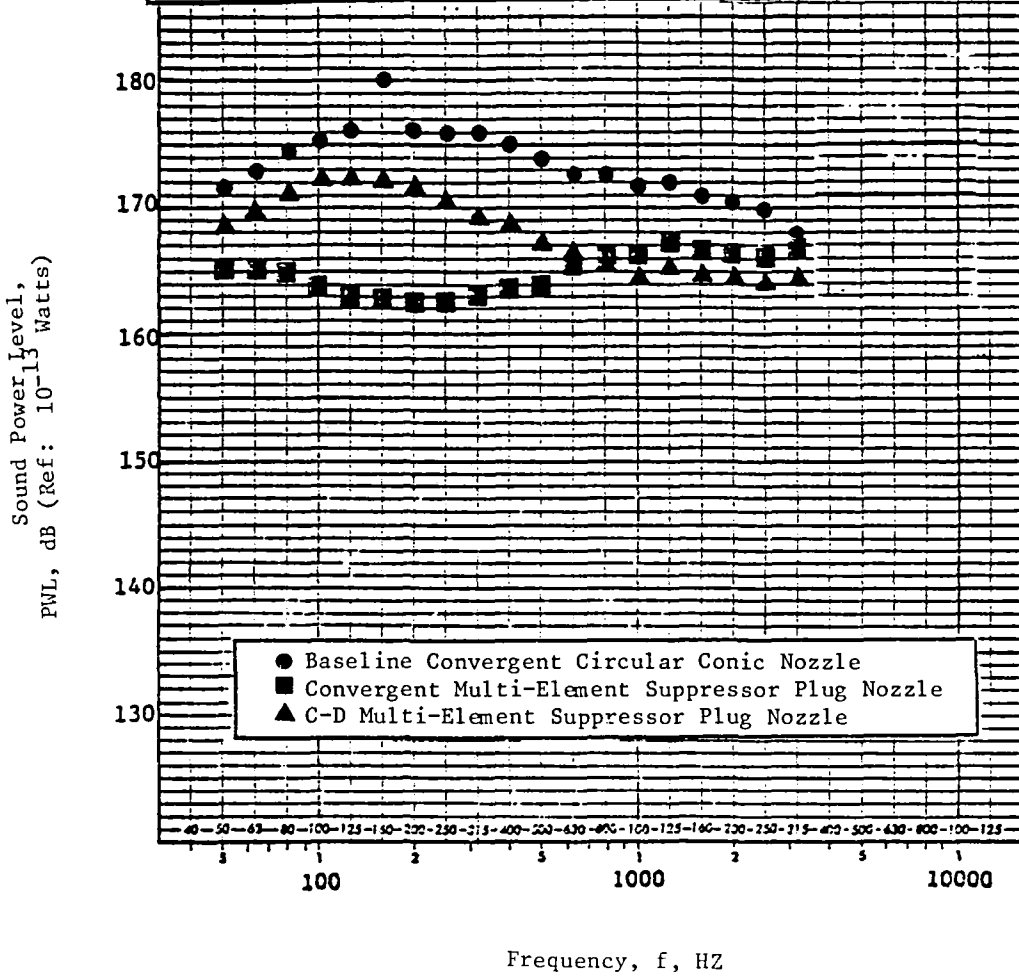


Figure 5-21. PWL Comparison Between Baseline Convergent Circular Nozzle, Convergent Multi-Element Suppressor Plug Nozzle, and C-D Multi-Element Suppressor Plug Nozzle. (Static)

- At the C-D design condition, the multi-element C-D suppressor plug nozzle yielded suppression to the extent of 9 PNdB at $\theta = 130^\circ$ during both static and simulated flight tests relative to the baseline convergent circular nozzle. The corresponding reductions by the multi-element convergent suppressor plug nozzle were somewhat larger than those of its C-D counterpart and 12 and 9 PNdB reductions were observed at $\theta = 130^\circ$ under static and simulated flight conditions, respectively.
- The C-D annular plug nozzle possibly produces shock noise even at the C-D design condition because of the shock system formed downstream of the plug due to the plug curvature.
- Complete shock noise suppression was not achieved by the C-D termination in the chute flowpath incorporated in the multielement suppressor plug nozzle tested during the present program.

5.2 INFLUENCE OF FLIGHT, JET TEMPERATURE AND NOZZLE GEOMETRY ON SHOCK-CELL NOISE

In this subsection, discussions on the influence of simulated aircraft motion, plume temperature and nozzle geometry on the shock-cell noise are presented. As before, unless otherwise stated, all the acoustic data presented in this subsection are scaled to a typical engine size of 1400 in.² at a 2400 foot sideline distance.

5.2.1 INFLUENCE OF FLIGHT ON SHOCK-CELL NOISE

In this subsection, static-to-flight comparisons are made in order to determine whether acoustic benefits of various nozzles over the baseline convergent circular nozzle under static conditions are retained in flight. PNL directivity and acoustic spectra are compared for typical underexpanded and overexpanded conditions, in addition to the ideally expanded flow condition.

5.2.1.1 C-D Circular Nozzle (Model 2)

The influence of flight on the shock associated noise produced by the C-D circular nozzle (Model 2) is first examined. Figures 5-22 through 5-27 illustrate static-to-flight PNL and spectral comparisons between the C-D circular and the baseline convergent circular nozzle data.

Figure 5-22 presents static-to-flight PNL comparison between these nozzles at overexpanded flow conditions. An examination of this figure indicates that the flight amplification in the front quadrant for the convergent circular nozzle is significantly larger compared to that for its C-D counterpart under the given operating conditions. This result indicates that the convergent circular nozzle has a stronger broadband shock noise contribution. Consequently, in the front quadrant, larger noise reduction due to the C-D termination is observed under the simulated flight conditions than under the static conditions. A typical mixing noise attenuation is noted, in this figure, for the PNL data in the aft quadrant. Up to $\theta = 130^\circ$ where PNL takes a maximum value, the same trend as that observed in the forward quadrant is noted. At the emission angles larger than $\theta = 130^\circ$, no systematic trend is observed.

Static-to-flight spectral comparisons of the C-D circular nozzle acoustic data to the baseline convergent circular nozzle under identical flow conditions are presented in Figure 5-23 at twelve selected acoustic angles. A typical front quadrant spectrum comparison (e.g., at $\theta = 60^\circ$) shows that a significant mitigation of sound pressure level due to the C-D termination is observed, primarily in the high frequency region for both static and simulated flight cases. Again, larger reduction in SPL due to the C-D termination is observed for the simulated flight case compared to the static case. In the aft quadrant (e.g., at $\theta = 130^\circ$), in-flight noise reduction over the entire frequency range is noted. However, practically no influence of flight is observed on the magnitude of the noise reduction due to the convergent-divergent termination, which is negligible.

Corresponding PNL and spectral static-to-flight comparisons at the C-D design point are presented in Figures 5-24 and 5-25. We note, by comparing Figures 5-22 and 5-24, that somewhat less PNL amplification by flight is observed in the front quadrant at the C-D design point, as compared to that

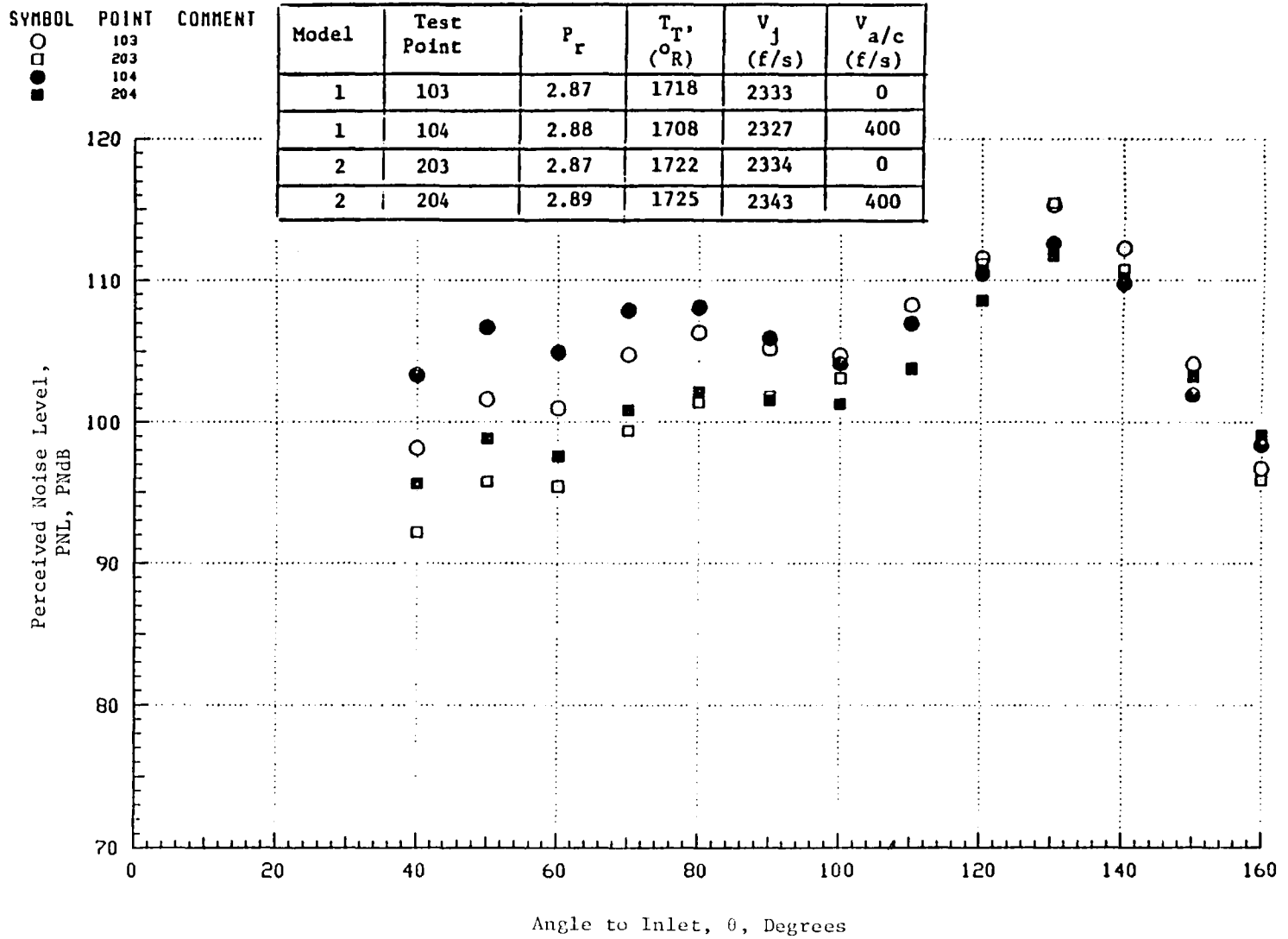


Figure 5-22. Static-to-Flight PNL Comparison at Overexpanded Flow Conditions; Convergent Circular (Model 1) and C-D Circular (Model 2) Nozzles.

SYMBOL POINT
 ○ 103
 □ 203
 ⊙ 104
 ■ 204

Model	Test Point	P_r	T_{T^*} (°R)	V_j (ft/s)	$V_{a/c}$ (ft/s)
1	103	2.87	1718	2333	0
1	104	2.88	1708	2327	400
2	203	2.87	1722	2334	0
2	204	2.89	1725	2334	400

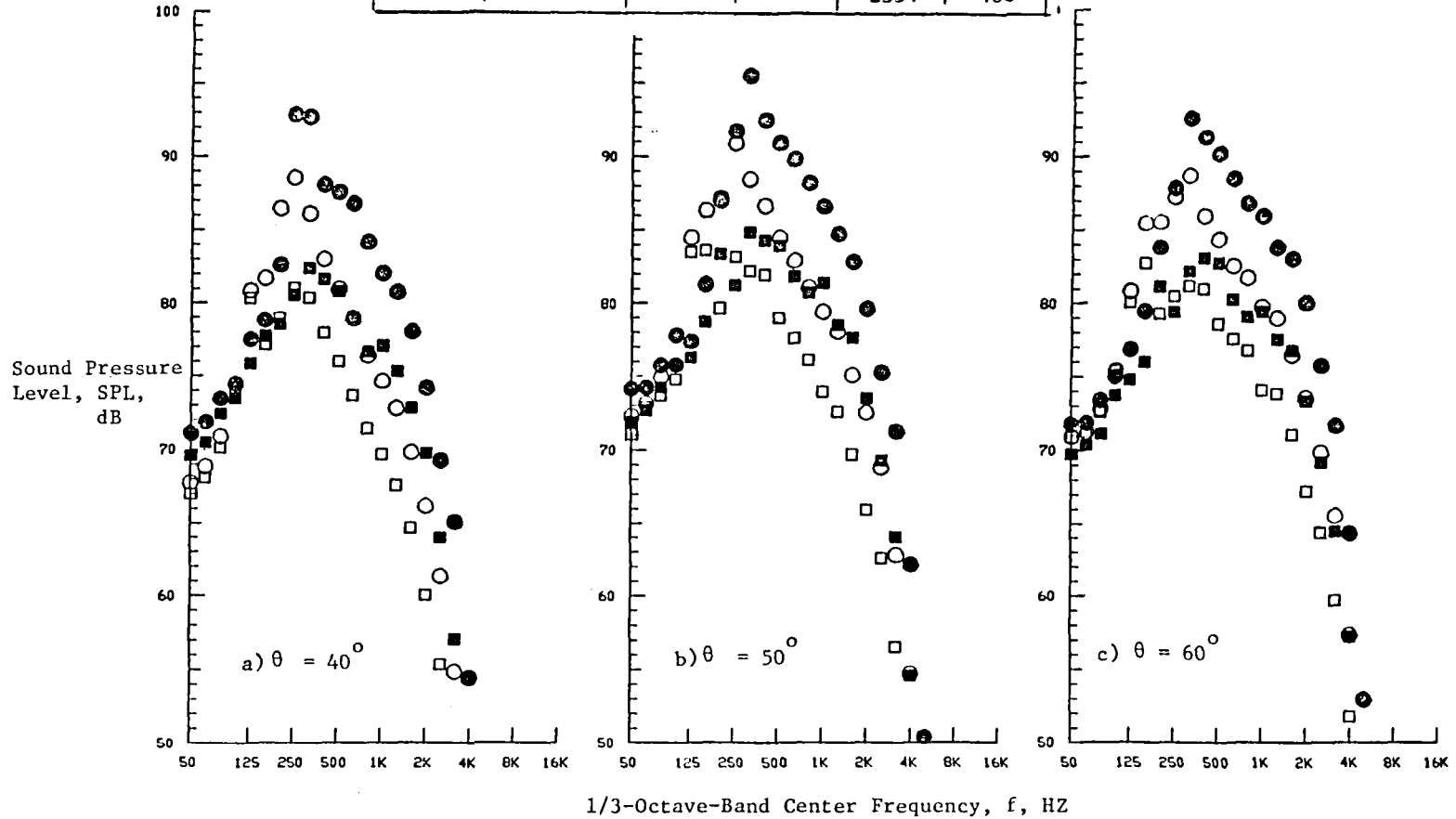
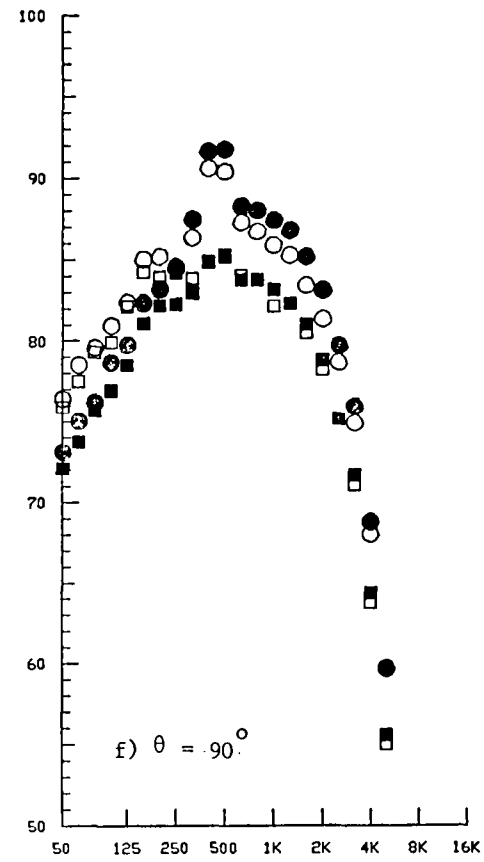
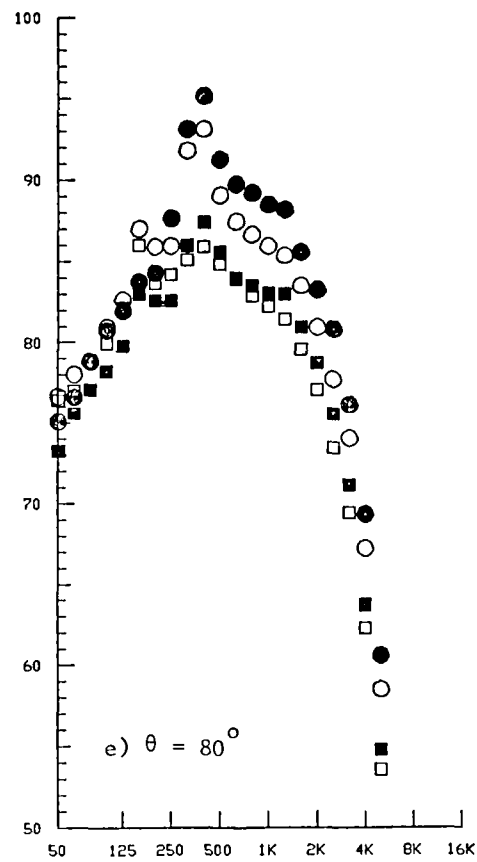
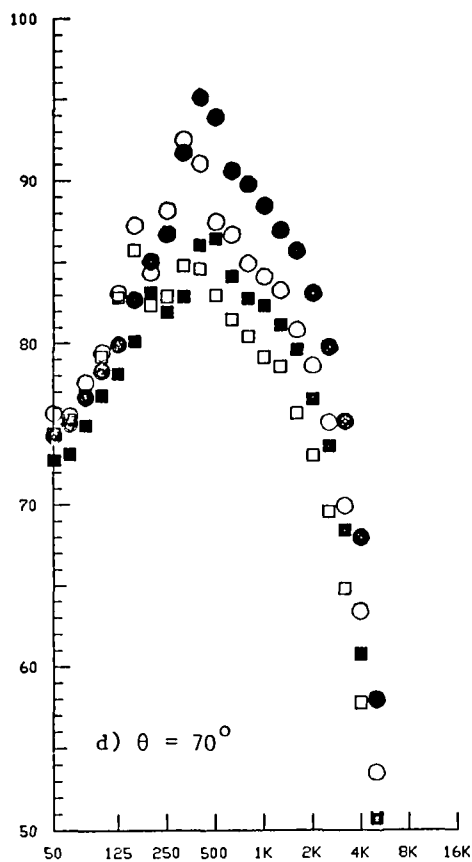


Figure 5-23. Static-to-Flight Spectral Comparison at Overexpanded Flow Conditions; Convergent Circular (Model 1) and C-D Circular (Model 2) Nozzles.

SYMBOL	POINT
○	103
□	203
●	104
■	204

Sound
Pressure
Level, SPL,
dB

94



1/3-Octave-Band Center Frequency, f, Hz

Figure 5-23. (Cont'd.) Static-to-Flight Spectral Comparison at Overexpanded Flow Conditions, Convergent Circular (Model 1) and C-D Circular (Model 2) Nozzles.

SYMBOL	POINT
○	103
□	203
●	104
■	204

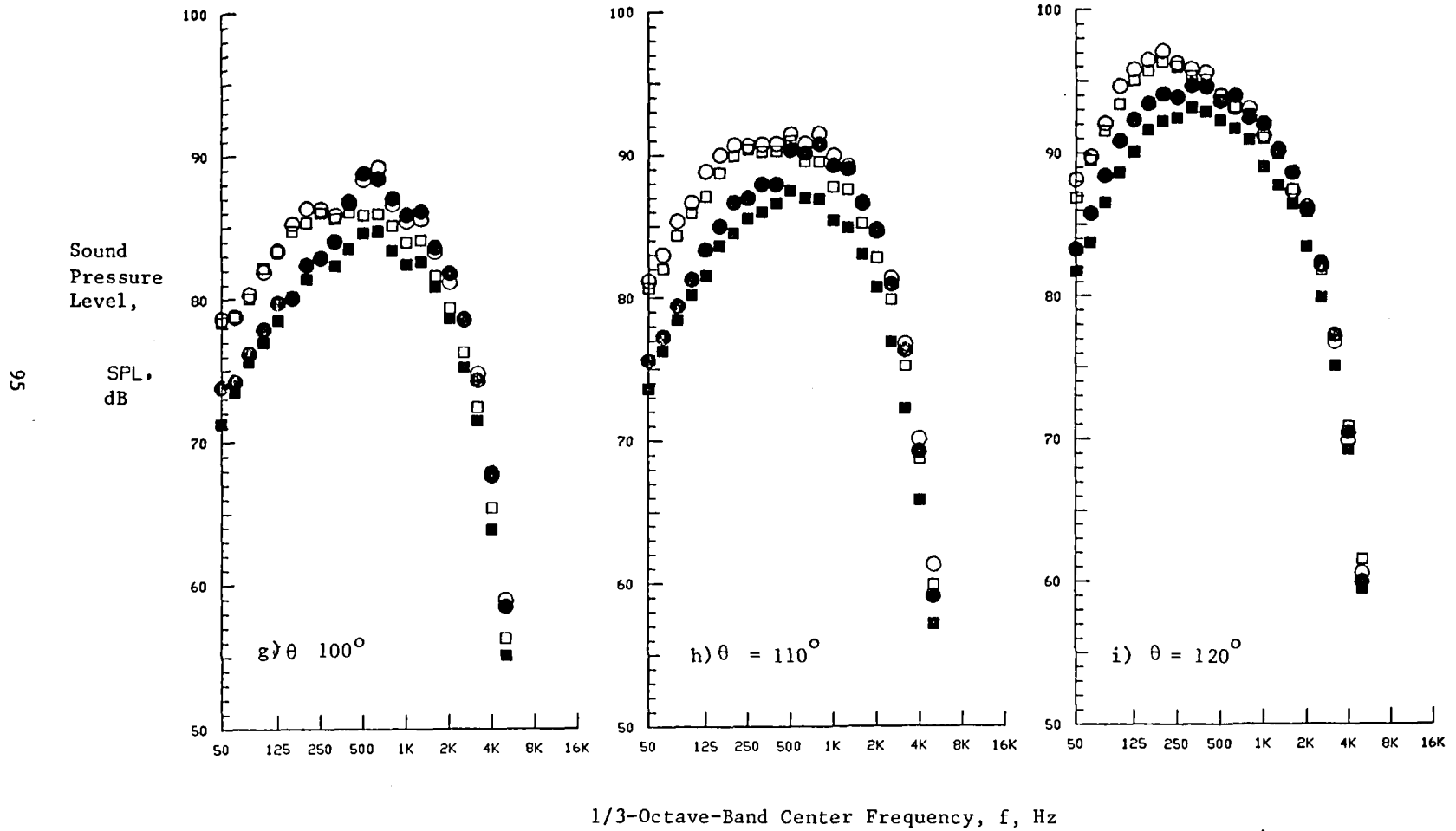


Figure 5-23. (Cont'd). Static-to-Flight Spectral Comparison at Overexpanded Flow Condition, Convergent Circular (Model 1) and C-D Circular (Model 2) Nozzles.

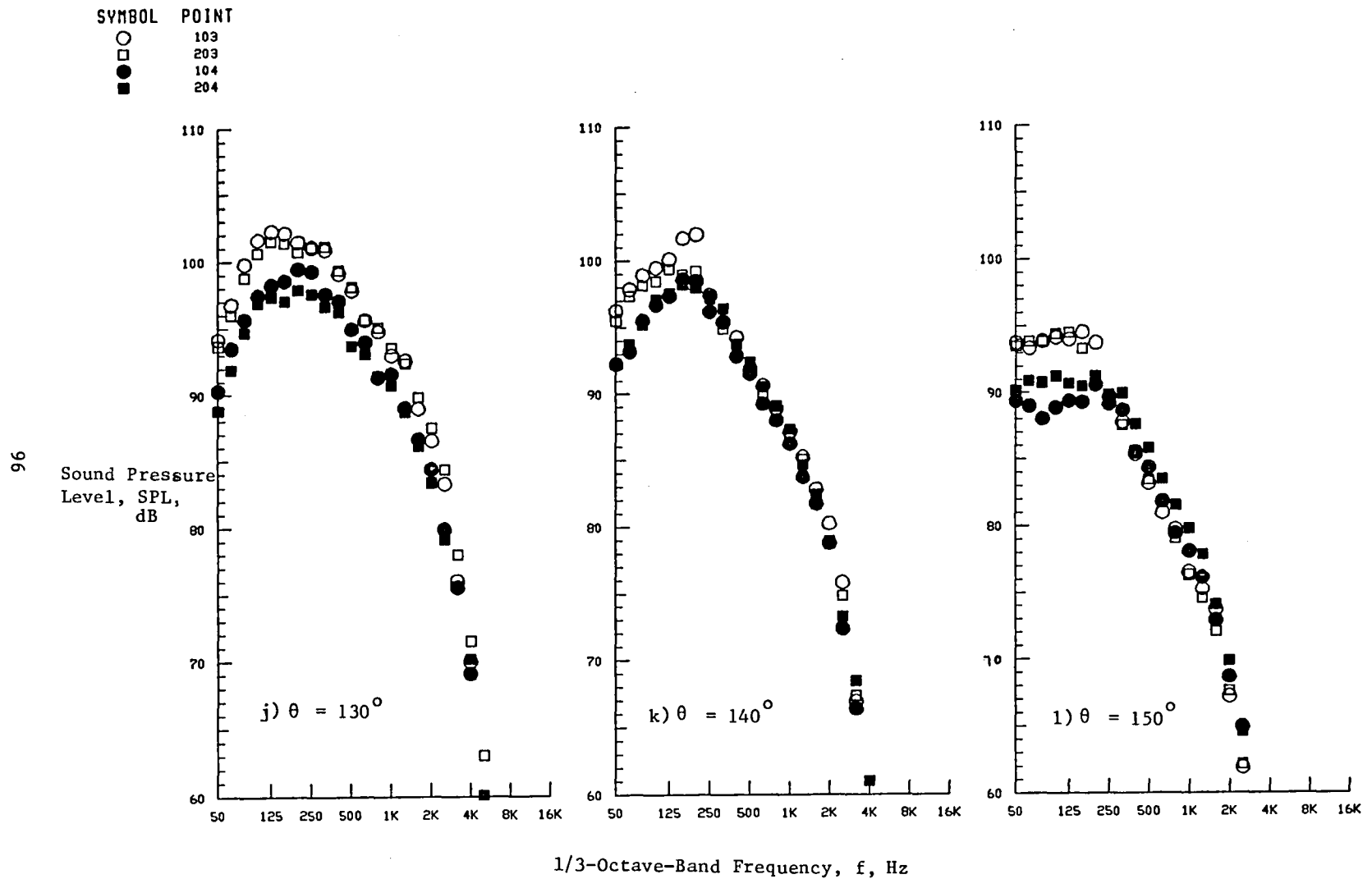


Figure 5-23. (Concluded). Static-to-Flight Spectral Comparison at Overexpanded Flow Condition, Convergent Circular (Model 1) and C-D Circular (Model 2) Nozzles.

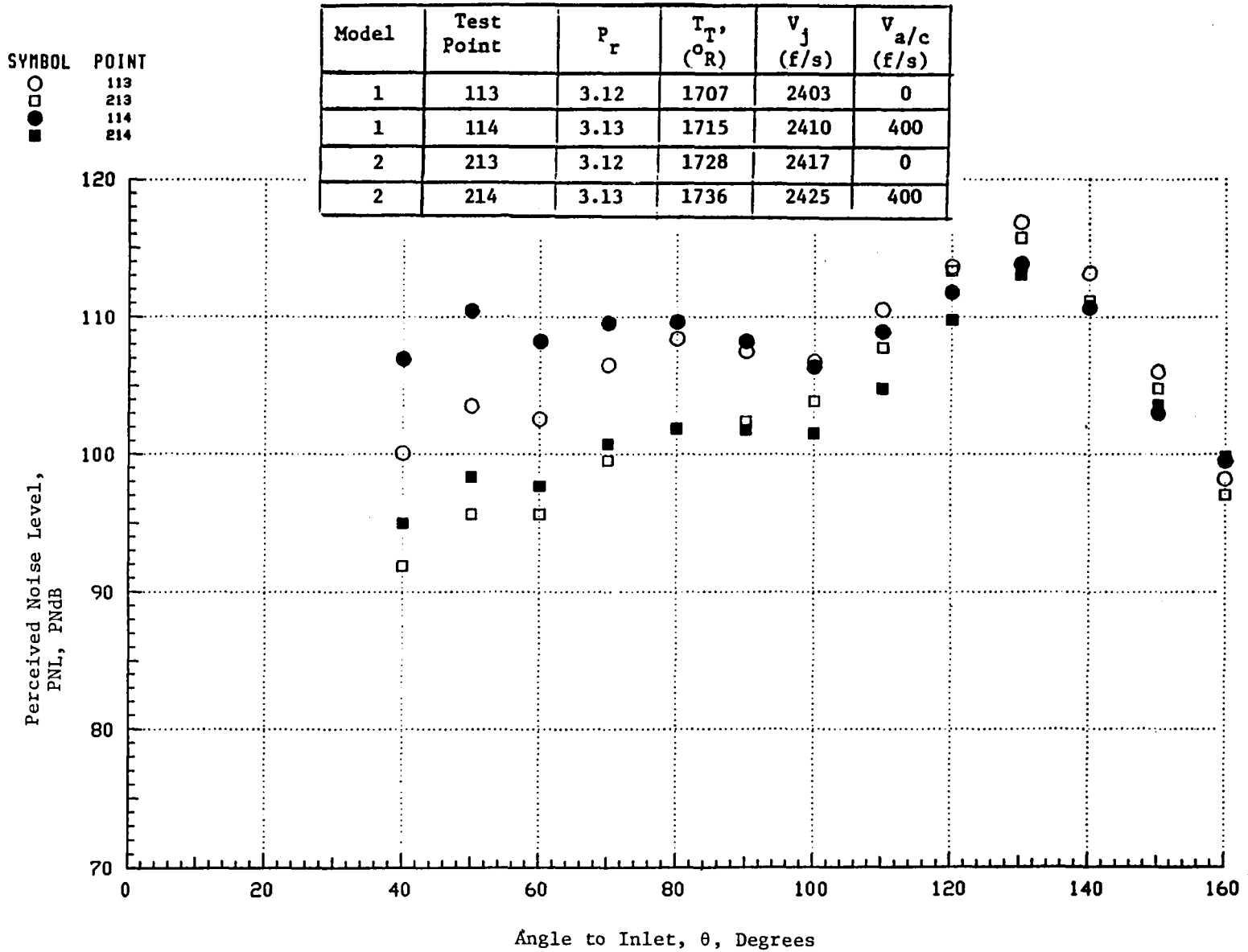


Figure 5-24. Static-to-Flight PNL Comparison at Design Operating Conditions; Convergent Circular (Model 1) and C-D Circular (Model 2) Nozzles.

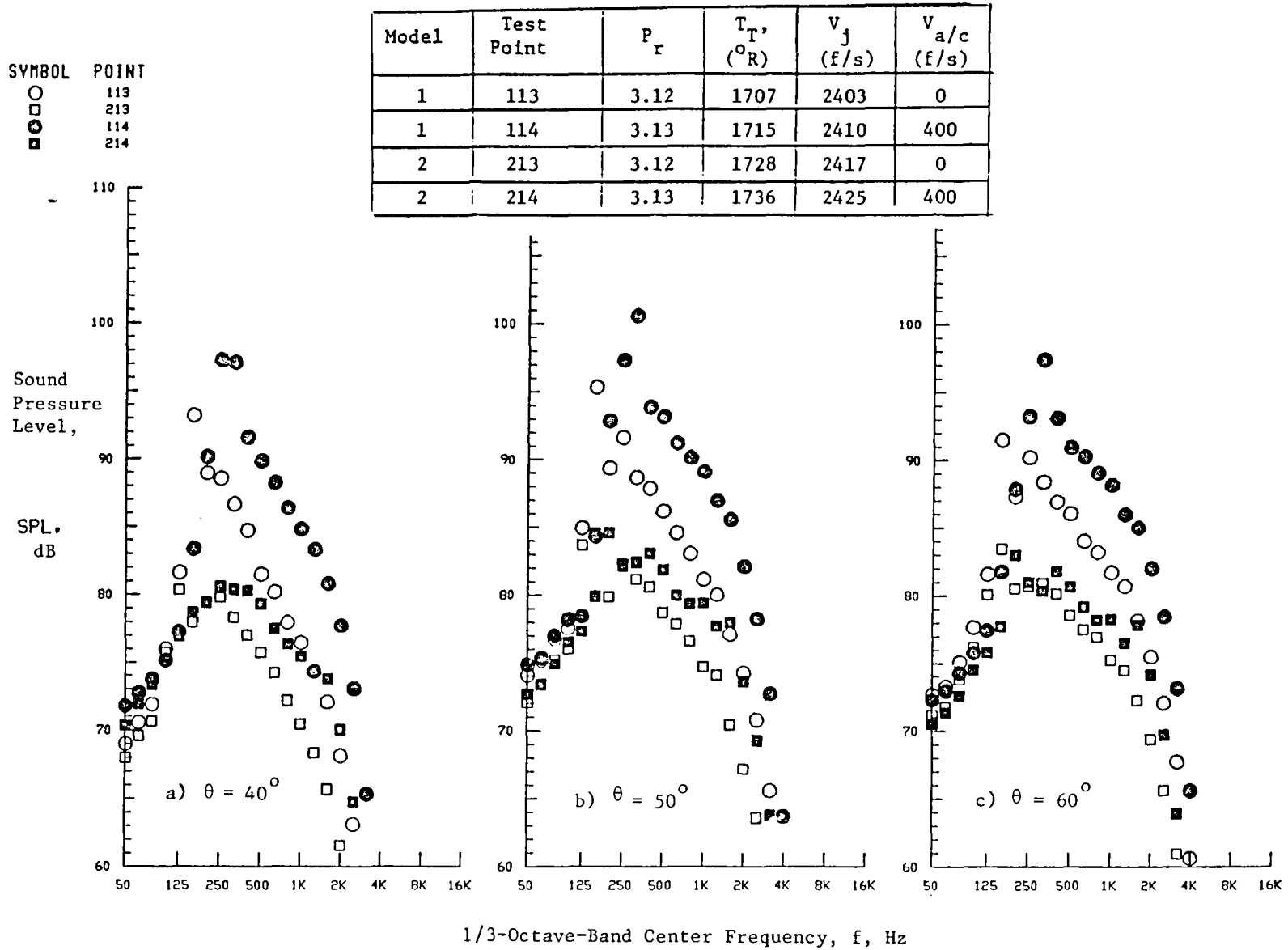


Figure 5-25. Static-to-Flight Spectral Comparison at Design Operating Conditions; Convergent Circular (Model 1) and C-D Circular (Model 2) Nozzles.

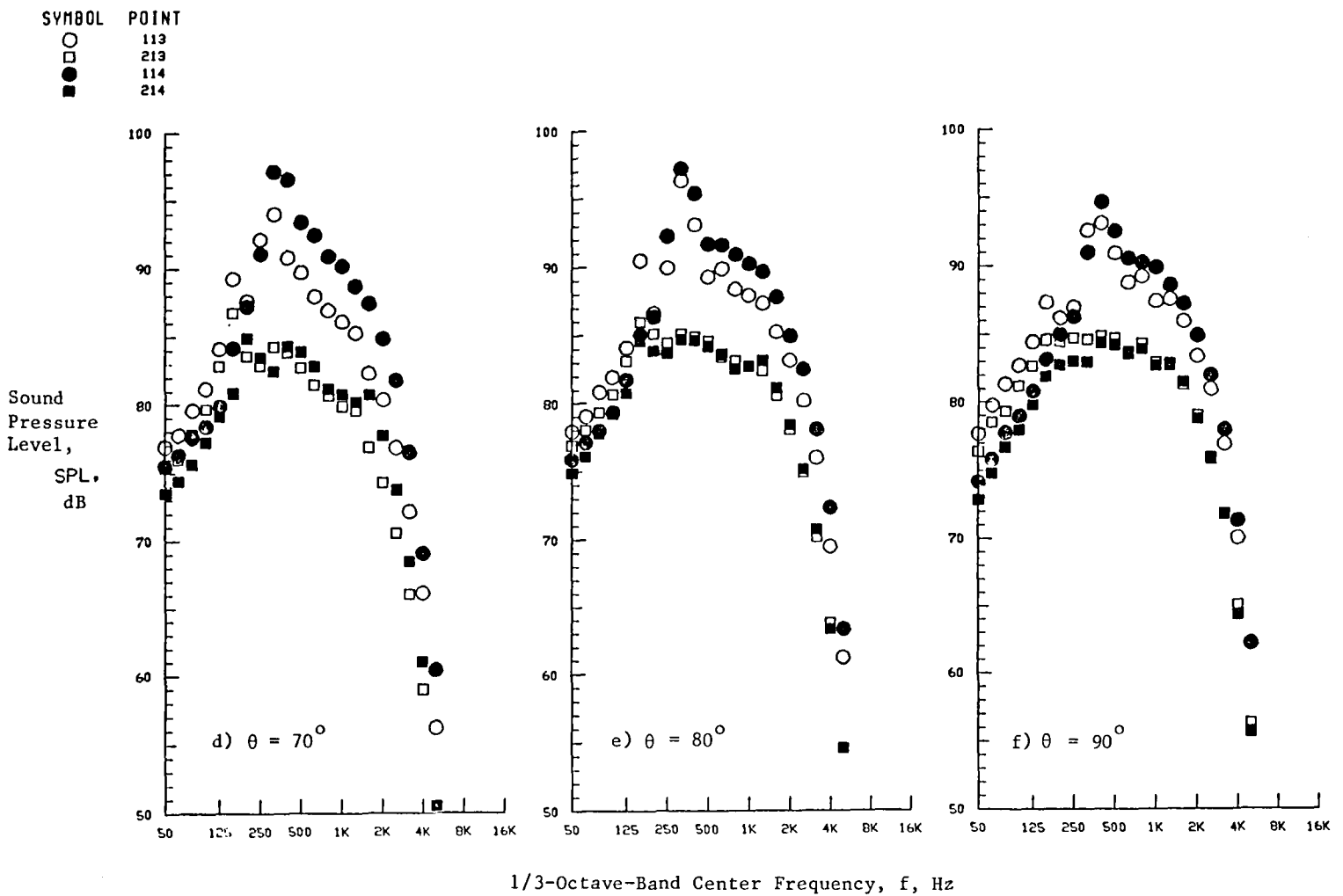


Figure 5-25. (Cont'd.) Static-to-Flight Spectral Comparison at Design Operation Conditions; Convergent Circular (Model 1) and C-D Circular (Model 2) Nozzles.

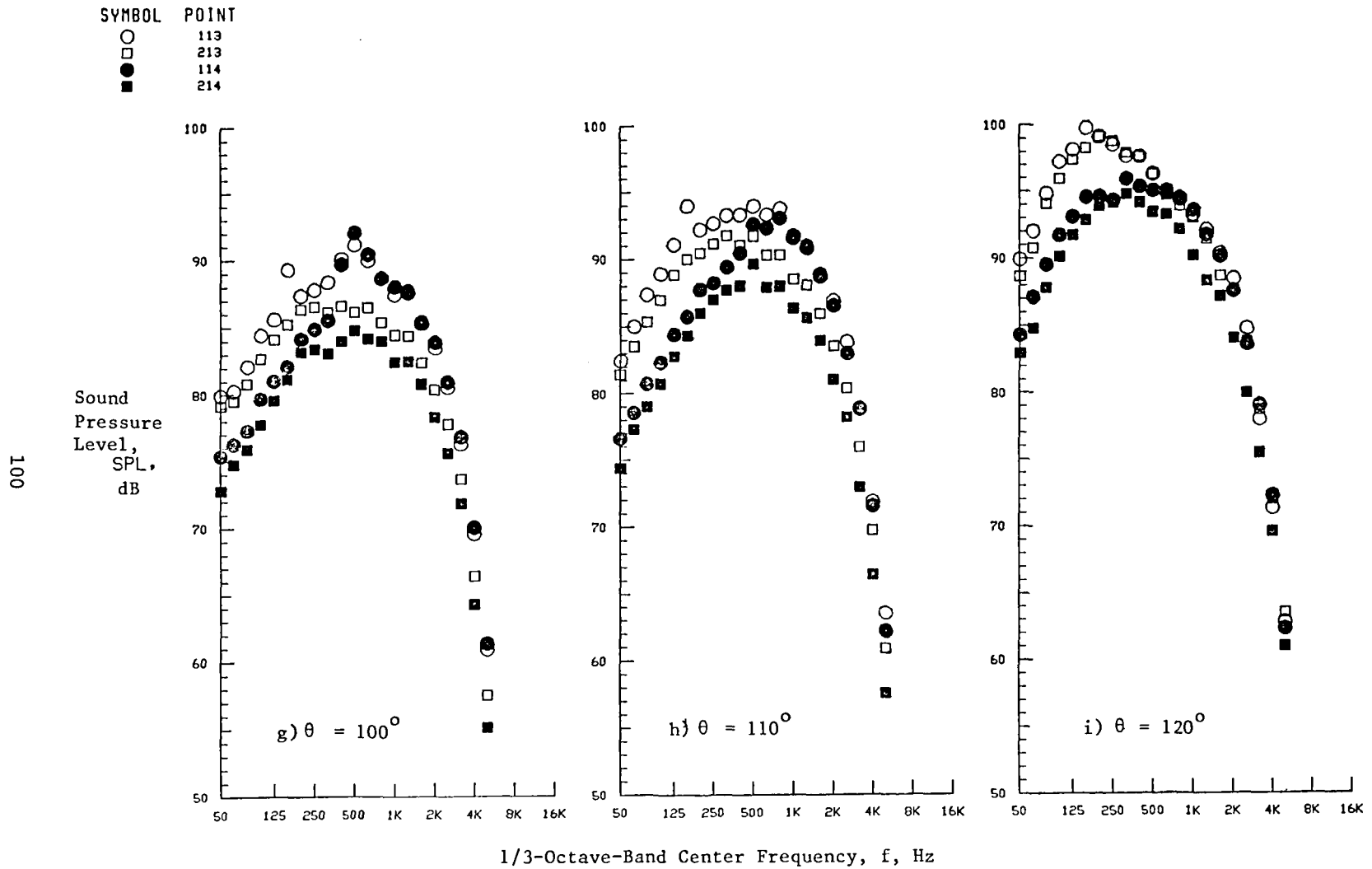


Figure 5-25. (Cont'd.) Static-to-Flight Spectral Comparison at Design Operating Conditions; Convergent Circular (Model 1) and C-D Circular (Model 2) Nozzles.

SYMBOL	POINT
○	113
□	213
●	114
■	214

101

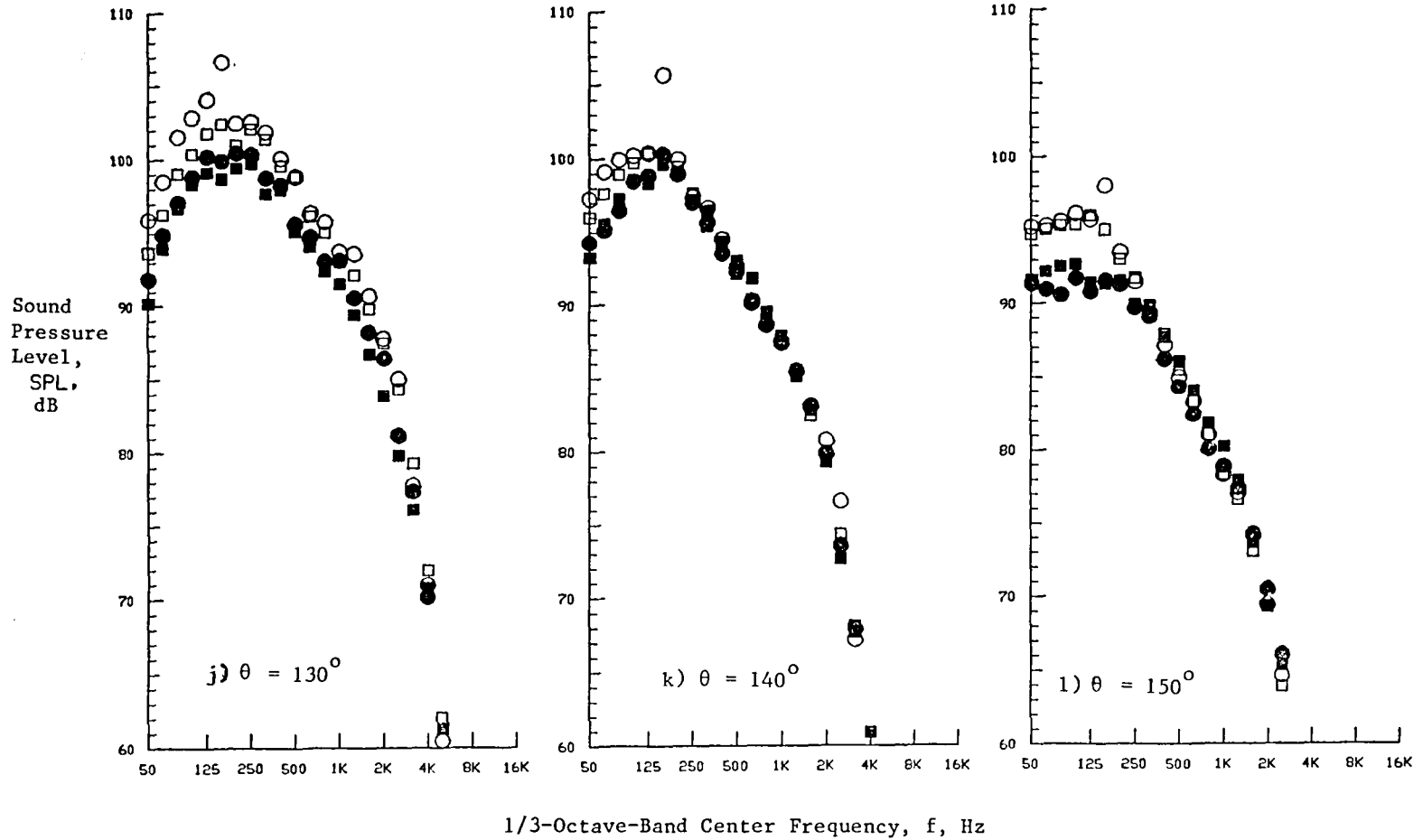


Figure 5-25. (Concluded) Static-to-Flight Spectral Comparison at Design Operating Conditions; Convergent Circular (Model 1) and C-D Circular (Model 2) Nozzles.

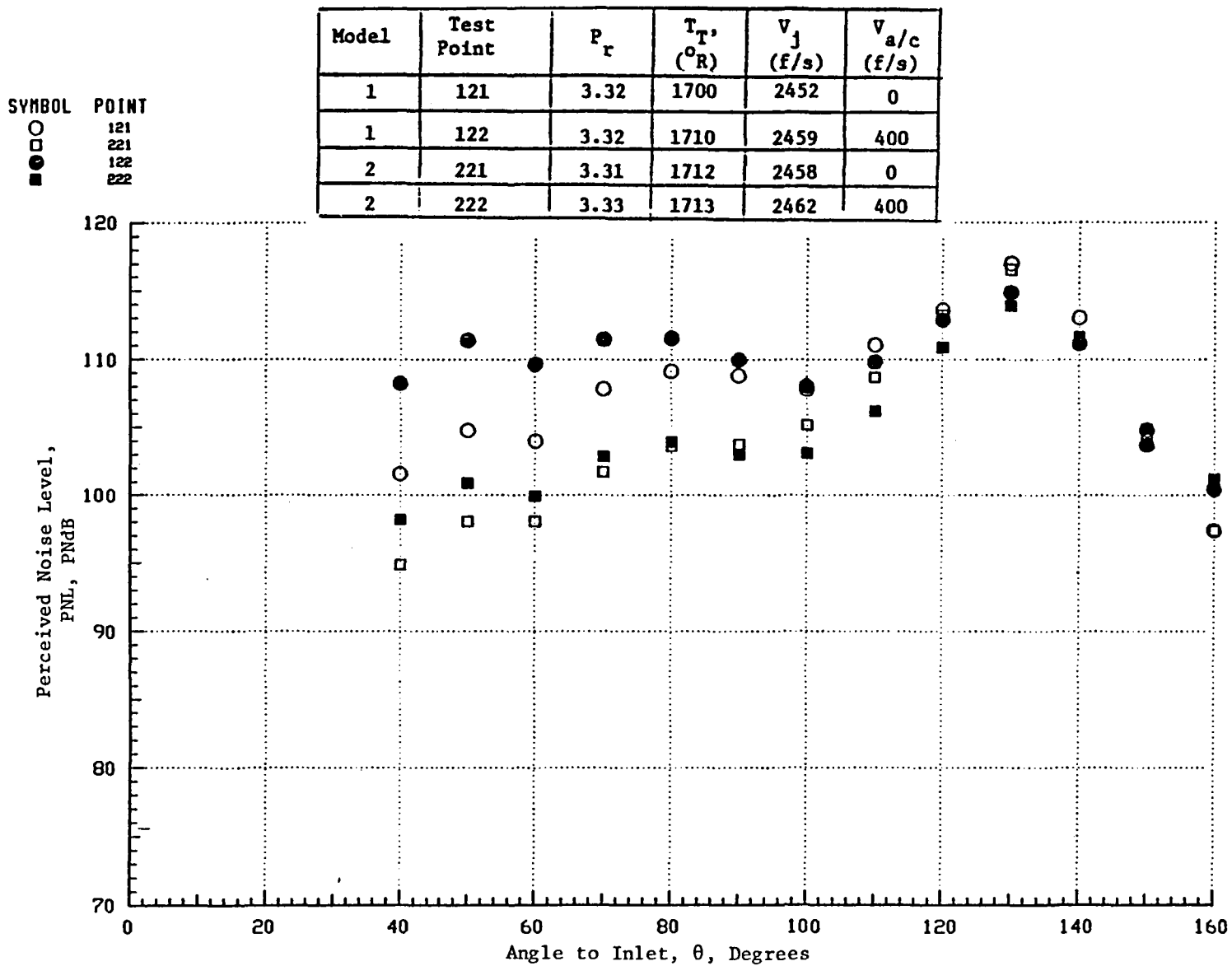


Figure 5-26. Static-to-Flight PNL Comparison at Underexpanded Flow Conditions; Convergent Circular (Model 1) and C-D Circular (Model 2) Nozzles.

SYMBOL POINT
 ○ 121
 □ 221
 ● 122
 ■ 222

Model	Test Point	P_r	T_T , (°R)	V_j (f/s)	$V_{a/c}$ (f/s)
1	121	3.32	1700	2452	0
1	122	3.32	1710	2459	400
2	221	3.31	1712	2458	0
2	222	3.33	1713	2462	400

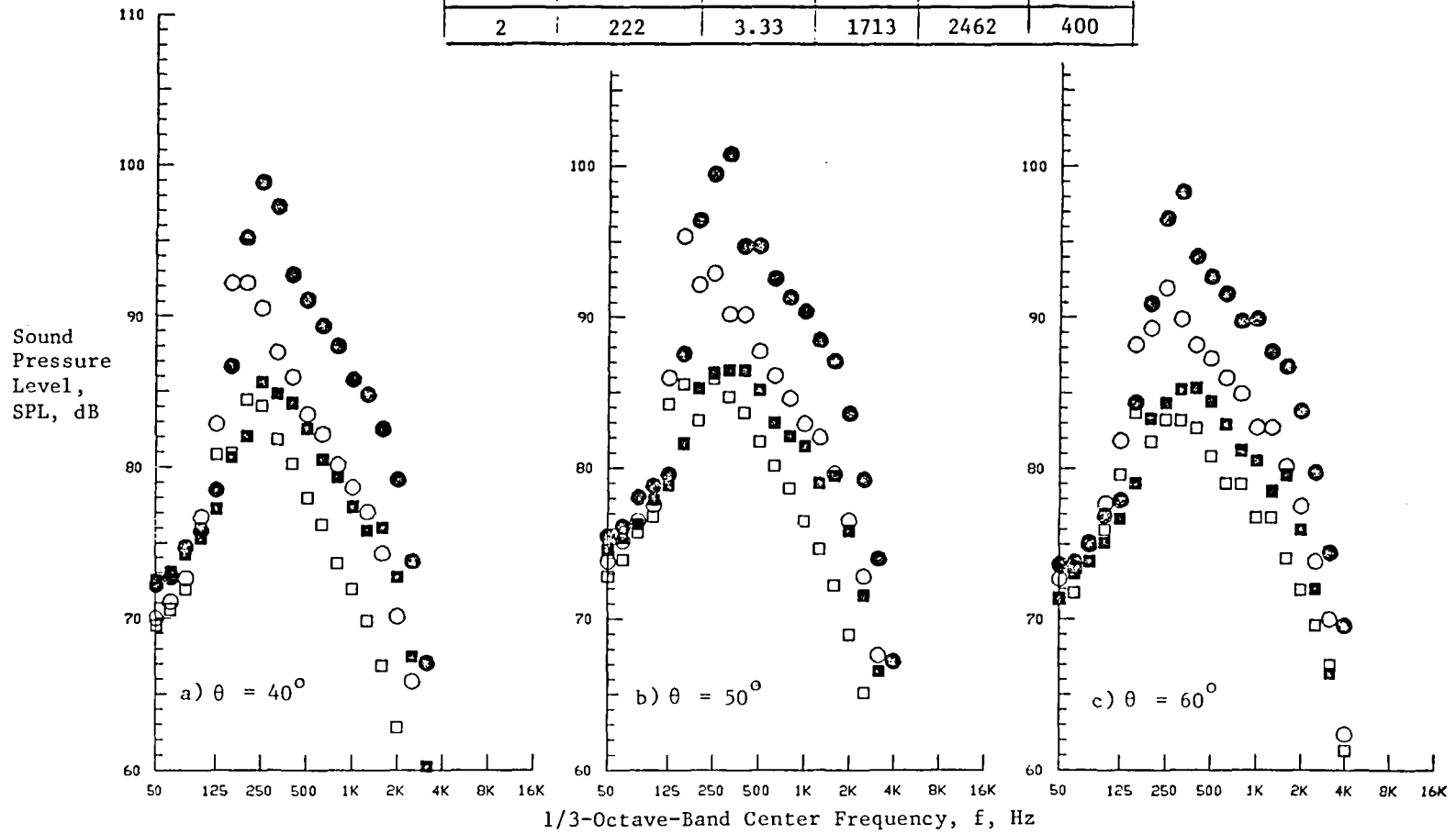


Figure 5-27. Static-to-Flight Spectral Comparison at Underexpanded Flow Conditions; Convergent Circular (Model 1) and C-D Circular (Model 2) Nozzles.

SYMBOL	POINT
○	121
□	221
●	122
■	222

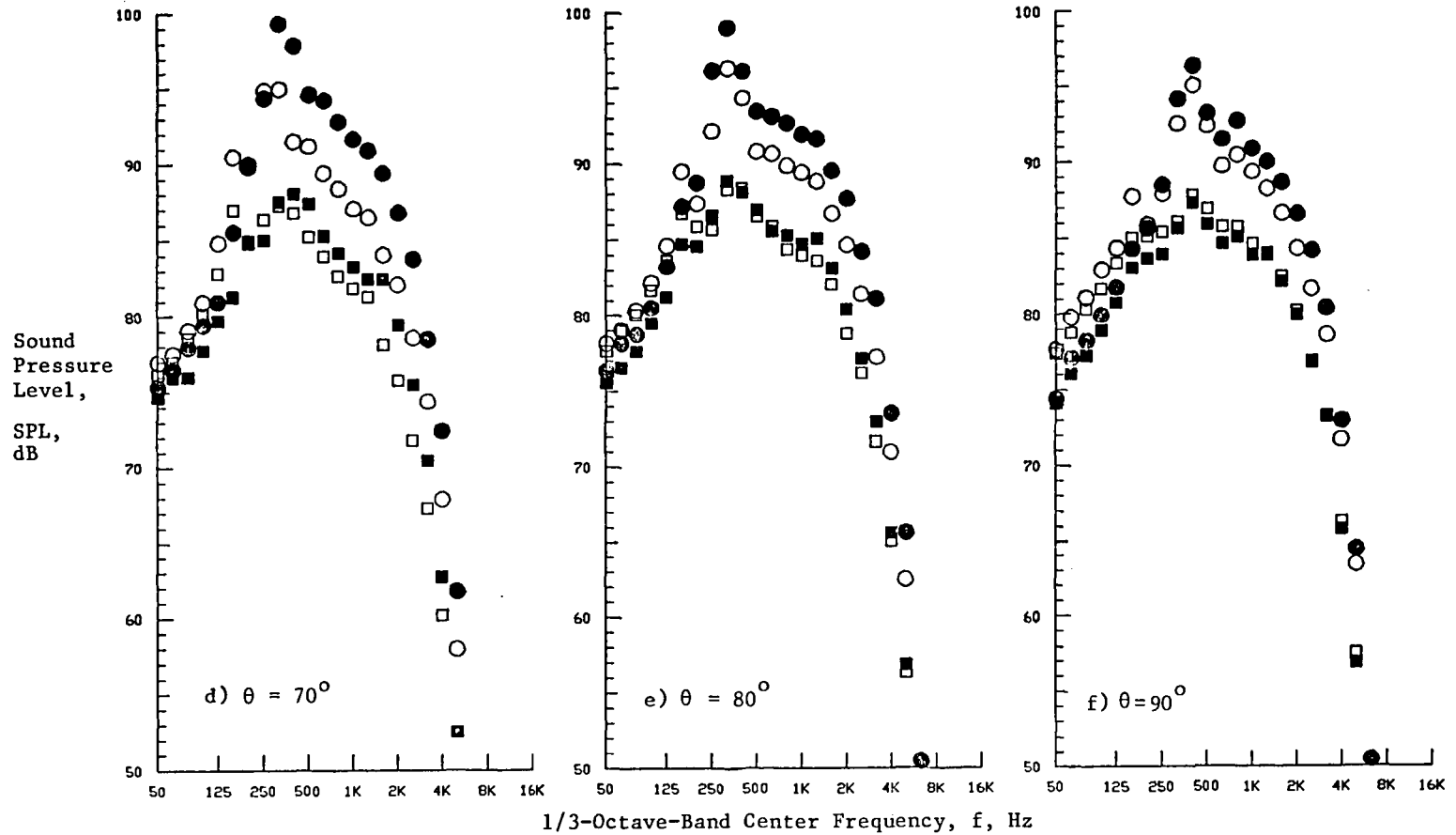


Figure 5-27. (Cont'd.) Static-to-Flight Spectral Comparison at Underexpanded Flow Conditions; Convergent Circular (Model 1) and C-D Circular (Model 2) Nozzles.

SYMBOL	POINT
○	121
□	221
●	122
■	222

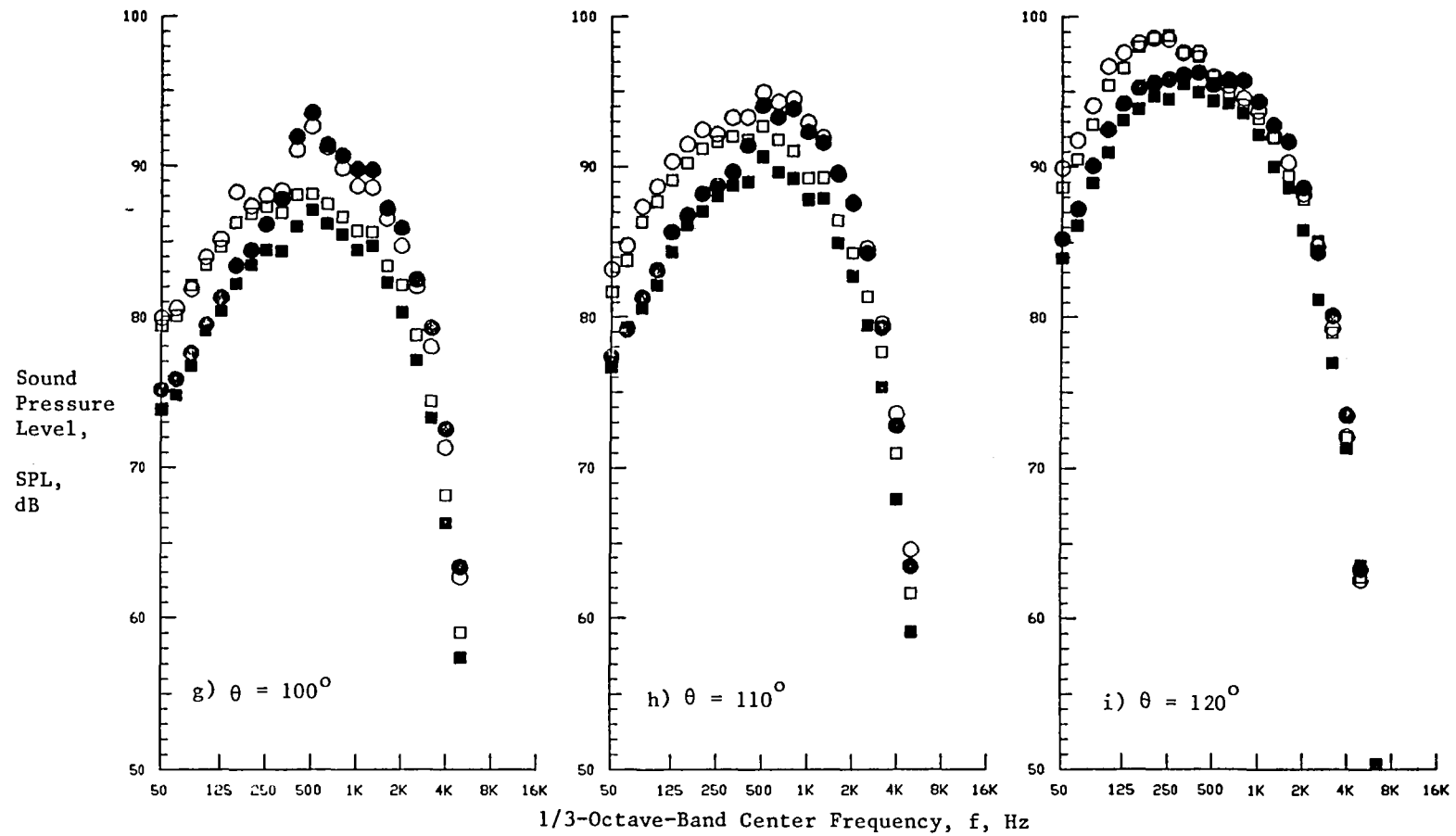


Figure 5-27. (Cont'd.) Static-to-Flight Spectral Comparison at Underexpanded Flow Conditions; Convergent Circular (Model 1) and C-D Circular (Model 2) Nozzles.

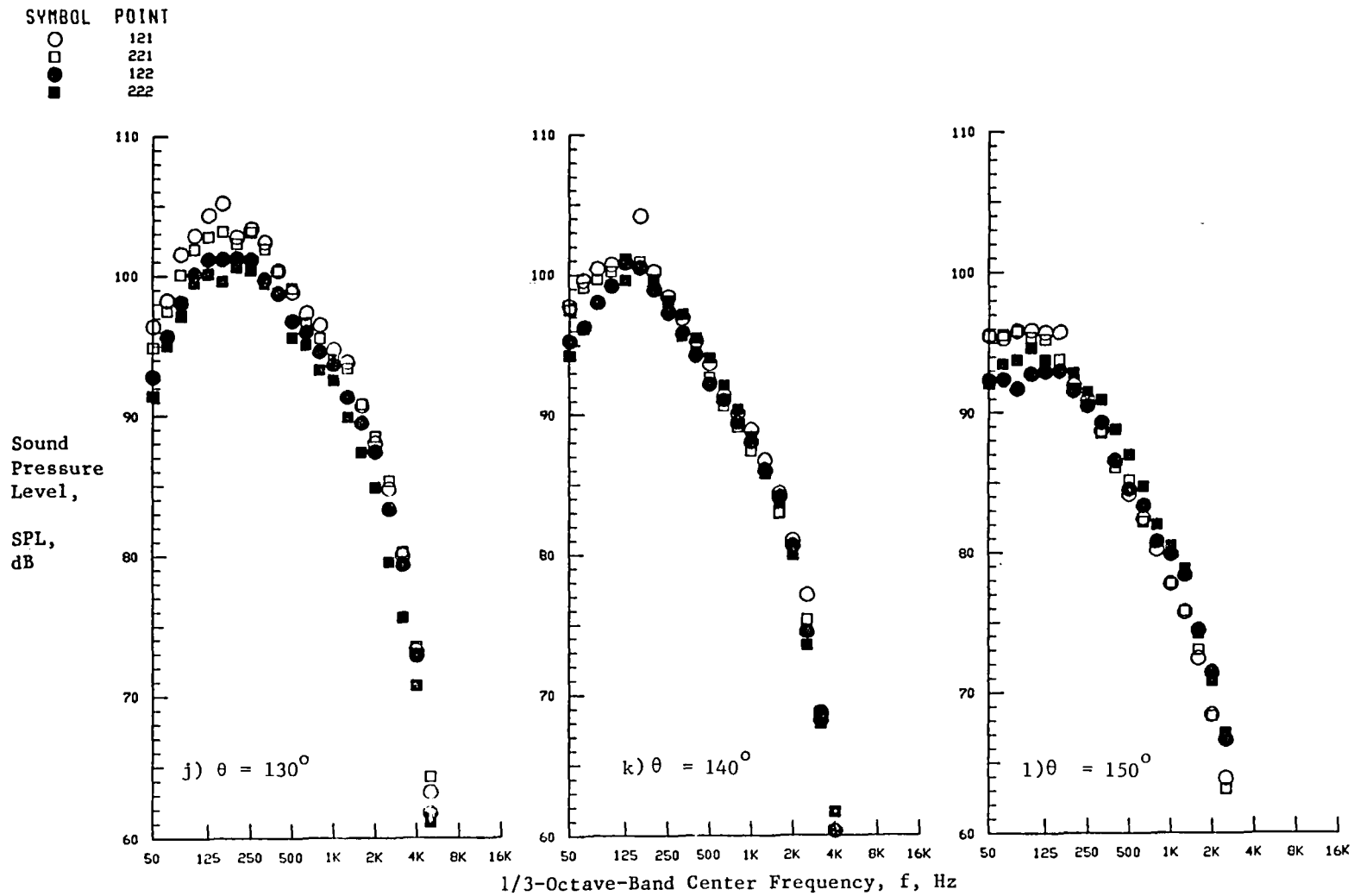


Figure 5-27. (Concluded) Static-to-Flight Spectral Comparison at Underexpanded Flow Conditions; Convergent Circular (Model 1) and C-D Circular (Model 2) Nozzles.

observed under overexpanded conditions. This is because of the fact that shocks were almost completely eliminated from the C-D circular nozzle plume at the C-D design point and, therefore, the sound produced by this nozzle does not experience the front quadrant amplification by flight. Accordingly, larger flight benefits correspond to the C-D circular nozzle at the C-D design point than that at overexpanded conditions. Corresponding static-to-flight spectral comparisons are illustrated in Figure 5-25. Comparing Figure 5-25 with Figure 5-23, we note that the flight amplification of shock noise observed at $\theta = 50^\circ$ is slightly less for the C-D design operating condition than for the overexpanded case.

Final static-to-flight PNL and spectral comparisons of C-D circular nozzle data with those of the baseline convergent circular nozzle are made at underexpanded plume conditions, results of which are provided in Figures 5-26 and 5-27. The observations made based on the data of Figures 5-22 and 5-23 correspond, in general, to the data presented in Figures 5-26 and 5-27.

5.2.1.2 Convergent Annular Plug Nozzle (Model 3)

Comparisons of the static and simulated flight PNL directivity and SPL spectral data of the convergent annular plug nozzle (Model 3) with those of the baseline convergent circular nozzle (Model 1) over the design and off-design C-D operating conditions are presented in Figures 5-28 through 5-33. The test results shown in these figures indicate that the flight amplification of shock-cell noise for the convergent annular plug nozzle is almost as much as observed for the convergent circular nozzle when pressure ratio is not large. However, at larger pressure ratios less flight amplification is observed for the convergent annular plug nozzle (Model 3) than for the baseline convergent circular nozzle (Model 1), indicating relative weak shocks associated with the former nozzle at these pressure ratios.

5.2.1.3 C-D Annular Plug Nozzle (Model 4)

Comparisons of the static and simulated flight PNL directivity and SPL spectral data of the C-D annular plug nozzle (Model 4) with those of the baseline convergent circular nozzle (Model 1) over the design and off-design operating conditions are presented in Figures 5-34 through 5-39.

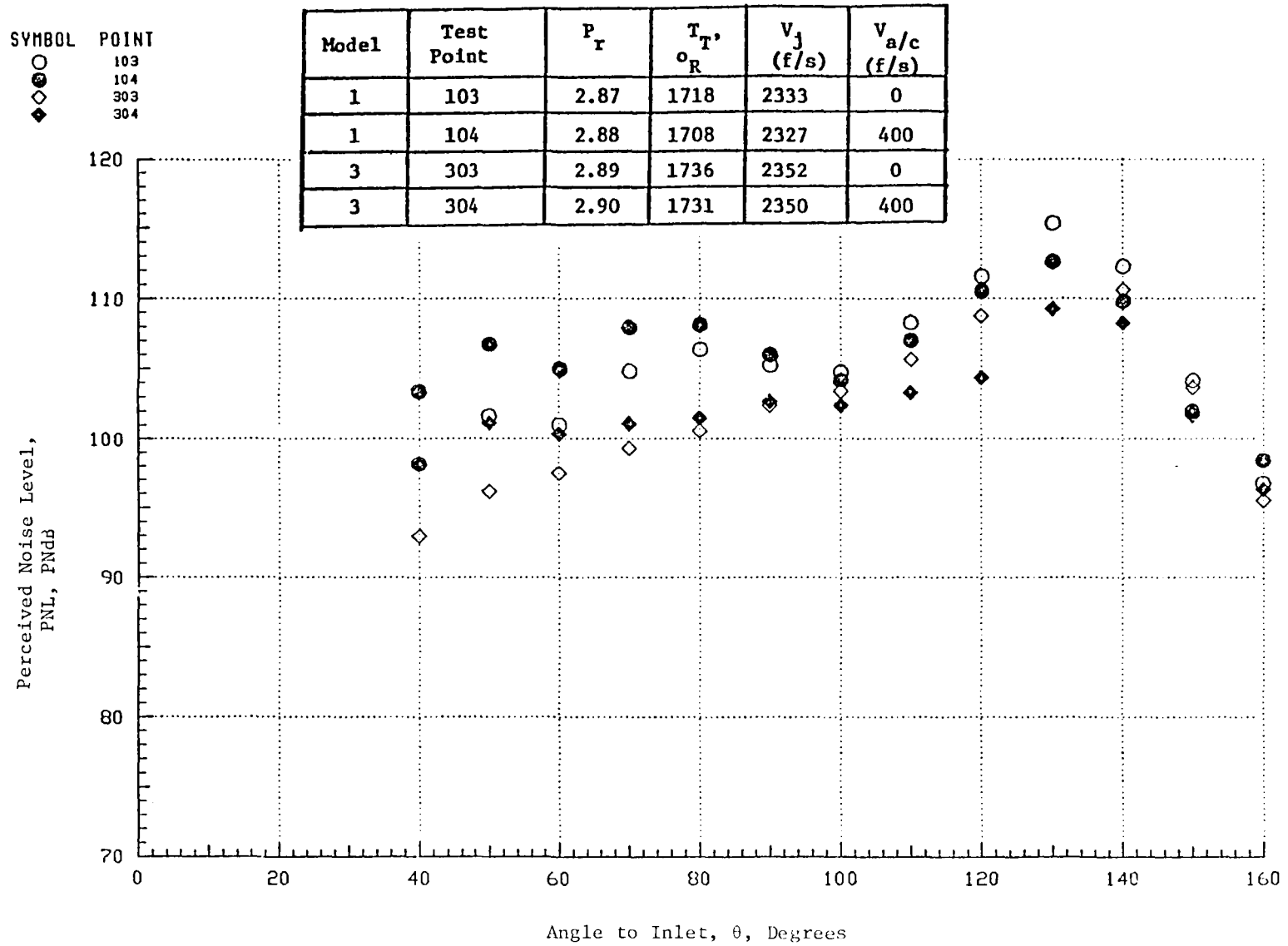


Figure 5-28. Static-to-Flight PNL Comparison Under Aerodynamic Conditions Corresponding to Overexpanded Conditions for C-D Nozzles; Convergent Circular (Model 1) and Convergent Annular Plug (Model 3) Nozzles.

SYMBOL	POINT
○	103
●	104
◇	303
◆	304

Model	Test Point	P_r	T_{T, o_R}	V_j (f/s)	V_a/c (f/s)
1	103	2.87	1718	2333	0
1	104	2.88	1708	2327	400
3	303	2.89	1736	2352	0
3	304	2.90	1731	2350	400

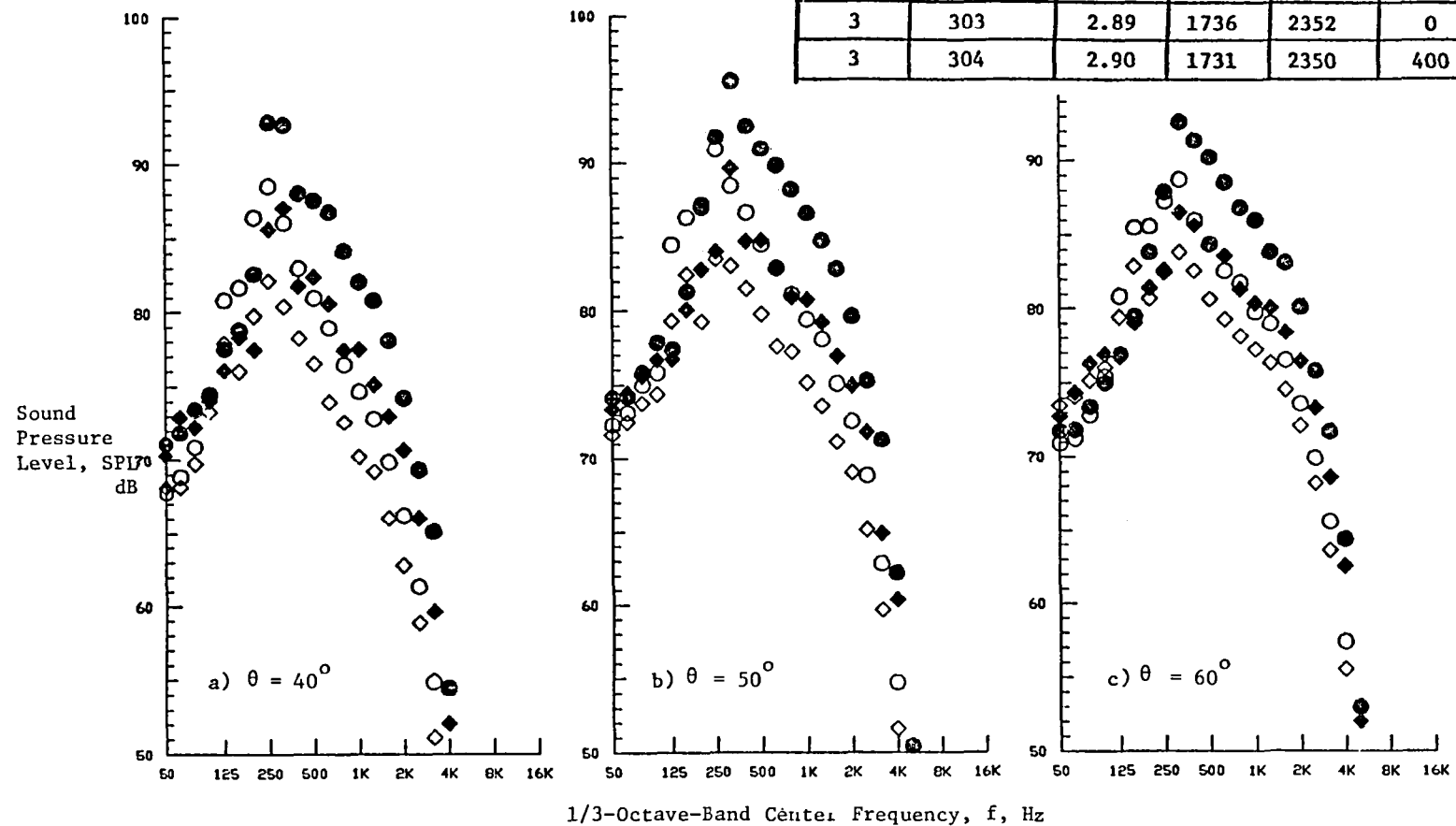


Figure 5-29. Static-to-Flight Spectral Comparison Under Aerodynamic Conditions Corresponding to Overexpanded Conditions for C-D Nozzles; Convergent Circular (Model 1) and Convergent Annular Plug (Model 3) Nozzles.

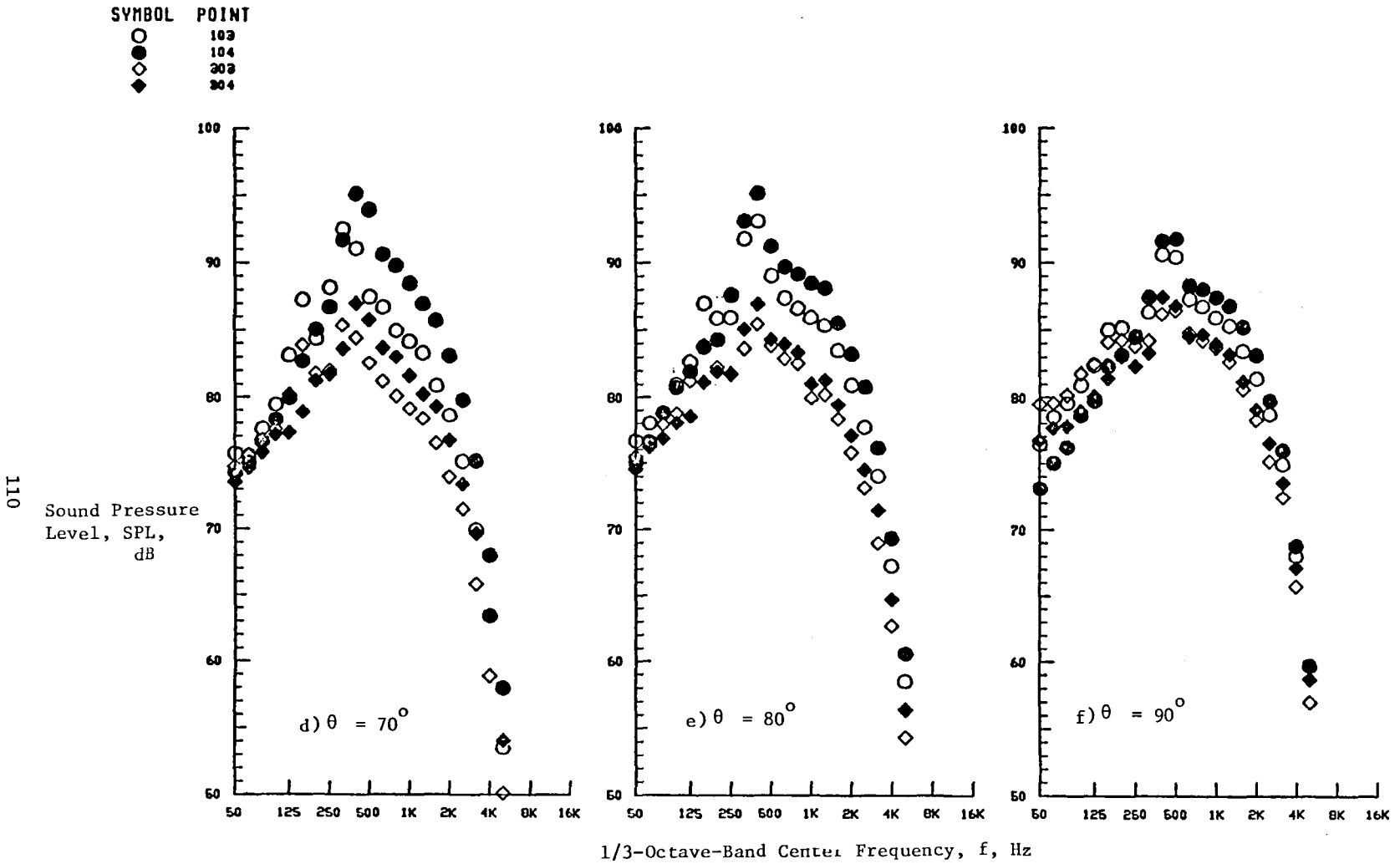


Figure 5-29. (Cont'd.) Static-to-Flight Spectral Comparison Under Aerodynamic Conditions Corresponding to Overexpanded Conditions for C-D Nozzles; Convergent Circular (Model 1) and Convergent Annular Plug (Model 3) Nozzles.

○	POINT
●	103
◇	104
◆	203
◆	204

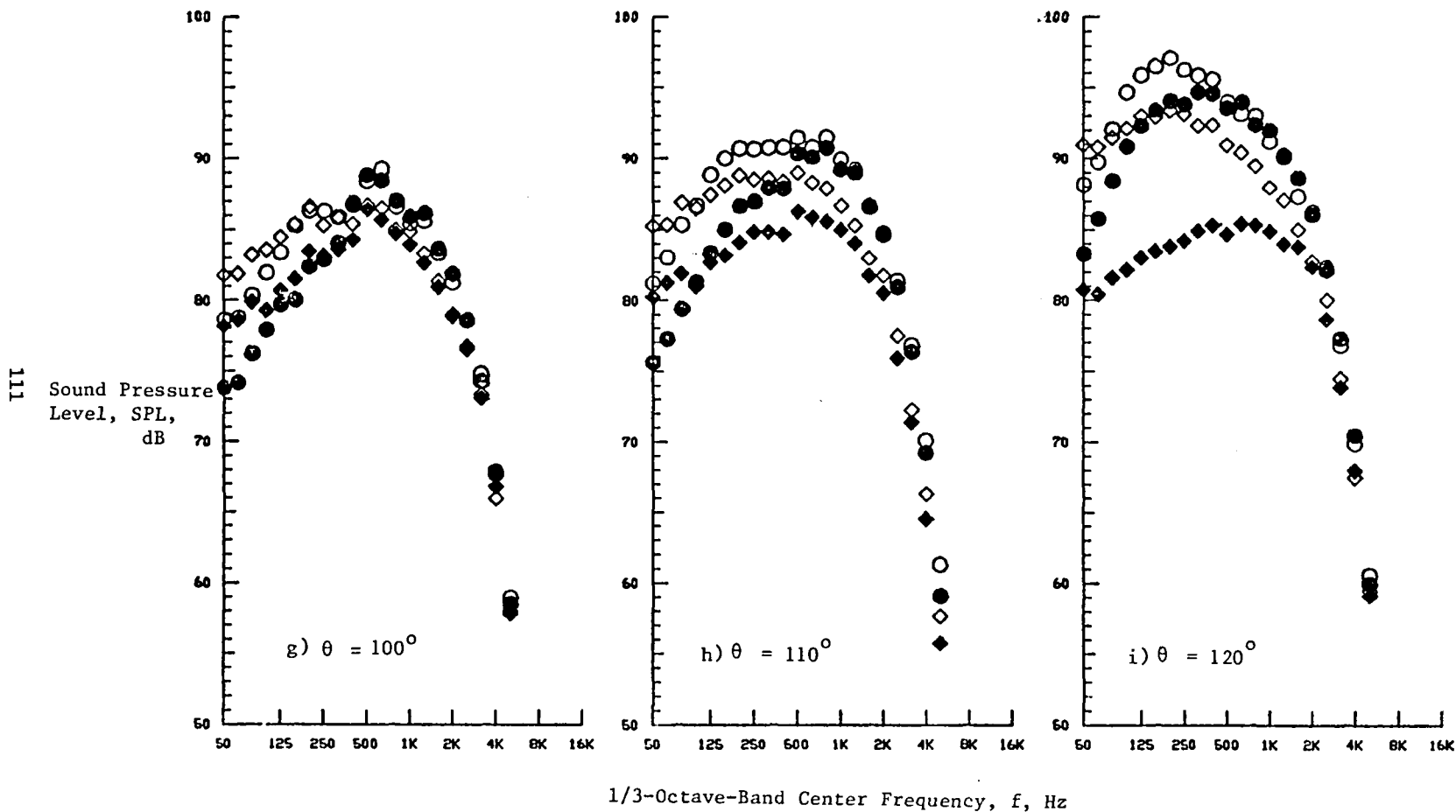


Figure 5-29. (Cont'd.) Static-to-Flight Spectral Comparison Under Aerodynamic Conditions Corresponding to Overexpanded Conditions for C-D Nozzles; Convergent Circular (Model 1) and Convergent Annular Plug (Model 3) Nozzles.

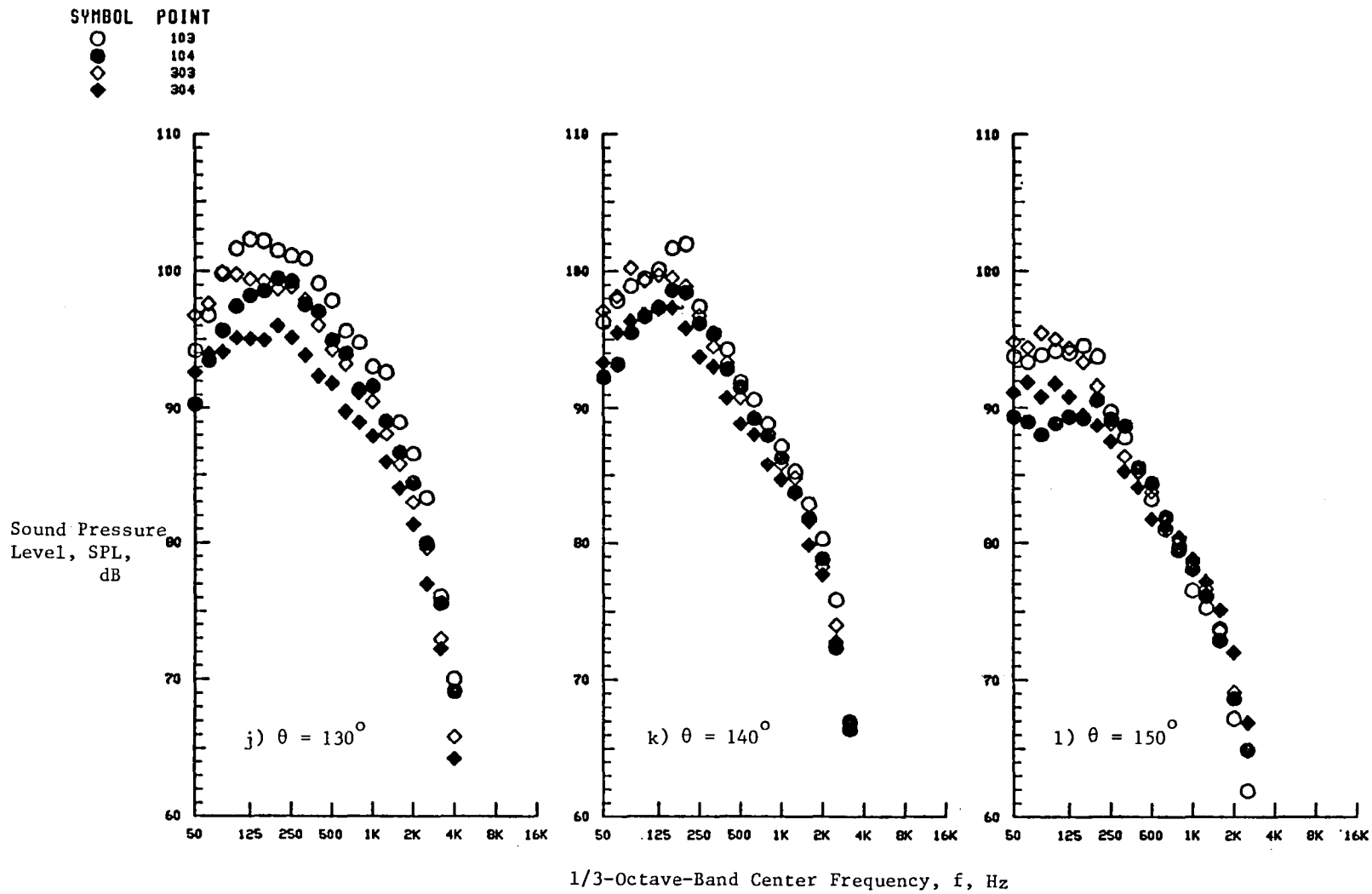


Figure 5-29. (Concluded.) Static-to-Flight Spectral Comparison Under Aerodynamic Conditions Corresponding to Overexpanded Conditions for C-D Nozzles; Convergent Circular (Model 1) and Convergent Annular Plug (Model 3) Nozzles.

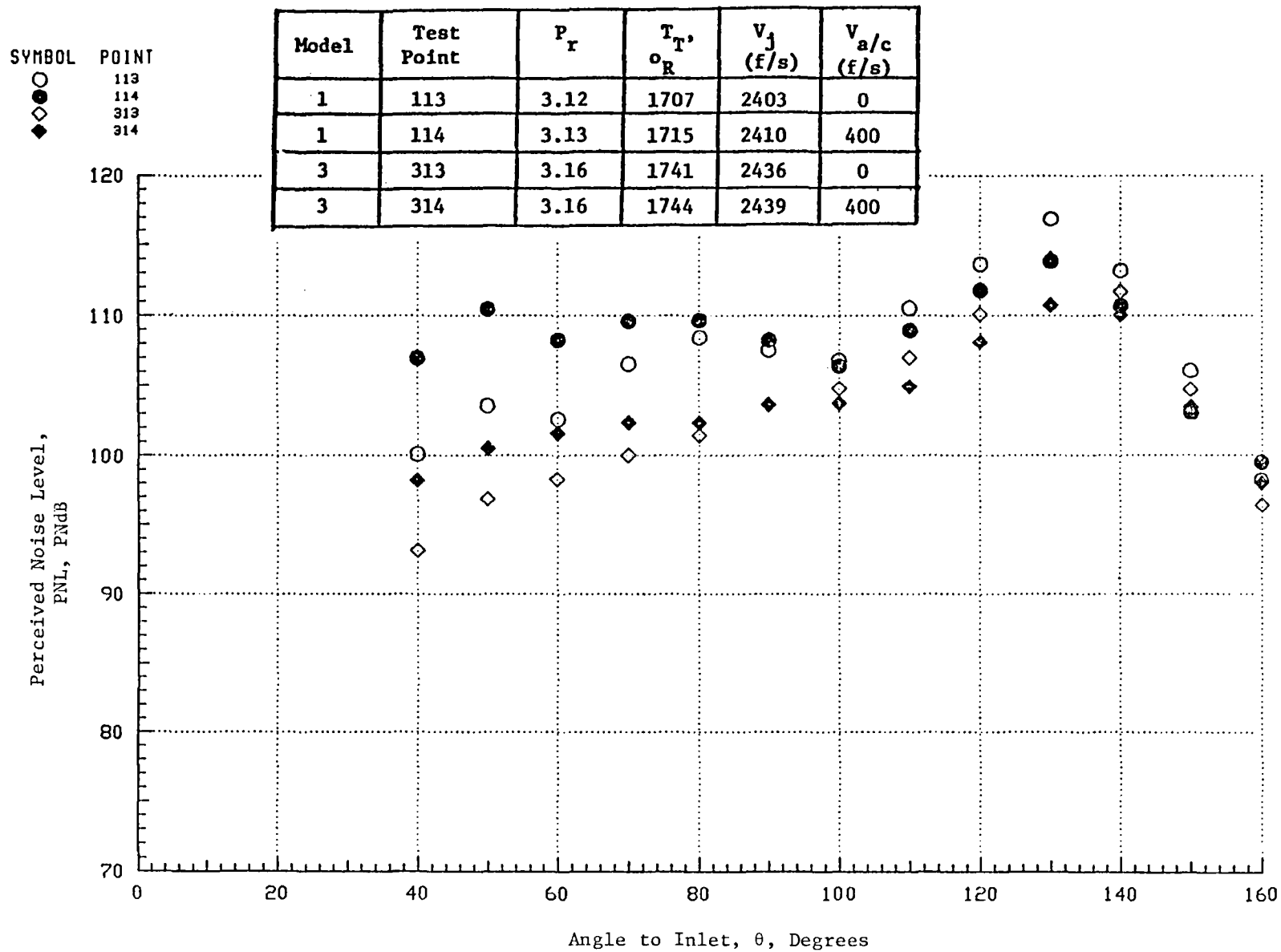


Figure 5-30. Static-to-Flight PNL Comparison Under Aerodynamic Conditions Corresponding to C-D Design Conditions for C-D Nozzles, Convergent Circular (Model 1) and Convergent Annular Plug (Model 3) Nozzles.

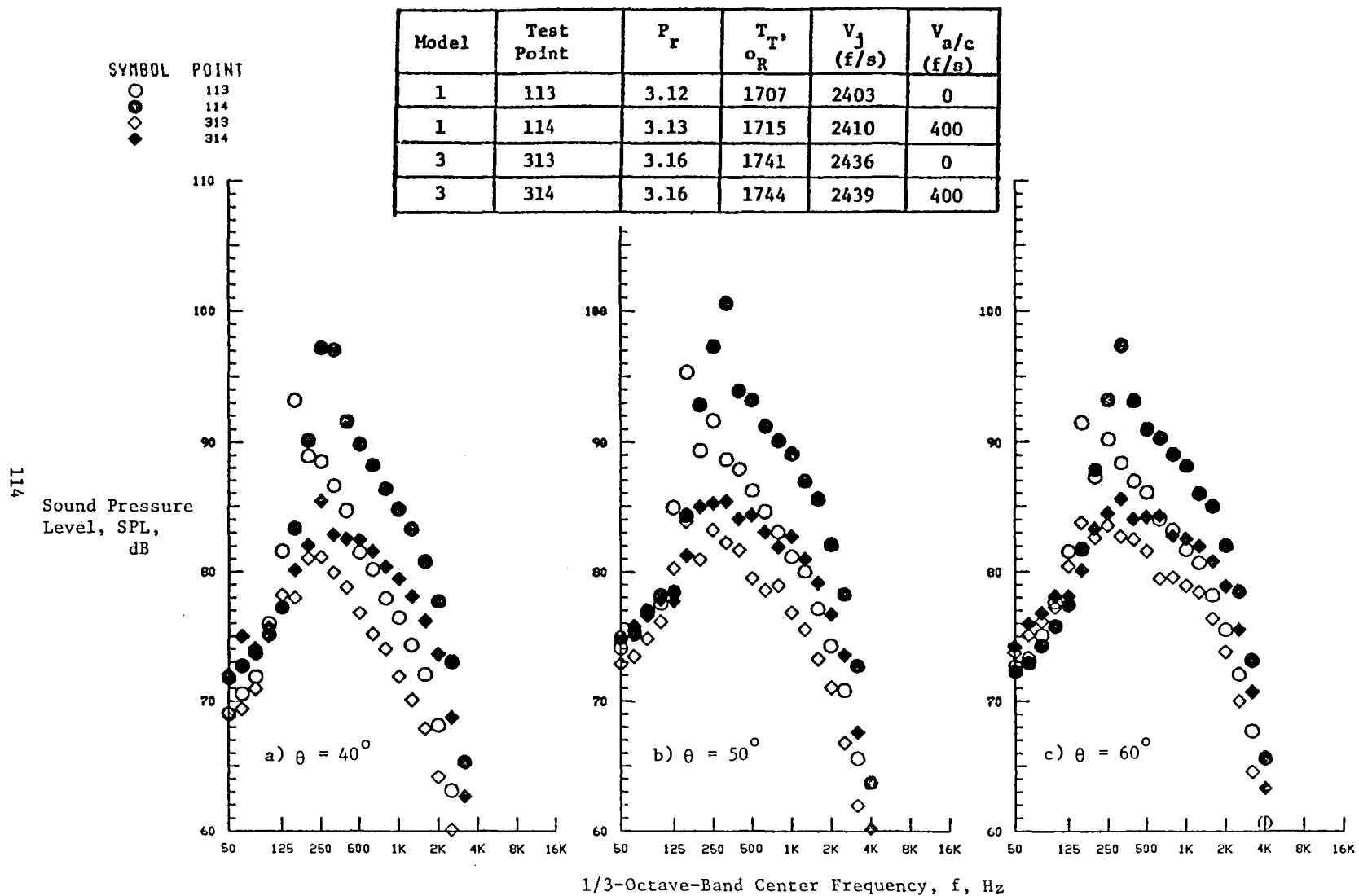


Figure 5-31. Static-to-Flight Spectral Comparison Under Aerodynamic Conditions Corresponding to C-D Design Conditions for C-D Nozzles; Convergent Circular (Model 1) and Convergent Annular Plug (Model 3) Nozzles.

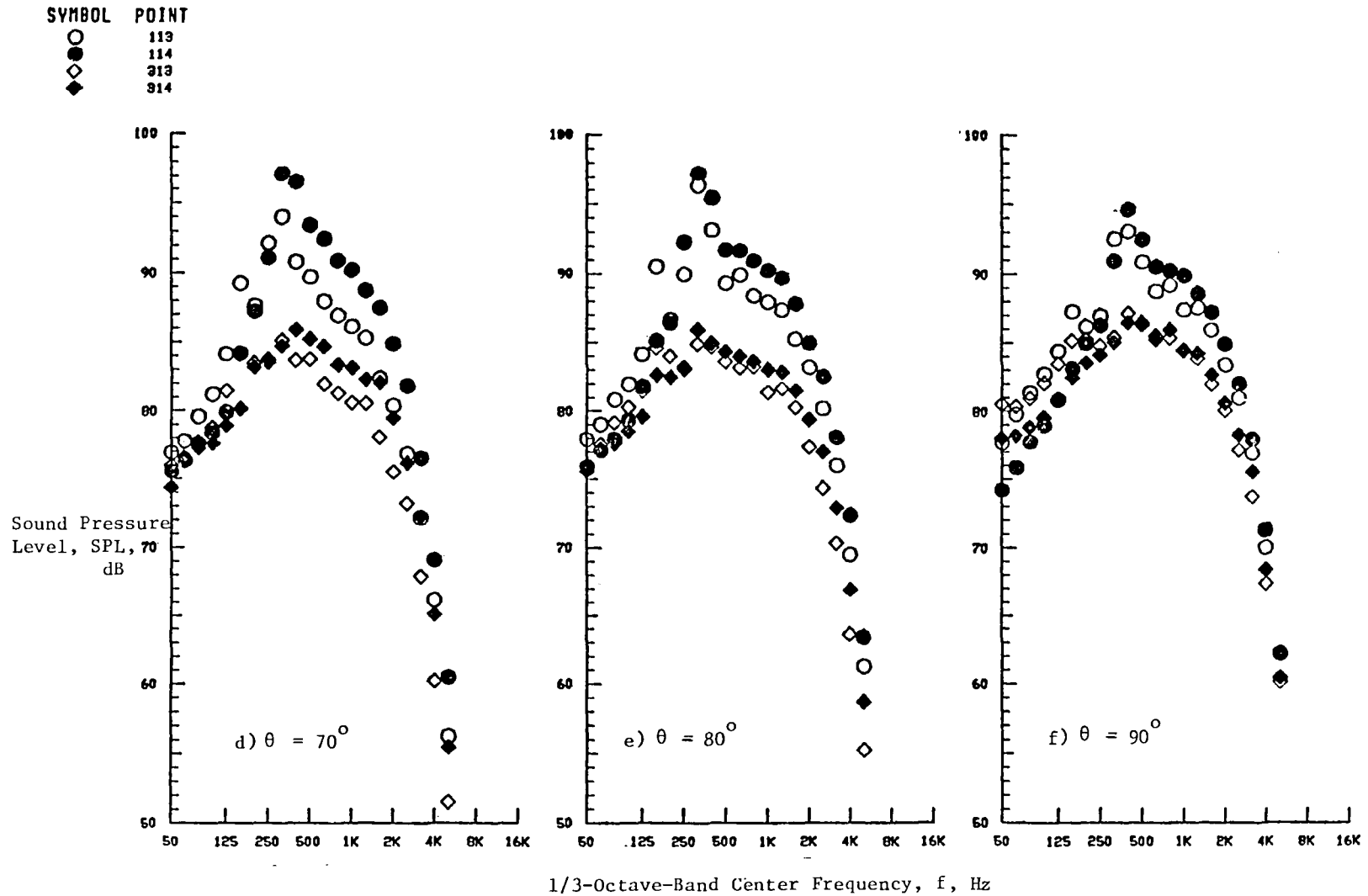


Figure 5-31. (Cont'd.) Static-to-Flight Spectral Comparison Under Aerodynamic Conditions Corresponding to C-D Design Conditions for C-D Nozzles; Convergent Circular (Model 1) and Convergent Annular Plug (Model 3) Nozzles.

SYMBOL	POINT
○	113
●	114
◇	313
◆	314

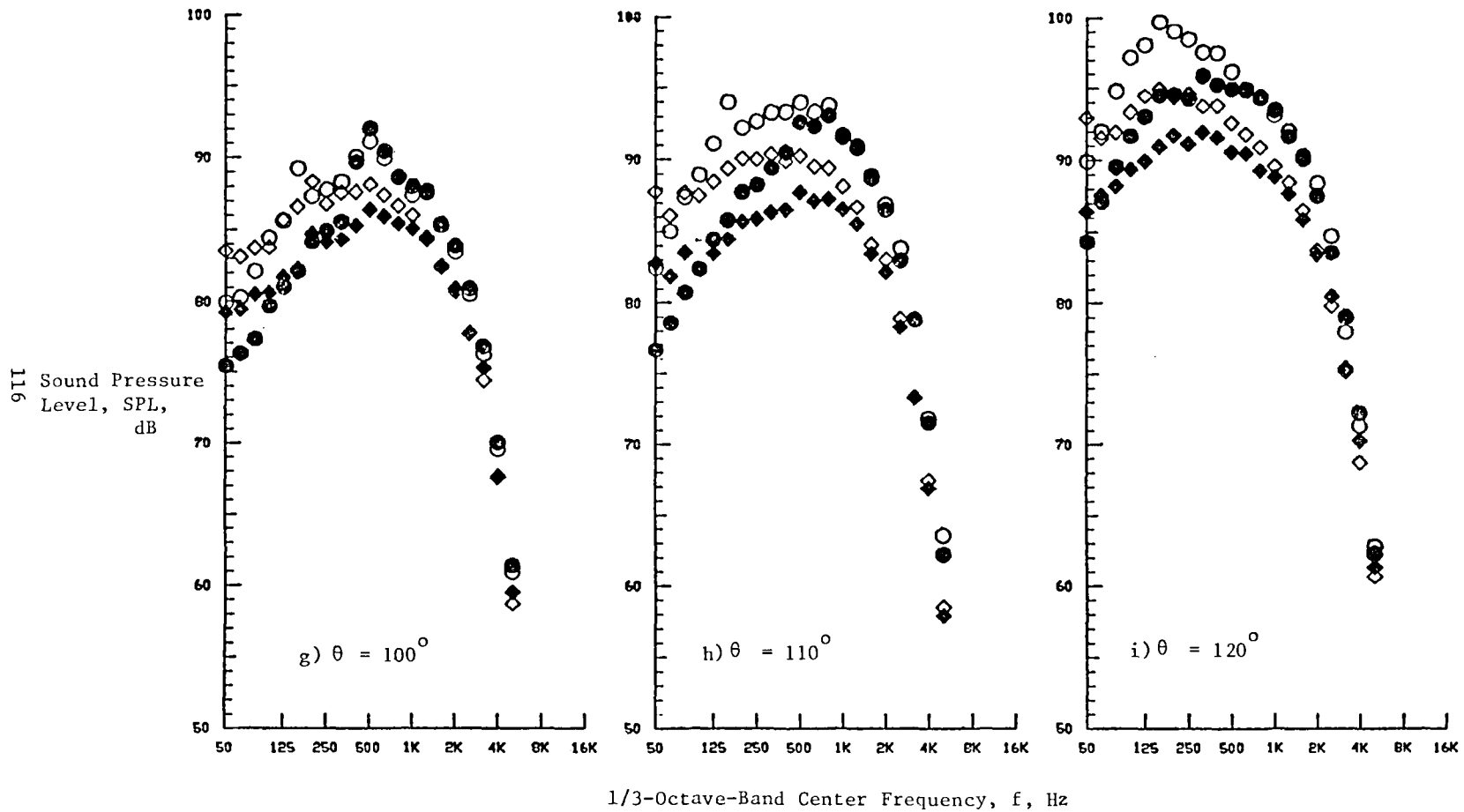


Figure 5-31. (Cont'd.) Static-to-Flight Spectral Comparison Under Aerodynamic Conditions Corresponding to C-D Design Conditions for C-D Nozzles; Convergent Circular (Model 1) and Convergent Annular Plug (Model 3) Nozzles.

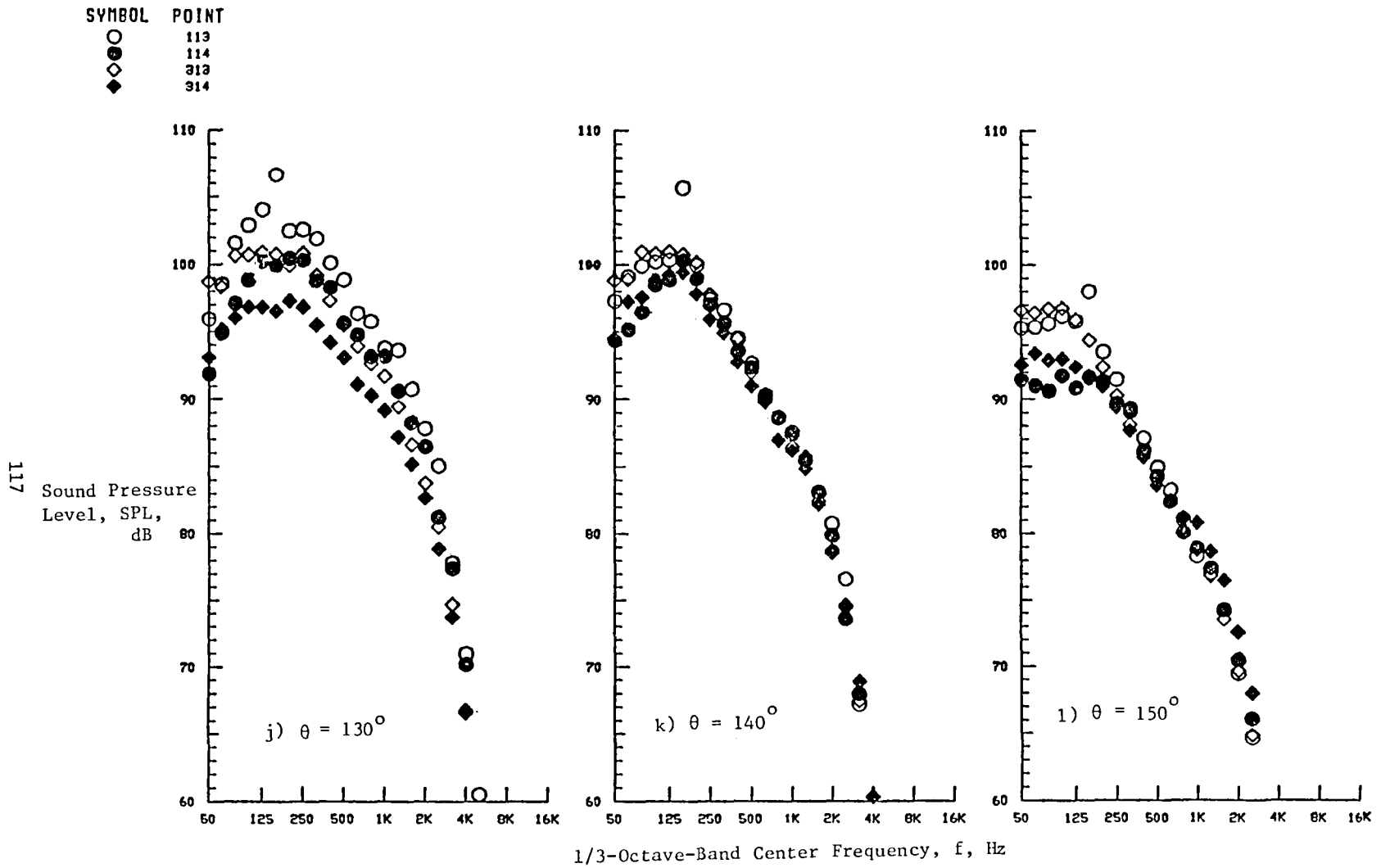


Figure 5-31. (Concluded.) Static-to-Flight Spectral Comparison Under Aerodynamic Conditions Corresponding to C-D Design Conditions for C-D Nozzles; Convergent Circular (Model 1) and Convergent Annular Plug (Model 3) Nozzles.

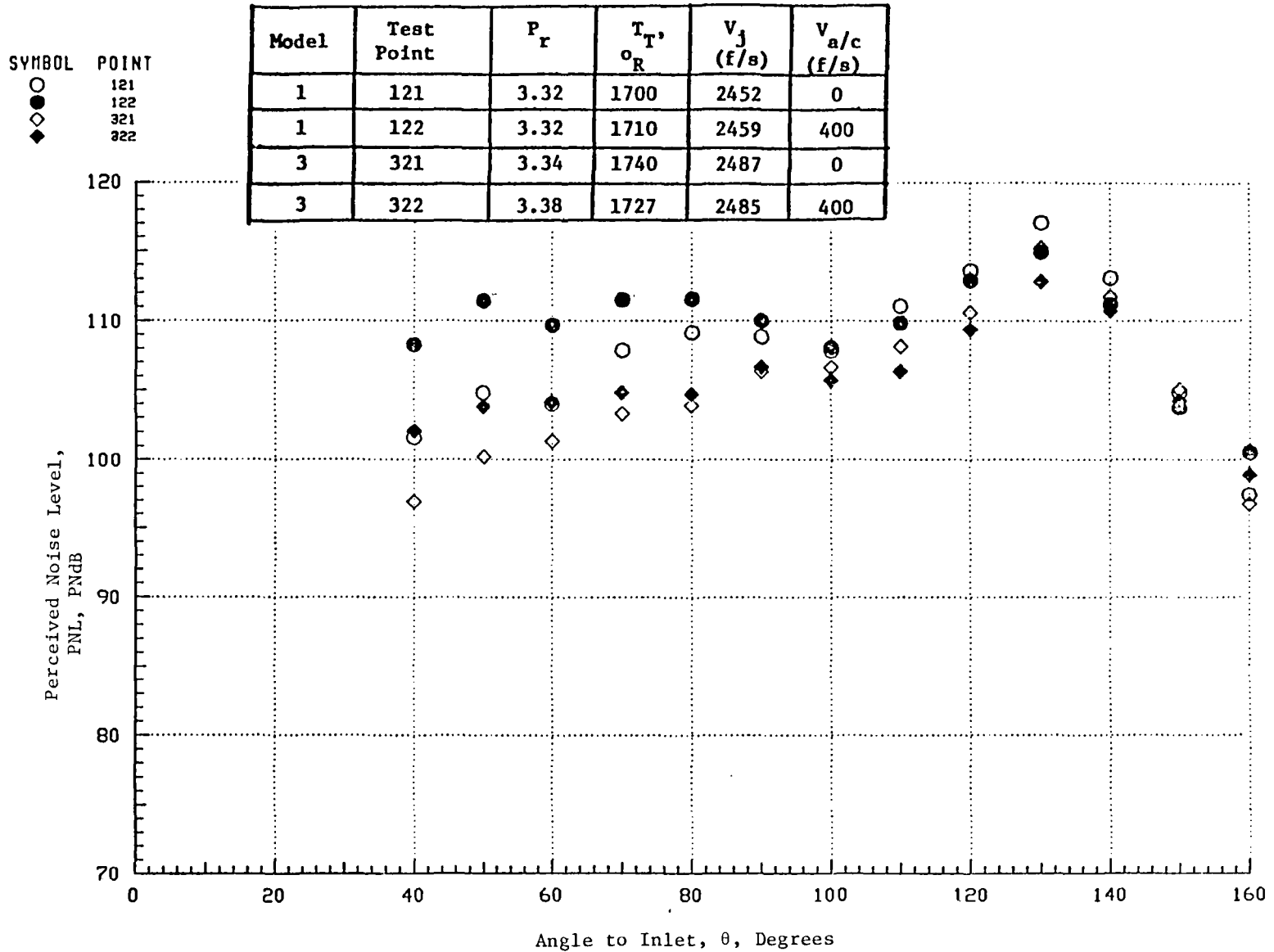


Figure 5-32. Static-to-Flight PNL Comparison Under Aerodynamic Conditions Corresponding to Underexpanded Conditions for C-D Nozzles; Convergent Circular (Model 1) and Convergent Annular Plug (Model 3) Nozzles.

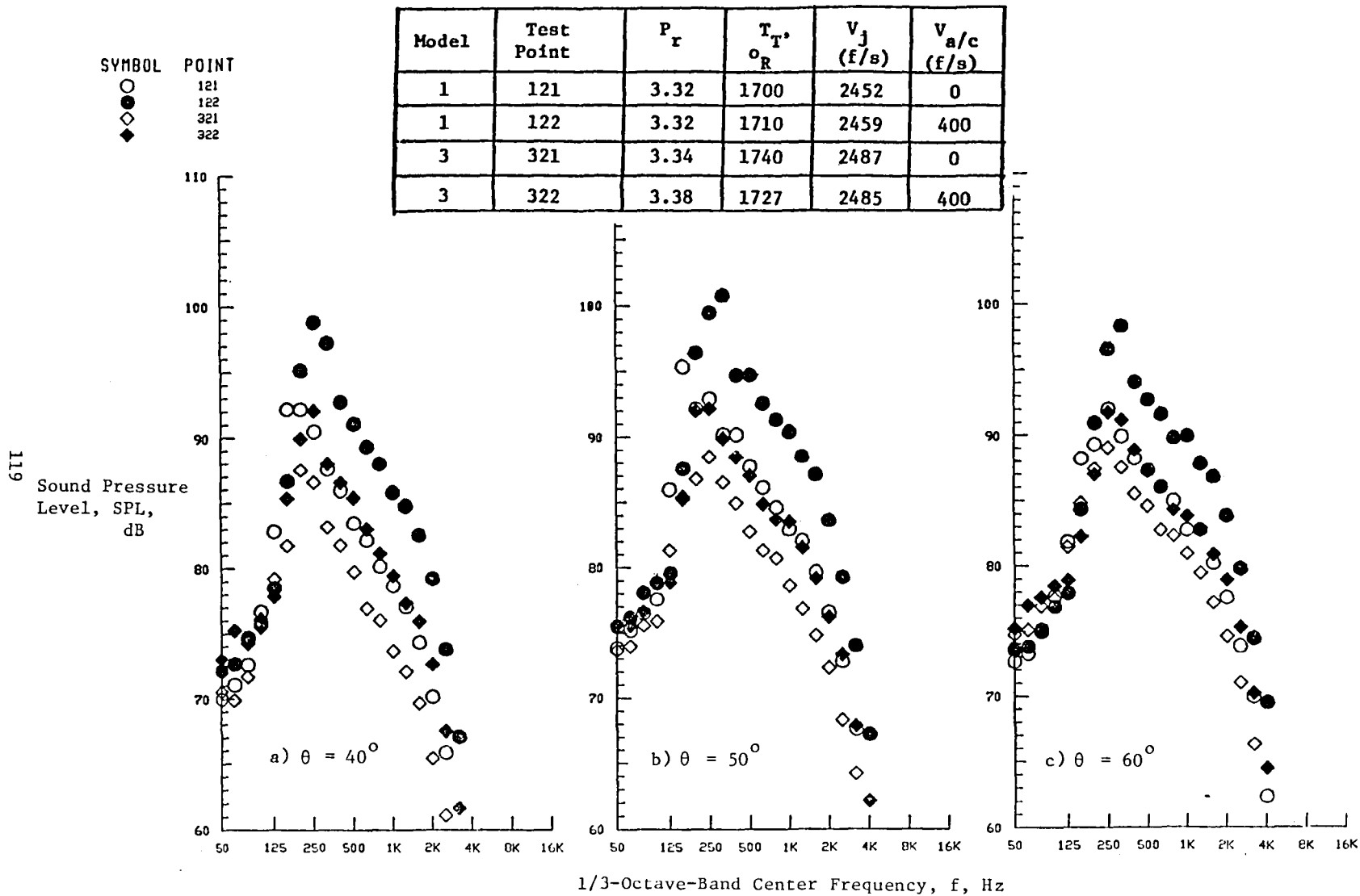


Figure 5-33. Static-to-Flight Spectral Comparison Under Aerodynamic Conditions Corresponding to Underexpanded Conditions for C-D Nozzles; Convergent Circular (Model 1) and Convergent Annular Plug (Model 3) Nozzles.

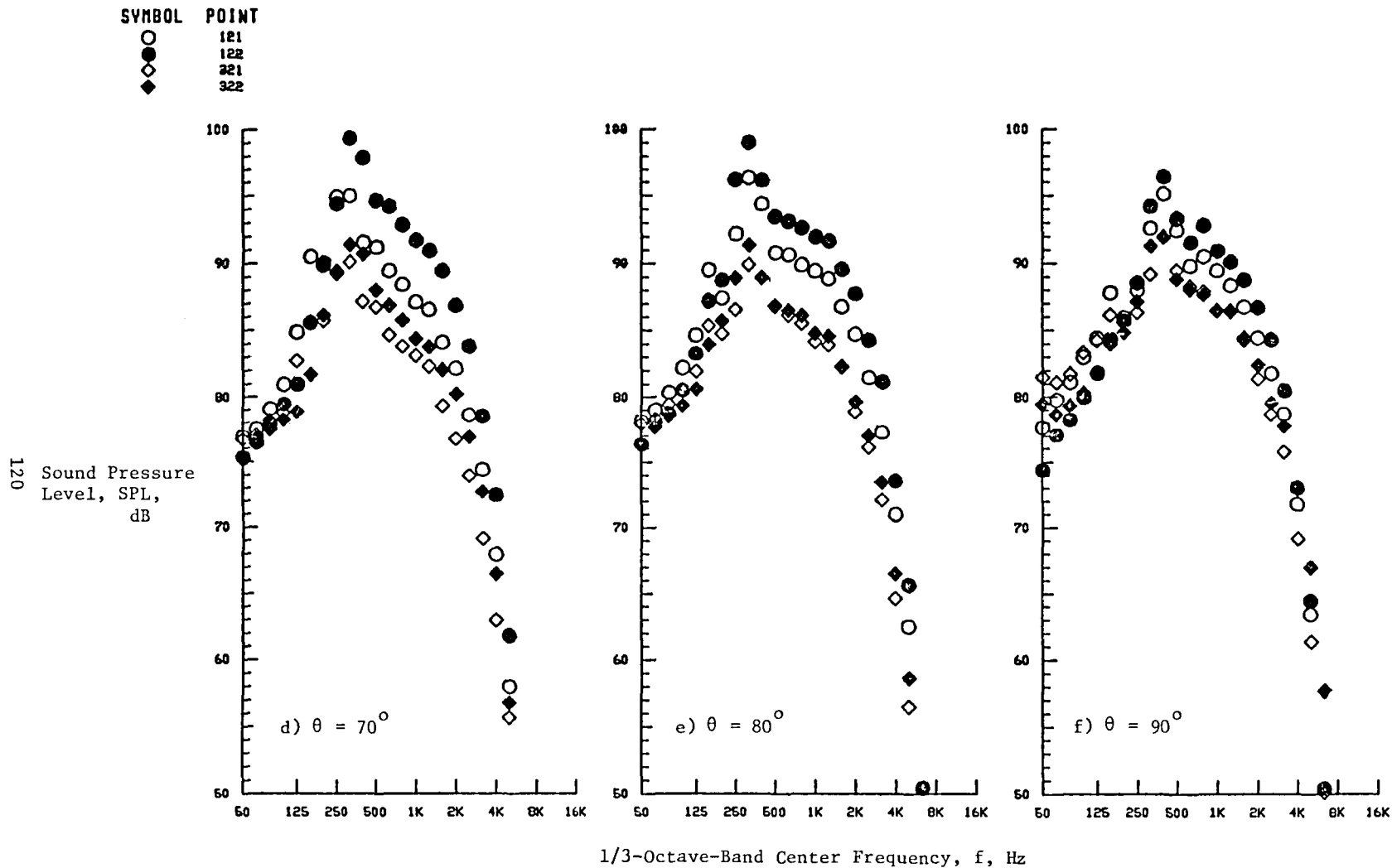
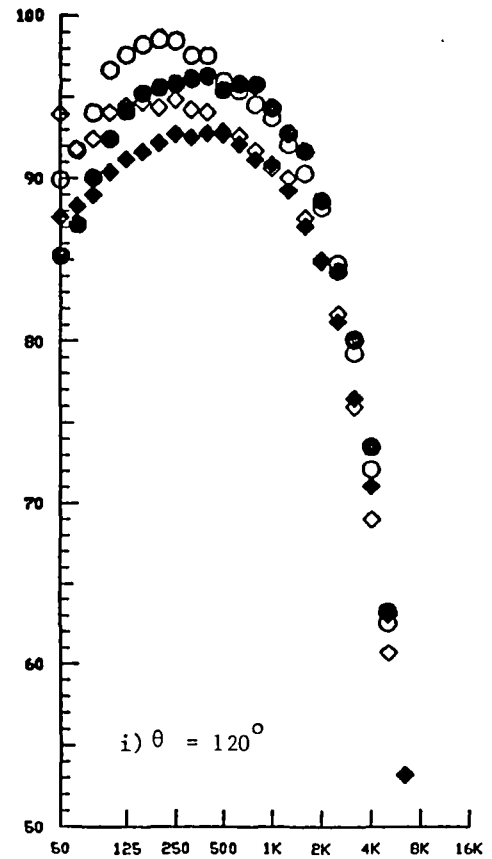
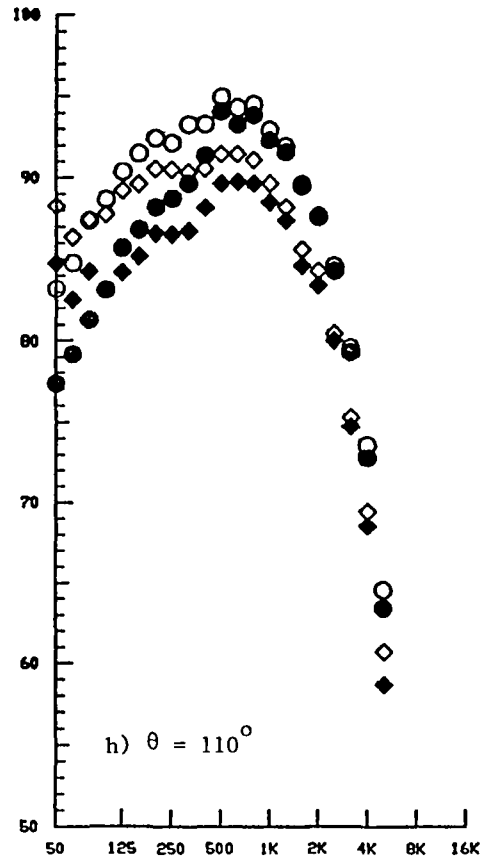
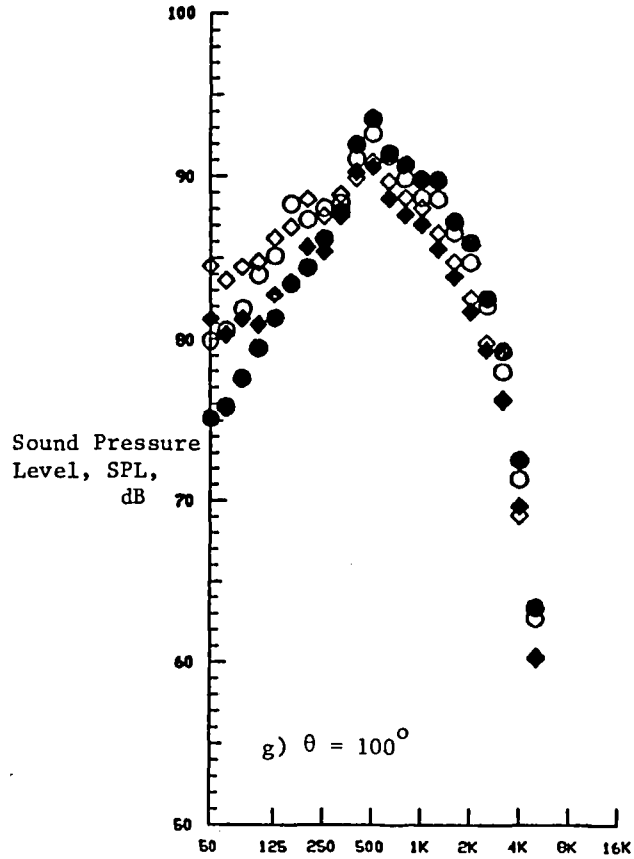


Figure 5-33. (Cont'd.) Static-to-Flight Spectral Comparison Under Aerodynamic Conditions Corresponding to Underexpanded Conditions for C-D Nozzles, Convergent Circular (Model 1) and Convergent Annular Plug (Model 3) Nozzles.

SYMBOL	POINT
○	121
●	122
◇	221
◆	222

121



1/3-Octave-Band Center Frequency, f, Hz

Figure 5-33. (Cont'd.) Static-to-Flight Spectral Comparison Under Aerodynamic Conditions Corresponding to Underexpanded Conditions for C-D Nozzles, Convergent Circular (Model 1) and Convergent Annular Plug (Model 3) Nozzles.

122

○	121
●	122
◇	321
◆	322

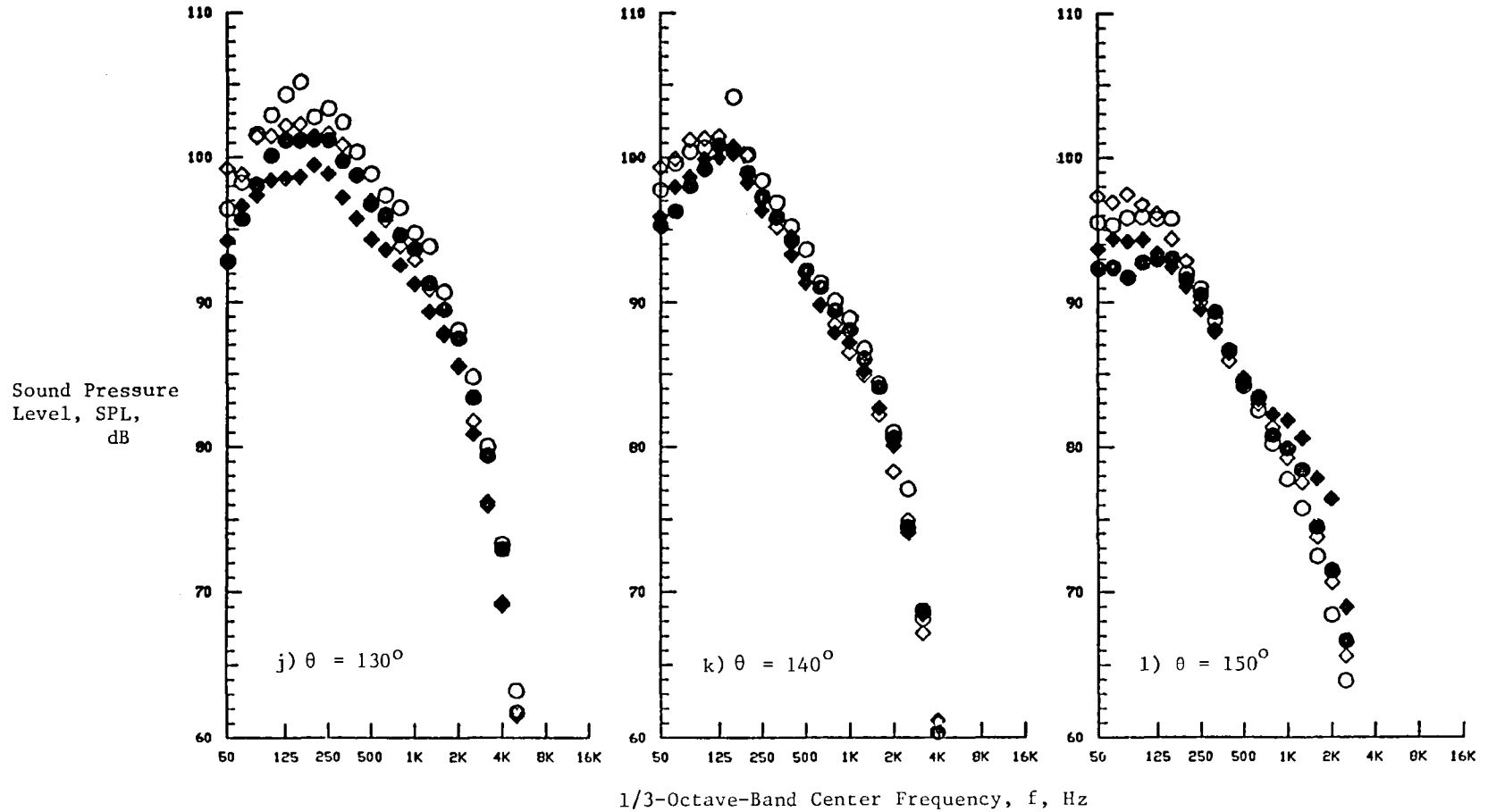


Figure 5-33. (Concluded.) Static-to-Flight Spectral Comparison Under Aerodynamic Conditions Corresponding to Underexpanded Conditions for C-D Nozzles, Convergent Circular (Model 1) and Convergent Annular Plug (Model 3) Nozzles.

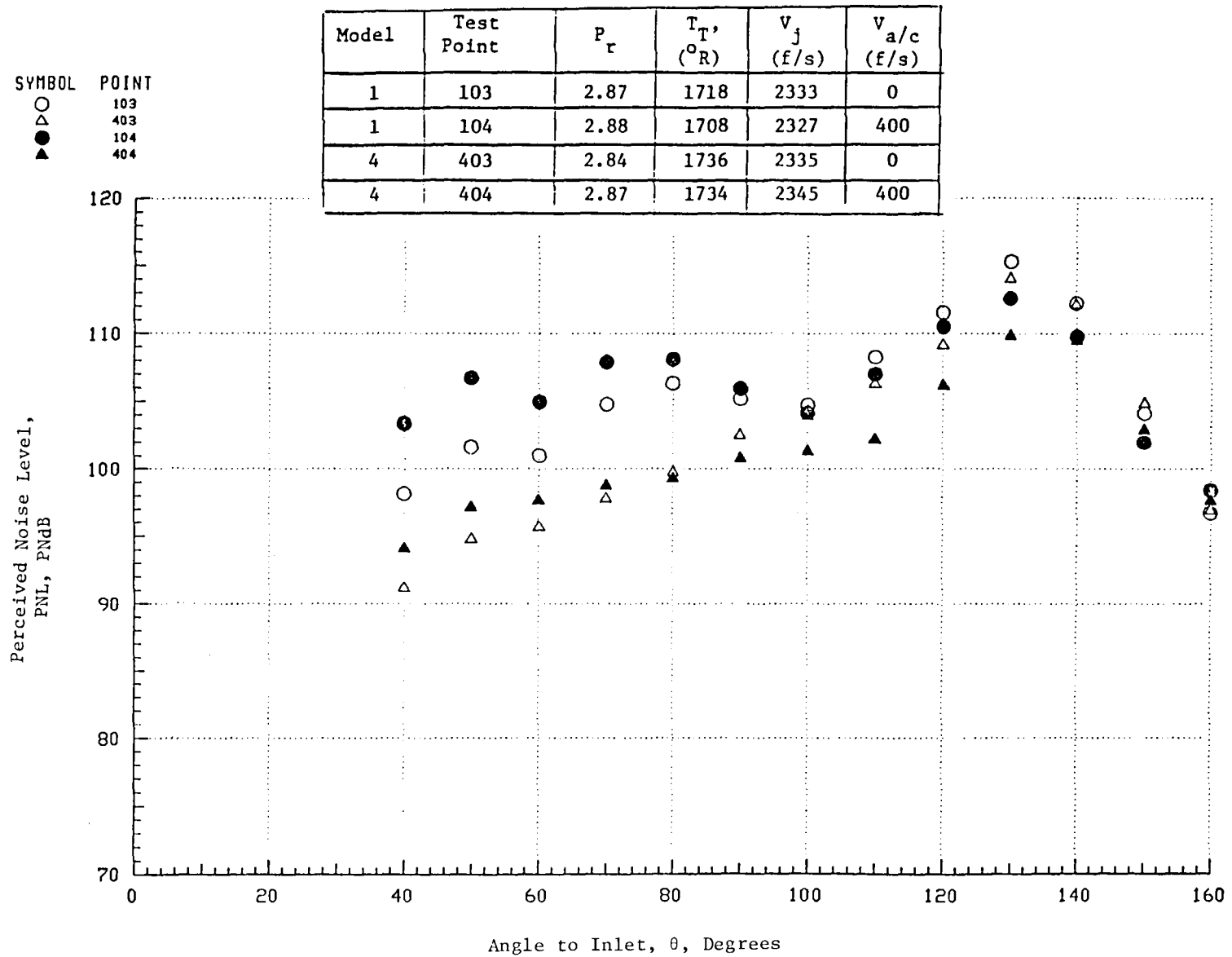


Figure 5-34. Static-to-Flight PNL Comparison at Overexpanded Flow Conditions, Convergent Circular (Model 1) and C-D Annular Plug (Model 4) Nozzles.

SYMBOL POINT
 ○ 103
 △ 403
 ● 104
 ▲ 404

Model	Test Point	P_r	T_T , (°R)	V_j (f/s)	$V_{a/c}$ (f/s)
1	103	2.87	1718	2333	0
1	104	2.88	1708	2327	400
4	403	2.84	1736	2335	0
4	404	2.87	1734	2345	400

124

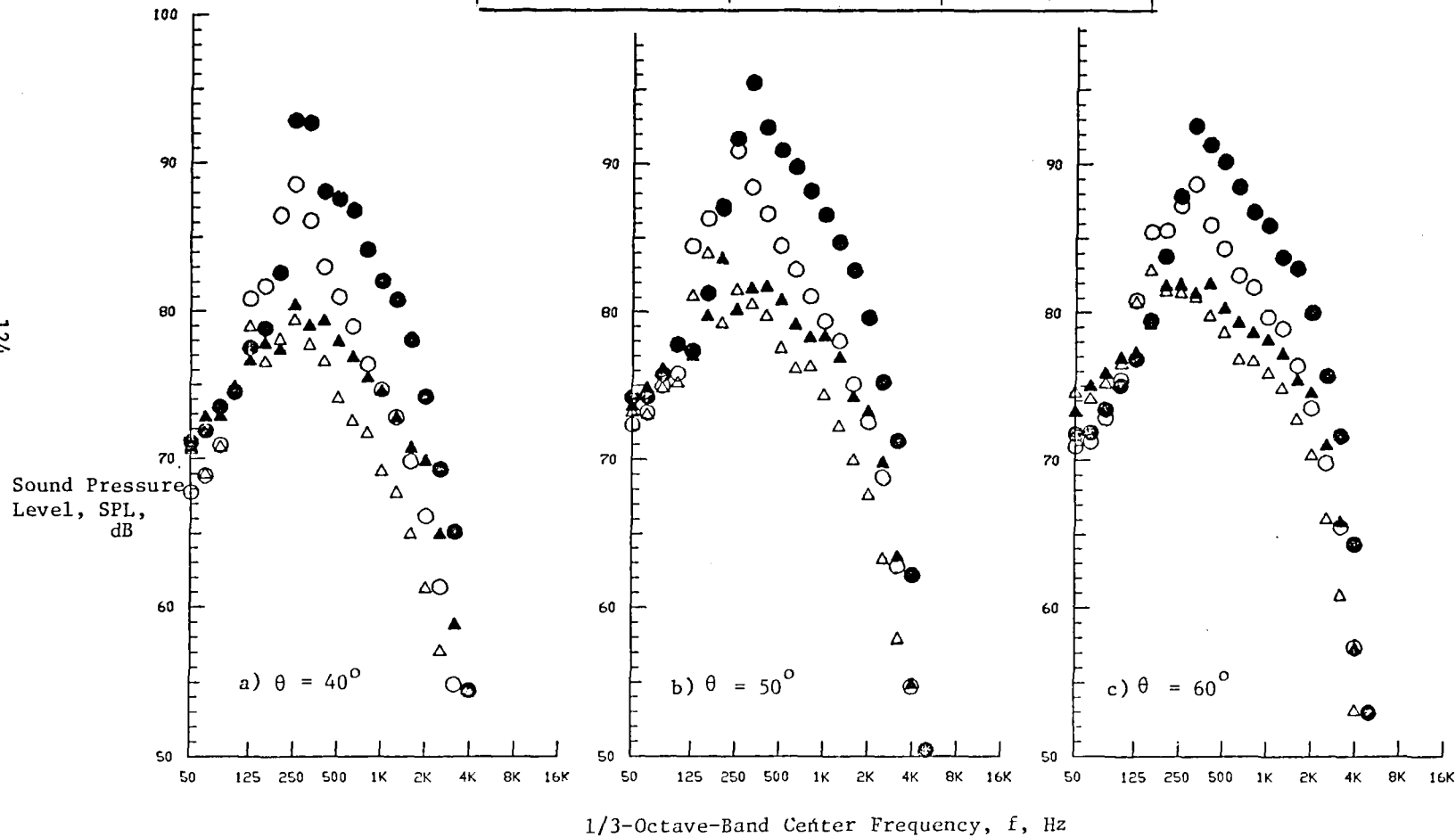
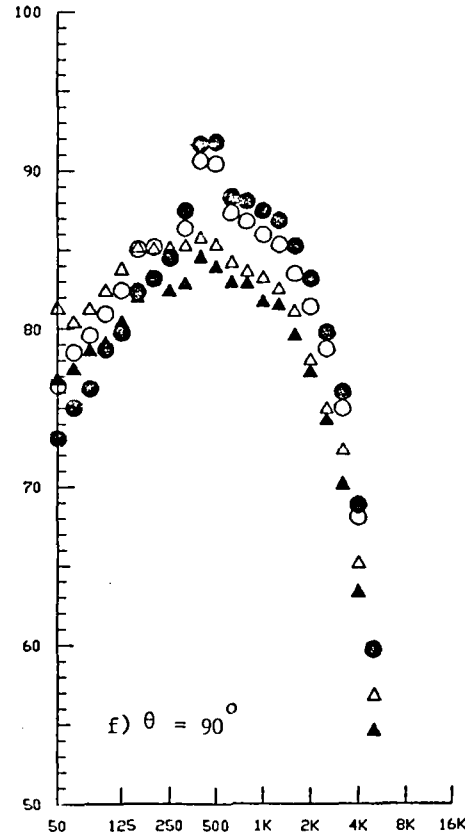
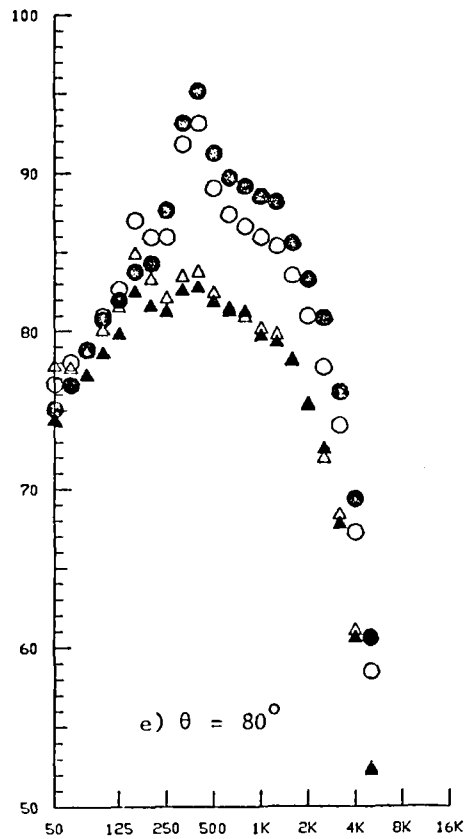
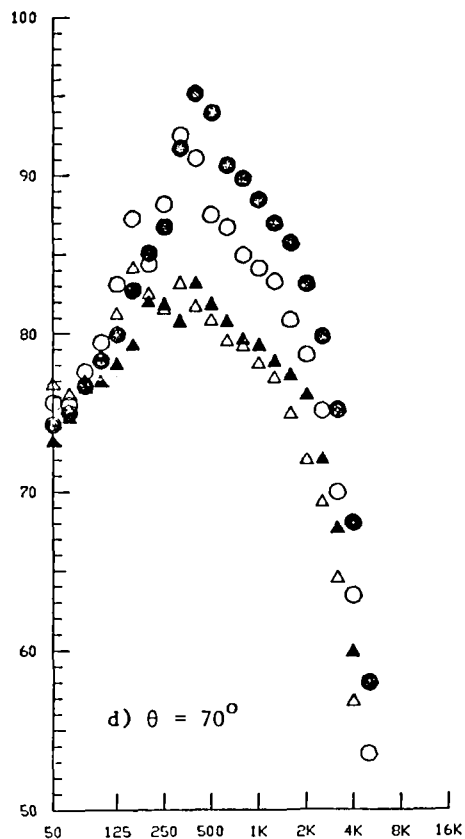


Figure 5-35. Static-to-Flight Spectral Comparison at Overexpanded Flow Conditions; Convergent Circular (Model 1) and C-D Annular Plug (Model 4) Nozzles.

SYMBOL	POINT
○	103
△	403
●	104
▲	404

Sound Pressure Level, SPL, dB

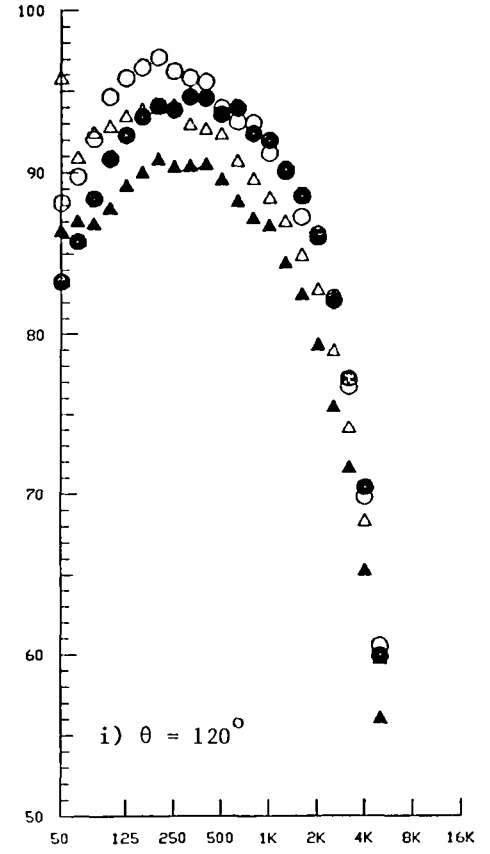
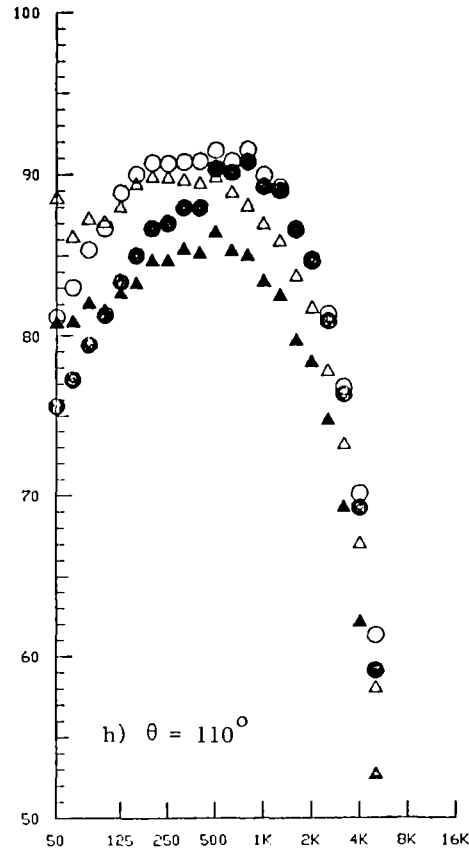
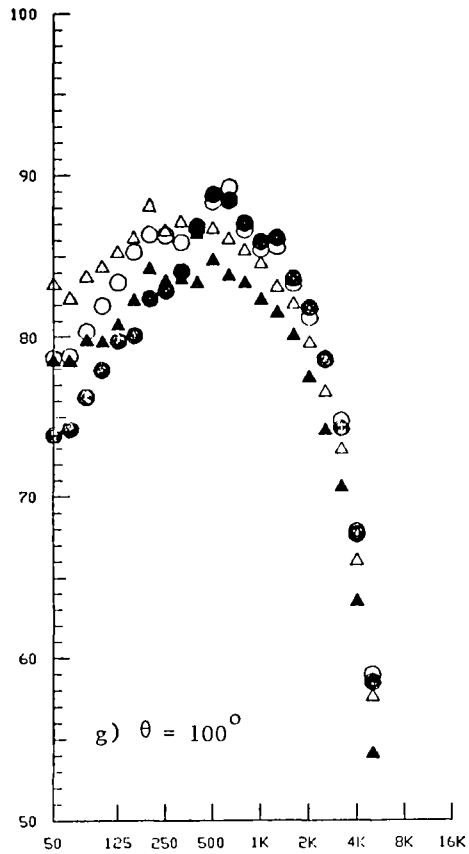


1/3-Octave-Band Center Frequency, f, Hz

Figure 5-35. (Cont'd.) Static-to-Flight Spectral Comparison at Overexpanded Flow Conditions; Convergent Circular (Model 1) and C-D Annular Plug (Model 4) Nozzles.

○	103
△	403
●	104
▲	404

Sound Pressure
Level, SPL,
dB



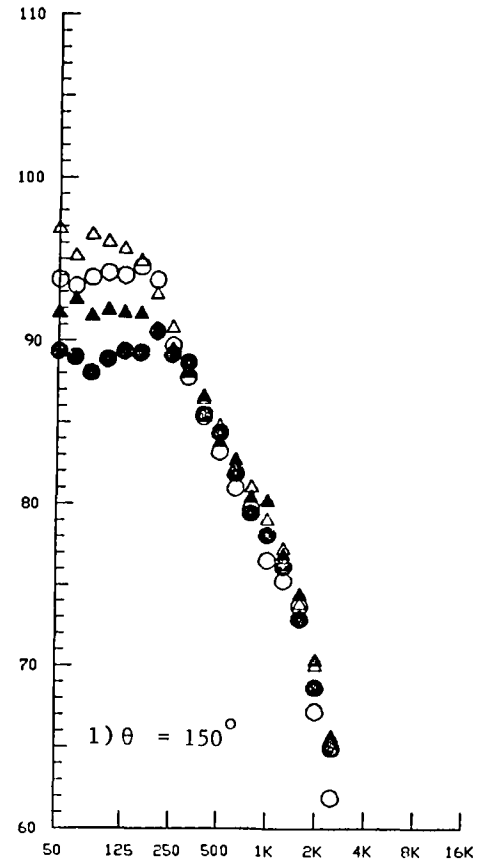
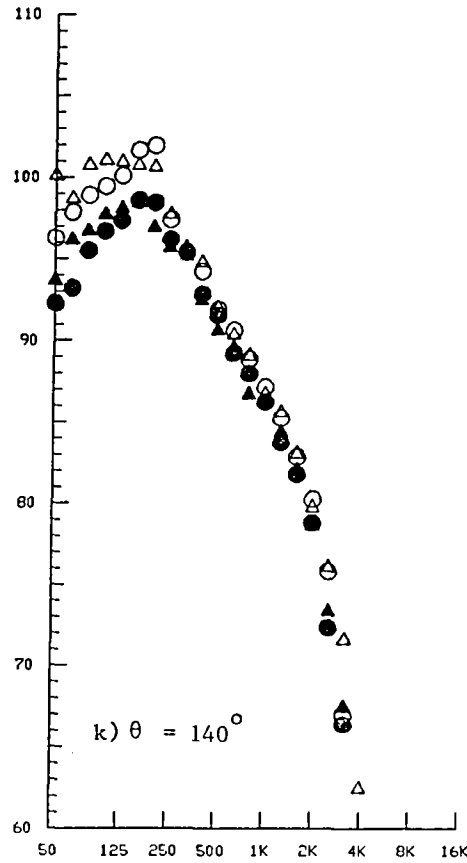
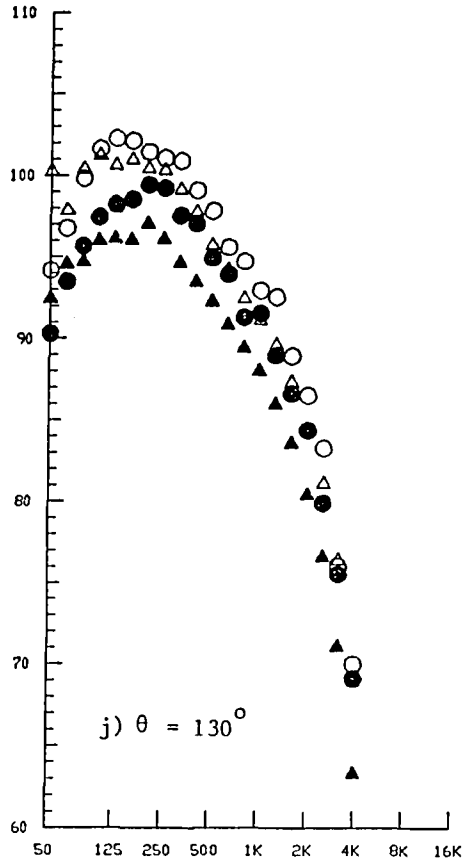
1/3-Octave-Band Center Frequency, f, Hz

Figure 5-35. (Cont'd.) Static-to-Flight Spectral Comparison at Overexpanded Flow Conditions; Convergent Circular (Model 1) and C-D Annular Plug (Model 4) Nozzles.

SYMBOL	POINT
○	103
△	403
●	104
▲	404

127

Sound Pressure
Level, SPL,
dB



1/3-Octave-Band Center Frequency, f , Hz

Figure 5-35. (Concluded.) Static-to-Flight Spectral Comparison at Overexpanded Flow Conditions; Convergent Circular (Model 1) and C-D Annular Plug (Model 4) Nozzles.

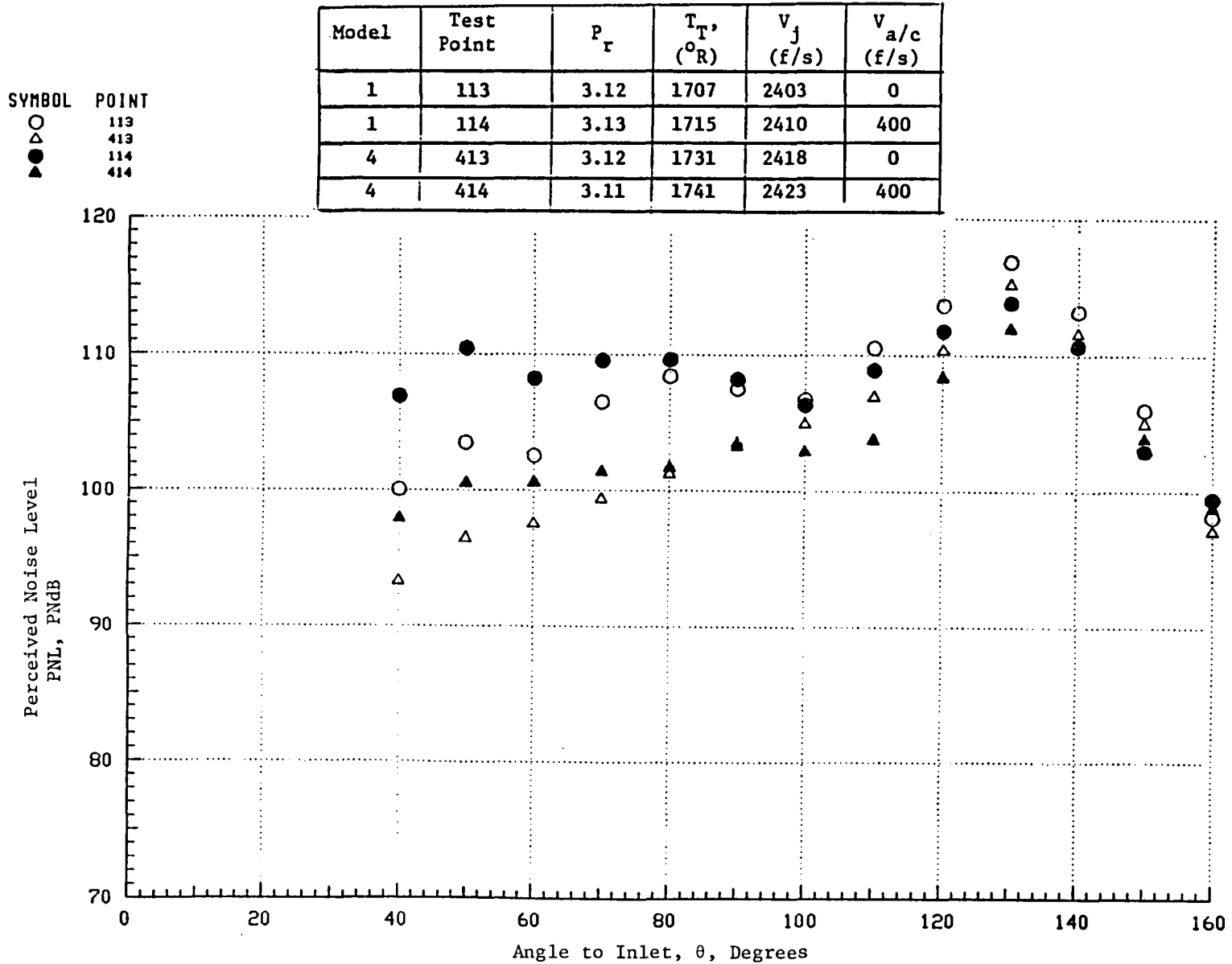


Figure 5-36. Static-to-Flight PNL Comparison at Design Operating Conditions; Convergent Circular (Model 1) and C-D Annular Plug (Model 4) Nozzles.

129 Sound Pressure Level, SPL, dB

SYMBOL POINT
 ○ 113
 △ 413
 ● 114
 ▲ 414

Model	Test Point	P_r	T_T ($^{\circ}R$)	V_j (f/s)	$V_{a/c}$ (f/s)
1	113	3.12	1707	2403	0
1	114	3.13	1715	2410	400
4	413	3.12	1731	2418	0
4	414	3.11	1741	2423	400

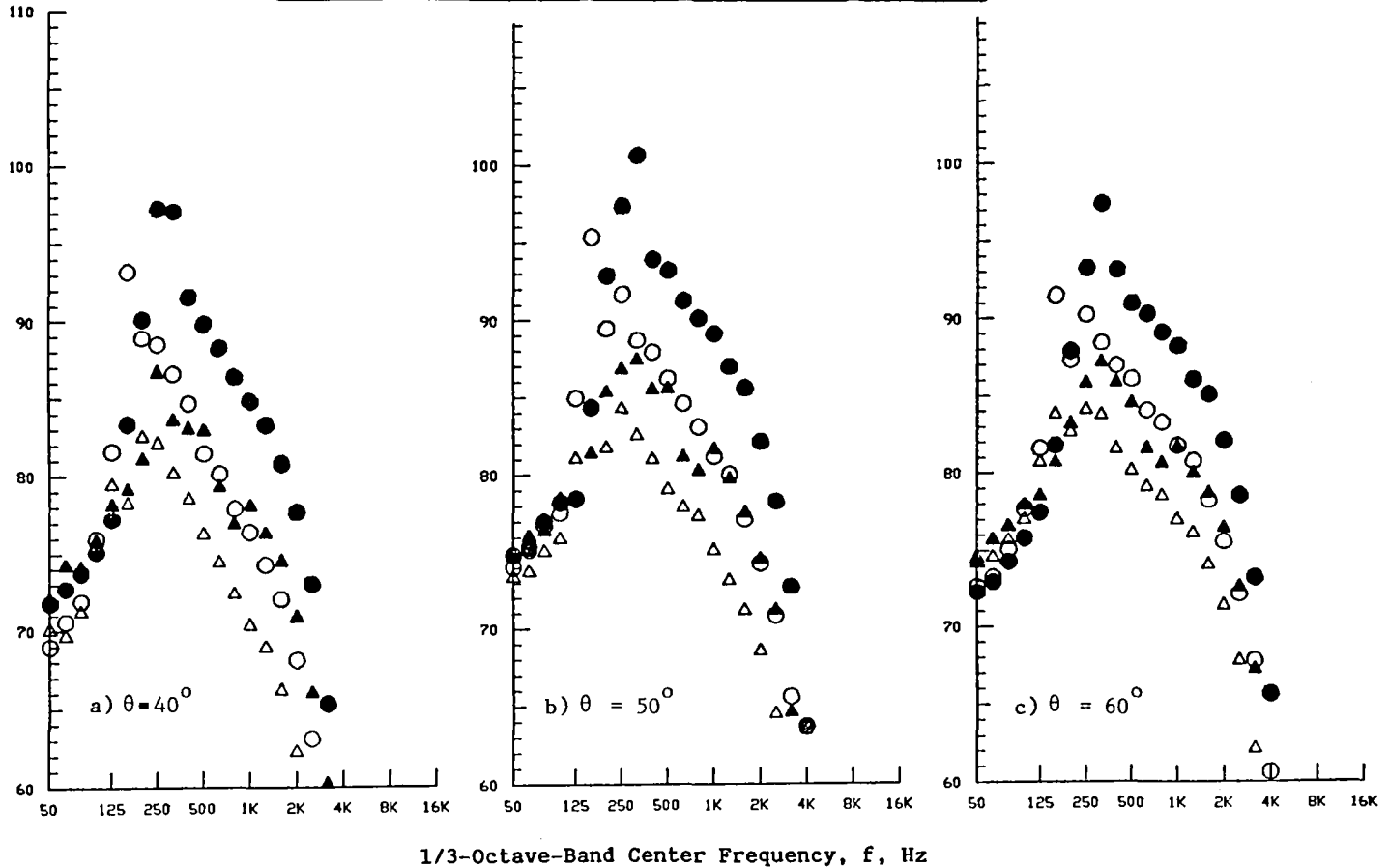


Figure 5-37. Static-to-Flight Spectral Comparison at Design Operating Conditions; Convergent Circular (Model 1) and C-D Annular Plug (Model 4) Nozzles.

SYMBOL	POINT
○	113
△	413
⊗	114
▲	414

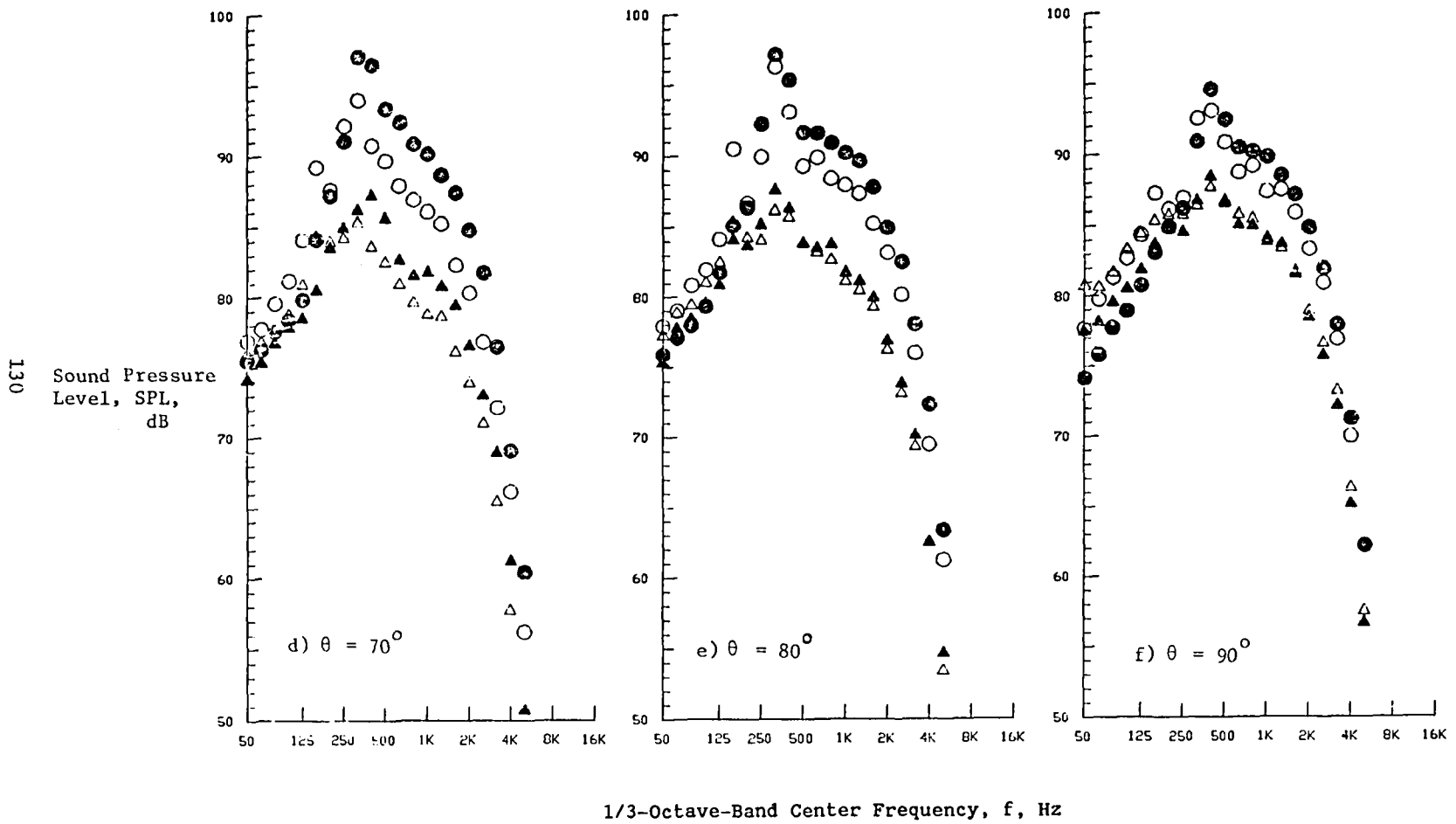


Figure 5-37. (Cont'd) Static-to-Flight Spectral Comparison at Design Operating Conditions; Convergent Circular (Model 1) and C-D Annular Plug (Model 4) Nozzles.

SYMBOL	POINT
○	113
△	413
●	114
▲	414

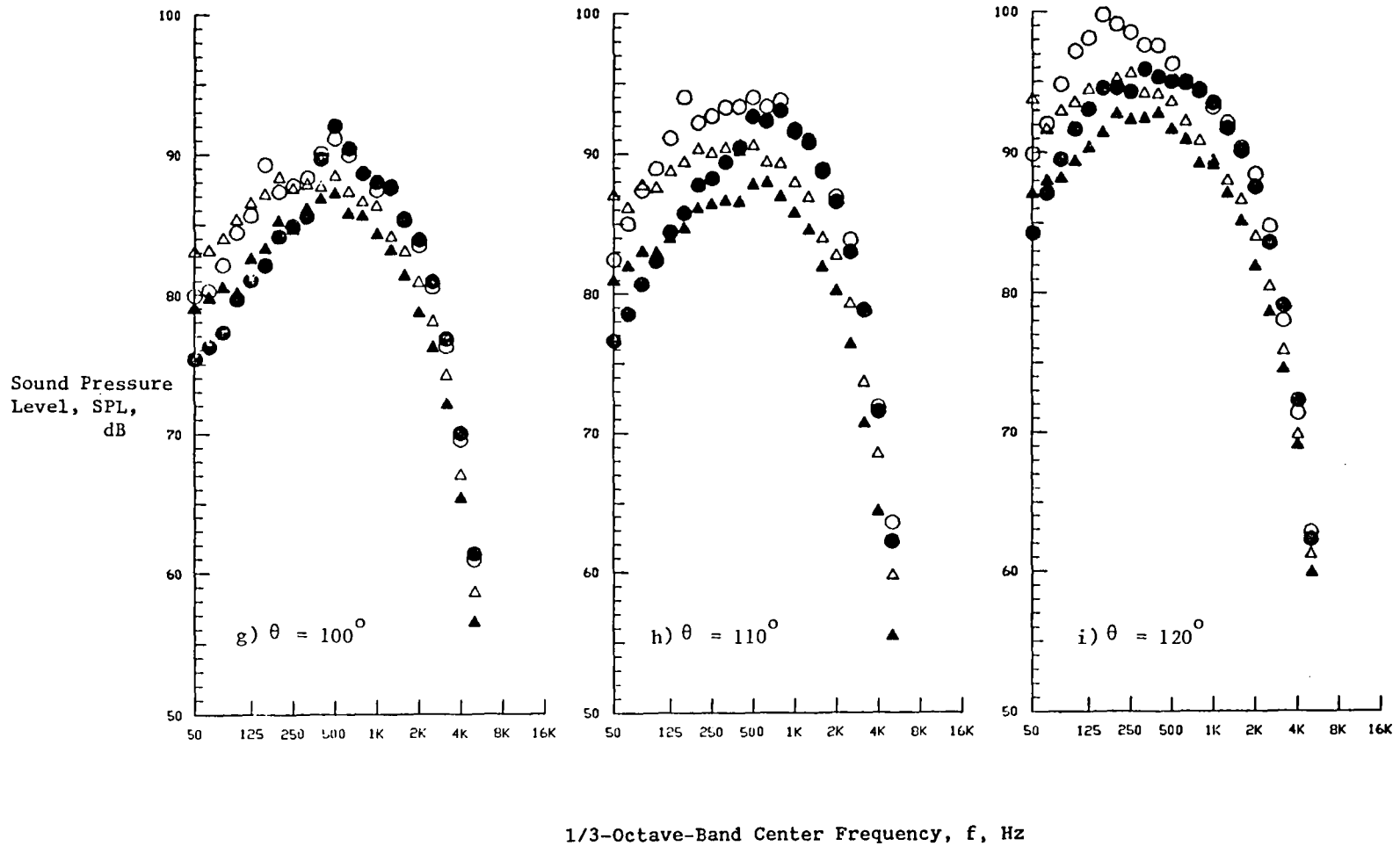


Figure 5-37. (Cont'd) Static-to-Flight Spectral Comparison at Design Operating Conditions; Convergent Circular (Model 1) and C-D Annular Plug (Model 4) Nozzles.

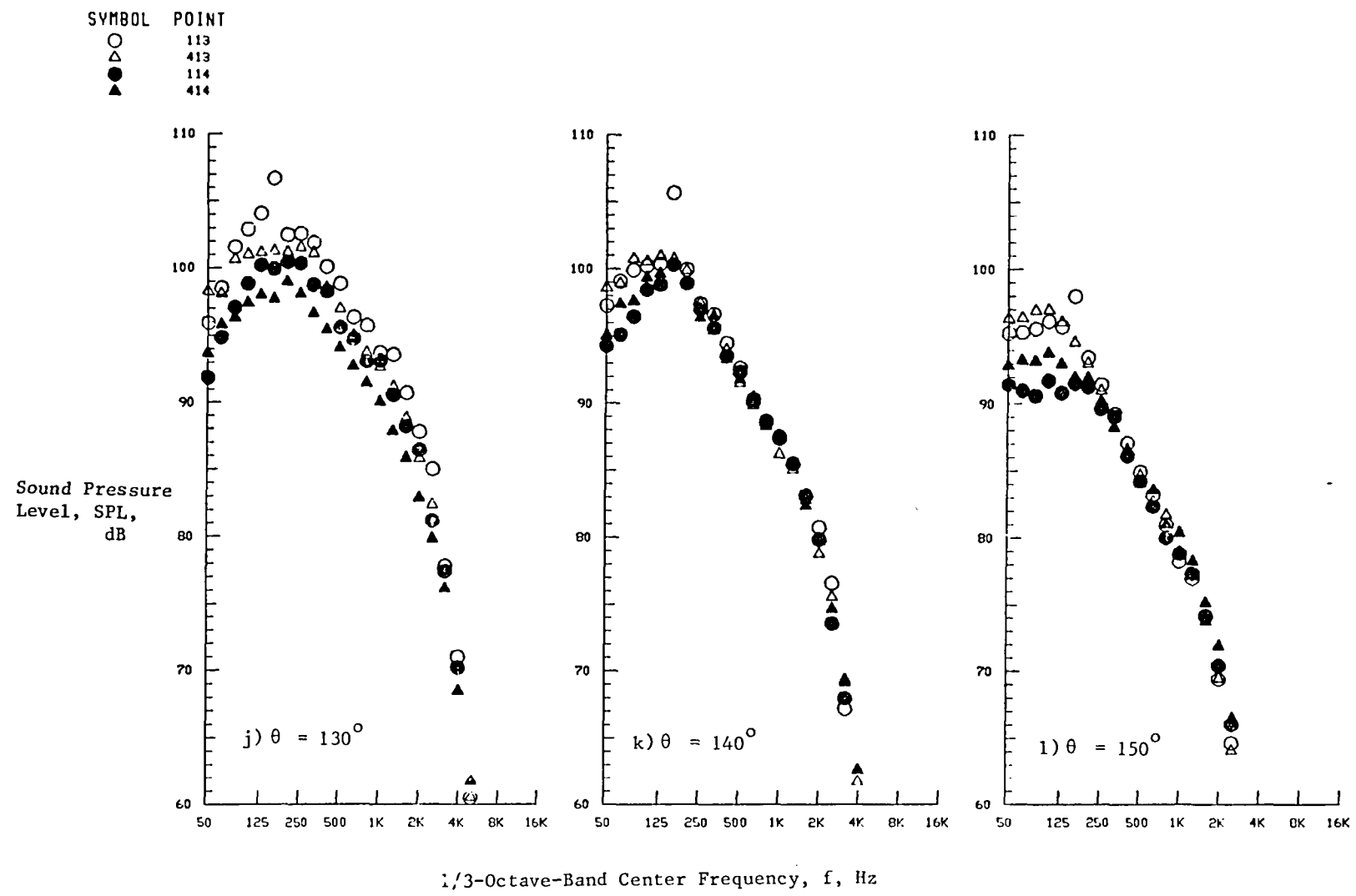


Figure 5-37. (Concluded) Static-to-Flight Spectral Comparison at Design Operating Conditions; Convergent Circular (Model 1) and C-D Annular Plug (Model 4) Nozzles.

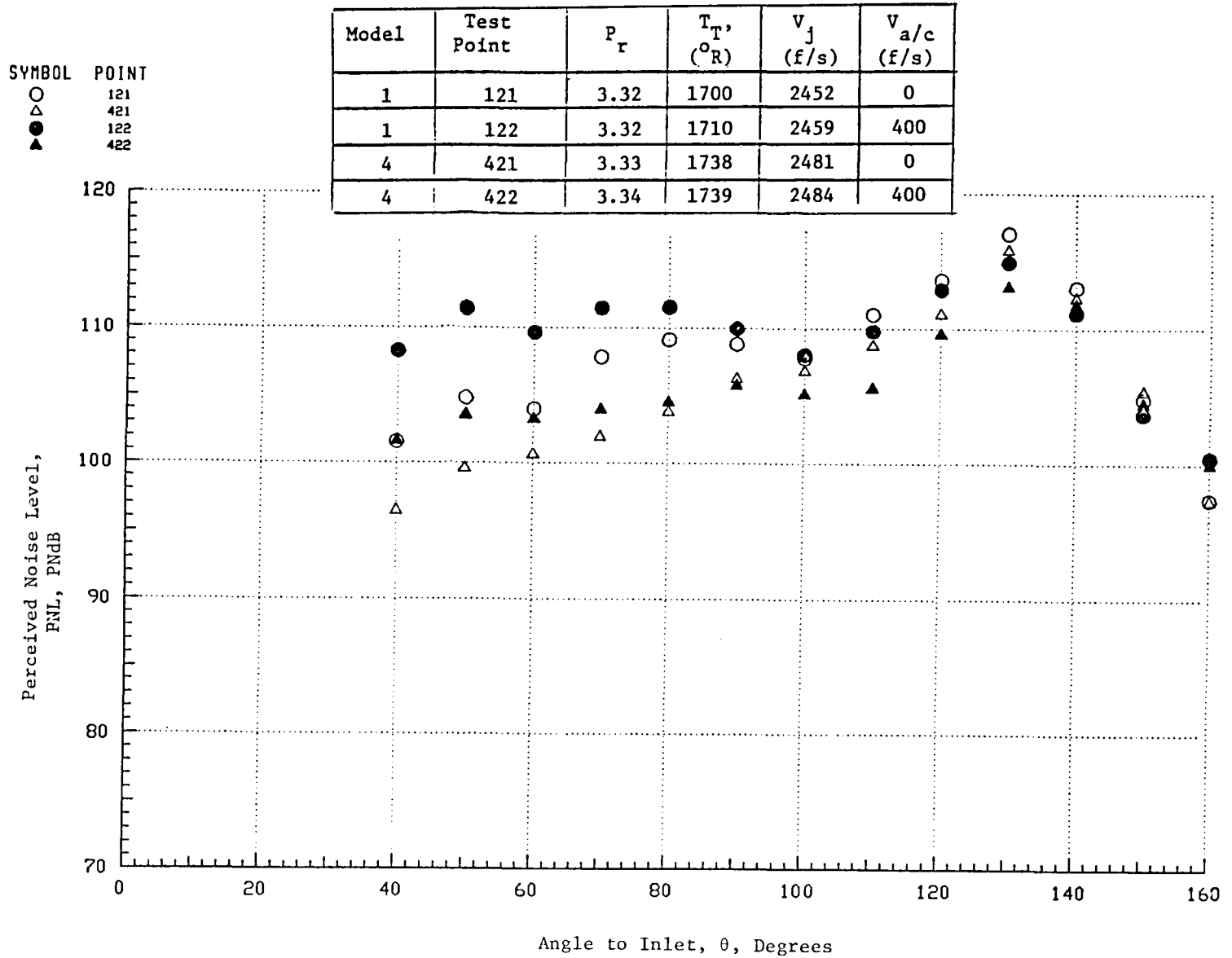


Figure 5-38. Static-to-Flight PNL Comparison at Underexpanded Flow Conditions; Convergent Circular (Model 1) and C-D Annular Plug (Model 4) Nozzles.

SYMBOL POINT
 ○ 121
 △ 421
 ● 122
 ▲ 422

Model	Test Point	P_r	T_T , (°R)	V_j (ft/s)	$V_{a/c}$ (ft/s)
1	121	3.32	1700	2452	0
1	122	3.32	1710	2459	400
4	421	3.33	1738	2481	0
4	422	3.34	1739	2484	400

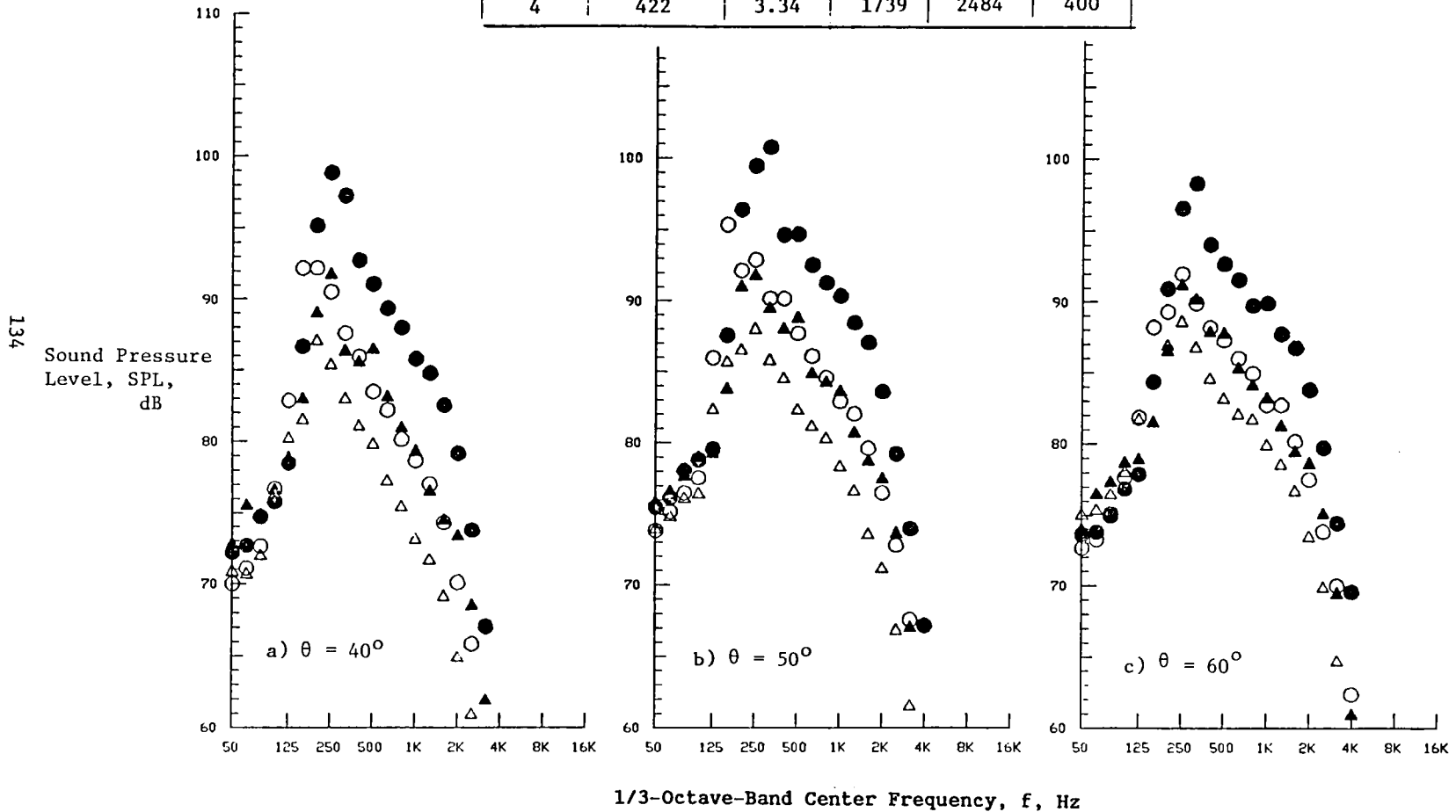
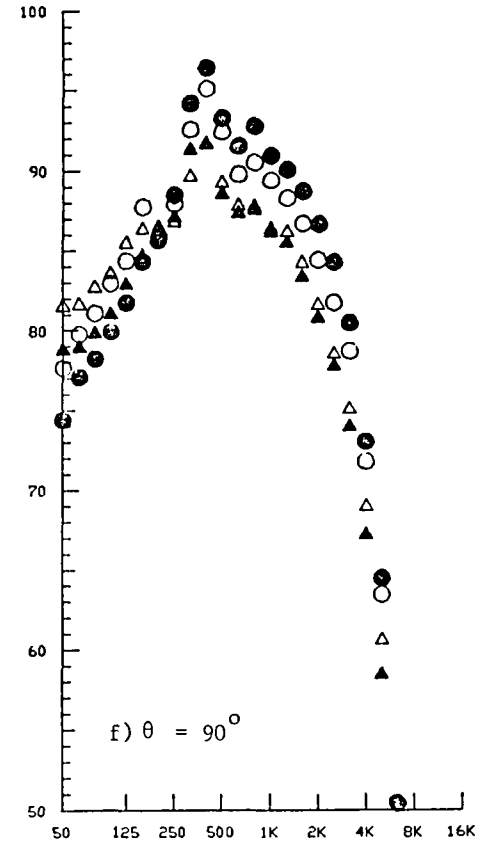
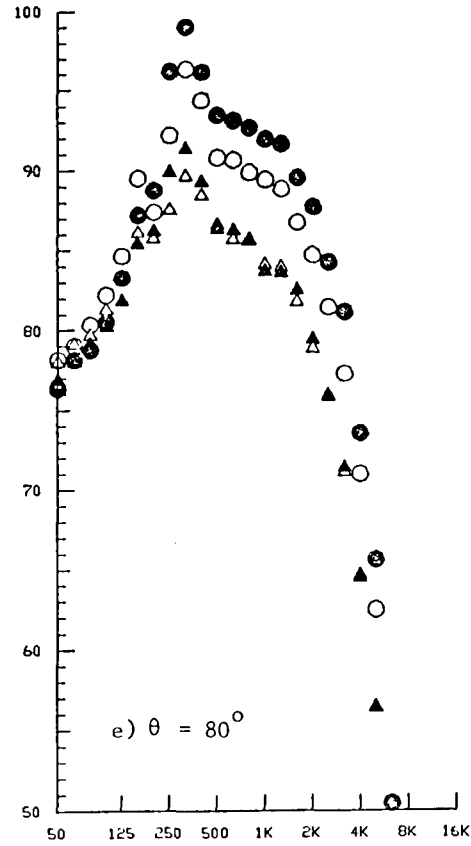
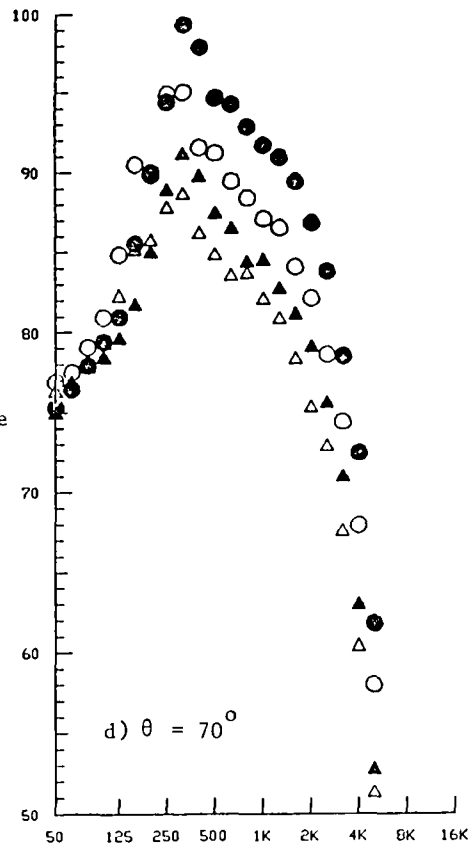


Figure 5-39. Static-to-Flight Spectral Comparison at Underexpanded Flow Conditions; Convergent Circular (Model 1) and C-D Annular Plug (Model 4) Nozzles.

Sound Pressure
Level, SPL,
dB

SYMBOL	POINT
○	121
△	421
●	122
▲	422



1/3-Octave-Band Center Frequency, f , Hz

Figure 5-39. (Cont'd) Static-to-Flight Spectral Comparison at Underexpanded Flow Conditions; Convergent Circular (Model 1) and C-D Annular Plug (Model 4) Nozzles.

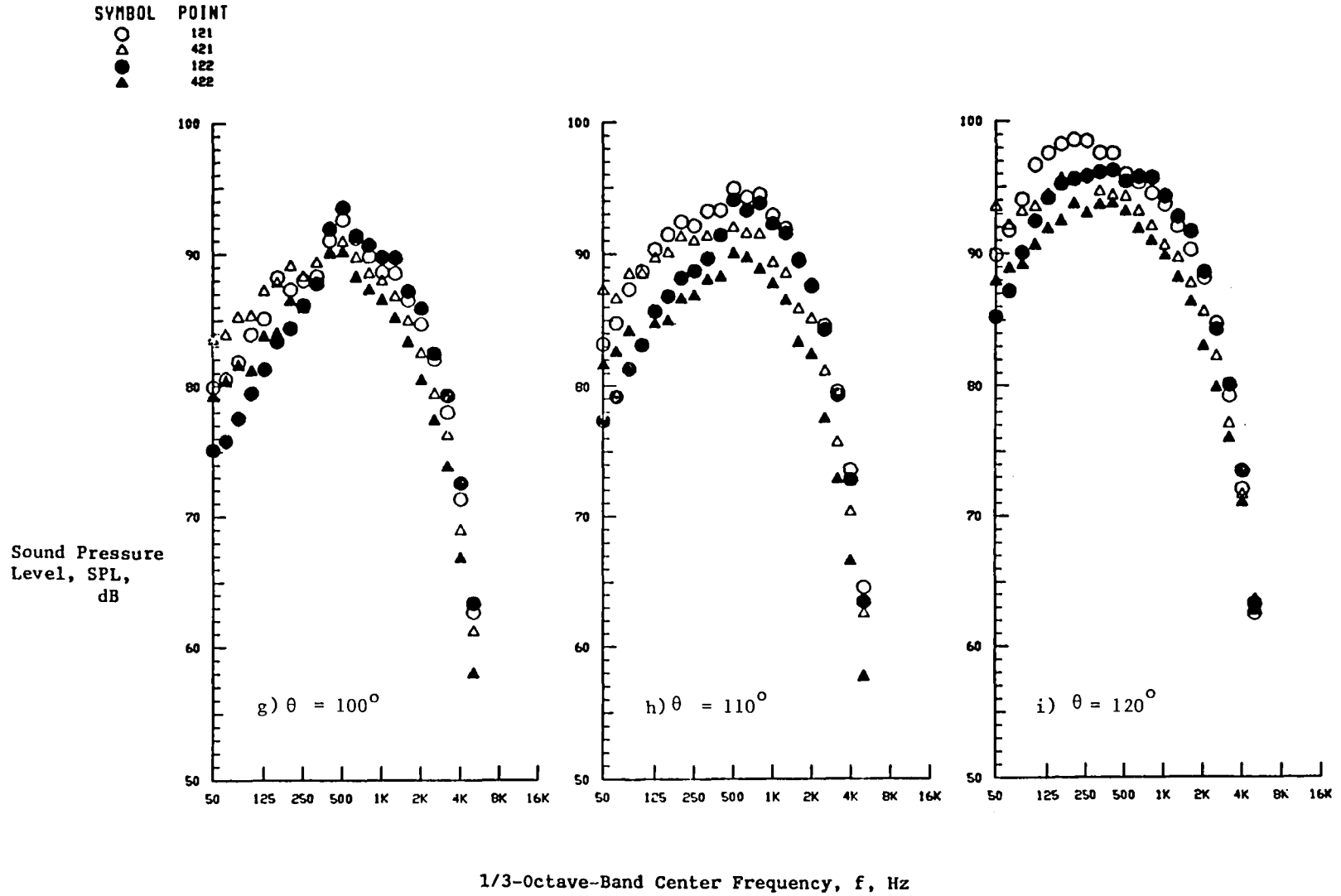


Figure 5-39. (Cont'd) Static-to-Flight Spectral Comparison at Underexpanded Flow Conditions; Convergent Circular (Model 1) and C-D Annular Plug (Model 4) Nozzles.

○	113
△	413
●	114
▲	414

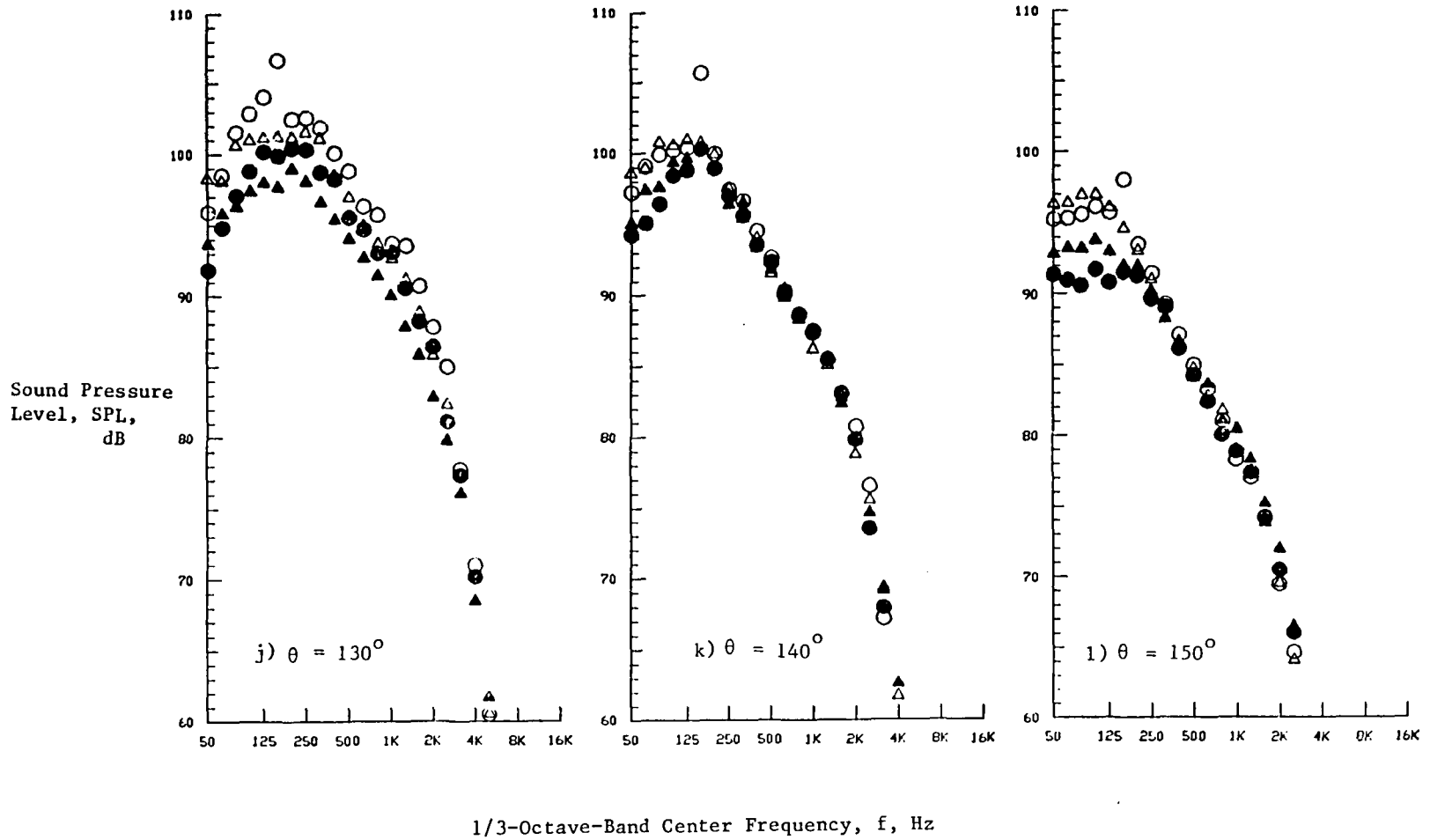


Figure 5-39. (Concluded) Static-to-Flight Spectral Comparison at Underexpanded Flow Conditions; Convergent Circular (Model 1) and C-D Annular Plug (Model 4) Nozzles.

The PNL directivity comparison presented in Figure 5-34 indicates a favorable PNL directivity pattern for the C-D annular plug nozzle over most observation angles at overexpanded plume conditions, as compared with the baseline convergent circular nozzle. Front quadrant amplification (of shock noise) and aft quadrant attenuation (of jet mixing noise) by flight is observed also. A small influence of forward velocity on the combined effect of the plug and the C-D termination is observed over the observation angle range of 40° through 130° . At 60° , for example, noise reduction due to the plug in combination with the C-D termination is 5 PNdB at the static condition, while at simulated flight the corresponding reduction amounts to 7 PNdB.

The implication of this result is that dominant shock noise source structure in the supersonic plume of the C-D annular plug nozzle is similar to that of the C-D circular nozzle. Since the equivalent diameter of the C-D annular plug nozzle ($Deq = 5.67''$) is roughly equal to the jet exit diameter (measured at throat) of the C-D circular nozzle and, in addition, the jet diameter is a principle length scale associated with the shock-cell structure, it is possible that the C-D annular plug nozzle major shock noise source location is not in the proximity of the jet exit but is downstream of the plug.

A static-to-flight spectral comparison of the C-D annular plug nozzle jet noise with the baseline convergent circular nozzle jet noise is presented in Figure 5-35 under identical aerodynamic conditions to those given in Figure 5-34. An examination of the typical front quadrant spectra (e.g., at $\theta = 60^\circ$) indicates a significant flight amplification of high frequency noise for both nozzles. In addition, the forward velocity tends to shift the peak frequency to the right (i.e., higher frequencies). This may be partly attributed to the elimination of the discrete shock noise components (screech). This trend is observed for both convergent circular and C-D annular plug nozzles. A relatively modest flight amplification observed for the C-D annular plug nozzle, as compared with that observed for the baseline convergent circular nozzle, may indicate a relatively small shock noise source region downstream of the plug. At $\theta = 130^\circ$ where observed PNL has a maximum value as shown in Figure 5-34, a favorable spectral profile for the C-D annular plug nozzle is noted. Over the entire frequency range of interest, the flight attenuation is larger for the C-D annular plug nozzle relative to that for the baseline convergent circular nozzle.

Figures 5-36 through 5-39 represent corresponding static-to-flight PNL and spectral comparisons between the C-D annular plug and the baseline convergent circular nozzles at the design and underexpanded flow conditions. No significant difference is observed in the results of these figures from those provided in Figures 5-34 and 5-35.

5.2.1.4 Convergent Multi-Element Suppressor Nozzle (Model 5)

Comparisons of the static and simulated flight PNL and SPL spectral data of the convergent multi-element suppressor nozzle (Model 5) with those of the baseline convergent circular nozzle (Model 1) are presented in Figures 5-40 and 5-41. Figure 5-40 illustrates PNL directivities for Models 1 and 5. Flight amplification observed over the front quadrant angles is similar to both nozzles. A rather flat directivity pattern over 50°-110° is noted for Test Point 514.

5.2.1.5 C-D Multi-Element Suppressor Nozzle (Model 6)

Comparisons of the static and simulated flight PNL and SPL spectral data of the C-D multi-element suppressor nozzle (Model 6) with those of the baseline convergent circular nozzle (Model 1) over the design and off-design operating conditions is provided in Figures 5-42 through 47. Figure 5-42 illustrates the static-to-flight PNL comparison of the C-D suppressor nozzle under a typical overexpanded plume condition ($P_r = 2.87$, $T_T = 1730^\circ R$). A general trend of the front quadrant amplification and the rear quadrant attenuation of PNL by flight is observed in this figure. However, as we note by comparing Figure 5-42 with Figures 5-22 and 5-28, significant reduction of PNL in the aft quadrant is observed only after about $\theta = 130^\circ$ in the case of the C-D suppressor nozzle. A similar observation can be made in the case of the design and underexpanded operating conditions (see Figures 5-44 and 5-46).

As far as the amount of flight amplification of PNL in the forward quadrant is concerned, as noted in Figure 5-42, no significant difference was demonstrated between the suppressor and convergent circular nozzle, in contrast to the case of the C-D annular plug nozzle (Figure 5-36).

A static-to-flight spectral comparison between the C-D suppressor and the baseline convergent circular nozzle acoustic data under a typical

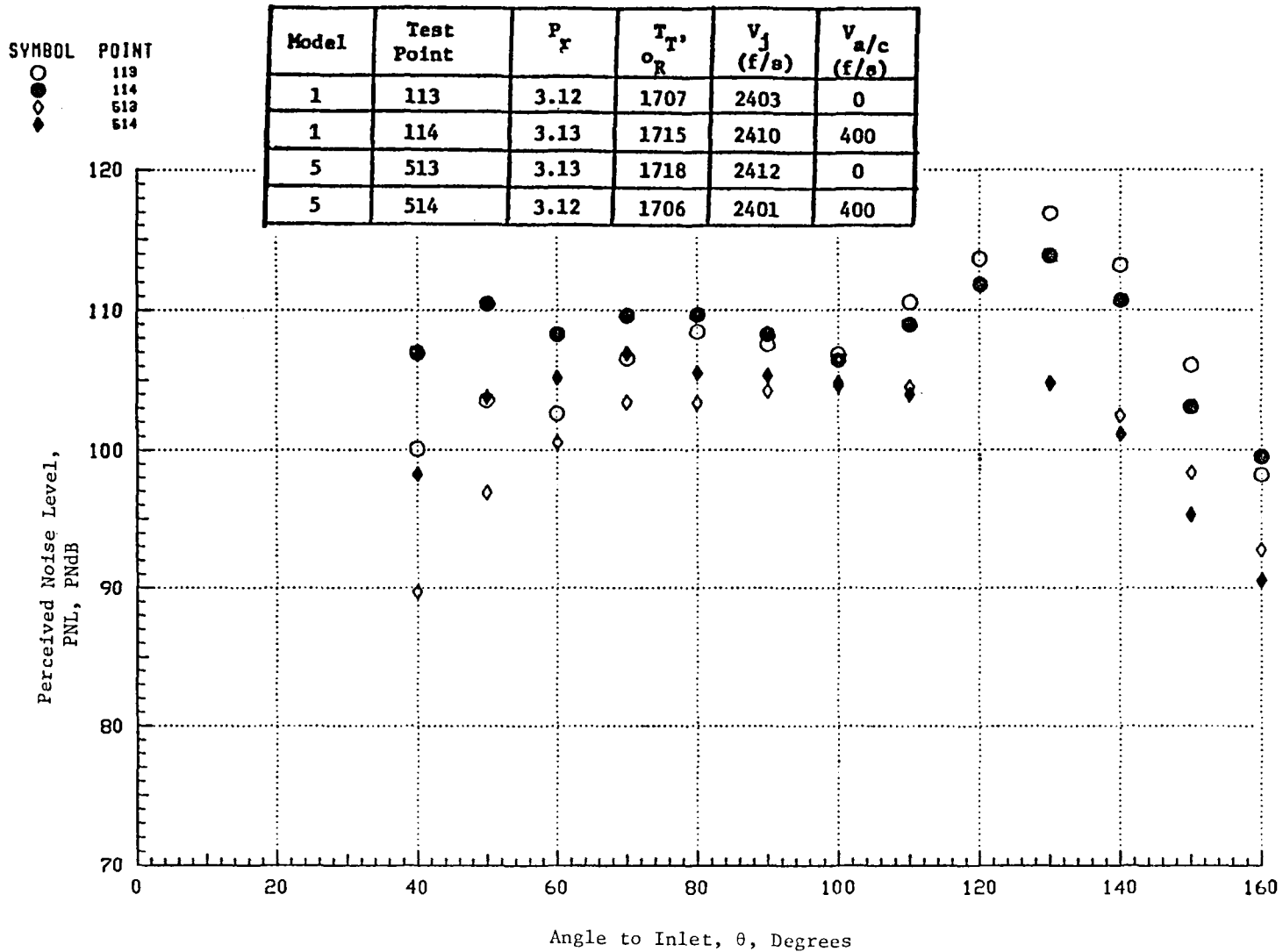


Figure 5-40. Static-to-Flight PNL Comparison Under Aerodynamic Conditions Corresponding to C-D Design Conditions for C-D Nozzles; Convergent Circular (Model 1) and Convergent Multi-Element Suppressor Plug (Model 5) Nozzles.

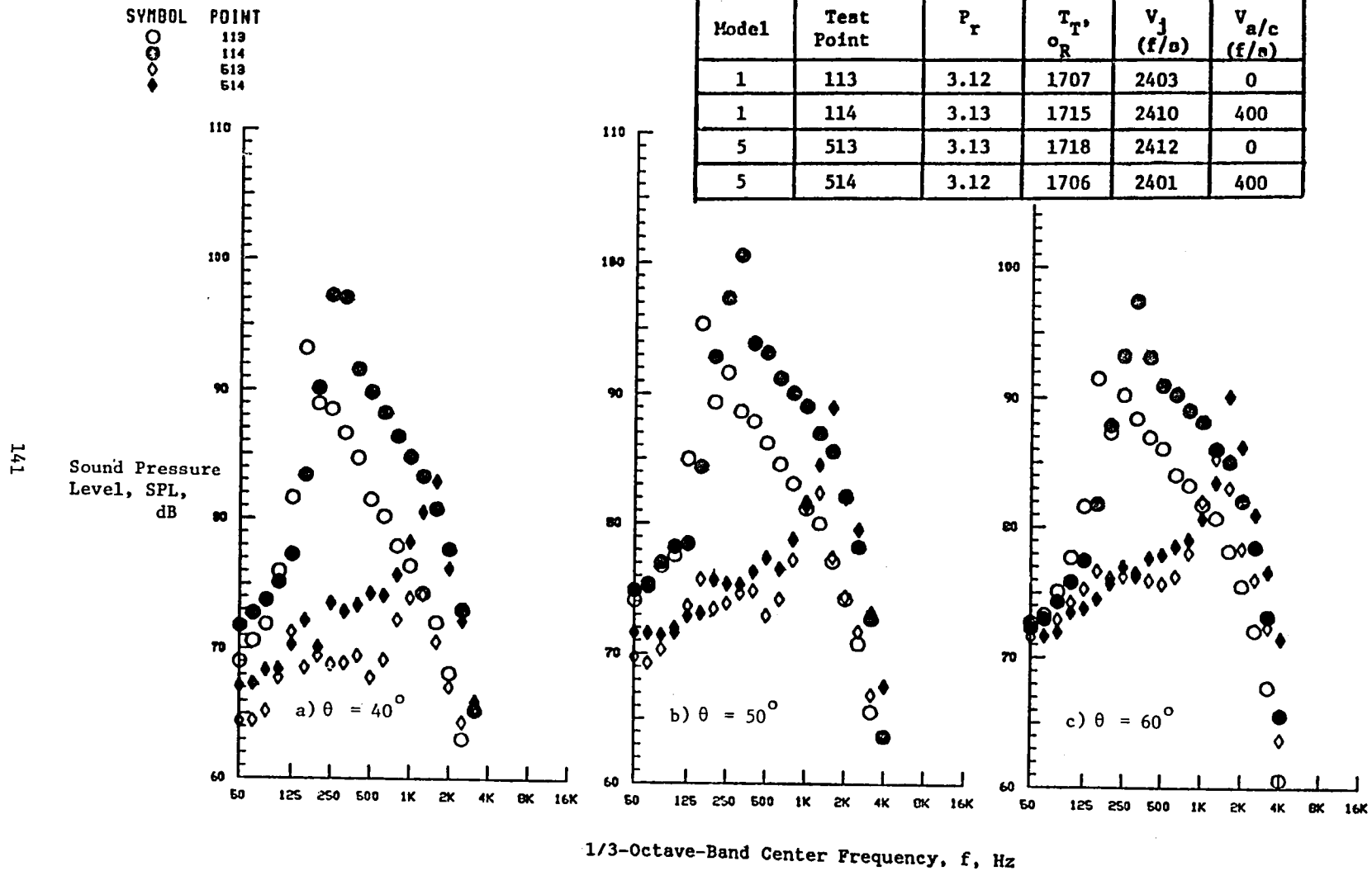


Figure 5-41. Static-to-Flight Spectral Comparison Under Aerodynamic Conditions Corresponding to C-D Design Conditions for C-D Nozzles; Convergent Circular (Model 1) and Convergent Multi-Element Suppressor Plug (Model 5) Nozzles

SYMBOL	POINT
○	113
●	114
◇	613
◆	614

142

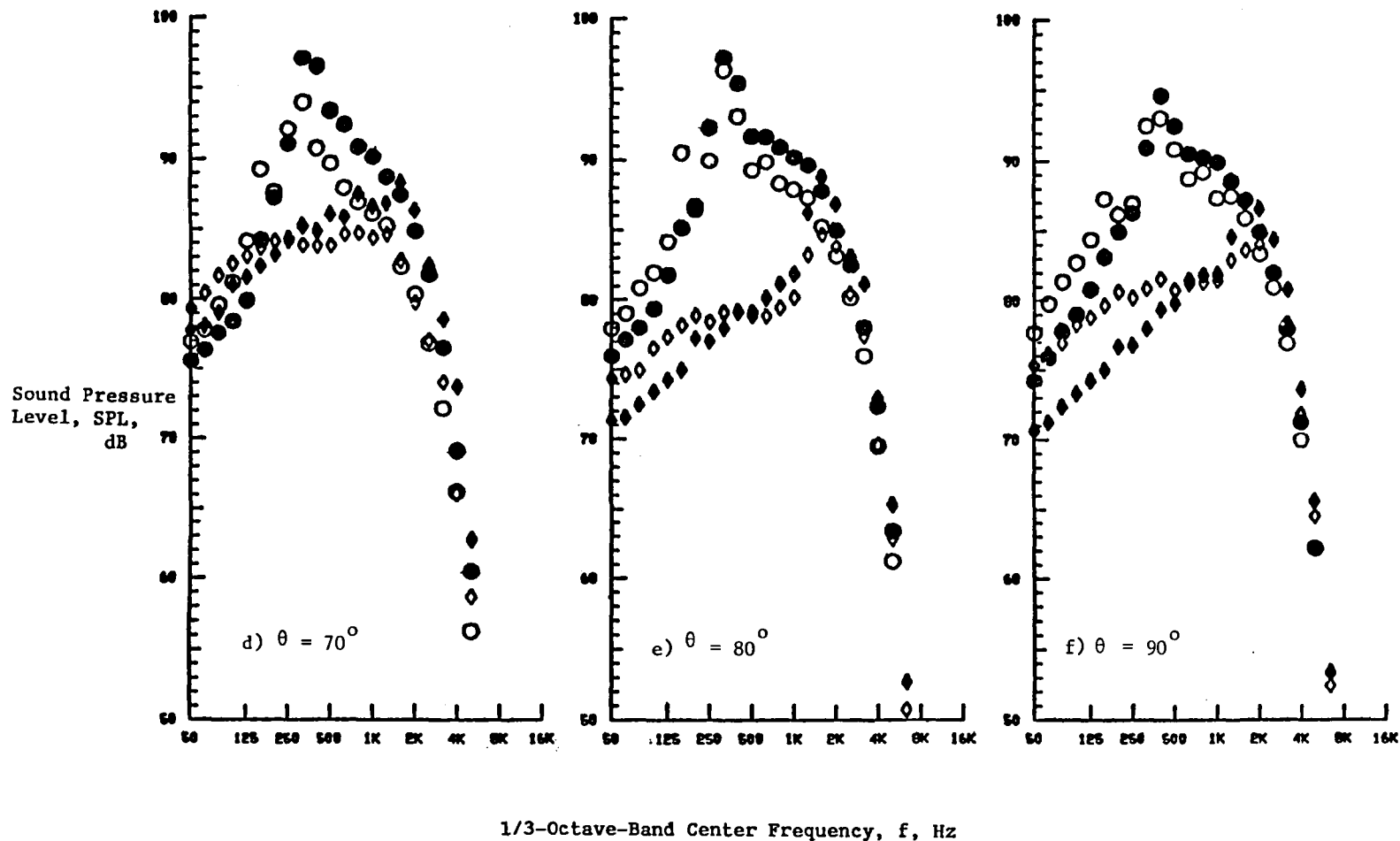
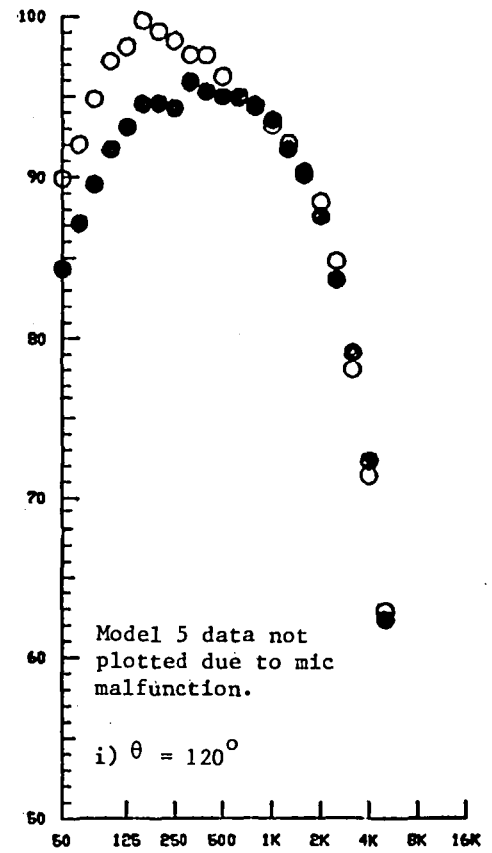
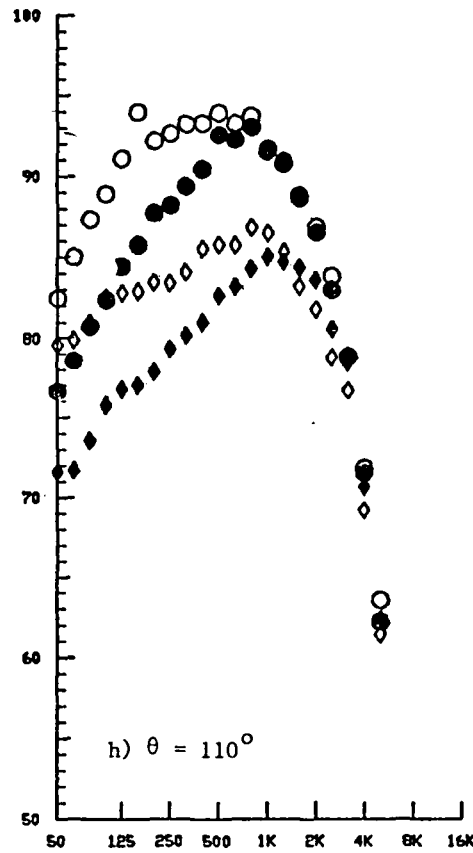
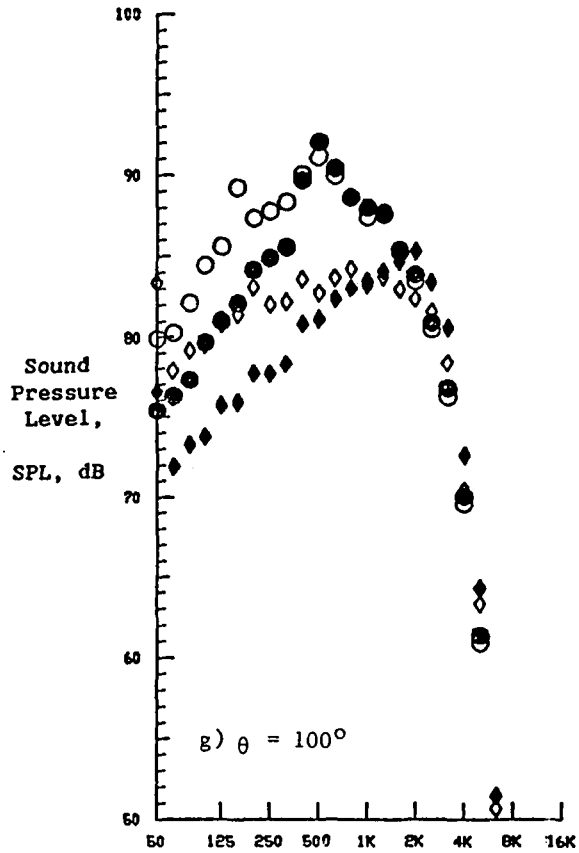


Figure 5-41. (Cont'd) Static-to-Flight Spectral Comparison Under Aerodynamic Conditions Corresponding to C-D Design Conditions for C-D Nozzles; Convergent Circular (Model 1) and Convergent Multi-Element Suppressor Plug (Model 5) Nozzles

SYMBOL	POINT
○	113
●	114
◊	513
◆	514



1/3-Octave-Band Center Frequency, f , Hz

Figure 5-41. (Cont'd) Static-to-Flight Spectral Comparison Under Aerodynamic Conditions Corresponding to C-D Design Conditions for C-D Nozzles; Convergent Circular (Model 1) and Convergent Multi-Element Suppressor Plug (Model 5) Nozzles

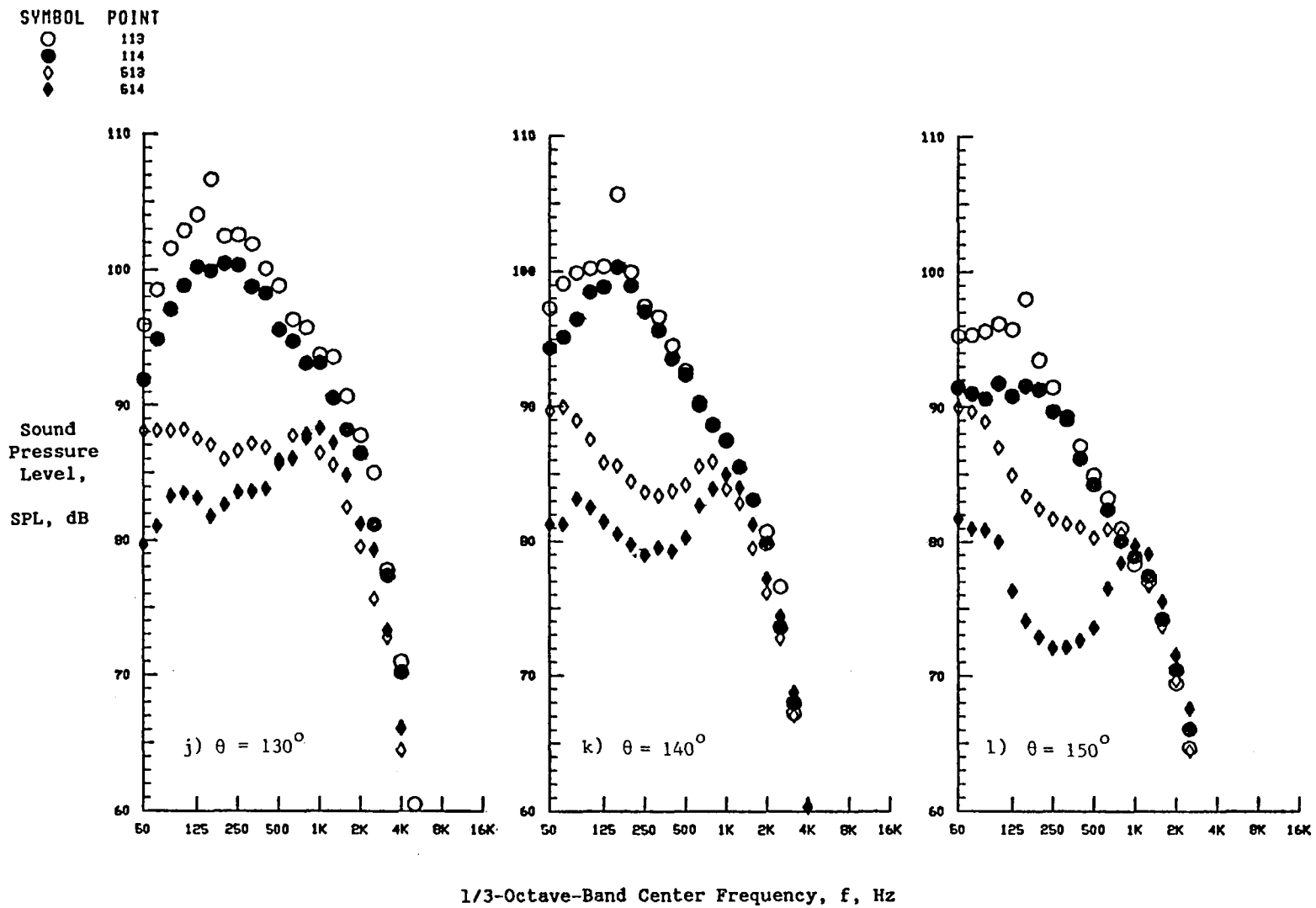


Figure 5-41. (Concluded) Static-to-Flight Spectral Comparison Under Aerodynamic Conditions Corresponding to C-D Design Conditions for C-D Nozzles; Convergent Circular (Model 1) and Convergent Multi-Element Suppressor Plug (Model 5) Nozzles

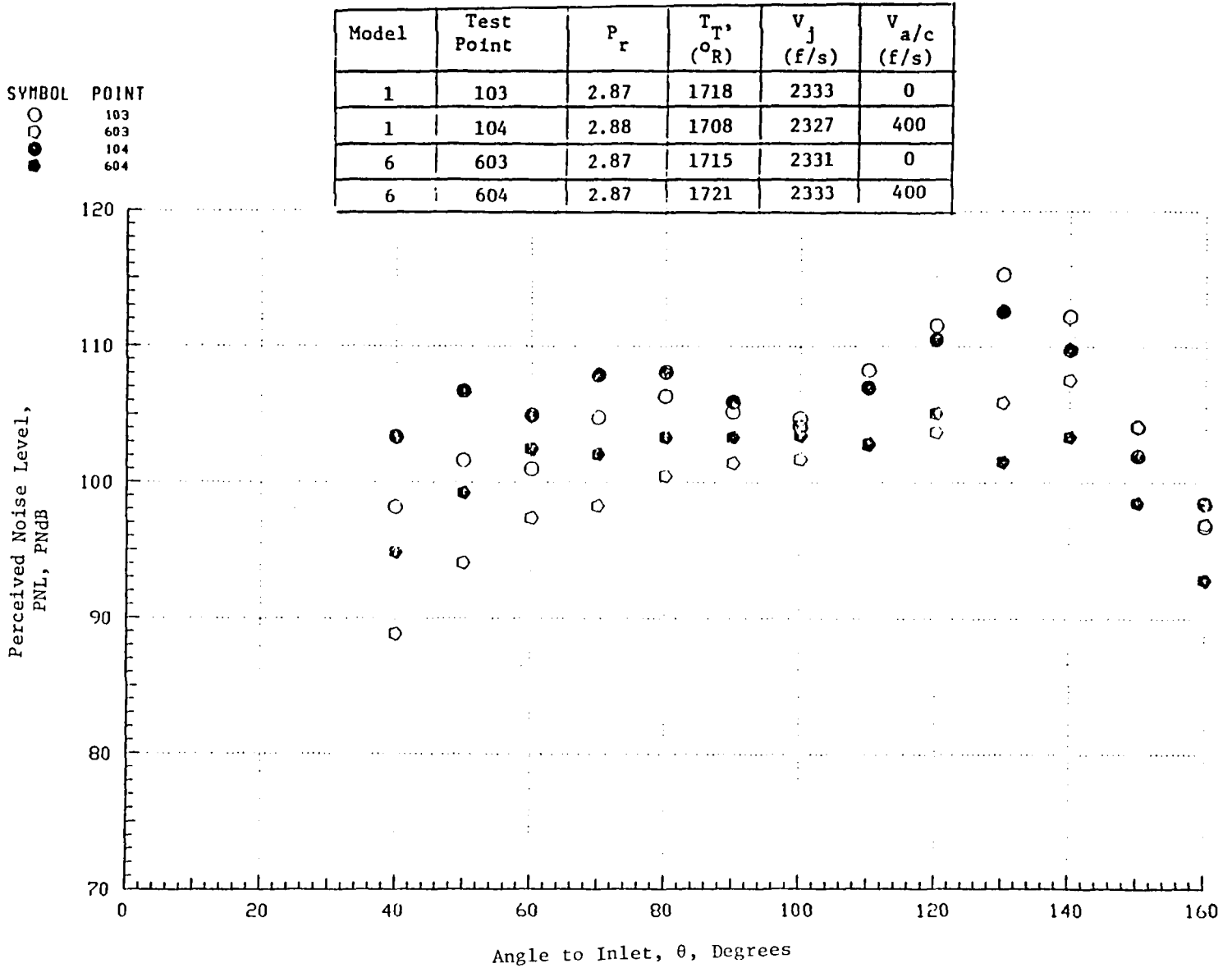


Figure 5-42. Static-to-Flight PNL Comparison at Overexpanded Flow Conditions, Convergent Circular (Model 1) and C-D Suppressor (Model 6) Nozzles.

SYMBOL POINT
 ○ 103
 ○ 603
 ● 104
 ● 604

Model	Test Point	P_r	$T_{T'} / T_{T'}^*$ (°R)	V_j (f/s)	$V_{a/c}$ (f/s)
1	103	2.87	1718	2333	0
1	104	2.88	1708	2327	400
6	603	2.87	1715	2331	0
6	604	2.87	1721	2333	400

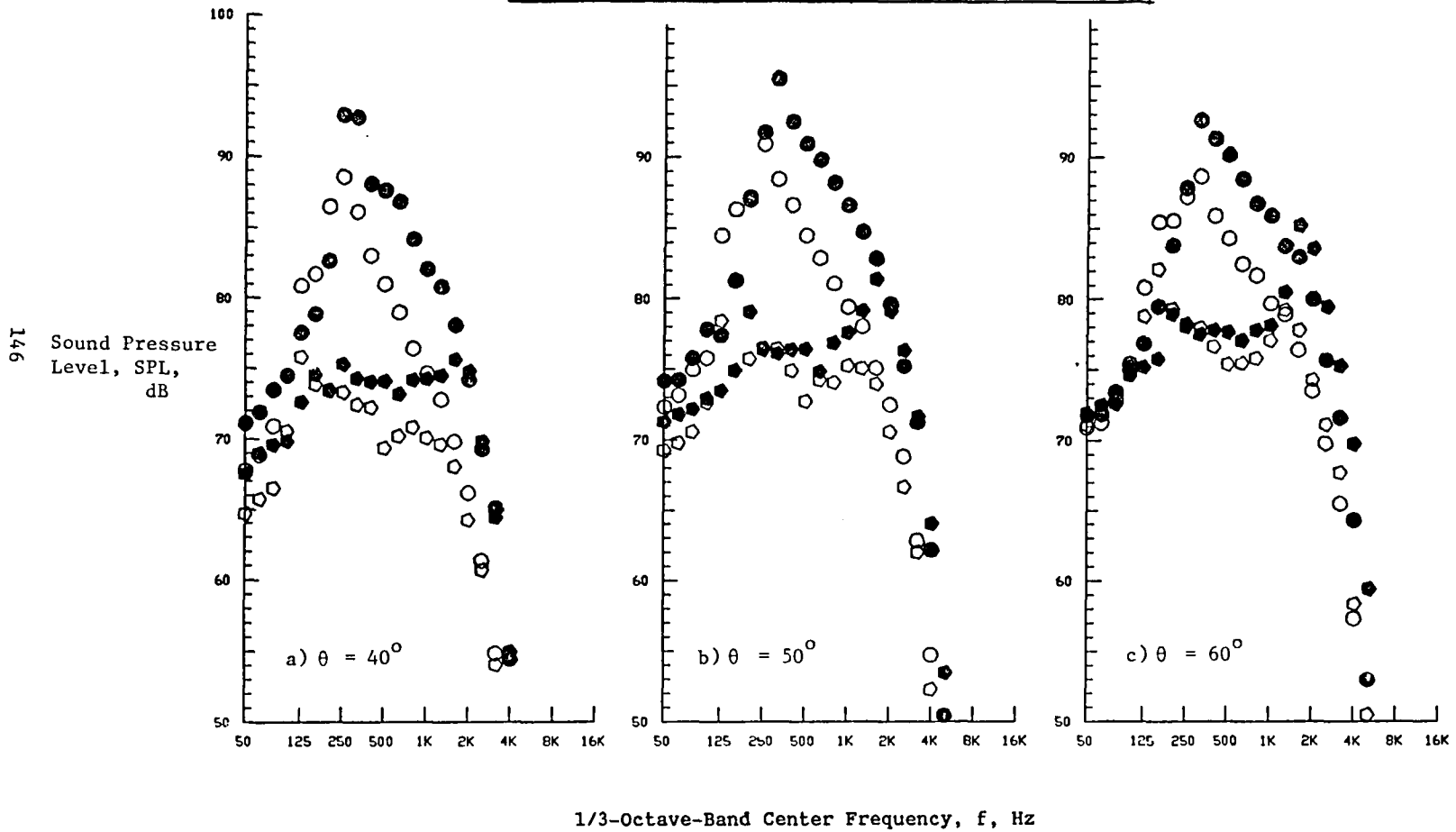


Figure 5-43. Static-to-Flight Spectral Comparison at Overexpanded Flow Conditions; Convergent Circular (Model 1) and C-D Suppressor (Model 6) Nozzles.

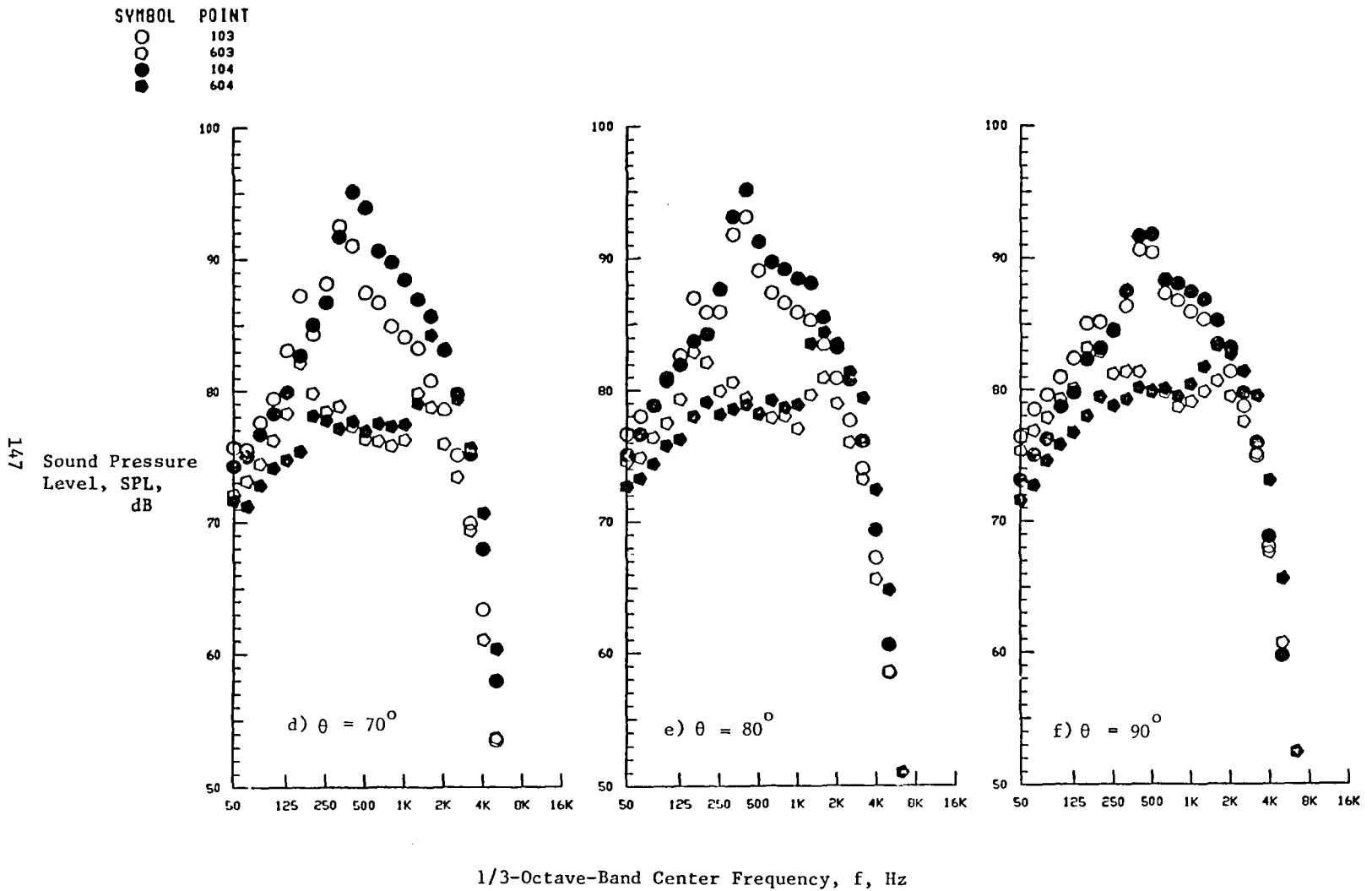
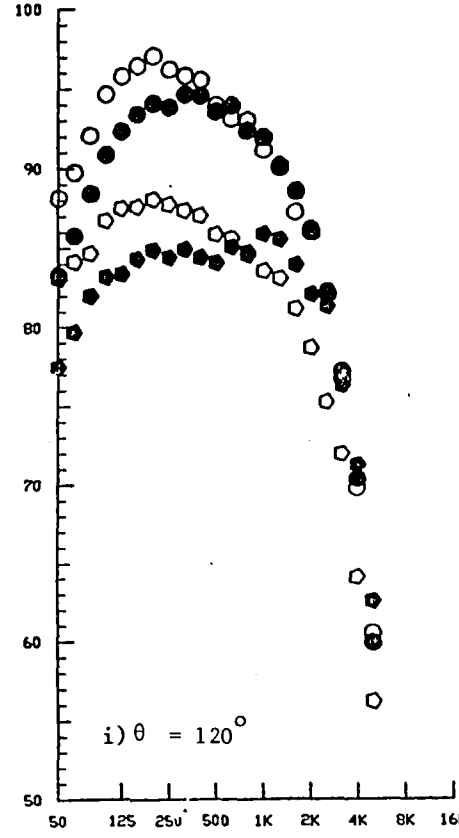
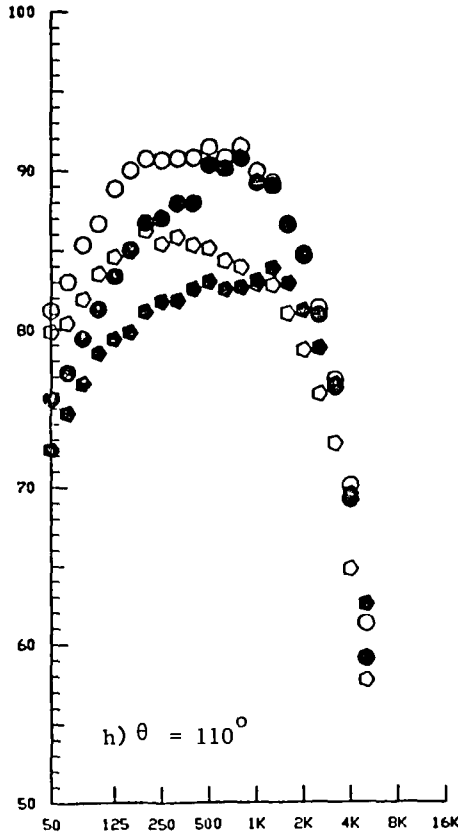
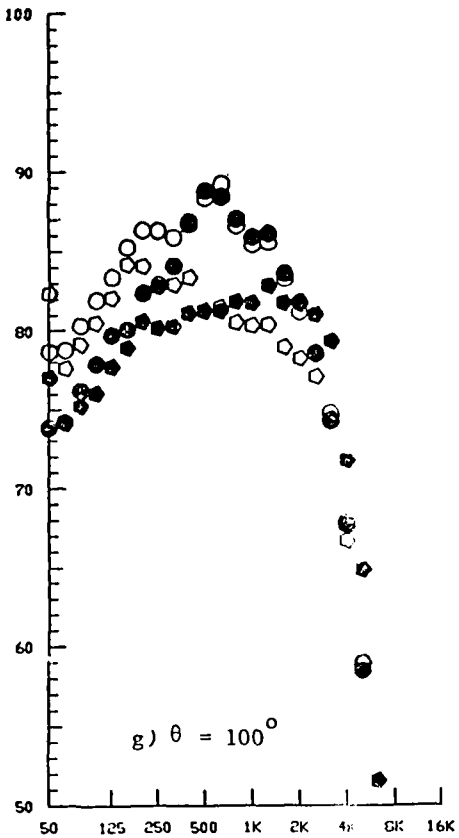


Figure 5-43. (Cont'd) Static-to-Flight Spectral Comparison at Overexpanded Flow Conditions; Convergent Circular (Model 1) and C-D Suppressor (Model 6) Nozzles.

SYMBOL	POINT
○	103
◊	603
●	104
◐	604

148

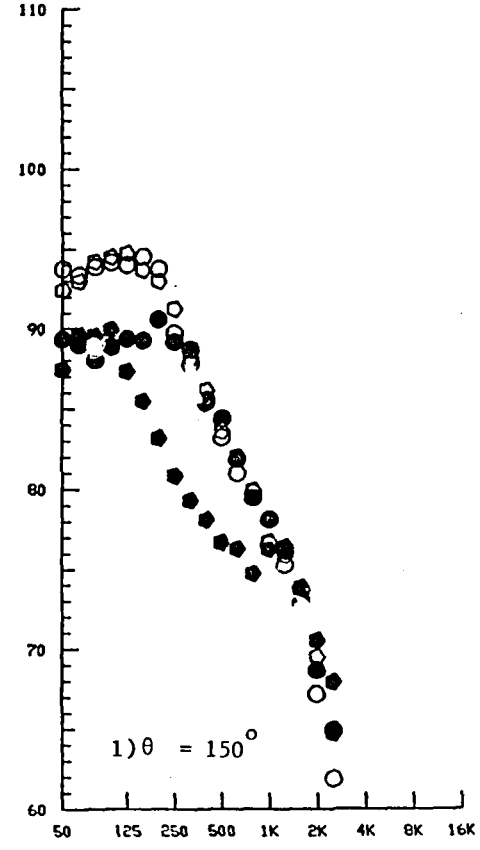
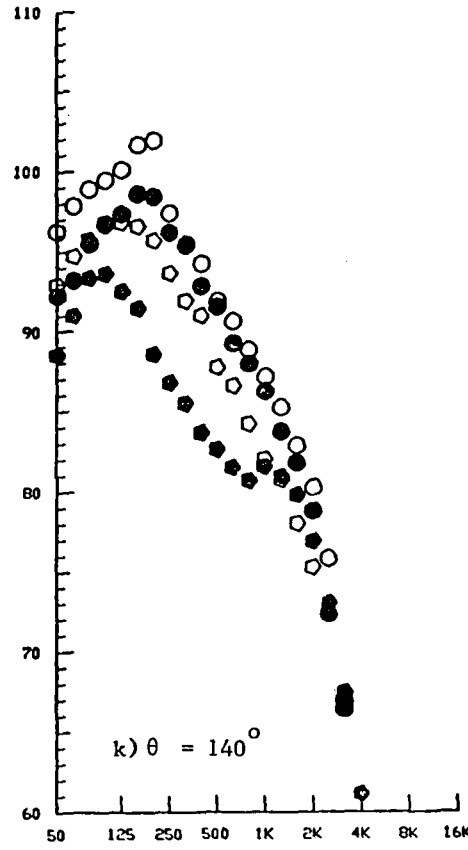
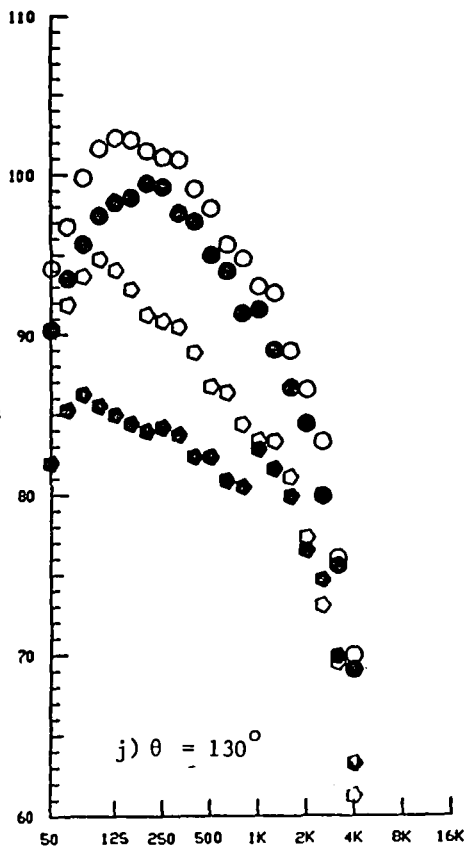
Sound Pressure
Level, SPL,
dB



1/3-Octave-Band Center Frequency, f, Hz

Figure 5-43. (Cont'd) Static-to-Flight Spectral Comparison at Overexpanded Flow Conditions; Convergent Circular (Model 1) and C-D Suppressor (Model 6) Nozzles.

SYMBOL	POINT
○	103
◊	603
●	104
◐	604



1/3-Octave-Band Center Frequency, f, Hz

Figure 5-43. (Concluded) Static-to-Flight Spectral Comparison at Overexpanded Flow Conditions; Convergent Circular (Model 1) and C-D Suppressor (Model 6) Nozzles.

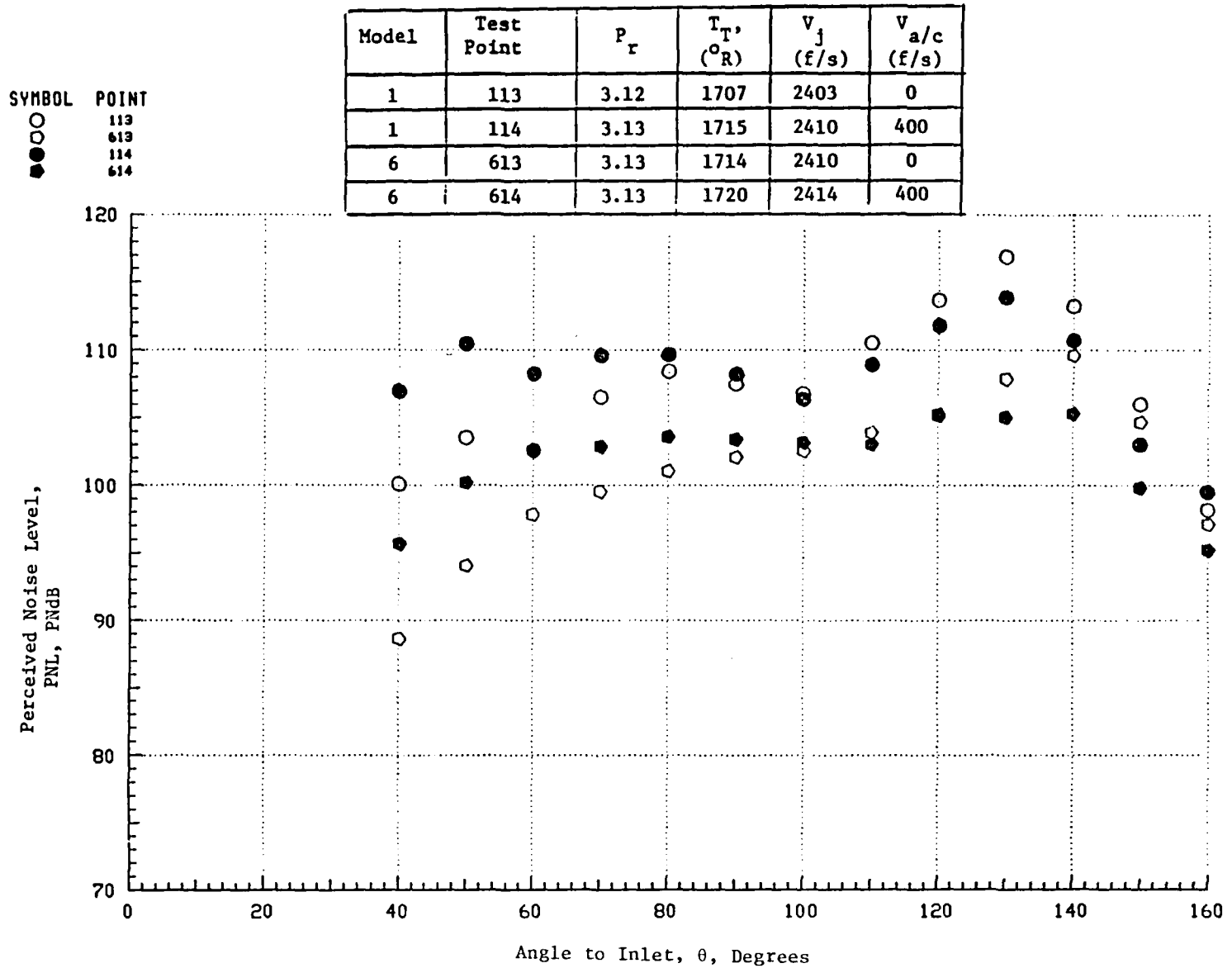


Figure 5-44. Static-to-Flight PNL Comparison at Design Operating Conditions; Convergent Circular (Model 1) and C-D Suppressor (Model 6) Nozzles.

Model	Test Point	P_r	$T_{T'} (^{\circ}R)$	V_j (f/s)	$V_{a/c}$ (f/s)
1	113	3.12	1707	2403	0
1	114	3.13	1715	2410	400
6	613	3.13	1714	2410	0
6	614	3.13	1720	2414	400

SYMBOL POINT
 ○ 113
 ○ 613
 ● 114
 ● 614

151

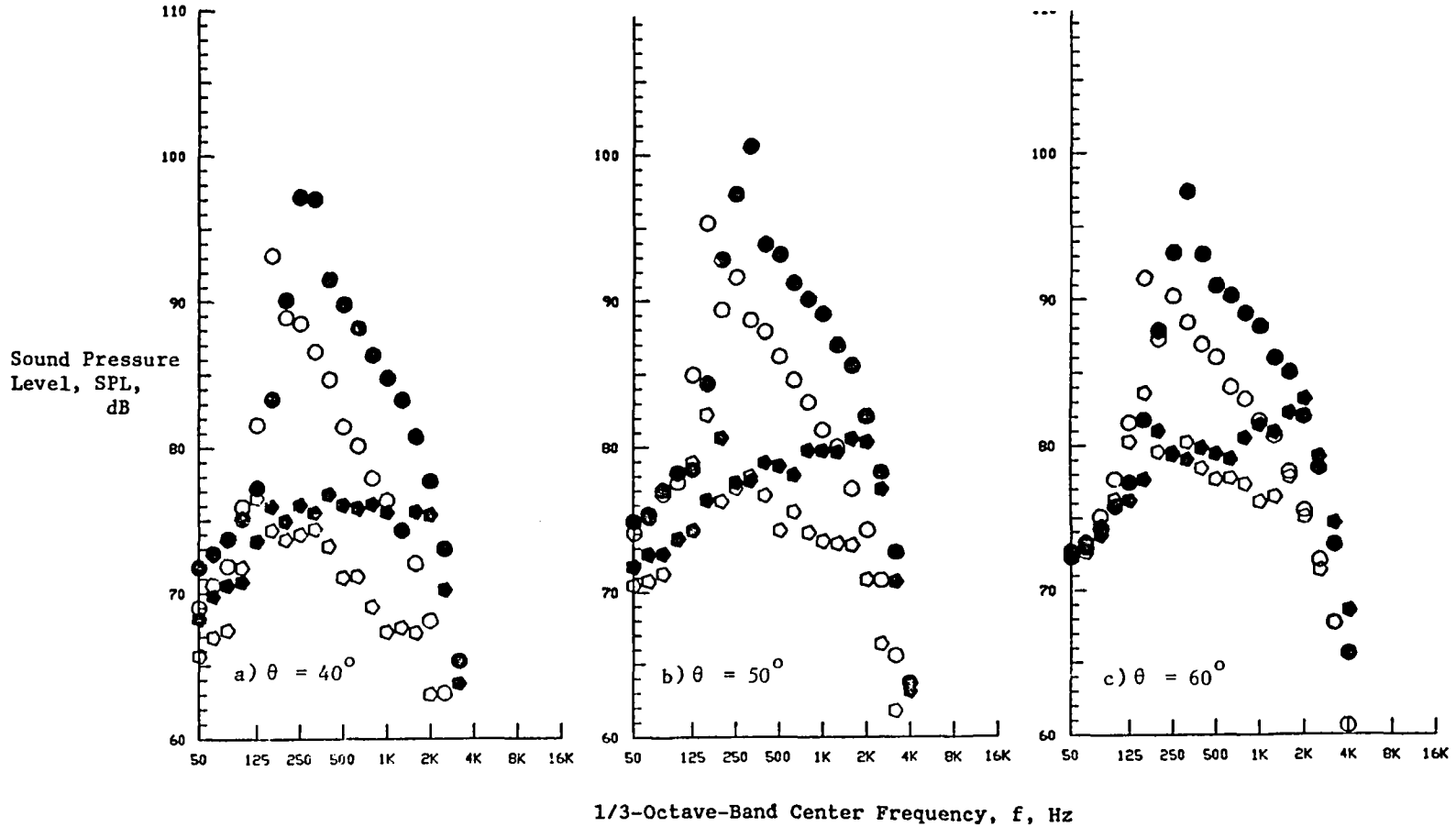
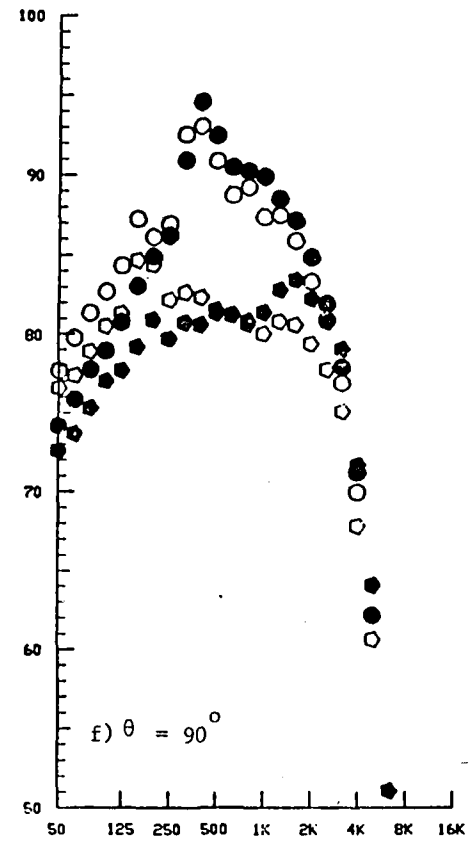
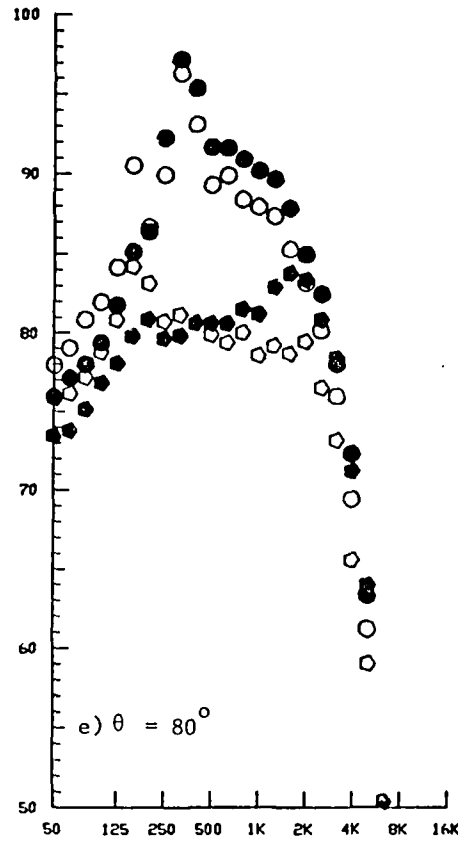
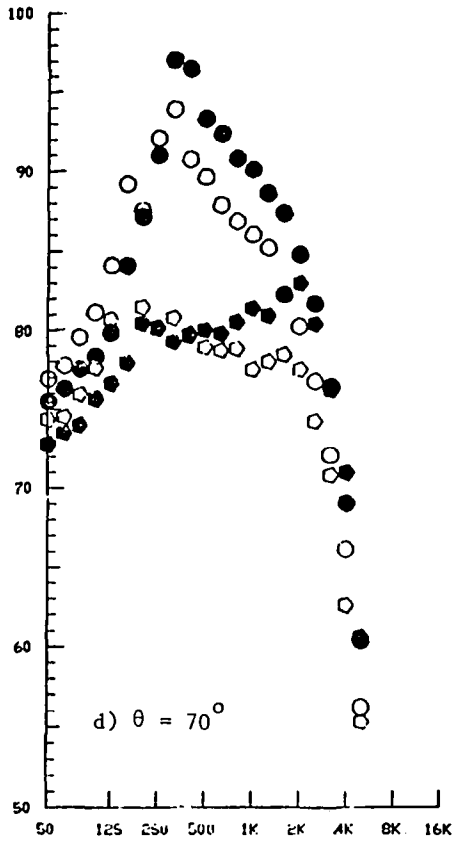


Figure 5-45. Static-to-Flight Spectral Comparison at Design Operating Conditions; Convergent Circular (Model 1) and C-D Suppressor (Model 6) Nozzles.

○	POINT 113
○	POINT 613
●	POINT 114
●	POINT 614

152

Sound Pressure
Level, SPL,
dB



1/3-Octave-Band Center Frequency, f, Hz

Figure 5-45. (Cont'd) Static-to-Flight Spectral Comparison at Design Operating Conditions; Convergent Circular (Model 1) and C-D Suppressor (Model 6) Nozzles.

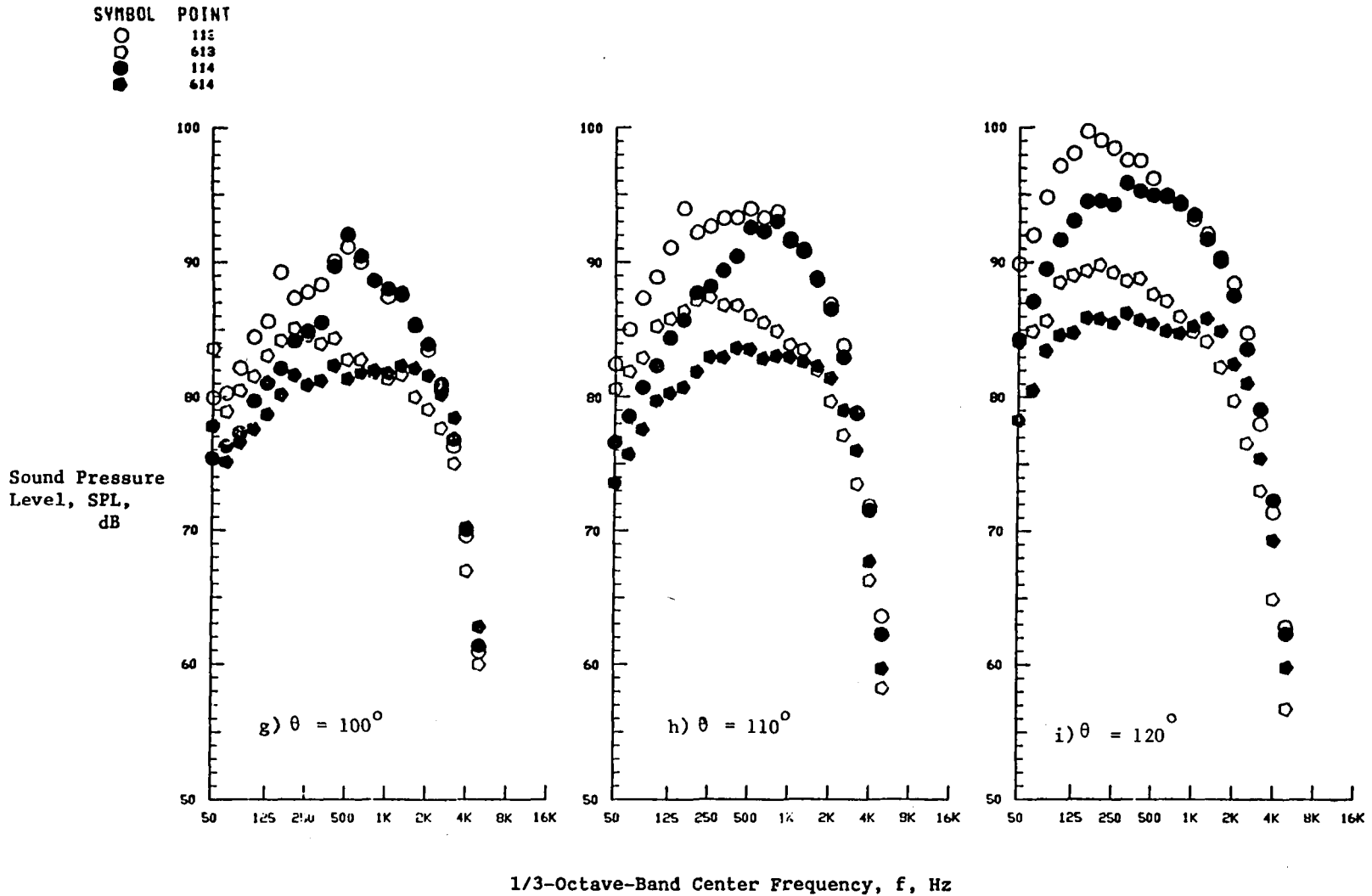
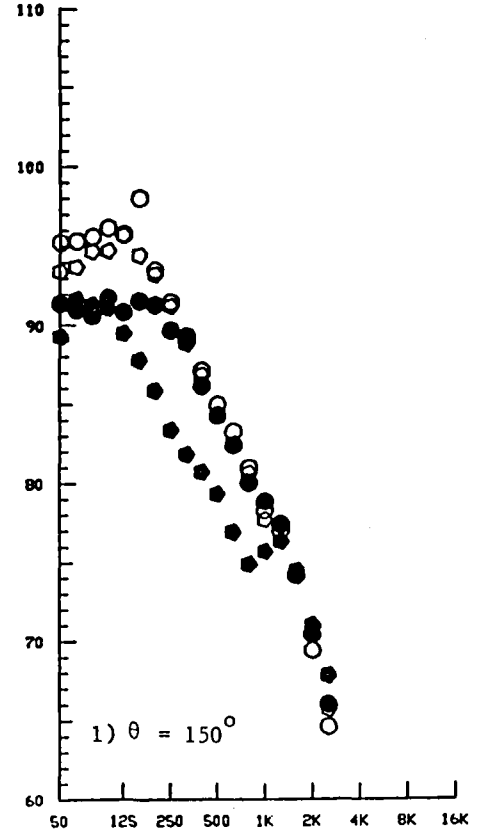
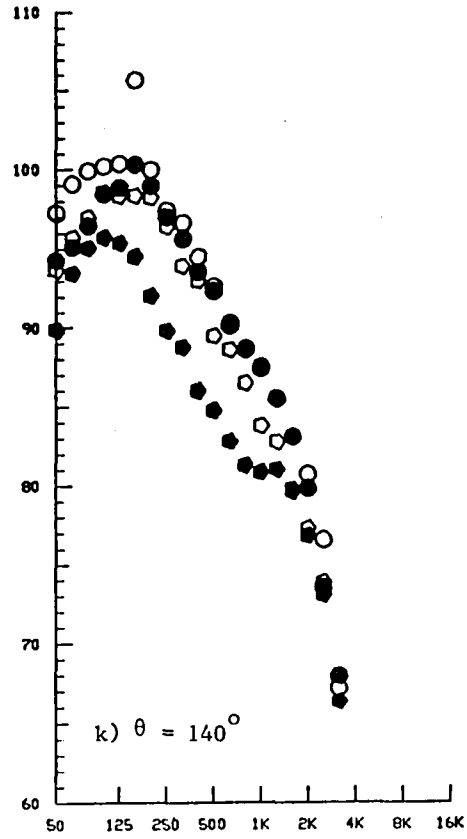
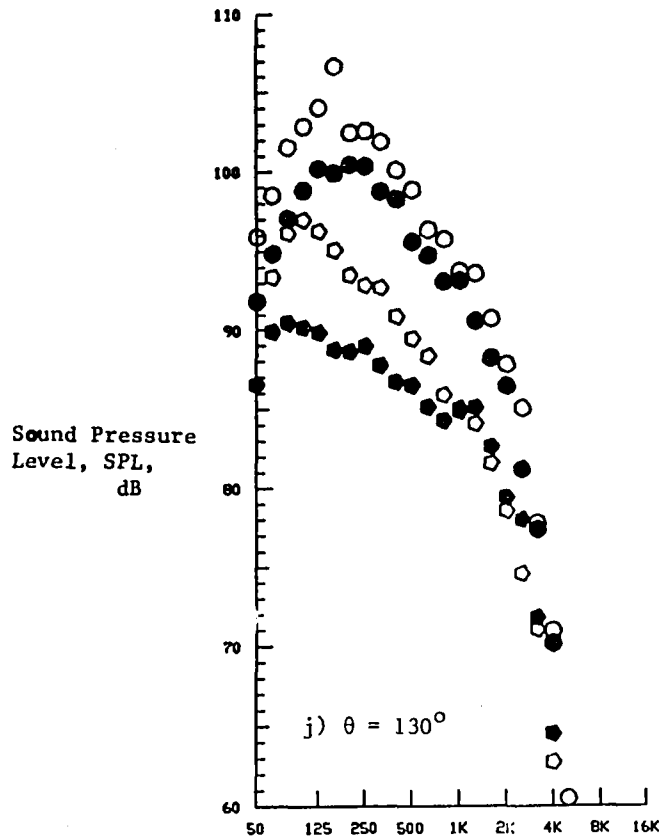


Figure 5-45. (Cont'd) Static-to-Flight Spectral Comparison at Design Operating Conditions; Convergent Circular (Model 1) and C-D Suppressor (Model 6) Nozzles.

SYMBOL POINT

○	113
◊	412
●	114
◐	614



1/3-Octave-Band Center Frequency, f, Hz

Figure 5-45. (Concluded) Static-to-Flight Spectral Comparison at Design Operating Conditions; Convergent Circular (Model 1) and C-D Suppressor (Model 6) Nozzles.

SYMBOL POINT
 ○ 121
 ○ 621
 ● 122
 ● 622

Model	Test Point	P_r	T_T , (°R)	V_j (f/s)	$V_{a/c}$ (f/s)
1	121	3.32	1700	2452	0
1	122	3.32	1710	2459	400
6	621	3.32	1714	2462	0
6	622	3.33	1709	2461	400

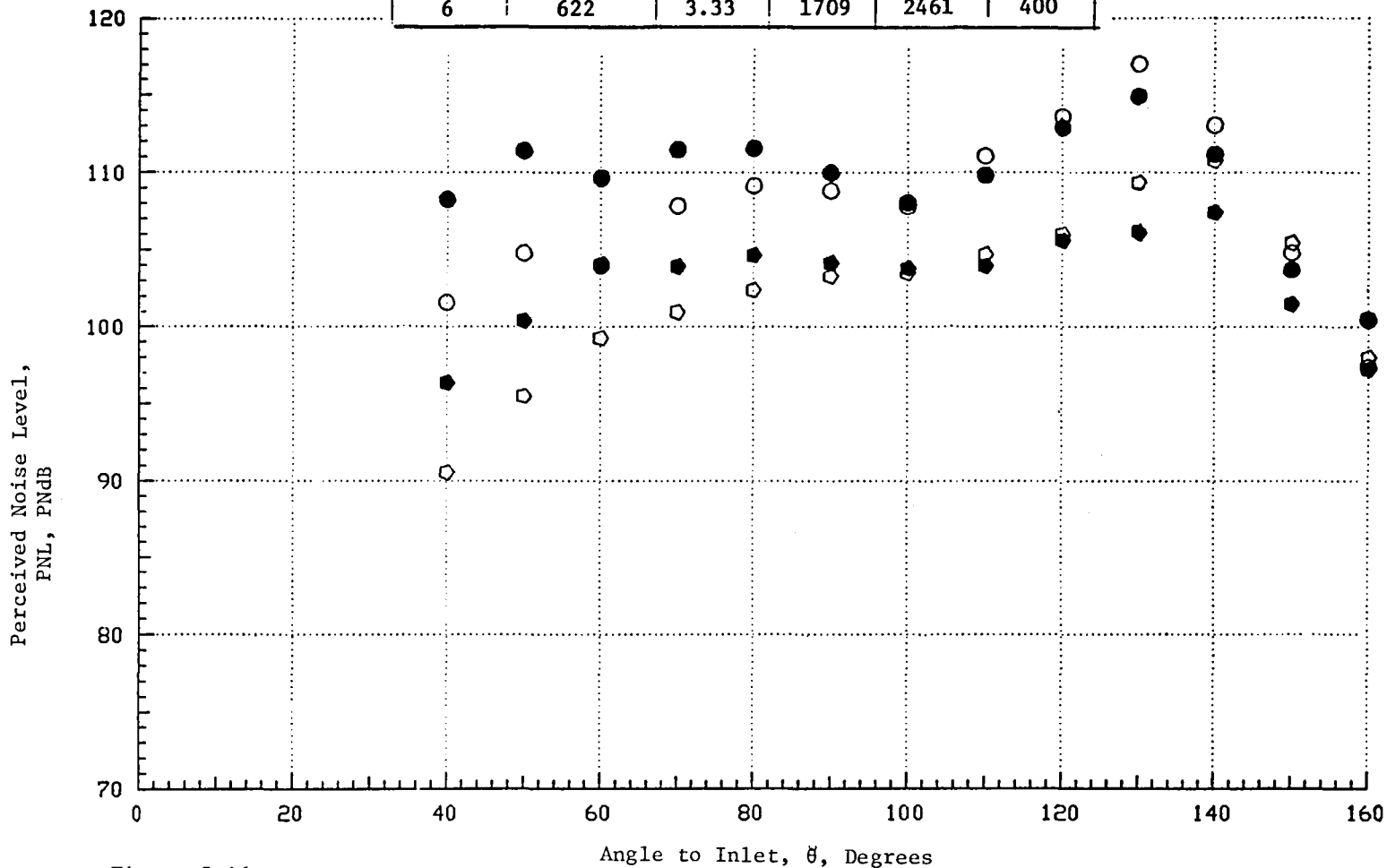


Figure 5-46. Static-to-Flight PNL Comparison at Underexpanded Flow Conditions; Convergent Circular (Model 1) and C-D Suppressor (Model 6) Nozzles.

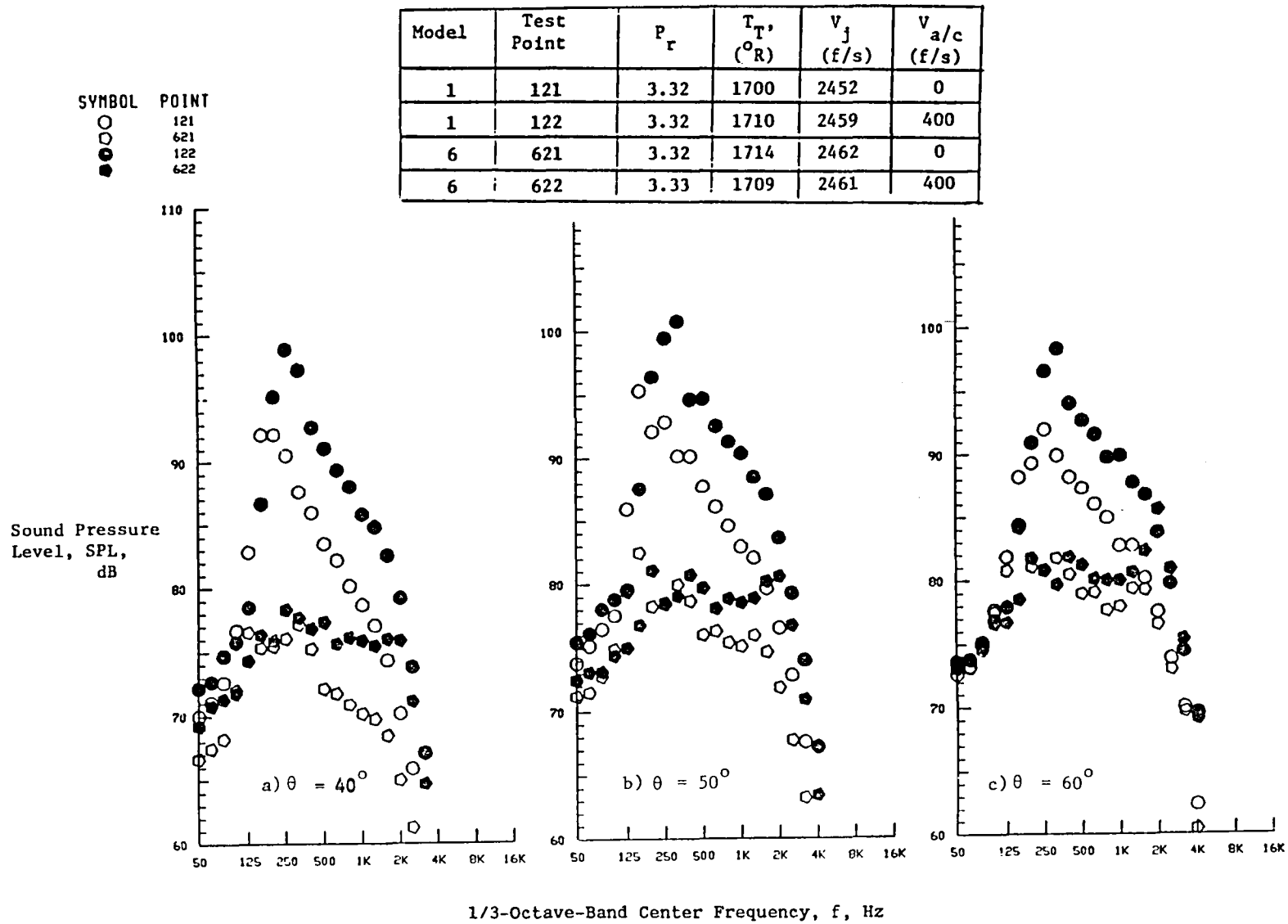
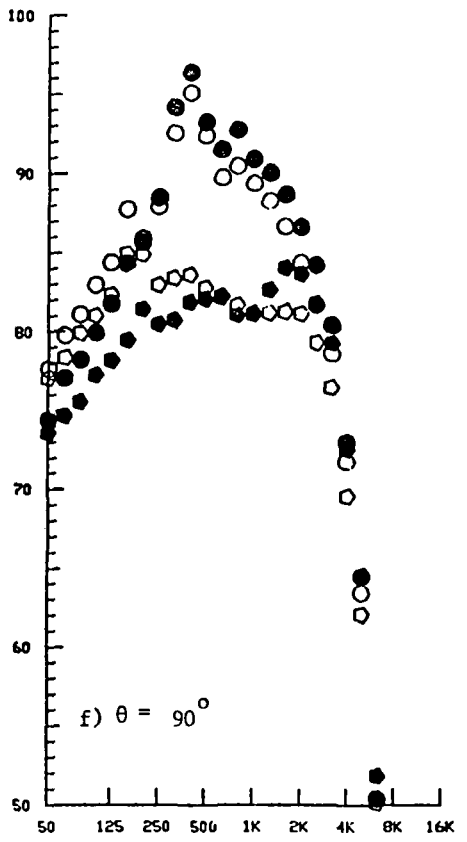
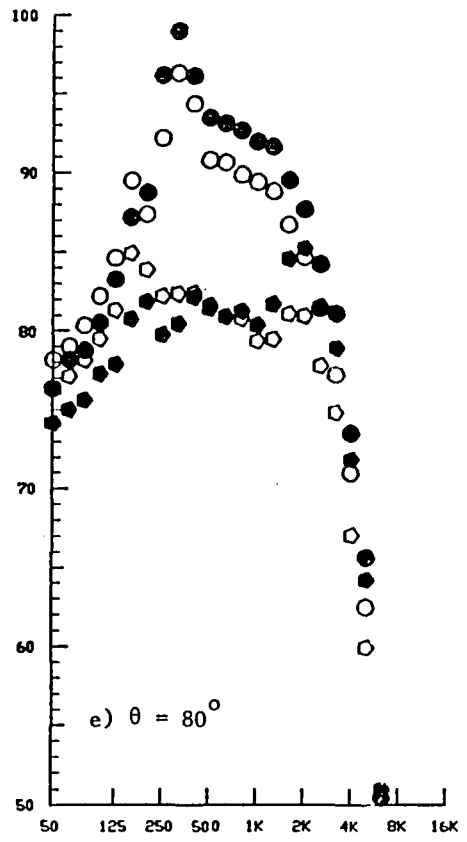
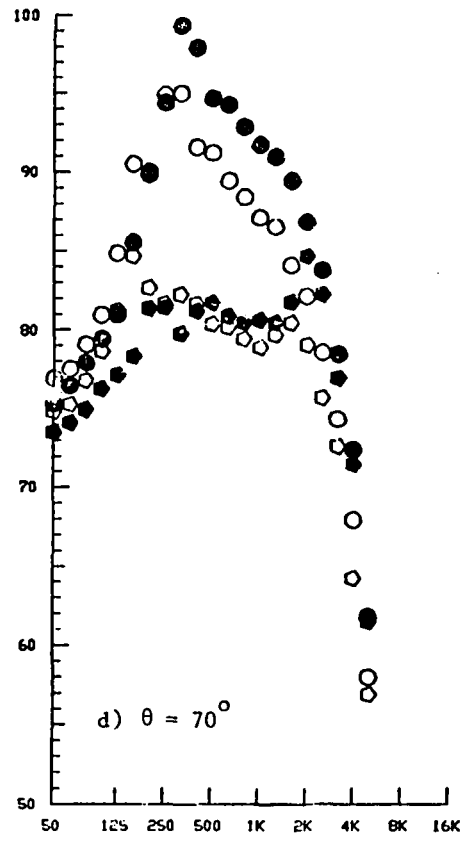


Figure 5-47. Static-to-Flight Spectral Comparison at Underexpanded Flow Conditions; Convergent Circular (Model 1) and C-D Suppressor (Model 6) Nozzles.

SYMBOL POINT
○ 121
○ 621
● 122
● 622

Sound Pressure Level, SPL, dB



1/3-Octave-Band Center Frequency, f, Hz

Figure 5-47. (Cont'd) Static-to-Flight Spectral Comparison at Underexpanded Flow Conditions; Convergent Circular (Model 1) and C-D Suppressor (Model 6) Nozzles.

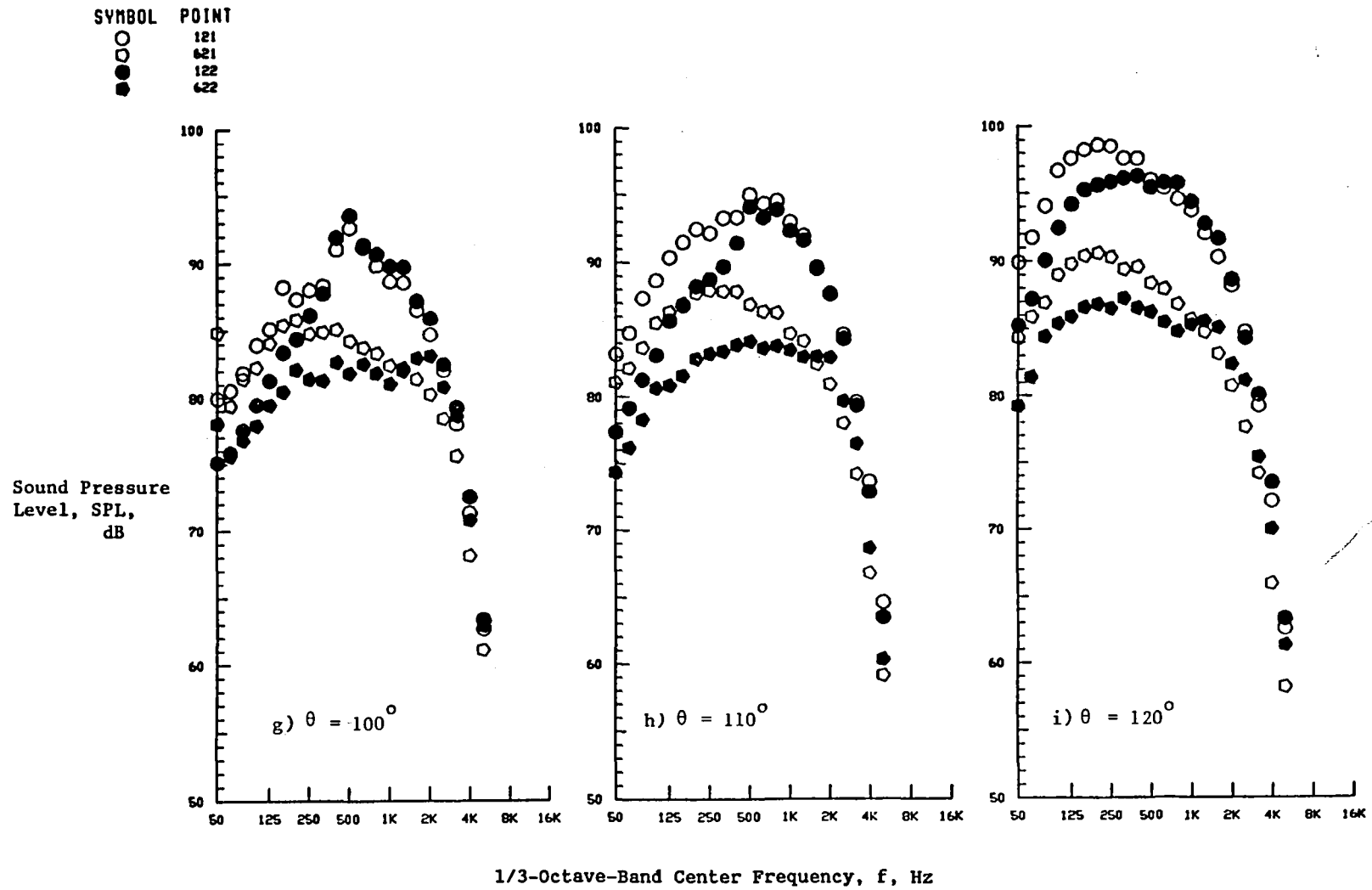


Figure 5-47. (Cont'd) Static-to-Flight Spectral Comparison at Underexpanded Flow Conditions; Convergent Circular (Model 1) and C-D Suppressor (Model 6) Nozzles.

○	121
○	621
●	122
●	622

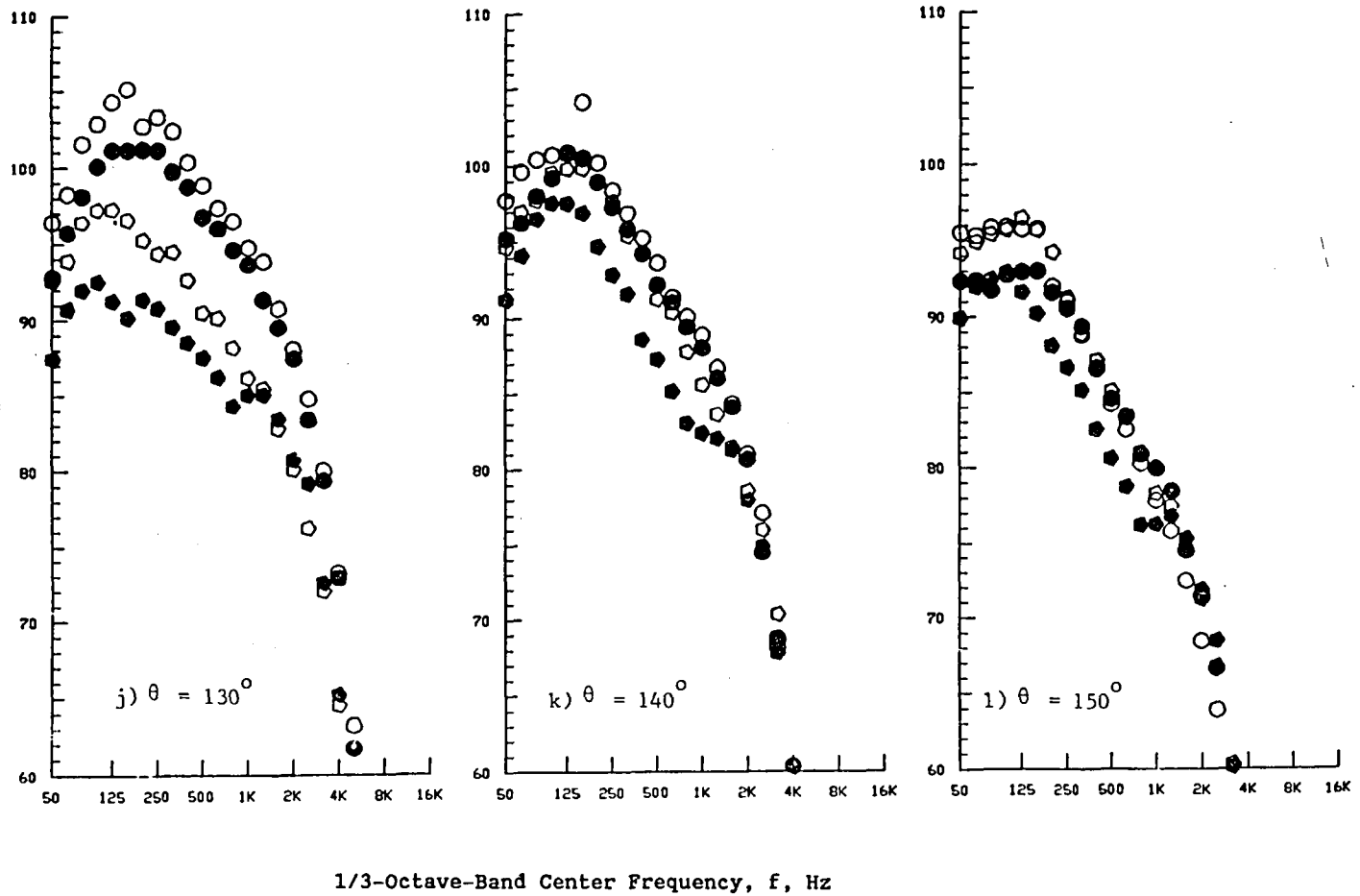


Figure 5-47. (Concluded) Static-to-Flight Spectral Comparison at Underexpanded Flow Conditions; Convergent Circular (Model 1) and C-D Suppressor (Model 6) Nozzles.

overexpanded plume condition is presented in Figure 5-43. In the spectrum corresponding to Test Point 603, a prominent peak is observed near the center frequency of 160 Hz ($\theta = 60^\circ$) which is regarded as a screech tone, possibly generated in the flow region downstream of the center plug. This screech tone is effectively suppressed in simulated flight. However, the shock noise produced by the shock system formed on the plug surface is significantly amplified, as indicated by an increased level of the high frequency components whose peak is located at near 1.6 kHz. This may be partly due to the Doppler amplification of shock noise in the front quadrant and partly due to the enlargement of the supersonic mixing layer thickness by flight which is one of the key aerodynamic parameters associated with the shock noise generation (References 2-6 and 5-11).

Corresponding spectral comparisons at design and underexpanded conditions are presented in Figure 5-45 and 5-47, respectively. It should be noted that SPL attenuation by C-D termination under the simulated conditions observed in high frequency is more significant for the design operating conditions than either overexpanded or underexpanded operating conditions, as anticipated, because of significant reduction of shock noise by the C-D termination at this operating condition.

Some significant differences, regarding jet mixing noise between C-D suppressor nozzle (configuration 6) and C-D annular plug nozzle (configuration 4) were identified by comparing test results presented in Figure 5-47 ($\theta = 140^\circ$) and Figure 5-39 ($\theta = 140^\circ$). We note that a significant mixing noise reduction by SPL by flight is observed over a wide range of frequencies for the C-D suppressor nozzle which is in contrast to the corresponding results by the C-D annular plug nozzle where only modest reduction by flight is noted in low frequencies. This could be understandable in view of the fact that suppressor redistributes mixing noise to higher frequencies.

5.2.1.6 Summary of Flight Effects Results

To conclude the discussions on the influence of flight on front-quadrant noise, principal results from the analyses of this subsection are summarized below:

- Perceived noise level measured with the convergent-divergent circular nozzle indicated comparatively smaller flight amplification of broadband shock noise than those for the baseline convergent circular nozzle over a wide range of operating conditions.
- Almost the same magnitude of flight amplification was observed for the PNL measured with the convergent annular plug nozzle as that for the C-D annular nozzle.
- In the case of the multi-element suppressor nozzle, the flight amplification of shock-cell noise was found to be almost identical to those for the baseline convergent circular nozzle.

5.2.2 JET TEMPERATURE EFFECTS ON SHOCK-CELL NOISE

One of the issues relevant to shock associated noise is the effect of jet plume temperature on shock-turbulence interactions. Based upon his work on shock associated noise from imperfectly expanded jets, Tanna (Reference 5-6) concluded that the overall intensity of shock associated noise is essentially independent of the jet efflux temperature. However, the analytical work on the noise generated by an imperfectly expanded supersonic jet by Howe and Ffowcs Williams (Reference 2-6), indicates that the total radiated sound power, p , of shock associated noise is approximated by

$$p = \frac{\pi a^2 \beta^2 p^2 V_c}{2\rho V^2}$$

where p is the excess pressure at the jet exit, β is the shock strength parameter, V and V_c represents the jet efflux velocity and the convection velocity, respectively, and ρ corresponds to the local flow density which is inversely proportional to the local flow temperature.

The complexity of the issue lies in the fact that the shock-cell noise component of imperfectly expanded supersonic jet noise is not easily isolated from the jet mixing noise components in the measurements. Since the jet

mixing noise follows the V^8 law and increasing jet temperature (at a given pressure ratio) increases jet velocity, heated jets are generally noisier than their cold counterparts.

In this subsection the results of a comparative study of shock-cell noise characteristics between moderately heated ($T_T \sim 850^\circ\text{R}$) and high temperature ($T_T \sim 1750^\circ\text{R}$) jets are presented. The overall and spectral characteristics produced, under different flow temperatures, by convergent annular plug nozzle (Model 3), C-D annular plug nozzle (Model 4) and convergent suppressor nozzle (Model 5) are discussed.* These three configurations are determined to contain respectively, shock-cells on the plug and downstream of the plug (Model 3), downstream of the plug (Model 4), and on the plug (Model 5). (Refer to the discussion on the diagnostic data for details.)

Typical front quadrant spectral comparison between the data obtained with the two stream temperatures for the convergent annular plug nozzle is provided in Figure 5-48. The data indicates that in the high frequency region the spectral data agree with one another. The higher SPL at the peak frequency observed with the moderately heated flow is due to the first harmonic of the observed screech fundamental that coincided with the shock-cell broadband peak frequency. This is made clear by the data of Figure 5-49. In this figure the on-line narrowband data at $\theta = 60^\circ$ obtained during the tests at the two stream temperatures are presented to indicate the presence of screech and its harmonic with the moderately heated jet.

PNL- and OASPL-directivities and typical front quadrant spectra of C-D annular plug nozzle under ideally expanded flow conditions but at three different stream temperatures are presented in Figures 5-50, 5-51 and 5-52, respectively. As pointed out in Section 5.1.2, this C-D configuration which had no shock-cells on the plug at these conditions was determined to have shock-cells downstream of the plug. Hence, this set of front-quadrant data demonstrates the effect of temperature on the noise due to these downstream

*No such comparisons are provided with the convergent circular nozzle data as tests with moderately heated jets were not conducted with this configuration.

SYMBOL POINT
 ◆ 322
 ● 1324

MODEL	TEST POINT	P_r	$T_T, ^\circ R$	V_j, fps	$V_{a/c}, \text{fps}$
3	322	3.38	1727	2485	400
3	1324	3.45	873	1767	400

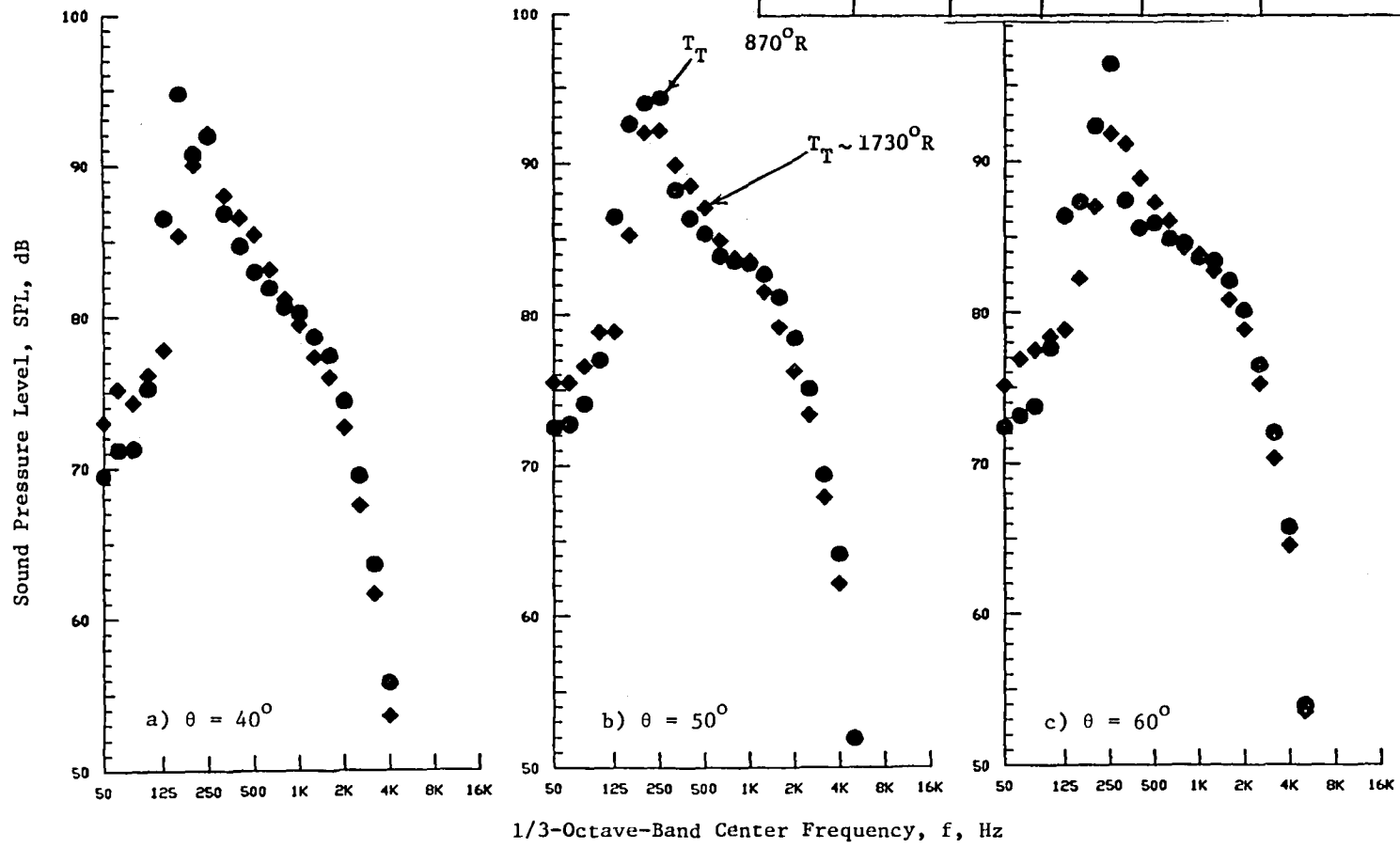
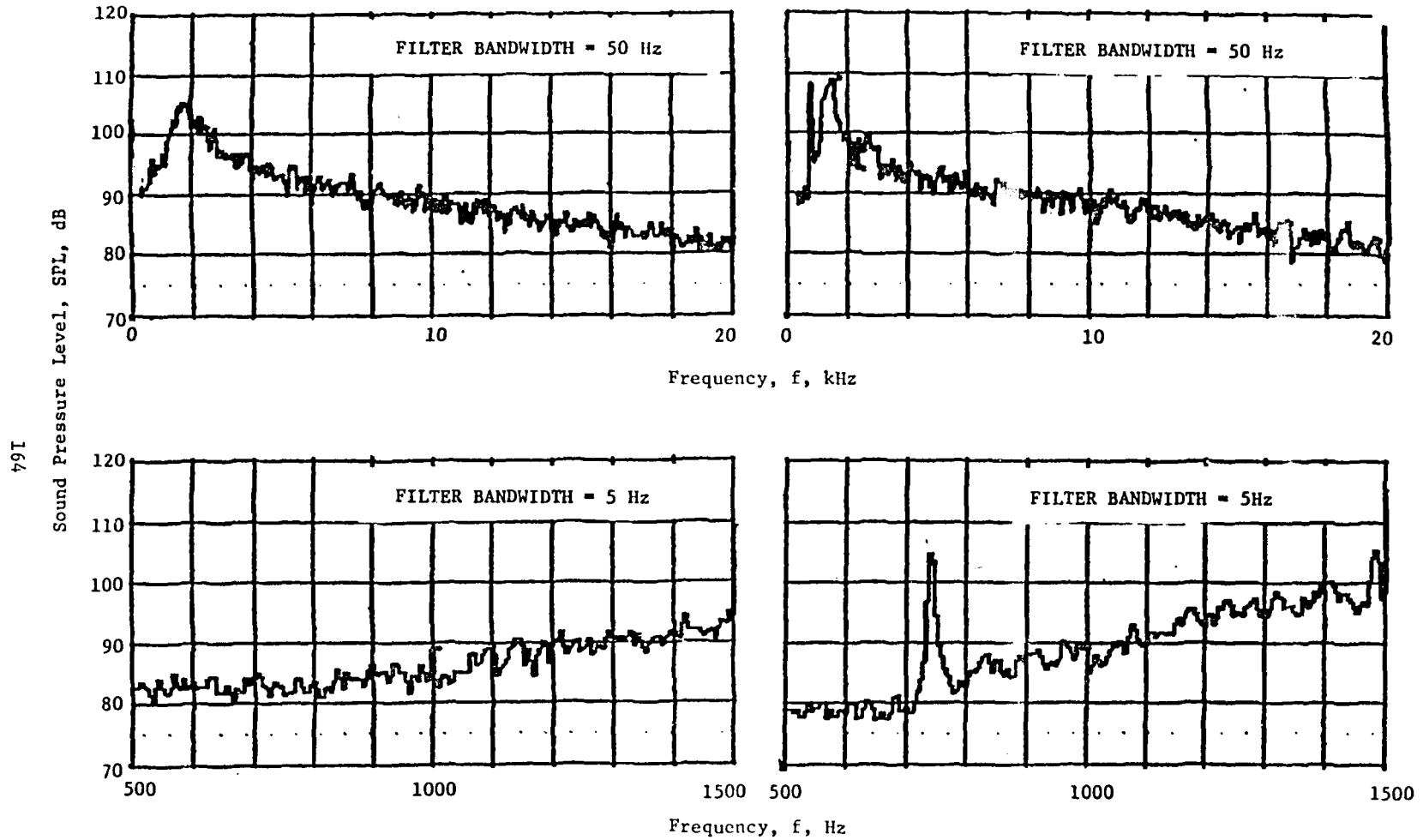


Figure 5-48. Typical Front-Quadrant Spectra of Convergent Annular Plug Nozzle at Two Plume Temperatures.

MODEL DATA

$\theta = 60^\circ$

(SEE FIGURE 5-54 FOR AERODYNAMIC FLOW CONDITIONS)



(a) Heated Jet, $T_T = 1730^\circ\text{R}$ (TP 322)

(b) Moderately Heated Jet, $T_T = 870^\circ\text{R}$ (TP 1324)

Figure 5-49. On-Line Narrowband Spectra ($\theta = 60^\circ$) Obtained with Convergent Annular Plug Nozzle at Two Plume Temperatures.

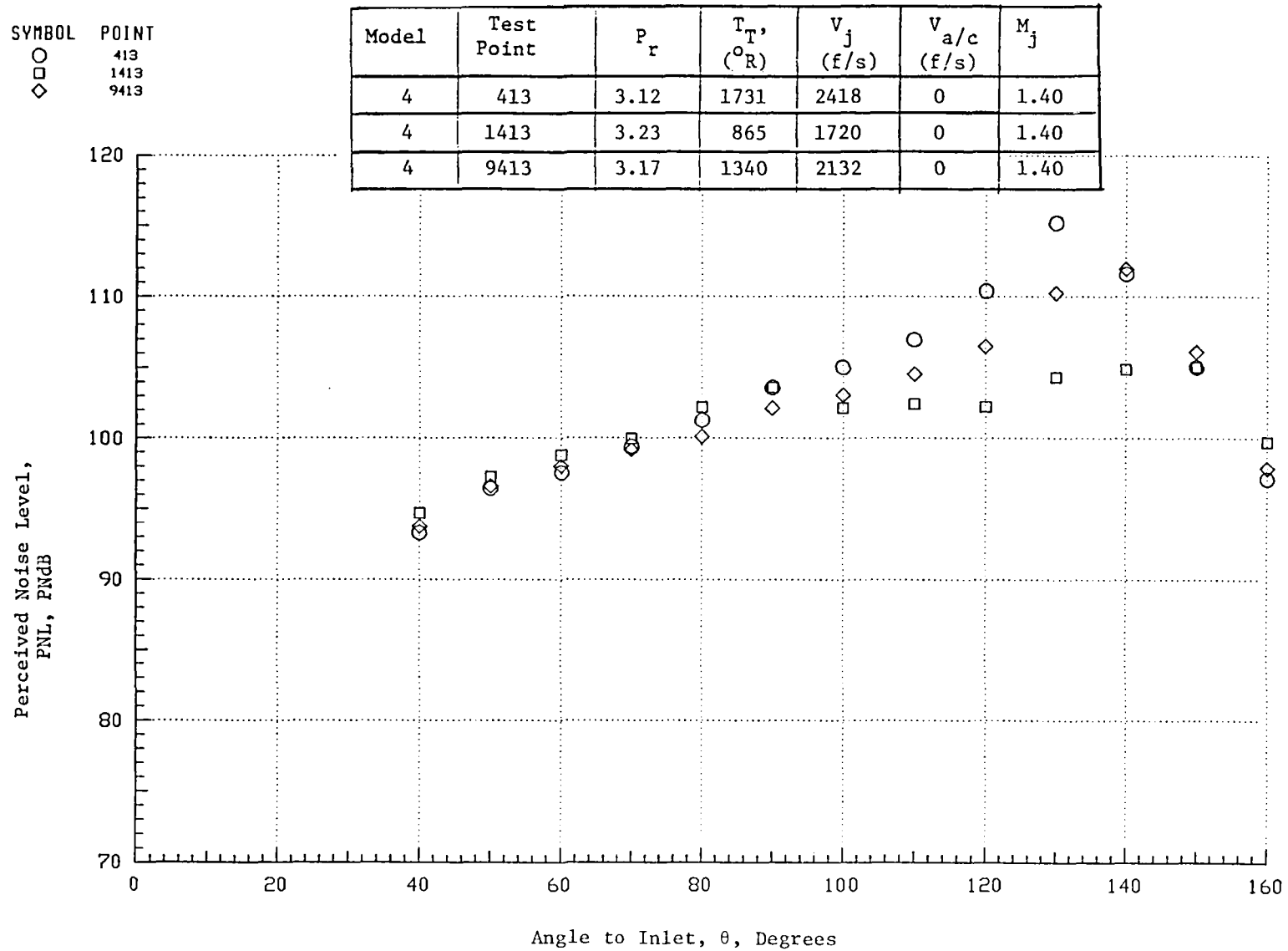


Figure 5-50. PNL Directivity of C-D Annular Plug Nozzle For Various Plume Temperatures at Design Operating Conditions.

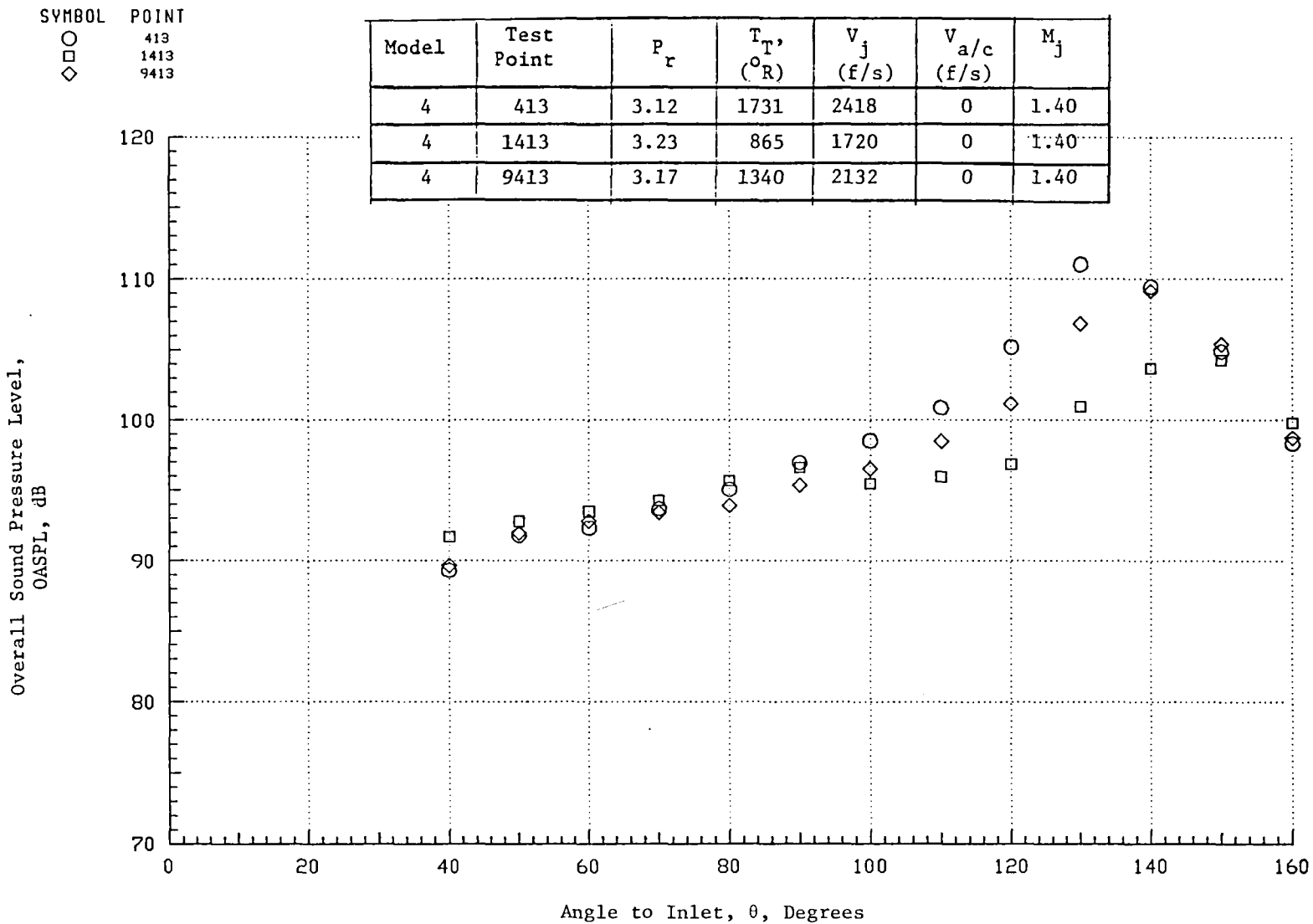


Figure 5-51. OASPL Directivity of C-D Annular Plug Nozzle for Various Plume Temperatures at Design Operating Conditions.

SYMBOL POINT
 ○ 413
 □ 1413
 ◇ 9413

Model	Test Point	P_r	T_T , ($^{\circ}R$)	V_j (f/s)	$V_{a/c}$ (f/s)	M_j
4	413	3.12	1731	2418	0	1.40
4	1413	3.23	865	1720	0	1.40
4	9413	3.17	1340	2132	0	1.40

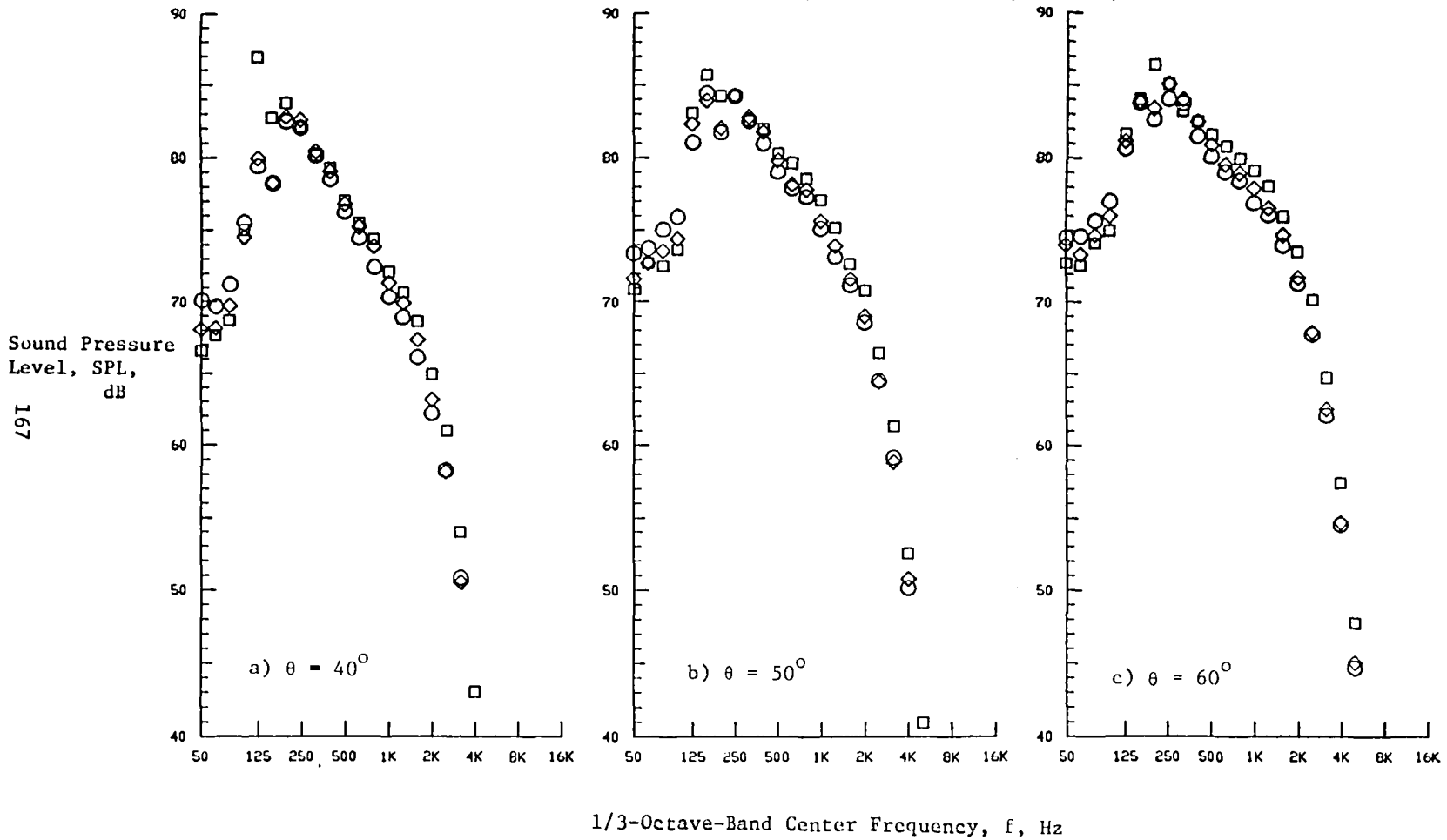


Figure 5-52. Front-Quadrant Spectra of C-D Annular Plug Nozzle for Various Plume Temperatures at Design Operating Conditions.

SYMBOL	POINT
○	413
□	1413
◇	9413

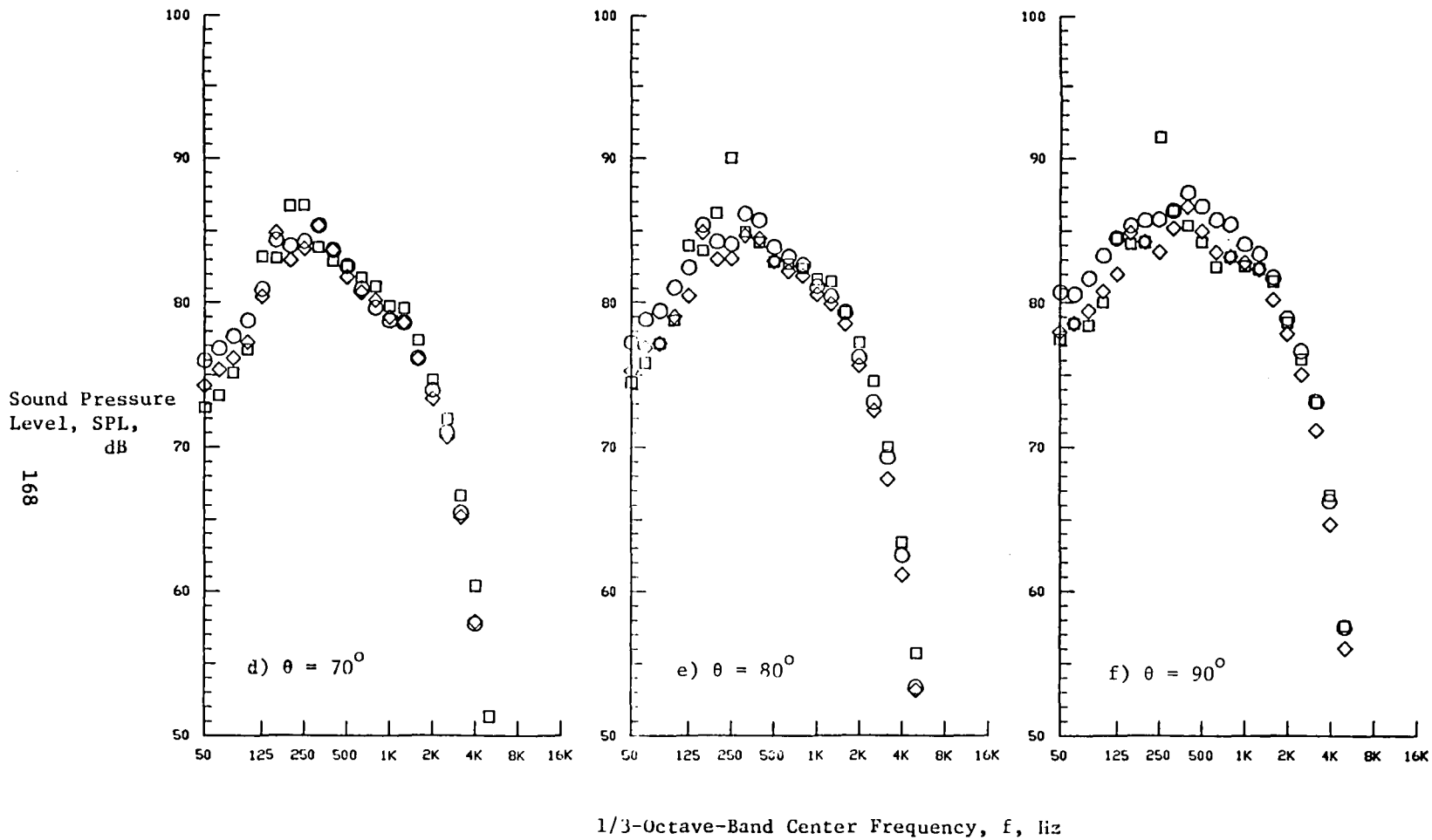


Figure 5-52. (Concluded) Front-Quadrant Spectra of C-D Annular Plug Nozzle for Various Plume Temperatures at Design Operating Conditions.

shock-cells. The data indicate little effect of temperature on shock-cell associated noise. On-line narrowband data measured at $\theta = 90^\circ$ for these test conditions are presented in Figure 5-53 to indicate the presence of screech and its harmonic with moderately heated jet ($T_T \sim 865^\circ\text{R}$) and absence of screech with the other two heated jets.

Typical PNL- and OASPL-directivities and typical front quadrant spectra of convergent suppressor nozzle are presented in Figures 5-54, 5-55 and 5-56, respectively. As discussed later in Section 6.0, this convergent suppressor configuration under the test conditions of the presented data was observed to have 6 to 8 shock-cells on the plug and no shock-cells downstream of the plug. Hence, this set of data indicate no effect of temperature on the noise due to the shock-cells on the plug. On-line narrowband measured at $\theta = 60^\circ$ for these test conditions are presented in Figure 5-57 to indicate the absence of screech for both moderately heated and high temperature jets of the convergent suppressor configuration.

To conclude this subsection, principal results from the above discussions are summarized below:

- Heating has little effect on the shock-cell noise level.
- These results are observed with convergent and C-D annular plug nozzles and convergent suppressor nozzle.

5.2.3 INFLUENCE OF NOZZLE CONFIGURATION ON SHOCK-CELL NOISE

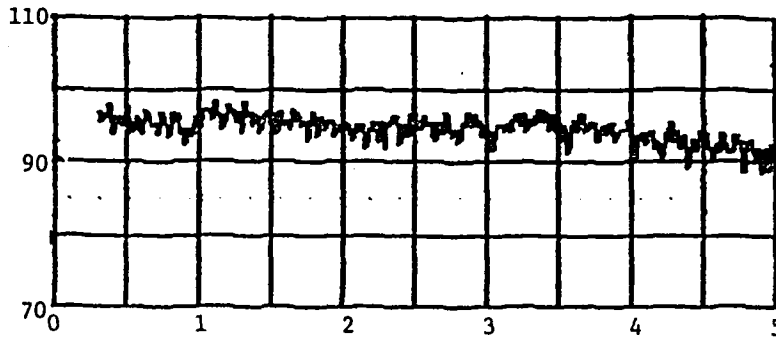
This subsection provides data comparisons between the three tested C-D nozzles and similar comparisons between the three convergent nozzles of this program. In each of these comparisons, the data of the baseline convergent circular nozzle is given as a reference at comparable test conditions.

5.2.3.1 Convergent-Divergent Nozzles

Figure 5-58 comparatively illustrates a typical front quadrant perceived noise level as a function of $10 \log \beta$ for four different nozzles. The aerodynamic conditions of the selected test points were: $T_T \approx 1730^\circ\text{R}$, $2.8 < Pr < 3.9$. The results indicate that multi-element C-D suppressor

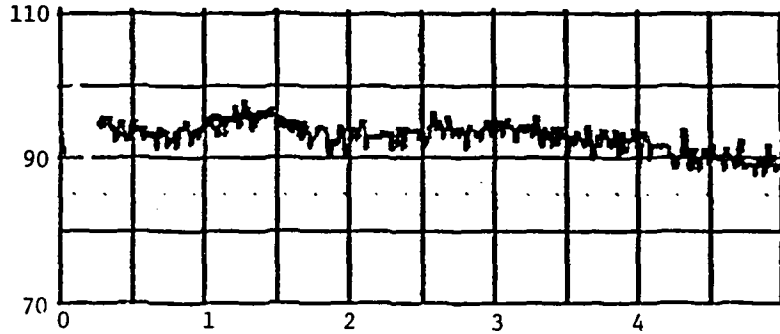
(SEE FIGURE 5-54 FOR AERODYNAMIC CONDITIONS)

MODEL DATA $\theta = 90^\circ$ FILTER BANDWIDTH = 12.5 Hz

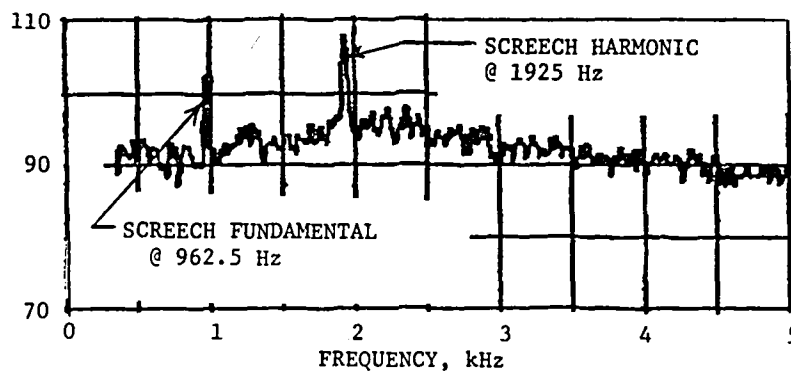


(a) HEATED JET, $T_T \sim 1730^\circ\text{R}$ (TEST POINT 413)

Sound Pressure Level, SPL, dB



(b) HEATED JET, $T_T \sim 1340^\circ\text{R}$ (TEST POINT 9413)



(c) MODERATELY HEATED JET, $T_T \sim 865^\circ\text{R}$ (TEST POINT 1413)

Figure 5-53. On-Line Narrowband Spectra (at $\theta = 90^\circ$) Obtained with C-D Annular Plug Nozzle at Three Plume Temperatures.

SYMBOL POINT
 ◊ 513
 ○ 1513

MODEL	TEST POINT	P_R	$T_T, ^\circ R$	V_j, fps	$V_{a/c}, \text{fps}$
5	513	3.13	1718	2412	0
5	1513	3.22	851	1704	0

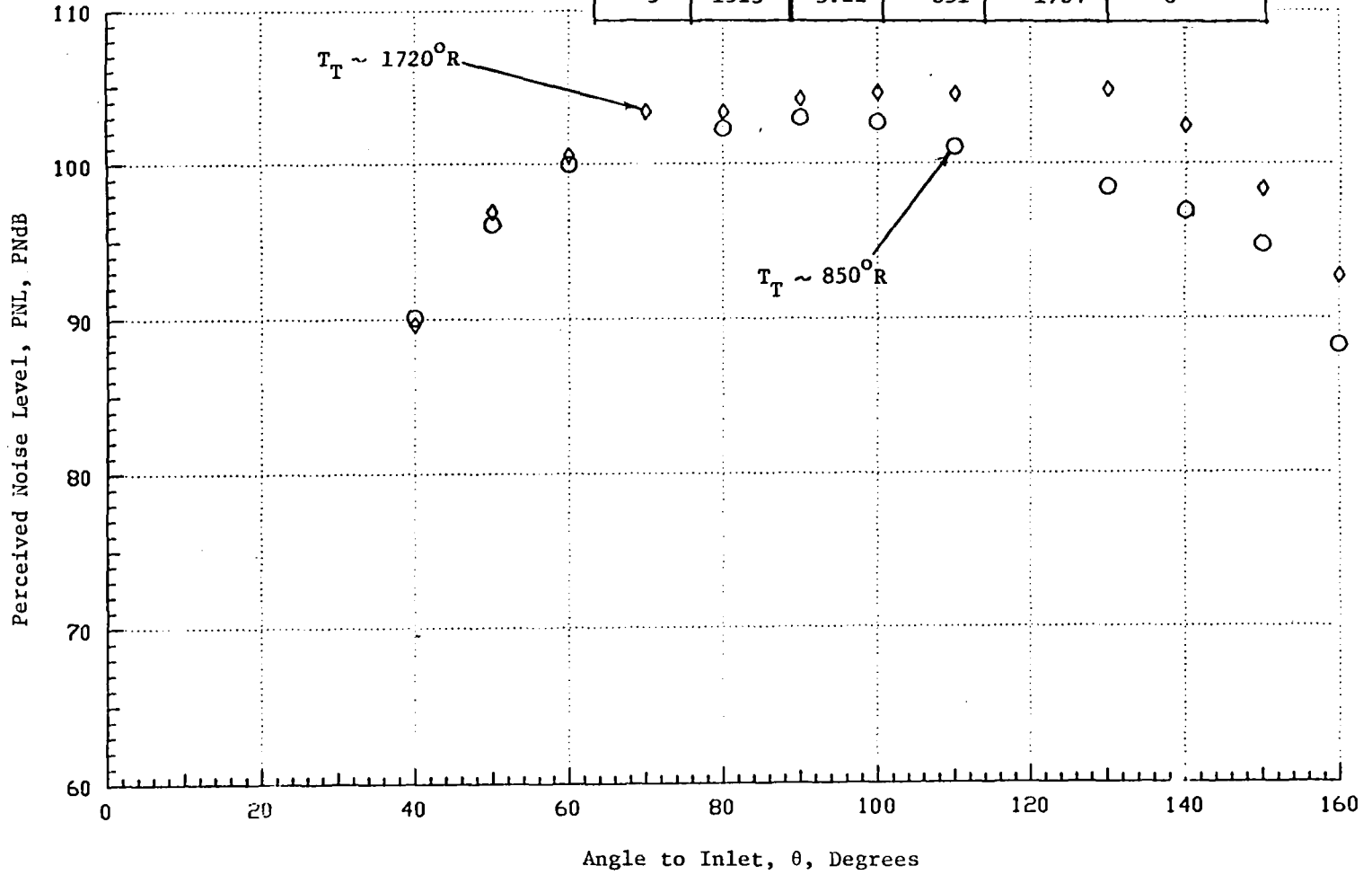
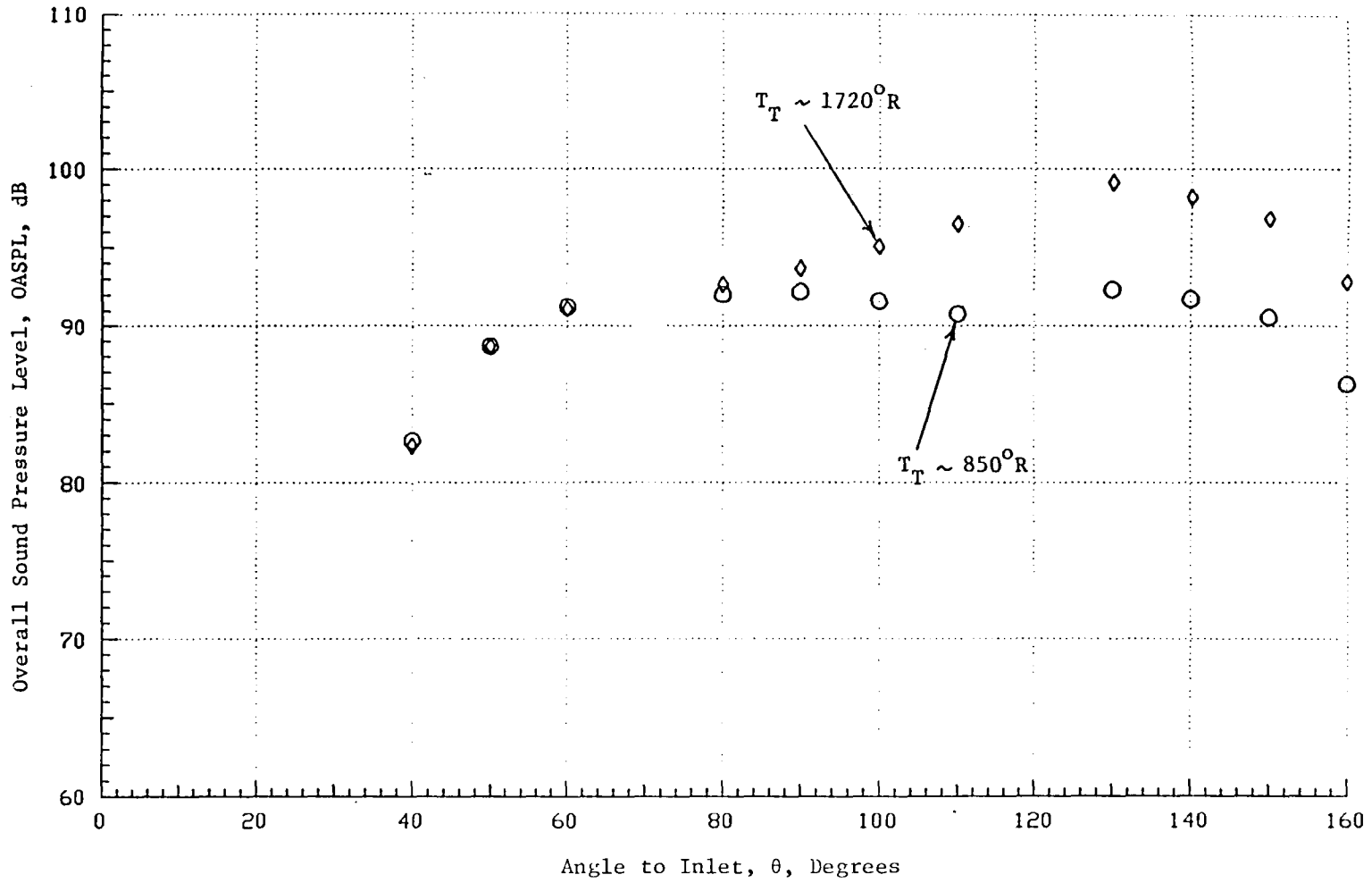


Figure 5-54. PNL Directivity of Convergent Suppressor Nozzle at Two Plume Temperatures.

SYMBOL POINT
 ◊ 513
 ○ 1513

(SEE FIGURE 5-54 FOR AERODYNAMIC CONDITIONS)



172

Figure 5-55. OASPL Directivity of Convergent Suppressor Nozzle at Two Plume Temperatures.

SYMBOL POINT
 ◊ 513
 ○ 1513

(SEE FIGURE 5-54 FOR AERODYNAMIC CONDITIONS)

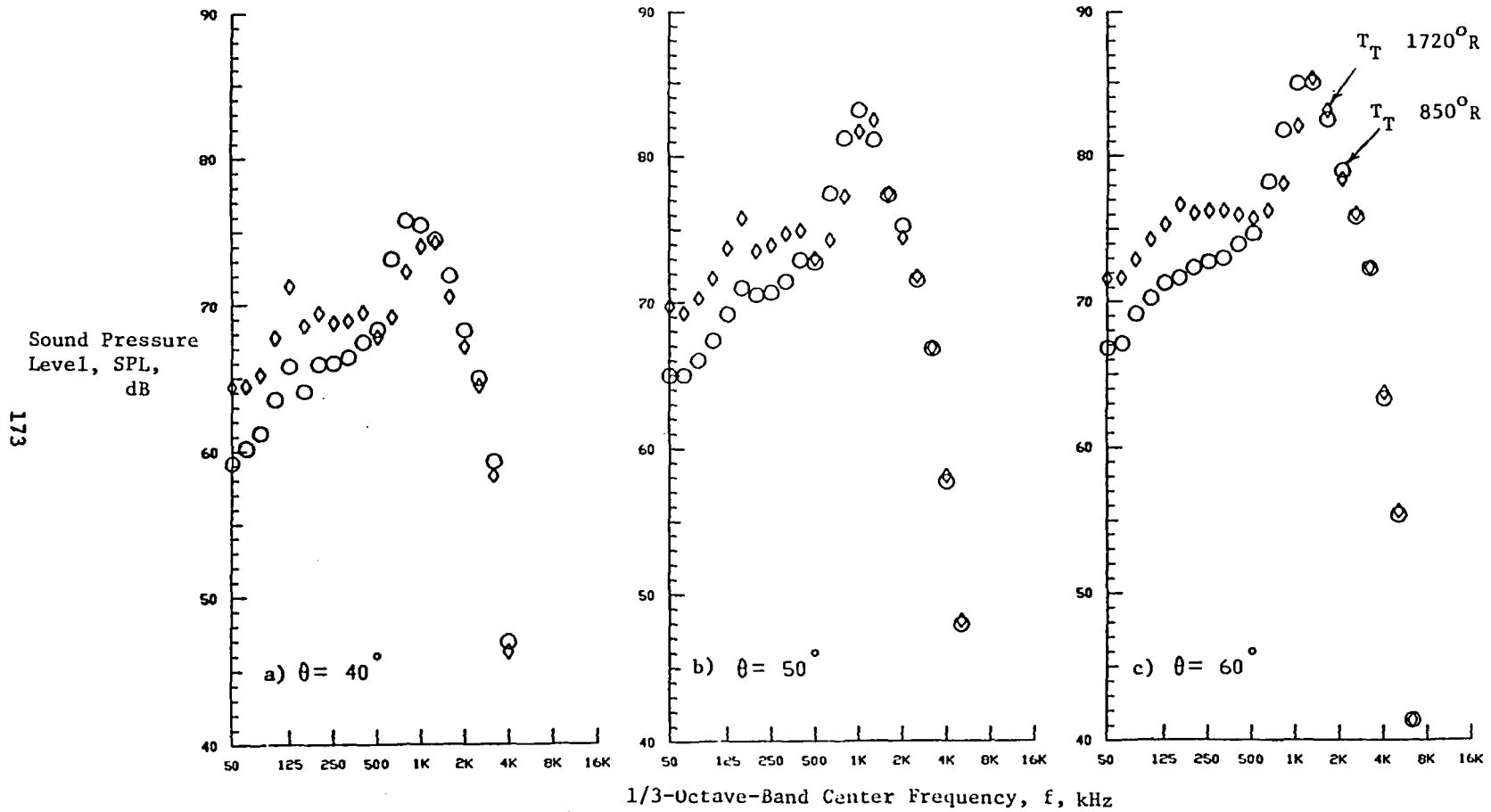


Figure 5-56. Typical Front-Quadrant Spectra of Convergent Suppressor Nozzle at Two Plume Temperatures.

(SEE FIGURE 5-54 FOR AERODYNAMIC CONDITIONS)

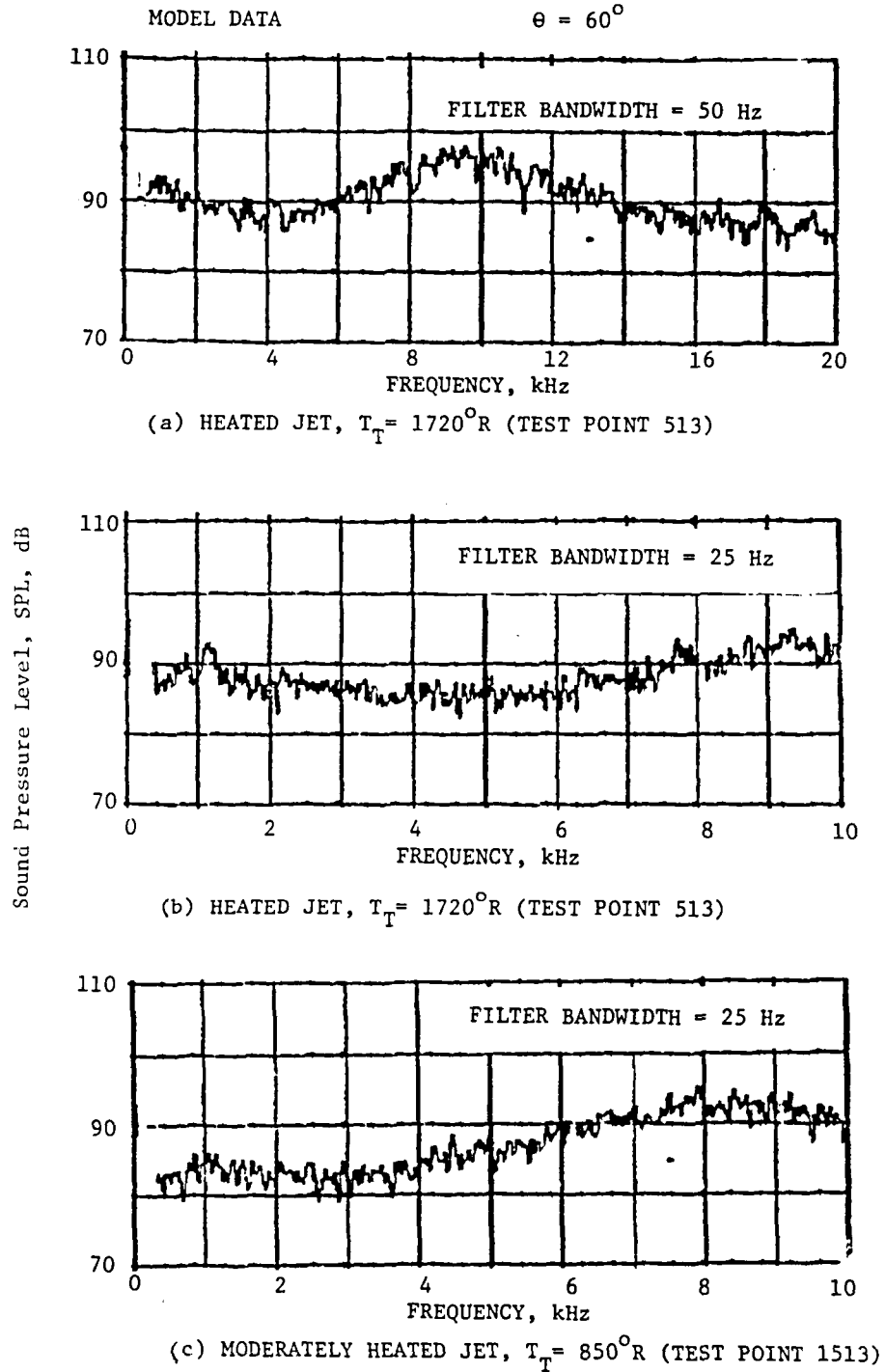


Figure 5-57. On-Line Narrowband Spectra (@ $\theta = 60^\circ$) Obtained with Convergent Suppressor Nozzle at Two Plume Temperatures.

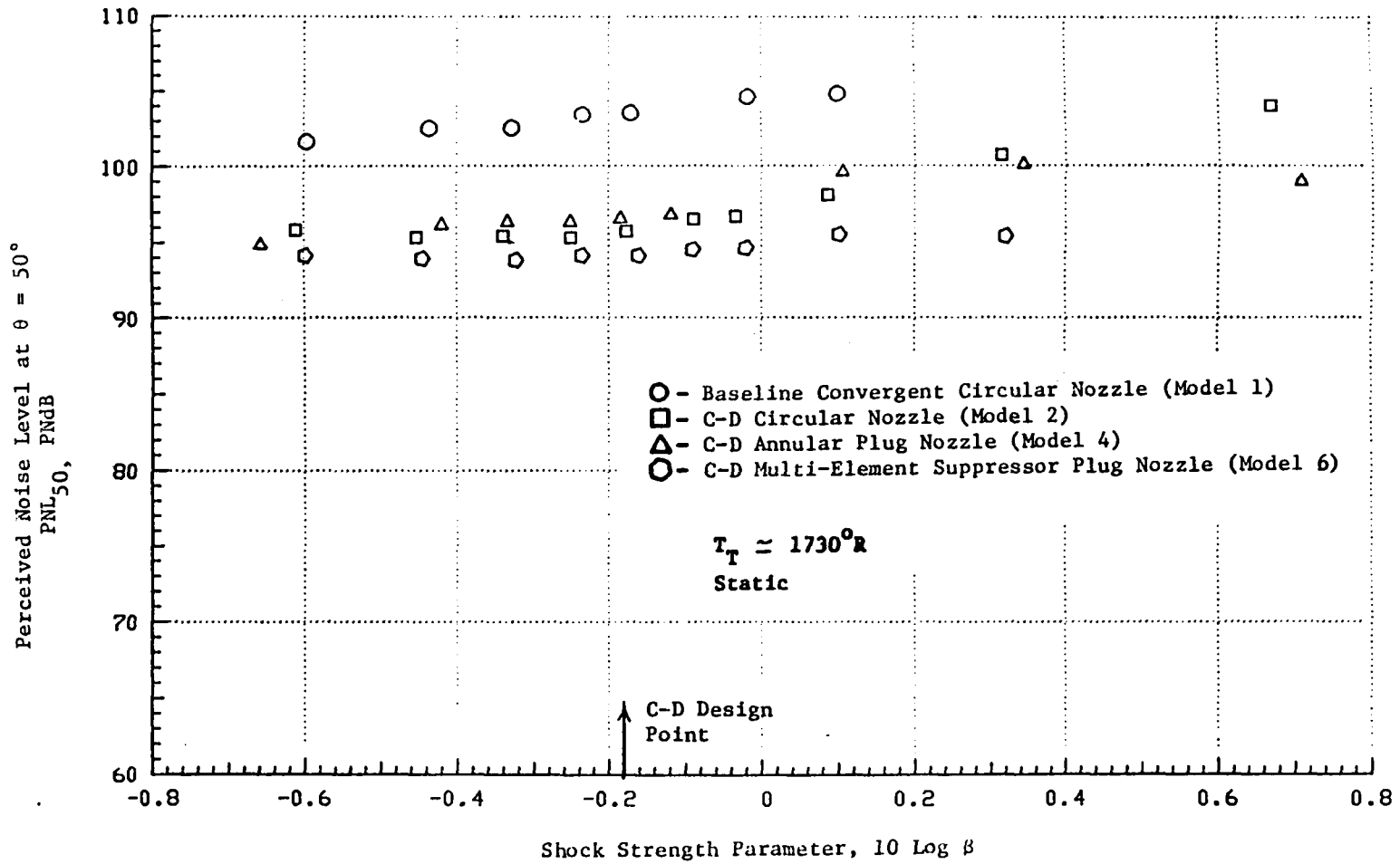


Figure 5-58. PNL at $\theta = 50^\circ$ as a Function of Shock Strength Parameter for Various C-D Nozzles (Static).

nozzle (Model 6) has the lowest front quadrant noise levels over the entire range of pressure ratio among the four nozzles shown in the figure. We note a maximum noise reduction of 9.5 PNdB for this nozzle relative to the baseline convergent circular nozzle, while the C-D circular and the C-D annular plug nozzles show almost an identical amount of reduction near the C-D design point. About 7-7.5 PNdB reduction is observed for these nozzles relative to the convergent circular nozzle. A corresponding simulated flight case is presented in Figure 5-59. The C-D circular nozzle shows the lowest noise level near the C-D operating pressure ratio and as much as 12 PNdB reduction is observed, relative to the baseline convergent circular nozzle.

In order to examine the geometry effects of various C-D nozzles on the jet mixing noise, the normalized perceived noise level was plotted versus $10 \log (V_j/a_{amb})$ at a typical aft quadrant observation angle ($\theta = 130^\circ$) for both static and simulated flight cases. The results are provided in Figures 5-60 and 5-61. An examination of these figures indicates that the convergent-divergent terminations in the flowpaths of Model 2 and 4 have no effects on the suppression of the jet mixing noise. Apparently, significantly lower PNLN_{130°} values for the C-D multi-element suppressor plug nozzle (Model 6) are due to the suppressor (20 shallow chutes) itself and not due to the C-D termination in the flowpath of the chutes.

It is useful to review, at this point, the effects of center plug and the radius ratio of annular plug nozzles on jet mixing noise. Usefulness of employing a center plug in annular jets has been known for some time. Its presence prevents vortices forming in the vicinity of the jet exit plane. Williams et al. (Reference 5-9) reported that the employment of a center plug whose length is twice the diameter of the nozzle reduces the noise level of an annular jet with zero plug length by about 1 dB. Also, shorter length plugs show practically little improvement relative to zero bullet length. On the other hand, the analytical results obtained by means of the MGB-model (Reference 5-13) and by Yamamoto (Reference 5-10) show that a plug shorter than that suggested by Williams et al. is effective in reducing jet mixing noise.

A recent GE study of jet noise of inverted velocity profile coannular plug nozzles (Reference 5-14) has indicated that outer stream radius ratio is a key coannular (or annular) plug nozzle noise reduction parameter; the higher

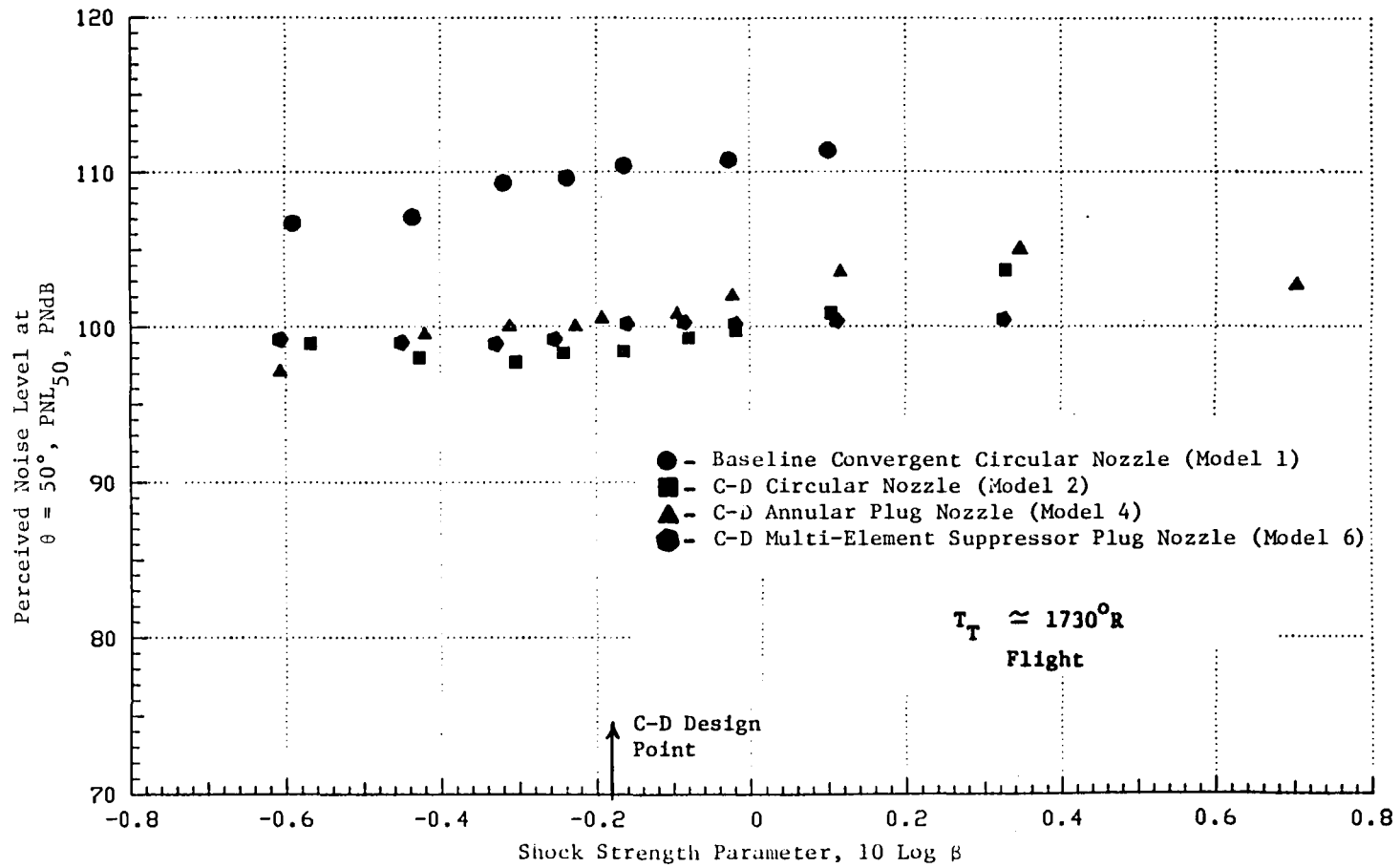


Figure 5-59. PNL at $\theta = 50^\circ$ as a Function of Shock Strength Parameter for Various C-D Nozzles (Flight).

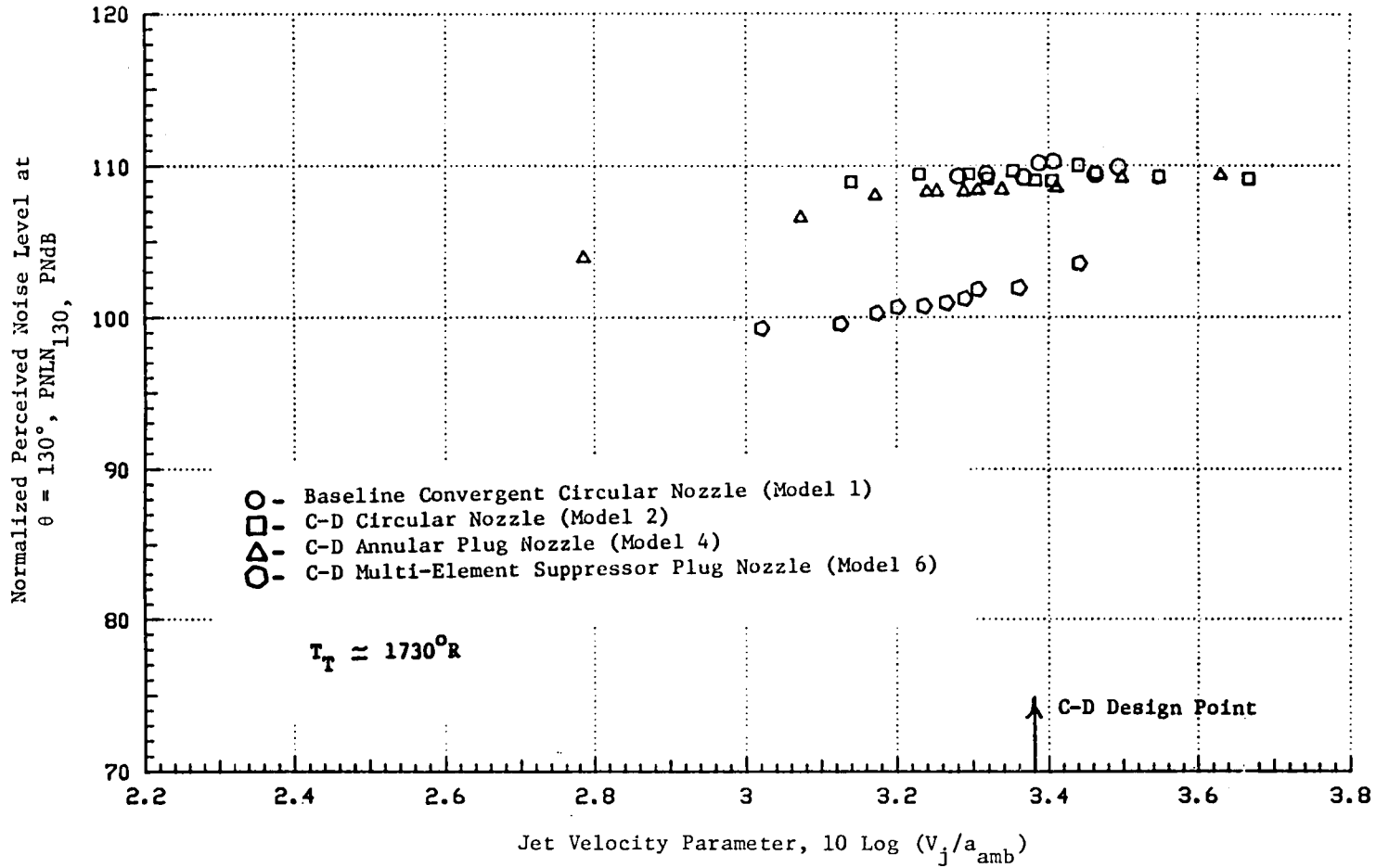


Figure 5-60. Normalized PNL at $\theta = 130^\circ$ as a Function of Jet Exit Velocity for Various C-D Nozzles (Static).

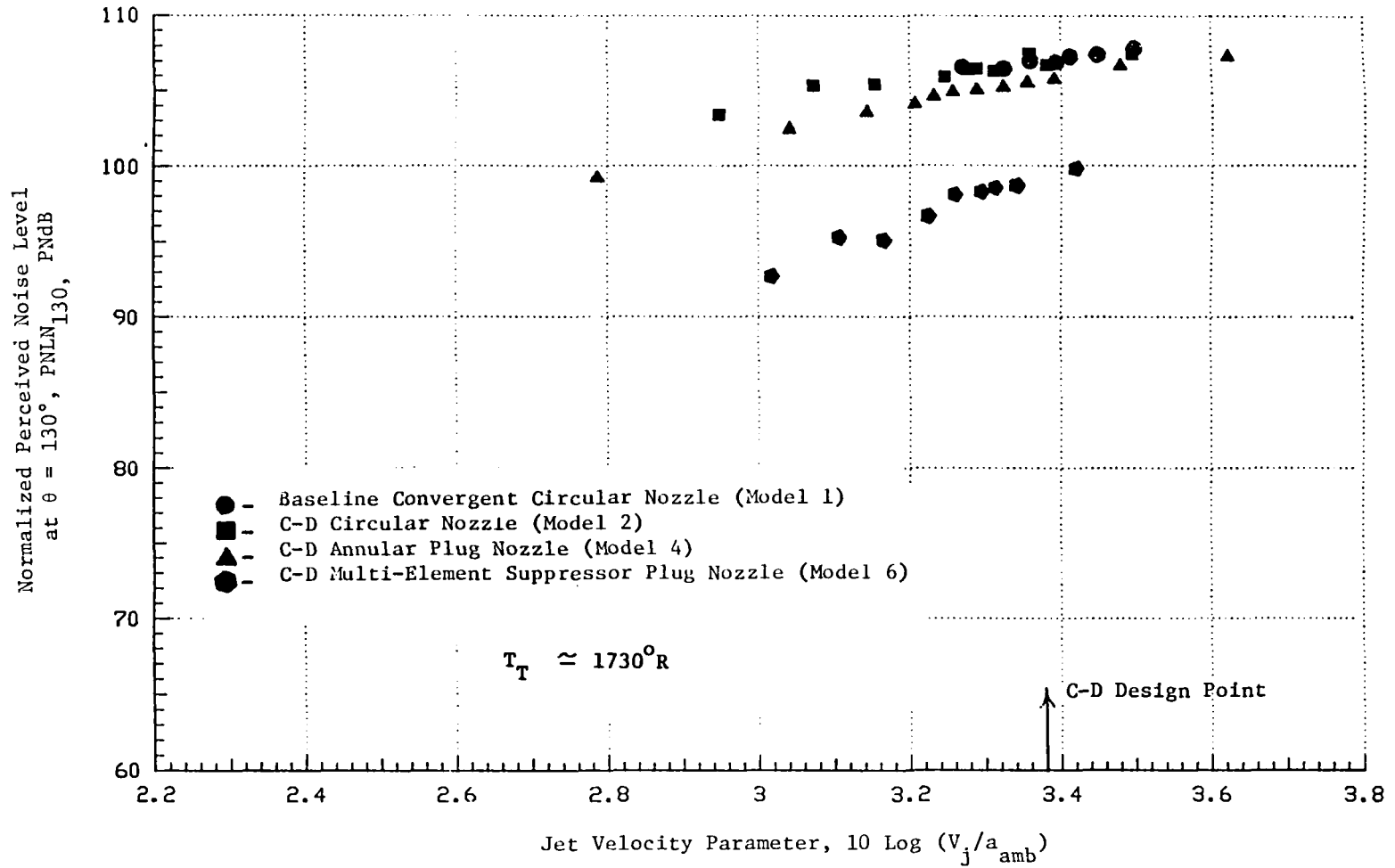


Figure 5-61. Normalized PNL at $\theta = 130^\circ$ as a Function of Jet Exit Velocity for Various C-D Nozzles (Flight).

the radius ratio the greater the noise reduction at a fixed thrust. These results, hence, indicate that annular nozzles are quieter than circular nozzles, and, furthermore, annular plug nozzles have an advantage over annular nozzles with truncated centerbodies as far as jet mixing noise suppression is concerned.

Next, the C-D effectiveness at the design operating conditions is examined for the three different C-D nozzle configurations in terms of PNL and OASPL directivities. The results are presented in Figures 5-62 through 5-67. Here again, a greater effectiveness of the C-D suppressor nozzle than other C-D nozzles is demonstrated over the entire range of observed angles. In the front quadrant, the C-D circular nozzle appears to be less noisy compared to the annular C-D nozzle. However, this trend is reversed in the aft quadrant where, generally, jet mixing noise is predominant. Data for the corresponding flight case are presented in Figure 5-63. Here we note a favorable front quadrant directivity pattern for the C-D circular nozzle. Compared to the plug nozzles, 1 to 2 PNdB lower noise level is observed for this nozzle. This is due to a better shock elimination by the C-D termination in the flowpath of the C-D circular nozzle. In the aft quadrant, however, the C-D suppressor nozzle still maintains its superiority over the rest of the nozzles. An important conclusion from this study is that, under simulated flight conditions, the C-D circular nozzle is the most efficient nozzle among the C-D nozzles tested as far as shock-cell noise suppression is concerned, while the C-D multi-element suppressor is by far the better nozzle in terms of jet mixing noise mitigation.

Figures 5-64 and 5-65 present OASPL directivities for various C-D nozzles at the design operating conditions for static and simulated flight cases. The general trends observed in the results given in these figures is not significantly different from that noted in Figures 5-62 and 5-63, except that in the flight case, the C-D suppressor nozzle shows lower noise level than the circular C-D nozzle in the front quadrant. This is attributed to the difference in the way of handling high frequency components in the OASPL and PNL calculations.

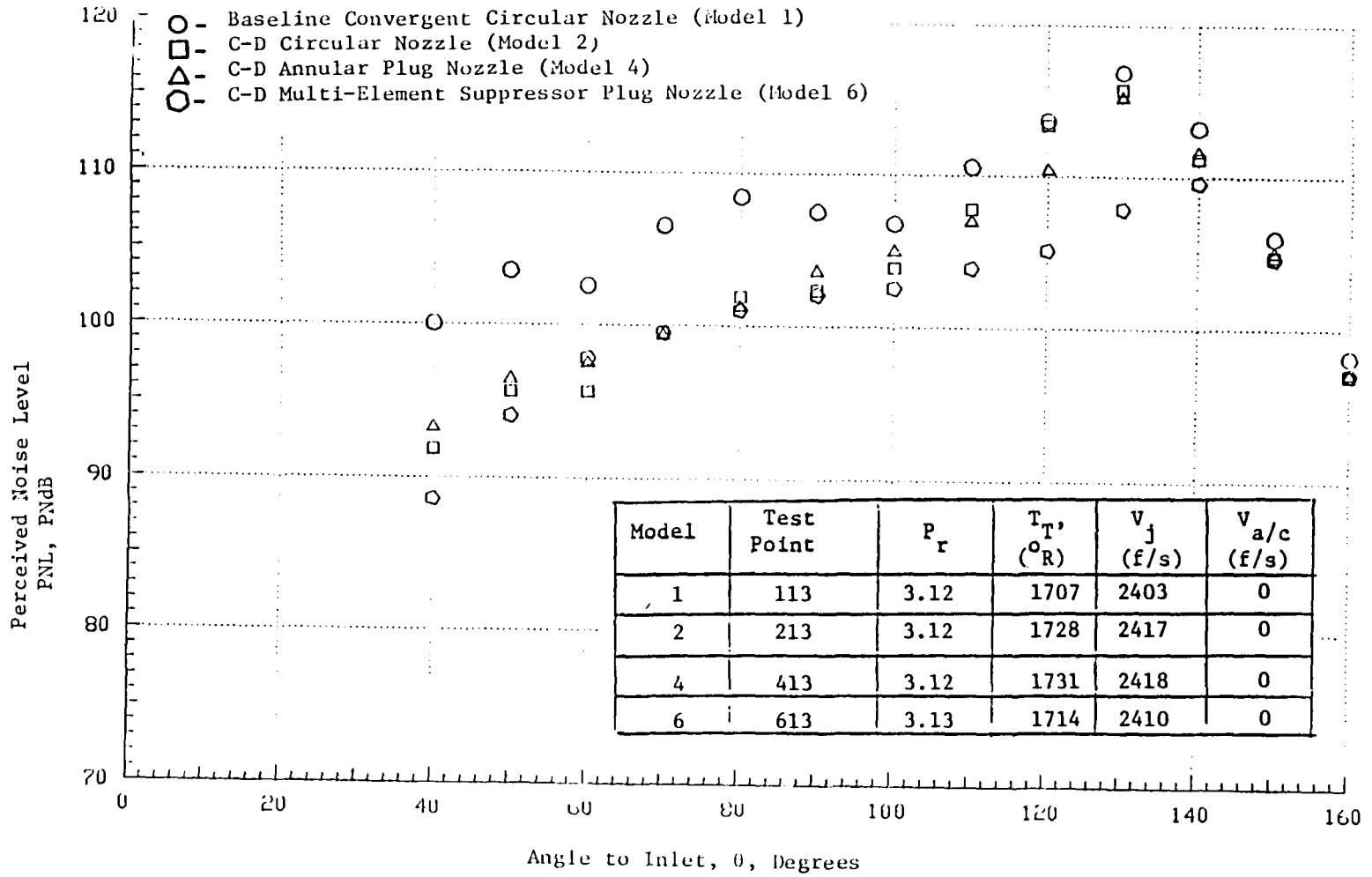


Figure 5-62. PNL Directivities for Various C-D Nozzles at Design Operating Condition (Static).

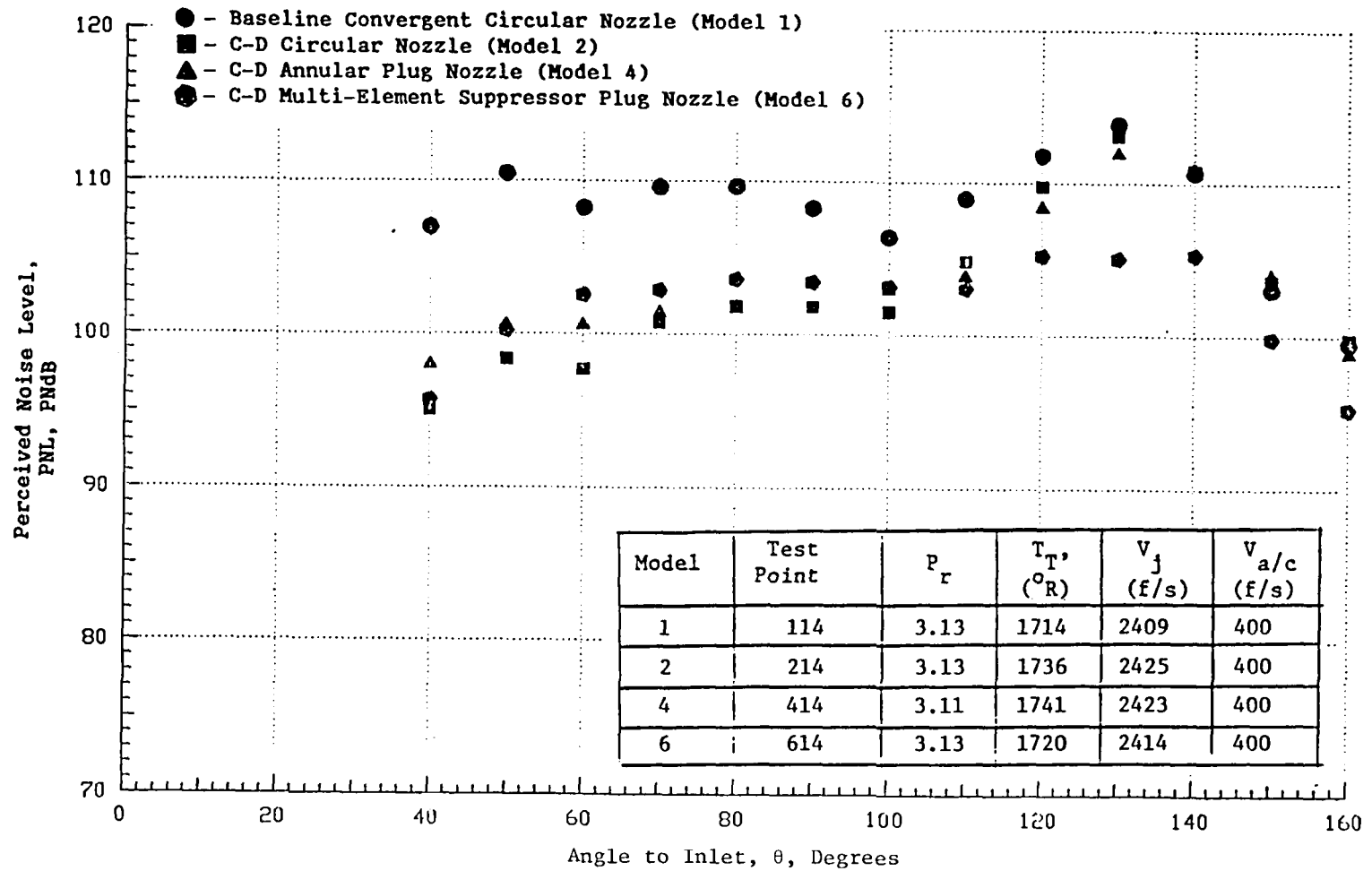


Figure 5-63. PNL Directivities for Various C-D Nozzles at Design Operating Condition (Flight).

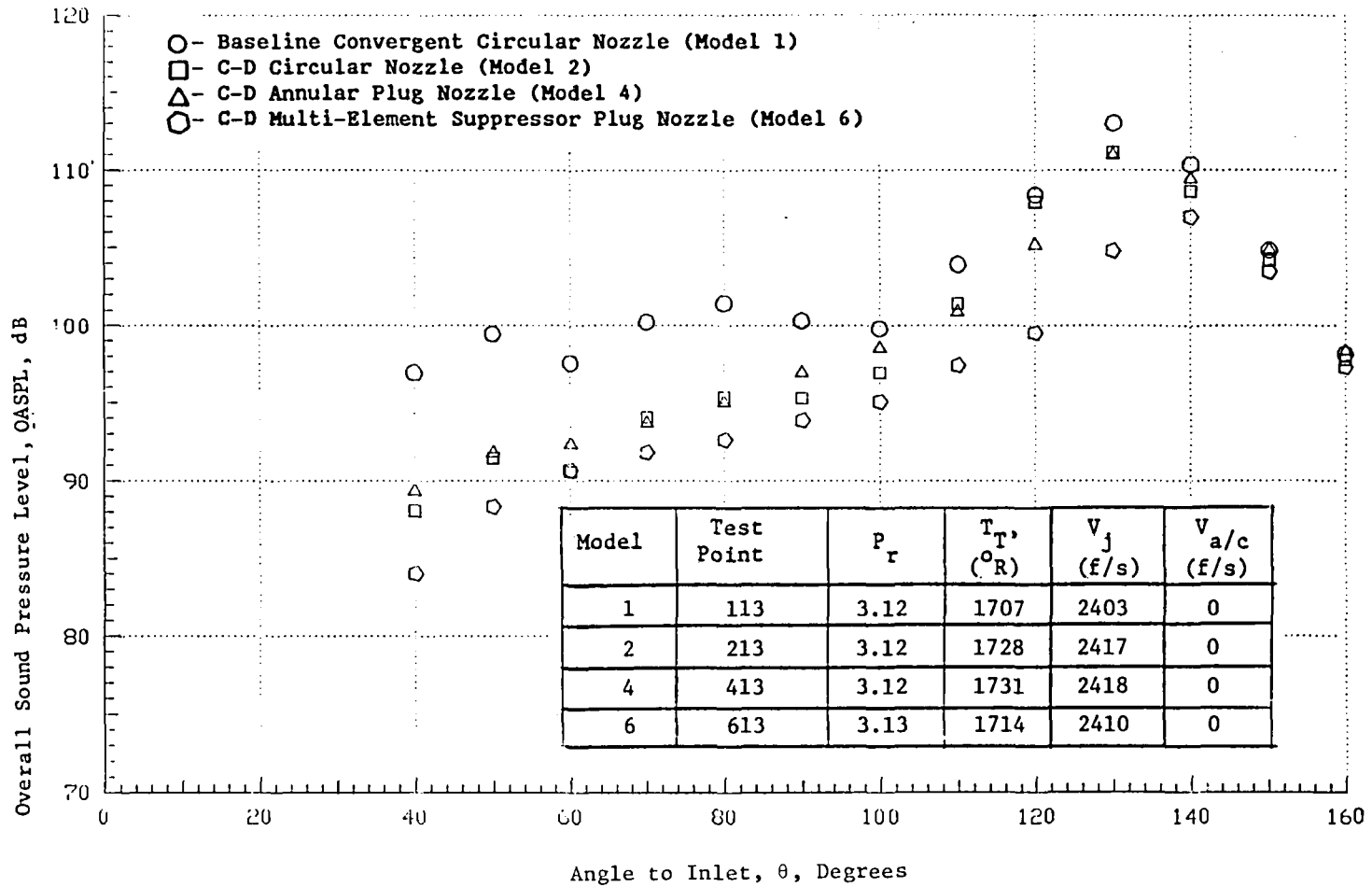


Figure 5-64. OASPL Directivities for Various C-D Nozzles at Design Operating Condition (Static).

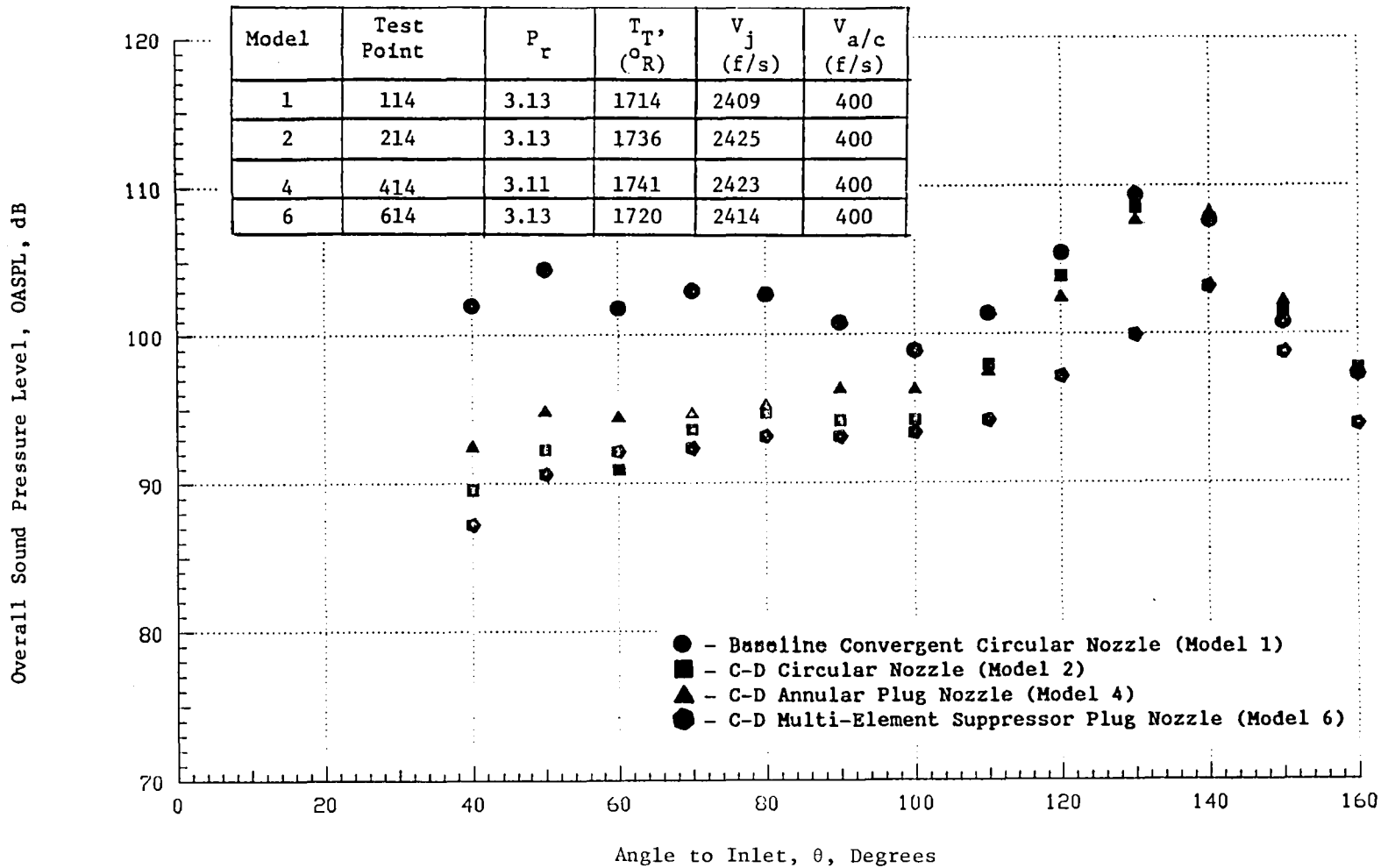


Figure 5-65. OASPL Directivities for Various C-D Nozzles at Design Operating Condition (Flight).

- - Baseline Convergent Circular Nozzle (Model 1)
- - C-D Circular Nozzle (Model 2)
- △ - C-D Annular Plug Nozzle (Model 4)
- - C-D Multi-Element Suppressor Plug Nozzle (Model 6)

Model	Test Point	P_r	$T_{T'}$ ($^{\circ}R$)	V_j (f/s)	$V_{a/c}$ (f/s)
1	113	3.12	1707	2403	0
2	213	3.12	1728	2417	0
4	413	3.12	1731	2418	0
6	613	3.13	1714	2410	0

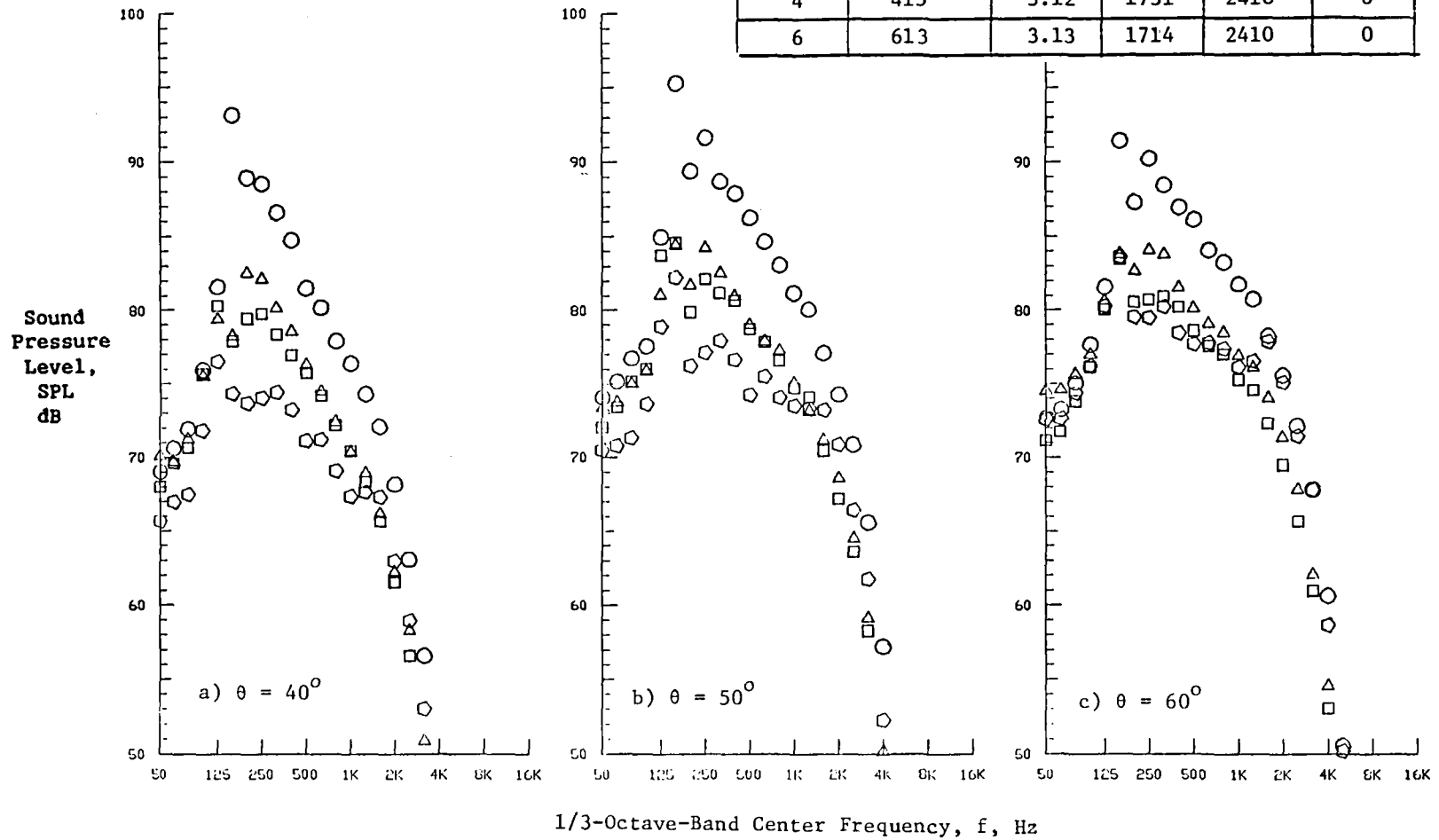


Figure 5-66. One-Third-Octave Spectra for Various C-D Nozzles at Design Operating Condition (Static).

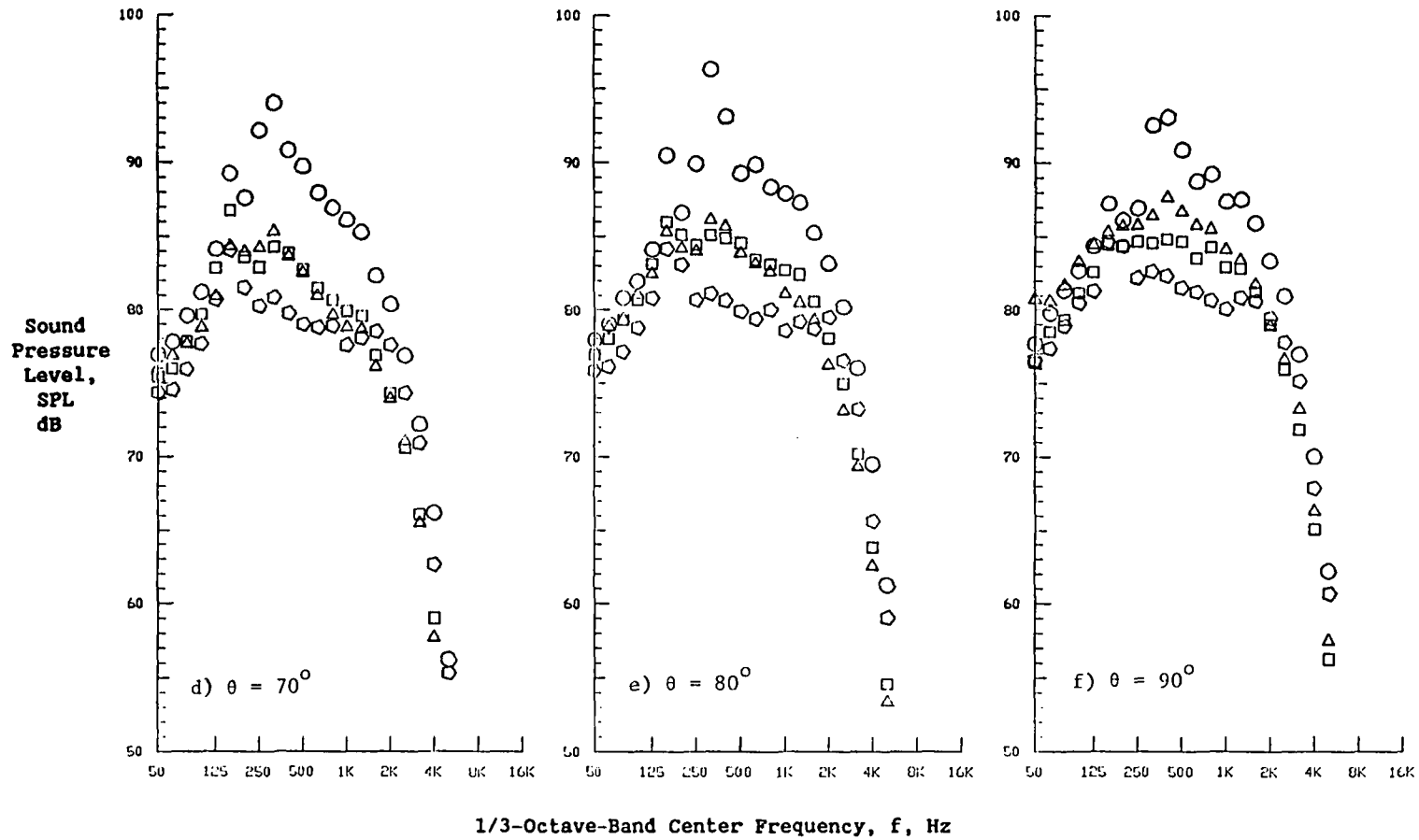


Figure 5-66. (Cont'd) One-Third-Octave Spectra for Various C-D Nozzles at Design Operating Condition (Static).

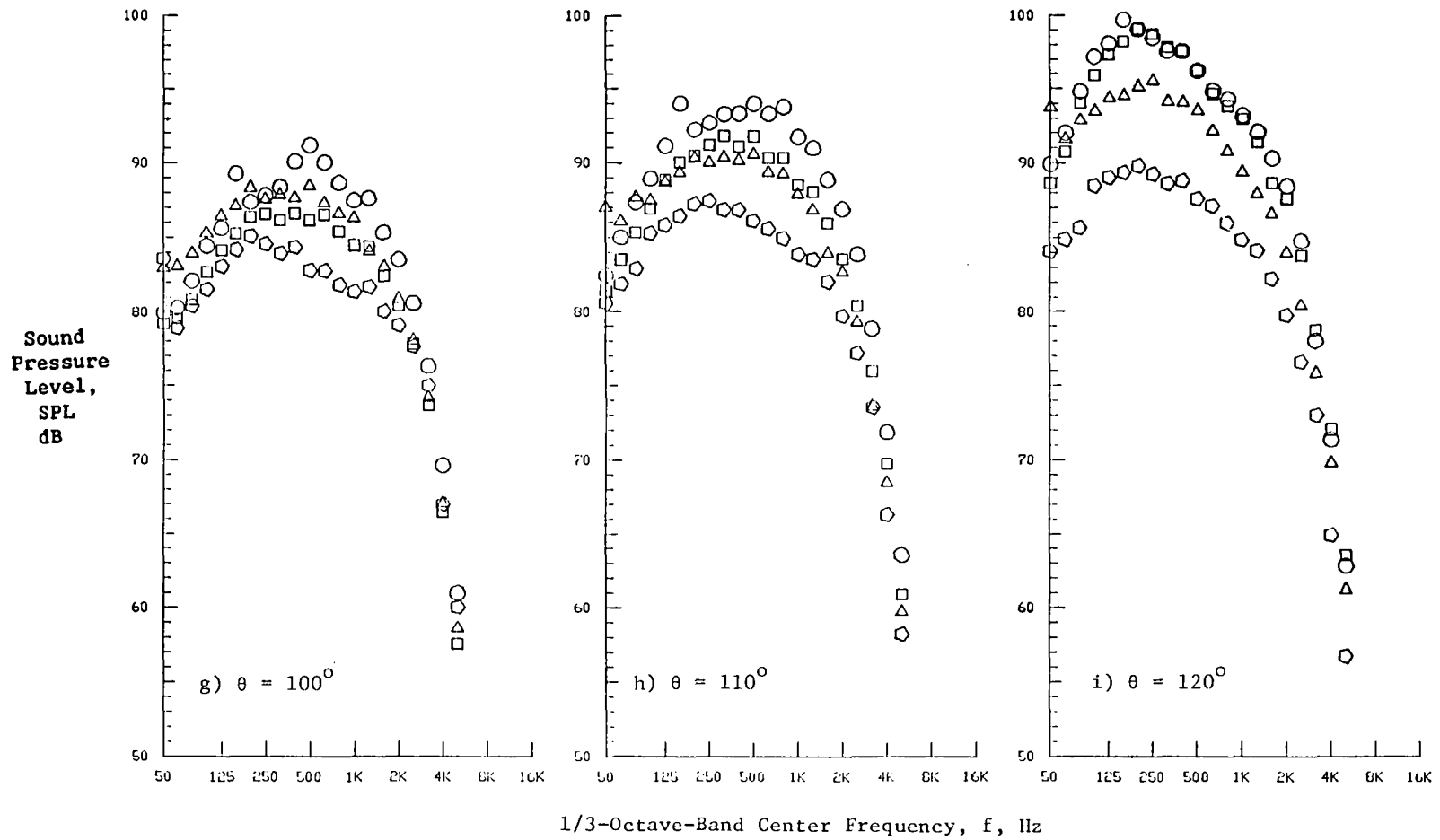


Figure 5-66. (Cont'd) One-Third-Octave Spectra for Various C-D Nozzles at Design Operating Condition (Static).

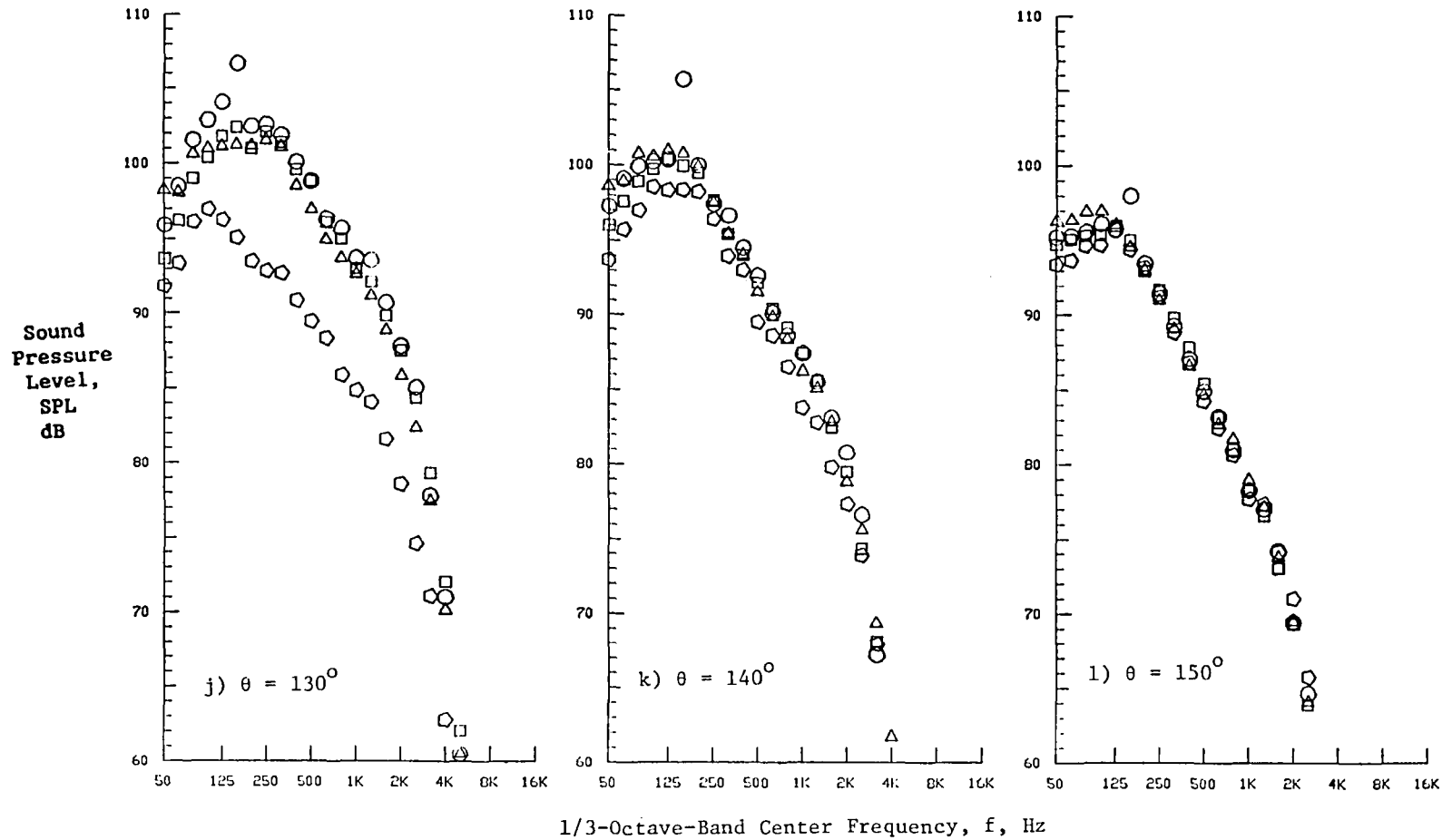


Figure 5-66. (Concluded) One-Third-Octave Spectra for Various C-D Nozzles at Design Operating Condition (Static).

- - Baseline Convergent Circular Nozzle (Model 1)
- - C-D Circular Nozzle (Model 2)
- ▲ - C-D Annular Plug Nozzle (Model 4)
- - C-D Multi-Element Suppressor Plug Nozzle (Model 6)

Model	Test Point	P_r	T_T , ($^{\circ}R$)	V_j (f/s)	$V_{a/c}$ (f/s)
1	114	3.13	1714	2409	400
2	214	3.13	1736	2425	400
4	414	3.11	1741	2423	400
6	614	3.13	1720	2414	400

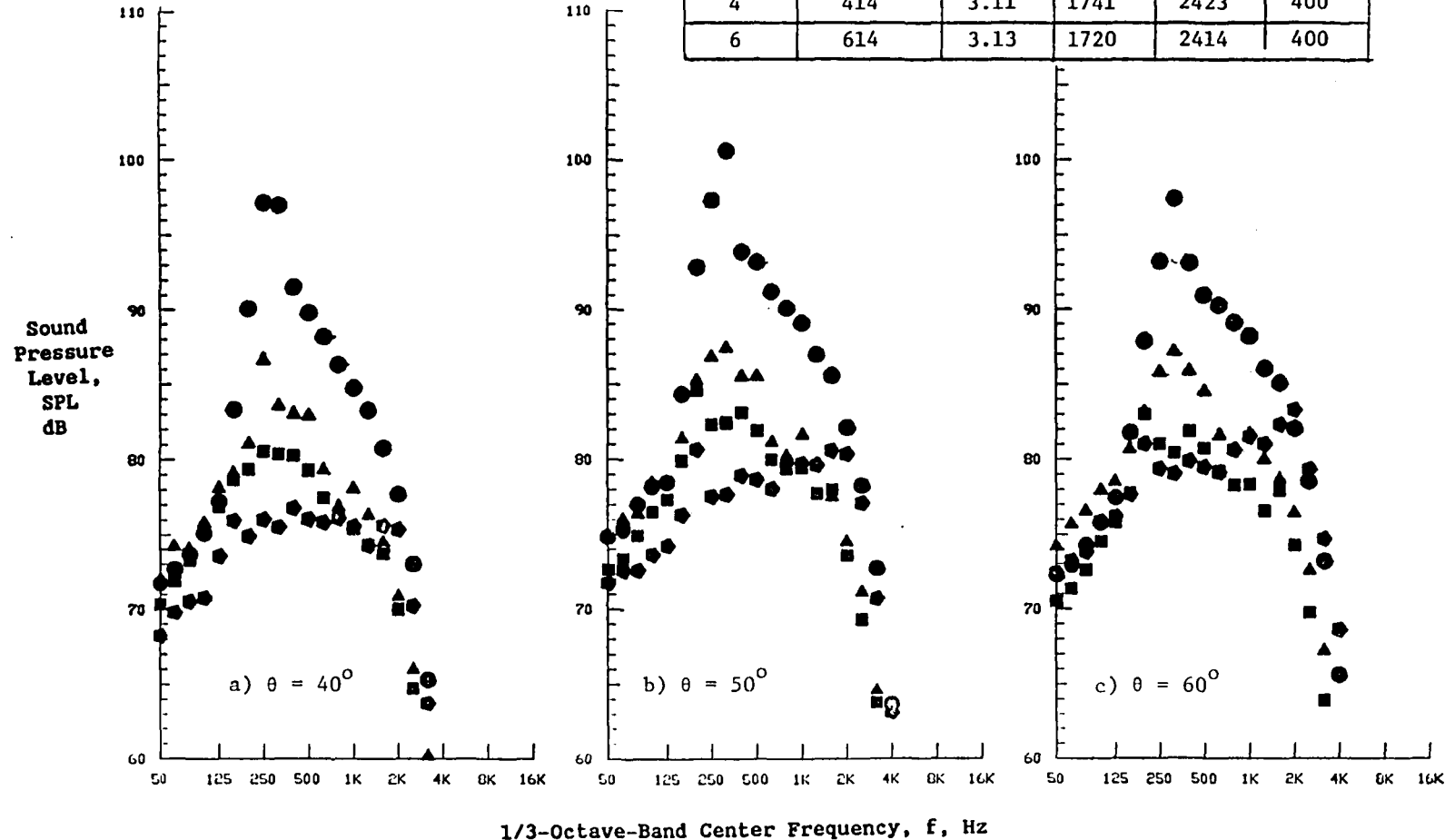


Figure 5-67. One-Third-Octave Spectra for Various C-D Nozzles at Design Operating Condition (Flight).

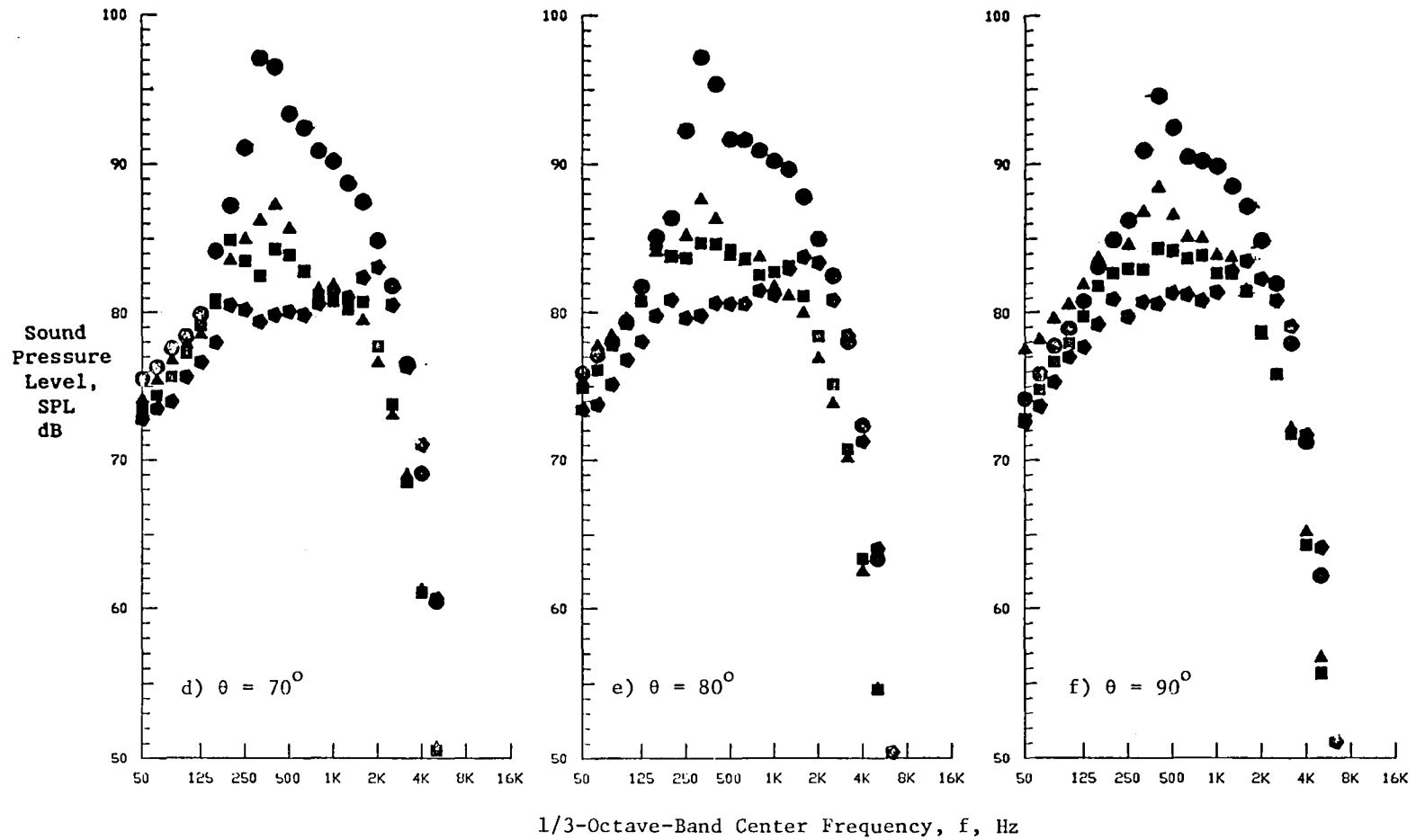


Figure 5-67. (Cont'd) One-Third-Octave Spectra for Various C-D Nozzles at Design Operating Condition (Flight).

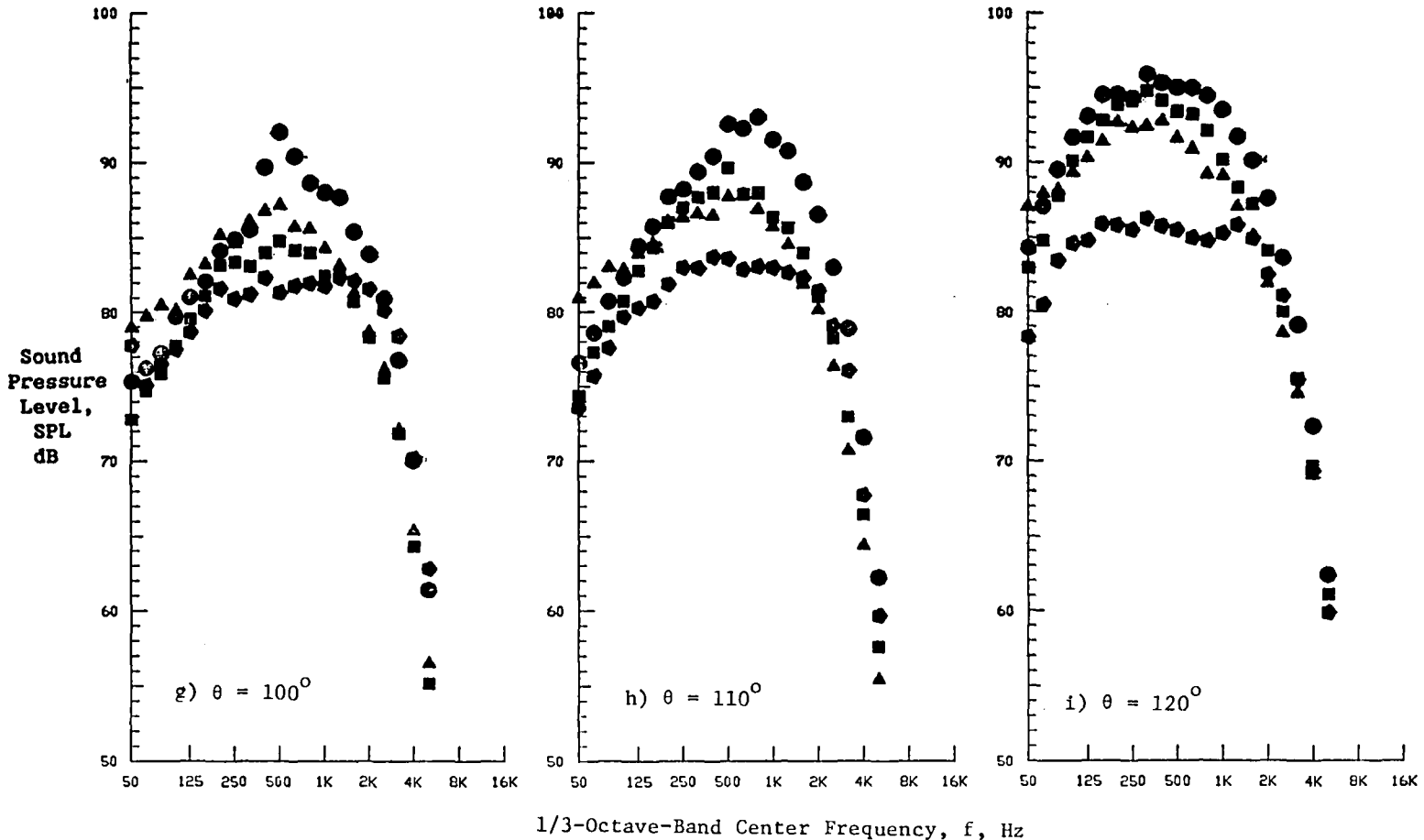


Figure 5-67. (Cont'd) One-Third-Octave Spectra for Various C-D Nozzles at Design Operating Condition (Flight).

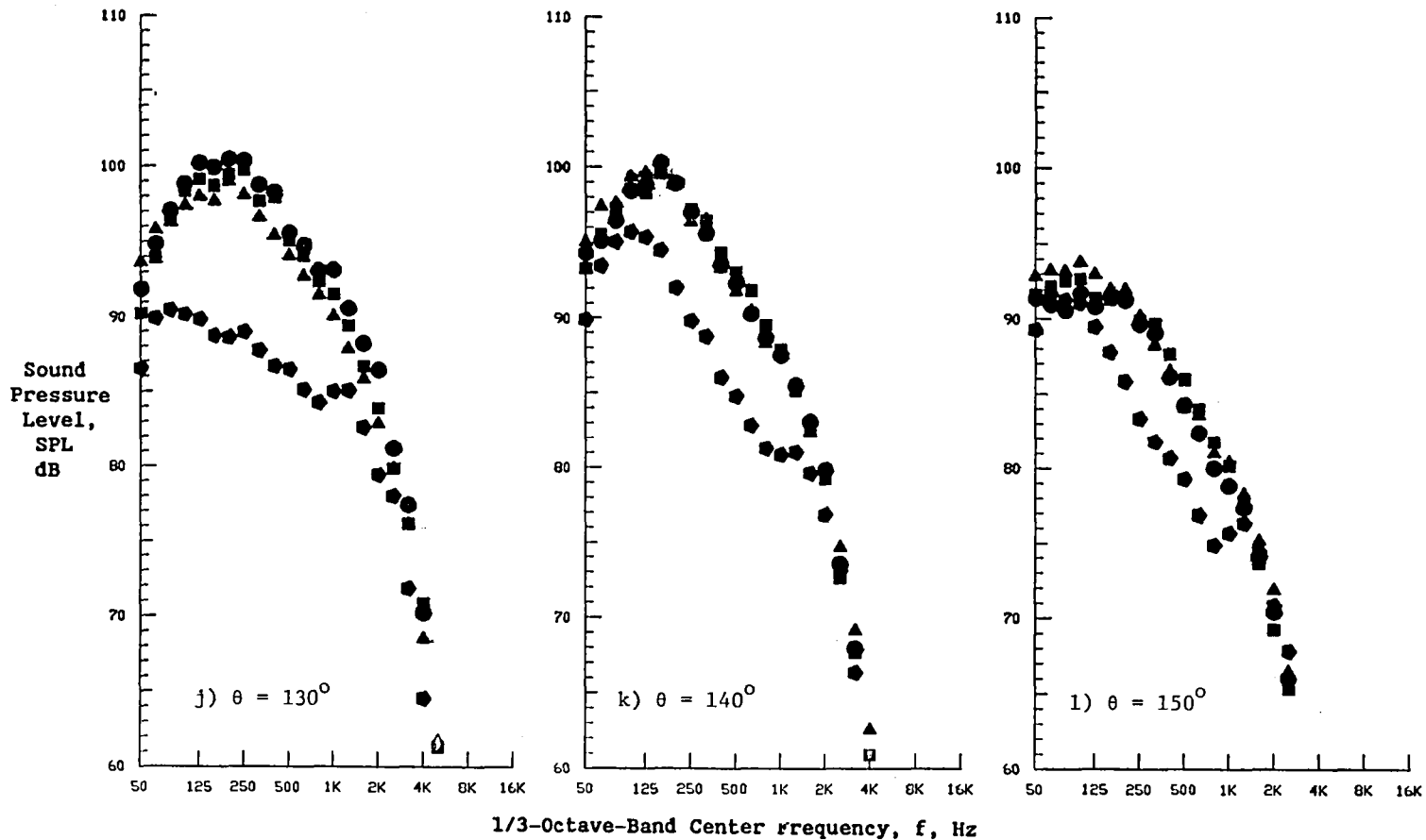


Figure 5-67. (Concluded) One-Third-Octave Spectra for Various C-D Nozzles at Design Operating Condition (Flight).

Corresponding one-third-octave spectra for various C-D nozzles observed at the design operating conditions are presented in Figure 5-66 (static) and 5-67 (flight). Examination of the figures indicates that:

In the front quadrant spectrum (e.g., at $\theta = 50^\circ$)

- Over the mid to low frequency range, the C-D suppressor nozzle shows the lowest noise level; however, in the high frequency range, the C-D circular nozzle is the quietest.
- In the mid frequency range (i.e., $250 \text{ Hz} < f < 1000 \text{ Hz}$), SPL for the C-D annular plug nozzle is generally higher than that for the C-D circular nozzle.
- SPL flight amplification varies depending upon frequency and nozzle type as illustrated in Figure 5-68.

In the aft quadrant spectrum (e.g., at $\theta = 130^\circ$)

- Over the entire range of frequencies, the C-D suppressor nozzle shows the lowest SPL both at static and flight conditions.
- In the mid to high frequency range, the C-D annular plug nozzle jet is slightly quieter than the C-D circular nozzle jet.
- The C-D circular nozzle has a spectral profile basically identical to that of the baseline convergent circular nozzle, indicating that the C-D termination does not play any significant role in jet mixing noise suppression.

At this point, further remarks can be made about the results illustrated in Figure 5-68. How flight affects the spectral contents of the front quadrant noise is illustrated in this figure for the test points selected in Figures 5-66 and 5-67. An examination of this figure indicates a general shock noise amplification by flight over a wide range of frequencies for all of the selected nozzles, except near 160 Hz. In addition, the C-D circular nozzle (Model 2) shows the least flight amplification over the entire

Model 1, Baseline Convergent Circular Nozzle
 Model 2, C-D Circular Nozzle
 Model 4, C-D Annular Plug Nozzle
 Model 6, C-D Multi-Element Suppressor Plug Nozzle

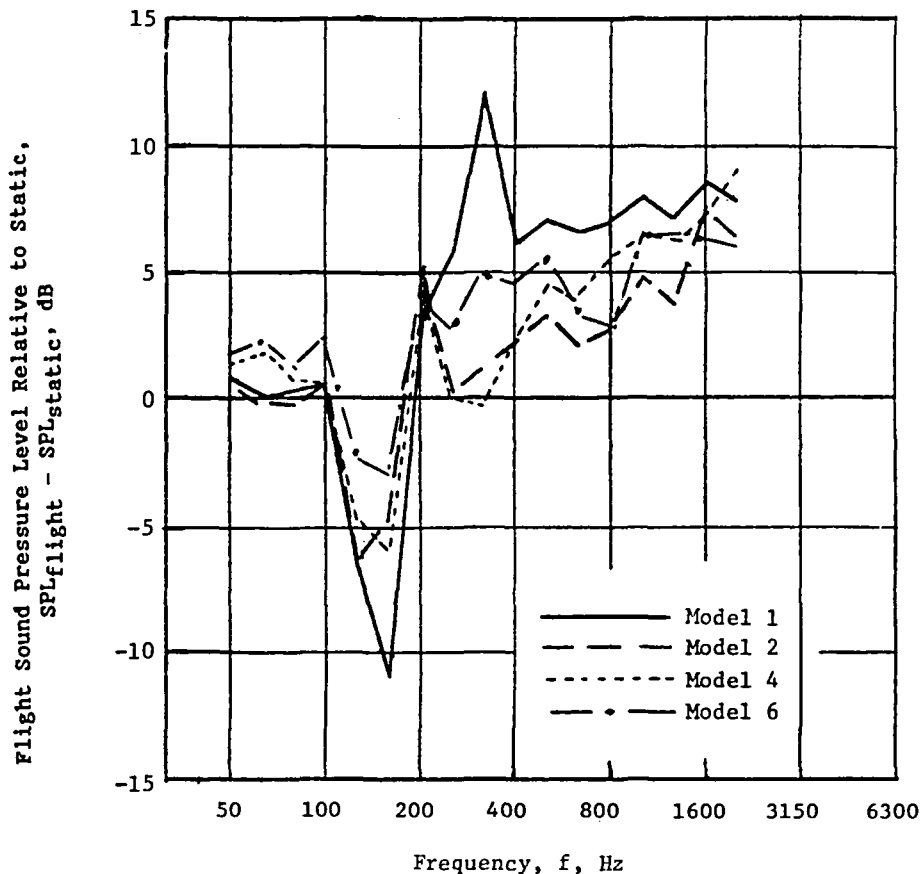


Figure 5-68. Typical Front Quadrant ($\theta = 50^\circ$) SPL Amplification by Flight for Various C-D Nozzles (Selected Test Points are Identical to Those Given in Figures 5-66 and 5-67).

frequency range of interest, indicating shock suppression by the C-D termination of this nozzle. The apparent negative amplification in flight observed near 160 Hz is attributed to the fact that screech was eliminated under simulated flight conditions. This is verified in Figure 5-69, where the model size on-line narrowband acoustic data of Test Points 113 and 114 are presented. A strong screech is observed in the narrowband spectrum of Test Point 113 whose frequency was identified to be 1320 Hz and which falls in the 160 Hz range (one-third-octave band) when scaled to a product size. The screech tone and its harmonic appear to be completely suppressed under simulated flight conditions.

5.2.3.2 Convergent Nozzles

Figure 5-70 comparatively illustrates a typical front quadrant PNL as a function of $10 \log \beta$ for the three convergent nozzles tested during this program. The aerodynamic test conditions of the selected test points were $T_T \approx 1730^\circ R$ and $2.8 < P_r < 3.9$. The results indicate that both the convergent annular plug nozzle and the convergent multi-element suppressor plug nozzle have an almost equal amount of reduction relative to the baseline convergent circular nozzle at this radiation angle over a wide range of pressure ratios. A maximum noise reduction of 8 dB for these nozzles relative to the baseline convergent circular nozzle is noted.

A corresponding simulated flight case is presented in Figure 5-71. A maximum of 10 dB reduction relative to the baseline convergent circular nozzle is observed for the annular plug nozzle (Model 3).

In order to examine the effect of various convergent nozzles on the jet mixing noise, the normalized PNL was plotted versus $\log (V_j/a_{amb})$ at a typical aft quadrant observation angle ($\theta = 130^\circ$) for both static and simulated flight cases. The results are provided in Figures 5-72 and 5-73. An examination of these figures indicates that, for a given thrust, aft quadrant PNL for the convergent multi-element suppressor nozzle is by far the lowest among the three tested convergent nozzles. This is observed both at static and simulated flight cases. Decreased PNL values corresponding to the convergent annular plug nozzle relative to those for the baseline convergent circular nozzle may be attributed to the annular jet effect.

Model	Test Point	P_r	$T_{T^{\circ}}$ ($^{\circ}$ R)	V_j (f/s)	$V_{a/c}$ (f/s)
1	113	3.12	1707	2403	0
1	114	3.13	1715	2410	400

ON-LINE DATA (Filter Bandwidth = 12.5 Hz)
MODEL SIZE

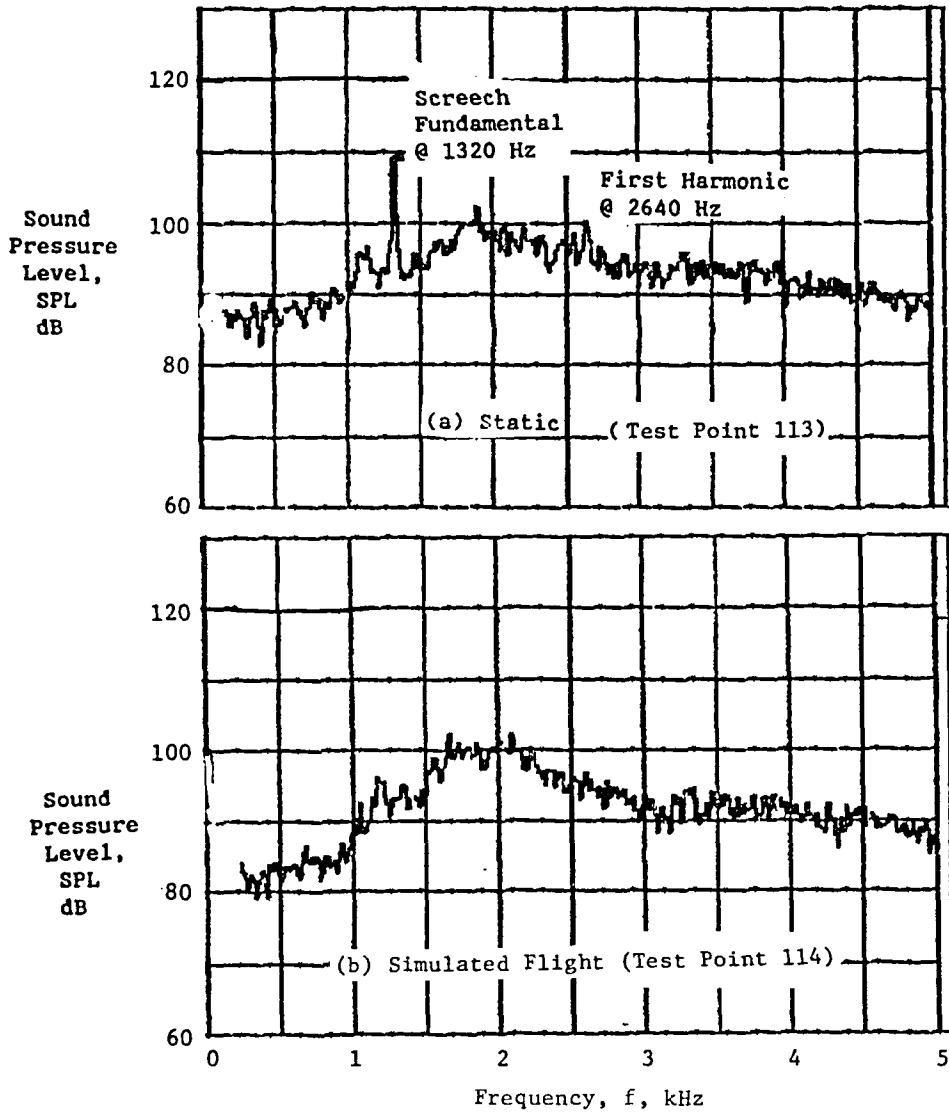


Figure 5-69. An Illustration on the Effect of Flight on Screech at $\theta = 60^{\circ}$.

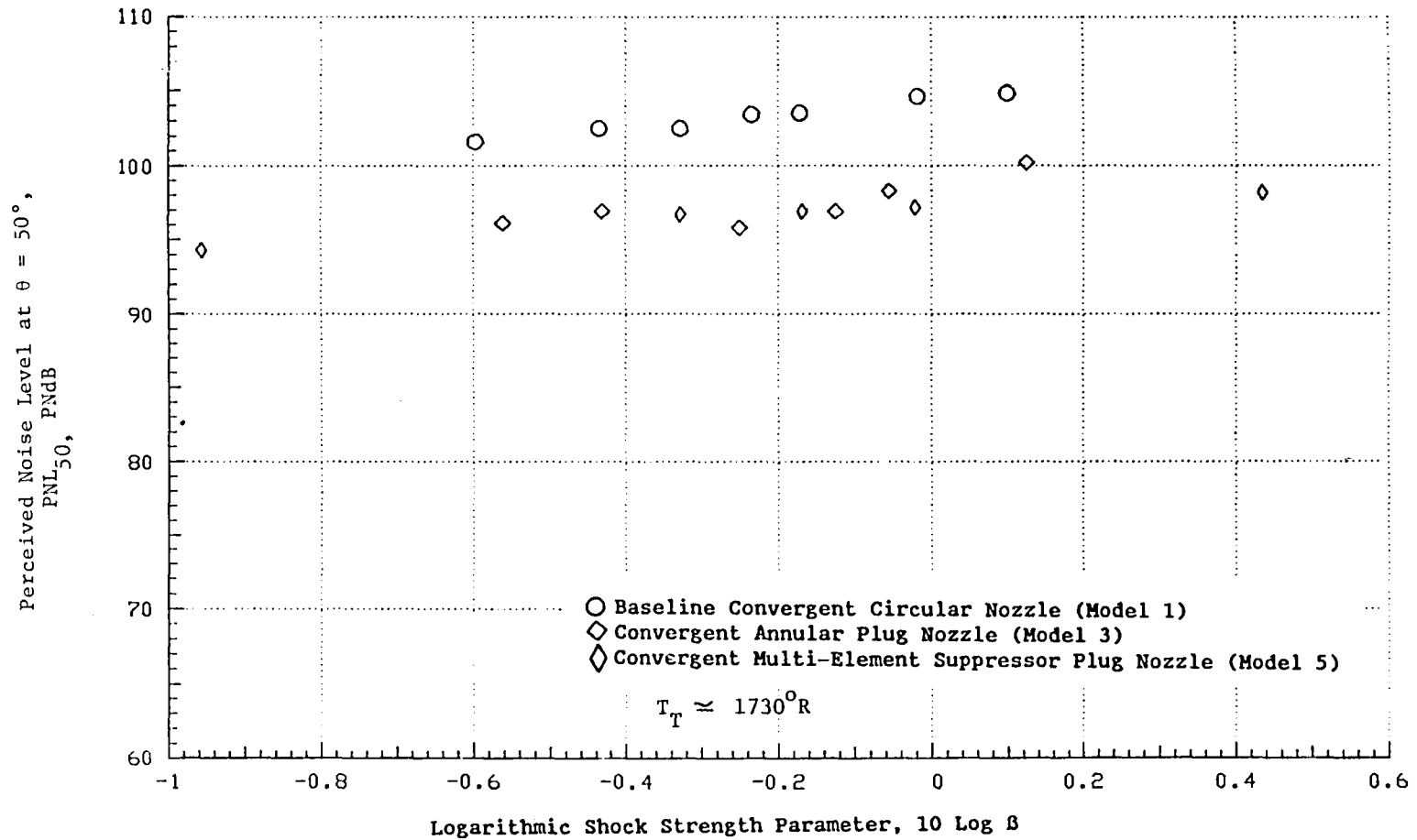


Figure 5-70. PNL at $\theta = 50^\circ$ as a Function of Shock Strength Parameter for Various Convergent Nozzles (Static).

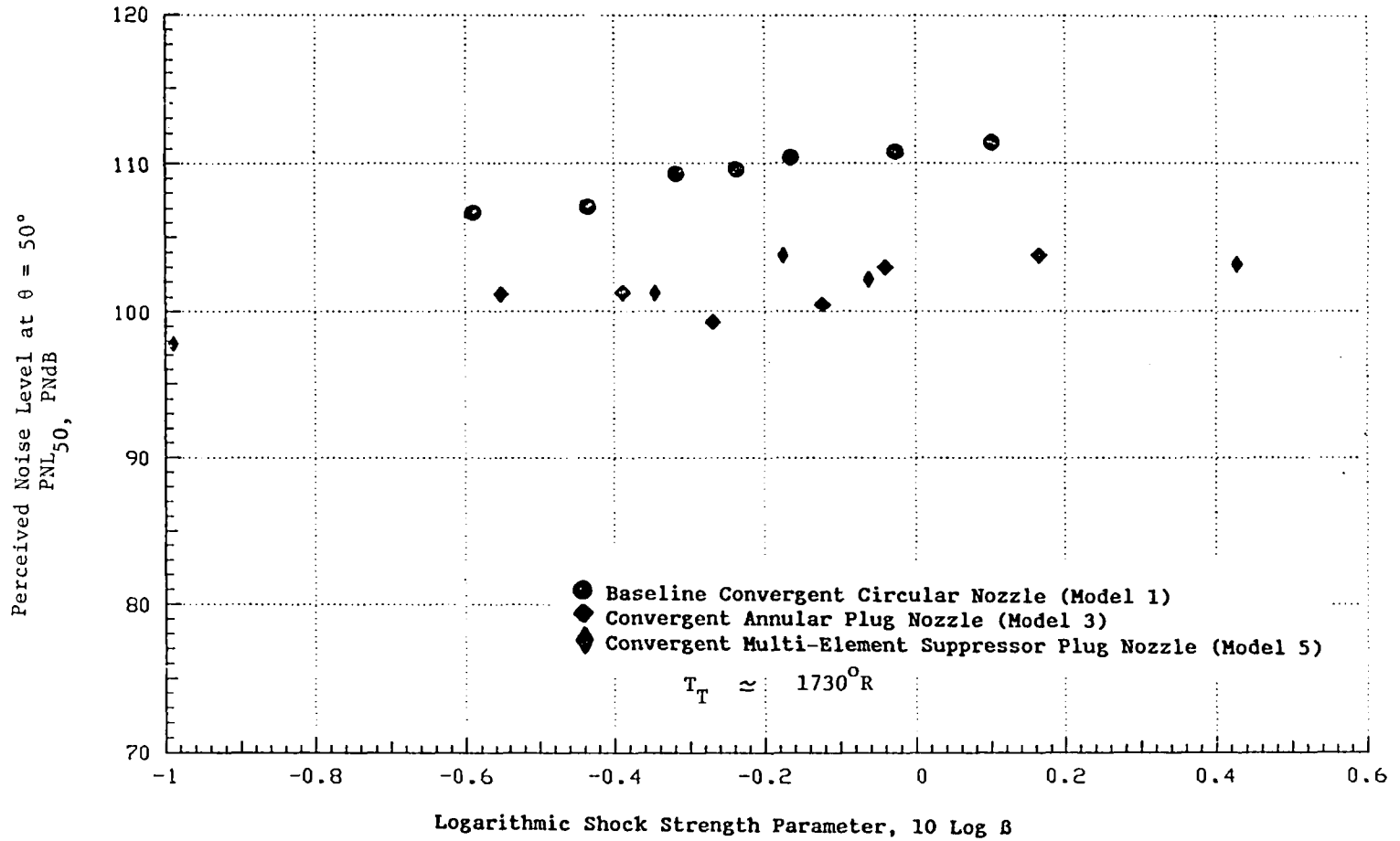


Figure 5-71. PNL at $\theta = 50^\circ$ as a Function of Shock Strength Parameter for Various Convergent Nozzles (Flight).

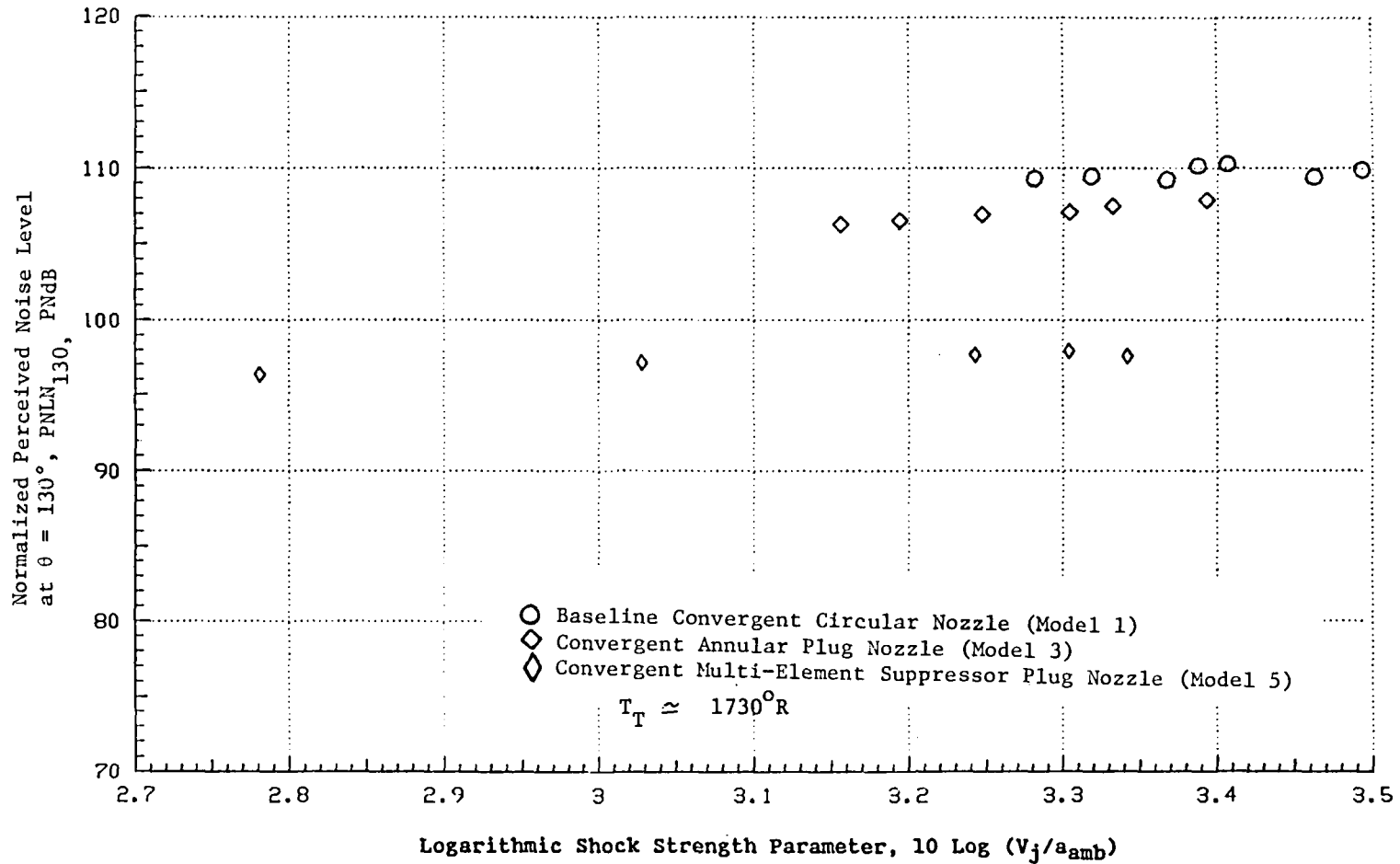


Figure 5-72. Normalized PNL at $\theta = 130^\circ$ as a Function of Jet Exit Velocity for Various Convergent Nozzles (Static).

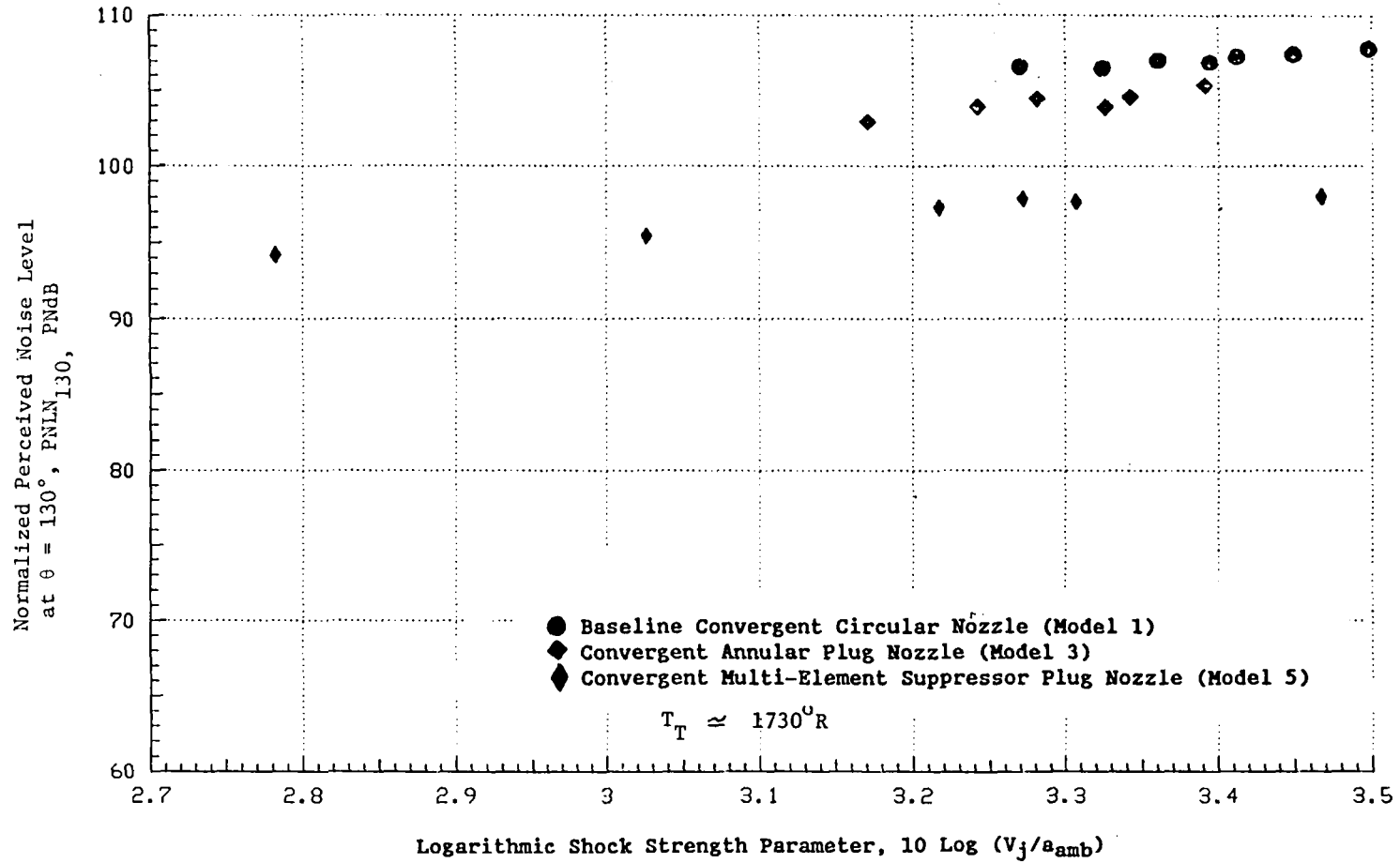


Figure 5-73. Normalized PNL at $\theta = 130^\circ$ as a Function of Jet Exit Velocity for Various Convergent Nozzles (Flight).

Next, geometry effects on PNL and OASPL directivities are examined over three different convergent nozzles. The results are presented in Figures 5-74 through 5-77. The OASPL directivity presented in Figure 5-76 indicates that the suppressor nozzle (Model 5) has an edge over the non-suppressor nozzles (Models 1 and 3) over the entire observation angles of interest. However, if noise signature is expressed in terms of the perceived noise level, as is illustrated in Figure 5-74, the annular nozzle (Model 3) shows a favorable directivity pattern in the front quadrant. This is because of less high frequency contents of the noise generated by the nozzle, as compared to the noise produced by the suppressor nozzle (Model 5). Corresponding flight cases for PNL and OASPL directivities are presented in Figures 5-75 and 5-77. It appears that the noise from the suppressor nozzle (Model 5) undergoes larger front quadrant flight amplification than that from the convergent annular nozzle (Model 3). To examine how each frequency component is affected by flight, one-third-octave spectra over various radiation angles are illustrated in Figures 5-78 and 5-79. Comparison of the spectra at $\theta = 50^\circ$, for example, between static and flight cases indicates that in the case of the convergent annular plug nozzle flight affects mid to high frequencies, whereas flight predominantly affects high frequencies of noise generated by the convergent multi-element suppressor nozzle. These results, hence, indicate that the convergent annular plug nozzle produced shocks downstream of the plug as well as on the plug at supercritical conditions while the convergent multi-element suppressor nozzle produced shocks only in the close proximity of the nozzle exit, as illustrated by the laser velocimeter results to be discussed later.

To conclude discussions of this subsection, major results are summarized below:

- The convergent-divergent circular nozzle was identified to be quietest at the design operating condition among the three types of C-D nozzles tested in simulated flight, as far as front quadrant noise measured in terms of PNL is concerned.
- The convergent-divergent multi-element suppressor plug nozzle was identified to be quietest among the three test C-D nozzles as far as aft quadrant noise is concerned, both at static and simulated flight conditions.

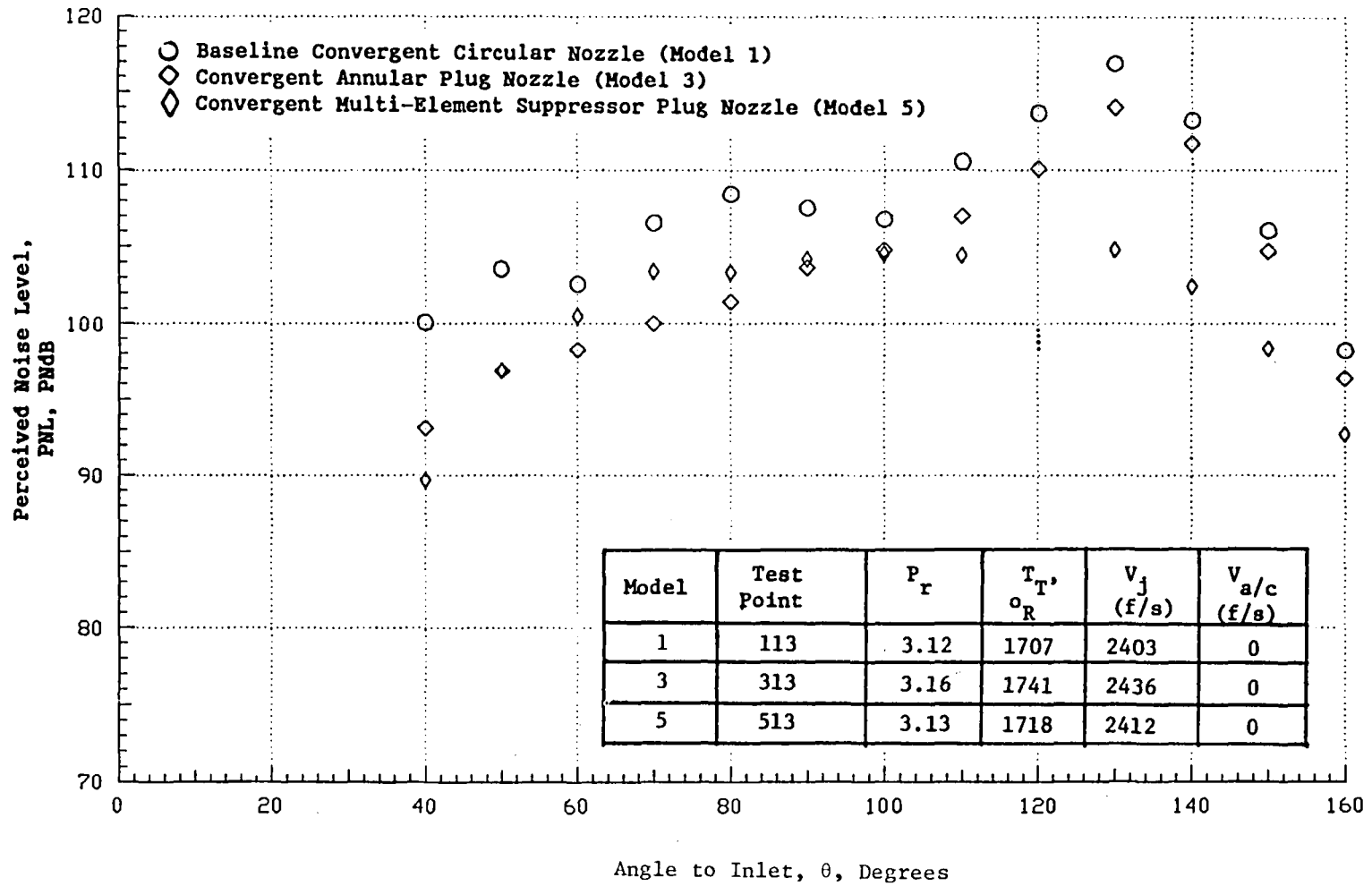


Figure 5-74. PNL Directivities for Various Convergent Nozzles at Aerodynamic Conditions Corresponding to the C-D Design Operating Conditions (Static).

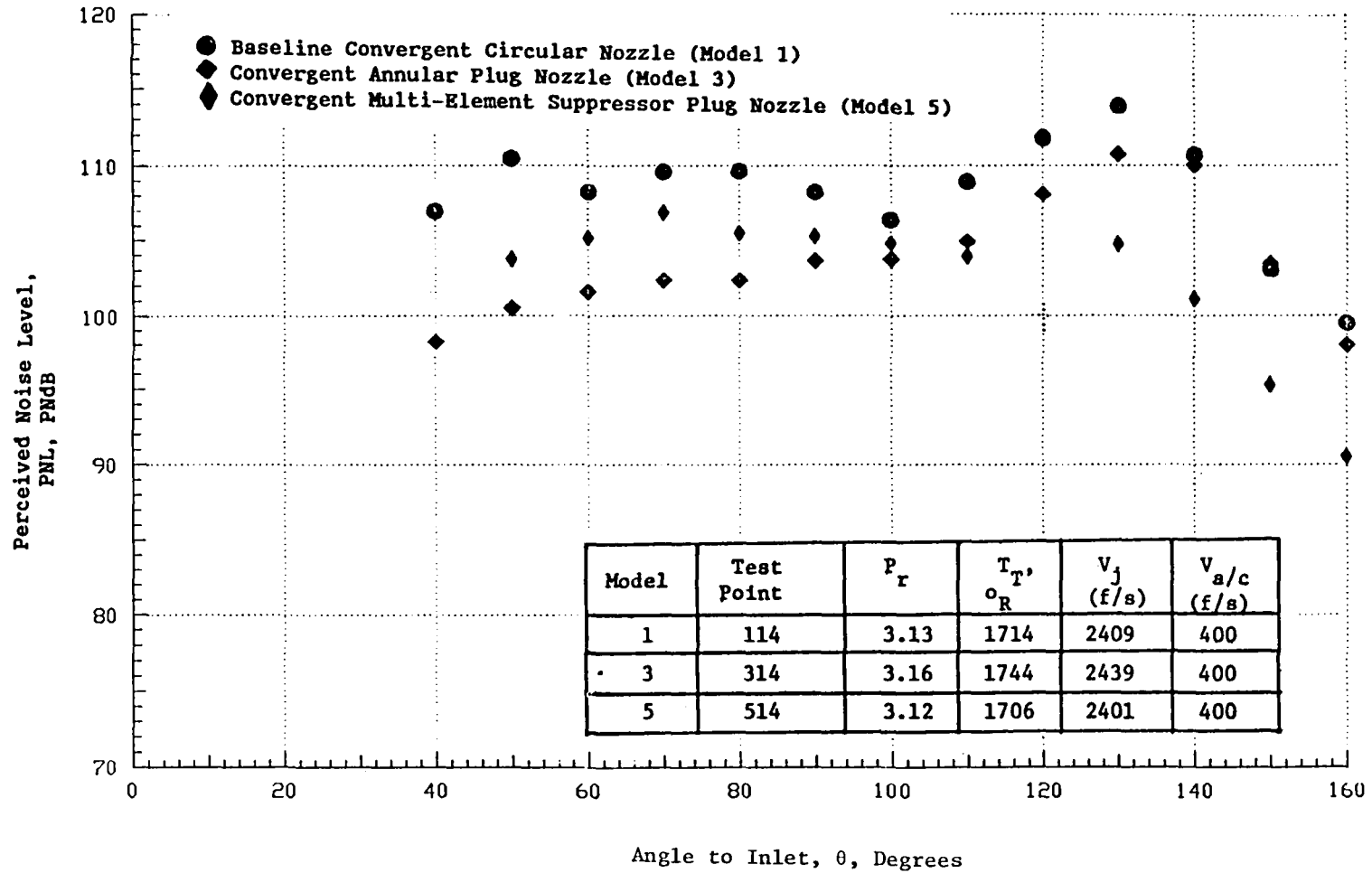


Figure 5-75. PNL Directivities for Various Convergent Nozzles at Aerodynamic Conditions Corresponding to the C-D Design Operating Conditions (Flight).

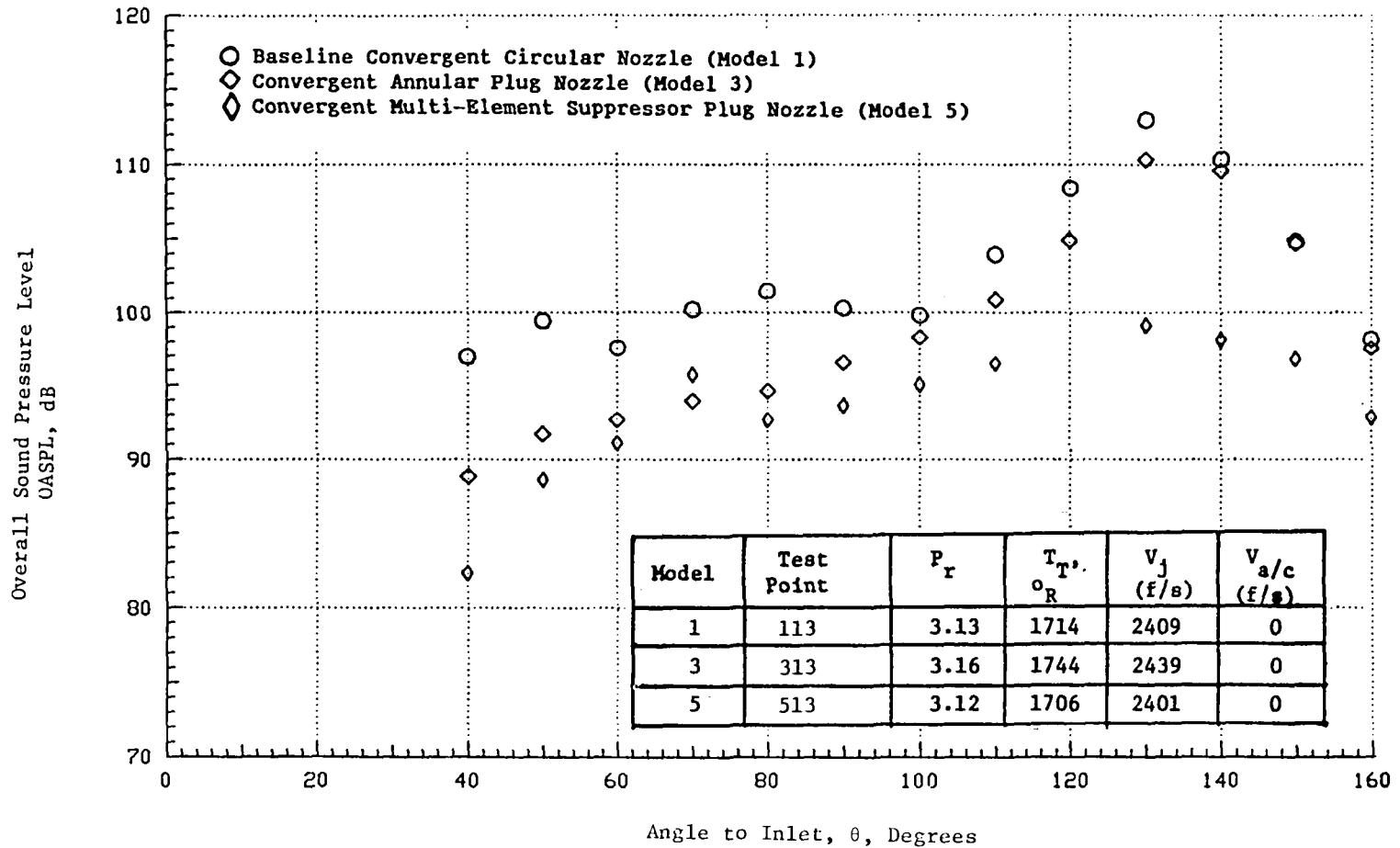


Figure 5-76. OASPL Directivities for Various Convergent Nozzles at Aerodynamic Conditions Corresponding to the C-D Design Operating Conditions (Static).

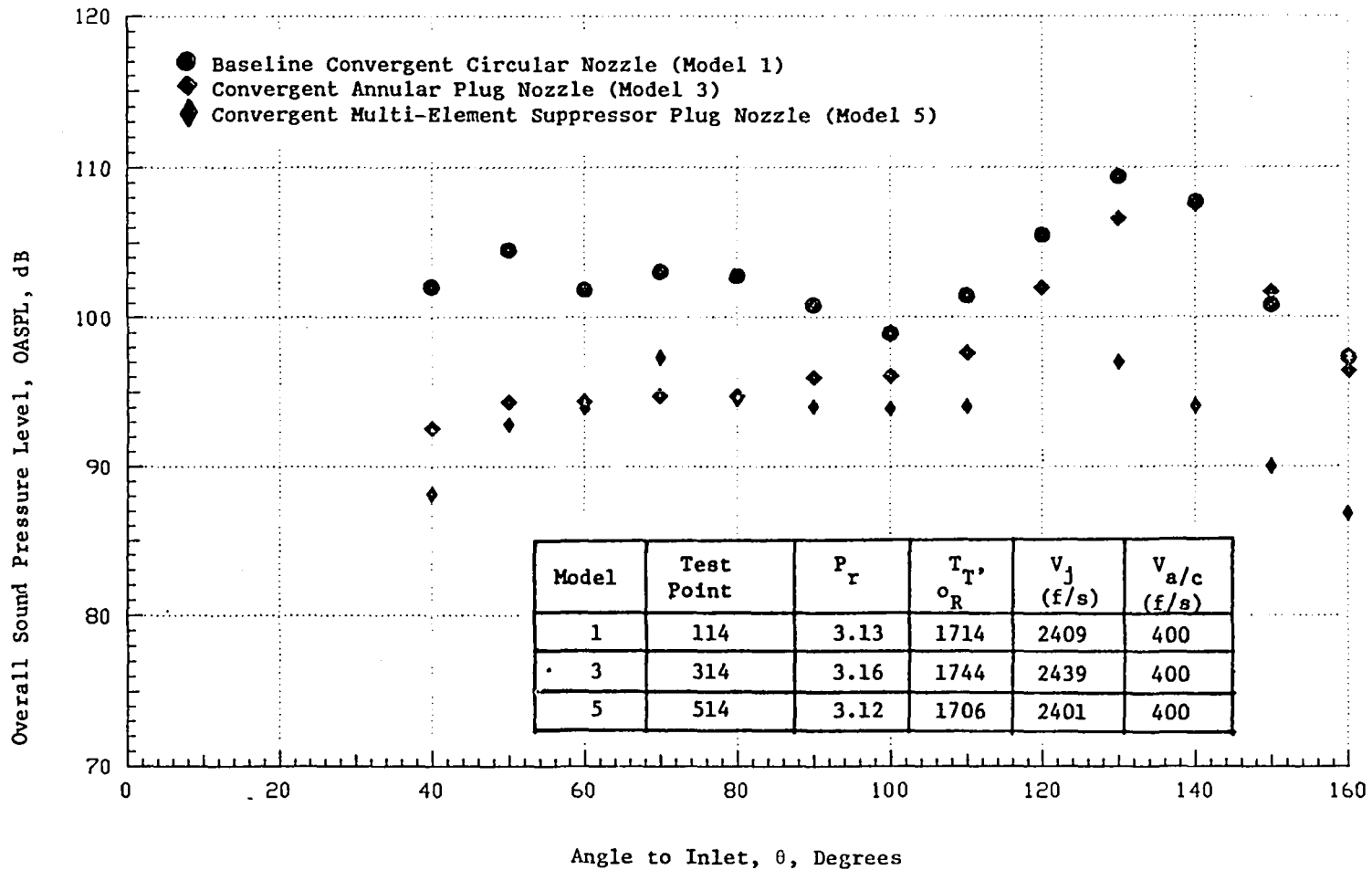


Figure 5-77.

OASPL Directivities for Various Convergent Nozzles at Aerodynamic Conditions Corresponding to the C-D Design Operating Conditions (Flight).

Model	Test Point	P_r	T_{T^*} $^{\circ}R$	V_j (f/s)	$V_{a/c}$ (f/s)
1	113	3.12	1707	2403	0
3	313	3.16	1741	2436	0
5	513	3.13	1718	2412	0

- Baseline Convergent Circular Nozzle (Model 1)
- ◇ Convergent Annular Plug Nozzle (Model 3)
- ◊ Convergent Multi-Element Suppressor Plug Nozzle (Model 5)

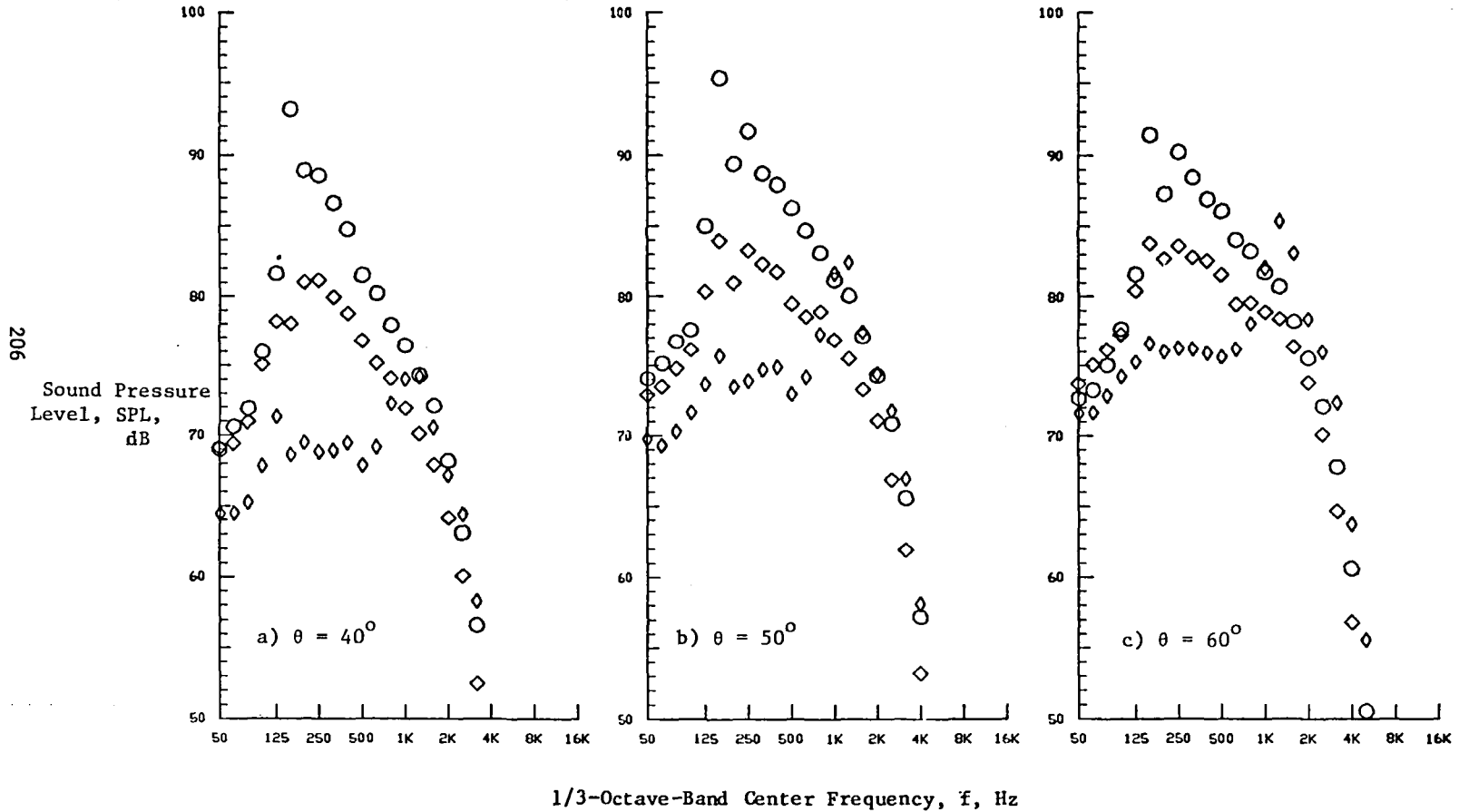


Figure 5-78. One-Third Octave Spectra for Various Convergent Nozzles at Aerodynamic Conditions Corresponding to the C-D Design Operating Conditions (Static).

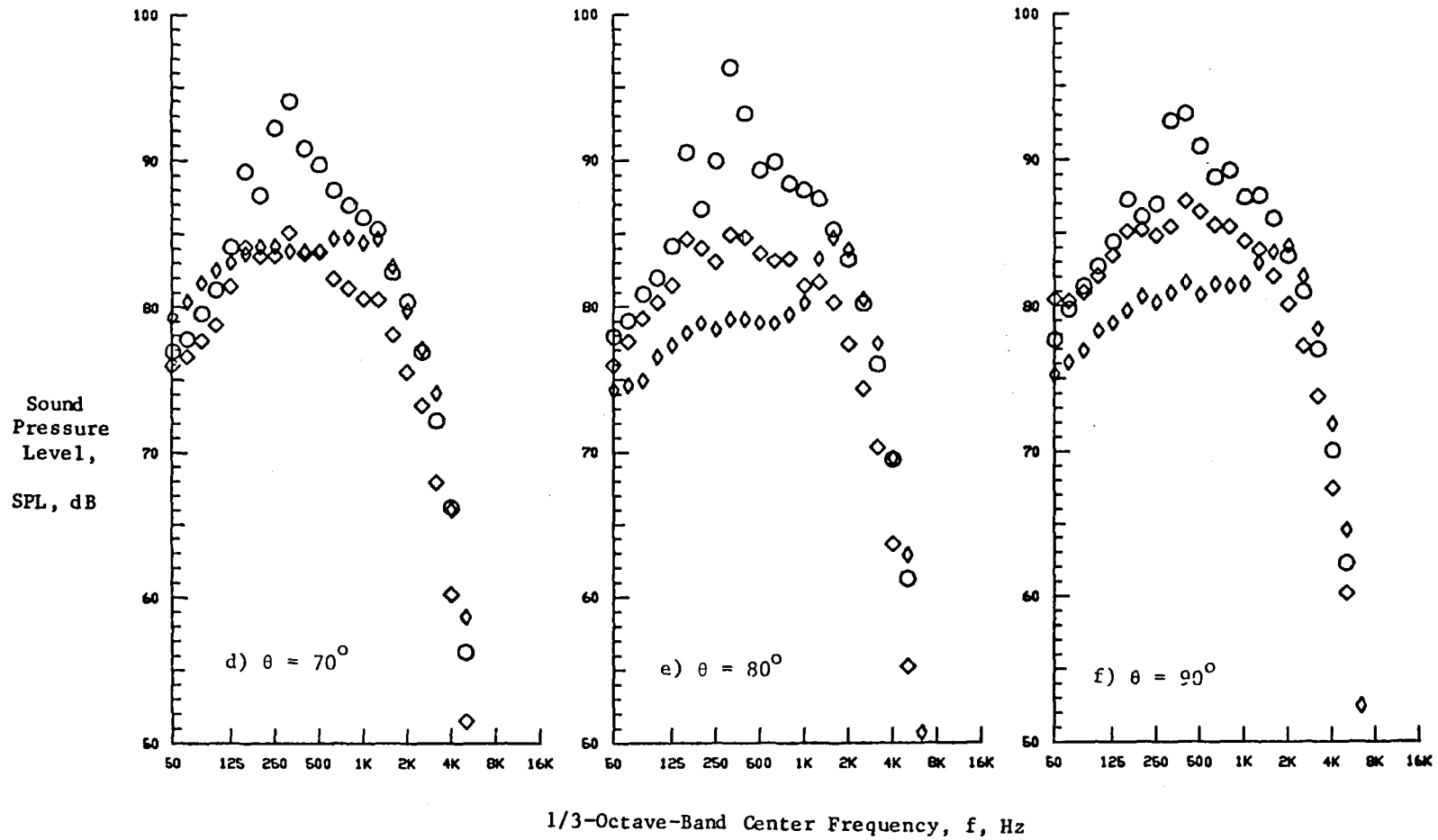


Figure 5-78. (Cont'd) One-Third Octave Spectra for Various Convergent Nozzles at Aerodynamic Conditions Corresponding to the C-D Design Operating Conditions (Static).

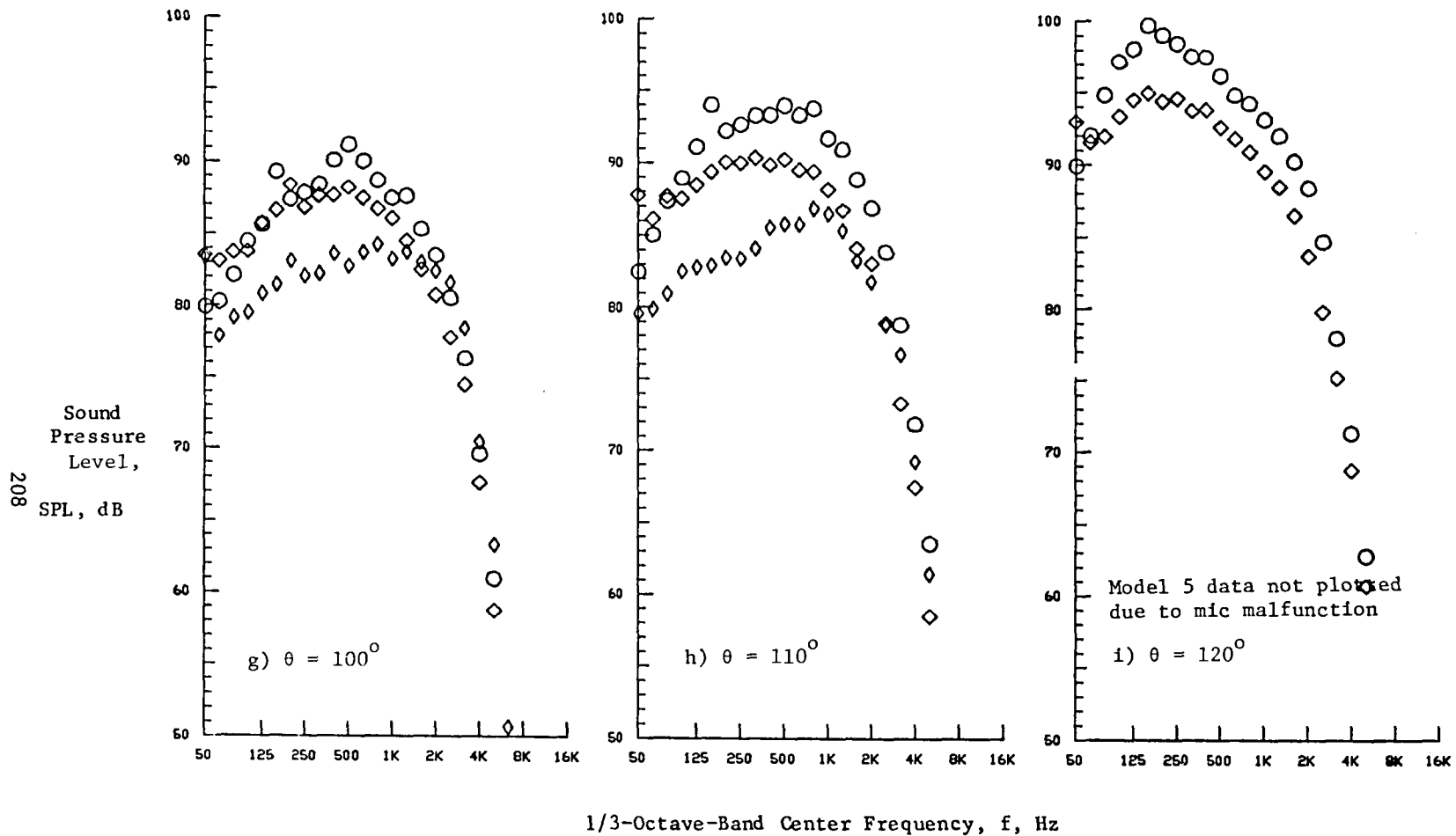


Figure 5-78. (Cont'd) One-Third Octave Spectra for Various Convergent Nozzles at Aerodynamic Conditions Corresponding to the C-D Design Operating Conditions (Static).

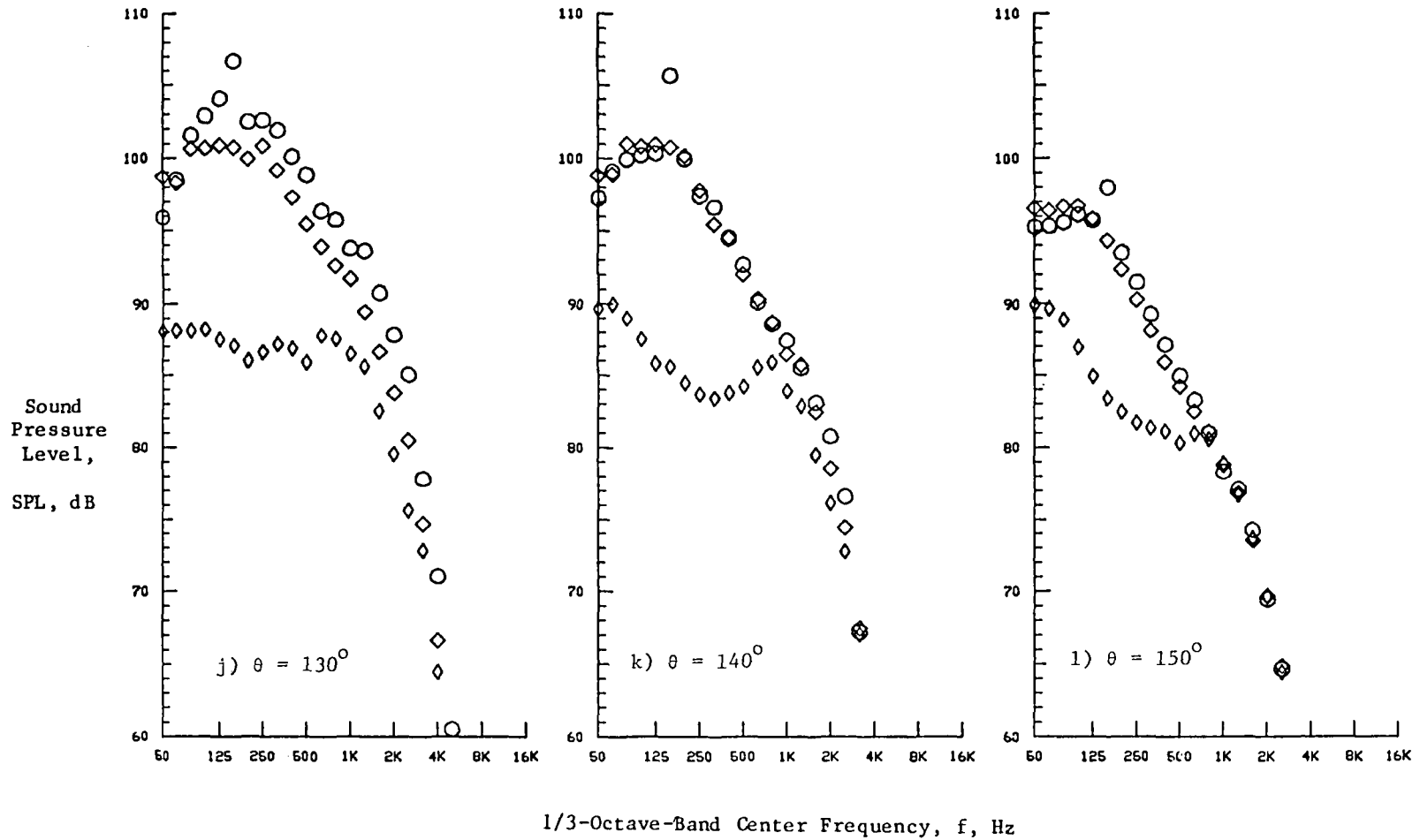


Figure 5-78. (Concluded) One-Third Octave Spectra for Various Convergent Nozzles at Aerodynamic Conditions Corresponding to the C-D Design Operating Conditions (Static).

Model	Test Point	P_T	$T_{T, \circ R}$	V_j (f/s)	$V_{a/c}$ (f/s)
1	114	3.13	1714	2409	400
3	314	3.16	1744	2439	400
5	514	3.12	1706	2401	400

- Baseline Convergent Circular Nozzle (Model 1)
- ◊ Convergent Annular Plug Nozzle (Model 3)
- ◈ Convergent Multi-Element Suppressor Plug Nozzle (Model 5)

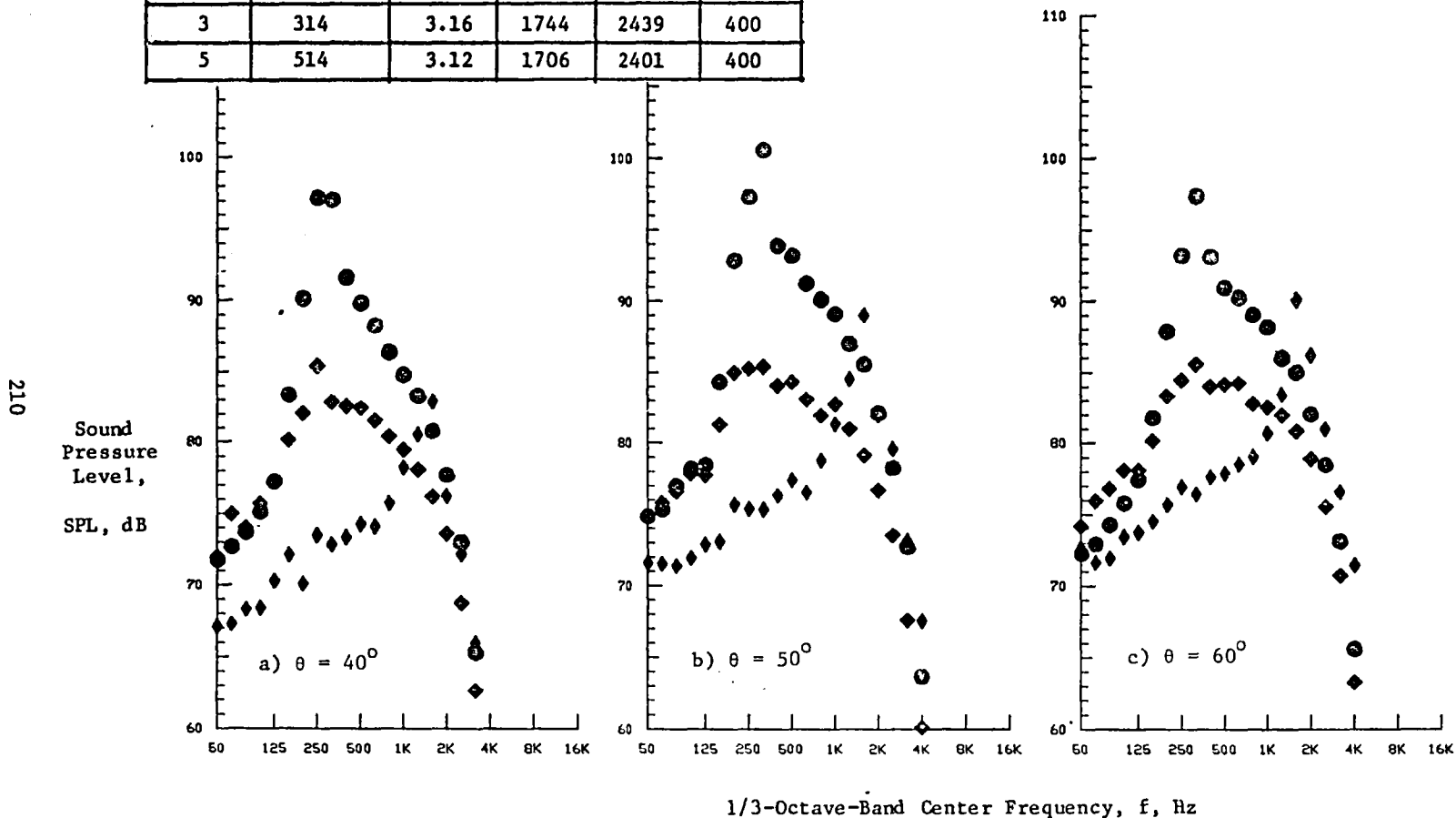


Figure 5-79.

One-Third Octave Spectra for Various Convergent Nozzles at Aerodynamic Conditions Corresponding to the C-D Design Operating Conditions (Flight).

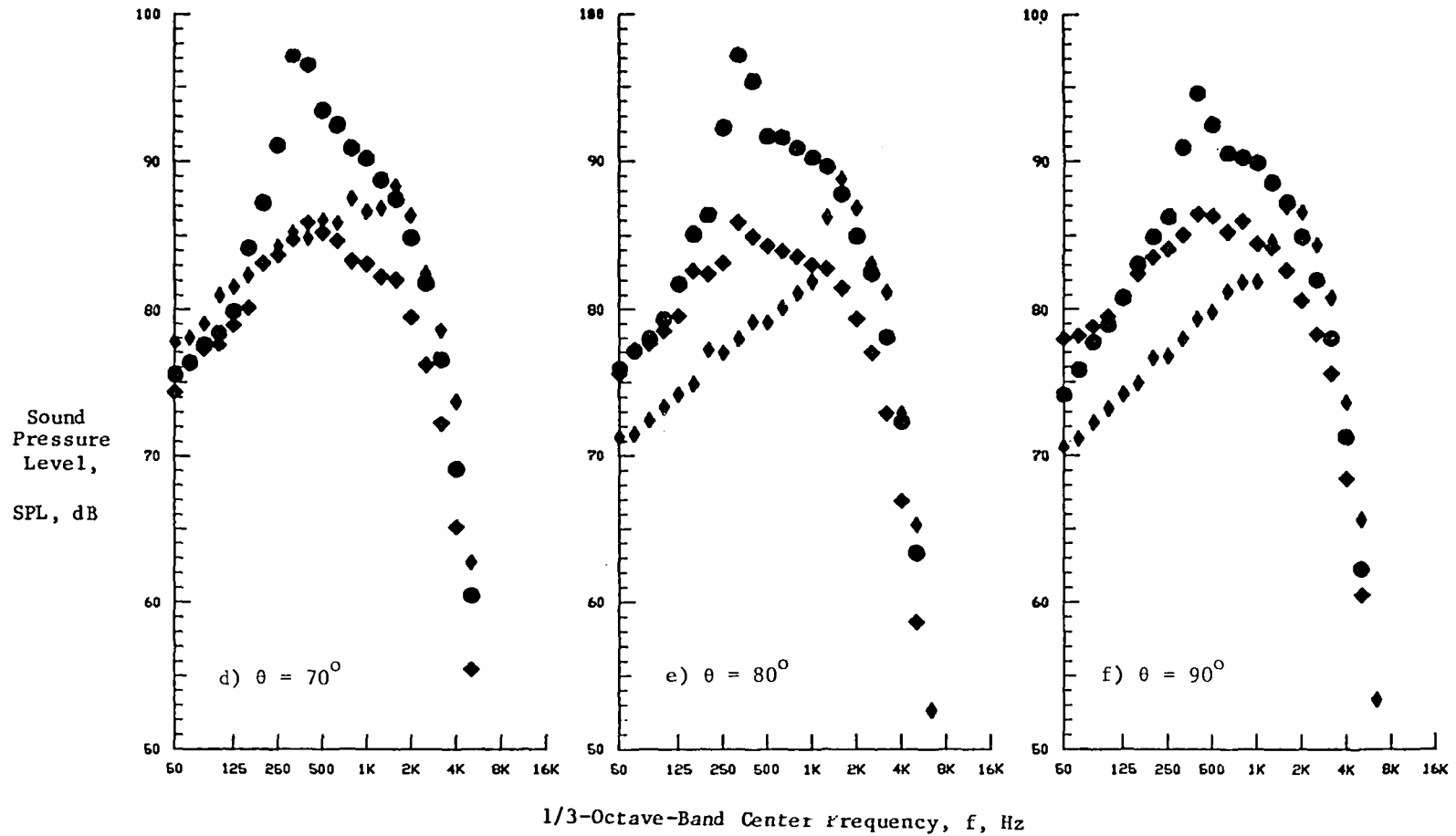


Figure 5-79. (Cont'd) One-Third Octave Spectra for Various Convergent Nozzles at Aerodynamic Conditions Corresponding to the C-D Design Operating Conditions (Flight).

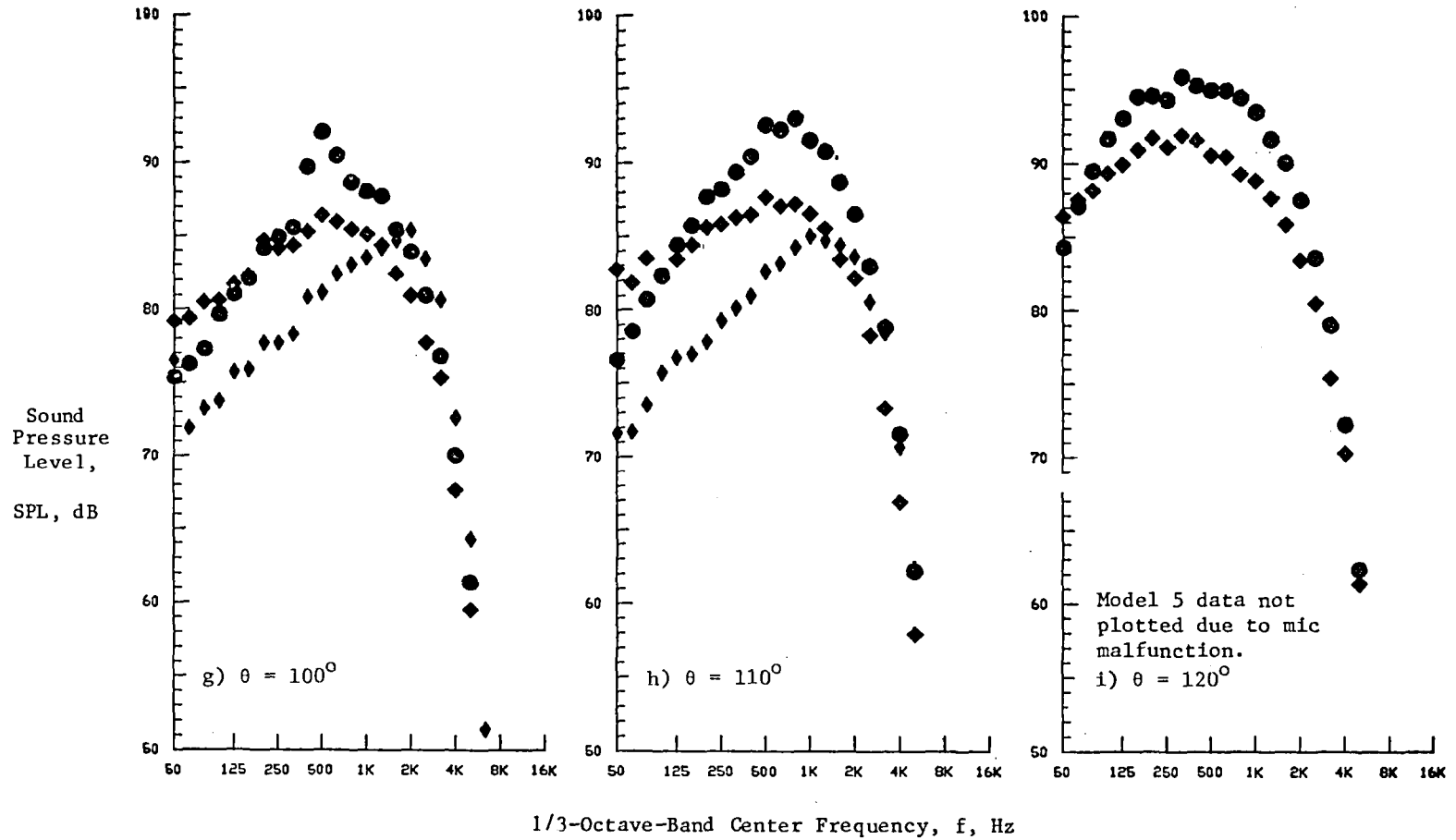


Figure 5-79. (Cont'd) One-Third Octave Spectra for Various Convergent Nozzles at Aerodynamic Conditions Corresponding to the C-D Design Operating Conditions (Flight).

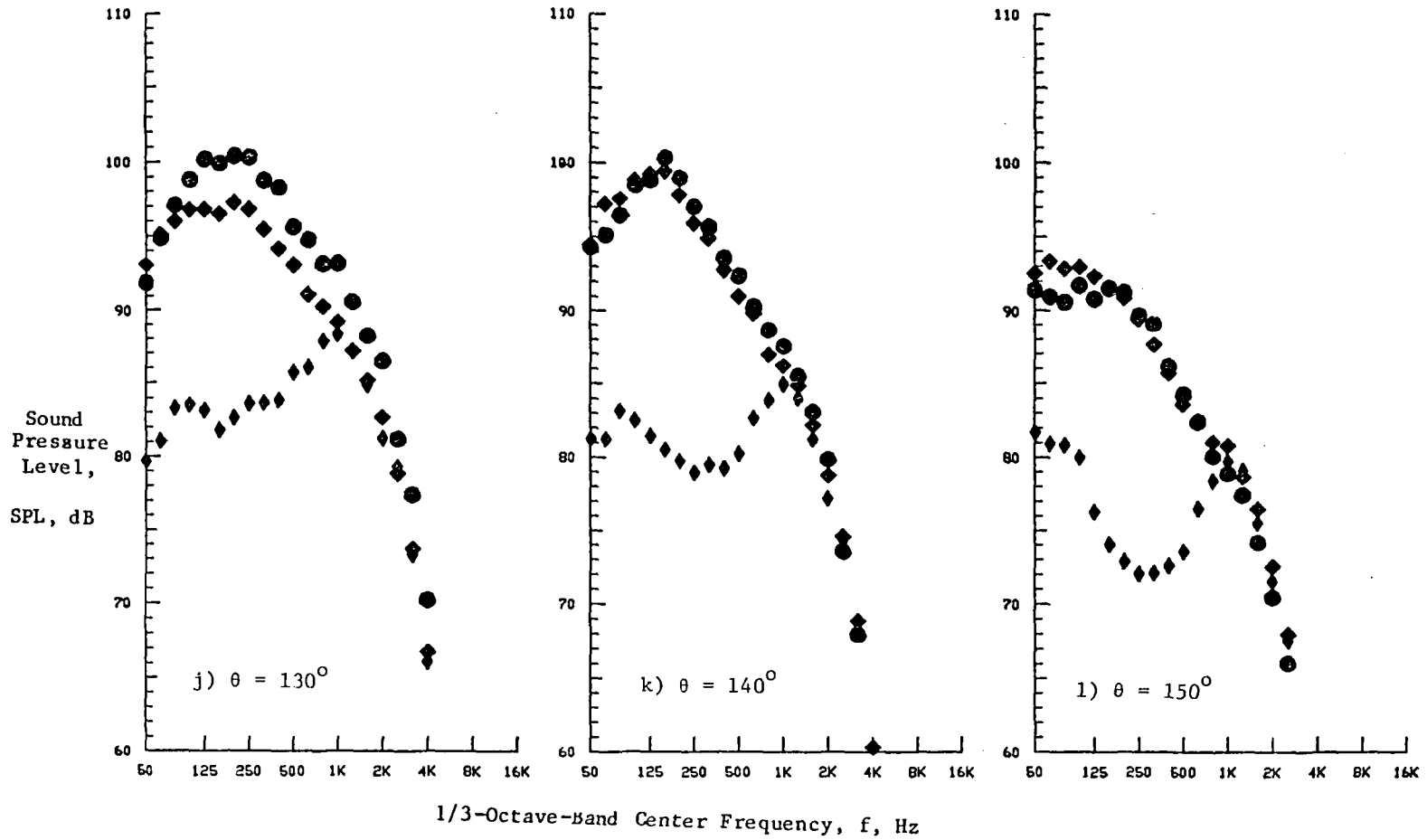


Figure 5-79. (Concluded) One-Third Octave Spectra for Various Convergent Nozzles at Aerodynamic Conditions Corresponding to the C-D Design Operating Conditions (Flight).

5.3 DISCUSSION ON SHOCK SCREECH

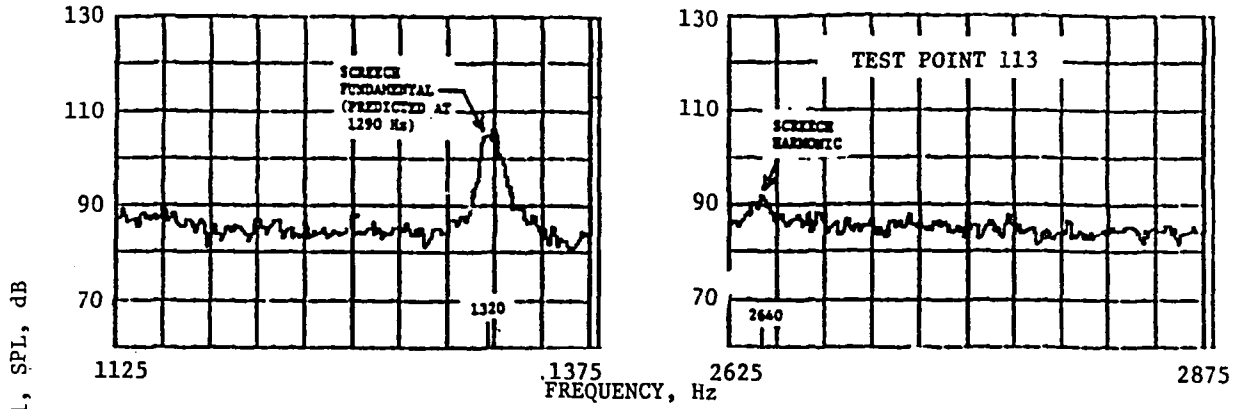
The shock noise, generally, can be divided into two distinct categories, namely, broadband shock associated noise and shock screech. While the former is broadband in nature with a well-defined peak frequency of $V_c/L(1+M_c \cos\theta)$ (Reference 5-2), shock screech is discrete and usually has several harmonics. When a turbulent eddy is shed from the nozzle and collides with a shock, a sound wave is generated which propagates upstream of the jet. The sound wave tends to release another eddy as it passes the nozzle, and, thus, a feedback cycle is formed. This process generates sound at a fundamental screech frequency of $V_c/L(1+M_c)$, and harmonics thereof.

Shock screech is not present normally in full-scale engine configurations due to physical irregularities, such as surface roughness, which generally weaken the feedback mechanism between the acoustic signal and shear layer disturbance. Hence, in order to develop a prediction model for the shock associated noise for full-scale engines based on acoustic data acquired from model jets, the characteristic properties of the broadband shock noise should be known. For this reason, during the acoustic tests of model jets, screech should be carefully eliminated by appropriate means.

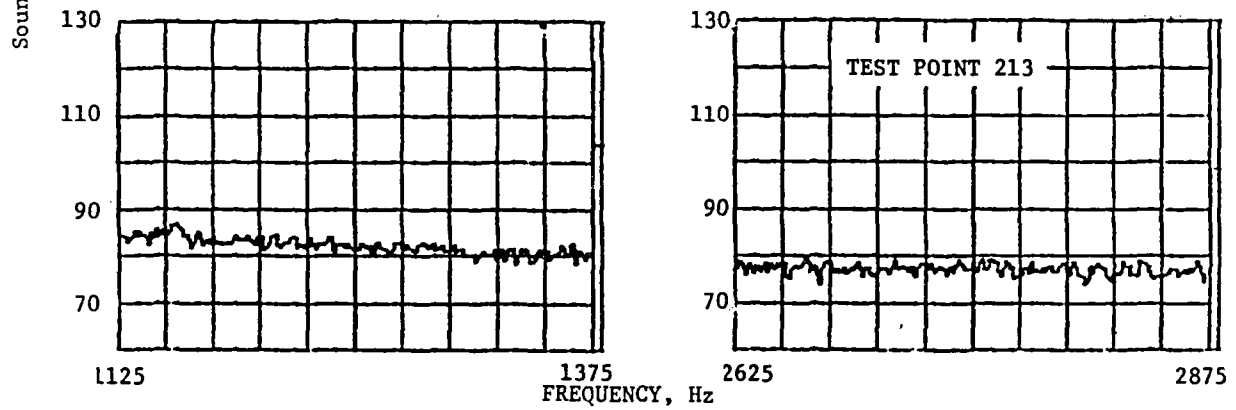
Tanna (Reference 5-6) was able to successfully eliminate screech for a convergent model nozzle by wrapping all surfaces surrounding the nozzle exit with sound absorbing material and inserting a small projection inside the nozzle lip. However, the assumption that the two shock noise components are mutually independent has not been verified; and it is not clear, therefore, whether screech-eliminated shock noise actually reveals intrinsic properties of the broadband shock noise.

A typical comparison between the front-quadrant narrowband spectra of convergent and C-D circular nozzles under static tests is presented in Figure 5-80. The aerodynamic conditions correspond to those of the design conditions of the C-D configuration. A strong discrete screech tone is noted with circular convergent nozzle at 1320 Hz with a harmonic at 2640 Hz (refer to Figure 5-69 for comparison between the static and simulated flight data). The corresponding C-D nozzle data indicates no such screech tones. This absence of screech with the C-D nozzle was noted over the range of test

FILTER BANDWIDTH = 1.25 Hz STATIC MOD L DATA $\theta = 60^\circ$



(a) Convergent Circular Nozzle (P_r 3.12, T_T 1730°R)



(b) Convergent-Divergent Circular Nozzle (P_r 3.12, T_T 1730°R;
C-D Design Condition)

Figure 5-80. Comparison of Front Quadrant On-Line Narrowband Spectra of Convergent and C-D Circular Nozzles.

pressure ratios and under both heated ($T_T \sim 1750^\circ \text{ R}$) and moderately heated ($T_T \sim 850^\circ \text{ R}$) test conditions.

During the present study, a limited effort was conducted with the aim to identify screech tones with the test configurations and to determine the effect, if any, of projections (tabs) on both broadband and discrete shock noise components of the convergent annular plug nozzle. A spectral analyzer (Spectral Dynamics: SD-345) was used for shock-screech detection. In what follows, some representative results of this study are presented.

The effect of the tabs was determined with the convergent annular plug nozzle (Model 3) with the tabs applied, as illustrated in Figure 4-5. The acoustic data obtained with and without tabs are compared to identify the effects of tabs on the shock associated noise. Figure 5-81 illustrates typical narrowband SPL spectra of shock associated noise produced by the convergent annular plug nozzle with and without tabs (on-line data; model scale). The aerodynamic flow conditions were $P_r = 3.44$, $T_T = 870^\circ \text{ R}$ for the test without tabs and $P_r = 3.41$, $T_T = 865^\circ \text{ R}$ with tabs. At $f = 937.5$ Hz, a strong discrete-tone is observed in the spectrum without tabs, while this screech is almost completely missing in the spectrum with tabs. In addition, the frequency of the broadband peak is noted to have shifted to a higher value with the use of tabs. This frequency shift with the tabs is associated also with a reduction in the sound pressure level at the broadband peak relative to the level without the tabs.

Effects of tabs on the PNL directivity and one-third-octave-band spectrum of shock associated noise at the moderately heated test conditions of Figure 5-81 can be seen in the results presented in Figures 5-82 and 5-83. In Figure 5-82, we note a significant PNL reduction by tabs. It is rather surprising to see that the PNL reduction is observed not only in the front quadrant where shock noise is generally dominant but also in the aft quadrant where jet mixing noise is important. An examination of the corresponding one-third-octave-band spectra depicted in Figure 5-83 indicates that the tabs apparently suppressed the screech as is seen at a typical front quadrant angle of $\theta = 50^\circ$. However, it is not clear at this point how the tabs favorably alter the mixing noise mechanism in the aft quadrant.

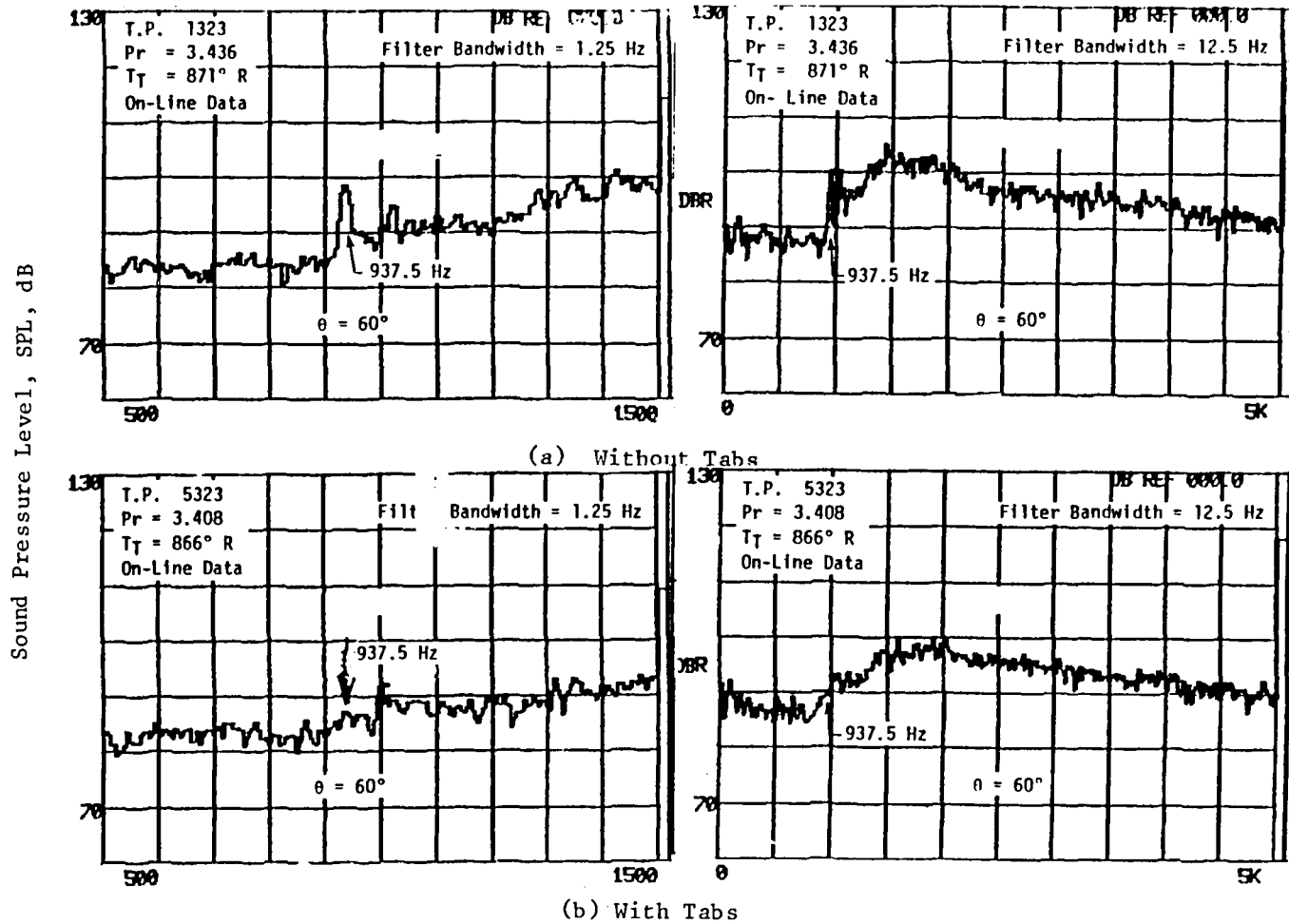


Figure 5-81. On-Line Narrowband Spectra for Convergent Annular Plug Nozzle With and Without Tabs (Moderately Heated Jet $T_T \sim 870^\circ\text{R}$)

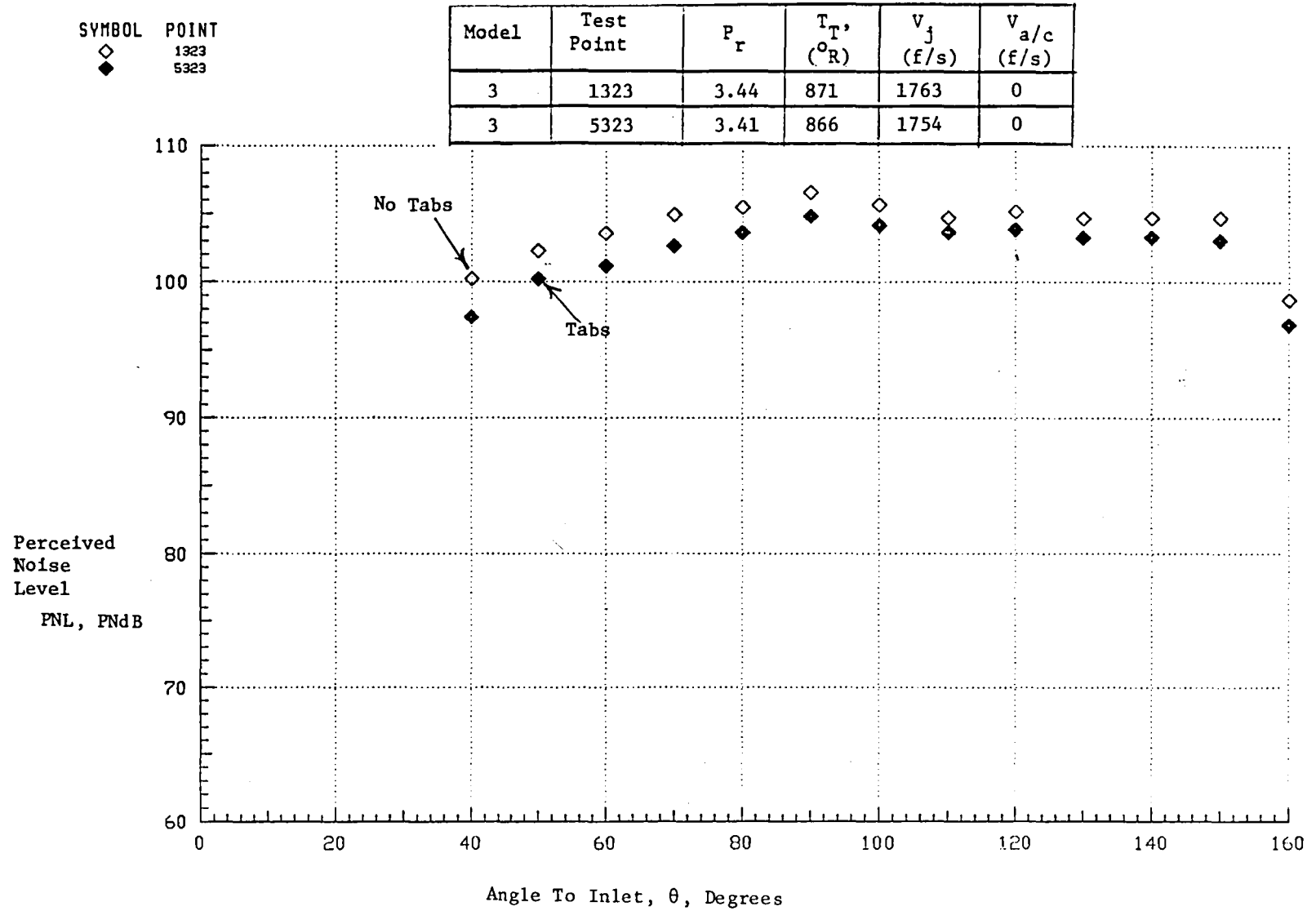


Figure 5-82. Effects of Screech Tabs on PNL Directivity: Convergent Annular Plug Nozzle (Moderately Heated Jet).

SYMBOL POINT
 ◊ 1323
 ◆ 5323

Model	Test Point	P_r	$T_{T'} (^\circ R)$	$V_j (f/s)$	$V_{a/c} (f/s)$
3	1323	3.44	871	1763	0
3	5323	3.41	866	1754	0

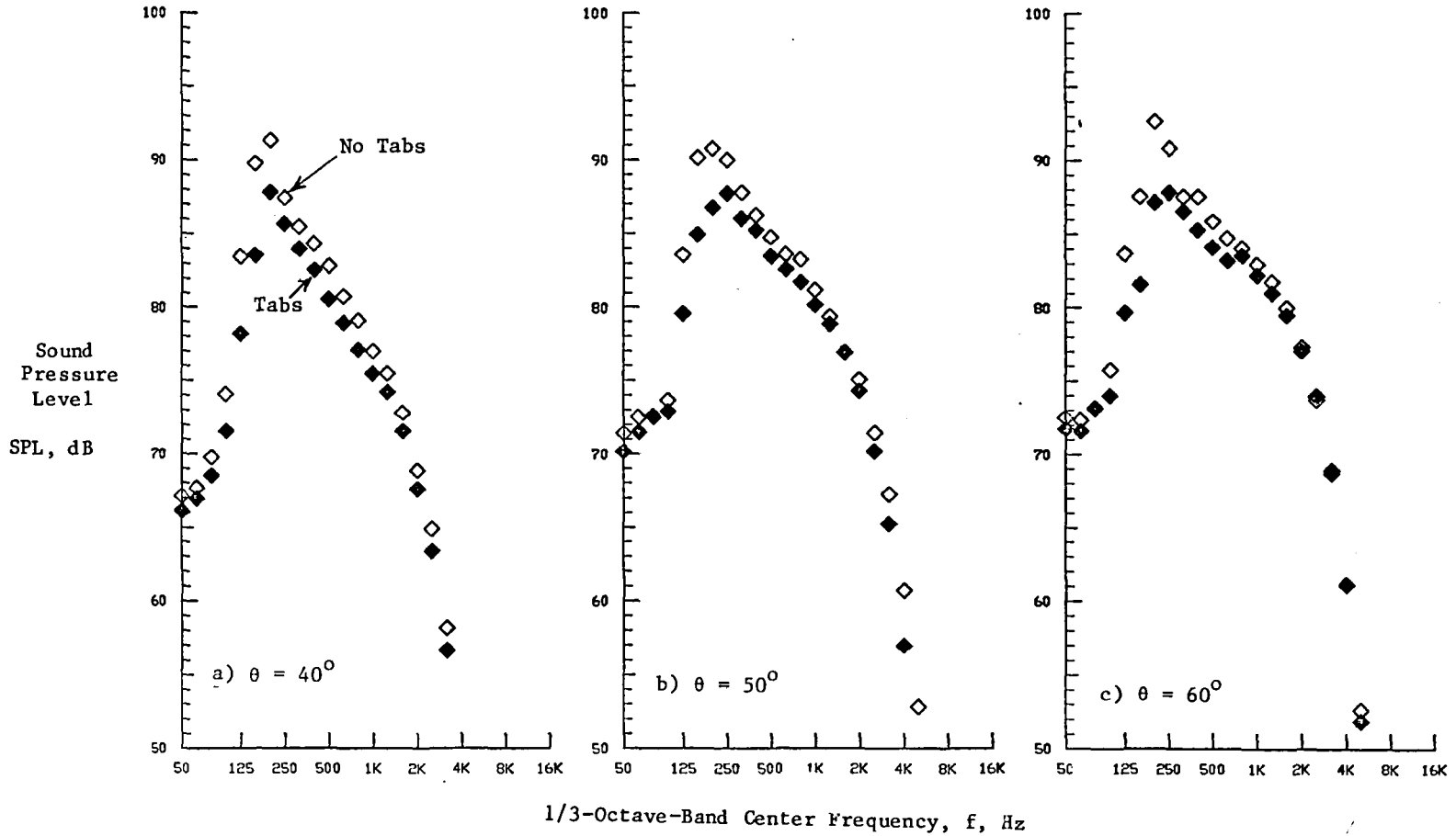


Figure 5-83. Effects of Screech Tabs on SPL Spectra: Convergent Annular Plug Nozzle (Moderately Heated Jet).

◇	POINT
◇	1323
◆	5323

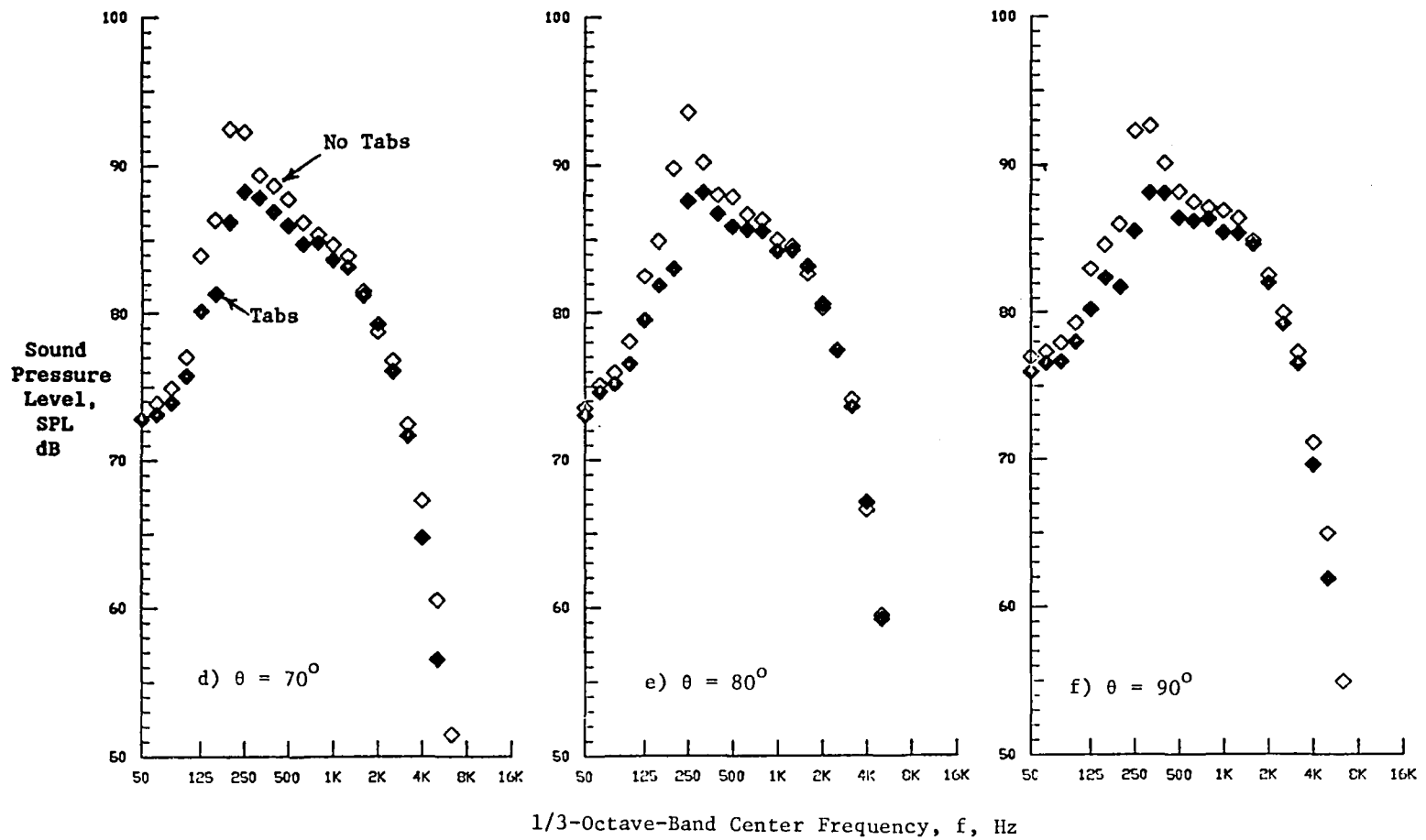


Figure 5-83. (Cont'd) Effects of Screech Tabs on SPL Spectra: Convergent Annular Plug Nozzle (Moderately Heated Jet).

◇	POINT
◇	1323
◆	5323

221

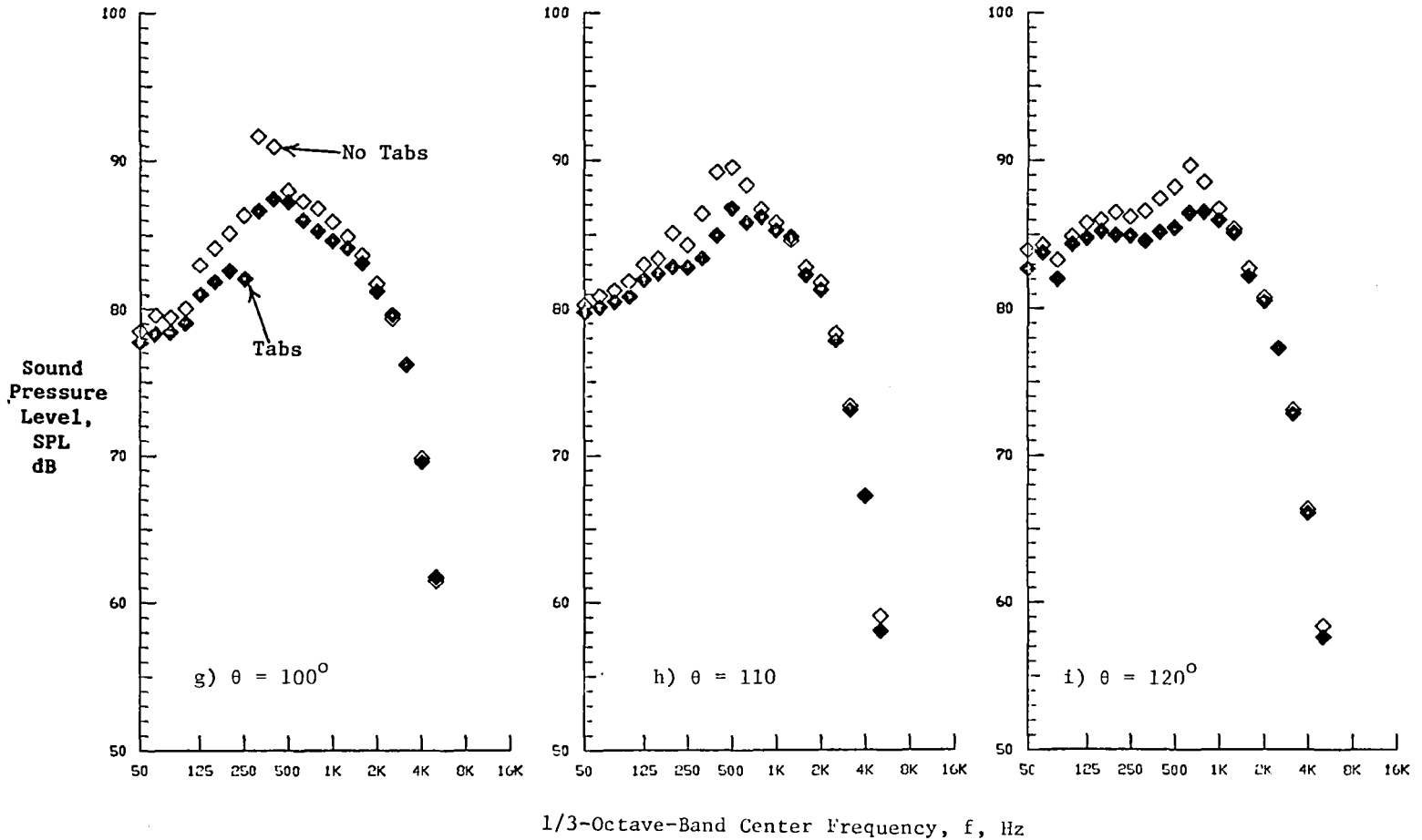
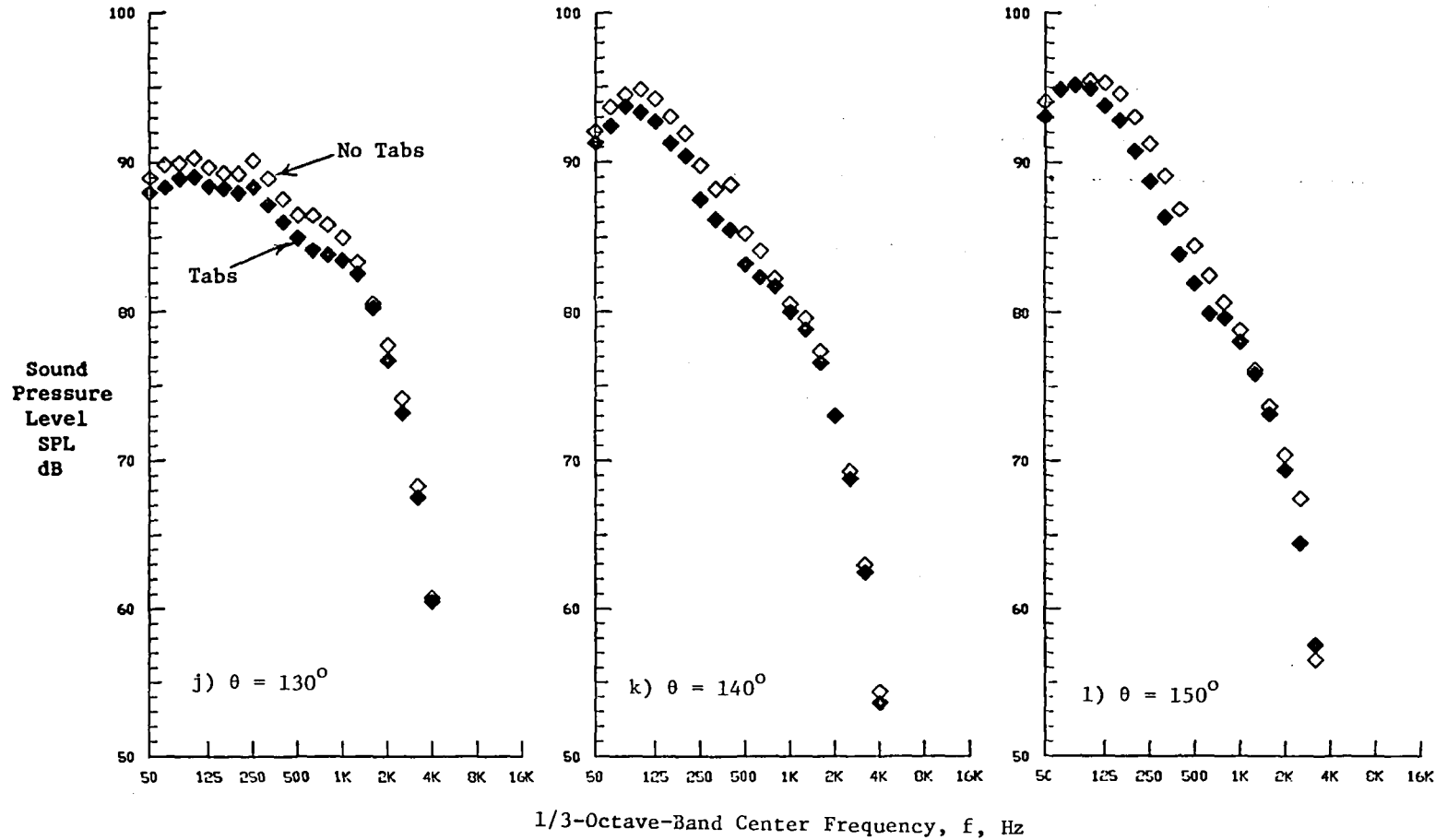


Figure 5-83. (Cont'd) Effects of Screech Tabs on SPL Spectra: Convergent Annular Plug Nozzle (Moderately Heated Jet).

SYMBOL POINT
 ◊ 1323
 ◆ 5323



222

Figure 5-83. (Concluded) Effects of Screech Tabs on SPL Spectra: Convergent Annular Plug Nozzle (Moderately Heated Jet).

Corresponding data obtained with the high temperature jets ($T_T \sim 1750^\circ\text{R}$) are presented in Figures 5-84 through 5-86. Observations with the data of moderately heated jets are seen to be valid for the case of the high temperature jets.

Next, the peak screech frequency from the convergent-divergent annular plug nozzle (Model 4) is examined in the light of Powell's model (Reference 5-1).

Powell suggested that the peak frequency of screech is scaled by the expression

$$f_p = \frac{V_c}{L(1+M_c)}$$

where V_c is the convection velocity and M_c is the convection Mach number calculated based on ambient sound speed. L represents the characteristic length associated with screech generation, which is usually taken to be equal to the averaged shock-cell spacing. The shock-cell spacing, however, is known to be correlated to the shock strength parameter β as

$$L = k\beta D$$

where D and k are the nozzle diameter and a numerical constant which may be related to the mode of screech (Reference 5-15), respectively.

Utilizing on-line narrowband acoustic spectra obtained with the convergent-divergent annular plug nozzle (Model 4), the peak screech frequency at $\theta = 60^\circ$ was plotted as a function of shock strength parameter, β . The results are presented in Figure 5-87 together with corresponding predictions of Powell. There are two sets of data in this figure; one was obtained at static conditions and the other in simulated flight. Selected pressure ratios for these plots were $3.07 < P_r < 3.37$, and plume temperature was maintained at $T_T \approx 850^\circ\text{R}$. An excellent agreement between data and Powell's prediction is noted. For these predictions, the convection velocity was chosen to be equal to 51 percent of the fully expanded flow velocity. Furthermore, values of 1.1 (static) and 1.33 (free-jet) were assigned to the constant k which is in the Powell's prediction expression.

STATIC MODEL DATA

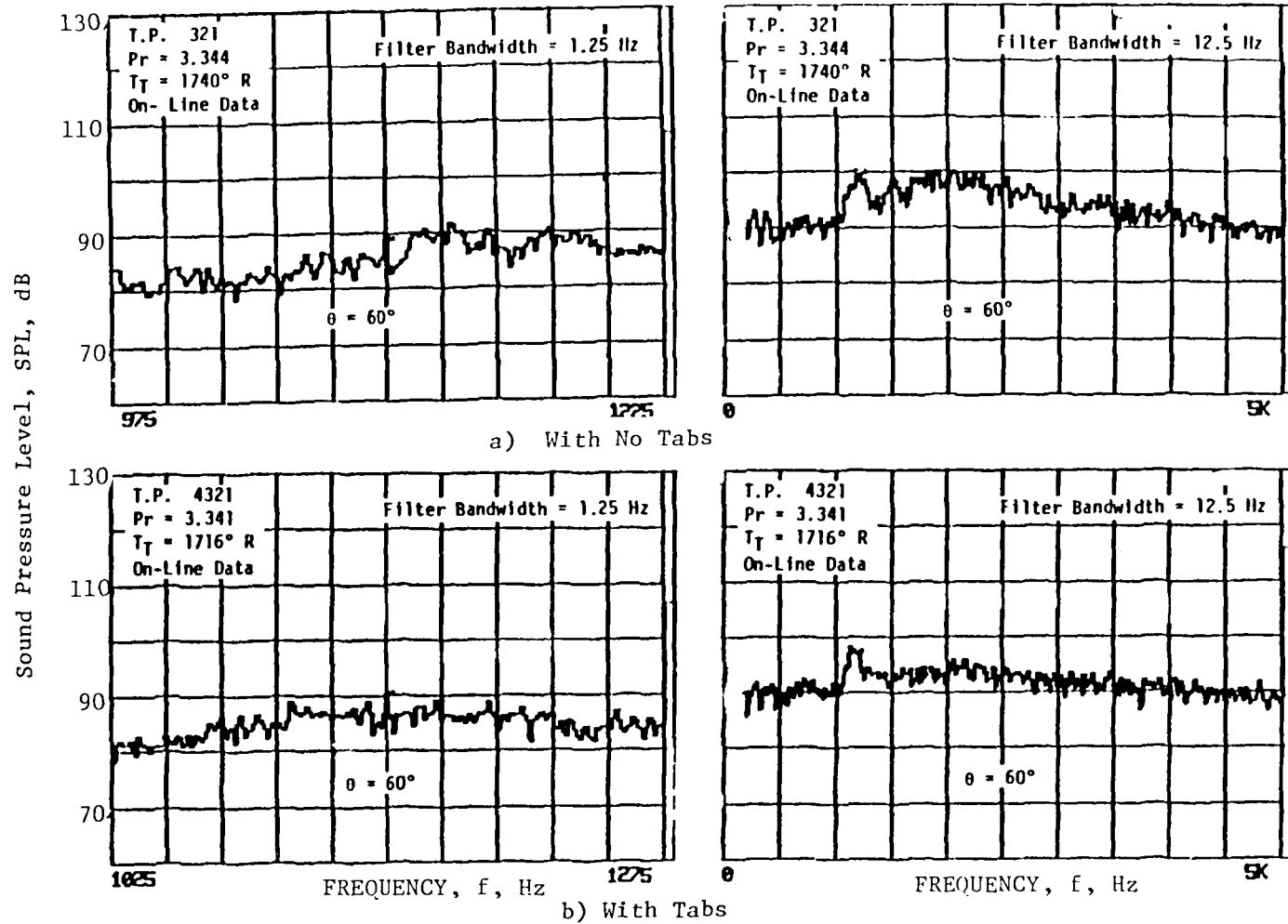


Figure 5-84. Narrowband SPL Spectra for Convergent Annular Plug Nozzle with and Without Tabs (High Temperature Jet, $T_T \sim 1750^\circ R$).

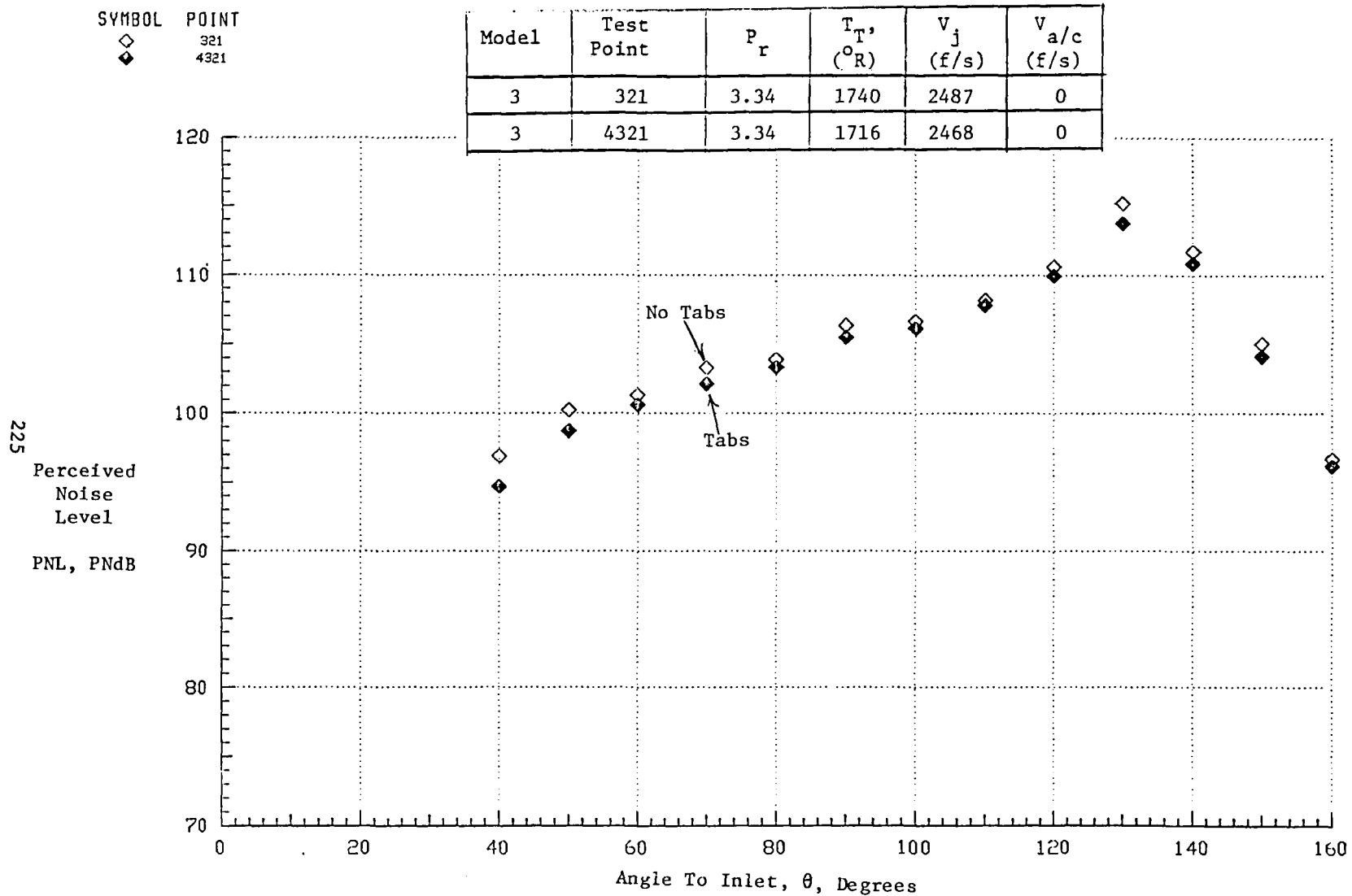


Figure 5-85. Effect of Screech Tabs on PNL Directivity: Convergent Annular Plug Nozzle (High Temperature Jets).

SYMBOL POINT
 ◊ 321
 ◆ 4321

Model	Test Point	P_r	T_{T^*} (°R)	V_j (ft/s)	$V_{a/c}$ (ft/s)
3	321	3.34	1740	2487	0
3	4321	3.34	1716	2468	0

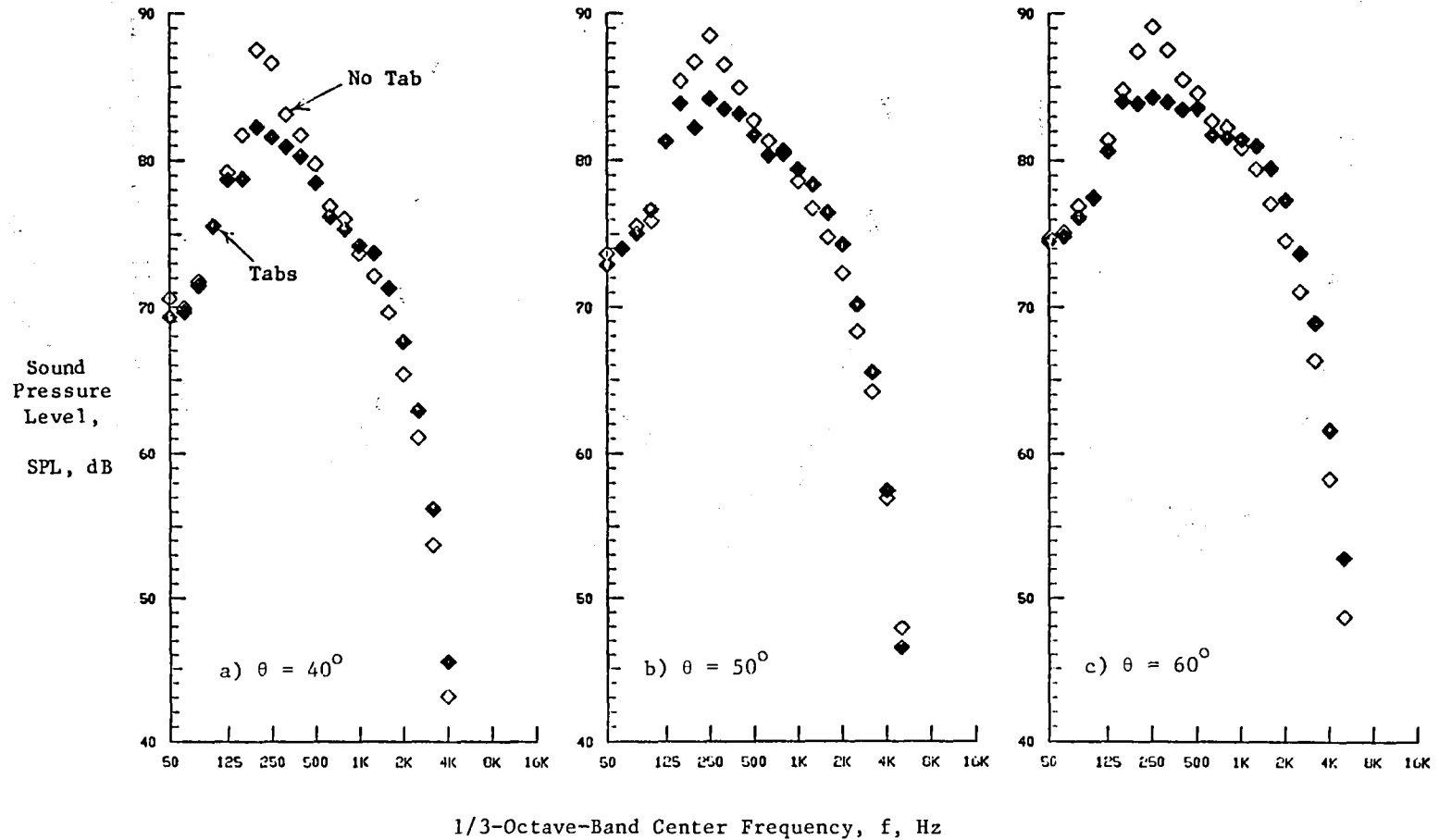


Figure 5-86. Effect of Screech Tabs on Spectrum: Convergent Annular Plug Nozzle (High Temperature Jets).

SYMBOL POINT
 ◊ 321
 ◊ 4321

227

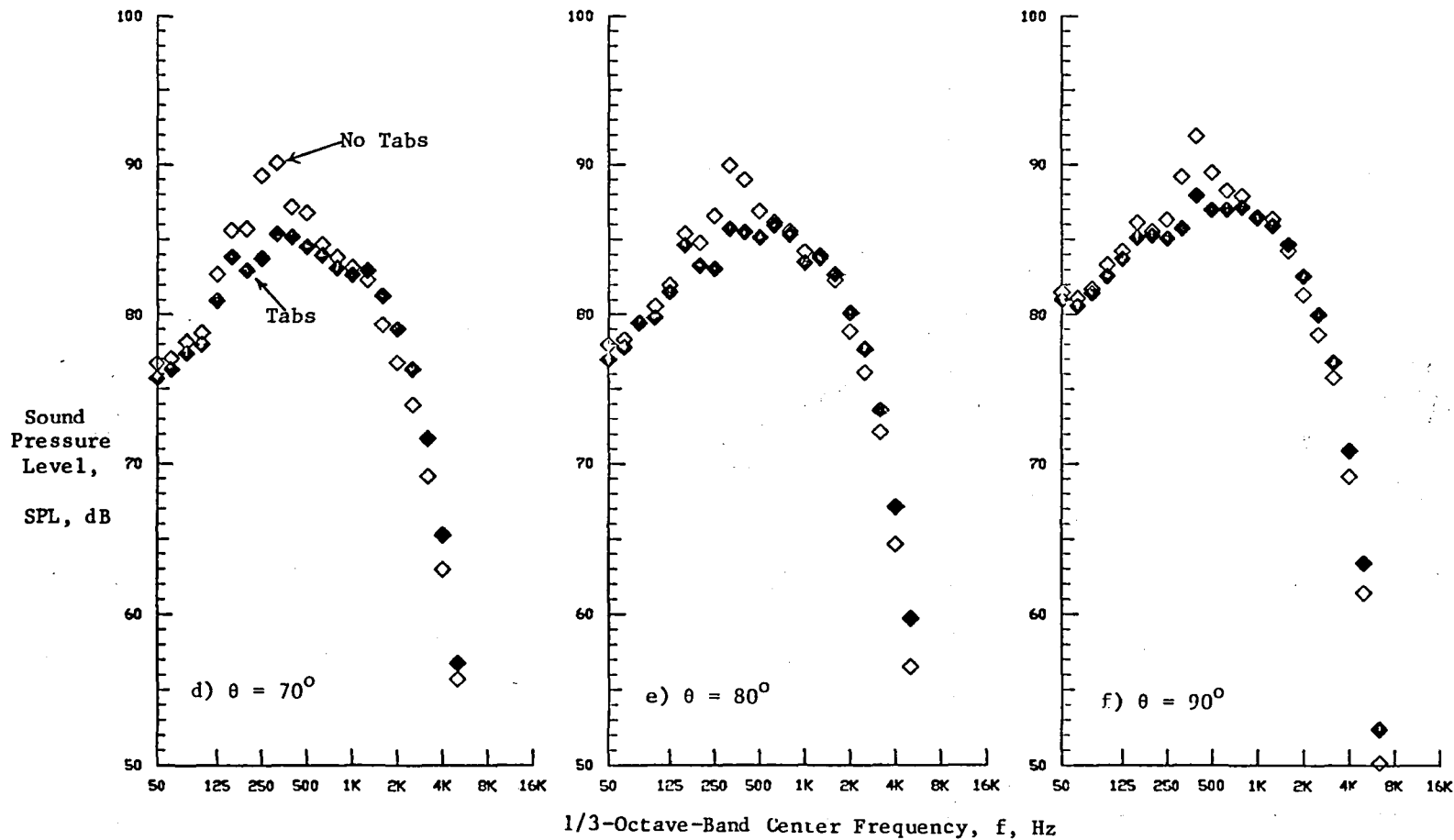


Figure 5-86. (Cont'd) Effect of Screech Tabs on Spectrum: Convergent Annular Plug Nozzle (High Temperature Jets).

SYMBOL POINT
 ◊ 921
 ◆ 4321

228

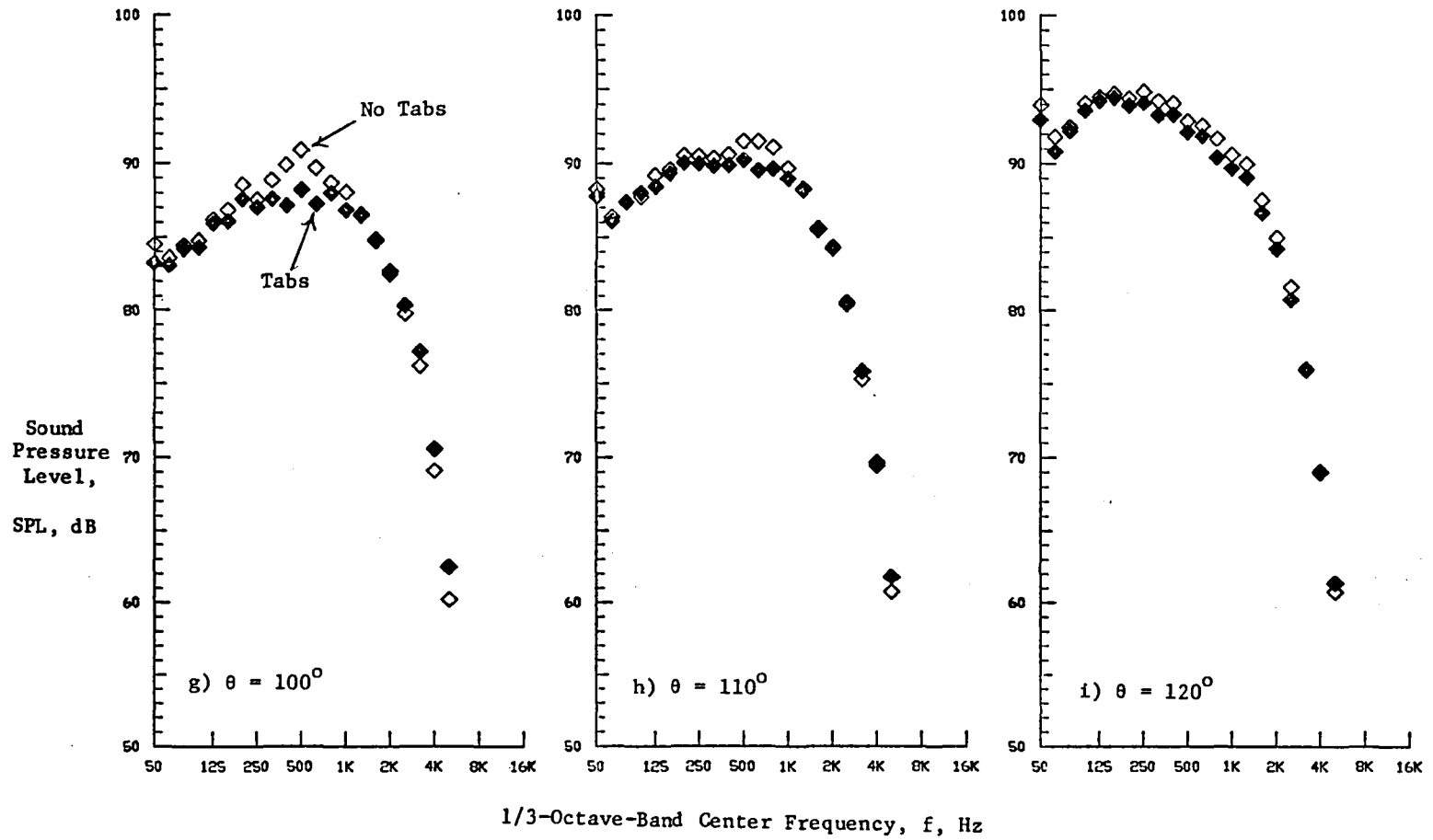


Figure 5-86. (Cont'd) Effect of Screech Tabs on Spectrum: Convergent Annular Plug Nozzle (High Temperature Jets).

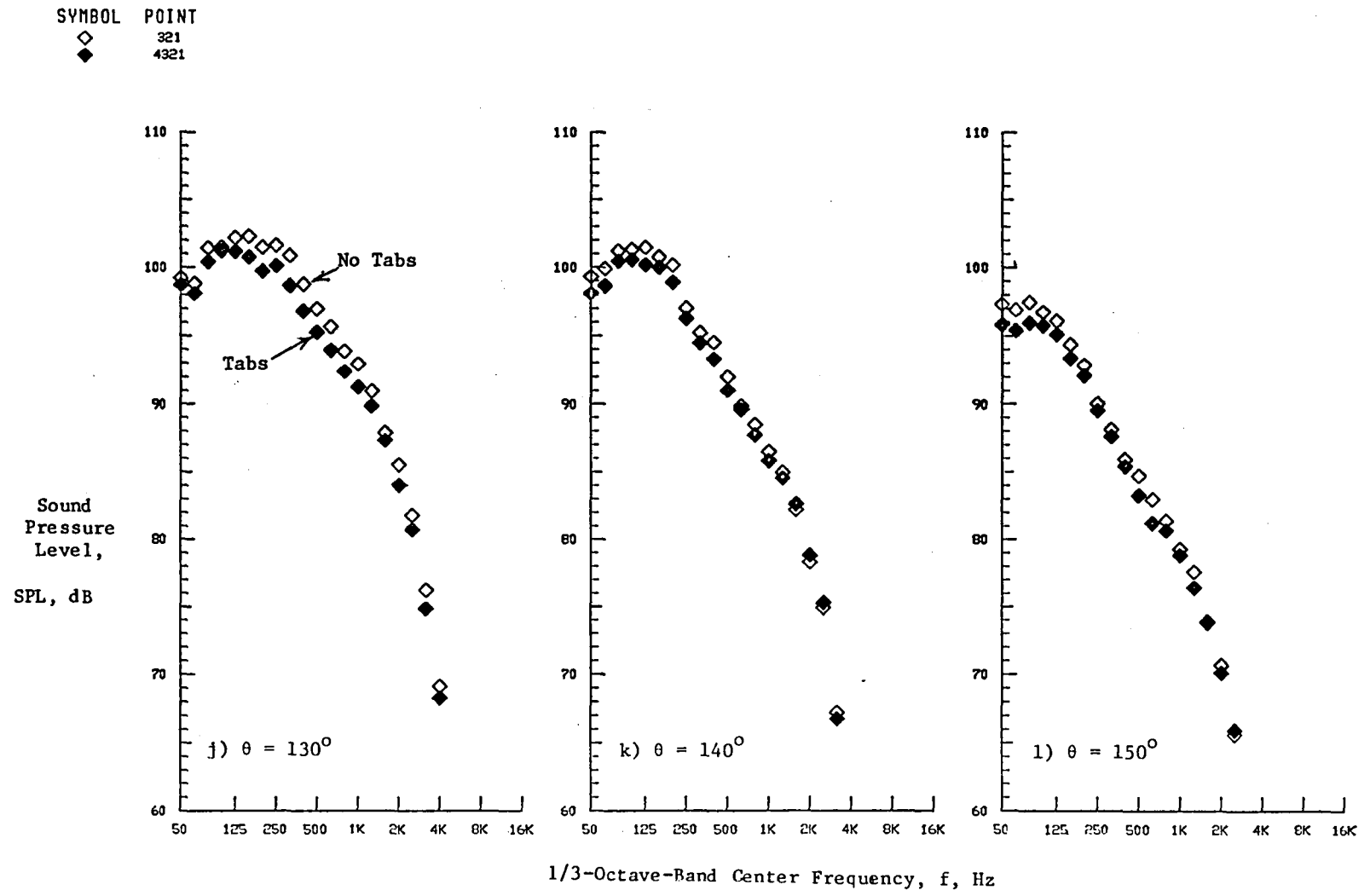


Figure 5-86. (Concluded) Effect of Screech Tabs on Spectrum: Convergent Annular Plug Nozzle (High Temperature Jets).

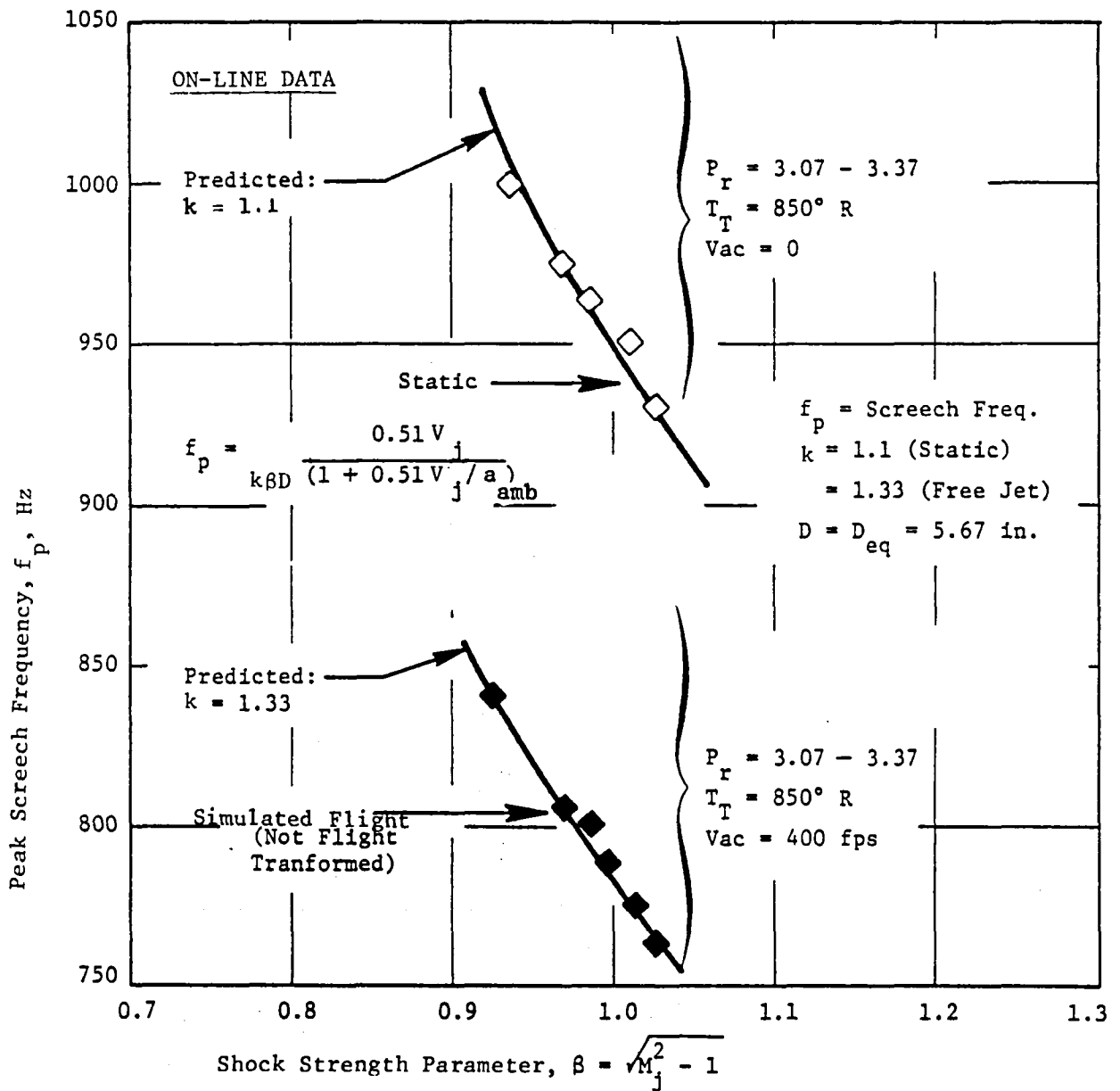


Figure 5-87. Peak Screech Frequency at $\theta = 60^\circ$ as a Function of Shock Strength Parameter; C-D Annular Plug Nozzle (Model 4).

Since the selected nozzle for this survey was the convergent-divergent annular plug nozzle (Model 4), the jet diameter which defines the shock-cell spacing together with the shock strength parameter was accordingly replaced by the equivalent diameter defined based on the total flow area of the annular plug nozzle. It should be noted that at a given condition, peak screech frequency corresponding to the simulated flight case is smaller than that for static case, indicating shock-cell stretching by the free-jet flow. With a free-jet speed of 400 fps, averaged stretching amounts to 20 percent.

It has been well established that both screech and broadband shock noise peak frequencies can be adequately correlated to the shock strength parameter in terms of Helmholtz number (H) which is defined as

$$H = \frac{f \cdot D}{\frac{p_{eq}}{a_{amb}}}$$

Figure 5-88 illustrates the correlation between Helmholtz number and shock strength parameter based on screech data obtained with conic and C-D annular plug (Model 4) nozzles. The conic data are replotted from Reference 5-16. It appears that the correlation may be approximated by

$$H = 0.85e^{-0.8\beta}$$

Following is the summary of the observations made during present screech survey:

- Screech tabs appear to suppress both the discrete and broadband shock noise components.
- Tabs tends to shift the peak broadband frequency to higher values.
- They also alter jet mixing noise process to some extent.
- Effects of tabs on shock associated noise are less significant for high temperature jets as compared to their low temperature counterparts.
- A good correlation exists between screech-peak frequency and the parameter β .

Nozzle	Type Data	Diam. (Cm)
○ Conic	Narrow Band	5.1
■ Conic	Broad Band	9.5
◆ Conic	"	7.6
▲ Conic	"	10.2
+ C-D Plug	Narrow Band	14.4

From Fig. 2 of
Ref. 5-16.

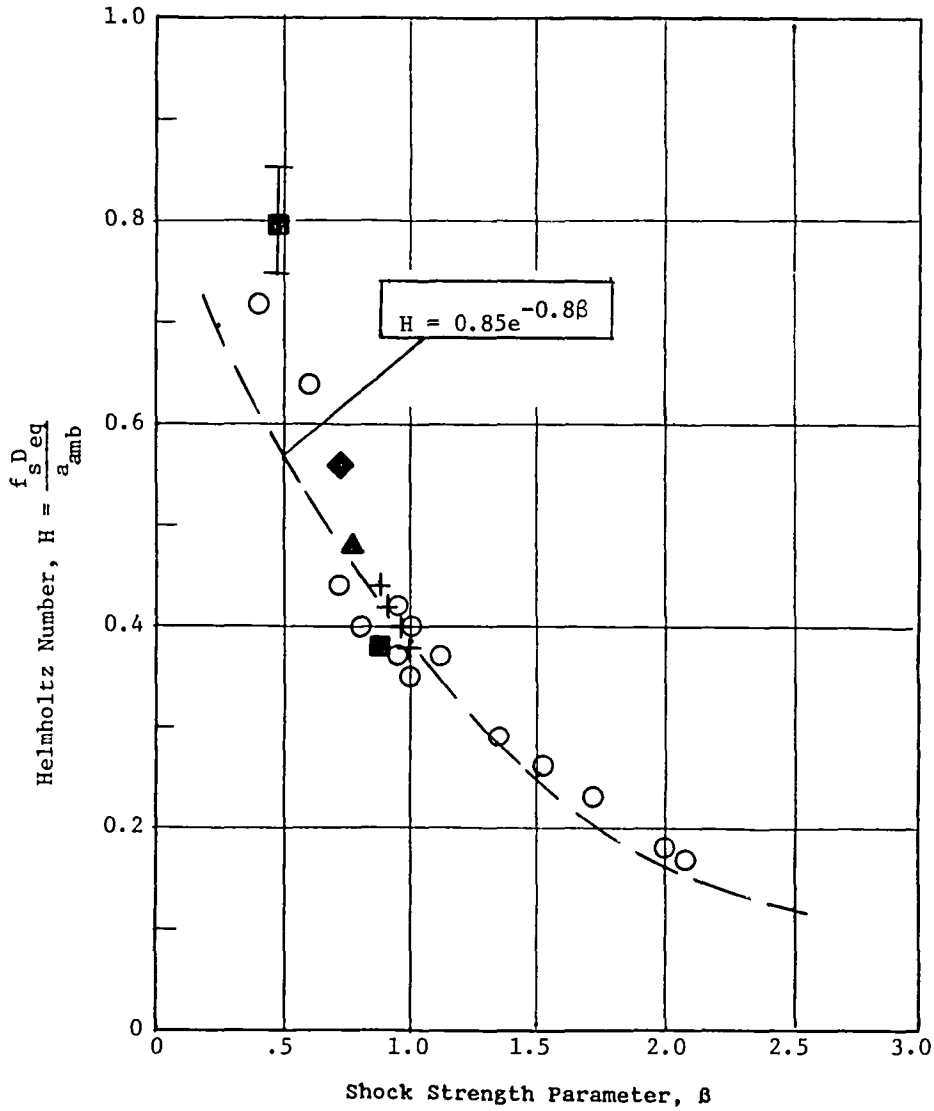


Figure 5-88. Correlation of Screech Tone Helmholtz Number with Shock Strength Parameter C-D Annular Plug Nozzles.

5.4 COMPARISON OF MEASURED SHOCK-CELL NOISE DATA WITH PREDICTIONS FROM EXISTING MODELS

In this subsection results of a comparative study of the existing predictive models of shock-cell noise with measured data are summarized.

It has been well established that the Harper-Bourne Fisher Model* (Reference 5-2) is the most directly applicable model to predict broadband shock noise produced by convergent circular nozzle jets. This is illustrated in Figures 5-89 and 5-90. In these figures the measured static and simulated flight total noise data of the convergent circular nozzle in a forward quadrant are compared with the predicted shock-cell noise data obtained from M & S program of Reference 5-13. This program essentially uses the HBF model to predict the shock-cell noise component. An examination of these figures also indicates that in the forward quadrant, shock-cell noise tends to dominate the total jet noise spectrum at middle to high frequencies. As described before, the strong peak located at 160 Hz in the static data is the shock screech that was identified earlier in Figure 5-69.

Because of the success of the predictive HBF scheme, many attempts have been made to apply its concept to the prediction of shock noise produced by other types of nozzles, with appropriate modifications (References 5-17 to 5-20). During this study, a similar attempt has been made with the aim of developing an applicable model to predict shock-cell noise generated by annular nozzle jets. In what follows, a discussion on the model for annular nozzle jets and the rationale for the modifications (to the HBF model) incorporated in the model is given. For the development of this model the acoustic and diagnostic LV test data of Model 3 (convergent annular plug nozzle), Model 4 (C-D annular plug nozzle), Model 5 (convergent suppressor plug nozzle) and Model 6 (C-D suppressor plug nozzle) were utilized. The spectral comparison presented in this subsection is made with the acoustic data scaled to an engine size of 1400 in.² at a 2400 foot sideline distance.

*In what follows the Harper-Bourne Fisher Model is abbreviated as HBF model.

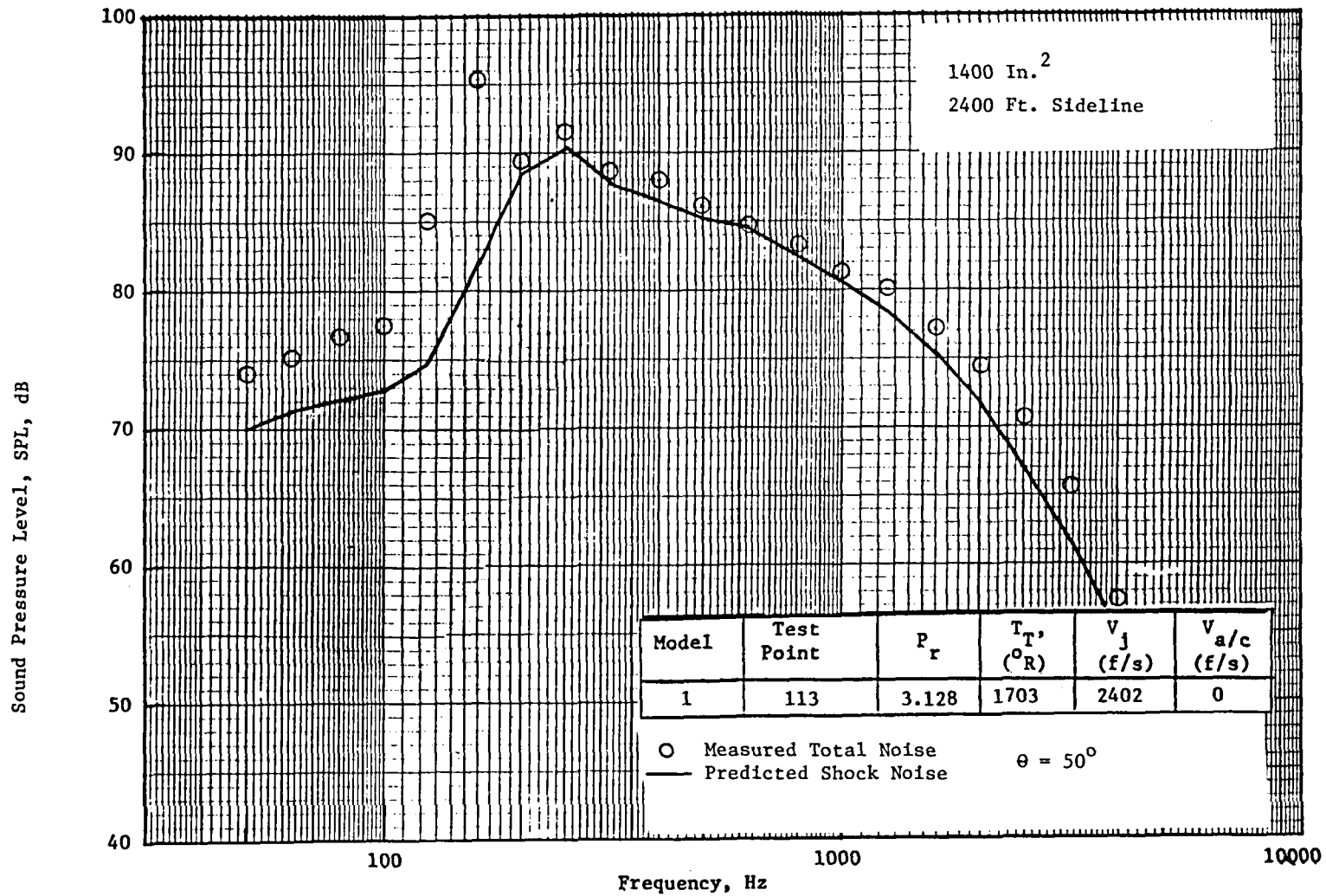


Figure 5-89. Comparison of M*S Prediction With Experimental Data of Shock Containing Jet Noise: Baseline Convergent Circular Conic Nozzle, Static.

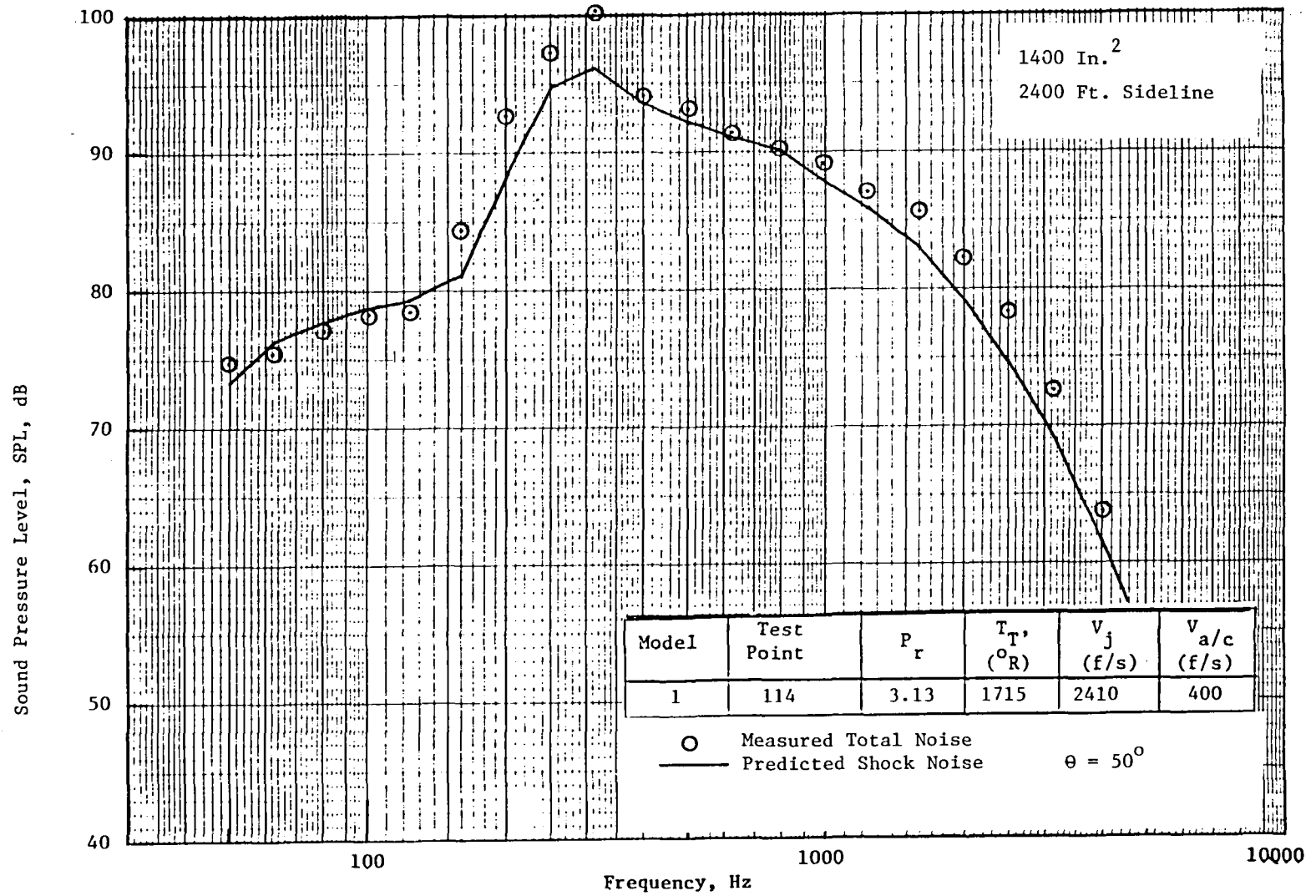


Figure 5-90. Comparison of M*S Prediction With Experimental Data of Shock Containing Jet Noise: Baseline Convergent Circular Conic Nozzle, Simulated Flight.

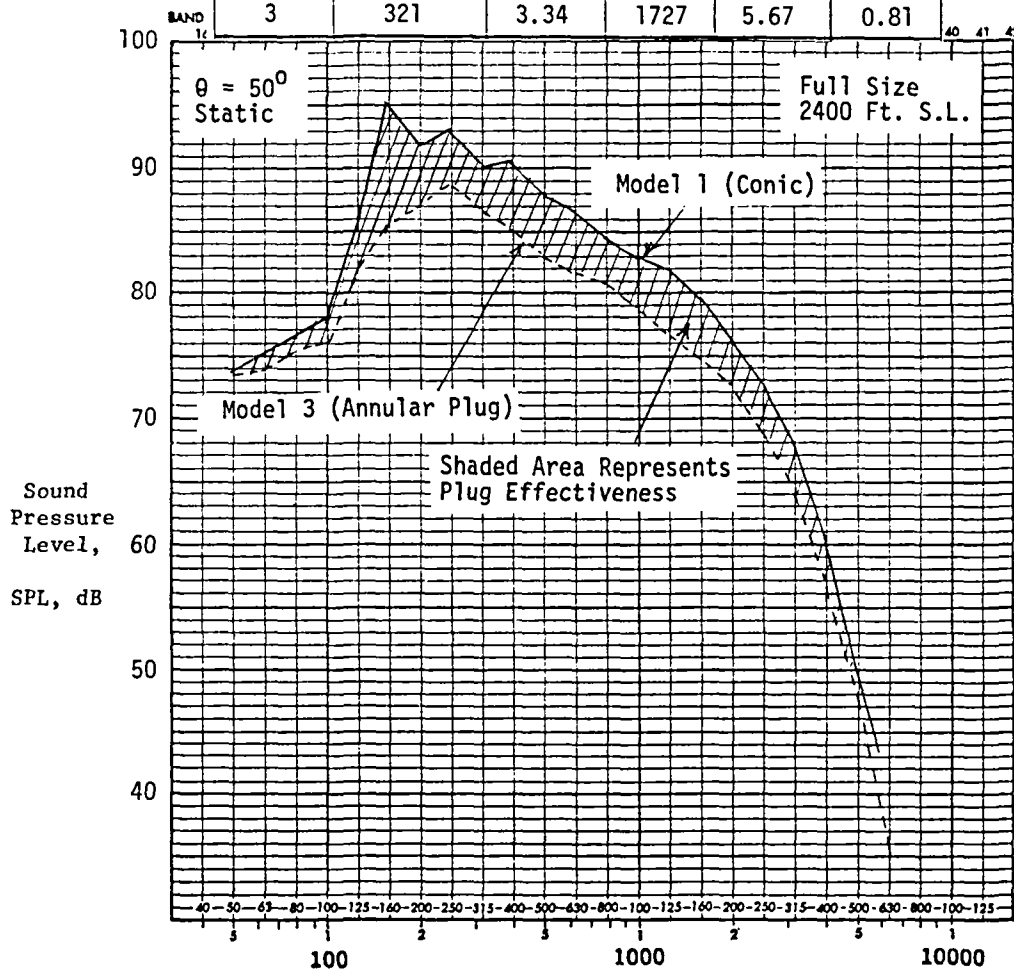
Figure 5-91 illustrates representative shock noise spectra for convergent circular (Model 1) and convergent annular plug (Model 3) nozzles. The comparison is made with almost identical flow conditions for both nozzles at emission angle of $\theta = 50^\circ$ under static condition. It is noted, in this figure, that over the frequency range of interest the convergent annular plug nozzle shows lower SPL values to the extent of 1 to 5 dB relative to the baseline convergent circular nozzle. Since shock-cell noise is generally predominant at this emission angle (i.e., $\theta = 50^\circ$), the difference in SPL observed between the circular and annular plug nozzles may be attributed mainly to lower shock-cell noise level corresponding to the annular plug nozzle.

A similar spectral comparison between Model 3, convergent annular plug nozzle, and Model 4, convergent-divergent (C-D) annular plug nozzle, is presented in Figure 5-92. The selected aerodynamic flow conditions correspond to the C-D operating conditions of Model 4. It should be noted that, shock-cell noise level corresponding to Model 3 is slightly higher only in the high frequency range. As the diagnostic LV test results (see Section 6.0) with these nozzles indicated, under the given flow conditions Model 4 is practically shock-free on the plug. However, downstream of the plug, both Model 3 and Model 4 have shock-cells. This implies that the SPL difference observed between the two nozzles in the high frequency range may be attributed to the shock noise generated on the plug surface of the convergent configuration.

The above-mentioned discussions on front quadrant noise from convergent annular plug nozzle are summarized as follows:

- Under identical aerodynamic flow conditions, the convergent annular plug nozzle jet is quieter by 1 to 5 dB in the mid to high frequency range relative to the baseline circular convergent nozzle jet.
- Shock-cell noise produced by the convergent annular plug nozzle jet have two components; one is associated with the shocks on the plug and the other with the shocks downstream of the plug.

Model	Test Point	P_r	T_T , ($^{\circ}R$)	D_{eq} (Inch)	h (Inch)
1	121	3.32	1700	5.10	-
3	321	3.34	1727	5.67	0.81



1/3-Octave-Band Center Frequency, f , Hz

Figure 5-91. Spectral Comparison of Shock-Cell Noise Between Model 1 and Model 3, Illustrating Plug Effects on Shock-Cell Noise.

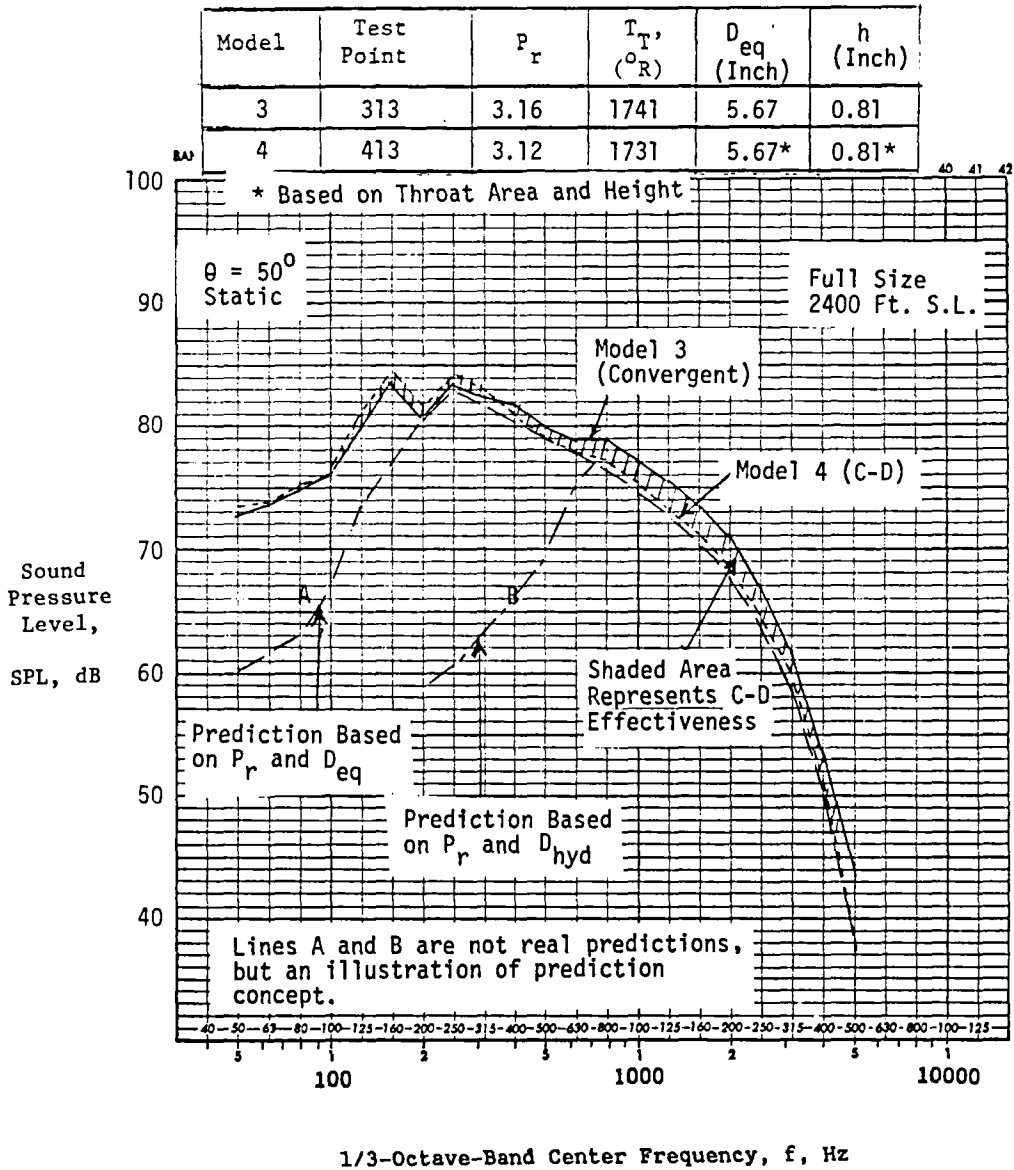


Figure 5-92. Spectral Comparison of Shock-Cell Noise Between Model 3 and Model 4, Illustrating Spectral Contribution of Shocks Formed on the Plug.

These findings suggest a prediction scheme for the shock noise on convergent annular plug nozzles. First, two appropriate length scales associated with shock noise generation on the plug and downstream of the plug have to be defined. Then, the two predictions have to be combined. Finally, the combined sound pressure levels have to be decreased by 5 dB over the mid to high frequency range. Obviously the best choice for the length scale associated with the shocks downstream of the plug is the equivalent diameter. It is a common practice to use the hydraulic diameter as a characteristic length scale in the jet mixing noise prediction scheme for the suppressor nozzles. This hydraulic diameter may be used also to define the length scale associated with shocks in the close proximity of annular plug nozzle exit, though its rationale is open to question.

Based on this scheme, spectral prediction of shock-cell noise of the convergent annular plug nozzle has been made after incorporating the above suggested modifications into the HBF model. Comparison of the predicted shock-cell noise data with the measured front quadrant data for a set of test conditions are provided in Figures 5-93 through 5-97. The test conditions range over pressure ratios of $2.96 < P_r < 3.34$ at $T_T \sim 1730^\circ R$. It should be noted that the measured data is the composite of jet and shock-cell noise. An examination of these figures indicates good agreement between the measured and predicted data. Since the shock-cell noise is known to dominate in the forward quadrant, this acceptable agreement justifies the suggested prediction scheme for shock-cell noise of convergent annular plug configurations.

Next, a limited assessment of this prediction scheme for suppressor nozzles is presented. Figure 5-98 illustrates a typical front quadrant spectral comparison of shock-cell noise between the convergent 20-shallow-chute suppressor nozzle (Model 5) and the C-D 20-shallow-chute suppressor plug nozzle (Model 6). Selected aerodynamic plume conditions correspond to the C-D operating conditions for Model 6. It should be noted in this figure that the C-D termination of the flow elements of Model 6 has both favorable and adverse effects on shock-cell noise suppression. In view of the relatively small characteristic length associated with the shock noise produced by the chute, the peak frequency of this shock noise is shifted to higher frequencies, as compared with the case of the unsuppressed annular plug

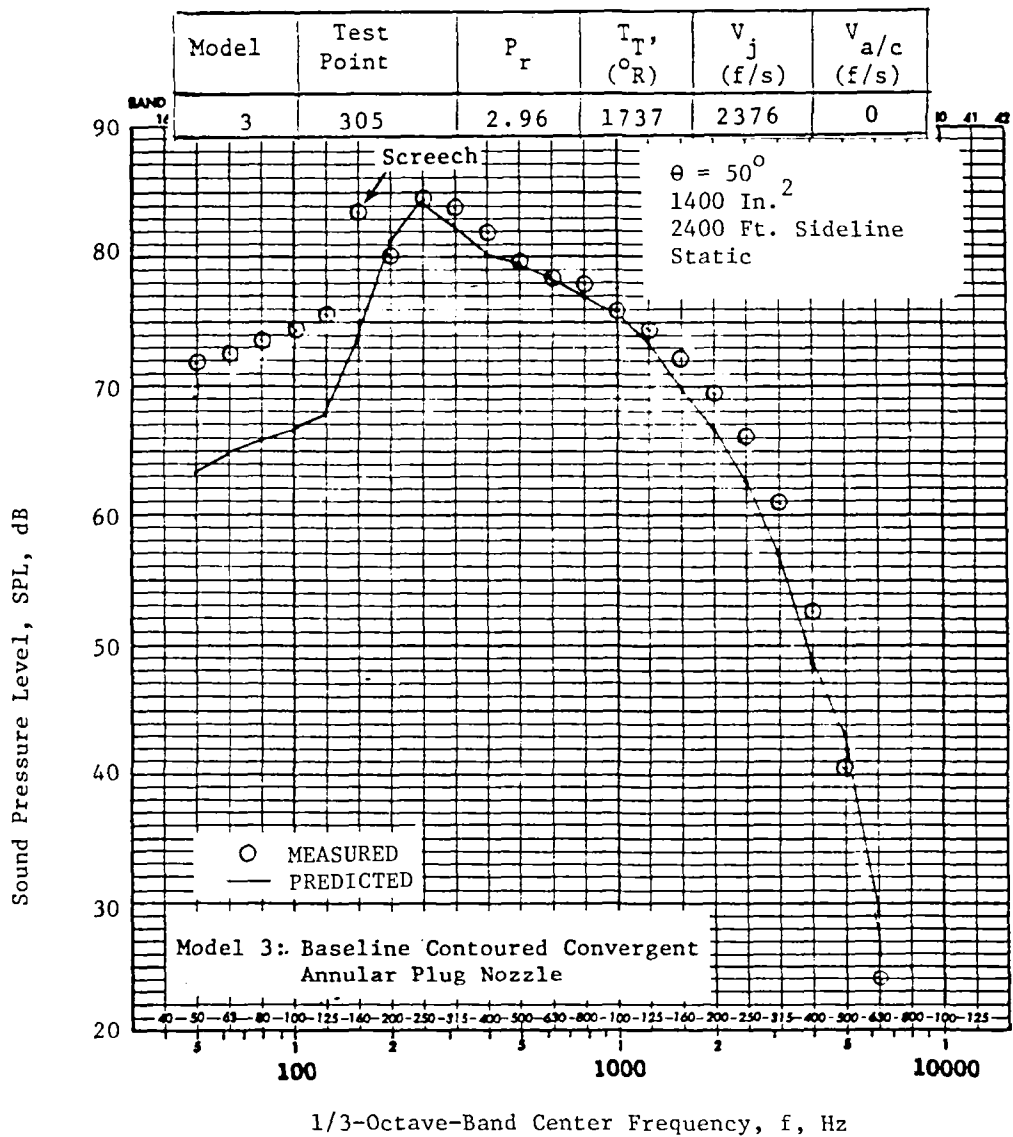


Figure 5-93. Comparison of Predicted Shock-Cell Noise Spectra of Convergent Annular Plug With Measured Data; $P_r = 2.96$.

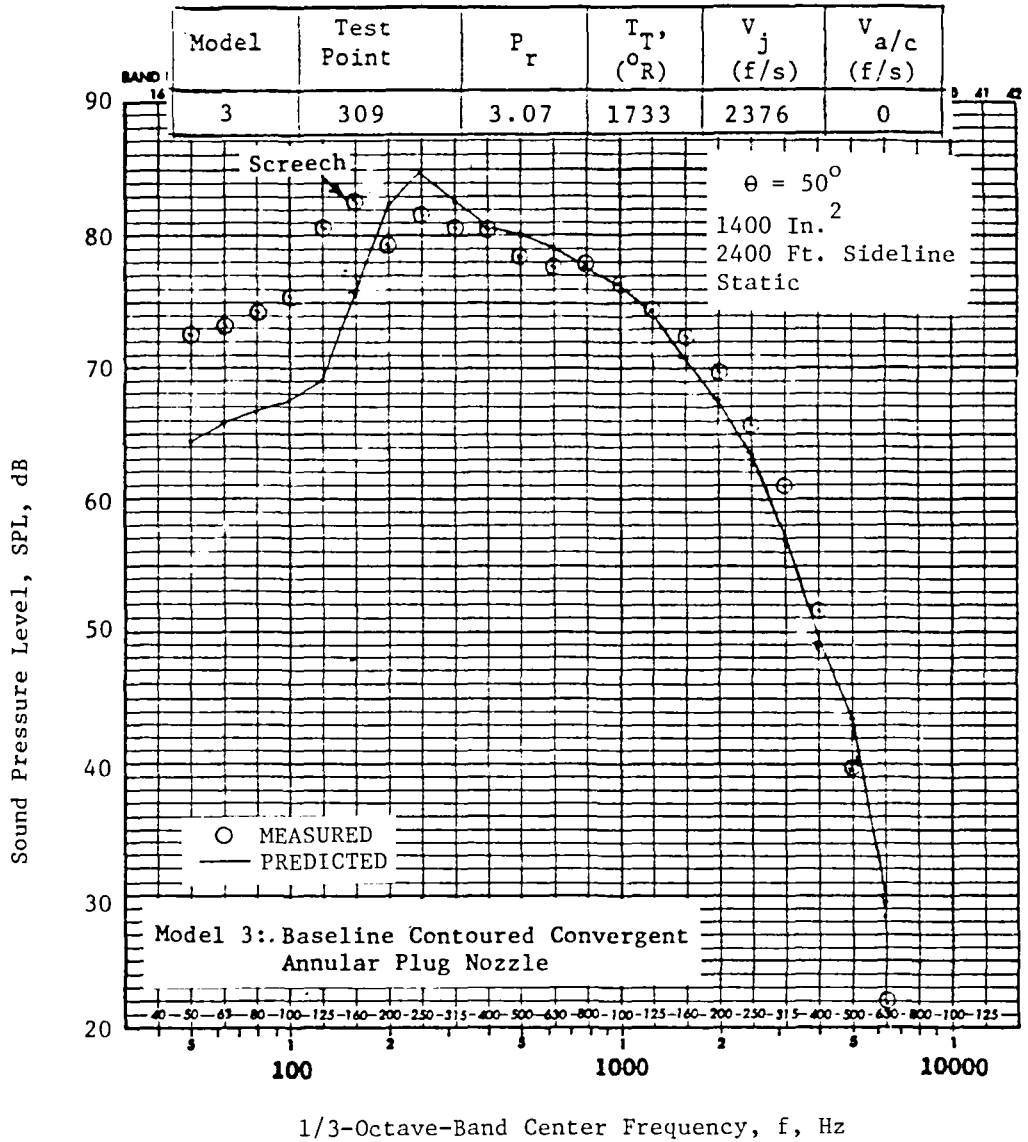


Figure 5-94. Comparison of Predicted Shock-Cell Noise Spectra of Convergent Annular Plug With Measured Data; $P_r = 3.07$.

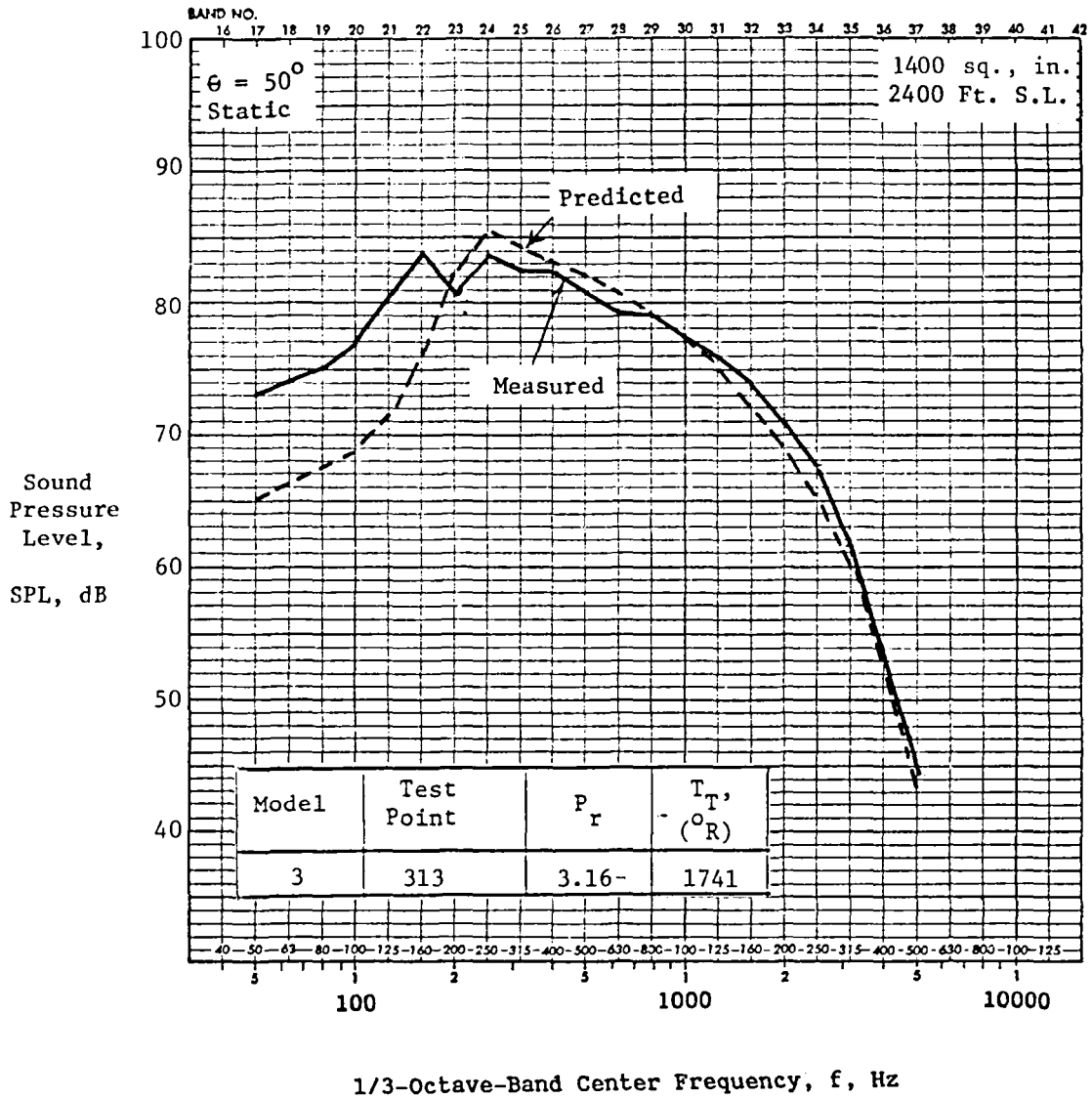


Figure 5-95. Comparison of Predicted Shock-Cell Noise Spectra of Convergent Annular Plug With Measured Data; $P_r = 3.16$.

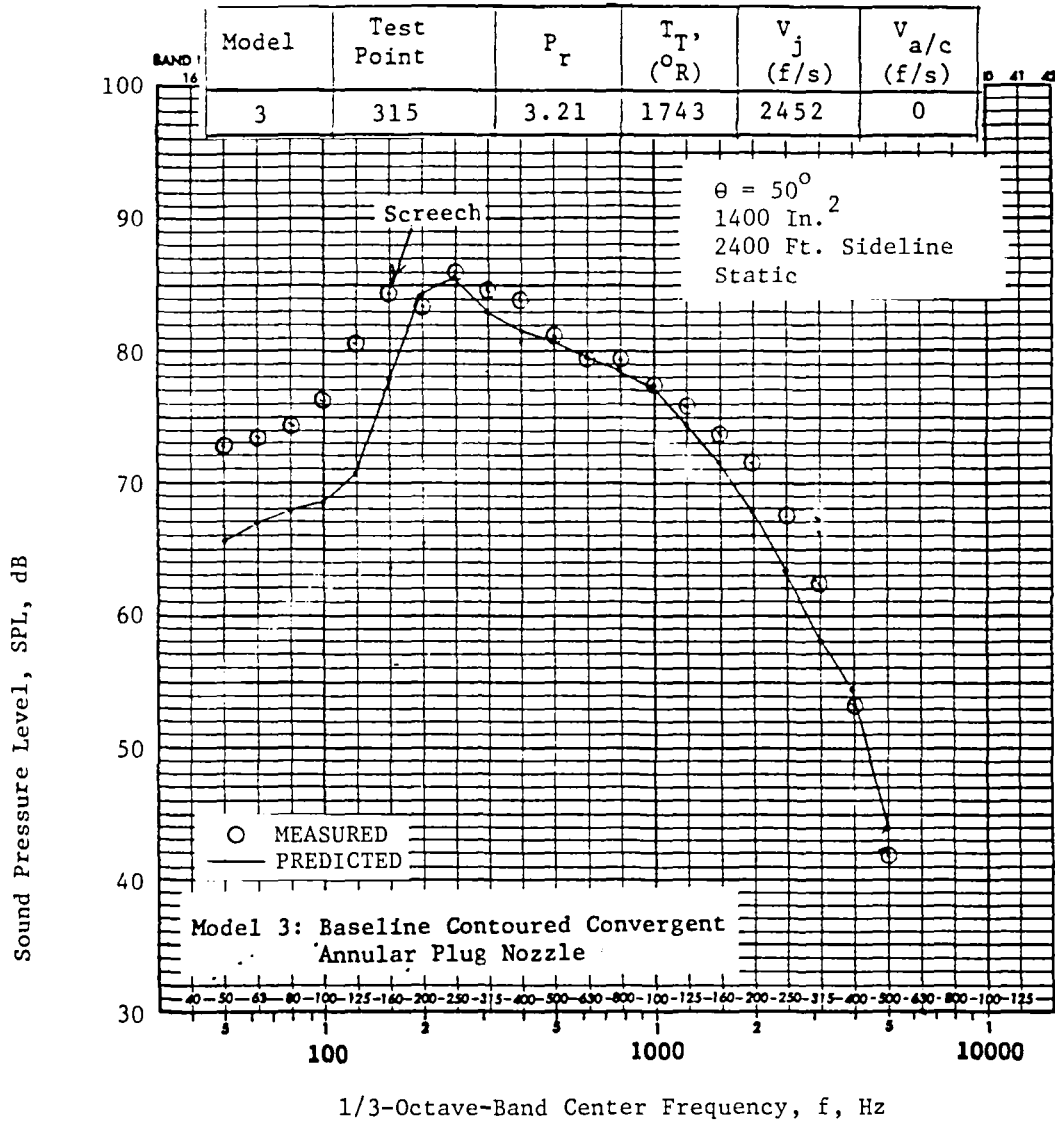


Figure 5-96. Comparison of Predicted Shock-Cell Noise Spectra of Convergent Annular Plug With Measured Data; $P_r = 3.21$.

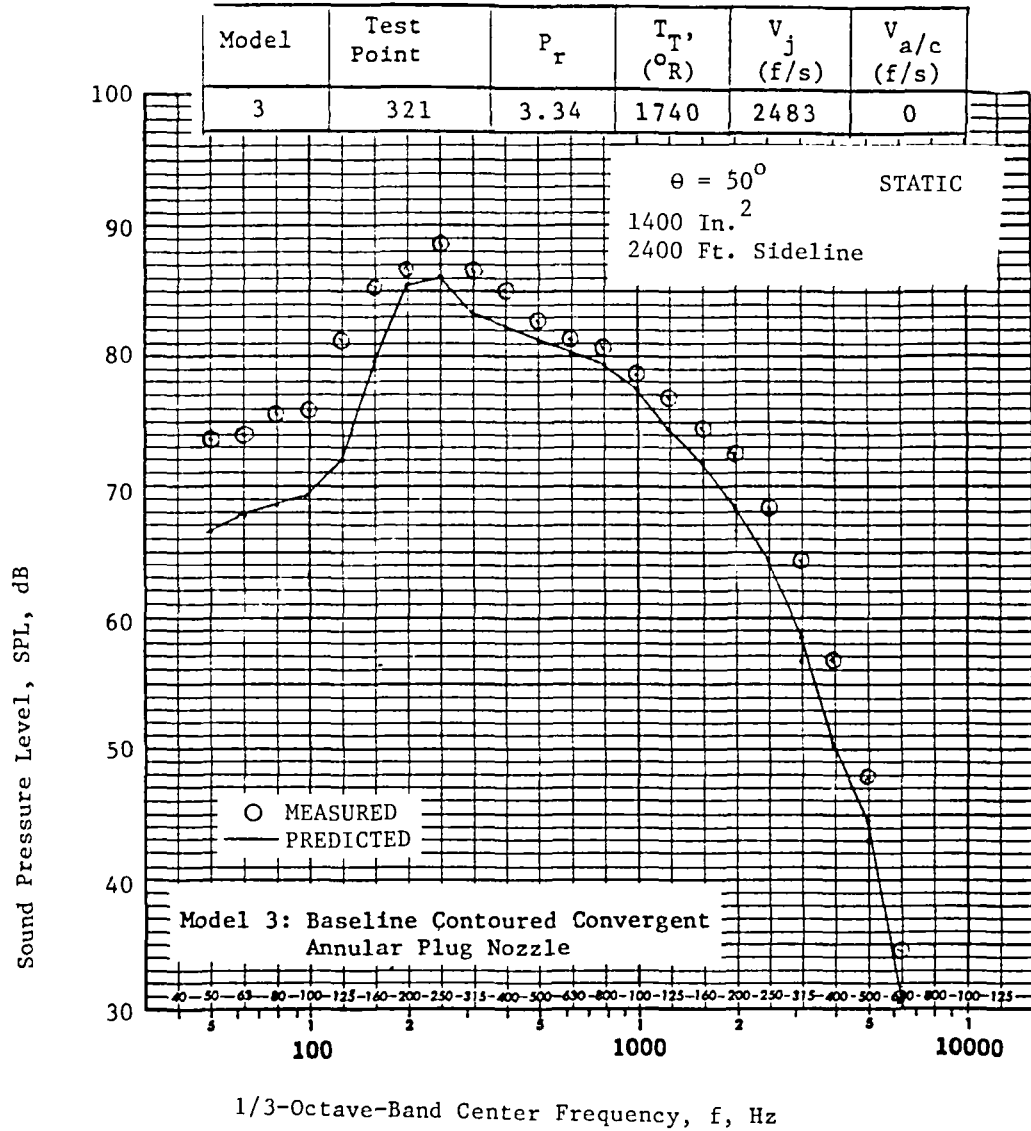


Figure 5-97. Comparison of Predicted Shock-Cell Noise Spectra of Convergent Annular Plug Nozzle with Measured Data; $P_r = 3.34$.

nozzle. Obviously, the C-D termination in the flowpath of the suppressor elements mitigates shocks on the plug, to some extent,* and an appreciable difference of high frequency SPL is noted between Model 5 and Model 6. However, as indicated by the laser velocimeter test results, the axial mean velocity of the flow for Model 5 is already subsonic at the plug tip, and, consequently, no shocks are formed downstream of the plug. This is in contrast to the case of Model 6 where substantially higher axial mean velocity is observed downstream of the plug. Hence, as indicated in Figure 5-98, the C-D termination has an adverse effect on shock noise suppression in the low to mid frequency range due to shock downstream of the plug. The results of Figure 5-98 indicates the following regarding a prediction scheme for shock-cell noise of suppressor configurations:

- When the mean velocity decay rate is large enough so that the flow speed downstream of the plug is subsonic, shock-cell noise may be adequately predicted by the HBF model, incorporating a suitable length scale associated with a suppressor element.
- When flow speed downstream of the plug is still supersonic, however, a composite of two predictions (with weak shocks on the plug and downstream of plug) may be appropriate.

Figure 5-99 illustrates a sample prediction of shock-cell noise from the convergent suppressor plug nozzle (Model 5) based on the HBF model, utilizing the hydraulic diameter of chute element as a characteristic length associated with shocks formed near the jet exit.

The selected aerodynamic flow conditions are identical to those for Figure 5-98. It should be noted that for the prediction shown in Figure 5-99 it was assumed that shock noise produced by each chute is mutually uncorrelated. A satisfactory agreement seen in this figure is encouraging. However, to fully establish the validity of prediction concept of shock-cell noise, more work, both theoretical and experimental, is needed in the future.

*The diagnostic LV and shadowgraph tests have indicated that shock suppression by the C-D termination is not as complete for Model 6 as for Model 2, circular C-D nozzle.

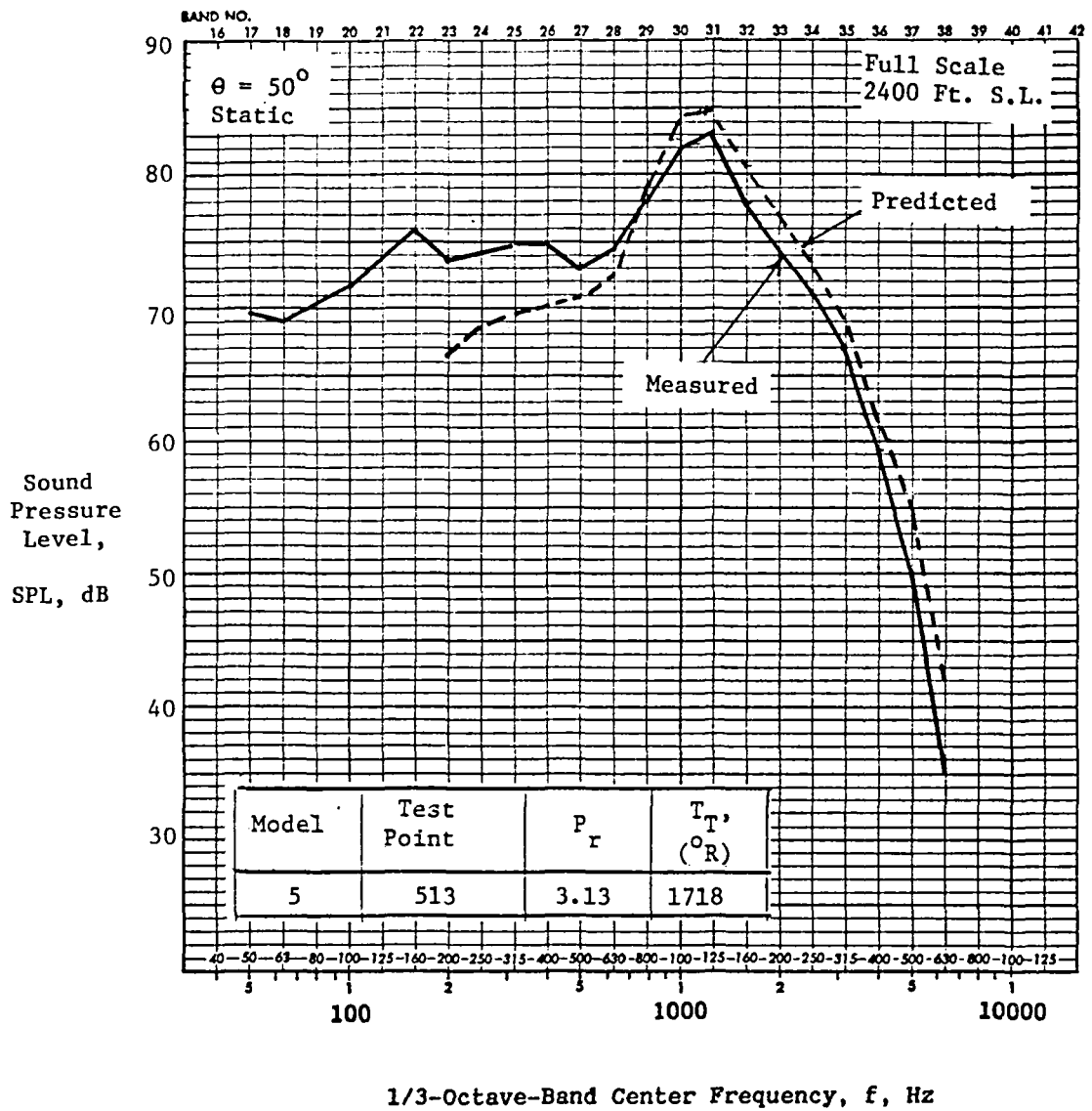


Figure 5-99. Spectral Comparison of Shock-Cell Noise from Convergent Suppressor Plug Nozzle (Model 5) Between Measured Data and Predicted.

6.0 DIAGNOSTIC TEST RESULTS

To better understand shock associated noise generation mechanism and also to aid in the development of an analytical prediction model for shock noise, flow visualization using shadowgraph photography and mean velocity and turbulent velocity measurements using a laser velocimeter were employed.

Scope and test matrices of the diagnostic tests with six model nozzles are given in Appendix II and III. Detailed diagnostic data are in the companion Comprehensive Data Report (Reference 2-1).

Guidelines of the diagnostic tests were:

- From on-line acoustic sensitivity studies, determine the value of shock-free pressure ratio and range of sensitivity.
- Identify regions of strongest shock formation (example: in the region of the annular plug or downstream of the plug).
- By means of the laser velocimeter measurements, determine the mean and turbulent velocity distributions to assess the general shock-cell structure of the various types of configurations.
- Identify the difference in shock structure in the flow, if any, between static and simulated flight cases.

The results of the diagnostic data analysis of the model nozzle configurations described in Section 4.0 are presented in this section.

This section consists of two subsections. Subsection 6.1 contains a discussion on the laser velocimeter test results and Subsection 6.2 contains discussions on the flow visualization shadowgraph test results.

6.1 LASER VELOCIMETER TEST RESULTS

In an imperfectly expanded nozzle flow rapid variation in the mean pressure occurring at the nozzle exit is accommodated by a system of steady

waves emanating from the nozzle lip. The cell-like structure of the jet arises from the subsequent multiple internal reflections of the system at the jet boundaries. This cell structure is damped out generally before the centerline velocity has become subsonic. At the relatively high Reynolds numbers encountered in aeronautical applications, turbulent diffusion is probably the dominant mechanism responsible for the degradation of the cell structure. For this reason, current effort has been directed toward understanding of the flow behavior in the vicinity of an equivalent lip-line in jets. The study on supersonic flow field by Seiner and Norum (Reference 5-19) is referenced in the present discussions wherever possible with the aim of identifying temperature effects, if any, on shock formation and shock-turbulence interactions in the supersonic jet flows.*

The equivalent lip-line is defined as the line downstream of the plug being parallel to the jet axis and offset from it by half of the equivalent diameter. In what follows, the term "lip-line" is used; and, wherever the term is referenced downstream of the plug, it should be interpreted as "equivalent lip-line."

Prior to discussions on the flow characteristics in the vicinity of the lip-line, general flow characteristics of supersonic jets from various nozzle configurations are discussed.

6.1.1 GENERAL FLOW CHARACTERISTICS OF SUPERSONIC JETS

In this subsection discussions on the mean flow characteristics of supersonic jets with and without shocks emanating from various single-stream nozzles are presented.

6.1.1.1 Centerline Mean Velocity Distributions

The axial mean velocity distributions of various nozzle jets are first examined. Figures 6-1 through 6-4 illustrate some representative results of the axial mean velocity measurements in the baseline convergent circular

*Seiner and Norum used cold jets for their study while the discussions herein are mostly based on the test results for heated jets.

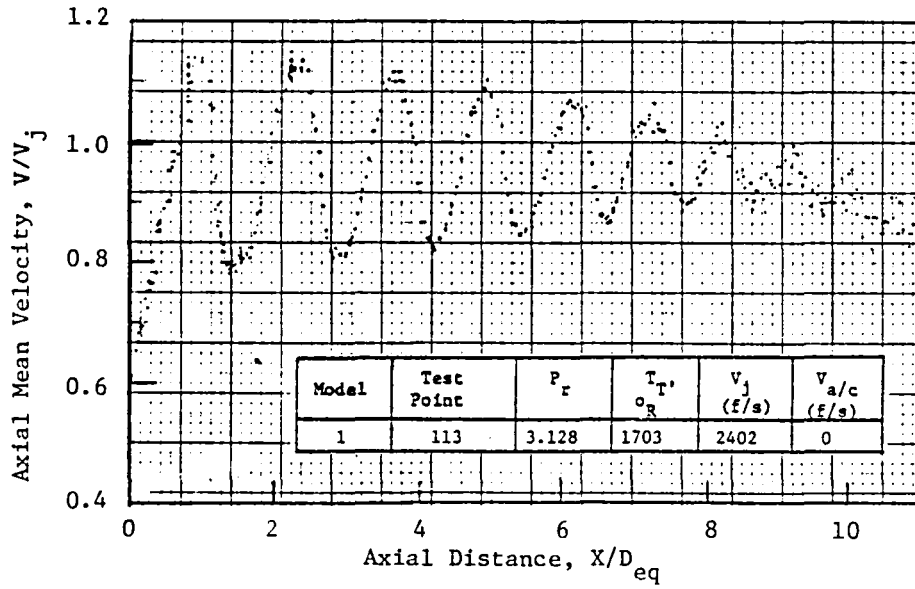


Figure 6-1. Axial Mean Velocity Distribution on Jet Axis for Baseline Convergent Circular Nozzle at Aerodynamic Flow Conditions Matched to C-D Design Conditions of Model 2 (Static).

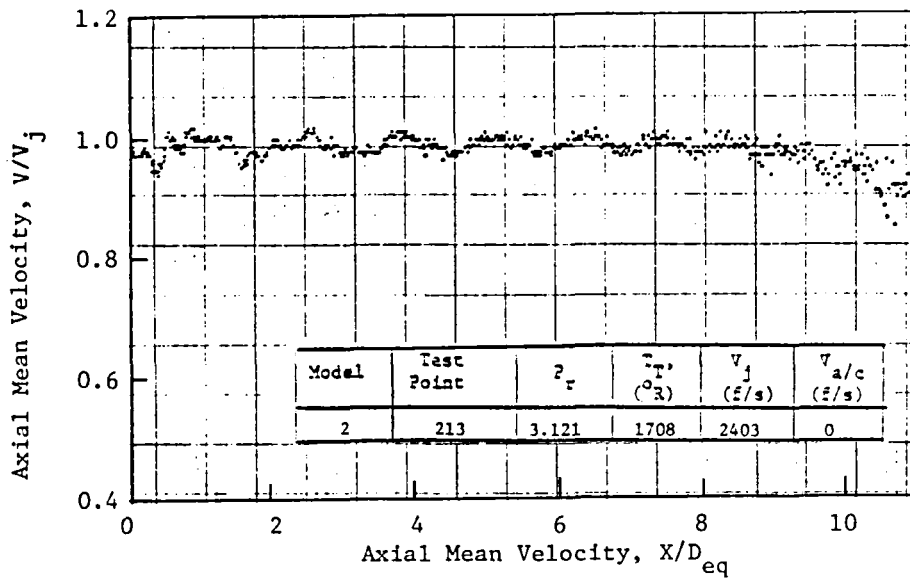


Figure 6-2. Axial Mean Velocity Distribution on Jet Axis for C-D Circular Nozzle at Design Conditions (Static).

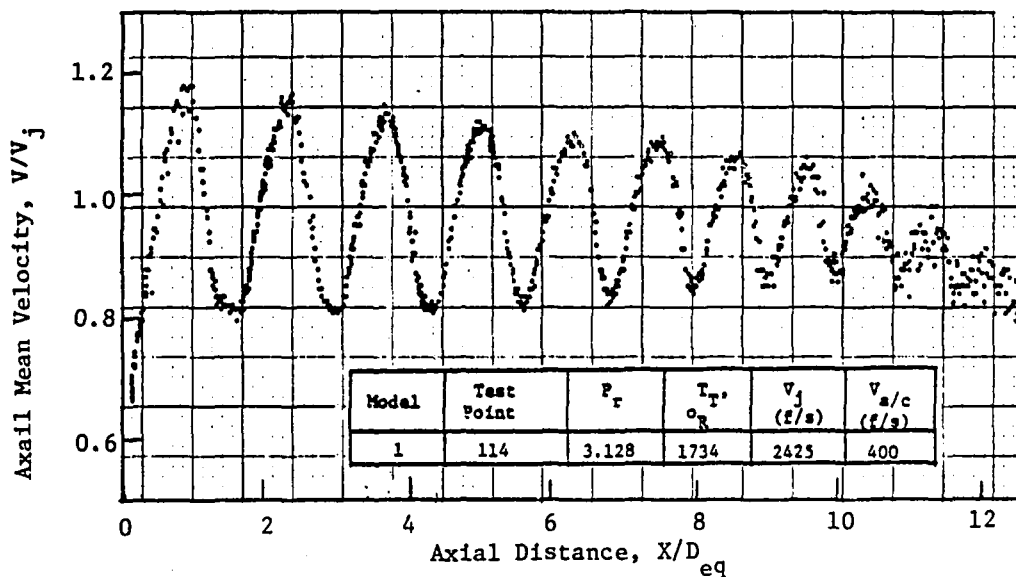


Figure 6-3. Axial Mean Velocity Distribution on Jet Axis for Baseline Convergent Circular Nozzle at Aerodynamic Flow Conditions Matched to C-D Design Conditions of Model 2 (Simulated Flight).

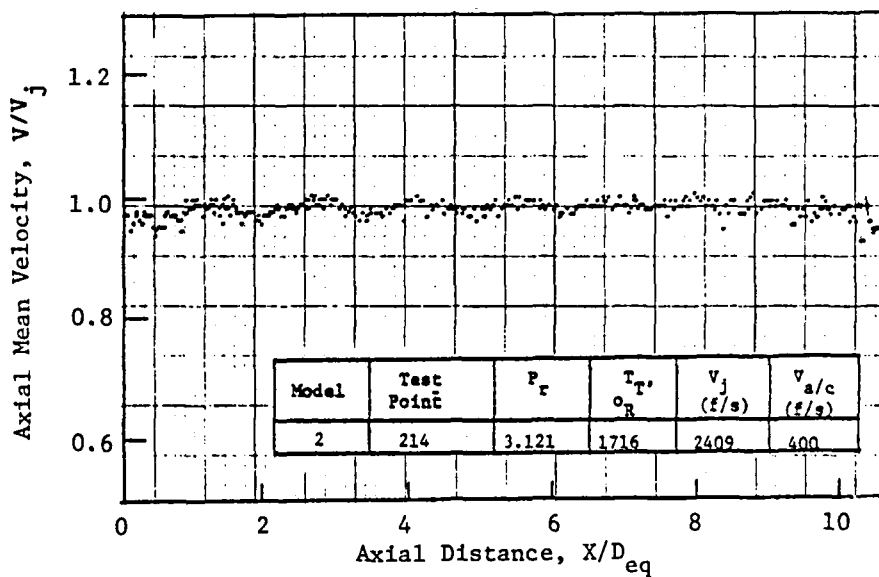


Figure 6-4. Axial Mean Velocity Distribution on Jet Axis for C-D Circular Nozzle at Design Conditions (Simulated Flight).

nozzle and the C-D circular nozzle jet. The selected test points have the aerodynamic flow conditions which correspond to the C-D operating conditions of the C-D circular nozzle ($P_r \sim 3.12$ and $T_T \sim 1700^\circ\text{R}$).

The axial mean velocity variations on the jet axis for a typical supercritical jet is presented in Figure 6-1. Over a length of ten diameters from the nozzle exit, as many as eight shocks are observed. Gradual decrease of shock-cell spacing is also noted in this figure. Similar mean velocity distribution for the C-D circular nozzle jet (Model 2) at its C-D operating conditions is illustrated in Figure 6-2. Practically no shocks are observed, and the fully expanded flow velocity is maintained as far as near ten diameters downstream from the nozzle exit. These results were obtained from the LV measurements conducted under static conditions. With practically identical flow conditions to those shown in Figures 6-1 and 6-2 but with a simulated flight velocity of 400 fps, similar mean velocity distributions were measured with Model 1 and Model 2. The results of these measurements are presented in Figures 6-3 and 6-4. Again, strong shocks are noted in the mean flow for Model 1. Over a length of twelve diameters downstream of jet axis, nine or ten shocks are observed. Corresponding axial mean velocity distribution for Model 2 obtained in simulated flight is presented in Figure 6-4. No significant difference is observed between static and free-jet cases.

Figures 6-5 through 6-8 represent the axial mean velocity distributions for the convergent circular (Model 1) and C-D circular (Model 2) nozzles at off-design conditions of Model 2, obtained with and without free-jet flow. Comparison of the results of these figures to those of Figures 6-1 through 6-4 indicates that with a larger pressure ratio shock-cell spacing increases.

The axial mean velocity distributions of the jet downstream of the plug measured with the convergent annular plug nozzle (Model 3) and the C-D annular plug nozzle (Model 4) with and without free-jet flow are presented next. Figures 6-9 through 6-12 illustrate these axial mean velocity distributions obtained at the C-D design conditions of Model 4 ($P_r \sim 3.12$, $T_T \sim 1730^\circ\text{R}$). It should be noted that both convergent and C-D nozzles have an almost identical shock pattern in the flow region downstream of the plug. Due to the plug step, a supersonic flow produces a series of expansion

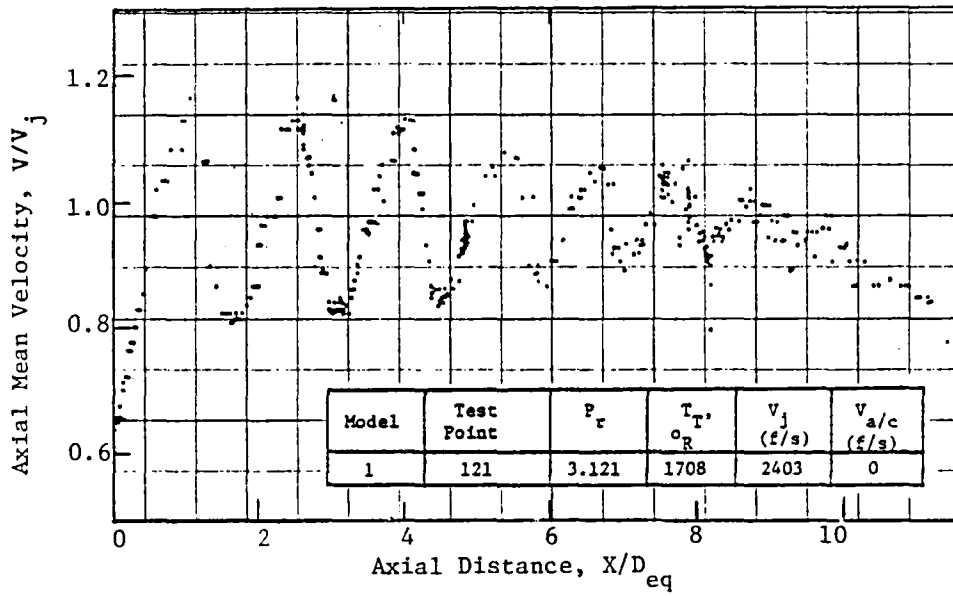


Figure 6-5. Axial Mean Velocity Distribution on Jet Axis for Baseline Convergent Circular Nozzle at Aerodynamic Flow Conditions Matched to C-D Design Conditions of Model 2 (Static).

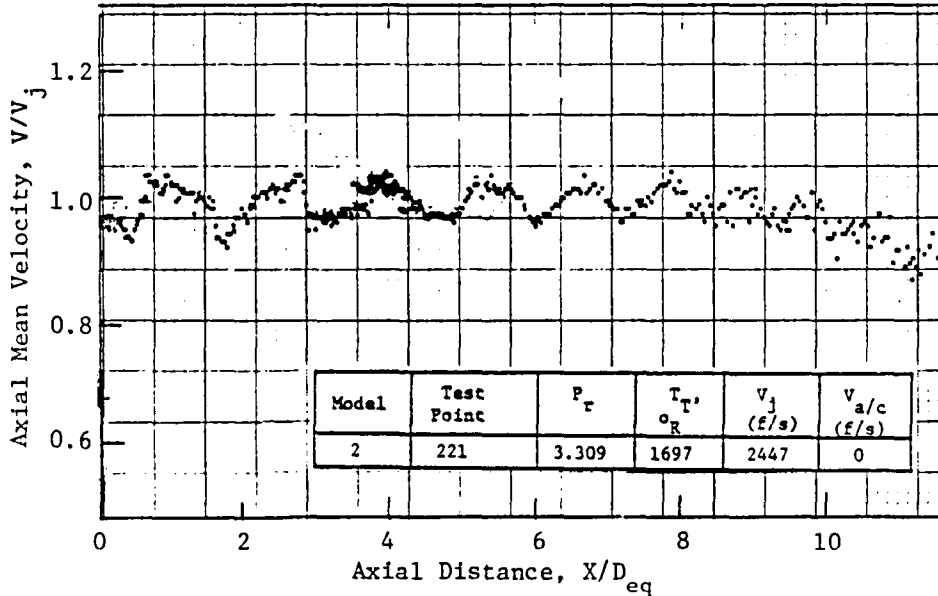


Figure 6-6. Axial Mean Velocity Distribution on Jet Axis for C-D Circular Nozzle at Design Conditions (Static).

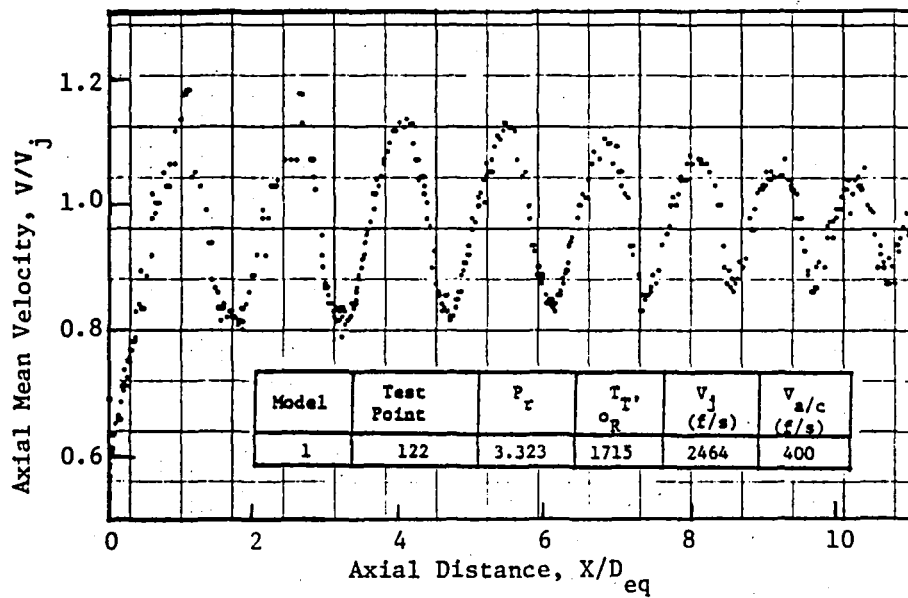


Figure 6-7. Axial Mean Velocity Distribution on Jet Axis for Baseline Convergent Circular Nozzle at Aerodynamic Flow Conditions Matched to the Off-Design Conditions of Model 2 (Simulated Flight).

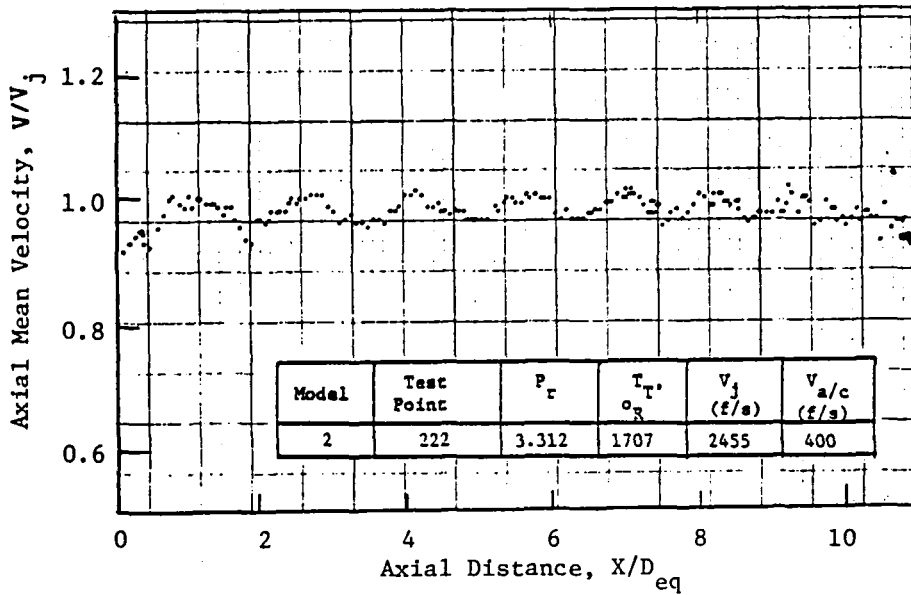


Figure 6-8. Axial Mean Velocity Distribution on Jet Axis for C-D Circular Nozzle at Off-Design Conditions (Simulated Flight).

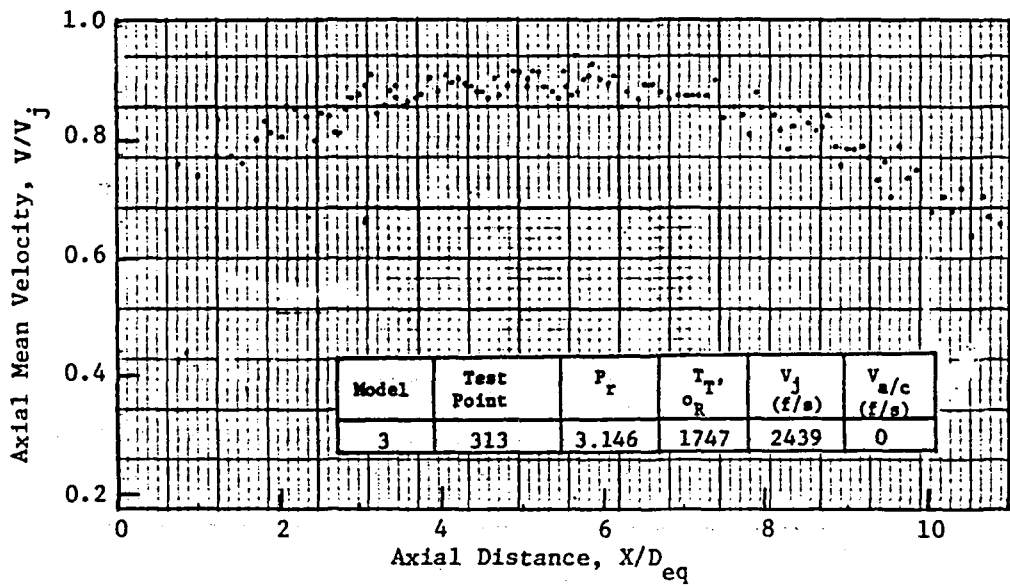


Figure 6-9. Axial Mean Velocity Distribution on Jet Axis for Convergent Annular Plug Nozzle at Aerodynamic Flow Conditions Matched to the C-D Design Conditions of Model 4 (Static).

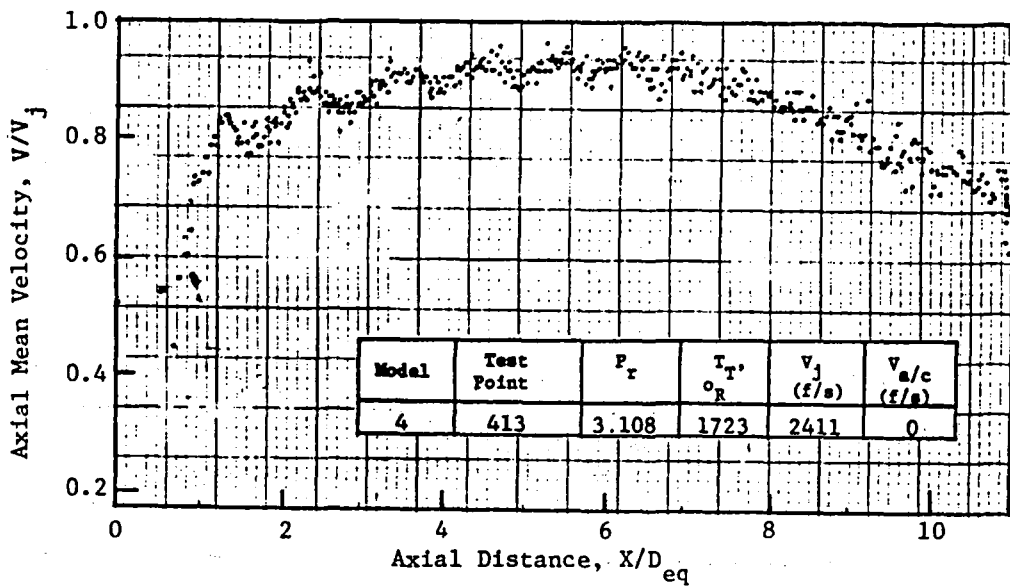


Figure 6-10. Axial Mean Velocity Distribution on Jet Axis for C-D Annular Plug Nozzle at Design Conditions (Static).

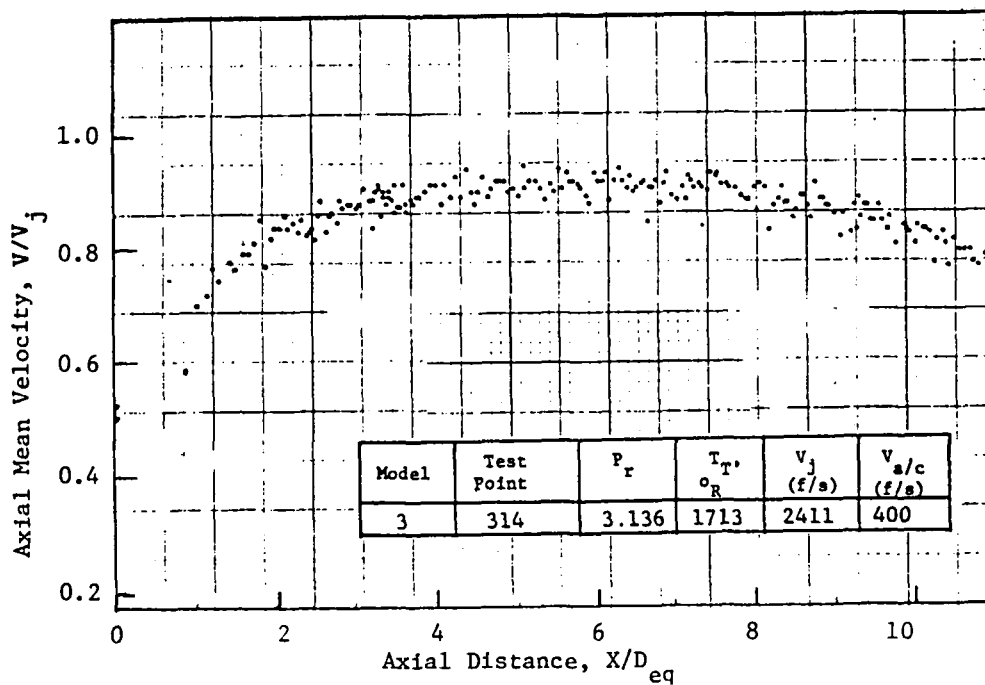


Figure 6-11. Axial Mean Velocity Distribution on Jet Axis for Convergent Annular Plug Nozzle at Aerodynamic Flow Conditions Matched to the C-D Design Conditions of Model 4 (Simulated Flight).

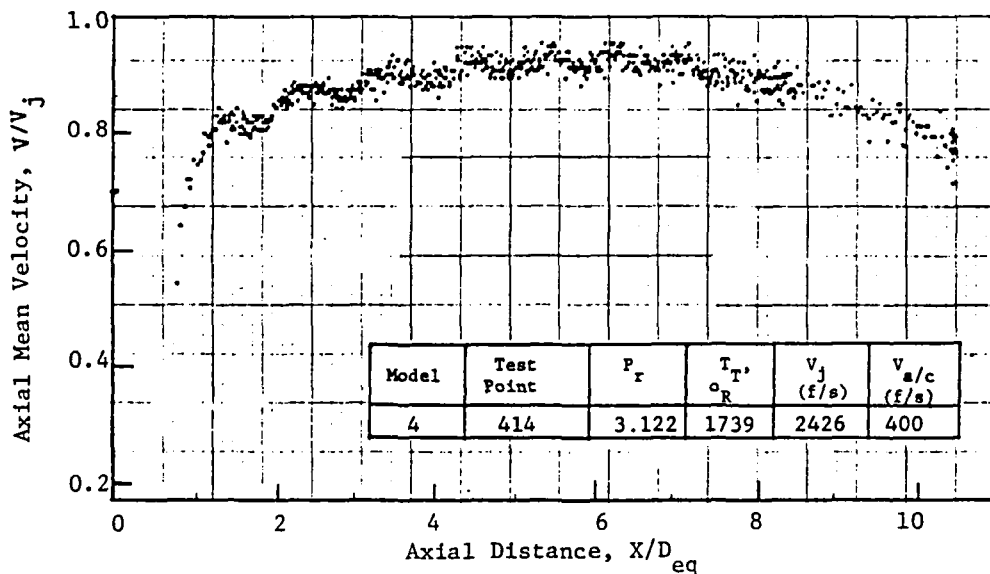


Figure 6-12. Axial Mean Velocity Distribution on Jet Axis for C-D Annular Plug Nozzle at Design Conditions (Simulated Flight).

and subsequent shock waves downstream of the plug. The multiple internal reflections of these waves at the jet boundaries give rise to the cell-like structure in the flow. No appreciable difference can be noted between static and simulated flight cases.

Corresponding axial mean velocity distributions measured with Models 3 and 4 at off-design conditions are presented in Figures 6-13 through 6-16. More pronounced shocks are observed for Model 3, under both static and free-jet conditions, relative to those of Model 4.

Finally, a similar survey was made with the two multi-chute suppressor nozzles. The axial mean velocity distributions for the convergent 20-shallow-chute suppressor nozzle (Model 5) and the C-D 20-shallow-chute suppressor nozzle (Model 6) are presented in Figures 6-17 through 6-20. The aerodynamic conditions for the selected test points correspond to the C-D design conditions of Model 6 ($P_r \sim 3.12$ and $T_T \approx 1730^\circ R$). Significantly, no shocks are observed downstream of the plug under the given aerodynamic conditions for both static and free-jet cases. Furthermore, we note that the axial mean velocity on the jet axis for Model 5 is already subsonic within the first ten diameters from the plug tip,* in contrast to the case of Model 6 where the flow maintains a supersonic speed as far as ten equivalent jet diameters from the plug tip, though no shocks are distinctly observed in this flow region.

6.1.1.2 Radial Mean Velocity Distributions

A limited number of radial traverses of the mean velocity were performed during this investigation. Some representative results of these measurements are presented in this subsection.

*In this case the sonic velocity corresponds to $V/V_j \approx 0.73$ which was calculated on the assumption that the flow temperature is uniform throughout the flow region and equal to the static temperature of the ideally expanded flow.

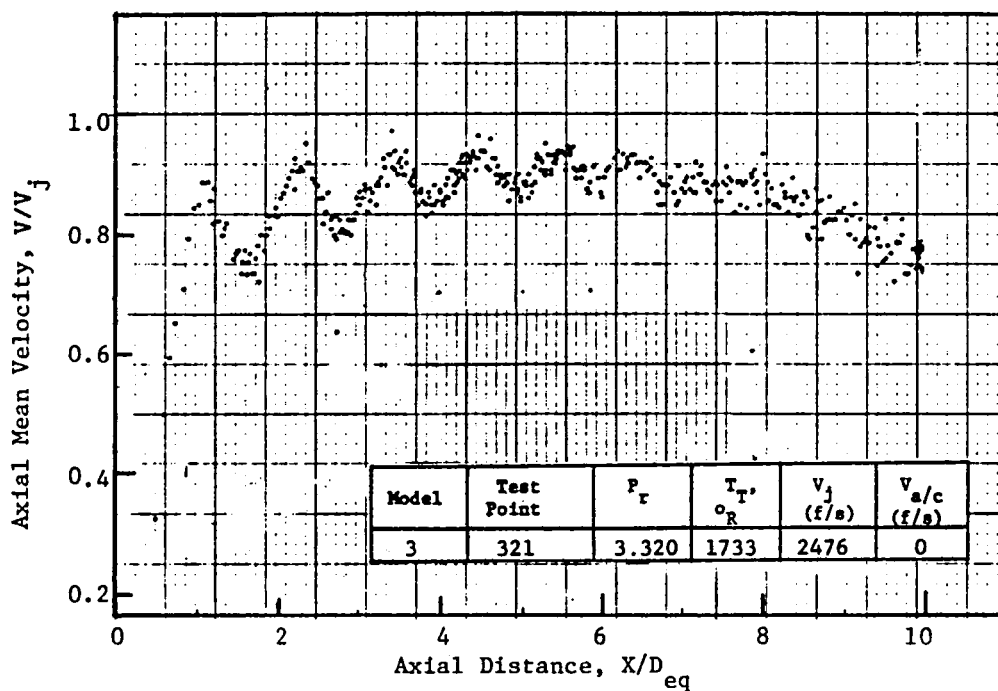


Figure 6-13. Axial Mean Velocity Distribution on Jet Axis for Convergent Annular Plug Nozzle at Aerodynamic Flow Conditions Matched to Off-Design Conditions of Model 4 (Static).

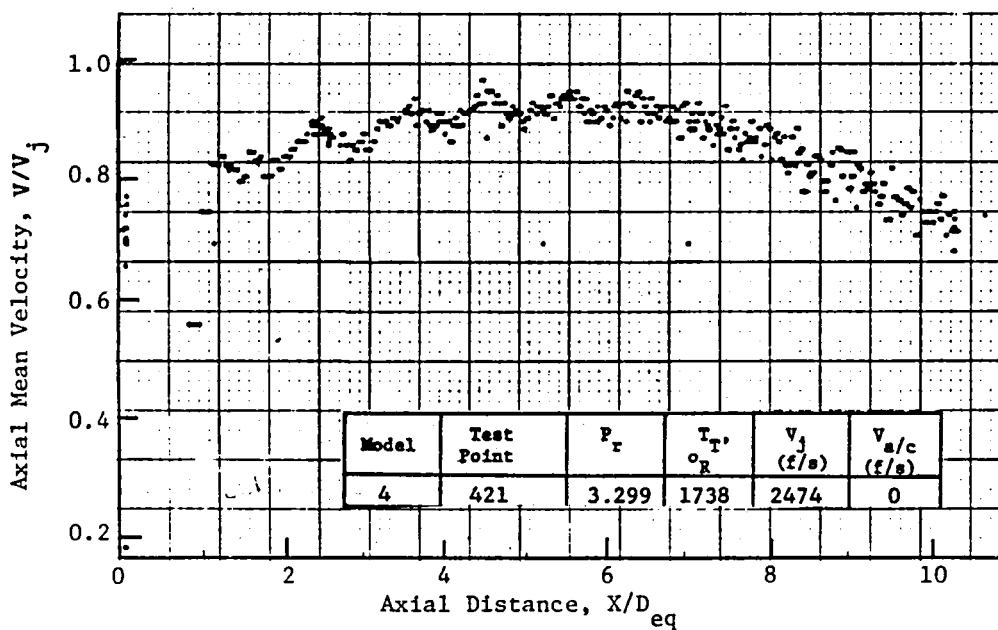


Figure 6-14. Axial Mean Velocity Distribution on Jet Axis for C-D Annular Plug Nozzle at Off-Design Conditions (Static).

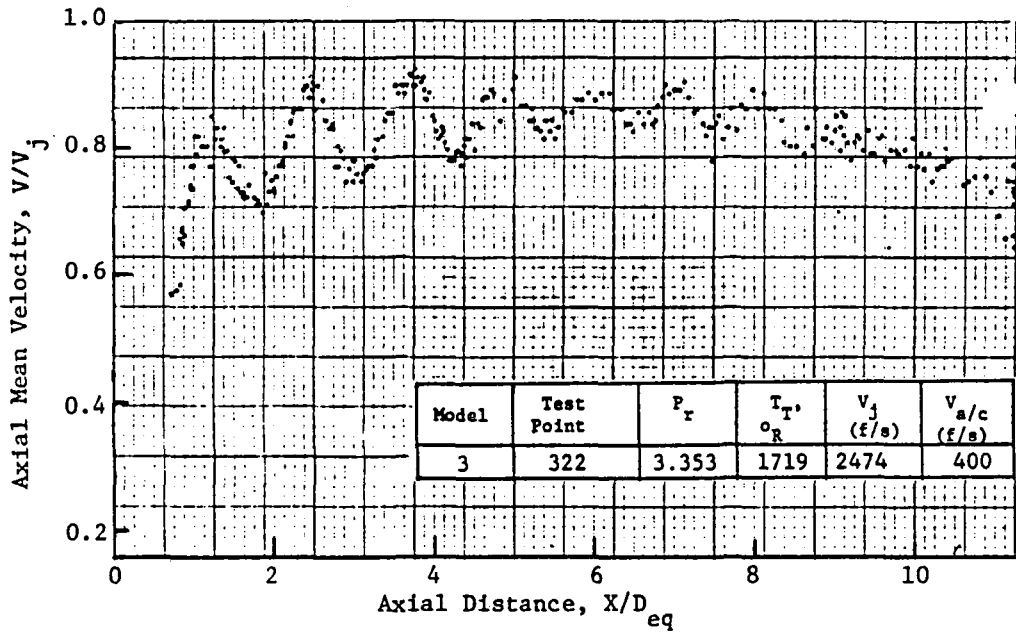


Figure 6-15. Axial Mean Velocity Distribution on Jet Axis for Convergent Annular Plug Nozzle at Aerodynamic Flow Conditions Matched to the Off-Design Conditions of Model 4 (Simulated Flight).

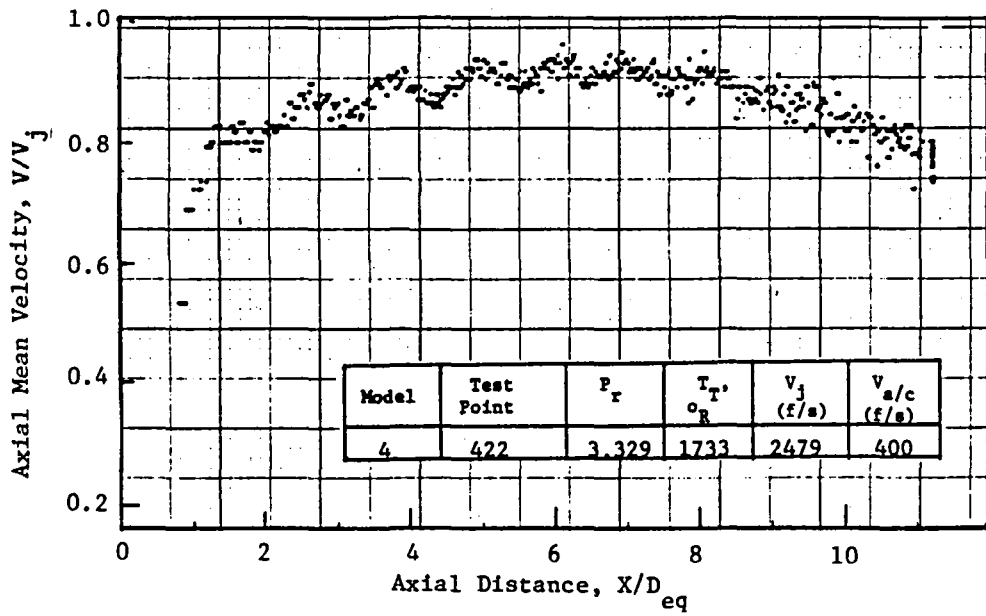


Figure 6-16. Axial Mean Velocity Distribution on Jet Axis for C-D Annular Plug Nozzle at Off-Design Conditions (Simulated Flight).

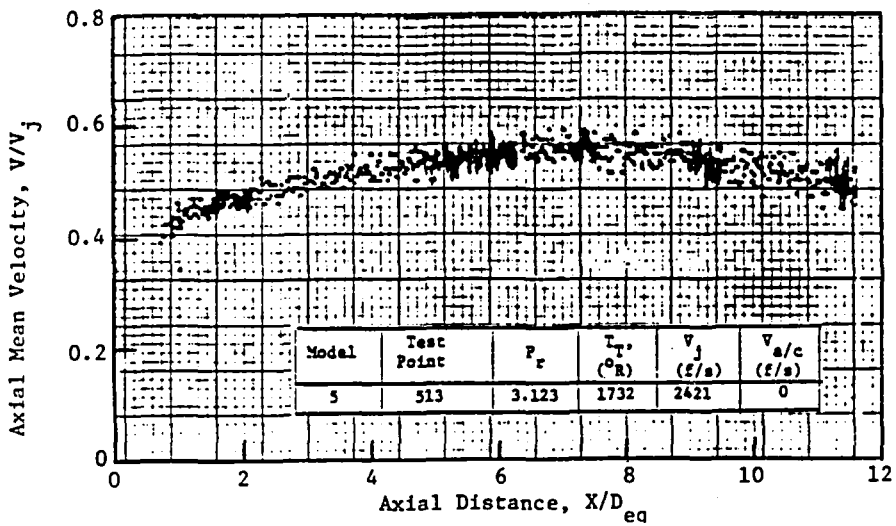


Figure 6-17. Axial Mean Velocity Distribution on Jet Axis for Convergent Multi-Element Suppressor Plug Nozzle (Static).

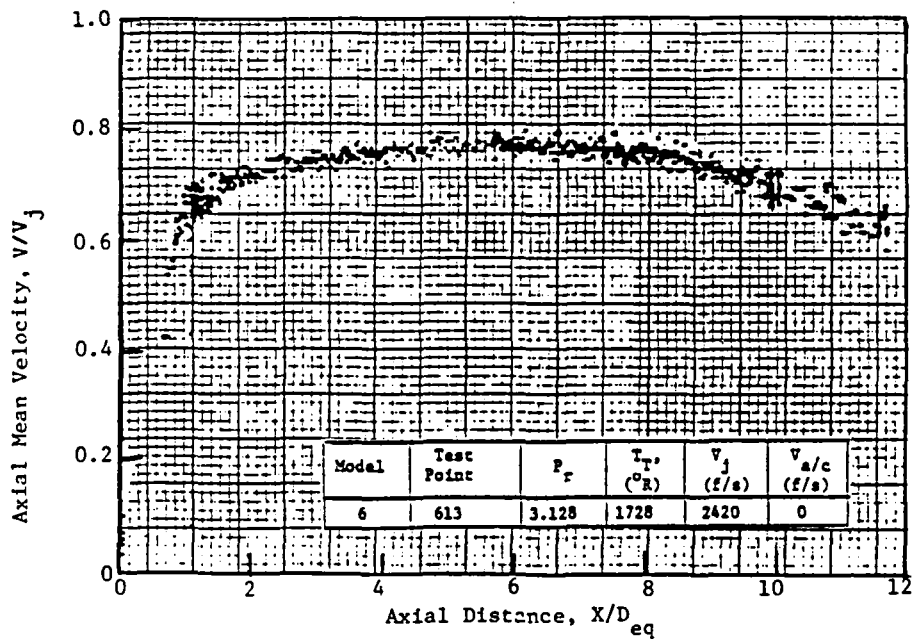


Figure 6-18. Axial Mean Velocity Distribution on Jet Axis for C-D Multi-Element Suppressor Nozzle (Static).

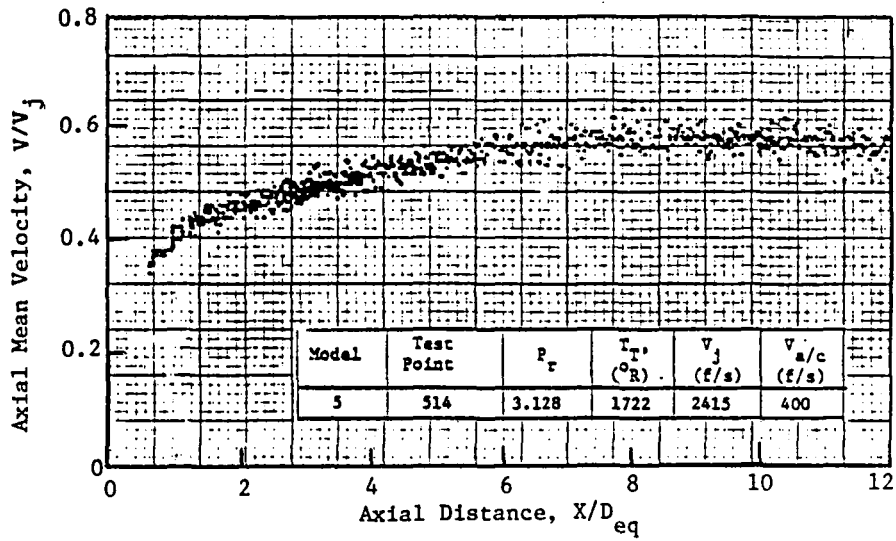


Figure 6-19. Axial Mean Velocity Distribution on Jet Axis for Convergent Multi-Element Suppressor Plug Nozzle (Simulated Flight).

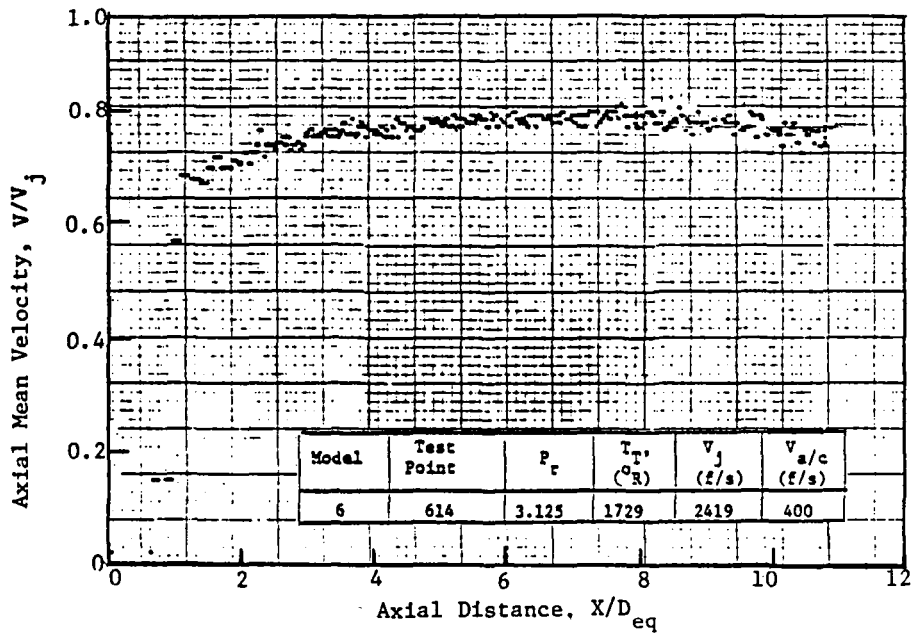


Figure 6-20. Axial Mean Velocity Distribution on Jet Axis for C-D Multi-Element Suppressor Nozzle (Simulated Flight).

Radial distributions of the mean velocity (axial component) for the convergent circular (Model 1) and C-D circular (Model 2) nozzles are illustrated in Figures 6-21 and 6-22. The selected test points correspond to the C-D operating point for Model 2.

The radial traverses by LV were made at four axial stations under static conditions and five in simulated flight. In Figure 6-21 one may note a series of radial mean velocity distribution profiles along the jet axis that are representative of flows in the presence of shock and expansion waves formed in the flow under the given aerodynamic conditions. Corresponding radial traverses with Model 2 are presented in Figure 6-22. The top-hat shape profiles which are typical for subsonic jets, indicating an isentropic expansion of the flow, is indicated in this figure.

The radial distributions of the mean velocity downstream of the plug for the suppressor nozzles are presented in Figures 6-23 and 6-24. Figure 6-23 illustrates the radial variations of the mean velocity for the convergent multi-element suppressor plug nozzle (Model 5) both at static and simulated flight conditions. Selected aerodynamic conditions correspond to the C-D design conditions of its C-D counterpart (Model 6). Two hump profile observed in this figure is due to the presence of the center plug. The free-jet flow is observed to stretch the profile in the axial direction. Similar results obtained with the C-D multi-element suppressor plug nozzle (Model 6) are presented in Figure 6-24. A comparison of the results between Figures 6-23 and 6-24 indicates that due to the turbulence-shock interaction some amount of energy was extracted from the mean flow near the plug surface and, consequently, the mean velocity of Model 5 is appreciably lower than that of Model 6.

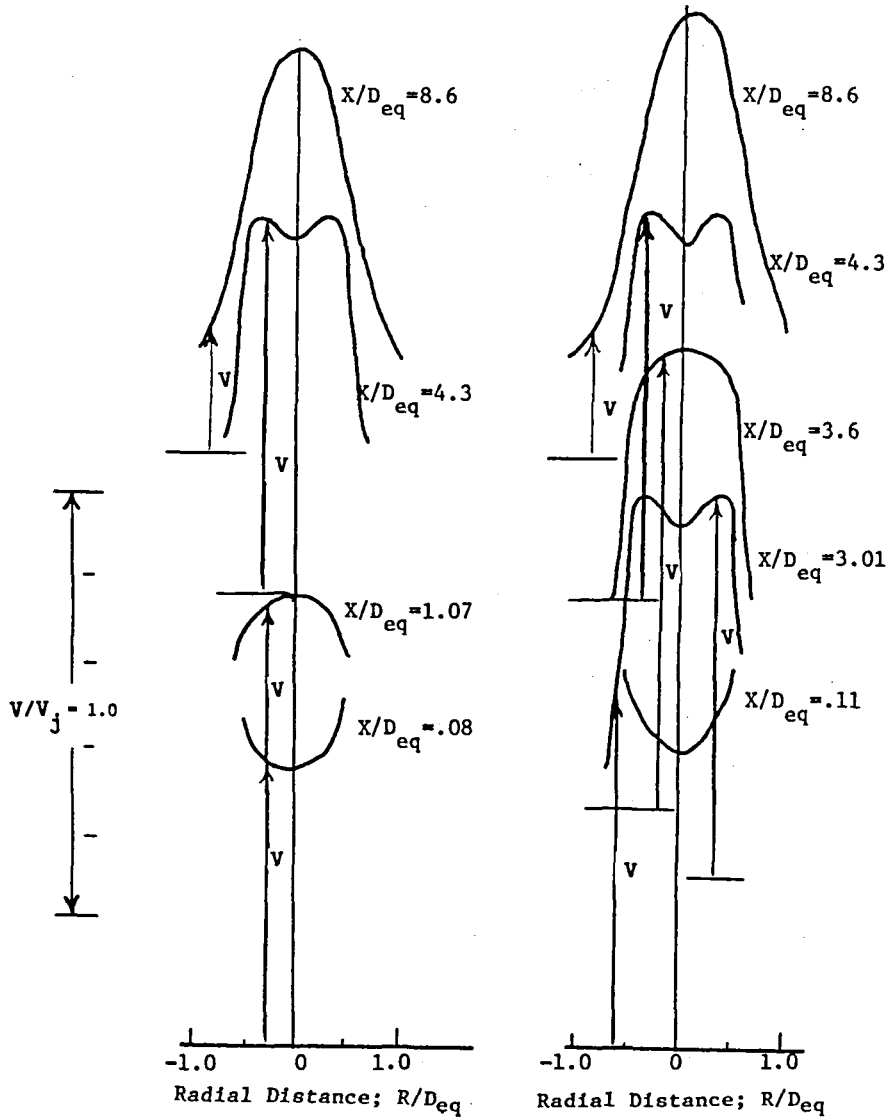
6.1.2 MEAN AND TURBULENT FLOW PROPERTIES IN TURBULENT SHEAR LAYER

By comparing the axial mean velocity and turbulent velocity distributions on the lip-line of C-D nozzles with those encountered with convergent nozzles, certain important features concerning the downstream development of supersonic turbulent mixing layer can be displayed. First, a comparison is made between the C-D circular nozzle and its convergent counterpart at the C-D design point, the results of which are presented in

Model	Test Point	P_r	$T_{T'}^{\circ} (R)$	V_j (f/s)	$V_{a/c}$ (f/s)
1	113	3.128	1703	2402	0
i	114	3.128	1734	2425	400

T.P. 113

T.P. 114



$D_{eq} = 5.09$ In.

Figure 6-21. Radial Distribution of Mean Velocity for the Baseline Convergent Circular Nozzle (Model 1).

Model	Test Point	P_r	T_T , (°R)	V_j (ft/s)	V_z/c (ft/s)
2	213	3.121	1708	2403	0
2	214	3.121	1716	2409	400

T.P. 213

T.P. 214

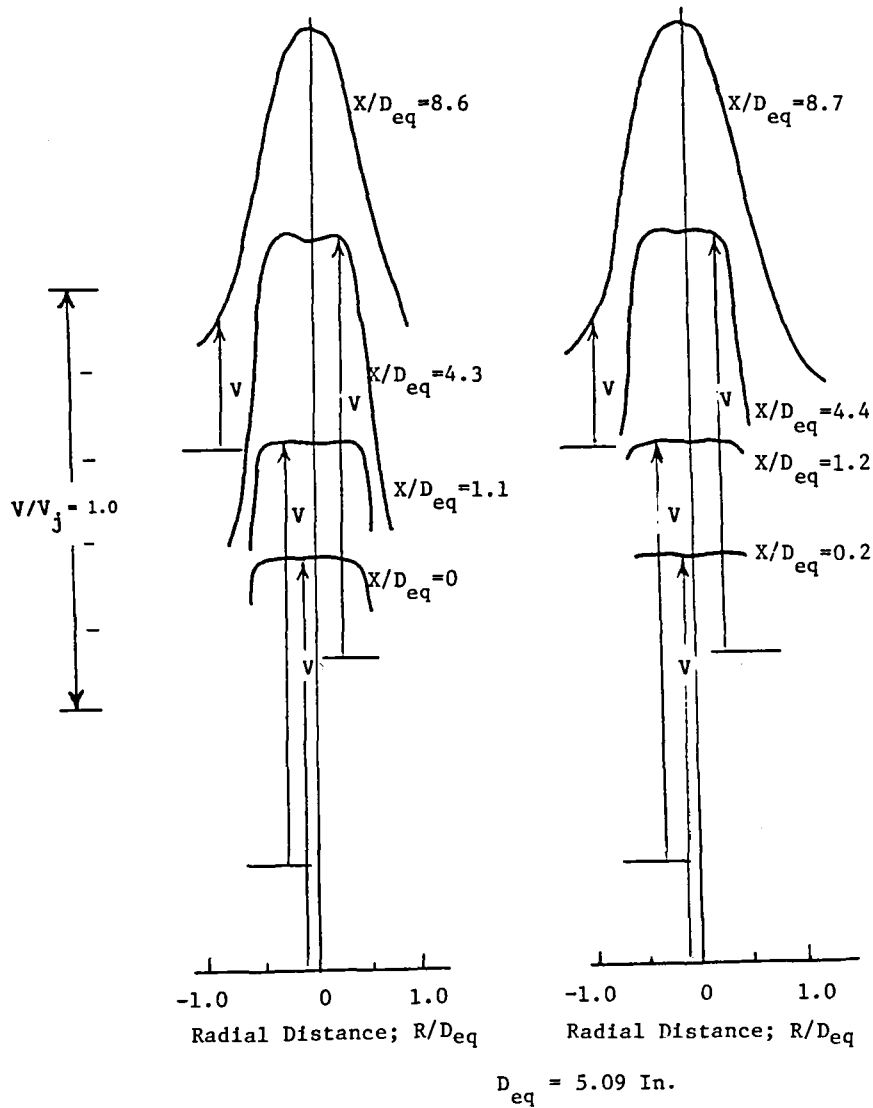
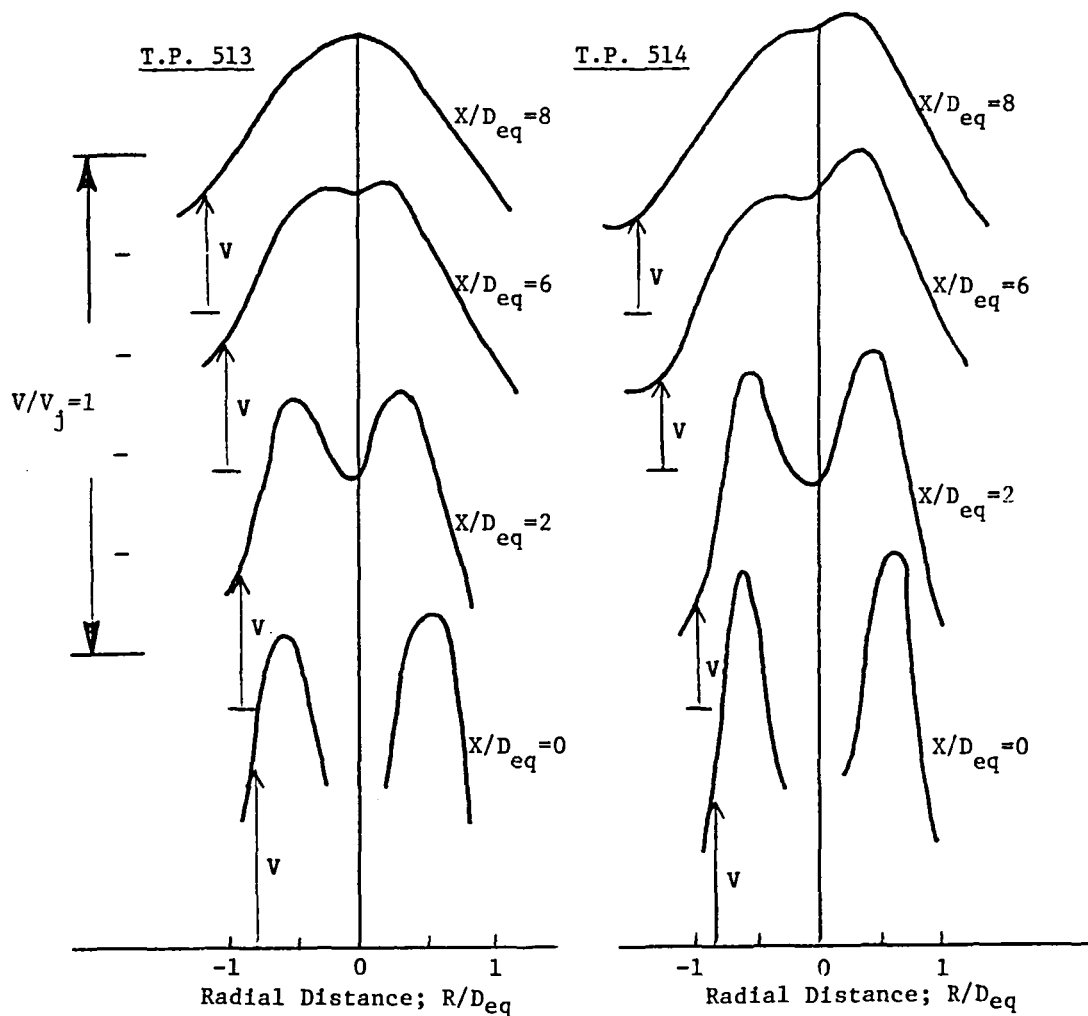


Figure 6-22. Radial Distribution of Mean Velocity for the C-D Circular Nozzle at Design Conditions (Model 2).

Model	Test Point	P_r	T_T , (°R)	V_j (f/s)	$V_{a/c}$ (f/s)
5	513	3.123	1732	2421	0
5	514	3.128	1722	2415	400



$D_{eq} = 5.03$ In.

Figure 6-23. Radial Distribution of Mean Velocity Downstream of the Plug: Convergent Multi-Element Suppressor Plug Nozzle (Model 5).

Model	Test Point	P_r	$T_{T'} (^\circ R)$	V_j (ft/s)	$V_{a/c}$ (ft/s)
6	613	3.128	1728	2420	0
6	614	3.125	1729	2419	400

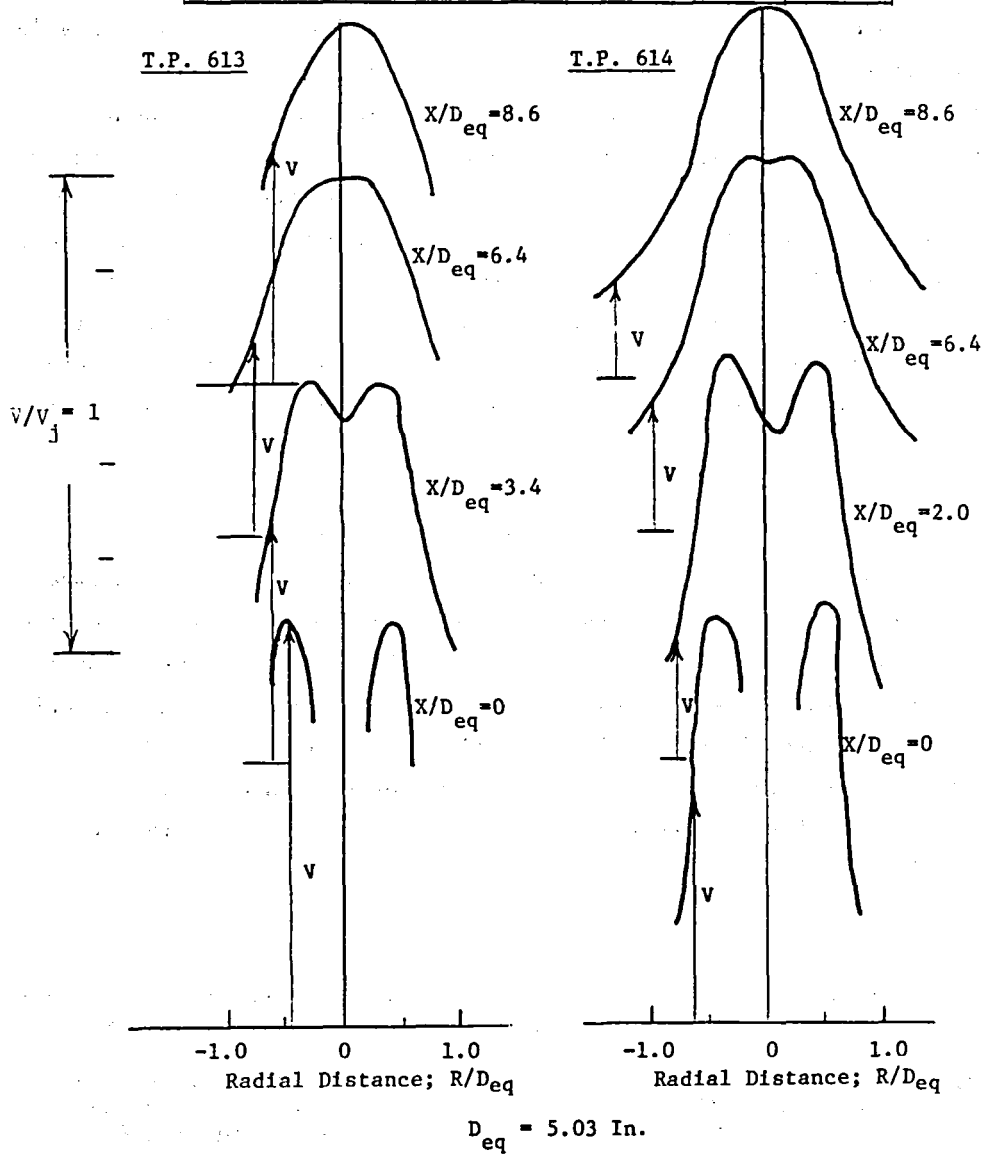


Figure 6-24. Radial Distribution of Mean Velocity Downstream of the Plug: C-D Multi-Element Suppressor Plug Nozzle (Model 6).

Figure 6-25 as a composite of the curves for the axial mean velocity and turbulence intensity distributions measured on the lip-line* at static conditions.** We note, in Figure 6-25, that at least four (4) shocks are observed for the convergent nozzle while a nearly shock-free pattern is seen for the C-D nozzle. It appears that at the end of each compression cycle the flow velocity converges to that obtained in the shock-free flow. Furthermore, the peak turbulence levels for shock-containing flow appears to locate near the end of a compression cycle and the minimum levels occur near the end of an expansion cycle.† These observations have been reported by Seiner and Norum in some detail in Reference 5-19. The turbulence level for a shock-free case is likely to be an average of the turbulence level of the shock-containing flow. A rather low turbulence level observed over the first one jet diameter of the convergent nozzle may be attributed to the fact that the supersonic mixing layer is extremely thin in this flow region and located off the lip-line.

Figure 6-26 presents the corresponding simulated flight cases for the convergent and C-D circular nozzles. Similar observations to those mentioned above can be made based on the results shown in this figure concerning general features of shock formation and shock-turbulence interactions. Some remarks, however, should be made in regard to observed differences between Figure 6-25 and Figure 6-26. A significant low level of the axial mean velocity distributions observed over the first five jet diameters downstream of the C-D nozzle exit was identified to be due to a slight offset of the LV traverse location away from the lip-line.

*As mentioned earlier, the equivalent lip-line traverse is defined as an axial traverse offset from the nozzle axis by one-half of equivalent diameter.

**The data presented on all of these figures are measured minihistogram LV data which get plotted as dots on the x-y plotter. When two sets of LV data are shown on one figure, then the data of one set (as obtained in dot form) is super-imposed by the second set (indicated by line obtained by a smooth curve drawn through the dots). The turbulence data were obtained from histograms.

†These maximum turbulence levels are primarily associated with mid to high frequency turbulence components, as pointed out in Reference 5-21.

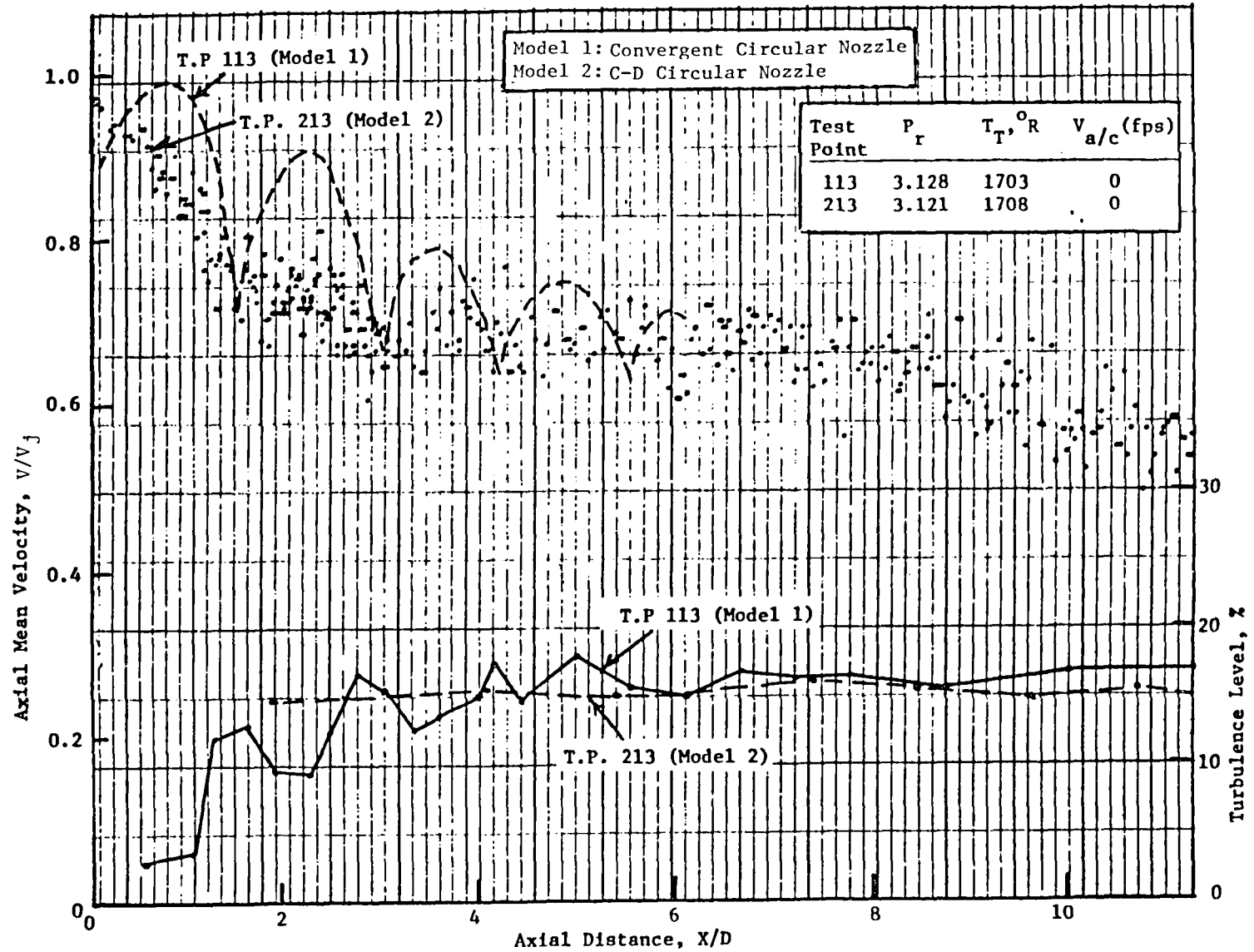


Figure 6-25. Comparison of Axial Mean Velocity and Turbulence Intensity Distributions Along Lip-Line for Shock Free and Shock Containing Cases: Model 1 and Model 2 - Static Test.

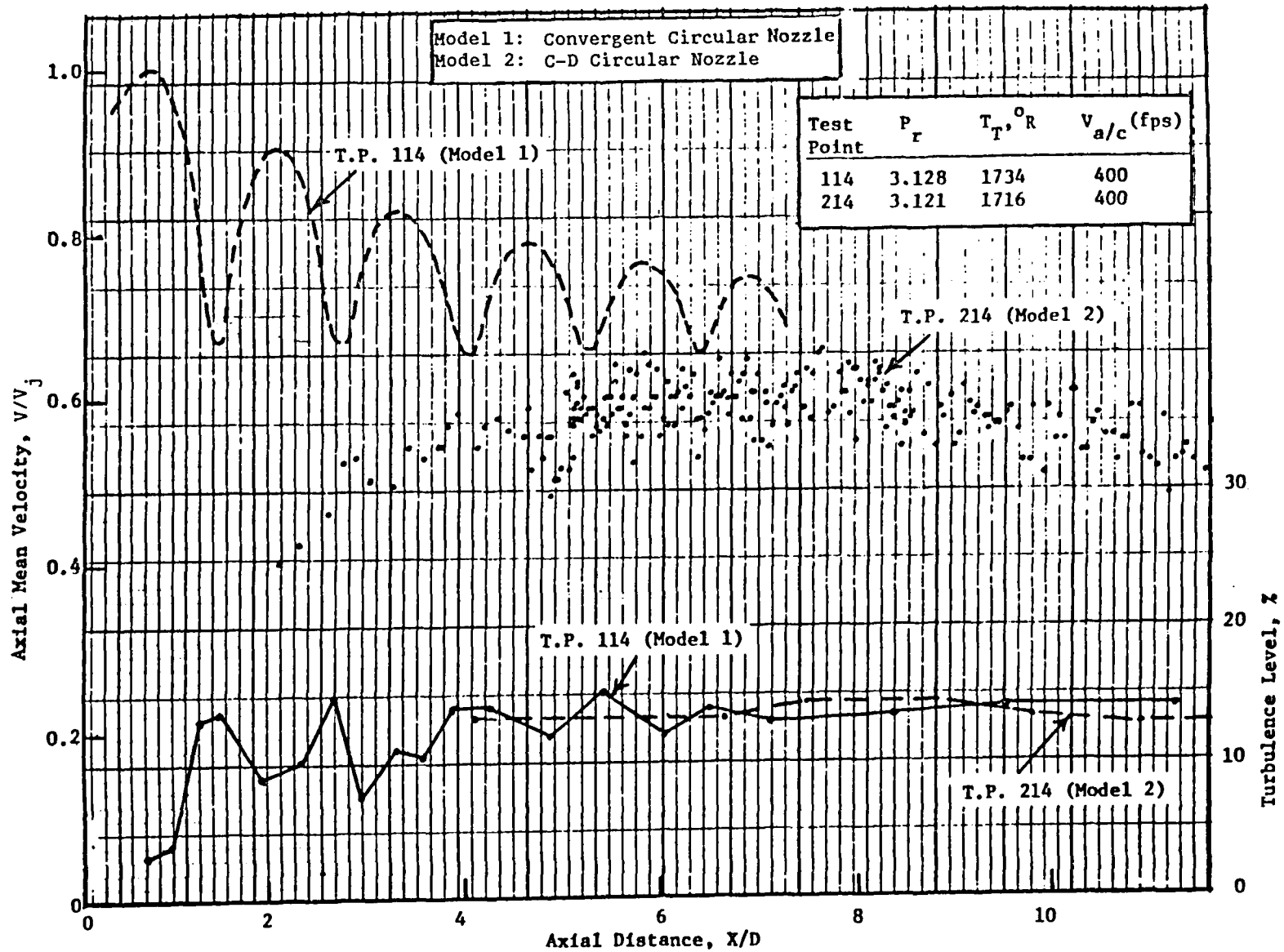


Figure 6-26. Comparison of Axial Mean Velocity and Turbulence Intensity Distributions Along Lip-Line for Shock Free and Shock Containing Cases: Model 1 and Model 2 - Simulated Flight Test.

It was noted earlier from Figure 6-1 that under the aerodynamic conditions of Test Point 113, eight (8) shocks were formed on the jet axis. However, referring to Figure 6-25, only the first four (4) or five (5) of these shocks are noted along lip-line. This, therefore, raises a question regarding the number of shocks that should be taken into account in a shock-cell noise prediction model.*

Figure 6-27 and Figure 6-28 represent similar mean velocity distributions in the lip-line parallel to the slant plug surface for the convergent and C-D annular plug nozzles. Due to lack of enough number of turbulence histograms to define the distribution of turbulence level, no turbulence data are given in these figures. The distance along the plug surface is normalized by the hydraulic diameter which is defined as four times the annulus area divided by the outer perimeter. The features of the oscillatory mean velocity distributions of shock-containing plumes for the circular nozzle, i.e., at the end of each compression cycle the mean velocity in the lip-line converges to that obtained in the shock-free plume, is also confirmed in the results shown in Figure 6-28, though in the static case (Figure 6-27) this is not very clear.

The supersonic turbulent mixing layer of the convergent and C-D multielement suppressor nozzle jets were also examined. Some representative results are illustrated in Figures 6-29 through 6-32. In contrast to the higher temperature jet plumes so far discussed, lower temperature test points were selected for the present study with the suppressor nozzles.

The lip-line mean velocity and turbulence level distributions parallel to the plug surface under static conditions are depicted in Figure 6-29, where the distance along the plug surface is normalized by the nozzle annulus height. In the case of the convergent suppressor nozzle, at least five (5) shocks are clearly observed. The turbulence levels of this convergent suppressor nozzle appear to be affected by the presence of shocks over the first four annulus heights from the core exit.

*Harper-Bourne and Fisher (Reference 5-3) model assumes the total number of shock-cells to be eight (8) for a conical nozzle.

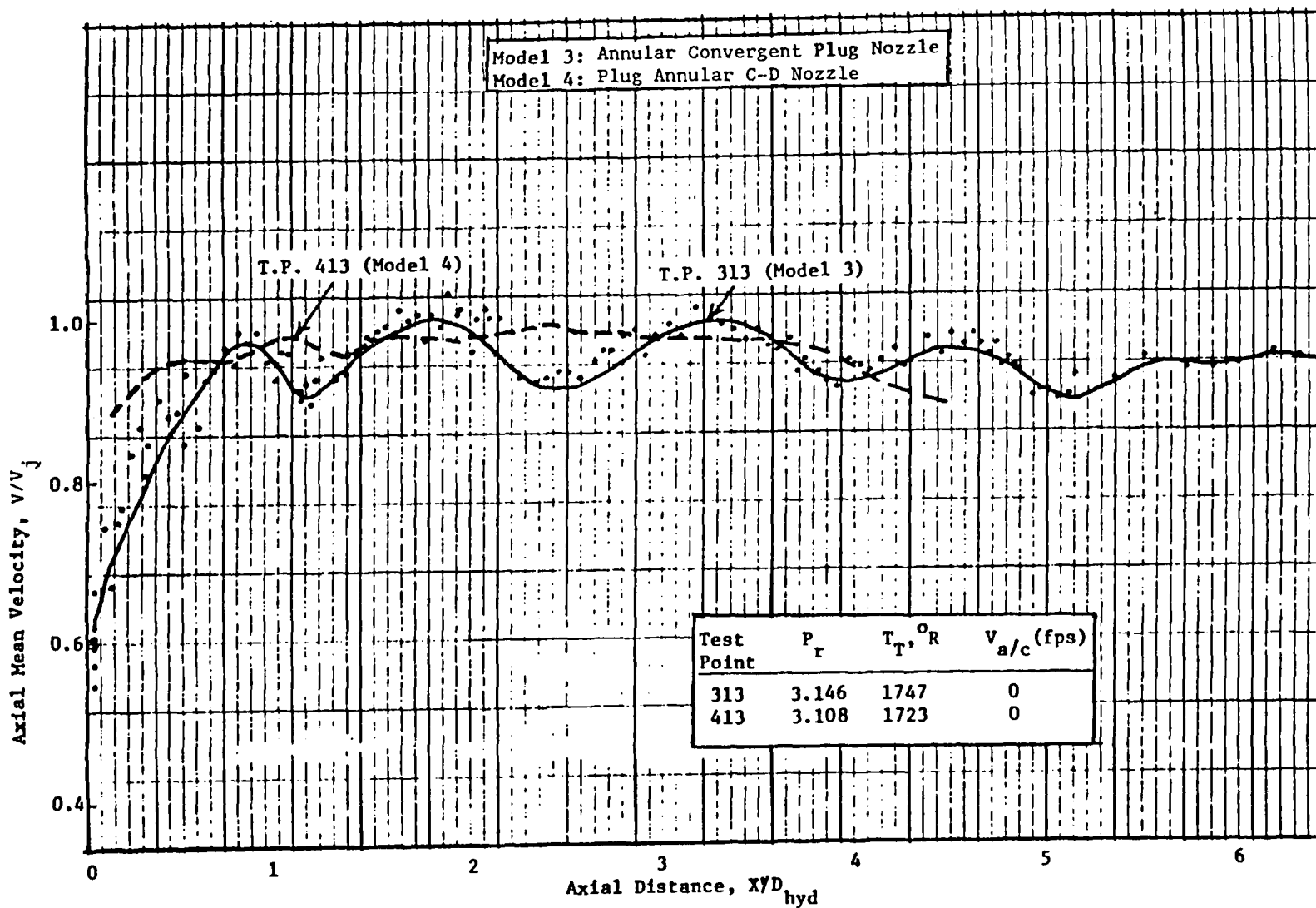


Figure 6-27. Comparison of Axial Mean Velocity Distributions Along Lip-Line for Shock Free and Shock Containing Cases: Model 3 and Model 4, On Plug Surface - Static Test.

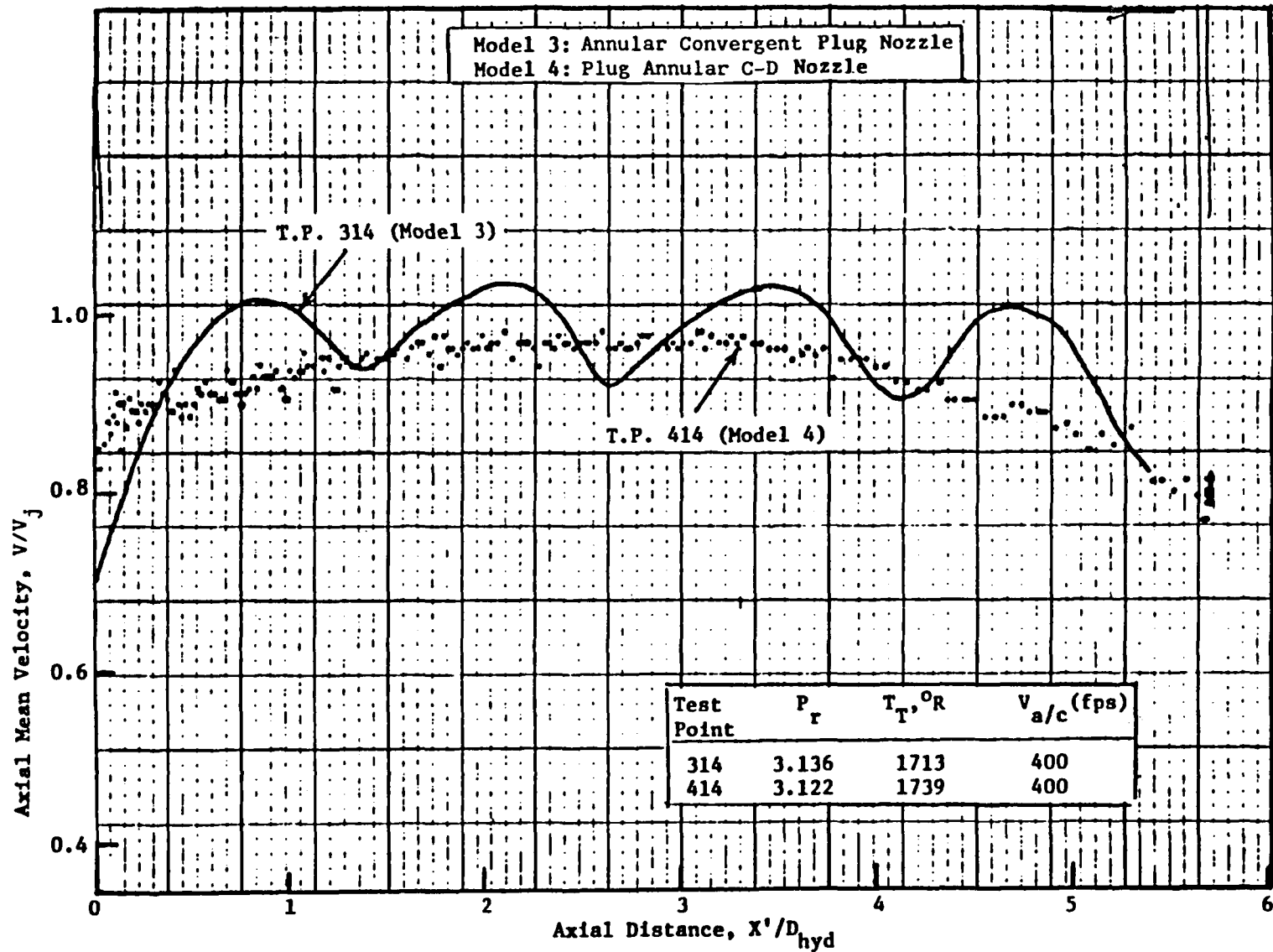


Figure 6-28. Comparison of Axial Mean Velocity Distribution Along Lip-Line for Shock Free and Shock Containing Cases: Model 3 and Model 4, On Plug Surface - Simulated Flight Test.

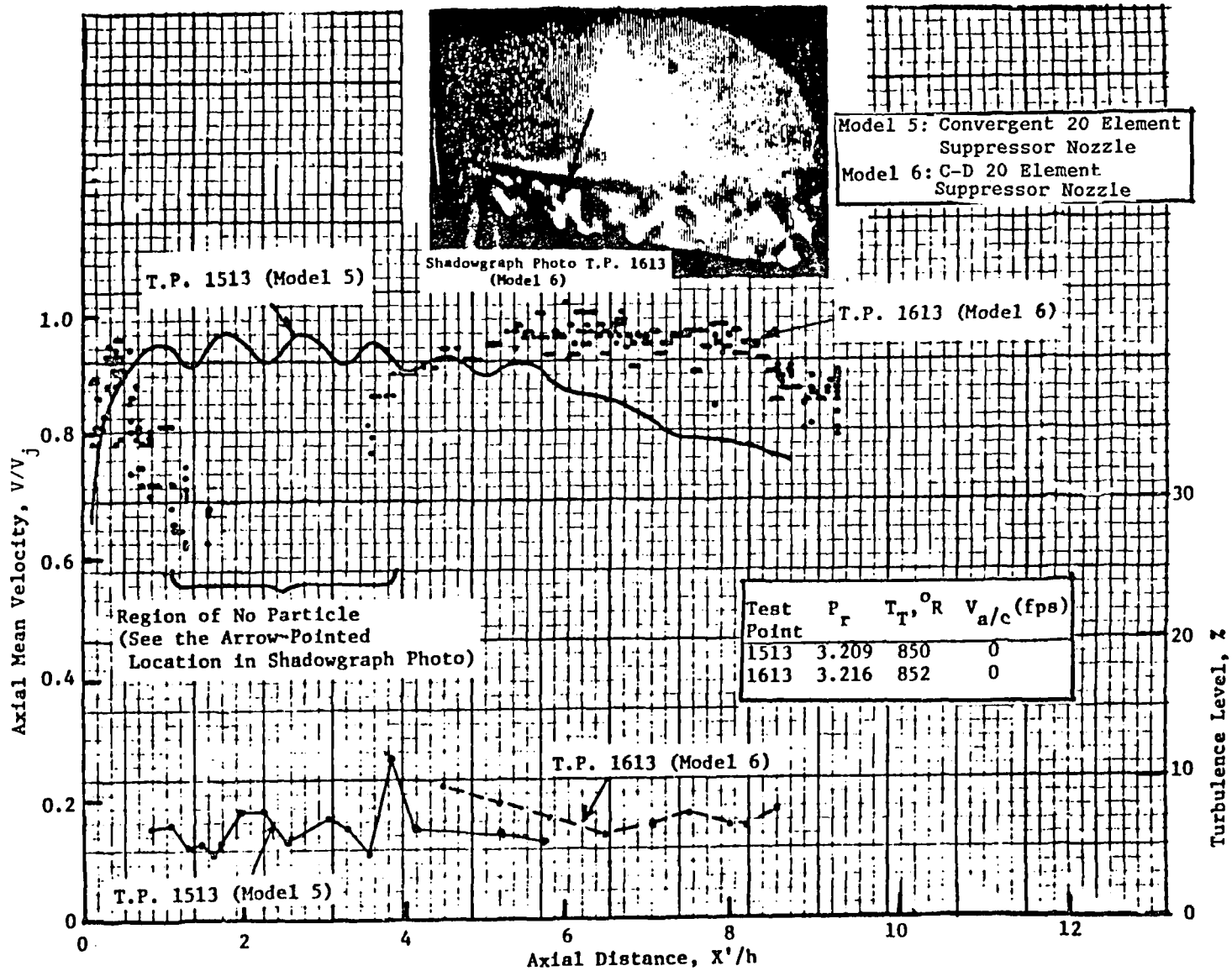


Figure 6-29. Comparison of Axial Mean Velocity and Turbulence Intensity Distributions Along Lip-Line for Shock Free and Shock Containing Case: Model 5 and Model 6, On Plug Surface - Static Test.

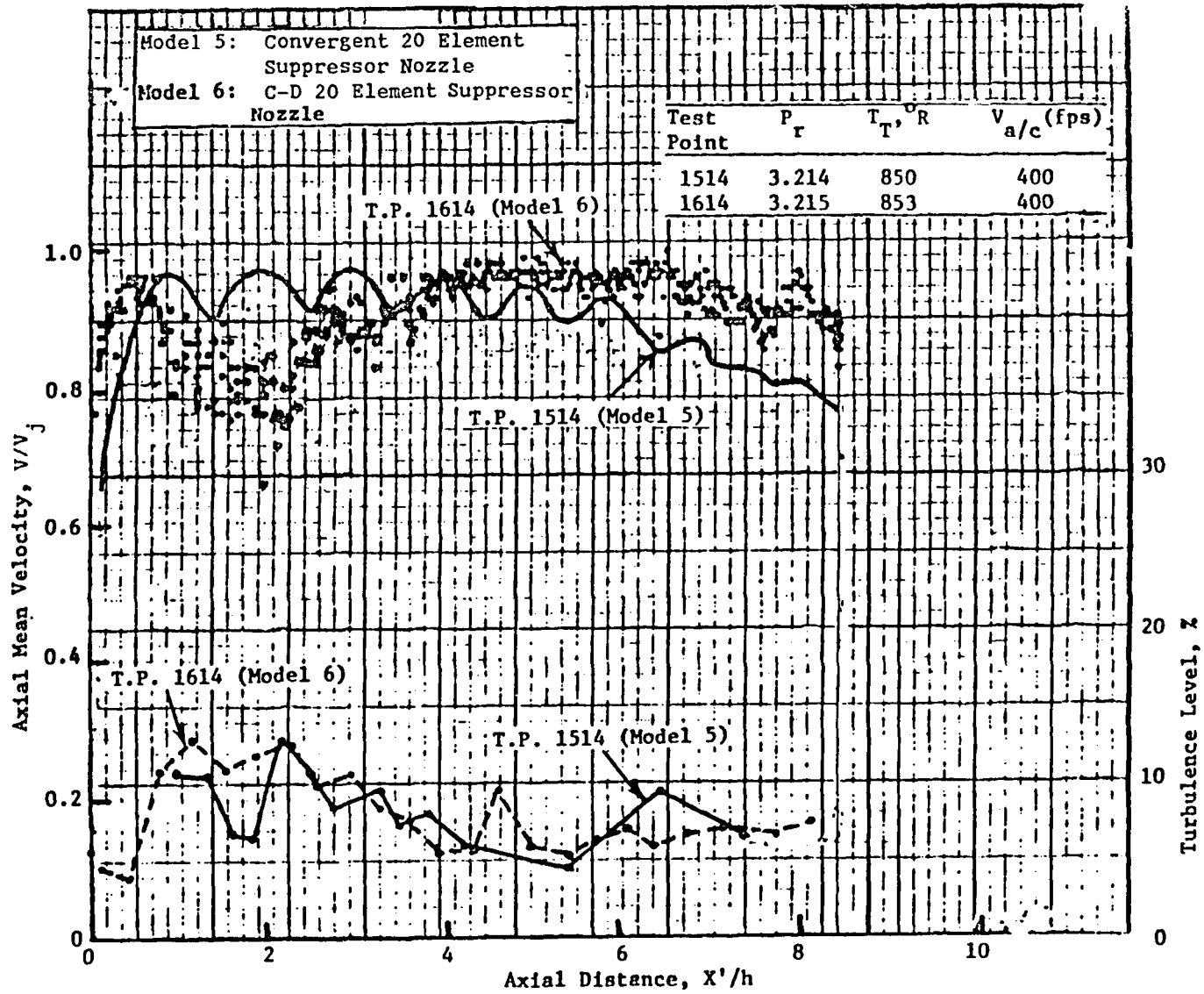


Figure 6-30. Comparison of Axial Mean Velocity and Turbulence Intensity Distributions Along Lip-Line for Shock Free and Shock Containing Cases: Model 5 and 6, On Plug Surface - Simulated Flight Test.

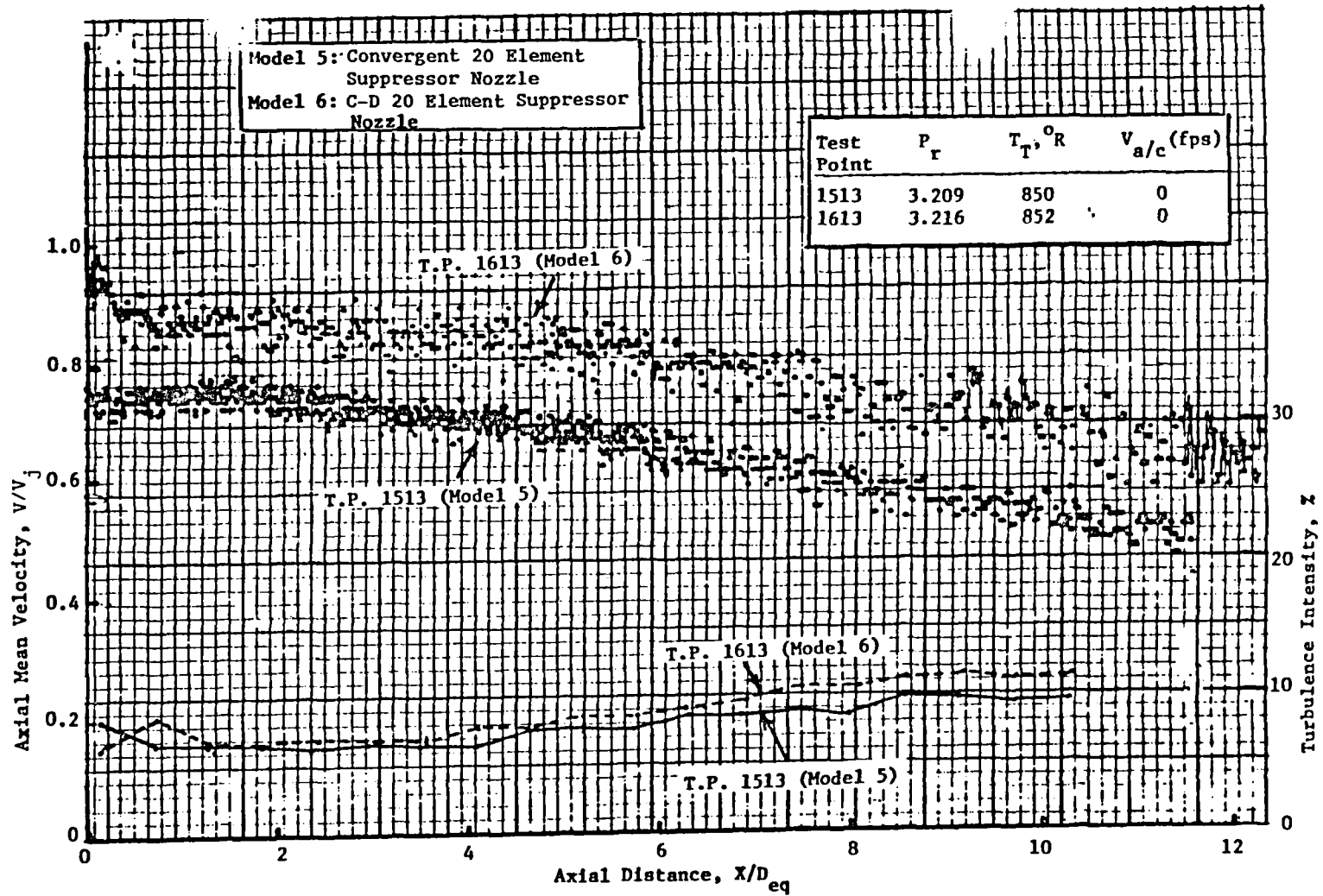


Figure 6-31. Comparison of Axial Mean Velocity and Turbulence Intensity Distributions Along Lip-Line for Shock Free and Shock Containing Cases: Model 5 and Model 6, Downstream of Plug - Static Test.

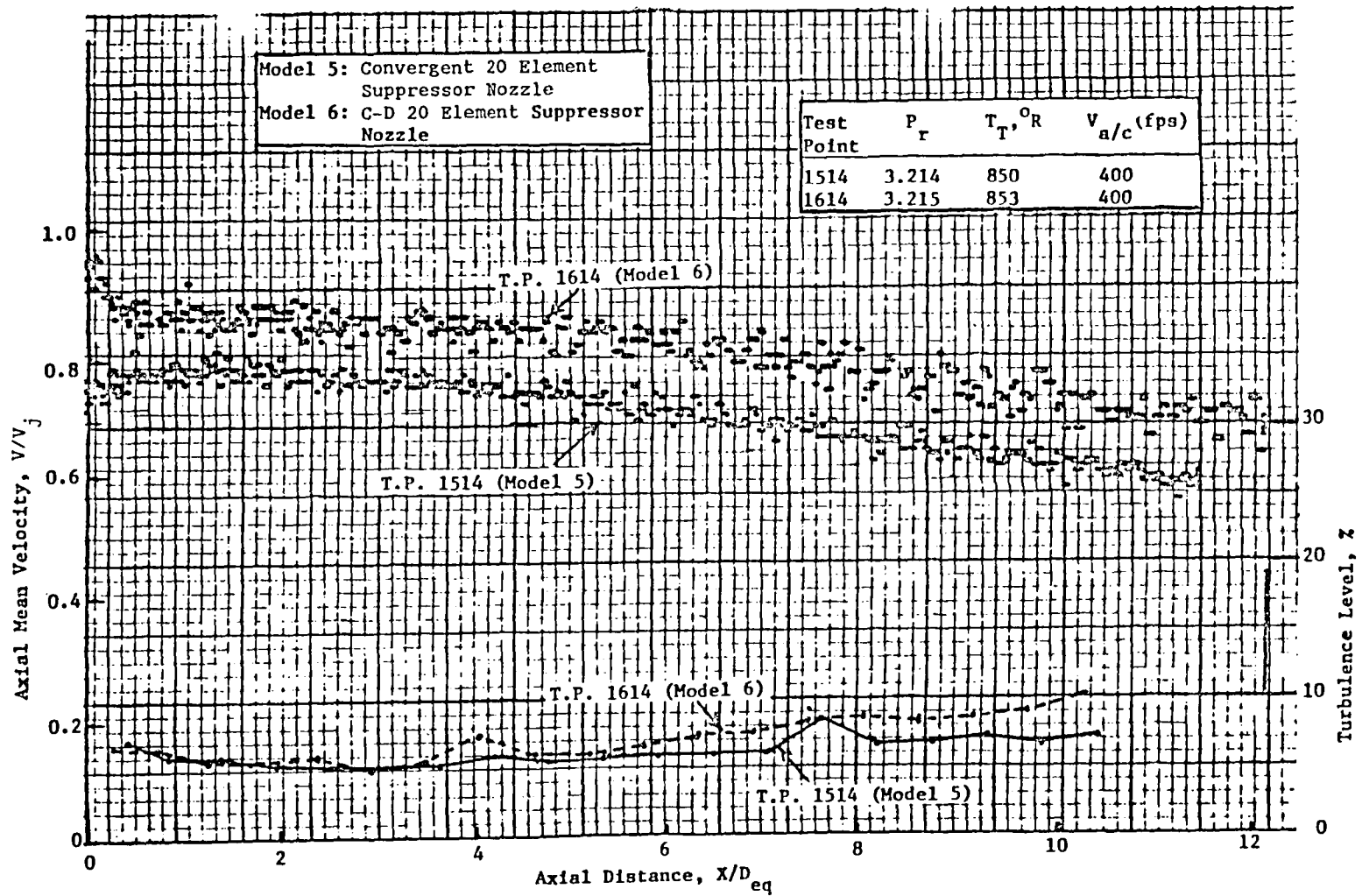


Figure 6-32. Comparison of Axial Mean Velocity and Turbulence Intensity Distributions Along Lip-Line for Shock Free and Shock Containing Cases: Model 5 and Model 6, Downstream of Plug - Simulated Flight Test.

The distributions of the mean velocity parallel to the plug surface for the C-D suppressor nozzle shows a rather complex pattern at the given test point. As is observed in the attached shadowgraph photo (see Figure 6-29), the plume appears to be squeezed at approximately two annulus heights downstream of the exit plane, so that the lip-line mean velocity traverse (which is parallel to the plug surface) may possibly be outside of the supersonic shear layer in this flow region.

Although the shock-cell patterns observed for Test Point 1613 (or Test Point 1614) are not so evident as those for Test Point 1513 (or Test Point 1514), the plume is not likely to be perfectly expanded in the former case. This could also be seen from the rather oscillatory turbulence intensity distributions in the lip-line (Figure 6-29 and Figure 6-30). Hence, it may not be appropriate to consider Test Point 1613 (or 1614) as a shock-free case.

Figure 6-30 represents the simulated flight counterpart of Figure 6-29. Comparison of Figure 6-30 with Figure 6-29 indicates that with simulated flight more shocks in the lip-line flow region are noted, as compared with the static case.

Lip-line flow field downstream of the plug for the suppressor nozzles is analyzed in Figure 6-31 (static) and Figure 6-32 (flight). A practically shock-free flow pattern is observed for the convergent suppressor nozzle (Model 5), while formation of weak shock-cells is noted for the C-D suppressor nozzle (Model 6). However, in the latter case, the observed shocks do not appear to be strong enough to modify the incoming turbulent eddies. It should be noted that Model 6 shows higher mean and turbulent velocity levels than Model 5, and this should be certainly correlated to the radiation field intensity, particularly in the directions near the downstream jet axis. It is interesting to note, comparing Figure 6-31 with Figure 6-32, that the simulated flight case has a slightly higher mean velocity level over the static case; nevertheless, a lower turbulence level is observed over the entire flow region downstream of the plug for the flight case. This is, of course, due to the reduced mean shear caused by the addition of free-jet flow.

Until now, discussions have been limited to the test points at C-D nozzle design operating conditions. In what follows test results of a limited number of test points at off-design conditions are discussed. Figures 6-33

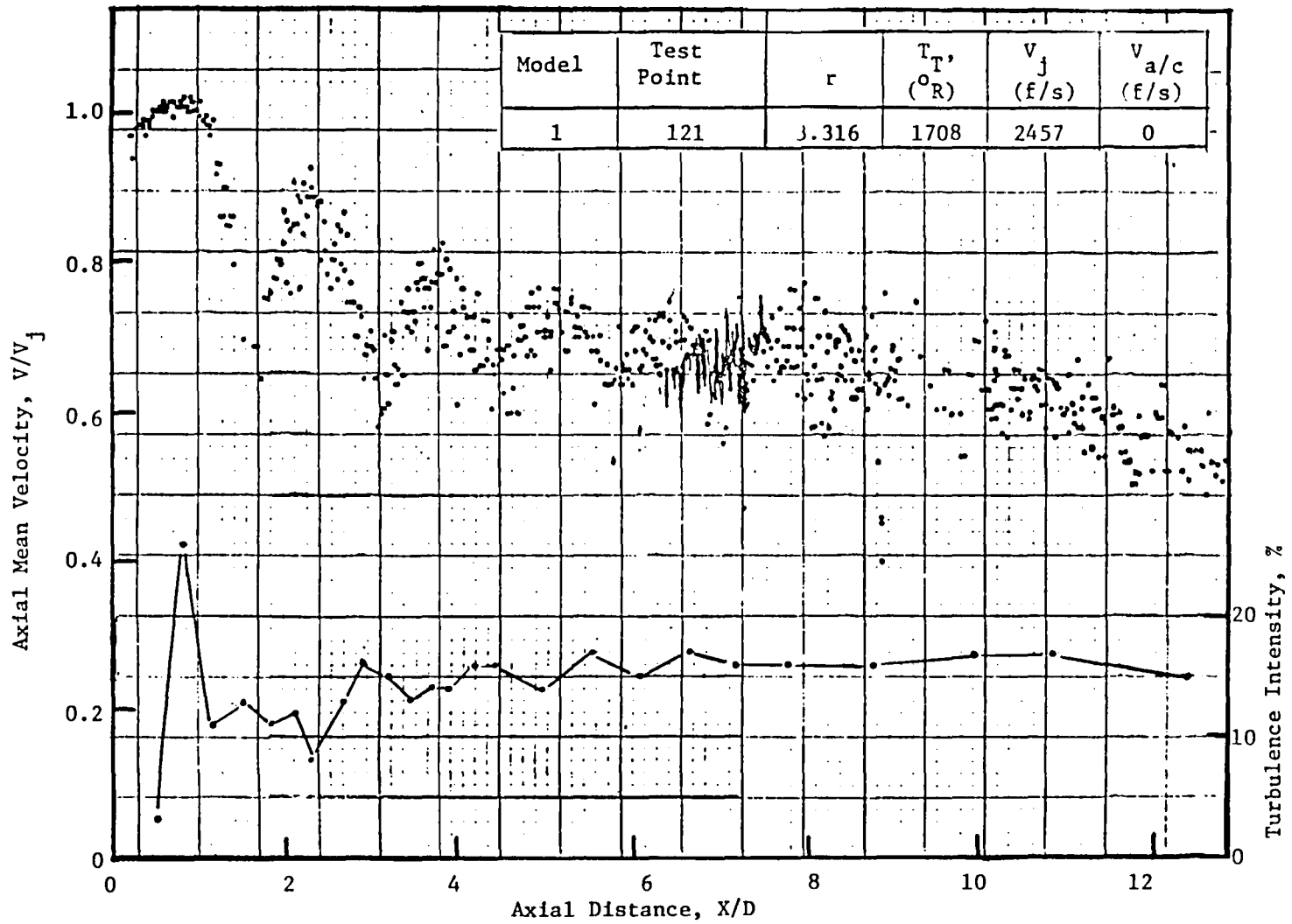


Figure 6-33. Axial Mean Velocity and Turbulence Intensity Distributions Along Lip-Line for Shock Containing Flow; Baseline Convergent Circular Nozzle (Model 1) - Static Test.

and 6-34 represent the axial mean velocity and turbulent velocity distributions for the baseline convergent circular nozzle (Model 1) at static and simulated flight conditions, respectively. Since Model 1 is a nozzle with the convergent flowpath termination, general flow field characteristics observed in the results presented in Figures 6-33 and 6-34 should be basically similar to those observed in Figures 6-25 and 6-26. Due to a higher pressure ratio, of course, the results presented in Figures 6-33 and 6-34 should show stronger shocks; and, therefore, more shocks should be detected both at static and simulated flight conditions. Corresponding test results with Model 2, circular C-D nozzle are presented in Figures 6-35 and 6-36. It should be noted, by comparing Figures 6-35 and 6-36 with Figures 6-33 and 6-34, that although the plume was underexpanded at the given test points, the circular C-D nozzle (Model 2) had much weaker shocks as compared with the baseline convergent circular nozzle (Model 1). For this reason, the observed forward quadrant noise level of the C-D circular nozzle at these test points is identified to be lower than the corresponding noise level for the baseline convergent circular nozzle, as is observed in Figures 5-1 and 5-3.

Major results of the present flow-field survey by the laser velocimeter which have been discussed above are summarized below:

Centerline Mean Velocity Distribution

For the baseline convergent circular nozzle (Model 1), eight shocks were observed on the jet axis, under the test conditions that match the design condition of C-D nozzle (Model 2). At the C-D design condition, the C-D circular nozzle was identified to be shock-free. At the C-D design conditions, the C-D annular plug nozzle was found to form shocks downstream of the plug, though near the jet exit (and on the plug) it was identified to be practically shock-free.

The downstream flow regions of the convergent and C-D multi-element suppressor nozzle were identified to be practically shock-free. The level of the centerline mean velocity downstream of the plug was found to be significantly sensitive to the flowpath geometry of the suppressor chute.

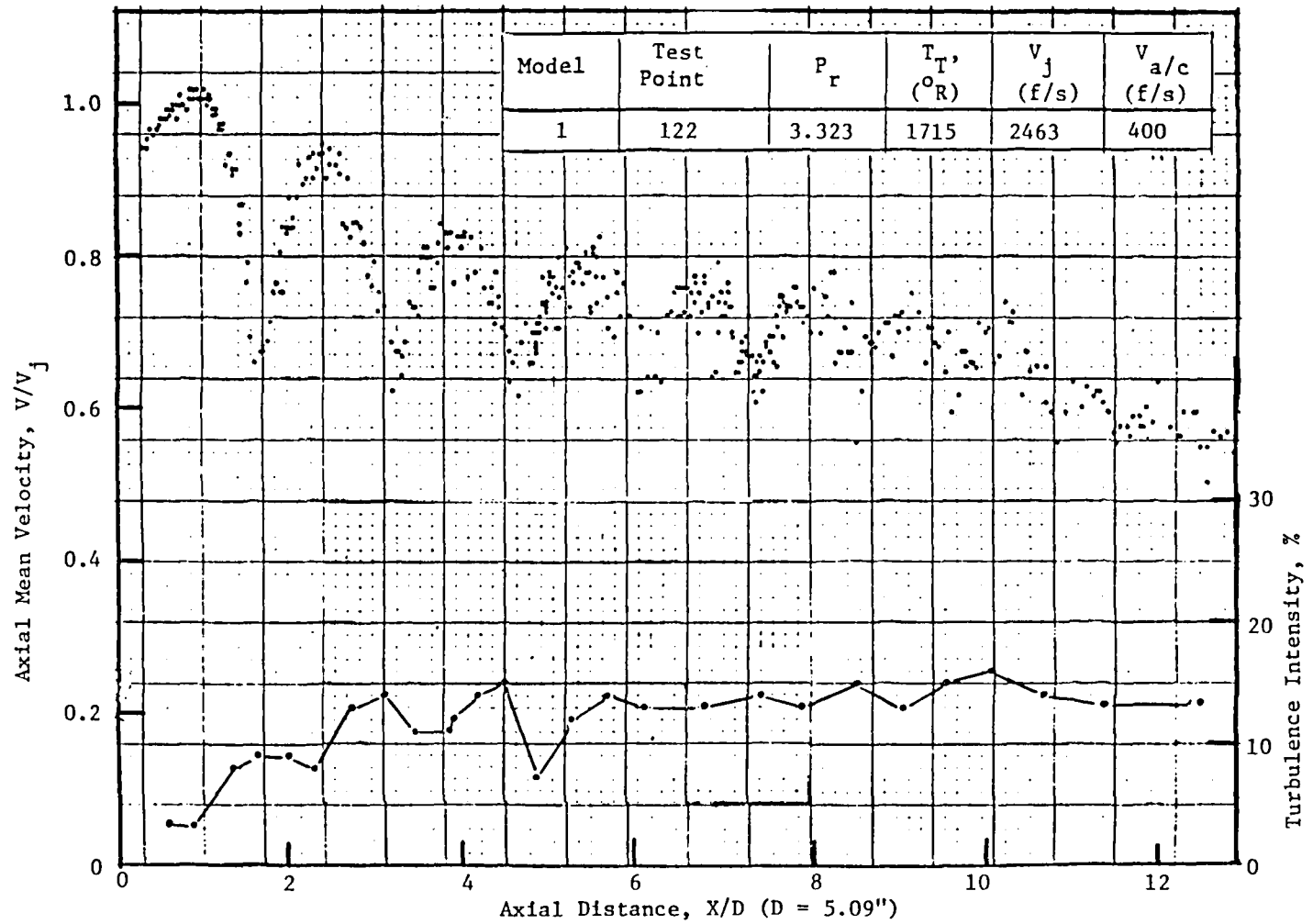


Figure 6-34. Axial Mean Velocity and Turbulence Intensity Distributions Along Lip-Line for Shock Containing Flow; Baseline Convergent Circular Nozzle (Model 1) - Simulated Flight Test.

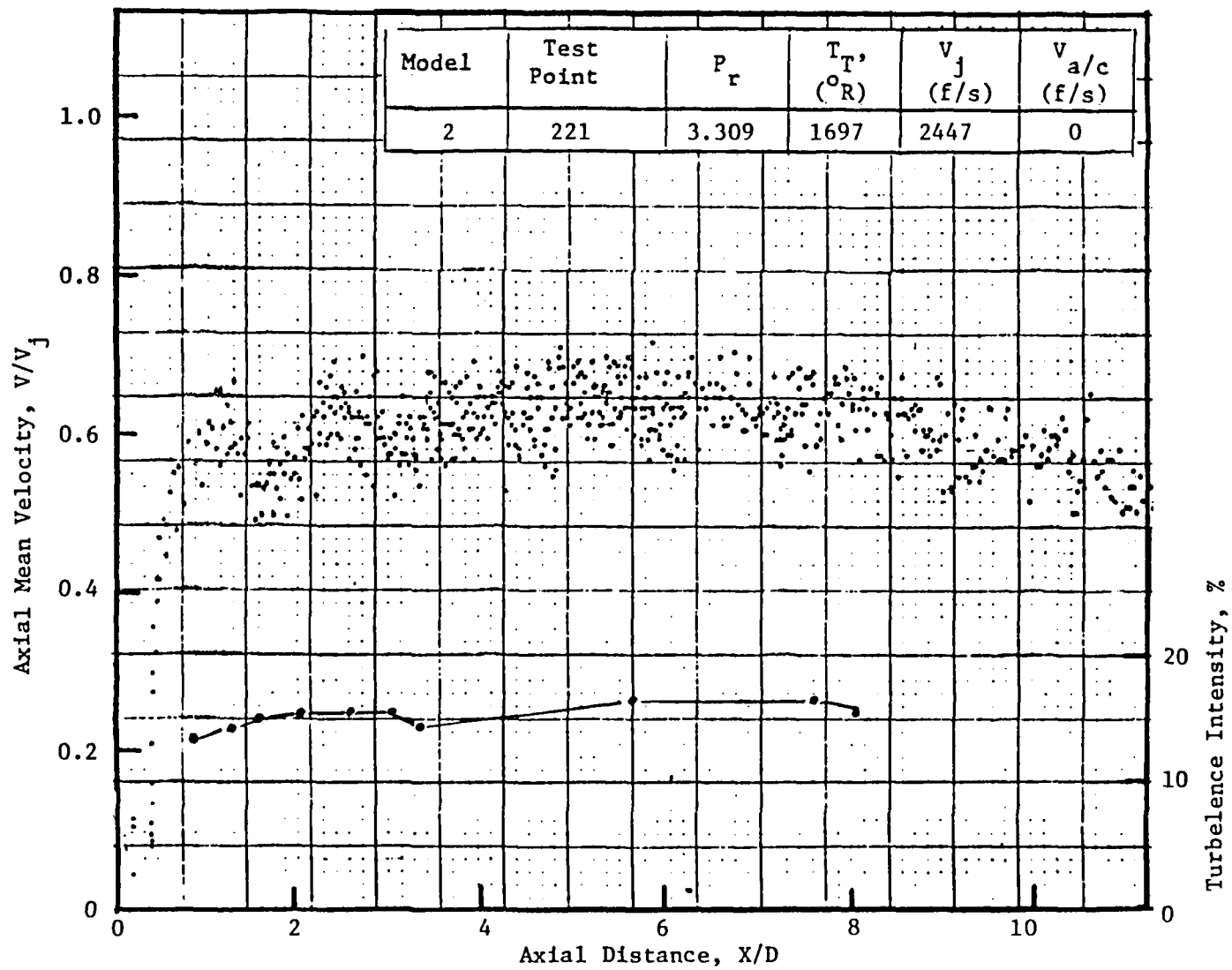


Figure 6-35. Axial Mean Velocity and Turbulence Intensity Distributions Along Lip-Line for Shock Containing Flow; C-D Circular Nozzle (Model 2) - Static Test.

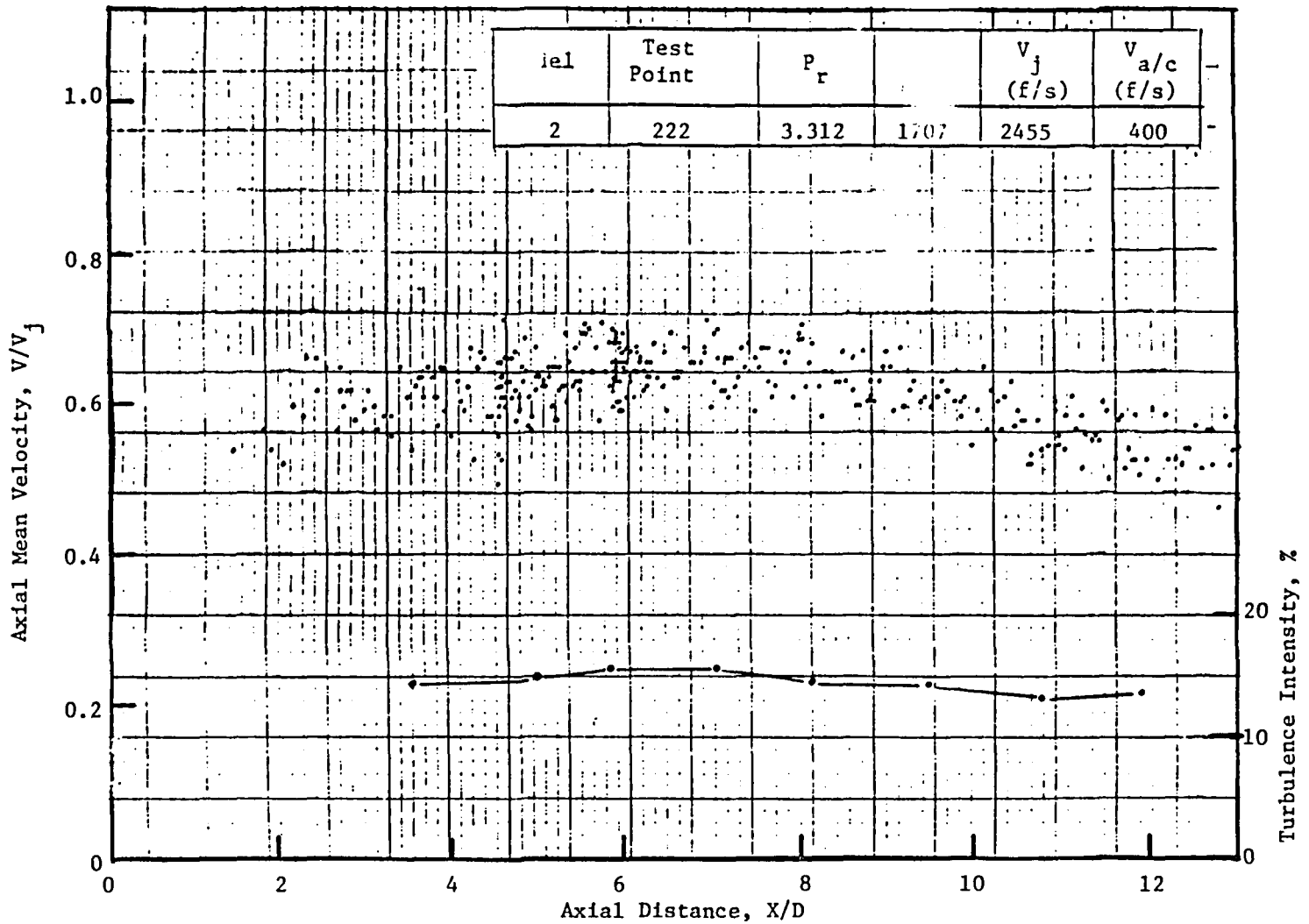


Figure 6-36. Axial Mean Velocity and Turbulence Intensity Distributions Along Lip-Line for Shock Containing Flow; C-D Circular Nozzle (Model 2) - Simulated Flight Test.

Free-jet flow tends to stretch shock-cell spacing axialwise.

Radial Variations of Mean Velocity Distributions

At the C-D design condition, the radial mean velocity distribution profile for the C-D circular nozzle was found to be almost identical to that of a typical subsonic jet.

Lip-Line Mean and Turbulent Velocity Distributions

On the lip-line, at the end of each compression cycle, the local axial mean velocity in the shock-containing flow converges to that obtained in the shock-free flow.

For the circular nozzles it was observed that turbulence levels of the shock-free flow give average values of the turbulence level of the shock-containing flow. It was also noted for the convergent circular nozzle that peak turbulence level on the lip-line occurs near the end of the compression cycle, whereas a minimum level is observed near the end of the expansion cycle.

Judging from the fluctuating turbulence intensity distribution profile obtained from the lip-line traverse of the convergent circular nozzle, four to five shocks appear to interact with turbulent eddies.

6.2 SHADOWGRAPH PHOTO TEST RESULTS

Diagnostic flow visualization shadowgraph photos were taken for six model nozzles. In this subsection, some representative shadowgraph photos* are presented with the aim to illustrate the effectiveness of the convergent-divergent termination in the flowpath of the C-D nozzles. Consequently, selected photos are limited to those corresponding to the plumes whose pressure ratio is equal to the C-D design pressure ratio (or for convergent nozzles, matched to the C-D design pressure ratio of their C-D counterparts).

*For exact locations of the presented shadowgraphs, refer to the test matrix of shadowgraph photo testing given in Appendix III.

Figures 6-37 and 6-38 represent shadowgraph photos taken near the jet exit of the baseline convergent circular nozzle (Model 1) with and without free-jet flow. Apparently a system of compression and expansion waves emanating from the nozzle lip is noted in the flow which is produced to accommodate rapid variation in the mean pressure occurring at the nozzle exit. The shadowgraphs under simulated flight conditions appear to have more clarity, in general.

Corresponding shadowgraph photos of the C-D circular nozzle are presented in Figures 6-39 and 6-40 where the aerodynamic conditions of the plumes correspond to the C-D design condition of the nozzle. It should be noted that strong shocks observed for the baseline convergent circular nozzle are eliminated.

Shadowgraph photos taken with the convergent and C-D annular plug nozzles with and without free-jet flow are presented in Figures 6-41 through 6-44. The aerodynamic flow conditions of the plumes correspond to the C-D design condition of the C-D annular plug nozzle. In these figures, we observe the shock-cell structure on the plug surface and an expansion fan near the plug tip which indicates possible shock noise emission from the downstream of the plug. In the case of the C-D annular plug nozzle (Figures 6-43 and 6-44), the shocks observed on the plug appear to be significantly weaker than those for the convergent annular plug nozzle (also demonstrated by the LV data of Figures 6-27 and 6-28). This is attributed to the C-D termination in the flowpath of the C-D annular plug nozzle. However, as indicated by expansion waves observed near the plug tip, the C-D termination in the nozzle flowpath is not enough for the plug nozzles completely to suppress shocks. Figures 6-45 and 6-46 illustrate the static and simulated flight axial mean velocity distributions on the jet axis downstream of the plug obtained by LV measurements for the C-D annular plug nozzle where the aerodynamic flow conditions are almost identical to those shown in Figures 6-43 and 6-44. Although not significantly strong, five to six shocks are observed in these figures. Also, the centerline mean velocity maintains its supersonic speed as far as ten equivalent jet diameters.*

*Sonic velocity corresponds to $V/V_j \approx 0.7$.

Model	Test Point	P_r	$T_{T'}$ (°R)	V_j (f/s)	$V_{a/c}$ (f/s)
1	113	3.12	1704	2396	0

Configuration 1
 Test Point 113
 Shadowgraph No. 3

Configuration 1
 Test Point 113
 Shadowgraph No. 2

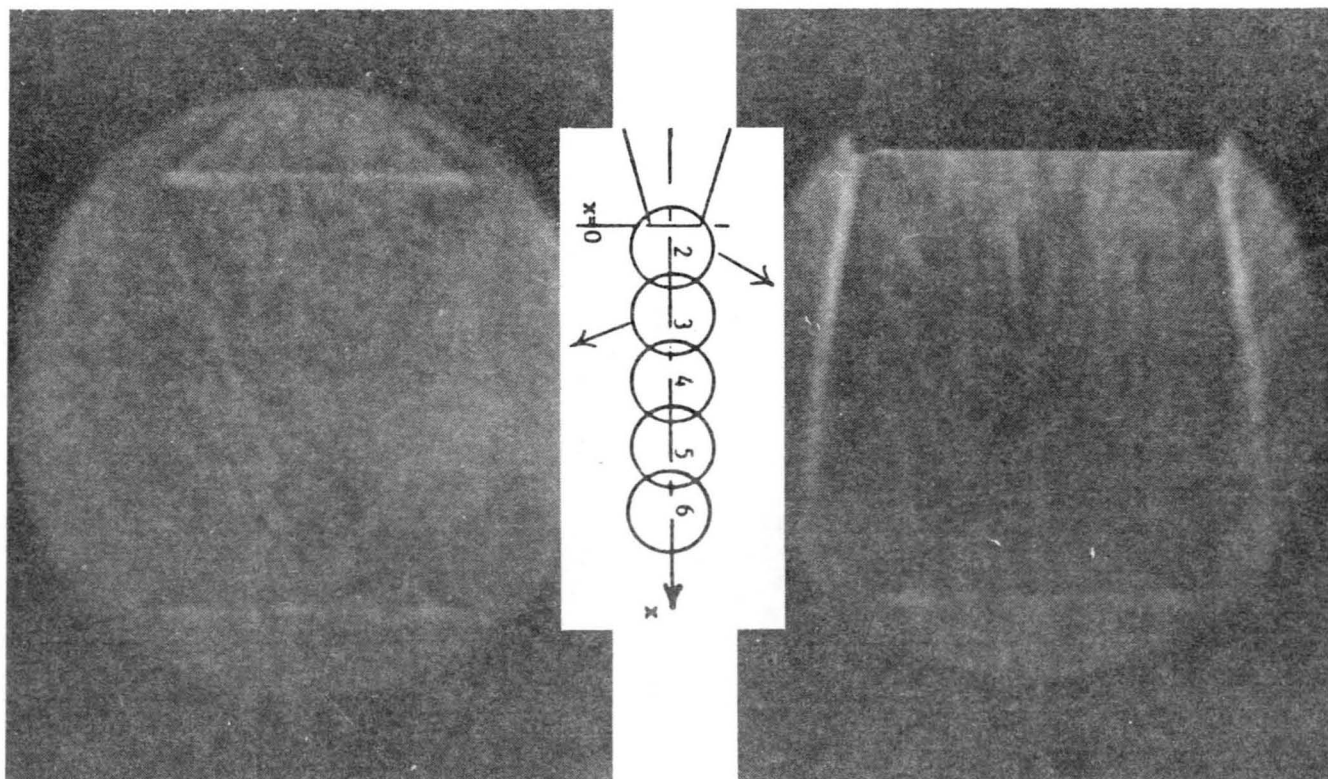


Figure 6-37. Shadowgraph Photos: Convergent Circular Nozzle (Model 1): Static Test.

Model	Test Point	P_r	T_T , ($^{\circ}R$)	V_j (f/s)	$V_{a/c}$ (f/s)
1	114	3.12	1703	2396	400

Configuration 1
 Test Point 114
 Shadowgraph No. 11

Configuration 1
 Test Point 114
 Shadowgraph No. 10

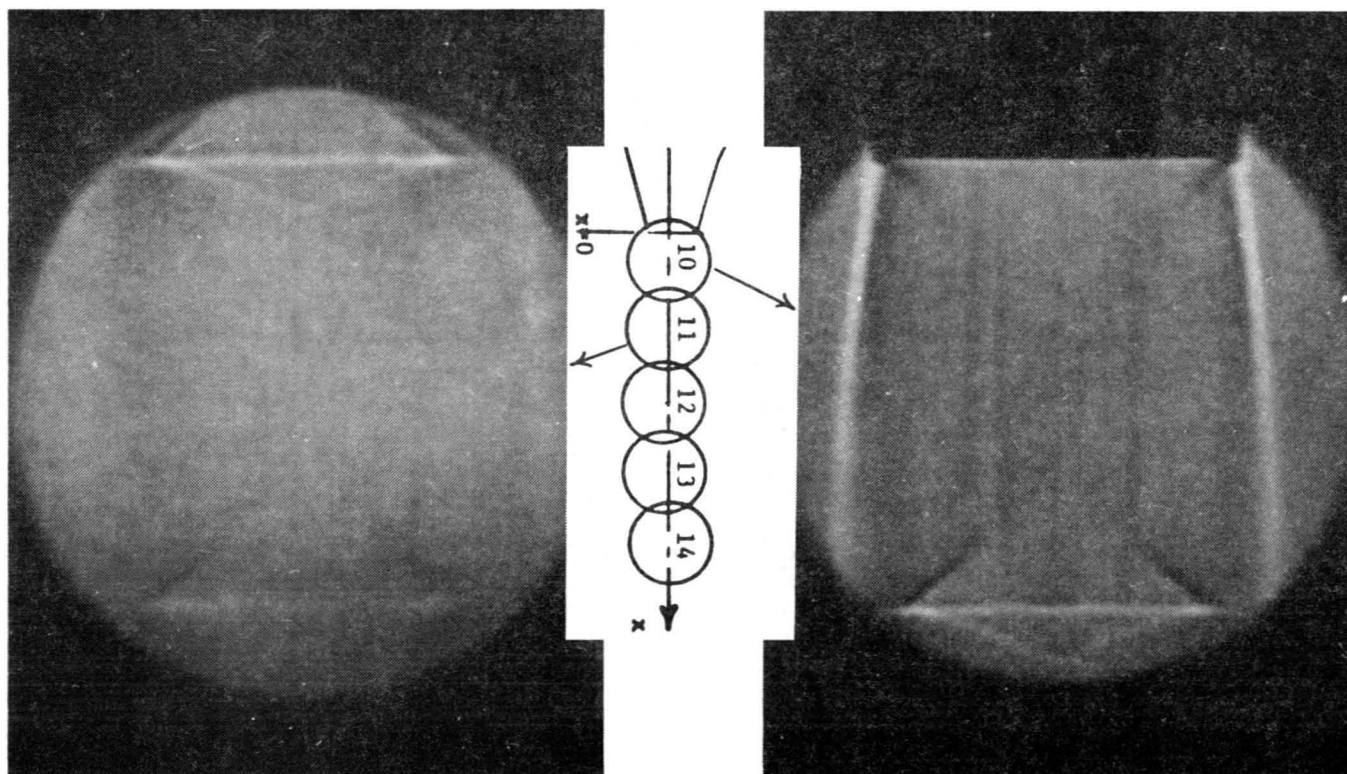


Figure 6-38. Shadowgraph Photos: Convergent Circular Nozzle (Model 1): Simulated Flight.

Model	Test Point	P_r	T_T , (°R)	V_j (f/s)	$V_{a/c}$ (f/s)
2	213	3.12	1716	2405	0

Configuration 2
 Test Point 213
 Shadowgraph No. 2

Configuration 2
 Test Point 213
 Shadowgraph No. 1

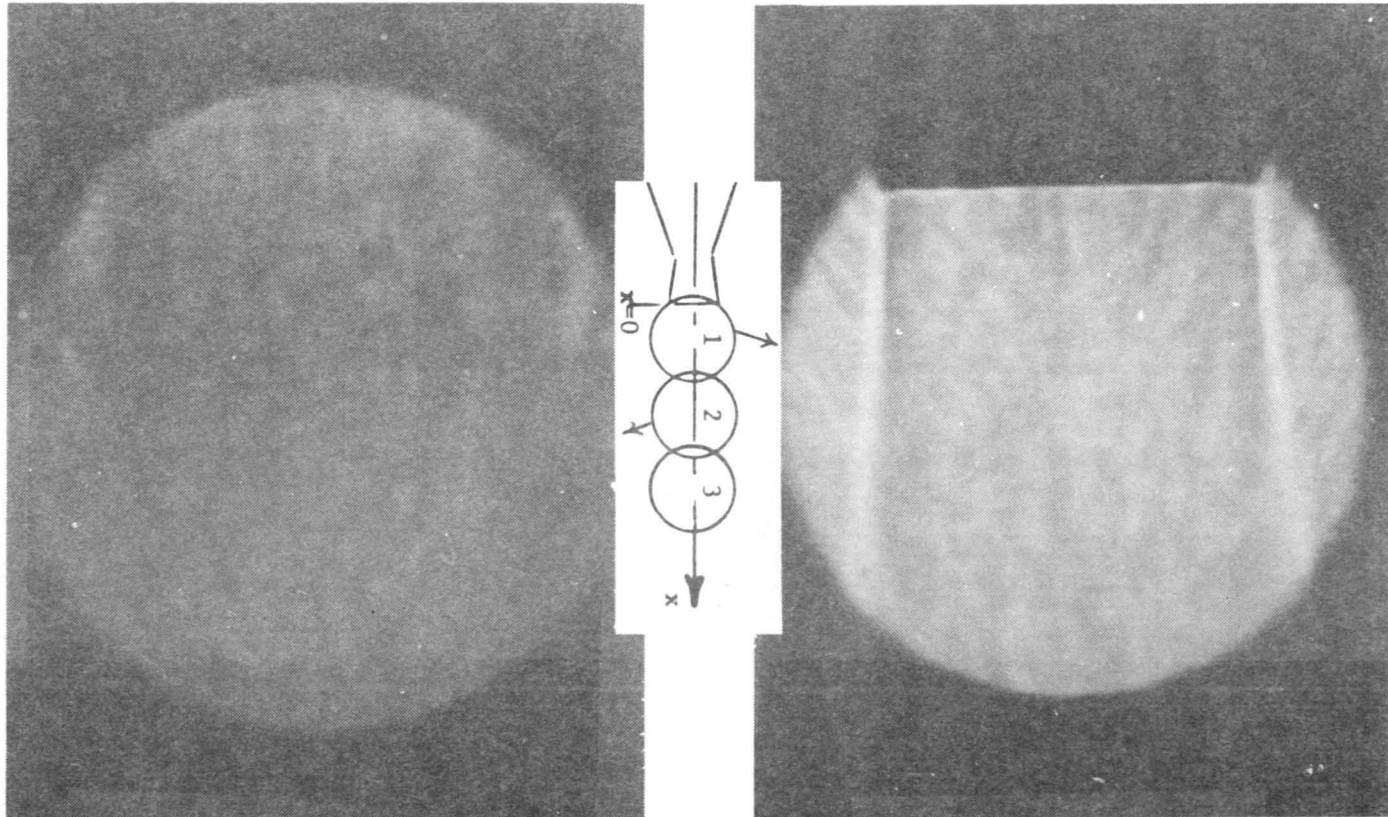


Figure 6-39. Shadowgraph Photos: C-D Circular Nozzle (Model 2): Static Test.

Model	Test Point	P_r	T_T , (°R)	V_j (f/s)	$V_{a/c}$ (f/s)
2	214	3.12	1707	2398	400

Configuration 2
 Test Point 214
 Shadowgraph No. 11

Configuration 2
 Test Point 214
 Shadowgraph No. 10

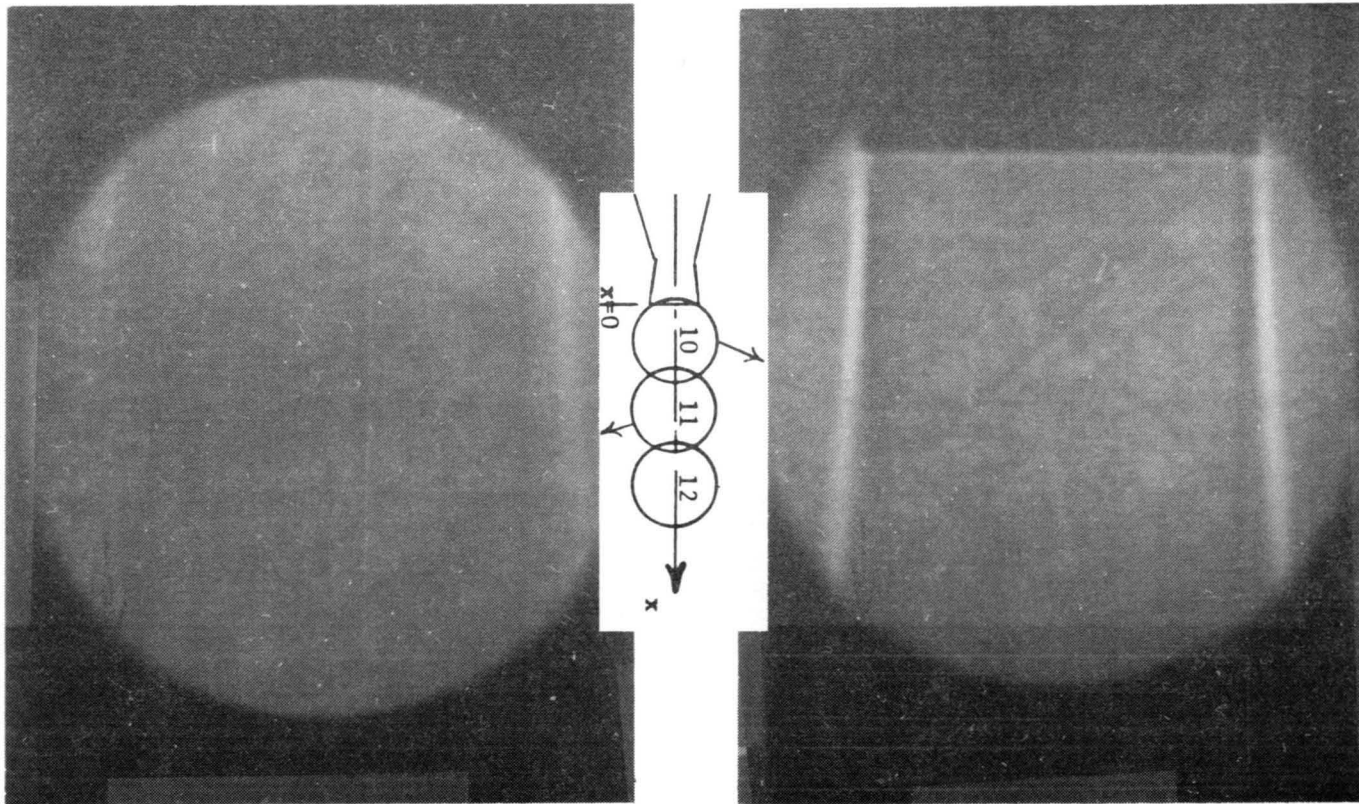


Figure 6-40. Shadowgraph Photos: C-D Circular Nozzle (Model 2):
 Simulated Flight.

Model	Test Point	P_r	$T_{T'}$ (°R)	V_j (f/s)	$V_{a/c}$ (f/s)
3	313	3.13	1731	2418	0

Configuration 3
 Test Point 313
 Shadowgraph No. 21

Configuration 3
 Test Point 313
 Shadowgraph No. 20

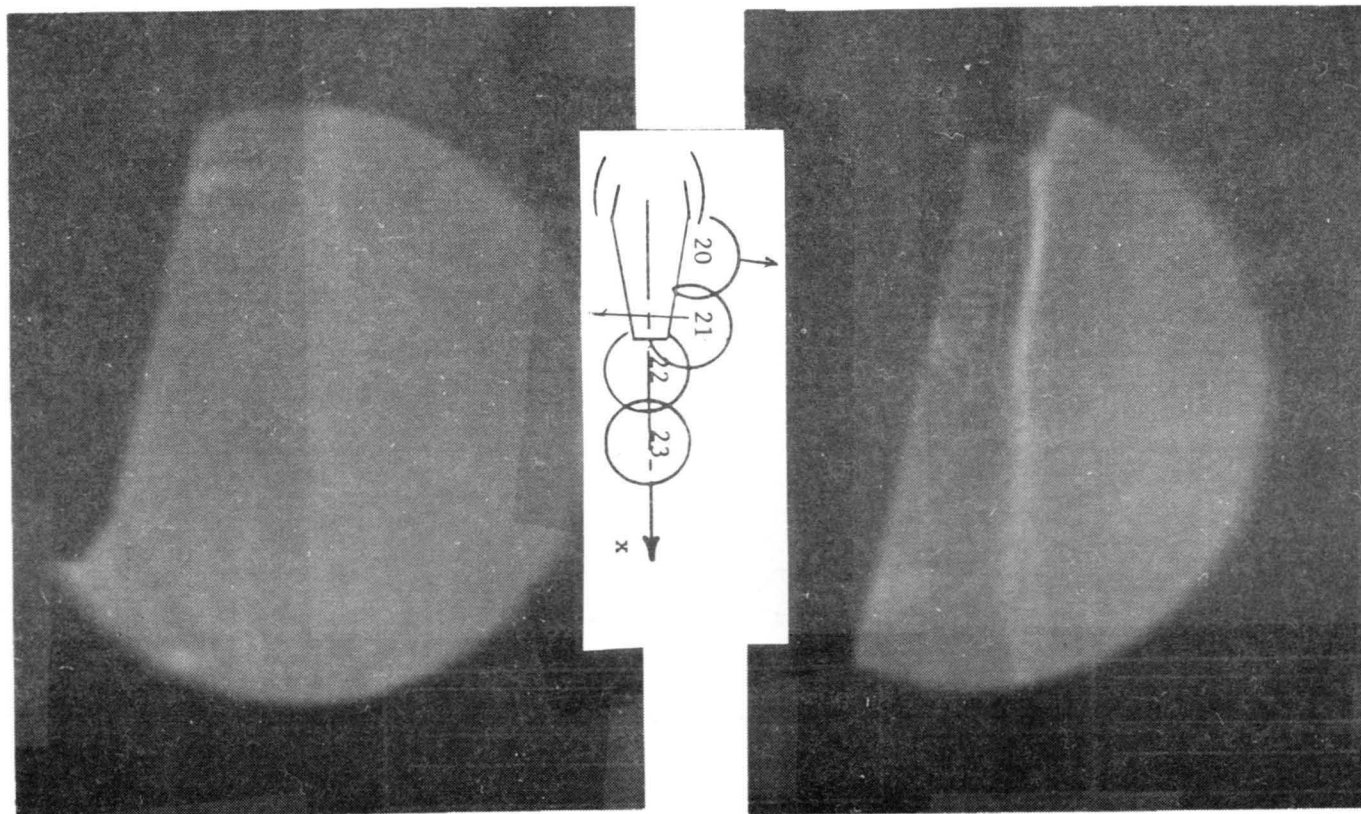


Figure 6-41. Shadowgraph Photos: Convergent Annular Plug Nozzle (Model 3): Static Test.

Model	Test Point	P_r	$T_{T'}^{(OR)}$	V_j (f/s)	$V_{a/c}$ (f/s)
3	314	3.14	1708	2405	400

Configuration 3
 Test Point 314
 Shadowgraph No. 26

Configuration 3
 Test Point 314
 Shadowgraph No. 25

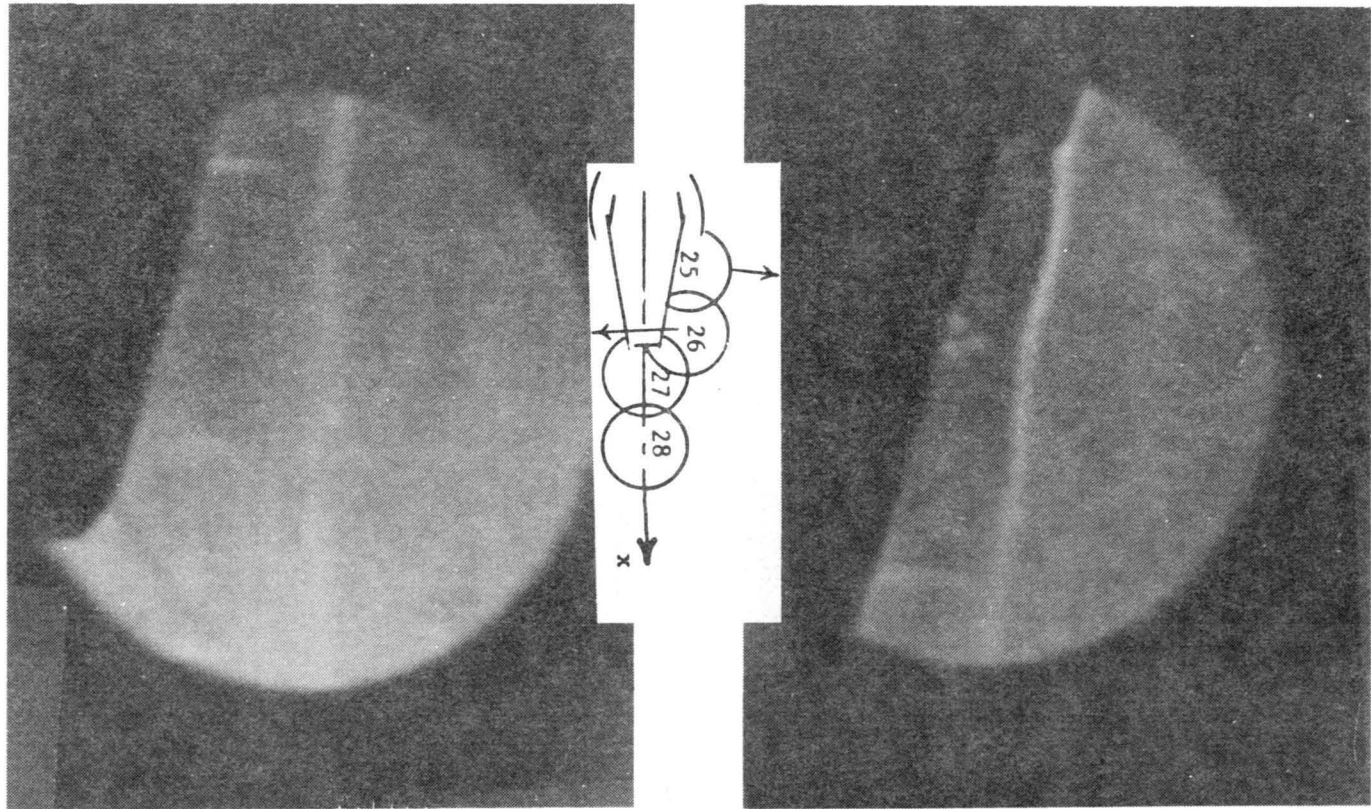


Figure 6-42. Shadowgraph Photos: Convergent Annular Plug Nozzle (Model 3): Simulated Flight.

Model	Test Point	P_r	$T_{T'}$ (°R)	V_j (f/s)	$V_{a/c}$ (f/s)
4	413	3.10	1687	2378	0

Configuration 4
 Test Point 413
 Shadowgraph No. 4

Configuration 4
 Test Point 413
 Shadowgraph No. 3

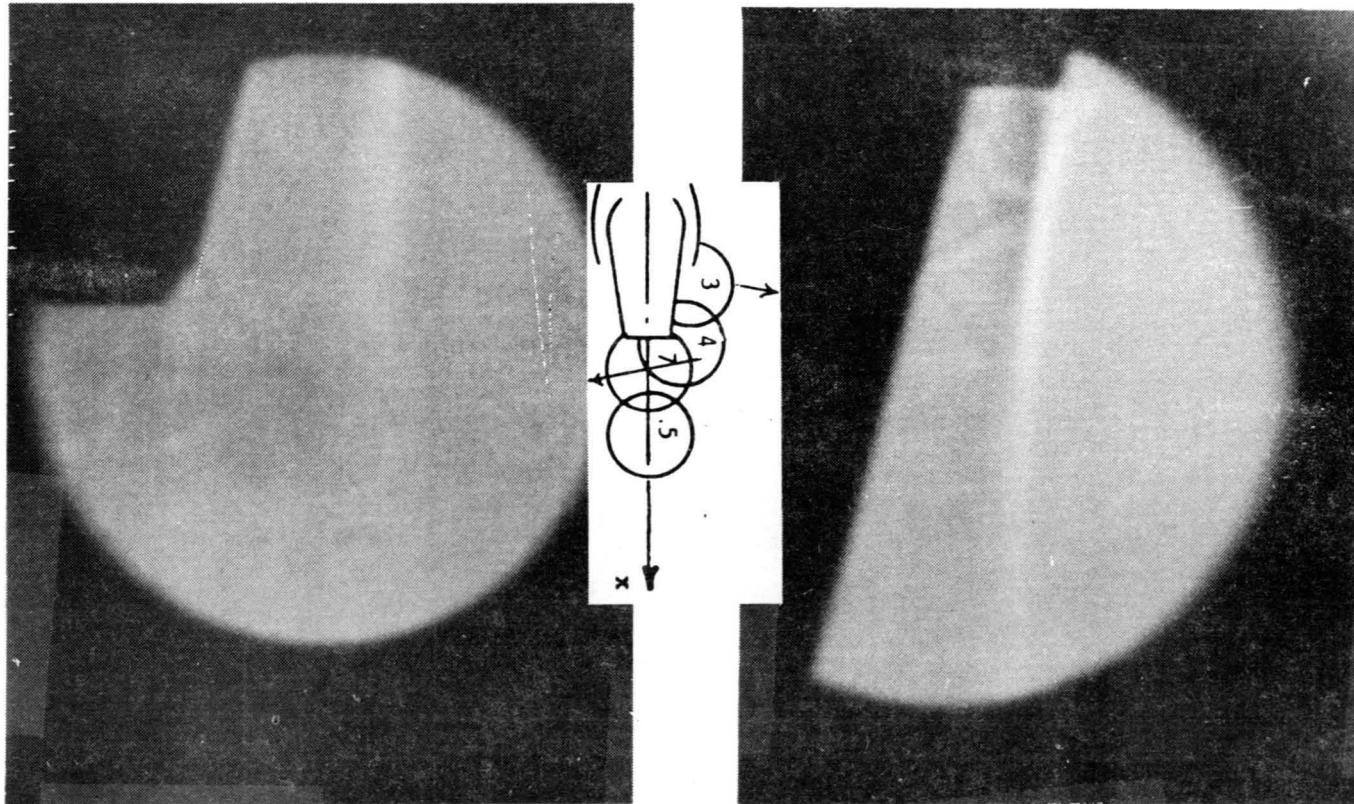


Figure 6-43. Shadowgraph Photos: C-D Annular Plug Nozzle (Model 4): Static Test.

Model	Test Point	P_r	T_T , (°R)	V_j (f/s)	$V_{a/c}$ (f/s)
4	414	3.09	1700	2384	400

Configuration 4
 Test Point 414
 Shadowgraph No. 22

Configuration 4
 Test Point 414
 Shadowgraph No. 21

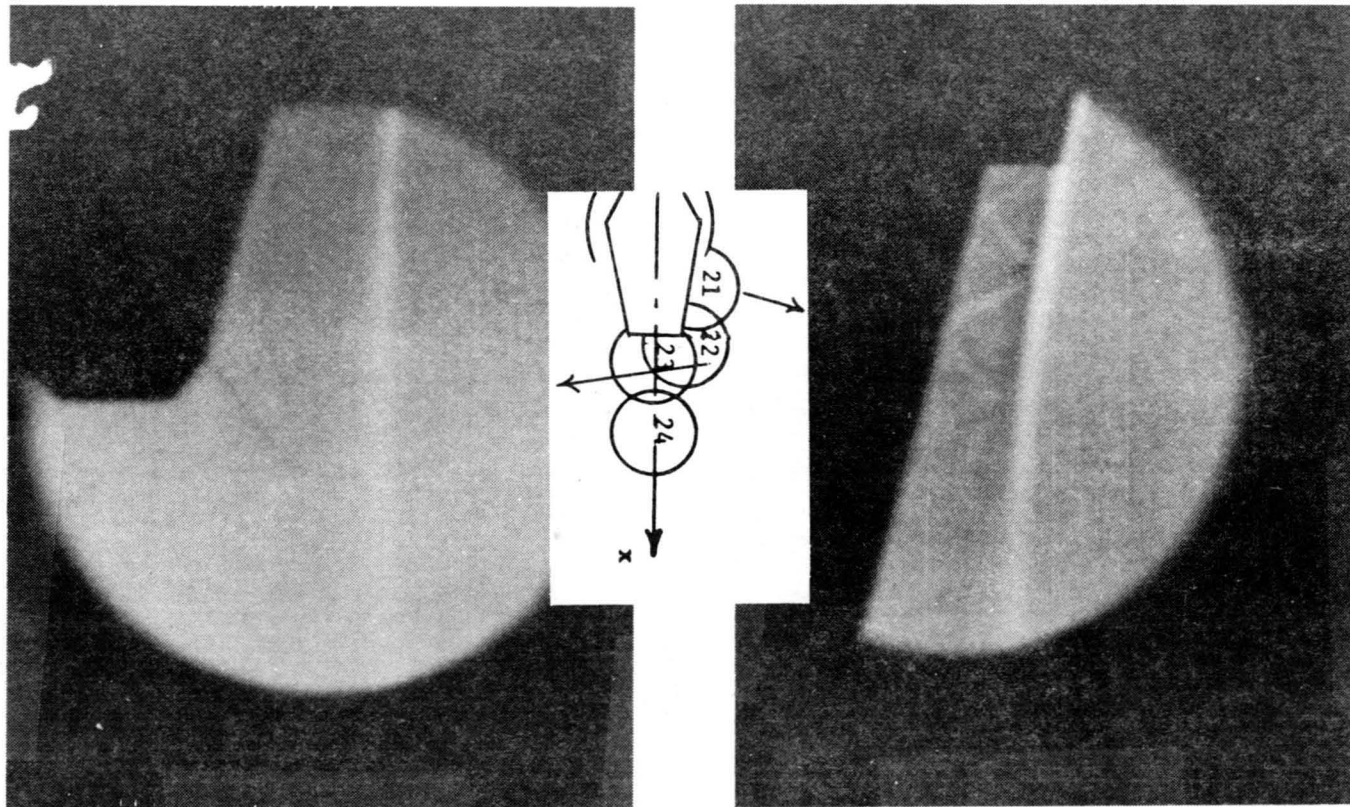


Figure 6-44. Shadowgraph Photos: C-D Annular Plug Nozzle (Model 4): Simulated Flight.

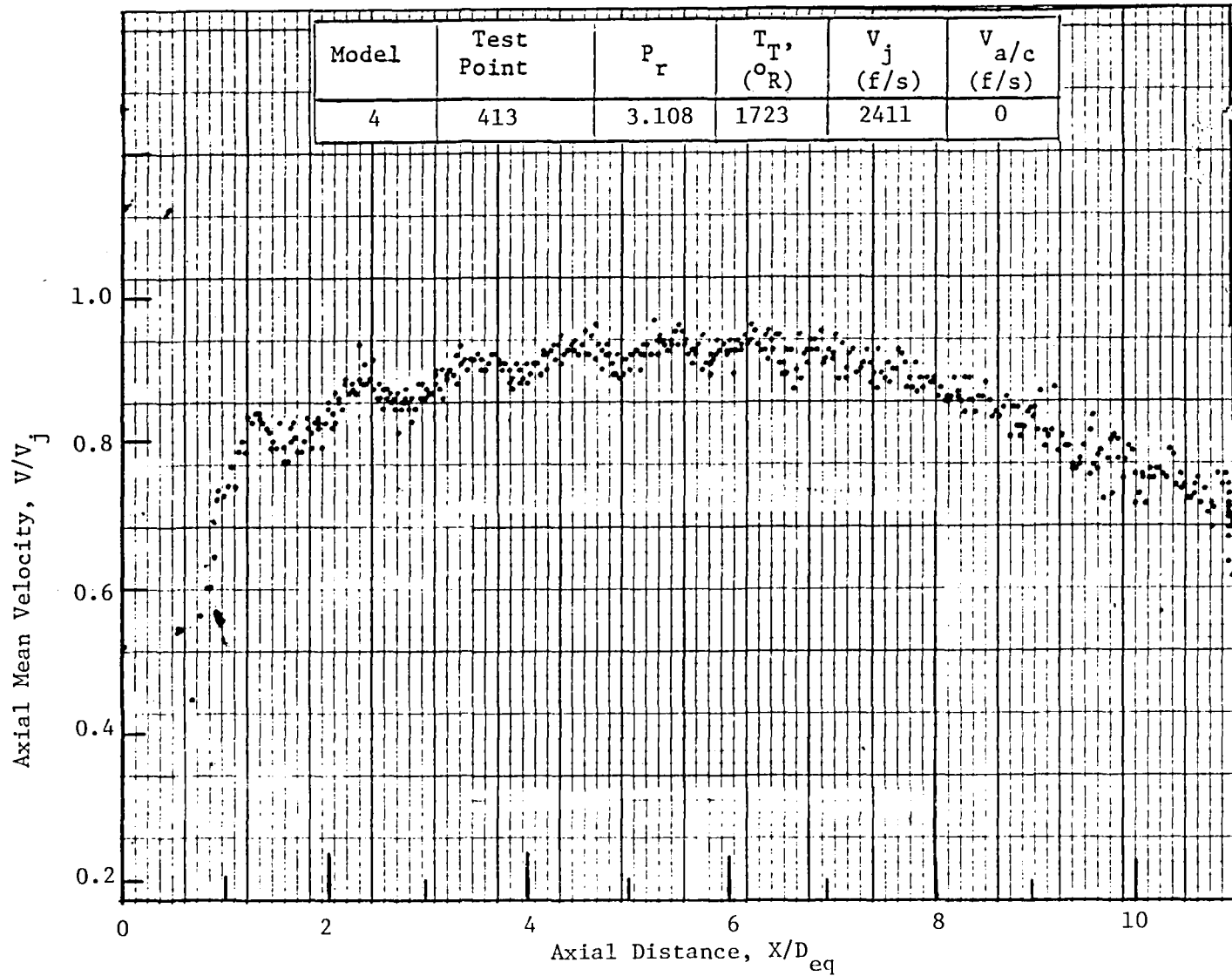


Figure 6-45. Axial Mean Velocity Distributions on the Jet Axis of C-D Annular Plug Nozzle (Model 4) - Static Test. (Repeated from Figure 6-10)

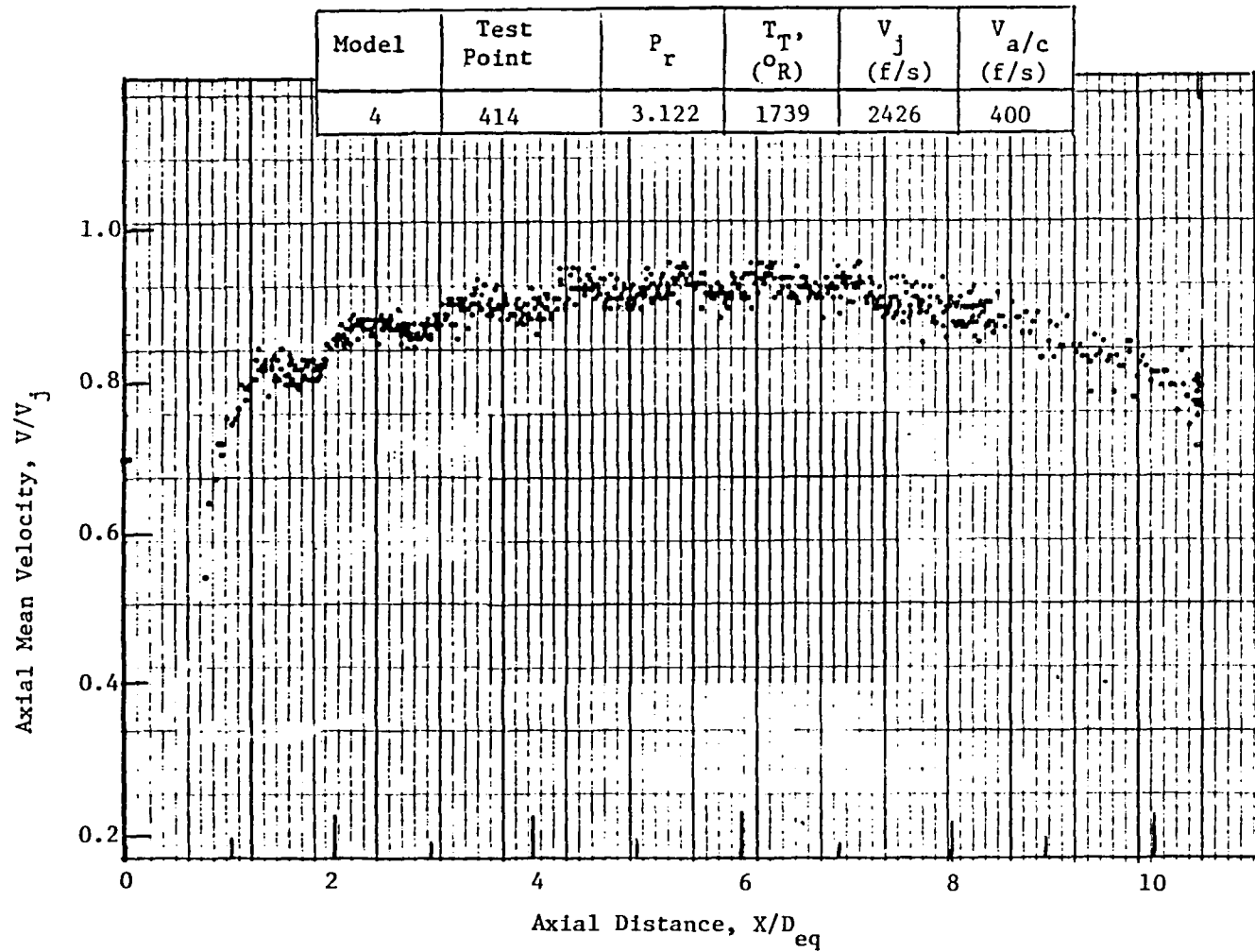


Figure 6-46. Axial Mean Velocity Distributions on the Jet Axis of C-D Annular Plug Nozzle (Model 4) - Simulated Flight. (Repeated from Figure 6-12)

A rather complex shock-cell structure is observed for the multi-element suppressor plug nozzles presented in Figures 6-47 through 6-50. Shocks produced by more than one chute are shown possibly in a shadowgraph photo. It should be noted that rather strong shocks are observed on the plug surface of the convergent suppressor nozzle, but practically no shock is formed downstream of the plug, indicating that the axial mean velocity has already decayed to a subsonic velocity before flow reaches the plug end, in contrast to the case of the C-D suppressor nozzle (Figures 6-49 and 6-50) where an expansion fan at the plug tip is noted, which is indicative of the flow being still supersonic there. The weak shocks observed on the plug surface of the C-D suppressor nozzle may be attributed to the convergent termination of the chute flowpath projected on the radial cross section.

To conclude the discussions of this section, it may be said that a high degree of consistency was identified concerning aerodynamic characteristics of shock-containing flow between laser velocimeter and shadowgraph test results.

Model	Test Point	P_r	$T_{T'} (^\circ R)$	$V_j (f/s)$	$V_{a/c} (f/s)$
5	513	3.12	1717	2405	0

Configuration 5
 Test Point 513
 Shadowgraph No. 7

Configuration 5
 Test Point 513
 Shadowgraph No. 6

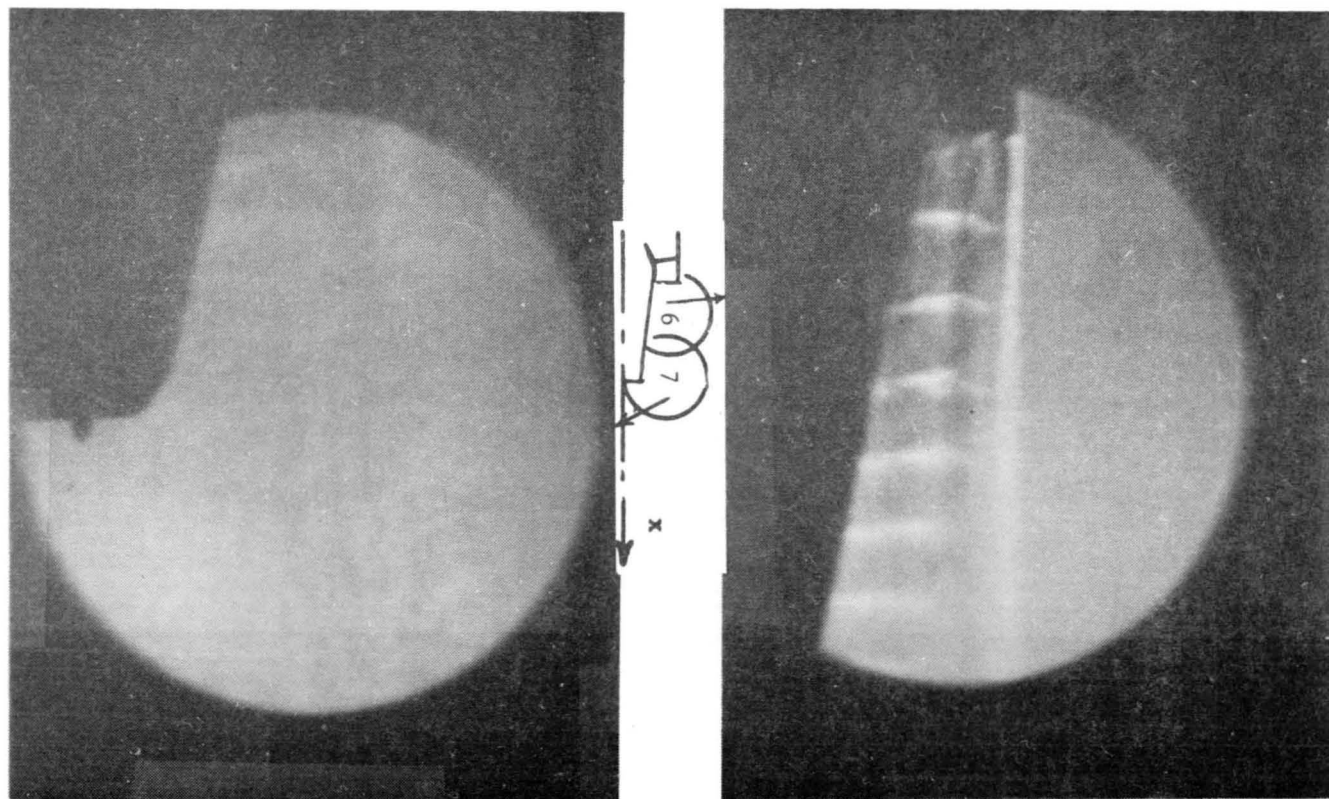


Figure 6-47. Shadowgraph Photos: Convergent Multi-Element Suppressor Plug Nozzle: Model 5: Static Test.

Model	Test Point	P_r	$T_{T,}$ ($^{\circ}R$)	V_j (f/s)	$V_{a/c}$ (f/s)
5	514	3.13	1725	2414	400

Configuration 5
 Test Point 514
 Shadowgraph No. 8

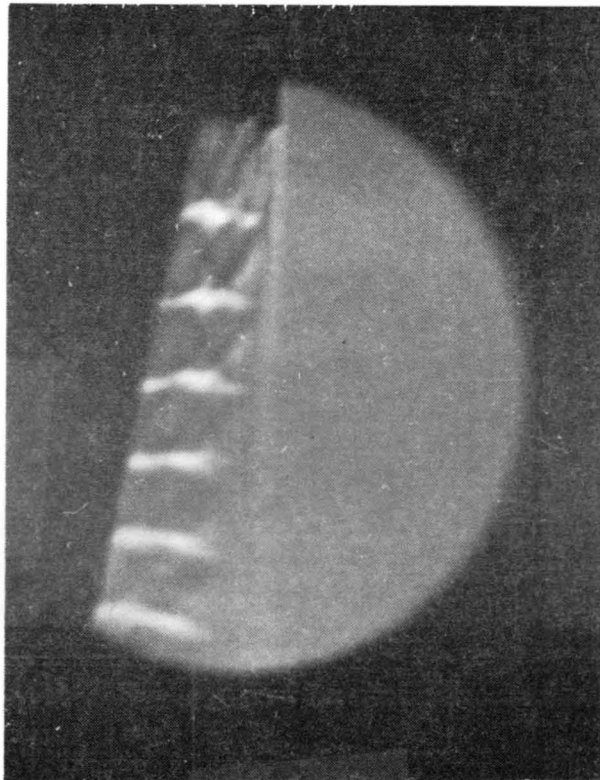


Figure 6-48. Shadowgraph Photos: Convergent Multi-Element Suppressor Plug Nozzle: (Model 5): Simulated Flight.

Model	Test Point	P_r	$T_{T'}$ (°R)	V_j (f/s)	$V_{a/c}$ (f/s)
6	613	3.12	1735	2418	0

Configuration 6
 Test Point 613
 Shadowgraph No. 2

Configuration 6
 Test Point 613
 Shadowgraph No. 1

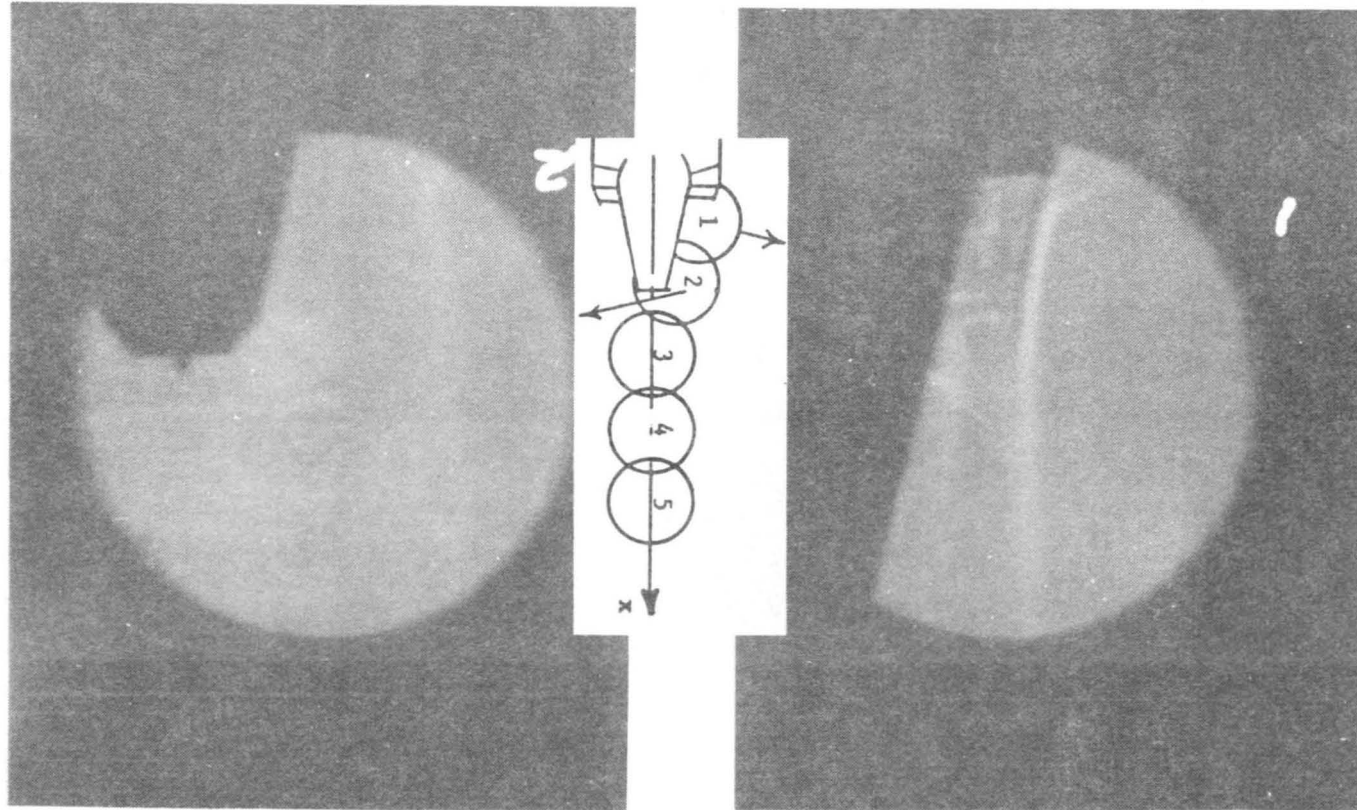


Figure 6-49. Shadowgraph Photos: C-D Multi-Element Suppressor Plug Nozzle: (Model 6): Static Test.

Model	Test Point	P_r	$T_{T,}$ ($^{\circ}R$)	V_j (f/s)	$V_{a/c}$ (f/s)
6	614	3.13	1711	2404	400

Configuration 6
 Test Point 614
 Shadowgraph No. 7

Configuration 6
 Test Point 614
 Shadowgraph No. 6

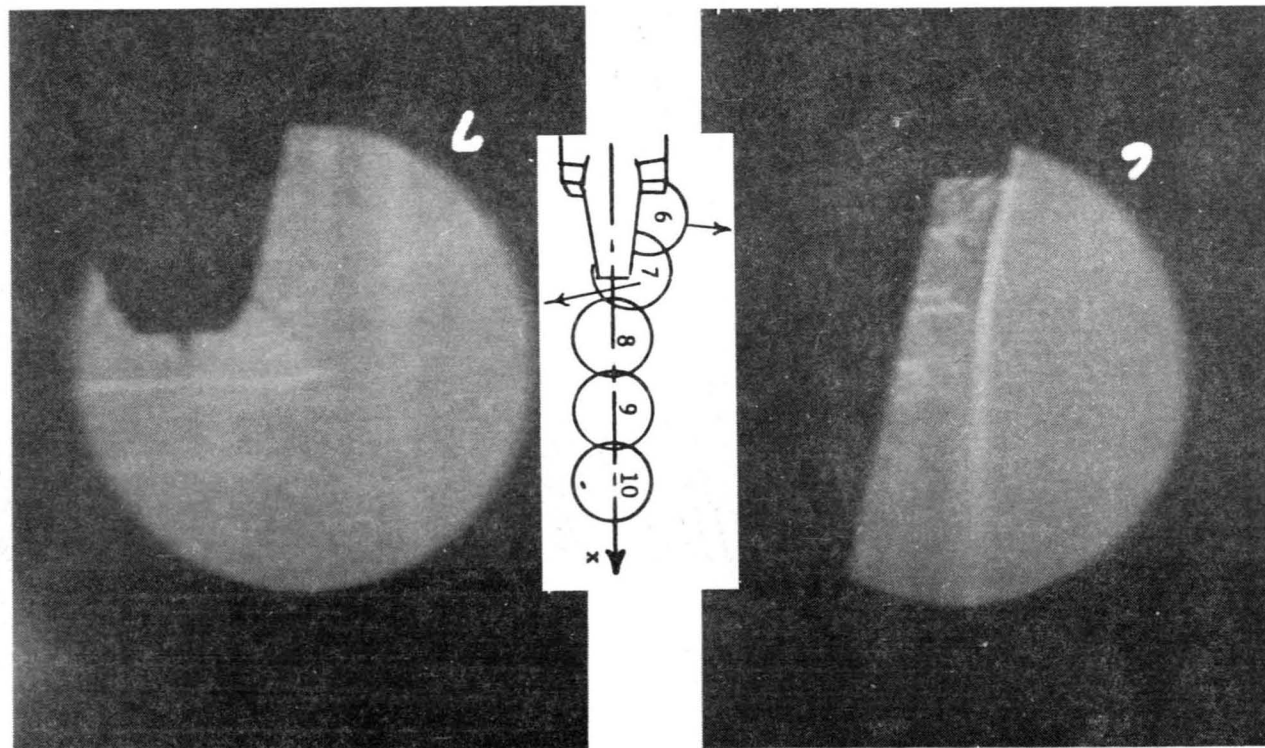


Figure 6-50. Shadowgraph Photos: C-D Multi-Element Suppressor Plug Nozzle: (Model 6): Simulated Flight.

7.0 PREDICTIVE MODELING*

Shock associated noise is a dominant contributor to the acoustic far field of high velocity jets operating at supercritical pressure ratios. The physical process by which shock noise is generated is as follows. In a convergent nozzle operating at supercritical pressure ratio, a pattern of regularly spaced shock formation exists. These shocks divide the plume into cells such that the spacing and strength of the shocks diminish in the downstream direction due to the mixing of the jet plume with the ambient air. The mixing process also produces turbulence in the form of statistically regular eddies which convect downstream with the flow. As these eddies pass through (or by) the shock fronts, they disturb the shocks, causing them to emit acoustic waves. The acoustic waves from the various shock-cells can constructively or destructively interfere, depending on the shock spacing, the eddy convection velocity and the lifetime of a given eddy.

As mentioned above, the primary physical mechanism for the production of broadband noise by the presence of shock-cells in the jet plume is the emission of acoustic waves by the shock fronts as they are disturbed by the passage of turbulent eddies. The eddies, produced in the mixing layers of the plume, are themselves unsteady fluctuating "blobs" of vorticity, so that the emitted acoustic waves from the shocks have characteristics which are related to the properties of the turbulent disturbances (e.g., their characteristic frequency and amplitude) as well as the shock structure. The purpose of this section is to establish one plausible relationship, based on a systematic but highly idealized model, among the acoustic field, shock structure and turbulence.

Almost thirty years ago, Lighthill (Reference 7-1) studied the properties of the scattered acoustic energy, resulting from the passage of a sound wave through a volume of turbulence, using his acoustic analogy. Lighthill also extended his results for a periodic wave train to an incident acoustic pulse propagating at the (constant) speed of sound and found that the

*This section was authored by T. F. Balsa of the General Electric Corporate Research and Development Center, Schenectady, New York.

energy scattered is infinite because of the "perfect resonance of the successive rays (i.e., wave fronts) emitted forward." But by permitting this pulse to be a weak, non-linear shock, he arrived at the total energy scattered and speculated that "the energy freely scattered when turbulence is convected through a stationary shock wave pattern in a supersonic jet may form an important part of the sound field of the jet." This last remark is certainly true.

Ribner, in a series of papers culminating in Reference 7-2, provides the flux of acoustic energy emanating from the downstream side of a stationary shock of finite strength as a body of isotropic turbulence passes through this shock. The ratio of the acoustic to the turbulent energy fluxes varies almost linearly with the shock density ratio reaching a maximum value of 0.062 when the incoming shock Mach number is infinity. Ribner's work was motivated by his desire to predict the intensity of sound waves generated by supersonic jets.

The works of Lighthill and Ribner are classic in the way that their results can be derived from the fundamentals of fluid mechanics and certain other generally accepted ideas. On the other hand, the somewhat more recent work of Harper-Bourne and Fisher (Reference 5-2) is highly heuristic in a sense that it postulates a simple but effective model of shock associated noise that needs, as input, certain experimentally measured quantities. There is little doubt, however, that the Harper-Bourne Fisher model is the most directly applicable to shock noise generated by supersonic jets and, given the empiricism that the model needs, it indeed predicts the noise of these jets in the far field.

The recent paper of Howe and Ffowcs-Williams (Reference 2-6) is clearly a compromise between these classic and intuitive studies; these authors approach the problem of shock associated noise from a fundamental perspective yet maintain enough realism so that their overall conclusions seem to be borne out qualitatively by experimental data. Howe and Ffowcs-Williams consider an ideal supersonic jet consisting of a perfect stream of air (i.e., slug flow) crisscrossed by a family of infinitesimally weak oblique shock and expansion waves. Turbulence, represented by a ring vortex of certain statistical description, is allowed to drift downstream and to pass through this wave

system; because of this, noise is radiated, and the shock waves in the jet decay due to turbulent diffusion. The ring vortex is a mathematical idealization of the coherent/large-scale structures, or axisymmetric puffs, that are so prevalent in supersonic jets.

According to Harper-Bourne and Fisher, a given turbulent eddy interacts with many (say eight to ten) shock-cells and the relatively coherent scattering of sound from these cells results in a sound spectrum characterized by a sequence of sharp peaks which are clearly related to the shock spacing and the convection speed of the eddy. Thus, this component of shock associated noise is almost diagonally opposite to that considered by Lighthill and Ribner; very loosely, they assume that the identity or lifetime of an eddy is so short that these eddies interact only with one shock at a time and multiple interactions with a family of shocks are additive in the mean square sense. Therefore, a more reasonable assumption, adopted by Howe and Ffowcs-Williams, is that the eddy is "frozen" and noise is radiated because energy is extracted from the shock structure by this frozen eddy.

Clearly the two essential ingredients of shock noise are an extensive shock structure and the interaction between (frozen) turbulence and these shocks. In order to have a shock system, a jet is needed; in this section, the jet is an ideal stream of air (i.e., slug flow), and the steady shock structure is calculated from linearized supersonic flow. These assumptions are the same as those of Howe and Ffowcs-Williams. However, in order to have an interaction between turbulence and the shocks, a jet is not needed and indeed, for the description of this interaction, we ignore the effects of jet flow in this section. This is in contrast to the work of Howe and FfowcsWilliams. Very roughly speaking, the present work may be thought of as an extension of Lighthill's work to a periodic system of shocks, but there are two very important differences that need to be emphasized: first, we consider a genuine interaction (i.e., a feedback) between the steady flow and the acoustic field (there was no such feedback in Lighthill's work); and second, our formalism differs quite considerably from Lighthill's (we use the acoustic analogy of Howe (Reference 7-3)).

There is a considerable body of experimental data which suggests that the shrouding effect of the jet flow is unimportant for shock associated noise (except, of course, for the determination of the shock structure per se). It

is well known that shock noise is the most dominant in the forward quadrant; in terms of the emission angle θ , this is defined by $\pi/2 < \theta < \pi$. Clearly, convective amplification effects are not very important in this region, therefore, to the extent that these effects are modified by the jet flow are also unimportant. Furthermore, shock noise is relatively insensitive to jet temperature (i.e., the noise depends on the pressure ratio of the jet alone) so that again the complicated temperature dependence of the noise created by the shrouding of the turbulence by the hot jet column is not needed (see Harper-Bourne and Fisher (Reference 5-2) and Tanna (Reference 5-6)). Thus, our model of shock associated noise seems quite plausible; indeed this model predicts many of the observed characteristics of shock associated noise in a simple and transparent fashion. The derivation of the theory is also quite direct and does not involve energy conversion arguments between the steady and unsteady flows.

7.1 PRELIMINARY REMARKS AND PERTURBATION EQUATIONS

The physical problem under consideration is shown in Figure 7-1.* We assume that an imperfectly expanded supersonic annular jet of velocity U_1 , and thickness a , exhausts into and mixes with the ambient. The characteristic mean speed of sound in the jet is taken to be c_1 so that the requirement of supersonic flow implies $M_1 = U_1/c_1 > 1$, a condition which is assumed to hold in the immediate vicinity of the jet exit. Because of locally supersonic flow in the jet, a well-known shock pattern is established within the jet. Of course, the strength of the shocks in the pattern decreases with distance downstream because of turbulent mixing. As a result of this mixing of the jet with the ambient, intense turbulence is created in the jet shear layer. This turbulence convects through the more or less spatially periodic shock structure thereby radiating noise. This is called shock associated noise and the purpose of this section is to describe its characteristics under highly idealized conditions.

*The symbols used in this section are defined in the text where they first appear and are not consistent with those of the rest of this report, which are listed in Section 9.0.

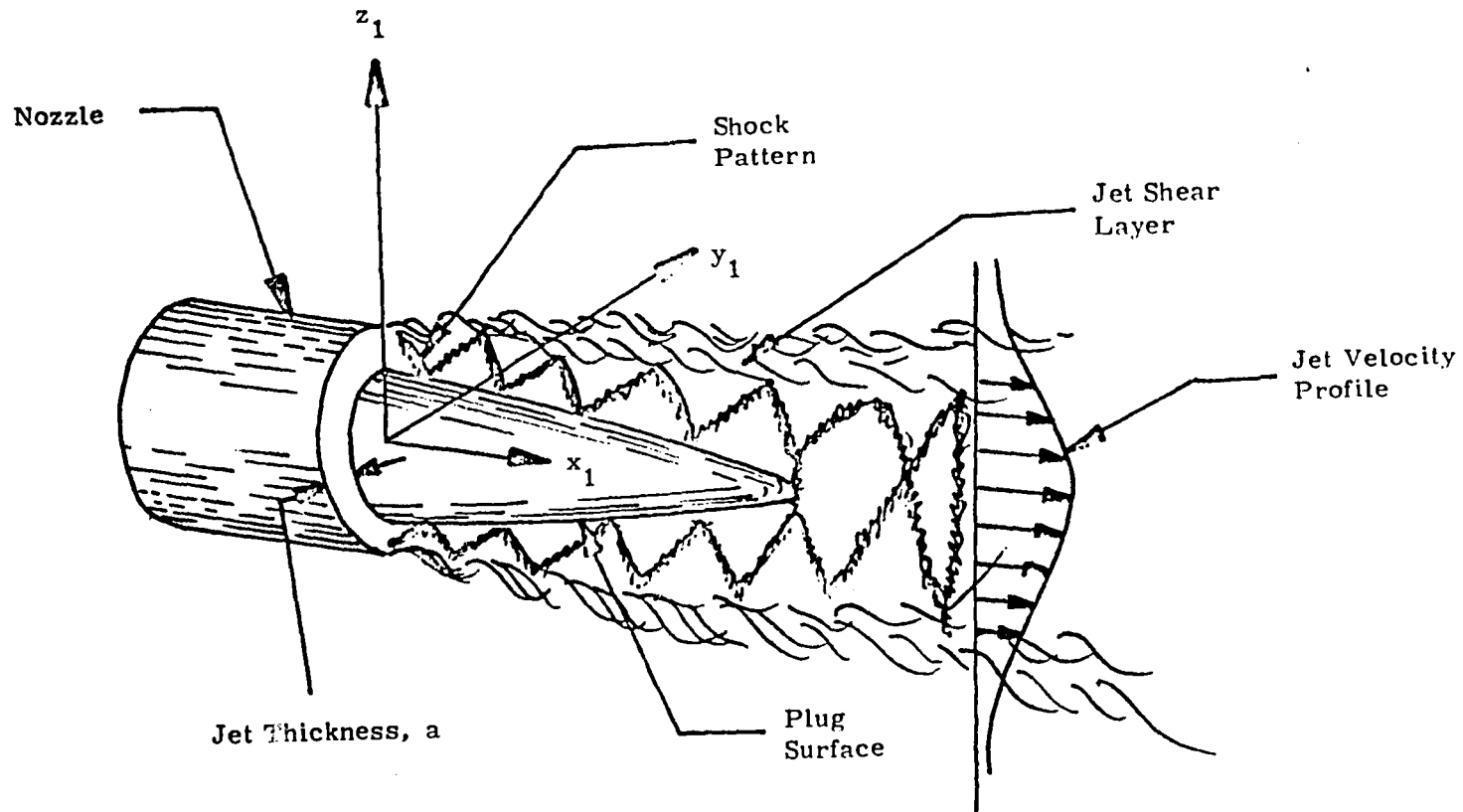


Figure 7-1. Geometry of Physical Problem

where $\gamma = \text{const}$ is the ratio of specific heats, the perturbation velocity components relative to the moving system are denoted by $\tilde{\mathbf{v}} = (\tilde{u}, \tilde{v}, \tilde{w})$ and the dots in (2a) stand for terms quadratic in the perturbations. In obtaining (2), it is assumed that the perturbed flow takes place at constant entropy (i.e., the perturbation entropy vanishes) and the fluid obeys the ideal gas law with constant specific heats. In regions of irrotational flow, the perturbation velocity components $(\tilde{u}, \tilde{v}, \tilde{w})$ are related to the enthalpy B via

$$\partial \frac{(\tilde{u}, \tilde{v}, \tilde{w})}{\partial t} = -\nabla B \quad (2c)$$

where ∇ denotes the usual spatial gradient operator and the perturbation pressure p is expressible as

$$\frac{1}{\rho} \frac{\partial \tilde{p}}{\partial t} = \frac{\partial B}{\partial t} + (U - U_c) \frac{\partial B}{\partial x} \quad (2d)$$

where the derivatives in (2c, 2d) are evaluated in the moving coordinate system. Equation (2c) comes from the Crocco form of the momentum equation whereas (2d) is obtained from the linearized Bernoulli equation. Note that the fluid velocity \mathbf{v} relative to the translating coordinate system has components $\mathbf{v} = (U - U_c + \tilde{u}, \tilde{v}, \tilde{w})$ and B is the perturbation stagnation enthalpy (but we leave the tilde off).

The wave equation describing the generation and propagation of sound through a turbulent jet is given by (Reference 7-3) as

$$\left[\frac{D}{Dt} \left(\frac{1}{c^2} \frac{D}{Dt} \right) + \frac{1}{c^2} \frac{D\mathbf{v}}{Dt} \cdot \nabla - \Delta \right] B^* = \nabla \cdot (\boldsymbol{\xi} \times \mathbf{v}) - \frac{1}{c^2} \frac{D\mathbf{v}}{Dt} \cdot (\boldsymbol{\xi} \times \mathbf{v}) \quad (3a)$$

where $\boldsymbol{\xi} = \nabla \times \mathbf{v}$ is the vorticity, c is the acoustic speed, Δ denotes the Laplacian operator and the convective derivative is defined as $D/Dt = \partial/\partial t + \mathbf{v} \cdot \nabla$. The vector \mathbf{v} is the velocity of the fluid relative to the moving coordinate system. The governing equation (3a) is valid when the entropy fluctuations in the jet, as sources of sound, are negligible.

The work of Howe and Ffowcs-Williams (Reference 2-6), which deals with this problem in a general and systematic way, suggests that the acoustic analogy of Howe (Reference 7-3) is a useful starting point. This implies that the physics of the sound generation and propagation process may be described by a suitable wave equation whose dependent variable is the stagnation enthalpy B^* .

Consider a laboratory coordinate system $(x_1, y_1, z_1; t_1)$ where x_1 is along the jet axis the t_1 denotes time and a translating coordinate system $(x, y, z; t)$ related by the Galilean transformation

$$x_1 = x + U_c t \quad (1a)$$

$$y_1 = y \quad (1b)$$

$$z_1 = z \quad (1c)$$

$$t_1 = t \quad (1d)$$

where $U_c = \text{const} > 0$ is the uniform speed of the moving coordinate system relative to the laboratory system. U_c will be assigned a physical meaning later in this section.

Suppose small perturbations are superimposed on an otherwise uniform flow with constant (i.e., independent of space and time) pressure p and density ρ . Let the unperturbed flow have velocity components $(U, 0, 0)$ relative to the laboratory coordinate system and assume that the tilde (\sim) above a quantity denotes an arbitrary perturbation associated with that quantity. Then from the usual definition of the stagnation enthalpy B^* "relative" to the moving coordinate system, we find

$$B^* = \frac{\gamma}{\gamma - 1} \frac{p}{\rho} + (U - U_c)^2 / 2 + B + \dots \quad (2a)$$

$$B = \frac{\tilde{p}}{\rho} + (U - U_c) \tilde{u} \quad (2b)$$

In order to obtain relatively simple closed form solutions to (3a), we must invoke two bold simplifications that are quite useful and frequent in the study of jet noise. First, the convective derivatives D/Dt of the fluid velocity \underline{V} and speed of sound c are replaced by zero; the implications are that in jet flows, on the average, the convective derivative means differentiation along the axis and, again in some average sense, the velocity \underline{V} and acoustic speed c change slowly in this direction (especially when compared to changes in the transverse plane); therefore, these changes are negligible. Thus, (3a) is replaced by

$$\left[\frac{1}{c^2} \frac{D^2}{Dt^2} - \Delta \right] B^* = \nabla \cdot (\underline{\xi} \times \underline{V}) \quad (3b)$$

where now the left-hand side of (3b) is recognized as a convected wave operator and the right-hand side is the source of sound; sound is generated by vorticity--a result first enunciated explicitly by Powell (Reference 7-4).

It is worthwhile to look at our first simplification from another perspective. For purely vortical flows, which a free-jet is, the acceleration of the fluid $D\underline{V}/Dt$ vanishes in the linear theory; in other words, these vortical disturbances in the linear theory carry no pressure fluctuations. It is known that in a free-jet the pressure fluctuations are quadratically small; and since these are balanced by the acceleration of the fluid, the latter must also be small. Furthermore, if the jet is nominally cold $c = c_\infty = \text{const}$ (c_∞ speed of sound in ambient), c^2 can be pulled out of the differentiation in the first term on the left-hand side of (3a). Thus, it can be argued that (3b), with c^2 replaced by c_∞^2 , describes the sound generation and propagation process in a cold jet reasonably well. Clearly neither of these phenomena is affected drastically by allowing the acoustic speed to vary, in which case we recover (3b). Of course, it must be recognized that by replacing (3a) with (3b) the effects of turbulent diffusion and the scattering of sound by the turbulence are largely ignored.

At this point, the acoustic speed c and fluid velocity \underline{v} in (3b) are still dependent on the space coordinates; all we have assumed so far is that, in a suitable average, the variation of these quantities along the axis of the jet is small. In order to go further in a way that is free from unnecessary algebraic complications, we invoke the second of our assumptions. We divide physical space into two regions--the jet and the ambient--and linearize (3b) in each of these regions about a uniform unperturbed state. This assumption will be discussed further in a following paragraph. For example, in the jet (whose extent in physical space will be defined momentarily) we assume that the unperturbed velocity components relative to the laboratory coordinate system are given by $(U_1, 0, 0)$ and the unperturbed pressure, density and speed of sound are denoted by p_1, ρ_1 and c_1 , respectively, all these quantities being constants in space and time. The ambient is assumed to be at rest with respect to laboratory space and the pressure, density and speed of sound are given by p_∞, ρ_∞ and c_∞ . Note that we also assume that the static pressure variation across the jet is negligible so that $p_1 = p_\infty$. Since the jet is generally hot, c_1 and c_∞ are usually unequal.

After linearizing the left-hand side of (3b) about the unperturbed state described above, we obtain, in the jet,

$$L_1 (B) = \left[\frac{1}{c_1^2} \left[\frac{\partial}{\partial t} + (U_1 - U_c) \frac{\partial}{\partial x} \right]^2 - \Delta \right] B = \nabla \cdot (\underline{\xi} \times \underline{v}) \quad (4a)$$

where $\underline{\xi} = \nabla \times \underline{\tilde{v}}$ is the perturbation vorticity. Similarly, in the ambient we have

$$L_\infty (B) = \left[\frac{1}{c_\infty^2} \left[\frac{\partial}{\partial t} - U_c \frac{\partial}{\partial x} \right]^2 - \Delta \right] B = 0 \quad (4b)$$

since there the vorticity perturbations vanish. Note that (4a, 4b) are written relative to the translating coordinate system. Governing equations (4a, 4b) have constant coefficients; therefore, they are amenable to simple analytical techniques.

The source term on the right-hand side of (4a) can be further separated into

$$\nabla \cdot (\tilde{\xi} \times \underline{V}) = \nabla \cdot [\tilde{\xi} \times (\underline{V} - \tilde{V})] + \nabla \cdot (\tilde{\xi} \times \tilde{V})$$

and since the problem is linear, we can deal with each of these sources independently and then superimpose the pertinent solutions. Now $(\underline{V} - \tilde{V}) = (U - U_c, 0, 0)$ so that the source term $\nabla \cdot [\tilde{\xi} \times (\underline{V} - \tilde{V})]$ is linear in the perturbation vorticity $\tilde{\xi}$. In the present paper, we wish to study only the effects of the quadratic source term $\nabla \cdot (\tilde{\xi} \times \tilde{V})$ --remember this can be done because of linearity--for reasons discussed momentarily.

The division of the physical space into the two regions (i.e., the jet and the ambient) is done in an obvious and conventional way: the jet is assumed to occupy a doubly infinite thin annular region of thickness a , bounded on the interior by a solid cylindrical surface corresponding to the nozzle plug (see Figure 7-1), and surrounded externally by the ambient. Clearly within this context, the left-hand sides of (4a, 4b) correspond to the well-known and frequently used assumptions of slug flow (Mani, Reference 7-5) or the vortex sheet analogy of Ffowcs-Williams (Reference 7-6); see also Dowling, Ffowcs-Williams and Goldstein, Reference 7-7).

Since the annular jet surrounding the plug is assumed to be thin, we "unwrap" the jet and solve the planar rather than the cylindrical problem; this is done to facilitate any calculation in the sense that easily calculable trigonometric functions take the place of Bessel functions. The governing equations for the stagnation enthalpy in the jet ($-\infty < x_1 < \infty, 0 \leq z_1 < a$) and ambient ($-\infty < x_1 < \infty, z_1 > a$) respectively are

$$L_1(B) = \nabla \cdot (\tilde{\xi} \times \tilde{V}) \quad (5a)$$

$$L_\infty(B) = 0 \quad (5b)$$

where the operators L_1 and L_∞ are defined in (4a, 4b). Note that because of the "unwrapping" of the thin jet, in the rest of this section the plug surface is taken to be at $z_1 = 0$, on which the condition $\partial B / \partial z_1 = 0$ is satisfied [see Equation (2c) and Figure 7-2].

The perturbation vorticity is expressed as

$$\tilde{\xi} = \zeta(x) \delta(z_1 - h) \mathbf{j} \quad (6)$$

where \mathbf{j} is the unit vector in the y_1 direction, $\delta(z_1 - h)$ is the delta function with support at $z_1 = h \leq a$ and $\zeta(x)$ is a random function describing the strength and spatial coherence of the vorticity. Since the entire flow field is assumed to be two dimensional (i.e., independent of the azimuthal angle and, because of "unwrapping," independent of the lateral coordinate y_1), equation (6) corresponds to a "ring" of concentrated vorticity (located at $z_1 = h$) traveling downstream with velocity U_c relative to the laboratory coordinate system. In some idealized sense, (6) represents the effects of axisymmetric coherent structures in the jet and (5a, 5b) describe the noise generated by these structures. Note that the physical dimensions for ζ is velocity, and it is assumed that $(\zeta / U_1) \ll 1$ where U_1 is the jet velocity. Furthermore, the vorticity is frozen in the translating reference frame so that in the laboratory reference frame $\zeta = \zeta(x_1 - U_c t_1)$. Clearly U_c is the convective velocity of the turbulent structures in the jet and our translating coordinate system is attached to these eddies. Generally $U_c \approx 0.6 U_1$ (Davis, Fisher and Barratt, Reference 7-8).

The task before us is to solve (5a, 5b), with the given vorticity (6), subject to certain boundary and matching conditions across the vortex sheet.

Since (5a) has a source or inhomogeneous term which is random, it is convenient to solve our governing equations by decomposing all perturbations into mean (i.e., into an average) and random parts. For example, let the (perturbation) stagnation enthalpy B be written as a sum $\overline{B} = B + B'$ where the overbar represents ensemble average and the prime denotes the random component such that $\overline{B'} = 0$. Then by averaging (5a), we obtain

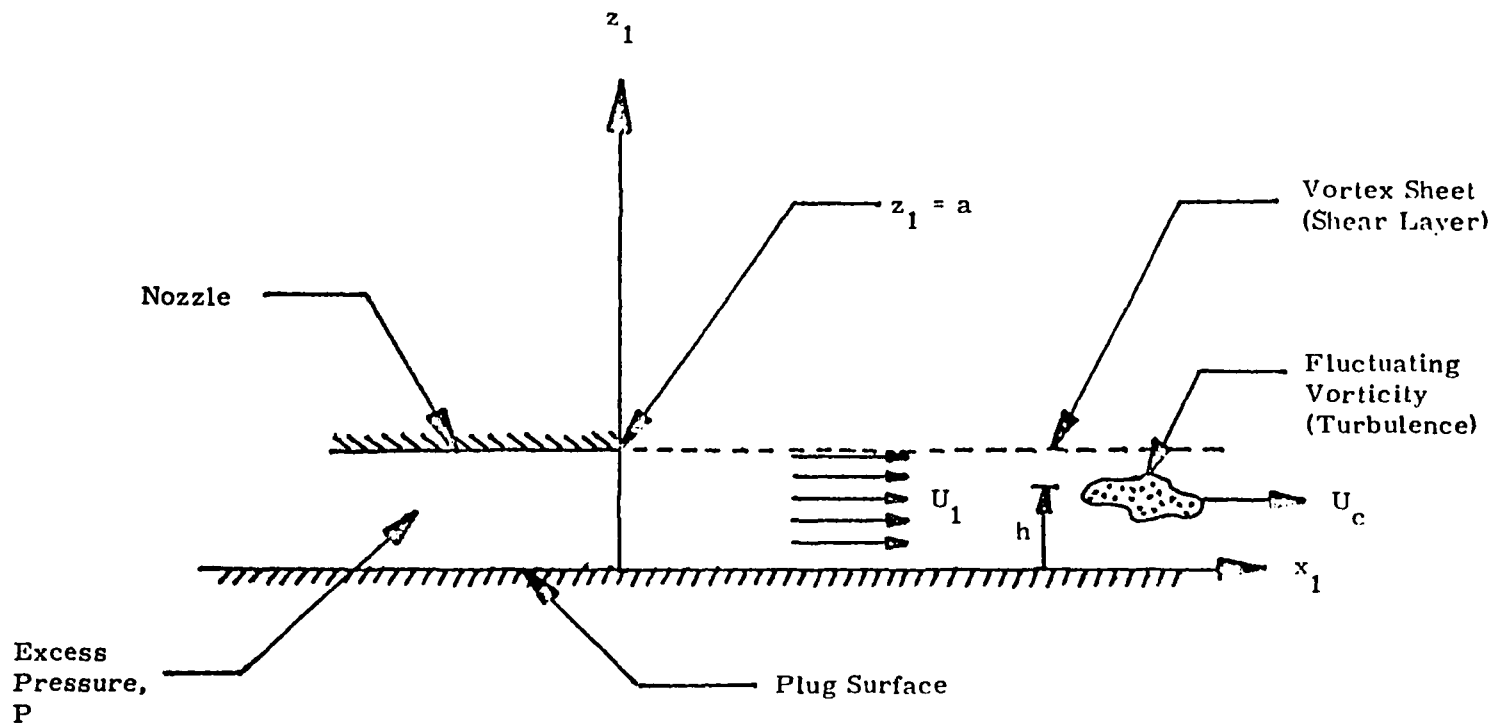


Figure 7-2. Idealized Planar Vortex Sheet Analogy
(y_1 coordinate is into paper)

$$L_1(\bar{B}) = \nabla \cdot \overline{(\tilde{\xi}' \times \tilde{V}')} \quad (7a)$$

since the mean part of the vorticity $\bar{\xi}$ is assumed to vanish. This is because in the vortex sheet analogy of Ffowcs-Williams (Reference 7-6), the mean vorticity in the jet shear layer is lumped into an infinitely thin vortex sheet that separates the jet from the ambient. After subtracting (7a) from (5a), we obtain the equation for the random part of the enthalpy field

$$L_1(B') = \nabla \cdot [\tilde{\xi}' \times \tilde{V}' + \tilde{\xi}' \times \tilde{V}' - \overline{\tilde{\xi}' \times \tilde{V}'}] \quad (7b)$$

Since the turbulent velocity fluctuations (ζ/U_1) are generally small, the last two terms in the right-hand side of (7b) may be ignored because they are quadratically small in (ζ/U_1) whereas the first term is linear. This approximation ignores the scattering of sound by jet turbulence.

Note that (7a, 7b) describe the mean and random components of the flow field in the jet. External to the jet, the relevant equations are

$$L_\infty(\bar{B}) = L_\infty(B') = 0 \quad (7c)$$

and across the vortex sheet interface suitable matching conditions are enforced. The relationships between the mean and random parts of the velocity components, pressure and enthalpy are readily obtained from (2c, 2d) by ensemble averaging. For example from (2c), we find

$$\frac{\partial \tilde{V}}{\partial t} = -\nabla \bar{B}, \quad \frac{\partial \tilde{V}'}{\partial t} = -\nabla B' \quad (8a, 8b)$$

Clearly governing equations (7a, 7b) are coupled since the random velocity \tilde{V}' in (7a) comes from the solution of (7b) for B' ; this latter equation cannot, however, be solved until the mean velocity \bar{V} is known from (7a). Very roughly speaking, the right-hand side of (7a) accounts for the effects of turbulent diffusion that lead to the decay of the shock structure in the jet. On the other hand, the right-hand side of (7b) represents the source of noise; specifically, noise is generated as turbulence interacts with the mean velocity field in the jet. In the study of shock associated noise, the relevant mean velocity is that due to the shock structure.

In the following sections, we outline the matching conditions across the shear layer and solve the governing equations.

7.2 SOLUTION FOR THE MEAN VELOCITY FIELD

In this section, the task before us is to solve for the mean enthalpy field \bar{B} which obeys, in the jet

$$L_1 (\bar{B}) = \nabla \cdot (\tilde{\xi}' \times \tilde{V}') \quad (9)$$

where the operator L_1 is defined in (4a). Since the right-hand side of (9) is unknown at this point (because the random velocity field \tilde{V}' is unknown), we write down the general formal solution. This is done by defining Fourier transform pairs in the translating coordinate x and time t as follows:

$$f(\omega, k) = \frac{1}{4\pi^2} \int_{-\infty}^{\infty} \int_{-\infty}^{\infty} f e^{-ikx} e^{+i\omega t} dx dt \quad (10a)$$

$$f(x, t) = \int_{-\infty}^{\infty} \int_{-\infty}^{\infty} \hat{f} e^{+ikx} e^{-i\omega t} dk d\omega \quad (10b)*$$

* $i = (-1)^{1/2}$

where $f = f(x, t)$ is an arbitrary function of time. Note that hat $\hat{}$ implies that the argument of a variable is ω (frequency) and k (axial wave number).

After applying Fourier transforms in the usual way to (9), we obtain

$$\left(\frac{d^2}{dz^2} + \Gamma^2 \right) \frac{\hat{B}}{B} = -\chi_1(\omega, k) \delta(z-h) - \chi_2(\omega, k) \delta'(z-h) \quad (11a)$$

where Γ is the transverse wave number

$$\Gamma^2 = \Gamma^2(\omega, k) = \frac{[\omega - k(U_1 - U_c)]^2}{c_1^2} - k^2 \quad (11b)$$

and the functions χ_1 and χ_2 are defined

$$\chi_1(\omega, k) = ik \overline{\zeta(x) \tilde{w}'_0(x, t)} \quad (11c)$$

$$\chi_2(\omega, k) = -\overline{\zeta(x) \tilde{u}'_0(x, t)} \quad (11d)$$

Note that \tilde{u}'_0 and \tilde{w}'_0 are the axial and transverse random velocity components [i.e., $\tilde{\mathbf{v}}' - (\tilde{u}', 0, \tilde{w}')$] evaluated at the transverse location of the vorticity $z = h \leq a$. Again we remark that the overbar represents ensemble averaging, U_1 and c_1 denote the velocity and acoustic speed of the jet with $M_1 = U_1/c_1 > 1$. The branch of Γ will be defined later.

The relationship between the Fourier transforms of the perturbation pressure \tilde{p} and enthalpy B follows from (2d).

$$\frac{\hat{B}}{B} = \frac{\omega}{\omega - (U - U_c)k} \frac{\tilde{p}}{\rho} \quad (12)$$

It is clear that in the ambient the mean value of the perturbation pressure vanishes. Since the pressure is continuous across the vortex sheet corresponding to the jet shear layer, we have

$$\overline{\tilde{P}} = 0 \text{ on } z_1 = a, x_1 > 0 \quad (13a)$$

Within the nozzle ($x_1 < 0$), the mean value of the perturbation pressure is taken to be $P = \text{const}$ for all values of the transverse coordinate $z_1 \leq a$. In other words, the mean flow field in our model is obtained by letting a high pressure ($P > 0$) supersonic jet expand in the ambient. P denotes the over (under) pressure in the jet depending on whether P is positive (negative).

After transforming the above boundary condition $\overline{\tilde{p}} = PH(-x_1)^*$ into the moving coordinate system $x_1 = x + U_c t$ and using Fourier transform (10a) and (12), we find

$$\frac{\hat{\Delta}}{\hat{B}} = S(\omega, k) = \frac{i P}{2\pi \rho_1} \frac{\omega}{\omega - (U_1 - U_c)k} \frac{\delta(\omega + U_c k)}{k} \quad (13b)$$

Clearly (13b) is to be satisfied on $z = a$; for $0 < z < a$, \hat{B} obeys (11a) and on $z = 0$, $\partial \hat{B} / \partial z = 0$ because of the rigid plug surface [see (2c)].

The solution for the Fourier transform of the mean stagnation enthalpy \hat{B} can be written down immediately. Across the location of the vorticity $z = h$, \hat{B} and its first derivative satisfy certain well-known jump conditions which are readily derivable from (11a) by integrating across $z = h$. We find, after some straightforward algebra arising from our previous remarks,

$$\frac{\hat{\Delta}}{\hat{B}} = A^{(3)} \cos \Gamma z \quad z < h \quad (14a)$$

$$\frac{\hat{\Delta}}{\hat{B}} = A^{(1)} \cos \Gamma z + A^{(2)} \sin \Gamma z \quad z > h \quad (14b)$$

where the coefficients $A^{(j)}$ ($j = 1, 2, 3$) are

* $H(\chi)$ denotes the Heaviside function; it is unity or zero depending on whether χ is positive or negative.

$$A^{(1)} = \frac{S}{\cos \Gamma a} + \frac{\chi_1}{\Gamma} \frac{\sin \Gamma a \cos \Gamma h}{\cos \Gamma a} + \chi_2 \frac{\sin \Gamma a \sin \Gamma h}{\cos \Gamma a} \quad (14c)$$

$$A^{(2)} = -\frac{\chi_1}{\Gamma} \cos \Gamma h - \chi_2 \sin \Gamma h \quad (14d)$$

$$A^{(3)} = \frac{S}{\cos \Gamma a} + \frac{\chi_1}{\Gamma} \frac{\sin \Gamma(a-h)}{\cos \Gamma a} + \chi_2 \frac{\cos \Gamma(a-h)}{\cos \Gamma a} \quad (14e)$$

Note that in (14) Γ , S , χ_1 and χ_2 are functions of the frequency ω and wave number k .

From (14) and the Fourier transform of (2c), we can readily derive mean velocities \hat{u} and \hat{w} . These velocities, evaluated at the location of the source $z = h$, will be needed in the solution of the random field [see (7b)]. Since \hat{B} and its derivative (d/dz) are discontinuous across $z = h$, we use the algebraic mean of \hat{B} and $d\hat{B}/dz$ at $z = h^\pm$ in order to obtain \hat{u}_0 and \hat{w}_0 . We find

$$\frac{\hat{u}}{\omega} = \frac{k}{\omega} \left(S \frac{\cos \Gamma h}{\cos \Gamma a} + \beta_{11} \frac{\chi_1}{\Gamma} + \beta_{12} \frac{\chi_2}{2} \right) \quad (15a)$$

$$\frac{\hat{w}}{\omega} = \frac{i\Gamma}{\omega} \left(S \frac{\sin \Gamma h}{\cos \Gamma a} + \beta_{21} \frac{\chi_1}{2\Gamma} + \beta_{22} \chi_2 \right) \quad (15b)$$

where

$$\beta_{11} = \sin \Gamma(a-h) \frac{\cos \Gamma h}{\cos \Gamma a} \quad (15c)$$

$$\beta_{12} = \cos^2 \Gamma h - \sin^2 \Gamma h + 2 \frac{\cos \Gamma h}{\cos \Gamma a} \sin \Gamma a \sin \Gamma h \quad (15d)$$

$$\beta_{21} = \beta_{12} \quad (15e)$$

$$\beta_{22} = \cos\Gamma(a - h) \frac{\sin\Gamma h}{\cos\Gamma a} \quad (15f)$$

Note that in (15), S , Γ , χ_1 and χ_2 are functions of ω and k .

This concludes the formal solution of the mean enthalpy and velocity fields. We shall return to them, however, in a later section once the coupling between the mean and random fields is explicitly established. This coupling is contained in the interaction functions χ_1 and χ_2 [see (11c, 11d)] which depend on the random field and are presently unknown.

7.3 SOLUTION FOR THE RANDOM VELOCITY FIELD

We now turn to the random enthalpy field B' which, in the jet and ambient, approximately obeys

$$L_1 (B') = \nabla \cdot (\tilde{\xi}' \times \tilde{V}) \quad (16a)$$

$$L_\infty (B') = 0 \quad (16b)$$

where operators L_1 and L_∞ are defined by (4a, 4b). Note that $\tilde{\xi}'$ is the random vorticity specified by (6) and \tilde{V} denotes the mean velocity field obtained in the previous section.

The above equations can be solved by enforcing the usual (and wellknown) matching of the pressure and particle displacement across the vortex sheet interface. In fact, for the case of cylindrical geometry, this was done by Howe and Ffowcs-Williams (Reference 2-6). Their results are extremely complicated, however, and our objective is to obtain simpler results that use many of their ideas but at the same time lie closer to the classic and successful works of Harper-Bourne and Fisher (Reference 5-2), Ribner (Reference 7-2) and Lighthill (Reference 7-1).

It is known from experimental data (see Harper Bourne and Fisher (Reference 5-2) and Tanna (Reference 5-6) that shock associated noise is the most dominant in the forward quadrant; in terms of the observation angle θ , measured relative to the jet axis, shock noise is important in the range $90^\circ < \theta < 180^\circ$. Furthermore, at a given jet Mach number $M_1 = U_1/c_1 > 1$, shock noise is largely insensitive to the temperature of the jet. This suggests that the shrouding effects of the mean flow are not important for shock associated noise; of course, exactly the opposite is true for pure mixing noise (Mani, Reference 7-9).

To state the above differently, it is known that the most important effect of the mean flow (i.e., jet velocity and temperature) on jet noise is the production of complicated convective amplification and temperature effects. For example, in the case of the mixing noise of hot jets, the so-called density exponent of the noise is an elaborate function of source frequency, observation angle, jet temperature, etc., (Mani, Reference 7-5) rather than the single value of 2 as predicted by Lighthill (Reference 7-9). Since neither of these two effects (i.e., convective and temperature) are particularly significant for shock noise, we may, to a good approximation, ignore the shrouding effects of the mean flow. Based on these remarks, the governing equation for the random field in the jet becomes, in place of (16a),

$$L_1 (B') = \nabla \cdot (\tilde{\mathbf{E}}' \times \tilde{\mathbf{V}}) \quad (17)$$

Clearly (17) holds throughout space because of (16b).

For our purposes (17) is most conveniently solved again by Fourier transforms [see (10)]; however, this time the frequency and axial wave number are denoted by Ω and K , respectively, in order to avoid confusion later on. Furthermore, the transform of a quantity f is denoted by f (rather than \hat{f}). Thus (17) becomes

$$\left(\frac{d^2}{dz^2} + \gamma^2 \right) B' = - \Lambda_1 (\Omega, K) \delta (z - h) - \Lambda_2 (\Omega, K) \delta' (z - h) \quad (18a)$$

where γ is a transverse wave number whose branch will be specified later:

$$\gamma^2 = \gamma^2(\Omega, K) = \frac{(\Omega + K U_c)^2}{c_\infty^2} - K^2 \quad (18b)$$

and the functions Λ_1 and Λ_2 are defined by

$$\Lambda_1(\Omega, K) = iK \left[\zeta(x) \overline{\overline{w}}_0(x, t) \right] \quad (18c)$$

$$\Lambda_2(\Omega, K) = - \left[\zeta(x) \overline{\overline{u}}_0(x, t) \right] \quad (18d)$$

where the inverted flex $\overline{\overline{}}$ on the right-hand sides of (18c, 18d) acts on the product enclosed by the square brackets.

Equation (18a) is solved by enforcing the Sommerfeld radiation condition* and the vanishing of the first derivative at infinity and the plug surface respectively. Clearly the scattering of the random field by the jet nozzle is ignored. After satisfying the usual jump conditions across the source $z = h$, we find

$$B' = [C^{(2)} - i C^{(1)}] \cos \gamma z, \quad z < h \quad (19a)$$

$$B' = - i C^{(1)} \exp(i\gamma z), \quad z > h \quad (19b)$$

*Actually, we assign a small imaginary value to Ω and invoke boundedness as $z \rightarrow \infty$.

where

$$c^{(1)}(\Omega, K) = \frac{1}{4\pi^2} \int_{-\infty}^{\infty} e^{i\Omega T} dT \int_{-\infty}^{\infty} [\bar{u}_0(x, T) \sin\gamma h - \frac{iK}{\gamma} \bar{w}_0(x, T) \cos\gamma h] \zeta(x) e^{-iKx} dx \quad (19c)$$

$$c^{(2)}(\Omega, K) = \frac{1}{4\pi^2} \int_{-\infty}^{\infty} e^{i\Omega T} dT \int_{-\infty}^{\infty} [-\bar{u}_0(x, T) \cos\gamma h - \frac{iK}{\gamma} \bar{w}_0(x, T) \sin\gamma h] \zeta(x) e^{-iKx} dx \quad (19d)$$

Note that γ , \wedge_1 , \wedge_2 , $c^{(1)}$ and $c^{(2)}$ are functions of the new Fourier transform variables (Ω, K) ; we emphasize this again in order to avoid total confusion later on. Observe also that the axial component of the mean velocity is denoted by $\bar{u}(x, z, t)$ and $\bar{u}_0(x, t)$ stands for $\bar{u}(x, h, t)$. If \bar{u} is discontinuous across $z = h$, \bar{u}_0 equals the algebraic average of \bar{u} across $z = h$. Similar remarks hold for $\bar{w}_0(x, t)$, $\bar{u}_0'(x, t)$ and $\bar{w}_0'(x, t)$.

After inverting (19a, 19b) to obtain the random enthalpy B' and using (2c), we find

$$\begin{aligned} \bar{u}_0'(x, t) = & -\frac{i}{2} \int_{-\infty}^{\infty} e^{-i\Omega t} d\Omega \int_{-\infty}^{\infty} \frac{K}{\Omega} e^{iKx} [c^{(1)} e^{i\gamma h} \\ & + (c^{(1)} + i c^{(2)}) \cos\gamma h] dK \end{aligned} \quad (20a)$$

$$\bar{w}_0'(x, t) = -\frac{i}{2} \int_{-\infty}^{\infty} e^{-i\Omega t} d\Omega \int_{-\infty}^{\infty} \frac{\gamma}{\Omega} e^{iKx} [c^{(1)} e^{i\gamma h}$$

$$+ i (c^{(1)} + i c^{(2)}) \sinh] dK \quad (20b)$$

Furthermore, by invoking the equivalent of (12) for the relationship between pressure and enthalpy and inverting (19b), the random pressure field in the moving coordinate system becomes

$$\frac{\tilde{p}'}{\rho_\infty} = - i \int_{-\infty}^{\infty} e^{-i\Omega t} d\Omega \int_{-\infty}^{\infty} \frac{\Omega + U_c K}{\Omega} c^{(1)} e^{i\gamma z} e^{iKx} dK \quad (20c)$$

whenever $z > h$. Note that in (20) γ , $c^{(1)}$ and $c^{(2)}$ are functions of (Ω, K) .

We have now derived expressions (20a, 20b) for the random velocity field at the source. These depend in a complicated way on the corresponding mean velocities \widetilde{u}_0 and \widetilde{w}_0 through coefficients $c^{(1)}$ and $c^{(2)}$ [see (19c, 19d)]. However, by the use of (11c, 11d) and (20a, 20b) the interaction functions χ_1 and χ_2 may be expressed (at least formally) in terms of mean velocities \widetilde{u}_0 and \widetilde{w}_0 by evaluating explicitly the right-hand sides of (11c, 11d). This is done in the following section.

7.4 INTERACTION BETWEEN MEAN AND RANDOM FIELDS

In Section 3, we have expressed the mean velocity field (15a, 15b) in terms of certain properties of the random field (i.e., χ_1 and χ_2). In Section 4, the situation is reversed in the sense that the random field is expressed in terms of the mean velocity field [see (19c, 19d) and 20a, 20b)]. The purpose of this section is to establish the correct simultaneous relationships between the mean and random fields by first evaluating interaction functions χ_1 and χ_2 via (11c, 11d) and (20a, 20b). This results in expressions for χ_1 and χ_2 in terms of the mean velocity fields. Next these expressions for χ_1 and χ_2 are substituted into

(15a, 15b) from which we obtain unique values for the mean velocity field. This procedure is algebraically complex since sometimes we deal with the velocity fields directly, other times we deal with their Fourier transforms.

A straightforward substitution of the transverse component \tilde{w}'_0 of the random velocity from (20b) into (11c) for χ_1 results in a six fold integral over (Ω, K) , (X, T) and (ω, k) . Incidentally, it now becomes apparent why we have chosen different symbols for the Fourier transforms of the mean and random fields. We must distinguish between the dummy variables of integration in order to avoid total chaos. The integrand for χ_1 will contain the two point correlation of turbulence, $\overline{\zeta(x) \zeta(X)}$. Because the turbulence is assumed to be homogeneous

$$\overline{\zeta(x) \zeta(X)} = R(X - x) \quad (21)$$

where R is the correlation function. By an obvious change of a variable of integration, one of the integrals reduces to a delta function. Because of this, a second integral can be immediately evaluated and using a third integral for the definition of the turbulence spectrum, the original six fold integration reduces to a three dimensional integral. By employing the definition of Fourier transforms and using the same procedure for χ_2 , the final results are

$$\chi_1(\omega, k) = \frac{\Lambda}{\tilde{u}_0} a_{11} + \frac{\Lambda}{\tilde{w}_0} a_{12} \quad (22a)$$

$$\chi_2(\omega, k) = \frac{\Lambda}{\tilde{u}_0} a_{21} + \frac{\Lambda}{\tilde{w}_0} a_{22} \quad (22b)$$

where

$$a_{11} = \frac{k}{\omega} \int_{-\infty}^{\infty} \gamma e^{i\gamma h} \sin\gamma h \Phi(K - k) dK \quad (22c)$$

$$a_{12} = -ik a_{21} \quad (22d)$$

$$a_{21} = \frac{1}{2\omega} \int_{-\infty}^{\infty} K e^{2i\gamma h} \Phi(K - k) dK \quad (22e)$$

$$a_{22} = \frac{1}{\omega} \int_{-\infty}^{\infty} \frac{K^2}{\gamma} e^{i\gamma h} \cos\gamma h \Phi(K - k) dK \quad (22f)$$

Note the following extremely important point: in (22c - 22f) $\gamma = \gamma(\omega, K)$. Because of this, coefficients α_{mn} ($m = 1, 2$; $n = 1, 2$) are functions of (ω, k) .

The wave number spectrum of the turbulence is defined by

$$\Phi(k) = \frac{1}{2\pi} \int_{-\infty}^{\infty} R(a) e^{-ika} da \quad -\infty < k < \infty \quad (23a)$$

and since R is an even function of its argument

$$\Phi(k) = \frac{1}{\pi} \int_0^{\infty} R(a) \cos ka da \quad (23b)$$

Φ is obviously real and an even function of the wave number k . From "energy" considerations, we must also have $\Phi \geq 0$.

Clearly (22a, 22b) provide an explicit representation of the interaction functions χ_1 and χ_2 as a linear combination of the Fourier transform of the mean velocities at the source. If we now take this representation to eliminate χ_1 and χ_2 from (15a, 15b), we obtain a system of linear equations for \hat{u}_0 and \hat{w}_0 . The inhomogeneous term in this system is clearly proportional to S ; S is the Fourier transform of the boundary condition for the mean enthalpy field at the edge of the jet (13b).

Since the turbulent velocity fluctuations (ζ/U_1) are small, the coefficients α_{mn} occurring in (22a, 22b) are quadratically small. Because of this, χ_1 and χ_2 are also quite small so that (15a, 15b) may be solved by perturbing about the $\zeta = 0$ state. Thus, in the complete absence of turbulence

$$\frac{\hat{u}}{\hat{u}_0} = \frac{k}{\omega} S \frac{\cos \Gamma h}{\cos \Gamma a} \quad (24)$$

and the mean field is generated by the shock pattern set up by the under (over) expanded jet. In order to obtain the axial component of the mean velocity, the inverse transform of (24) must be found. This is a simple task since the ω integral has a contribution only at the single point $\omega = -U_c k$ because of the occurrence of the delta function in the definition of S (13b). Therefore, from (11b), Γ in (24) may be replaced by $\beta_1 k$ where $\beta_1 = (M_1^2 - 1)^{1/2}$. Note that the last remark defines the proper branch of Γ . Now the remaining k integral associated with the inverse Fourier transform of (24) has contributions only from the poles of the integrand, namely, from points where $\cos \Gamma a = \cos \beta_1 a k = 0$. (Obviously, the k integral is most conveniently evaluated in the complex k plane.) These points are on the real axis at $\beta_1 a k_n = (n + 1/2) \pi$ ($n = 0, \pm 1, \pm 2, \dots$).

Clearly the above conclusions are not expected to be modified greatly in the presence of a "small" amount of turbulence in the jet (i.e., $\zeta/U_1 \ll 1$). It is well known that the randomness associated with turbulence leads to diffusion that results in the downstream weakening of the shock structure. Mathematically this will occur if the poles of the relevant integrand contain imaginary parts.

Of course, the already outlined mathematical procedure contains the physics to which we have briefly alluded; we now set out to demonstrate this. The solution of (15a, 15b) for \hat{u}_0 and \hat{w}_0 is straightforward when χ_1 and χ_2 are given by (22a, 22b) and coefficients α_{mn} ($m = 1, 2; n = 1, 2$) are small. In terms of the determinant D of the linear system of equations, we have

$$\frac{\hat{u}_0}{\omega} = \frac{k}{\omega} S \frac{\cos \Gamma h + O(\alpha_{mn})}{D} \quad (25a)$$

$$\frac{\hat{w}_0}{\omega} = \frac{i\Gamma}{\omega} S \frac{\sin \Gamma h + O(\alpha_{mn})}{D} \quad (25b)$$

where

$$D = [1 + O(\alpha_{mn})] \cos \Gamma a + [-\alpha_{11} \frac{k}{\omega} \frac{\cos^2 \Gamma h}{\Gamma} - \alpha_{12} \frac{i}{\omega} \frac{\cos \Gamma h \sin \Gamma h}{\Gamma} \quad (25c)$$

$$- \alpha_{21} \frac{k}{\omega} \cos \Gamma h \sin \Gamma h - \alpha_{22} \frac{i\Gamma}{\omega} \sin^2 \Gamma h + O(\alpha_{mn}^2)] \sin \Gamma a$$

Note that in the approximation contained in (25a, 25b), we ignore additive effects of $O(\alpha_{mn})$ due to turbulence; we simply look for the displacement of the poles, of the integrand of the inverse Fourier transform of \hat{u}_0 and \hat{w}_0 , away from the real axis. These poles are the zeroes of the determinant D on which we now concentrate.

Our objective is to obtain the simplest possible expressions for these zeroes while retaining the effects of turbulent diffusion to lowest order. This can be done by observing that the most likely location for the turbulence is at the edge of the shear layer $h \approx a$. Furthermore, based on what was said previously, the zeroes of D are expected to be very near $\beta_1 ak \approx (n + 1/2)\pi$ ($n = 0, \pm 1, \dots$) so that $\cos \Gamma h \approx 0$. Therefore, to a reasonable degree of approximation

$$D \approx [1 + O(\alpha_{mn})] \cos \Gamma a + [-\alpha_{22} \frac{i\Gamma}{\omega} \sin^2 \Gamma h + O(\alpha_{mn}^2)] \sin \Gamma a \quad (25d)$$

or

$$D \approx [1 + O(\alpha_{mn})] [\cos \Gamma(a + \frac{i}{\omega} \alpha_{22} \sin^2 \Gamma h) + O(\alpha_{mn}^2)] \quad (25e)$$

Finally we ignore terms of $O(\alpha_{mn})$ or smaller except the one effect of $O(\alpha_{mn})$ that leads to an imaginary part for the zeroes. Thus, in the desired approximation, the determinant of the system of linear equations becomes

$$D = \cos \Gamma \left[a + \frac{i}{\omega} \sin^2 \Gamma h \operatorname{Re}(\alpha_{22}) \right] \quad (26)$$

Where $\operatorname{Re}(\)$ denotes the real part of a complex number and $\alpha_{22} = \alpha_{22}(\omega, k)$ is defined by (22f).

We are now ready to obtain the mean component of the velocity field at the source. From (25a), (26) and the result for S (13b), we find that the Fourier inverse (10b) leads to

$$\bar{u}_0(x, t) = \frac{1}{2\pi i} \frac{P}{\rho_1 U_1} \int_{-\infty}^{\infty} e^{ik(x + U_c t)} \frac{\cos k \beta_1 h}{\cos k \beta_1 (a + i\Delta)} \frac{dk}{k} \quad (27a)$$

after evaluating the ω integral involving the delta function. The quantity $\Delta = \Delta(k)$ is defined as

$$\begin{aligned} \Delta(k) &= - \frac{\operatorname{Re}[\alpha_{22}(-U_c k, k)]}{U_c k} \sin^2 k \beta_1 h \\ &= \frac{\sin^2 k \beta_1 h}{U_c^2 k^2} \operatorname{Re} \int_{-\infty}^{\infty} \frac{K^2}{\gamma} e^{i\gamma h} \cos \gamma h \frac{1}{2} (K - k) dK \end{aligned} \quad (27b)$$

where in (27b) $\gamma = \gamma(-U_c k, K)$. Similarly, the transverse mean velocity and the mean pressure are given by

$$\tilde{w}_0(x, t) = \frac{\beta_1}{2\pi} \frac{P}{\rho_1 U_1} \int_{-\infty}^{\infty} e^{ik(x + U_c t)} \frac{\text{sink } \beta_1 h}{\text{cosk } \beta_1 (a + i\Delta)} \frac{dk}{k} \quad (27c)$$

and

$$\tilde{p} = \frac{iP}{2\pi} \int_{-\infty}^{\infty} e^{ik(x + U_c t)} \frac{\text{cosk } \beta_1 z}{\text{cosk } \beta_1 (a + i\Delta)} \frac{dk}{k} \quad (27d)$$

Note that (27d) is valid for $z < h$ and comes from (14a), (14e), (12) and the results of this section for χ_1 , χ_2 , and D . Finally, the integrals in (27a, 27c, 27d) will be evaluated in another section by the method of residues and a somewhat more explicit representation for $\Delta = \Delta(k)$ will be furnished also.

7.5 ACOUSTIC FIELD

In Section 7.3, we have obtained a representation of the random pressure field (20c) which is valid for $z > h$. Our immediate objective is to derive an expression for the random far field as $(x_1^2 + z_1^2)^{1/2} \rightarrow \infty$; clearly this will be the acoustic field. This is done by the method of stationary phase, once the pressure field is expressed in terms of laboratory coordinates.

From (20c), we find

$$\frac{\tilde{p}'}{\rho_\infty} = -i \int_{-\infty}^{\infty} e^{-i\Omega t} d\Omega \int_{-\infty}^{\infty} \frac{\Omega + U_c K}{\Omega} C^{(1)}(\Omega, K) e^{i\gamma z_1} e^{iK(x_1 - U_c t)} dK \quad (28)$$

where we have written t for t_1 (since a Galilean transformation does not alter time), $C^{(1)}(\Omega, K)$ is given by (19c) and \tilde{u}_0 and \tilde{w}_0 , required by (19c), can be obtained from (27a, 27c). The solution given by (28) is for the

planar problem with which we have been dealing. In the far field, the approximation of planar flow is not good because this approximation cannot predict the spherical decay of the acoustic field. Furthermore, the planar problem has associated with it a number of other "peculiarities" such as a convective amplification factor which is a fractional power of the usual Doppler factor (Howe, Reference 7-3). In order to avoid these unfamiliar (but correct for planar flow) effects and to obtain simply the familiar axisymmetric solution, we observe that $\exp(i\gamma z_1)$ in (28) is precisely the outgoing wave solution which should be replaced by $(2/\pi \gamma r)^{1/2} \exp[i\gamma(r-b) - i\pi/4]$ as $r \rightarrow \infty$ where r is the distance from the jet axis and b is the plug radius. In the rest of this paper, but only for the calculation of the far field, we make this replacement.

The inner or K integral of (28) may be evaluated by the method of stationary phase (Carrier, Krook and Pearson, Reference 7-10, p. 273). When the eddy convection Mach number is subsonic, $M_c = U_c/c_\infty < 1$, there is a single point of stationary phase at

$$K = K_* = \frac{\Omega}{c_\infty} \frac{\cos\theta}{1 - M_c \cos\theta} \quad (29a)$$

$$\gamma(\Omega, K_*) = \frac{\Omega}{c_\infty} \frac{\sin\theta}{1 - M_c \cos\theta} \quad (29b)$$

and θ is usually interpreted as the emission angle measured from the jet axis. After performing the well-known algebra associated with the stationary phase calculation, we find that the acoustic pressure in the far field reduces to

$$\frac{\tilde{p}'}{p_\infty} = -\frac{2i}{R} \frac{1}{(1 - M_c \cos\theta)^2} \int_{-\infty}^{\infty} C^{(1)}(\Omega, K_*) \quad (30)$$

$$\exp i\Omega [R/c_\infty - t - b \sin\theta/c_\infty (1 - M_c \cos\theta)] d\Omega$$

where $R \rightarrow \infty$ is the distance from the nozzle exit. It is worth emphasizing that, strictly speaking, R and θ are the length and direction (relative to the axis of the jet) of the vector to the observer from the emission location of the moving source; in other words, R and θ are retarded coordinates (Morse and Ingard, Reference 7-11, p. 723). This fact must be recalled in the following section when we discuss the implications of the theory. When the eddy convection Mach number is supersonic (i.e., $M_c > 1$), the necessary changes are explained in the next section.

The above expression (30) for the acoustic field can be simplified further by evaluating $C^{(1)}(\Omega, K_x)$ explicitly from (19c) and (27a, 27c). The three fold integral over (X, T, k) can be reduced to a double integral since the integration with respect to T results in a delta function, $\delta(\Omega + U_c k)$. After substituting $C^{(1)}$ into (30), the Ω integral is trivial; this yields a double integral for the acoustic field as follows

$$\frac{\tilde{p}'}{\rho_\infty} = - \frac{1}{2\pi^2 R} \frac{P}{\rho_1 U_1} \frac{1}{(1 - M_c \cos\theta)^2} \int_{-\infty}^{\infty} \zeta(X) dX \int_{-\infty}^{\infty} \frac{dk}{k}$$

$$\times \left[\frac{-\sin\gamma_0 h \cos k \beta_1 h + \frac{\beta_1 K_0}{\gamma_0} \cos\gamma_0 h \sin k \beta_1 h}{\cos k \beta_1 [a + i\Delta(k)]} \right] \quad (31a)$$

where

$$\times \exp ik [(X + M_c b \sin\theta)/(1 - M_c \cos\theta) - M_c R + U_c t]$$

$$K_0 = k \frac{M_c \cos\theta}{1 - M_c \cos\theta} \quad (31b)$$

$$\gamma_0 = k \frac{M_c \sin\theta}{1 - M_c \cos\theta} \quad (31c)$$

The quantity of physical interest is not the instantaneous acoustic pressure in the far field but its spectrum defined by

$$W(\omega) = \frac{1}{2\pi} \int_{-\infty}^{\infty} \overline{p'(t) p'(t + \tau)} e^{i\omega\tau} d\tau \quad (32)$$

where ω is the radian frequency and τ is an arbitrary time delay. The quantity $p'(t)$ is given by (31a). After substituting (31a) into (32), a five fold integral results over the dummy variables of integration (k , X), (k^+ , X^+) and τ . The integrand contains the factor $\zeta(X) \zeta(X^+) = R(X^+ - X)$, which is the two point correlation of the turbulence. An obvious change in the variables of integration X and X^+ leads to an integral which is calculable in terms of the delta function $\delta[(k + k^+)/(1 - M_c \cos\theta)]$. The evaluation of a second integral results in the appearance of the wave number spectrum Φ in place of the correlation R .

Based on the preceding remarks, the original five fold integral reduces to a three dimensional integral. Further progress is possible, however. The k^+ integration is trivial; the contribution arises from the point $k^+ = -k$. Because of this, the τ integration is simple, resulting in $\delta(\omega - U_c k)$ and the remaining integral over k has contribution at $k = \omega/U_c$ only. Therefore, the final result for the spectrum is

$$W(\omega) = \frac{\rho_\infty^2}{\pi^2 R^2 U_c} \frac{P^2}{(\rho_1 U_1)^2} \frac{1}{(1 - M_c \cos\theta)^3} \Phi\left(\frac{k}{1 - M_c \cos\theta}\right)$$

$$\frac{[\beta_1 \frac{K_0}{\gamma_0} \cos\gamma_0 h \operatorname{sinc} \beta_1 h - \sin\gamma_0 h \operatorname{cosec} \beta_1 h]^2}{k^2 |\operatorname{cosec} \beta_1 [a + i\Delta(k)]|^2} \quad (33)$$

where $k = \omega/U_c$. Recall $\beta_1 = (M_1^2 - 1)^{1/2}$ where $M_1 > 1$ is the jet Mach number, Φ is the wave number spectrum of the turbulence and K_0 and γ_0 are defined by (31b, 31c). Note that in arriving at (33) we have assumed that $\Delta(k)$ is an odd function k ; this will be proven in the next section.

7.6 DISCUSSIONS AND CONCLUSIONS

The spectrum of shock associated noise was derived in the previous section and is given by (33). In this section, we study, in detail, the implications of our theory when the turbulence spectrum is specified in a reasonable but completely ad hoc manner. Before we do this, however, there are a number of loose ends that need to be addressed.

First the choice for the branch cuts of the transverse wave number $\gamma = \gamma(\Omega, K)$ in the complex K plane must be decided. We do this through a procedure of Lighthill (Reference 7-12) in which Ω is assigned a small, positive imaginary part so that $\exp(-i\Omega t)$ will be growing in time [see (10b)]. We now choose that branch of γ which renders $\exp(i\gamma z)$ exponentially small as $z \rightarrow +\infty$. This fixes the desired branch at which point the small imaginary part may be set to zero. It is important to realize that the branch cuts are quite different when the eddy convection Mach number M_c is subsonic and supersonic. Roughly speaking when $M_c < 1$ one branch goes "up" and the other "down" in the complex K plane. On the other hand, for supersonic eddy convection, both branches go "down." The path of integration for the K integral is the real axis [e.g., (20 a, b, c)].

Based on these remarks, it is easy to show from (27b) that for $k > 0$

$$\Delta(k) = - \frac{\sin^2 k \beta_1 h}{(ak)^2 U_c^2} \int_{M_c \frac{ak}{1-M_c}}^{M_c \frac{ak}{1+M_c}} \frac{K^2}{\mu} \cos^2 \mu \Phi \left(\frac{K-ak}{a} \right) dK \quad (34a)$$

where

$$\mu = | M_c^2 (K - ak)^2 - K^2 |^{1/2} .$$

On the other hand for $k < 0$, we have

$$\Delta(k) = \frac{\sin^2 k \beta_1 h}{(ak)^2 U_c^2} \int_{M_c \frac{ak}{1+M_c}}^{- M_c \frac{ak}{1-M_c}} \frac{K^2}{\mu} \cos^2 \mu \Phi \left(\frac{K-ak}{a} \right) dK \quad (34b)$$

Replacing k by $(-k)$ in (34b), changing the variable of integration from K to $(-K)$ and also invoking the fact that Φ is an even function of its argument, we arrive at $\Delta(k) = -\Delta(-k)$; in other words, Δ is an odd function of the wave number k .

The above representations (34a, b) for $\Delta(k)$ are valid when the eddy convection Mach number is subsonic ($M_c < 1$). When the eddy convection Mach number is supersonic ($M_c > 1$), we similarly have

$$\Delta(k) = - \frac{\sin^2 k \beta_1 h}{(ak)^2 U_c^2} \int_{-\infty}^{ak \frac{M_c}{1+M_c}} \frac{K^2}{\mu} \cos^2 \mu \Psi \left(\frac{K-ak}{a} \right) dK$$

$$+ \frac{\sin^2 k \beta_1 h}{(ak)^2 U_c^2} \int_{ak \frac{M_c}{M_c-1}}^{\infty} \frac{K^2}{\mu} \cos^2 \mu \Psi \left(\frac{K-ak}{a} \right) dK \quad (34c)$$

whenever $k > 0$. We again have $\Delta(k)$ as an odd function of k so that we will not write out the expression for this quantity for negative wave numbers in the supersonic case. It is possible to show that for $k > 0$, $\Delta(k) < 0$ and (34a) and (34c) are equal and finite when $M_c = 1$.

A short physical interpretation for $\alpha_{22}(\omega, k)$, therefore, indirectly for $\Delta(k)$, has already been given in Section 5. There we state that α_{22} is responsible for shifting certain poles off the real axis and representing the effects of turbulent diffusion. We now elaborate on this by evaluating the mean pressure field (27d) in the jet.

Observe first $(x + U_c t) = x_1$ where x_1 is the laboratory coordinate measured along the axis of the jet. Thus, the mean pressure field in laboratory coordinates is independent of time as expected. The infinite sequence of poles associated with the integrand of (27d) occurs approximately at

$$\beta_1 ak = \left(n + \frac{1}{2}\right) \pi \left[1 - \frac{i \Delta(k)}{a} \right] \quad (35a)$$

since $\Delta(k)/a$ is small, where

$$\beta_1 a k_n = (n + \frac{1}{2}) \pi \text{ for } n = 0, \pm 1, \pm 2, \dots$$

These poles occur in the upper half plane for all values of n . The path of integration is the real axis, for reasons discussed above (in connection with the K plane), passing above the pole at $k = 0$. For a point within the nozzle, $x_1 < 0$, and the contour in the k plane is closed in the lower half plane. By the method of residues

$$\bar{p} = P \tag{35b}$$

so that indeed the mean pressure in the nozzle is given by the overpressure P . On the other hand, in the jet proper $x_1 > 0$ and the contour is closed in the upper half plane. By the method of residues we find

$$\bar{p} = \frac{2P}{\pi} \sum_{n=0}^{\infty} \frac{(-1)^n \cos [(n + \frac{1}{2}) \pi z/a] \cos [(n + \frac{1}{2}) \pi x_1/\beta_1 a]}{(n + \frac{1}{2})} \exp [\frac{\Delta(k_n)}{a} (n + \frac{1}{2}) \pi x_1/\beta_1 a] \tag{35c}$$

In the absence of turbulence (i.e., $\Delta = 0$), (35c) represents the well-known shock pattern in a planar jet. This pattern extends from the nozzle exit to downstream infinity without any change in strength; the pattern is created by the successive reflections of a shock wave from the plug surface and the jet shear layer. (Of course, in our linearized model, these shock reflections are simply Mach wave reflections.) In the presence of turbulence ($\Delta \neq 0$), the shock pattern decays in the downstream direction [recall $\Delta(k)$ is negative for k positive] because of the randomness or diffusion associated with the turbulence. This decay is the largest for the $n = 0$ term or "mode" of (35c) since $|\Delta(k)|$ is a decreasing function of positive wave

numbers k . Thus, the interaction between the mean and random fields, through the action of turbulence, removes energy from the lower order modes of the mean field. Clearly this energy shows up in the disturbances associated with the random field and we now turn to the examination of this effect.

The spectrum of the acoustic field is (33)

$$W(\omega) = \frac{\rho_\infty^2}{\pi^2 R^2 U_c} \frac{P^2}{(\rho_1 U_1)^2} \frac{1}{(1 - M_c \cos\theta)^3} \Phi\left(\frac{k}{1 - M_c \cos\theta}\right)$$

$$\times \frac{[\beta_1 \frac{K_0}{\gamma_0} \cos\gamma_0 h \sin k \beta_1 h - \sin\gamma_0 h \cos k \beta_1 h]^2}{k^2 |\cos k \beta_1 [a + i\Delta(k)]|^2} \quad (36)$$

where $k = \omega/U_c$, $\beta_1 = (M_1^2 - 1)^{1/2}$, Φ is the wave number spectrum of the turbulence (23a) and K_0 and γ_0 are defined by (31b, c). The jet velocity, density and over (under) pressure are given by U_1 , ρ_1 and P ; the spectrum is given for an observer located at a distant point in the far field at polar position (R, θ) relative to the nozzle exit. The eddy convection Mach number is $M_c = U_c/c_\infty$ and the location of the turbulence is near the edge of the shear layer at $z_1 = h \approx a$. The frequency ω is the angular frequency of the source (i.e., the source frequency) in its convecting reference frame.

Observe first that the spectrum W is generally of order Φ which in turn is proportional to the square of the turbulence fluctuations. Therefore, shock associated noise is quite negligible except at frequencies where the denominator of (36) becomes small. This occurs at

$$k = \frac{\omega}{U_c} \approx k_n = \frac{(n + \frac{1}{2}) \pi}{\beta_1 a} \quad n = 0, \pm 1, \dots \quad (37a)$$

In particular, since both the turbulence spectrum Φ and the last factor in (36) decreases rapidly with increasing frequency, shock associated noise is significant only at the source frequency

$$\omega = \frac{\pi}{2} \frac{U}{a \beta_1} \quad (37b)$$

The last remark agrees, at least qualitatively, with the experimental results of Harper-Bourne and Fisher (Reference 5-2) and Tanna (Reference 5-6). Note that the main contribution to the acoustic spectrum arises from the lowest "mode" of the shock-cell system.

In order to make additional progress, we must make reasonable assumptions for the turbulence spectrum Φ . Since this spectrum describes the vorticity fluctuations in the turbulence, it must be of the form (wave number)² ψ where ψ is the spectrum of the turbulent velocity fluctuations. There is, of course, no experimental information on Φ and we must make a crude (but perhaps not unrealistic) guess. This guess limits the accuracy of our theory; clearly this theory cannot be anything more than a qualitative model for shock associated noise. It also becomes immediately clear that detailed numerical calculations for the spectrum, sound pressure level, etc., are totally unwarranted since the accuracy of those calculations hinges on the form of the turbulence spectrum. We shall be content here with giving overall trends for the various features of shock associated noise.

Assume that the wave number spectrum of the vorticity is given by

$$\Phi(k) \sim (kL)^2 \exp(-k^2 L^2) \quad (38)$$

where L is the length scale of the turbulence. The proportionality sign in (38) may be replaced by an equal sign if certain constants, inessential for the present discussion, are included in (38). This spectrum attains its maximum at $k_{\max} = L^{-1}$, corresponding to a dominant vortical eddy size of length L . Since the shock associated noise of a supersonic jet is generated

by the large-scale coherent structures that originate in the jet instability wave, $L \gg a$. In other words, a typical eddy has a long lifetime and passes through several (say eight) shock-cells before it loses its coherence significantly. Therefore, $k_{\max} = L^{-1} \approx 0$ so that from (34b)

$$\frac{\Delta(k)}{a} \approx \frac{\sin^2 k \beta_1 h}{U_c^2} \frac{\cos^2 ak}{|ak|} \int_0^{-\infty} \Phi(\xi) d\xi \approx \frac{\int_{-\infty}^{\infty} \Phi(\xi) d\xi}{U_c^2 |ak|} \cos^2 \left(\frac{\pi}{2\beta_1} \right) \quad (39)$$

since $k \beta_1 h \approx k \beta_1 a = \pi/2$ at the peak frequency of shock associated noise. In other words, the dominant contribution to the integral in (34b) comes from the point where Φ is the maximum; this point is at $K \approx ak$. Therefore, $\Delta(k)/a = 0$ ($|ak|^{-1}$).

At the peak frequency of shock associated noise, $\cos k \beta_1 a \approx 0$ so that the denominator of the last factor in (36) is nearly independent of ak [see equation (39)]. On the other hand, the numerator of the last factor in (36) is of order unity at the peak frequency since it is a combination of trigonometric functions which are themselves of order one. Therefore, based on these remarks and (36), at the peak frequency, the last factor in $W(\omega)$ is nearly independent of the frequency.

Using this observation, converting (36) into one-third octave spectrum after multiplying by ω and integrating to obtain the overall sound pressure level, we find that

$$\int_{-\infty}^{\infty} W(\omega) \omega d\omega = \frac{\rho_{\infty}^2 U_c^2}{\pi^2 R^2} \frac{P^2}{(\rho_1 U_1)^2} \frac{1}{(1 - M_c \cos\theta)} \int_{-\infty}^{\infty} \Phi(\tilde{k}) \tilde{k} \frac{[\beta_1 \frac{k_0}{\gamma_0} \cos \gamma_0 h \sin k \beta_1 h - \sin \gamma_0 h \cos k \beta_1 h]^2}{k^2 | \cos k \beta_1 [a + i\Delta(k)] |^2} d\tilde{k} \quad (40)$$

where $\tilde{k} = k/(1 - M_c \cos\theta)$.

It is a most interesting consequence of the present theory that the overall sound pressure level of shock noise has associated with it a single power of the convective amplification factor $(1 - M_c \cos\theta)$. Generally one thinks of shock associated noise as being omnidirectional; but the data of Tanna (Reference 5-6) clearly show a slight non-omnidirectional pattern. Whether this is due to the contamination of shock associated noise by pure mixing noise as the observation angle θ is reduced from (say) 130° to 90° is not clear. In any case, Howe and Ffowcs-Williams (Reference 2-6) also obtain a directional pattern. Finally, it is seen from (40) that the sound pressure level is proportional to the square of the overpressure P^2 . Since the strength of the steady flow field (35c) is proportional to P [which in turn is proportional to $(M_1^2 - 1)$], we find that the noise scales on $P^2 \sim (M_1^2 - 1)^4$. This is also in agreement with experiment.

8.0 CONCLUSIONS AND RECOMMENDATIONS

8.1 CONCLUSIONS

Seven single stream model nozzles were tested to evaluate the effectiveness of convergent-divergent nozzle terminations in the reduction of shock-cell noise under static and simulated flight conditions. The test nozzles included a baseline convergent circular nozzle, a convergent-divergent circular nozzle, a convergent annular plug nozzle, a convergent-divergent annular plug nozzle, a convergent multi-element suppressor plug nozzle and a convergent-divergent multi-element suppressor plug nozzle. The seventh configuration was a modification of the convergent annular plug nozzle to evaluate a potential method for shock screech elimination.

One hundred forty acoustic test points were taken over the seven nozzle configurations for a wide range of exhaust velocities and temperatures. Diagnostic flow visualization with a shadowgraph and aerodynamic plume measurements with a laser velocimeter were performed also on the test nozzles to better quantify the effectiveness of C-D terminations for shock-cell noise control and to help formulate a proper physical model of the experimentally observed phenomena.

In addition to the acoustic and diagnostic studies, a theory of shockcell noise for annular plug nozzles in the vicinity of the plug was developed based on concepts of Howe and Ffowcs-Williams (Reference 2-6).

The significant results from the analyses of the measured data are:

- Effectiveness of convergent-divergent terminations in the flowpaths of circular, annular and suppressor nozzles in the reduction of front quadrant noise has been demonstrated under both static and simulated flight conditions. At an angle of 50 degrees relative to the inlet, the perceived noise level relative to the baseline convergent circular nozzle is reduced under static and simulated flight conditions, respectively, by a maximum of 7.5 and 11 dB with the C-D circular nozzle, 6 and 8 dB for the C-D annular nozzle and 9.5 and 10 dB for the C-D multi-element suppressor

nozzle. The shock noise suppression of these C-D nozzles is observed over a broad range of pressure ratios in the vicinity of their design condition.

- Smaller amplification of broadband shock noise of the C-D circular nozzle was observed in flight than for the convergent circular nozzle. However, equal magnitude of flight amplification of front quadrant noise was observed for convergent and C-D annular nozzles.
- Jet temperature does not appear to affect significantly the measured levels of shock-cell noise.
- The C-D circular nozzle was identified to be quietest among the test configurations in simulated flight as far as measured frontquadrant noise is concerned.
- The convergent multi-element suppressor nozzle was identified to be the quietest among the test configurations as far as aft-quadrant noise is concerned, under both static and simulated flight conditions.
- For the baseline convergent circular nozzle, eight shock-cells were observed on the nozzle axis while four to five shock-cells were noted along the lip-line. The C-D circular nozzle was noted to be completely shock-free at its design condition.
- The use of tabs with the convergent annular plug nozzle was found to suppress both the discrete and broadband shock noise components. However, the presence of tabs was found to shift the broadband peak frequency to a higher value.
- At the C-D design condition, the C-D annular nozzle was found to be free of shock-cells on the plug. However, shock-cells downstream of the plug were noted, indicating complete shock-cell noise reduction has not been achieved by the C-D termination on the annular plug nozzle.

8.2 RECOMMENDATIONS

Based on the studies conducted during this program, the following items are suggested for future investigation:

- In order to achieve further shock noise reduction with the plug nozzles, a systematic study should be carried out in search of an appropriate plug geometry design which effectively eliminates shocks in the flow region downstream of the plug.
- Diagnostic LV measurements should be conducted with a particular emphasis on the determination of the axial mean and turbulence velocity distributions in the center of shear layer and the clear definition of sonic line which plays an important role in the shock-cell noise generation mechanism. The latter could be achieved by detailed radial traverses of axial mean velocity in the proximity of the jet exit plane.

9.0 NOMENCLATURE

A	Cross-Sectional Area
a	Speed of Sound
AST	Advanced Supersonic Transport
C	Convective Amplification Factor
C-D	Convergent-Divergent
CDR	Comprehensive Data Report
D	Diameter
F	Thrust
F _{ref}	Reference Thrust, 5130 pounds
f	Frequency
FTFSDR	Flight Transformed, Full-Scale Data Reduction Computer Program
H	Helmholtz Number
h	Annular Step Height
k	Harper-Bourne and Fisher Constant
L	Shock Cell Spacing
LV	Laser Velocimeter
M	Mach Number
M _c	Convection Mach Number
n	Flight Amplification Exponent, or nth Shock Cell (Section 6.0)
OASPL	Overall Sound Pressure Level
OAPWL	Overall Sound Power Level
P	Pressure
p	Excess pressure
P _r	Defined = P_T/P_{amb}
PNL	Perceived Noise Level, PNdB
PNLN	Normalized PNL, Defined as $PNL - 10 \log (F/F_{ref})(\rho_j/\rho_{amb})^{\omega-1}$
RH	Relative Humidity
R	Radius
SL	Side Line
SPL	Sound Pressure Level

T	Temperature
V	Ideally Expanded Velocity
V _c	Convection Velocity
VCE	Variable Cycle Engine
\dot{w}	Mass Flow Rate
X	Axial Distance
X'	Axial Distance Measured Along Plug Surface
α	Atmospheric Absorption Coefficient
β	Shock Strength Parameter ($\beta^2 = M^2 - 1$)
Δ	Difference in Level
γ	Specific Heat Ratio
θ	Angle Measured Relative to the Inlet Centerline
ρ	Density
ω	Density Exponent

SUBSCRIPTS

ac, a/c	Aircraft
amb	Ambient Conditions
e	Exit
eq	Equivalent
hyd	Hydraulic
p	Peak
j	Based on Ideal Jet Conditions
r	Ratio
s	Static
T	Stagnation Condition
th	Throat
50°	Evaluated at $\theta = 50^\circ$
130°	Evaluated at $\theta = 130^\circ$

10.0 REFERENCES

- 2-1 Yamamoto, K., Brausch, J. F., Janardan, B. A., Hoerst, D. J., Price, A. O., and Knott, P. R., "Experimental Investigation of Shock-Cell Noise Reduction for Single-Stream Nozzles in Simulated Flight," Comprehensive Data Report, Volumes I, II and III, R82AEB491, August 1983 (NASA CR-168234).
- 2-2 Knott, P. R., "Supersonic Jet Exhaust Investigation - Volume I Summary Report," AFAPL-TR-76-68, July 1976.
- 2-3 Knott, P. R. and Mossey, P., "Parametric Laser Velocimeter Studies of High Velocity, High Temperature, Turbulent Jets," Second International Workshop on Laser Velocimeter, 28 March 1974, AFAPL-TR-68, Volume II, Chapter III.
- 2-4 Seiner, J. M., Norum, T. D., and Maestrello, L., "Effects of Noise Design from Supersonic Jets," NASA CP-2100, November 1979.
- 2-5 Janardan, B. A., Majjigi, R. K., Brausch, J. F., and Knott, P. R., "Free-Jet Investigation of Mechanically Suppressed, High Radius Ratio Co-annular Plug Model Nozzles," NASA CR-3596, 1983.
- 2-6 Howe, M. S. and Ffowcs-Williams, J. E., "On the Noise Generated by An Imperfectly Expanded Supersonic Jet," Phil. Trans. Roy. Soc. London, Volume 289, Number 1358, Pages 271-314 (1978).
- 3-1 Shields, F. D. and Bass, H. E., "Atmospheric Absorption of High Frequency Noise and Application to Fractional-Octave Bands," University of Mississippi, NASA CR-2760, June 1977.
- 4-1 Bediako, E. D., and Yamamoto, K., "Aerodynamic Design and Analysis for Shock-Cell Noise Reduction System," R81AEG543, General Electric Co., September 1981.

- 4-2 Brausch, J. F., Majjigi, R. K., and Bediako, E. D., "Model Hardware Design Report for a Thermal Acoustic Shield Concept for AST/VCE Application - Single Stream Nozzle Designs," R81AEG575, General Electric Co., July 1981.
- 4-3 Kozlowski, H. and Packman, A. B., "Flight Effects on the Aero/Acoustic Characteristics of Inverted Profile Coannular Nozzles," United Technologies Corp., NASA Contractor Report 3018, August 1978.
- 4-4 Janardan, B. A., et al., "Free-Jet Investigation of Mechanically Suppressed High-Radius-Ratio Coannular Plug Model Nozzles," R81AEG484, Volumes I and II, May 1981 (NASA CR-).
- 5-1 Powell, A., "On the Mechanism of Choked Jet Noise," Proc. Phys. Soc., B, Volume 66, Pages 1039-1056 (1953).
- 5-2 Harper-Bourne, M. and Fisher, M. J., "The Noise from Shock Waves in Supersonic Jets," AGARD-CP-131 (1973).
- 5-3 Seiner, J. M. and Norum, T. D., "Experiments of Shock-Associated Noise on Supersonic Jets," AIAA Paper Number 79-1526 (1979).
- 5-4 Lighthill, M. J., "On the Energy Scattered from the Interaction of Turbulence with Sound or Shock Waves," Proc. Camb. Phil. Soc., 49, Pages 531-551 (1953).
- 5-5 Ribner, H. S., "The Sound Generated by Interaction of a Single Vortex with a Shock Wave," UTIA Report Number 61 (1959).
- 5-6 Tanna, H. K., "An Experimental Study of Jet Noise, Part II ShockAssociated Noise," J. Sound Vib., Volume 50, Number 3, Pages 429-444 (1977).
- 5-7 Norum, T. D., and Seiner, J. M., "Location and Propagation of ShockAssociated Noise from Supersonic Jets," AIAA Paper, AIAA-80-0983, 1980.

- 5-8 Hay, J. A. and Rose, E. G., "In-Flight Shock-Cell Noise," J. Sound Vib., Volume II, Number 4, Pages 411-420 (1970).
- 5-9 Williams, T. J., Ali, M. R. M. H., and Anderson, J. S., "Noise and Flow Characteristics of Coaxial Jets," Journal of Mechanical Engineering Science II, 133-142, 1969.
- 5-10 Yamamoto, K., "High Bypass Jet Noise," GE Technical Report Number R81AEG197, 1980.
- 5-11 Yamamoto, K., "A Spectral Prediction Method for Low Velocity HighBypass Jet Noise," General Electric Company, R81AEG391, 1981.
- 5-12 Tam, C. D. W., and Tanna, H. K., "Shock-Associated Noise of Supersonic Jets from Convergent-Divergent Nozzles," J. Sound and Vib. 81(3), 1982.
- 5-13 Gliebe, P. R., Motsinger, R. E., and Sieckman, A., "High Velocity Jet Noise Source Location and Reduction," Task 6 Supplement - Computer Programs FAA-RD-78-79 VIA, (1979).
- 5-14 Knott, P. R., Janardan, B. A., Majjigi, R. K., Bhutiani, P. K., and Vogt, P., "Acoustic and Aerodynamic Performance Investigation of Inverted Velocity Profile Coannular Plug Nozzles," NAS3-19777, Final Technical Report, 1979.
- 5-15 Norum, T. D., "Screech Suppression in Supersonic Jets," AIAA Paper, AIAA-82-0052, 1982.
- 5-16 von Glahn, U., "New Interpretations of Shock-Associated Noise With and Without Screech," NASA Technical Memo. 81590, 1980.
- 5-17 Gliebe, P. R., et al., "High Velocity Jet Noise Source Location and Reduction," Final Report Submitted to U.S. Dept. of Transportation, Report No. FAA-RD-76-79, Task III, Vol. I, 1978.
- 5-18 Majjigi, R. K., "A Unique Spectral Acoustic Prediction Method for Jet and Shock-Cell Noise of Mechanical Suppressor Nozzles," GE Technical Report No. R81AEG363, 1981.

- 5-19 Seiner, J. M., and Norum, T. D., "Aerodynamic Aspects of Shock Containing Jet Plumes," AIAA Paper, AIAA-80-0965, 1980.
- 5-20 Bhutiani, P. K., "A Unique Coannular Plug Nozzle Jet Noise Prediction Procedure," AIAA Paper, AIAA-80-1007, 1980.
- 7-1 Lighthill, M. J., "On the Energy Scattered from the Interaction of Turbulence With Sound or Shock Waves," Proc. Camb. Phil. Soc., 49, pp. 531-551, 1953.
- 7-2 Ribner, H. S., "Acoustic Energy Flux from Shock Turbulence Interaction," J. Fluid Mech., 35, pp. 299-310, 1969.
- 7-3 Howe, M. S., "Contributions to the Theory of Aerodynamic Sound, With Application to Excess Jet Noise and the Theory of the Flute," J. Fluid Mech., 71, pp. 625-673, 1975.
- 7-4 Mani, R., "The Influence of Jet Flow on Jet Noise," J. Fluid Mech., 73, pp. 753-793, 1976.
- 7-5 Ffowcs-Williams, J. E., "Sound Production at the Edge of a Steady Flow," J. Fluid Mech., 66, pp. 791-816, 1974.
- 7-6 Dowling, A. P., Ffowcs-Williams, J. E., and Goldstein, M. E., "Sound Production in a Moving Stream," Phil. Trans. Roy. Soc. A., 288, pp. 321-410, 1978.
- 7-7 Davies, P. O. A. L., Fisher, M. J. and Barratt, M. J., "The Characteristics of Turbulence in the Mixing Region of a Round Jet," J. Fluid Mech., 15, pp. 337-367, 1963.
- 7-8 Powell, A., "Theory of Vortex Sound," J. Acoust. Soc. Am., 33, pp. 1672-1692, 1961.
- 7-9 Lighthill, M. J., "On Sound Generated Aerodynamically," Proc. Roy. Soc. A., 211, pp. 564-587, 1952.

- 7-10 Carrier, G. F., Krook, M. and Pearson, C. E., "Functions of a Complex Variable," McGraw-Hill, New York, 1966.
- 7-11 Morse, P. M. and Ingard, K. U., "Theoretical Acoustics," McGraw-Hill, New York, 1968.
- 7-12 Lighthill, M. J., "Studies on Magneto-Hydrodynamic Waves and Other Anisotropic Wave Motions," Phil. Trans. Roy. Soc. A., 252, pp. 397-430, 1960.

APPENDIX I: AERODYNAMIC AND ACOUSTIC TEST DATA

The aerodynamic flow conditions corresponding to the acoustic test points taken on each of the test configurations are tabulated in this appendix. The data are tabulated in both the SI and English units.

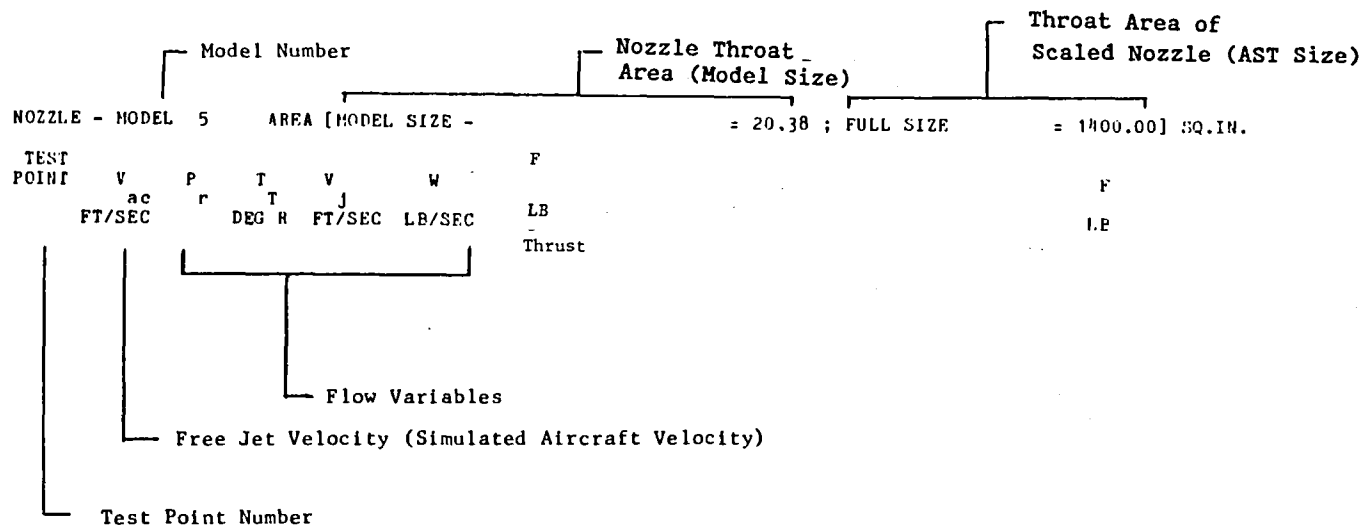
Sample sheets describing the variables listed in the aerodynamic data tables are presented in Tables I-1 and I-2.

The acoustic data that are summarized in the tables are far-field PNL results [scaled to an AST nozzle size of 9032 cm^2 (1400 in^2) and extrapolated to 731.5 m (2400 ft) sideline] at selected angles of $\theta = 50^\circ$, 60° , 70° , 90° , 120° , 130° , and 140° relative to engine inlet.

The test results are summarized in Tables I-3 through I-8. Detailed acoustic results are in Reference 2-1.

Table I-1. Description of Aerodynamic Data Sheet.

(English Units)



350

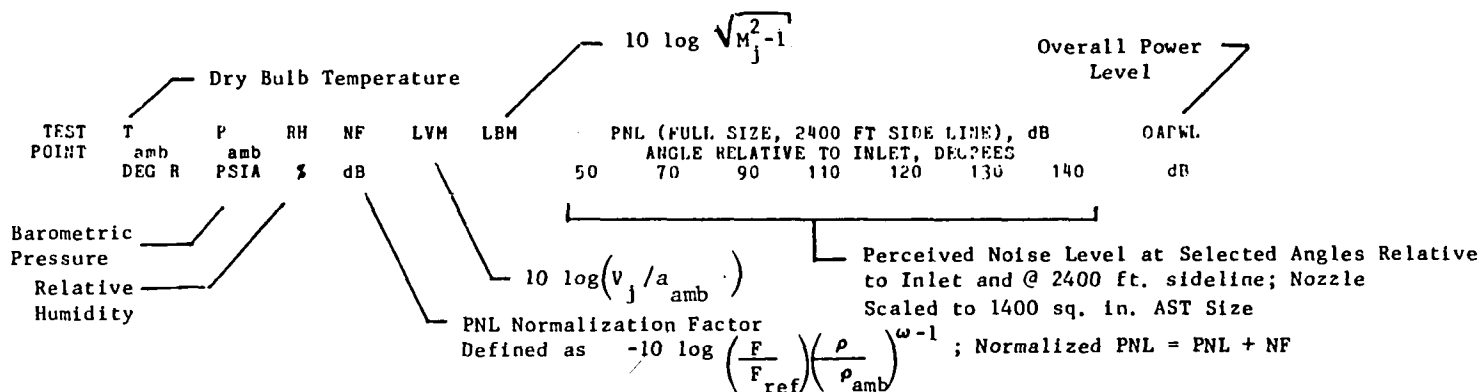


Table I-2. Description of Aerodynamic Data Sheet (Concluded).

(International Units)

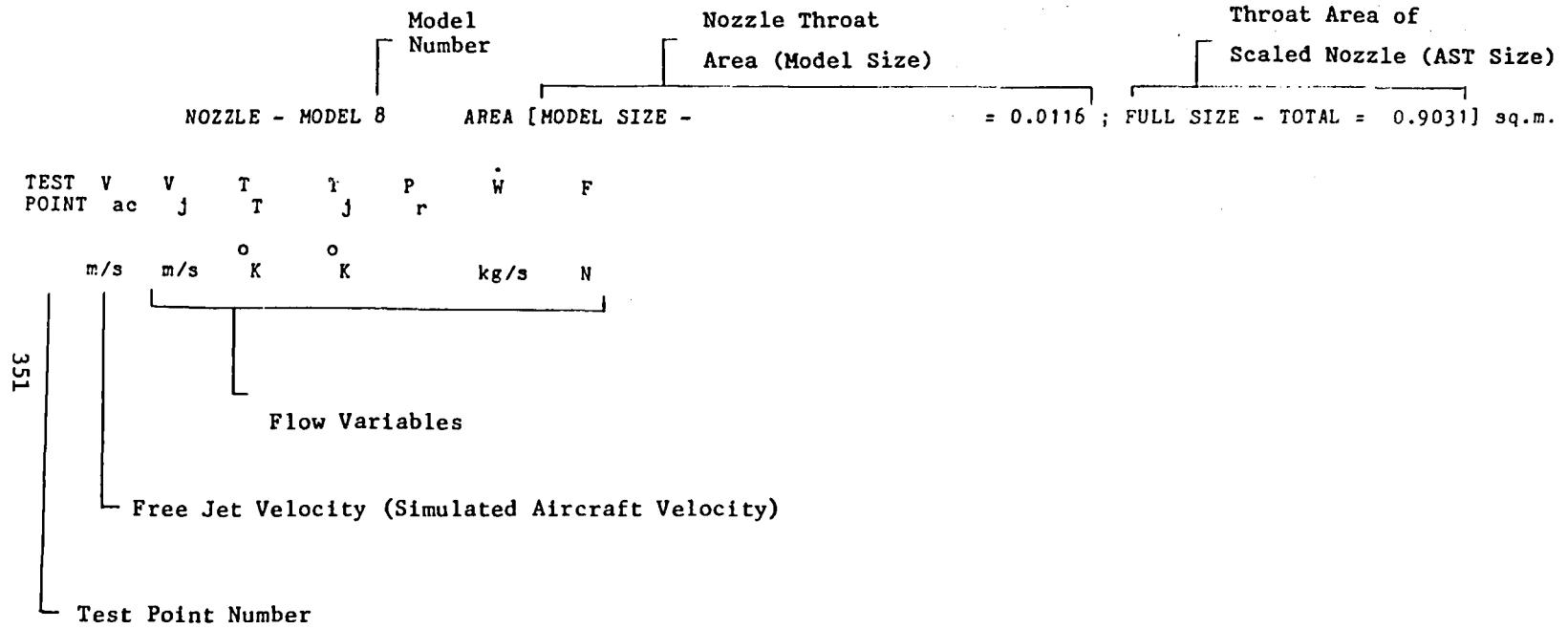


Table I-3. Aerodynamic and Acoustic Test Data - Model 1.

NOZZLE - MODEL 01 AREA [MODEL SIZE - INNER = 0. , OUTER = 20.38 ; FULL SIZE = 1400.00] SQ.IN.

TEST POINT	V _{ac} FT/SEC	P _r	T _T DEG R	V _J FT/SEC	W LB/SEC	F LB
103	0	2.87	1718	2333	733.1	53164
104	400	2.88	1708	2327	736.3	53258
105	0	2.96	1708	2354	758.2	55475
106	400	2.96	1714	2358	756.9	55485
107	0	3.02	1718	2381	772.2	57147
108	400	3.03	1711	2378	775.1	57282
111	0	3.08	1708	2392	789.3	58672
112	400	3.08	1715	2396	787.0	58609
113	0	3.12	1707	2403	800.5	59787
114	400	3.13	1715	2410	799.7	59894
119	0	3.23	1709	2434	827.6	62616
120	400	3.23	1707	2431	826.7	62466
121	0	3.32	1700	2452	852.8	64982
122	400	3.32	1710	2459	851.0	65039

TEST POINT	T _{amb} DEG R	P _{amb} PSIA	RH %	NF dB	LVM	LBM	PNL (FULL SIZE, 2400 FT SIDE LINE), dB							OAPWL dB
							ANGLE RELATIVE TO INLET, DEGREES							
							50	60	70	90	120	130	140	
103	499.9	14.43	92	-6.0	3.28	-0.60	101.6	101.0	104.8	105.2	111.6	115.3	112.2	185.9
104	500.0	14.42	92	-6.0	3.27	-0.59	106.7	104.9	107.9	106.0	110.5	112.6	109.8	184.5
105	500.5	14.43	92	-6.2	3.32	-0.44	102.5	101.6	105.8	106.3	112.8	115.7	112.3	186.6
106	500.9	14.43	92	-6.2	3.32	-0.43	107.1	105.8	108.2	107.0	111.0	112.7	109.7	184.9
107	500.6	14.43	92	-6.4	3.37	-0.33	102.5	101.7	106.2	106.6	112.5	115.6	113.8	187.0
108	500.6	14.42	92	-6.4	3.36	-0.32	109.3	107.2	108.8	107.8	111.0	113.4	110.4	185.6
111	500.3	14.43	92	-6.5	3.39	-0.23	103.4	102.1	106.3	106.9	112.9	116.7	114.5	187.5
112	500.6	14.42	92	-6.5	3.39	-0.24	109.6	108.0	109.8	108.2	111.5	113.4	110.2	185.9
113	500.6	14.43	92	-6.6	3.41	-0.17	103.5	102.6	106.5	107.5	113.7	116.9	113.2	187.5
114	502.1	14.43	92	-6.6	3.41	-0.16	110.4	108.3	109.6	108.3	111.8	113.9	110.7	186.3
119	500.7	14.43	92	-6.9	3.46	-0.02	104.6	103.7	107.3	108.5	113.8	116.3	112.8	187.7
120	502.4	14.43	92	-6.9	3.45	-0.03	110.8	109.0	110.9	109.2	112.2	114.3	111.1	187.0
121	500.6	14.43	92	-7.1	3.49	0.10	104.8	104.0	107.9	108.8	113.6	117.0	113.1	187.9
122	502.6	14.43	92	-7.1	3.50	0.10	111.4	109.7	111.5	110.0	112.9	114.9	111.2	187.6

Table I-3. (Cont'd)

***** S I.UNITS *****

NOZZLE - MODEL 01		AREA [MODEL SIZE		= 0 0131 ; FULL SIZE		= 0 9031] sq.m.	
TEST POINT	V ac	V j	T T	T j	P r	W	F
	m/s	m/s	K	K		kg/s	N
103	0.	711.1	954.4	725.6	2.8729	332.5	14780
104	122	709.3	948.9	720.7	2.8768	334.0	14806
105	0.	717.5	948.9	714.9	2.9610	343.9	15422
106	122	718.7	952.2	717.4	2.9616	343.3	15425
107	0.	725.7	954.4	715.3	3.0245	350.3	15887
108	122	724.8	950.6	711.6	3.0307	351.6	15925
111	0.	729.1	948.9	707.1	3.0834	358.0	16311
112	122	730.3	952.8	710.3	3.0815	357.0	16294
113	0.	732.4	948.3	704.1	3.1249	363.1	16621
114	122	734.6	952.8	707.1	3.1297	362.7	16651
119	0.	741.9	949.4	698.2	3.2331	375.4	17408
120	122	741.0	948.3	697.7	3.2268	375.0	17366
121	0.	747.4	944.4	688.9	3.3232	386.8	18065
122	122	749.5	950.0	693.0	3.3247	386.0	18081

353

TEST POINT	T amb DEG.K	P amb Pascal	RH %	NF dB	LVM	LBM	PNL (FULL SIZE, 2400 FT SIDE LINE) dB						OAPWL dB	
							ANGLE RELATIVE TO INLET DEGREES							
							50	60	70	90	120	130		140
103	277.7	99459.	92	-6.0	3.28	-0.60	101.6	101.0	104.8	105.2	111.6	115.3	112.2	185.9
104	277.8	99442	92	-6.0	3.27	-0.59	106.7	104.9	107.9	106.0	110.5	112.6	109.8	184.5
105	278.0	99475.	92	-6.2	3.32	-0.44	102.5	101.6	105.8	106.3	112.8	115.7	112.3	186.6
106	278.3	99472.	92	-6.2	3.32	-0.43	107.1	105.8	108.2	107.0	111.0	112.7	109.7	184.9
107	278.1	99502	92	-6.4	3.37	-0.33	102.5	101.7	106.2	106.6	112.5	115.6	113.8	187.0
108	278.1	99452	92	-6.4	3.36	-0.32	109.3	107.2	108.8	107.8	111.0	113.4	110.4	185.6
111	277.9	99465.	92	-6.5	3.39	-0.23	103.4	102.1	106.3	106.9	112.9	116.7	114.5	187.5
112	278.1	99445.	92	-6.5	3.39	-0.24	109.6	108.0	109.8	108.2	111.5	113.4	110.2	185.9
113	278.1	99506	92	-6.6	3.41	-0.17	103.5	102.6	106.5	107.5	113.7	116.9	113.2	187.5
114	278.9	99479.	92	-6.6	3.41	-0.16	110.4	108.3	109.6	108.3	111.8	113.9	110.7	186.3
119	278.2	99482	92	-6.9	3.46	-0.02	104.6	103.7	107.3	108.5	113.8	116.3	112.8	187.7
120	279.1	99506.	92	-6.9	3.45	-0.03	110.8	109.0	110.9	109.2	112.2	114.3	111.1	187.0
121	278.1	99459.	92	-7.1	3.49	0.10	104.8	104.0	107.9	108.8	113.6	117.0	113.1	187.9
122	279.2	99495.	92	-7.1	3.50	0.10	111.4	109.7	111.5	110.0	112.9	114.9	111.2	187.6

Table I-4. Aerodynamic and Acoustic Test Data - Model 2.

NOZZLE - MODEL 02 AREA [MODEL SIZE] = 20.43 ; FULL SIZE = 1400.00] SQ.IN.

TEST POINT	V _{ac} FT/SEC	P _r	T _T DEG R	V _J FT/SEC	Ẇ LB/SEC	F LB
201	0	2.72	1723	2282	693.3	49162
202	400	2.72	1747	2301	682.4	48794
203	0	2.87	1722	2334	730.5	52978
204	400	2.89	1725	2343	728.8	53074
205	0	2.95	1728	2365	751.3	55233
206	400	2.97	1732	2373	746.7	55072
207	0	3.02	1716	2378	770.8	56968
208	400	3.04	1730	2395	765.9	57000
211	0	3.07	1721	2398	783.7	58411
212	400	3.08	1736	2410	774.5	58013
213	0	3.12	1728	2417	794.2	59655
214	400	3.13	1736	2425	787.2	59323
215	0	3.18	1717	2426	812.3	61262
216	400	3.19	1722	2432	805.6	60890
219	0	3.22	1729	2446	819.6	62303
220	400	3.23	1734	2453	813.7	62033
221	0	3.31	1712	2458	847.1	64714
222	400	3.33	1713	2462	842.9	64508
223	0	3.51	1715	2508	896.1	69852
224	400	3.52	1737	2528	884.5	69498

TEST POINT	T _{amb} DEG R	P _{amb} PSIA	RH %	NF dB	LVM	LBM	PNL (FULL SIZE 2400 FT SIDE LINE), dB						OAPWL dB	
							ANGLE RELATIVE TO INLET, DEGREES							
							50	60	70	90	120	130		140
201	510.1	14.45	70	-5.6	3.14	-0.93	96.6	96.6	100.2	101.6	110.3	114.6	110.7	184.7
202	535.3	14.30	39	-5.8	3.07	-0.91	99.5	98.4	101.4	101.1	107.8	111.1	109.7	182.8
203	512.0	14.43	70	-6.1	3.23	-0.61	95.8	95.4	99.4	101.8	111.2	115.5	110.8	185.3
204	534.8	14.29	39	-6.3	3.15	-0.57	98.9	97.6	100.9	101.6	108.6	111.7	110.2	183.8
205	510.6	14.43	70	-6.3	3.29	-0.45	95.3	95.5	99.0	101.9	111.6	115.7	110.3	185.4
206	525.4	14.29	39	-6.4	3.25	-0.43	98.0	97.4	100.6	101.4	109.4	112.3	110.3	184.2
207	510.3	14.43	70	-6.4	3.32	-0.34	95.4	95.2	99.1	101.9	111.7	115.6	112.1	185.9
208	524.8	14.29	66	-6.5	3.29	-0.30	97.7	97.2	100.5	100.7	109.3	113.0	110.3	185.1
211	511.0	14.43	70	-6.6	3.35	-0.25	95.3	95.4	99.2	102.4	111.5	116.2	111.9	186.1
212	534.2	14.30	66	-6.7	3.28	-0.24	98.3	97.4	101.0	101.4	109.9	113.1	111.0	186.0
213	512.0	14.43	70	-6.7	3.38	-0.18	95.7	95.6	99.6	102.4	113.4	115.7	111.2	186.2
214	532.4	14.30	66	-6.8	3.31	-0.17	98.4	97.7	100.8	101.8	109.8	113.1	110.9	185.9
215	511.0	14.43	70	-6.8	3.40	-0.09	96.5	96.4	100.1	102.8	112.2	115.8	111.5	186.3
216	532.7	14.30	66	-7.0	3.32	-0.08	99.3	98.7	101.7	102.6	110.6	113.4	111.0	186.8
219	510.6	14.43	70	-6.9	3.44	-0.03	96.7	96.9	100.8	103.1	112.7	116.9	111.4	186.9
220	533.1	14.30	66	-7.0	3.36	-0.02	99.8	99.1	102.0	102.8	110.5	114.5	111.0	187.2
221	510.2	14.43	70	-7.1	3.46	0.09	98.1	98.1	101.7	103.8	113.3	116.6	111.4	187.0
222	531.5	14.30	66	-7.3	3.38	0.10	100.9	100.0	102.9	103.0	110.9	114.0	111.6	187.6
223	511.2	14.43	70	-7.5	3.55	0.31	100.7	100.2	103.8	105.8	113.9	116.8	112.5	187.6
224	531.7	14.29	66	-7.6	3.50	0.33	103.7	102.8	105.8	105.0	112.0	115.1	112.2	188.6

Table I-4. (Cont'd).

NOZZLE - MODEL 02 CONTINUED

TEST POINT	V _{ac} FT/SEC	P _r	T _T DEG R	V _j FT/SEC	Ẇ LB/SEC	F LB
226	400	2.62	1708	2235	664.1	46125
253	0	3.87	1705	2580	992.0	79554
1206	400	3.07	886	1709	1099.1	58389
1207	0	3.12	874	1708	1124.6	59709
1208	400	3.13	879	1714	1124.4	59895
1211	0	3.18	870	1714	1146.0	61055
1212	400	3.18	880	1725	1141.5	61189
1213	0	3.23	869	1723	1164.9	62387
1214	400	3.22	873	1726	1162.1	62354
1215	0	3.28	870	1734	1182.2	63715
1216	400	3.28	870	1735	1183.4	63801
1219	0	3.32	866	1738	1202.1	64953
1220	400	3.33	871	1744	1199.7	65032
1221	0	3.37	875	1756	1214.1	66265
1222	400	3.37	874	1755	1213.6	66208

355

TEST POINT	T _{amb}	P _{amb}	RH	NF	LVM	LBM	PNL (FULL SIZE, 2400 FT SIDE LINE), dB							OAPWL
	DEG R	PSIA	%	dB			ANGLE RELATIVE TO INLET, DEGREES							dB
							50	60	70	90	120	130	140	
226	534.5	14.30	39	-5.6	2.95	-1.18	99.6	98.7	101.2	100.3	106.3	109.0	108.8	181.5
253	511.9	14.42	70	-8.2	3.67	0.67	104.0	104.3	107.0	108.5	114.8	117.4	113.3	189.1
1206	530.0	14.30	77	-9.8	1.80	-0.25	99.1	96.5	99.4	97.9	99.7	99.4	99.1	175.6
1207	524.6	14.29	77	-10.0	1.82	-0.17	94.5	94.0	97.7	99.2	102.6	103.2	106.5	180.6
1208	529.6	14.30	77	-10.0	1.82	-0.16	97.0	96.1	99.0	97.6	99.8	99.1	99.2	175.2
1211	525.4	14.29	77	-10.1	1.83	-0.10	94.5	93.9	97.6	99.2	102.7	103.5	107.0	180.8
1212	529.6	14.30	77	-10.1	1.84	-0.09	96.4	95.7	98.8	97.7	100.0	99.6	99.5	175.1
1213	532.1	14.30	77	-10.3	1.83	-0.03	95.3	94.5	98.1	99.8	102.9	103.5	107.1	181.0
1214	528.7	14.30	77	-10.2	1.85	-0.03	96.5	96.1	99.3	98.2	100.3	99.6	99.9	175.5
1215	526.0	14.29	77	-10.3	1.88	0.04	96.2	95.6	99.2	100.3	103.3	104.0	108.0	181.7
1216	528.9	14.30	77	-10.3	1.87	0.04	97.7	97.0	99.8	98.8	101.0	99.8	100.0	176.1
1219	525.5	14.30	77	-10.4	1.89	0.10	97.3	96.6	100.5	101.0	103.7	104.1	107.5	181.9
1220	528.8	14.28	77	-10.4	1.90	0.11	99.0	98.1	101.2	99.7	101.5	100.6	100.9	176.9
1221	526.0	14.30	77	-10.5	1.94	0.16	98.2	97.6	101.1	101.6	104.3	104.5	108.3	182.3
1222	527.9	14.29	77	-10.5	1.93	0.16	100.7	99.2	102.1	100.6	102.2	101.2	101.7	177.8

Table I-4. (Cont'd)

***** S.I.UNITS *****

NOZZLE - MODEL 02 AREA [MODEL SIZE] = 0.0132 , FULL SIZE = 0.9031] sq.m.

TEST POINT	V _{ac}	V _j	T _T	T _J	P _r	Ẇ	F
	m/s	m/s	o K	o K		kg/s	N
201	0.	695.6	957.2	738.8	2.7162	314.5	13667
202	122.	701.3	970.6	749.6	2.7221	309.5	13565
203	0	711.4	956.7	727.8	2.8658	331.3	14728
204	122.	714.1	958.3	727.6	2.8882	330.6	14755
205	0.	720.9	960.0	724.3	2.9519	340.8	15355
206	122.	723.3	962.2	725.2	2.9662	338.7	15310
207	0.	724.8	953.3	715.0	3.0176	349.6	15837
208	122	730.0	961.1	719.7	3.0400	347.4	15846
211	0.	730.9	956.1	713.5	3.0734	355.5	16239
212	122	734.6	964.4	719.7	3.0784	351.3	16128
213	0	736.7	960.0	713.3	3.1212	360.2	16584
214	122.	739.1	964.4	716.3	3.1290	357.1	16492
215	0.	739.4	953.9	704.9	3.1820	368.5	17031
216	122.	741.3	956.7	706.7	3.1885	365.4	16928
219	0.	745.5	960.6	707.5	3.2214	371.8	17321
220	122.	747.7	963.3	709.2	3.2329	369.1	17246
221	0.	749.2	951.1	694.8	3.3133	384.2	17991
222	122.	750.4	951.7	694.4	3.3271	382.3	17934
223	0.	764.4	952.8	685.0	3.5067	406.5	19419
224	122	770.5	965.0	693.9	3.5190	401.2	19321

356

TEST POINT	T _{amb}	P _{amb}	RH	NF	LVM	LBM	PNL (FULL SIZE, 2400 FT SIDE LINE) dB						OAPWL	
	DEG.K	Pascal	%	dB			ANGLE RELATIVE TO INLET DEGREES						dB	
							50	60	70	90	120	130	140	
201	283.4	99613.	70	-5.6	3.14	-0.93	96.6	96.6	100.2	101.6	110.3	114.6	110.7	184.7
202	297.4	98573.	39	-5.8	3.07	-0.91	99.5	98.4	101.4	101.1	107.8	111.1	109.7	182.8
203	284.4	99465.	70	-6.1	3.23	-0.61	95.8	95.4	99.4	101.8	111.2	115.5	110.8	185.3
204	297.1	98556.	39	-6.3	3.15	-0.57	98.9	97.6	100.9	101.6	108.6	111.7	110.2	183.8
205	283.7	99482.	70	-6.3	3.29	-0.45	95.3	95.5	99.0	101.9	111.6	115.7	110.3	185.4
206	291.9	98526.	39	-6.4	3.25	-0.43	98.0	97.4	100.6	101.4	109.4	112.3	110.3	184.2
207	283.5	99506.	70	-6.4	3.32	-0.34	95.4	95.2	99.1	101.9	111.7	115.6	112.1	185.9
208	291.5	98556	66	-6.5	3.29	-0.30	97.7	97.2	100.5	100.7	109.3	113.0	110.3	185.1
211	283.9	99475.	70	-6.6	3.35	-0.25	95.3	95.4	99.2	102.4	111.5	116.2	111.9	186.1
212	296.8	98587	66	-6.7	3.28	-0.24	98.3	97.4	101.0	101.4	109.9	113.1	111.0	186.0
213	284.4	99462.	70	-6.7	3.38	-0.18	95.7	95.6	99.6	102.4	113.4	115.7	111.2	186.2
214	295.8	98576.	66	-6.8	3.31	-0.17	98.4	97.7	100.8	101.8	109.8	113.1	110.9	185.9
215	283.9	99472.	70	-6.8	3.40	-0.09	96.5	96.4	100.1	102.8	112.2	115.8	111.5	186.3
216	295.9	98597.	66	-7.0	3.32	-0.08	99.3	98.7	101.7	102.6	110.6	113.4	111.0	186.8
219	283.7	99486.	70	-6.9	3.44	-0.03	96.7	96.9	100.8	103.1	112.7	116.9	111.4	186.9
220	296.2	98576.	66	-7.0	3.36	-0.02	99.8	99.1	102.0	102.8	110.5	114.5	111.0	187.2
221	283.4	99459.	70	-7.1	3.46	0.09	98.1	98.1	101.7	103.8	113.3	116.6	111.4	187.0
222	295.3	98587.	66	-7.3	3.38	0.10	100.9	100.0	102.9	103.0	110.9	114.0	111.6	187.6
223	284.0	99489.	70	-7.5	3.55	0.31	100.7	100.2	103.8	105.8	113.9	116.8	112.5	187.6
224	295.4	98536	66	-7.6	3.50	0.33	103.7	102.8	105.8	105.0	112.0	115.1	112.2	188.6

Table I-4. (Concluded)

***** S I.UNITS *****

NOZZLE - MODEL 02 CONTINUED

TEST POINT	V ac	V j	T T	T j	P r	W	F
	m/s	m/s	K	K		kg/s	N
226	122	681.2	948.9	739.7	2.6173	301.2	12823
253	0.	786.4	947.2	661.9	3.8716	450.0	22117
1206	122.	520.9	492.2	357.2	3.0734	498.5	16232
1207	0.	520.6	485.6	350.8	3.1245	510.1	16599
1208	122	522.4	488.3	352.4	3.1300	510.0	16651
1211	0.	522.4	483.3	347.3	3.1761	519.8	16974
1212	122.	525.8	488.9	351.1	3.1805	517.8	17011
1213	0.	525.2	482.8	345.5	3.2259	528.4	17344
1214	122.	526.1	485.0	347.0	3.2240	527.1	17335
1215	0	528.5	483.3	344.4	3.2771	536.2	17713
1216	122	528.8	483.3	344.4	3.2792	536.8	17737
1219	0	529.7	481.1	341.3	3.3236	545.3	18057
1220	122	531.6	483.9	343.1	3.3290	544.2	18079
1221	0.	535.2	486.1	343.4	3.3727	550.7	18422
1222	122	534.9	485.6	343.0	3.3733	550.5	18406

357

TEST POINT	T amb DEG.K	P amb Pascal	RH %	NF dB	LVM	LBM	PNL (FULL SIZE, 2400 FT SIDE LINE) dB						OAPWL dB	
							ANGLE RELATIVE TO INLET DEGREES							
							50	60	70	90	120	130	140	
226	296.9	98590	39	-5.6	2.95	-1.18	99.6	98.7	101.2	100.3	106.3	109.0	108.8	181.5
253	284.4	99455.	70	-8.2	3.67	0.67	104.0	104.3	107.0	108.5	114.8	117.4	113.3	189.1
1206	294.4	98587.	77	-9.8	1.80	-0.25	99.1	96.5	99.4	97.9	99.7	99.4	99.1	175.6
1207	291.4	98556.	77	-10.0	1.82	-0.17	94.5	94.0	97.7	99.2	102.6	103.2	106.5	180.6
1208	294.2	98627	77	-10.0	1.82	-0.16	97.0	96.1	99.0	97.6	99.8	99.1	99.2	175.2
1211	291.9	98546	77	-10.1	1.83	-0.10	94.5	93.9	97.6	99.2	102.7	103.5	107.0	180.8
1212	294.2	98576.	77	-10.1	1.84	-0.09	96.4	95.7	98.8	97.7	100.0	99.6	99.5	175.1
1213	295.6	98583.	77	-10.3	1.83	-0.03	95.3	94.5	98.1	99.8	102.9	103.5	107.1	181.0
1214	293.7	98610.	77	-10.2	1.85	-0.03	96.5	96.1	99.3	98.2	100.3	99.6	99.9	175.5
1215	292.2	98553.	77	-10.3	1.88	0.04	96.2	95.6	99.2	100.3	103.3	104.0	108.0	181.7
1216	293.8	98600.	77	-10.3	1.87	0.04	97.7	97.0	99.8	98.8	101.0	99.8	100.0	176.1
1219	291.9	98573.	77	-10.4	1.89	0.10	97.3	96.6	100.5	101.0	103.7	104.1	107.5	181.9
1220	293.8	98476.	77	-10.4	1.90	0.11	99.0	98.1	101.2	99.7	101.5	100.6	100.9	176.9
1221	292.2	98600.	77	-10.5	1.94	0.16	98.2	97.6	101.1	101.6	104.3	104.5	108.3	182.3
1222	293.3	98492.	77	-10.5	1.93	0.16	100.7	99.2	102.1	100.6	102.2	101.2	101.7	177.8

Table I-5. Aerodynamic and Acoustic Test Data - Model 3.

NOZZLE - MODEL 03		AREA [MODEL SIZE		= 25.28 ; FULL SIZE		= 1400.00] SQ.IN.							
TEST POINT	V _{ac} FT/SEC	P _r	T _T DEG R	V _J FT/SEC	Ẇ LB/SEC	F LB							
303	0	2.89	1736	2352	732.1	53510							
304	400	2.90	1731	2350	732.3	53495							
305	0	2.96	1737	2376	748.4	55258							
306	400	2.99	1749	2392	751.2	55845							
309	0	3.07	1733	2407	777.0	58120							
310	400	3.06	1748	2413	769.1	57692							
313	0	3.16	1741	2436	796.0	60280							
314	400	3.16	1744	2439	794.6	60231							
315	0	3.21	1743	2452	806.7	61479							
316	400	3.22	1735	2449	812.0	61804							
321	0	3.34	1740	2487	841.7	65049							
322	400	3.38	1727	2485	854.7	66015							
349	0	2.38	1601	2064	625.8	40145							
1301	0	2.98	863	1666	1083.1	56092							
1302	400	2.98	873	1677	1079.1	56248							
1313	0	3.24	867	1723	1173.9	62864							
1314	400	3.24	870	1728	1174.7	63087							
1323	0	3.44	871	1763	1242.2	68072							
1324	400	3.45	873	1767	1245.4	68395							
4303	0	2.89	1734	2349	731.2	53396							

TEST POINT	T _{amb} DEG R	P _{amb} PSIA	RH %	NF dB	LVM	LBM	PNL (FULL SIZE, 2400 FT SIDE LINE), dB ANGLE RELATIVE TO INLET, DEGREES						OAPWL dB	
							50	60	70	90	120	130	140	
303	538.0	14.38	69	-6.3	3.16	-0.56	96.1	97.5	99.3	102.4	108.7	112.6	110.6	185.4
304	533.6	14.35	64	-6.3	3.17	-0.55	101.2	100.4	101.1	102.6	104.3	109.2	108.2	182.7
305	539.4	14.36	69	-6.5	3.19	-0.43	96.9	98.3	100.0	103.1	109.0	113.0	111.0	185.8
306	535.1	14.34	64	-6.5	3.24	-0.39	101.3	101.1	101.9	103.1	107.3	110.4	109.0	183.7
309	540.4	14.36	89	-6.8	3.25	-0.25	95.8	97.4	99.3	103.0	109.5	113.7	111.1	186.0
310	535.0	14.33	64	-6.6	3.28	-0.27	99.3	100.5	101.1	103.3	108.0	111.1	109.3	184.0
313	539.5	14.35	89	-6.9	3.30	-0.13	96.9	98.3	100.0	103.6	110.1	114.0	111.7	186.6
314	535.1	14.33	64	-6.9	3.33	-0.12	100.5	101.6	102.3	103.6	108.1	110.8	110.1	184.6
315	539.5	14.33	89	-7.0	3.33	-0.06	98.3	99.7	101.6	104.8	110.0	114.5	111.5	186.8
316	535.6	14.34	64	-7.0	3.34	-0.04	103.0	104.0	104.4	105.2	109.2	111.6	110.3	185.5
321	539.4	14.32	89	-7.3	3.39	0.12	100.2	101.3	103.3	106.4	110.6	115.2	111.7	187.8
322	539.1	14.35	64	-7.4	3.39	0.16	103.8	104.1	104.8	106.6	109.4	112.8	110.7	188.6
349	540.4	14.34	89	-5.2	2.58	-1.97	92.3	93.6	95.0	98.0	103.7	106.6	107.7	180.5
1301	539.7	14.35	89	-9.8	1.65	-0.41	99.4	100.2	101.6	103.0	101.4	101.3	101.2	180.9
1302	542.5	14.35	64	-9.8	1.67	-0.40	103.8	103.9	103.8	103.5	102.0	99.9	97.3	181.4
1313	540.2	14.34	89	-10.4	1.80	-0.01	99.2	100.1	101.7	103.6	97.3	103.0	103.0	182.8
1314	542.4	14.35	64	-10.4	1.80	-0.00	104.8	105.6	106.1	104.8	102.2	102.8	98.9	185.8
1323	540.7	14.33	66	-10.7	1.89	0.23	102.2	103.5	104.9	106.6	105.2	104.7	104.7	187.9
1324	541.5	14.34	66	-10.8	1.90	0.25	105.1	106.1	107.9	105.7	103.6	103.0	100.8	185.3
4303	537.0	14.38	68	-6.3	3.16	-0.57	94.7	97.0	98.7	102.3	107.7	111.0	109.7	184.5

Table I-5. (Cont'd)

NOZZLE - MODEL 03 CONTINUED

TEST POINT	V _{ac} FT/SEC	P _r	T _T DEG R	V _j FT/SEC	Ẇ LB/SEC	F LB
4313	0	3.13	1732	2423	793.7	59770
4321	0	3.34	1716	2468	850.6	65252
5301	0	2.97	865	1666	1080.8	55952
5313	0	3.23	864	1718	1174.8	62740
5323	0	3.41	866	1754	1238.5	67496

TEST POINT	T _{amb} DEG R	P _{amb} PSIA	RH %	NF dB	LVM	LBM	PNL (FULL SIZE, 2400 FT SIDE LINE), dB						OAPWL dB	
							ANGLE RELATIVE TO INLET, DEGREES							
							50	60	70	90	120	130	140	
4313	537.5	14.38	68	-6.9	3.29	-0.16	97.6	99.2	100.9	104.3	109.1	112.8	110.1	186.1
4321	536.9	14.38	68	-7.4	3.37	0.12	98.7	100.6	102.1	105.5	109.9	113.8	110.8	187.3
5301	539.0	14.38	69	-9.8	1.65	-0.42	97.7	98.6	100.1	101.7	100.9	100.6	100.0	178.4
5313	538.1	14.38	69	-10.4	1.79	-0.03	99.0	100.0	101.5	103.3	102.4	102.4	102.1	180.7
5323	538.1	14.36	68	-10.7	1.88	0.20	100.2	101.2	102.6	104.8	103.9	103.3	103.3	182.0

359

Table I-5. (Cont'd)

***** S.I.UNITS *****

NOZZLE - MODEL 03 AREA [MODEL SIZE - 0.0163 FULL SIZE - 0.9031] sq m.

TEST POINT	V ac	V J	T T	T J	P r	W	F
	m/s	m/s	o K	o K		kg/s	N
303	0	716.9	964.4	732.0	2.8923	332.1	14876
304	122.	716.3	961.7	729.7	2.8973	332.2	14872
305	0	724.2	965.0	727.6	2.9637	339.5	15362
306	122.	729.1	971.7	731.4	2.9885	340.7	15525
309	0	733.7	962.8	718.7	3.0733	352.4	16158
310	122.	735.5	971.1	726.1	3.0611	348.9	16039
313	0	742.5	967.2	716.8	3.1568	361.1	16758
314	122.	743.4	968.9	717.9	3.1585	360.4	16745
315	0	747.4	968.3	714.8	3.2061	365.9	17092
316	122	746.5	963.9	710.3	3.2174	368.3	17182
321	0	758.0	966.7	705.1	3.3438	381.8	18084
322	122.	757.4	959.4	697.4	3.3767	387.7	18353
349	0	629.1	889.4	709.7	2.3770	283.9	11160
1301	0	507.8	479.4	350.8	2.9785	491.3	15594
1302	122.	511.1	485.0	354.7	2.9843	489.5	15637
1313	0	525.2	481.7	344.2	3.2368	532.5	17477
1314	122.	526.7	483.3	345.5	3.2437	532.8	17539
1323	0	537.4	483.9	339.9	3.4359	563.5	18924
1324	122.	538.6	485.0	340.5	3.4461	564.9	19014
4303	0.	716.0	963.3	731.6	2.8885	331.7	14844

360

TEST POINT	T amb DEG K	P amb Pascal	RH %	NF dB	LVM	LBM	PNL (FULL SIZE 2400 FT SIDE LINE), dB							OAPWL dB
							ANGLE RELATIVE TO INLET DEGREES							
							50	60	70	90	120	130	140	
303	298.9	99179	69	-6.3	3.16	-0.56	96.1	97.5	99.3	102.4	108.7	112.6	110.6	185.4
304	296.4	98910.	64	-6.3	3.17	-0.55	101.2	100.4	101.1	102.6	104.3	109.2	108.2	182.7
305	299.7	98987.	69	-6.5	3.19	-0.43	96.9	98.3	100.0	103.1	109.0	113.0	111.0	185.8
306	297.3	98889.	64	-6.5	3.24	-0.39	101.3	101.1	101.9	103.1	107.3	110.4	109.0	183.7
309	300.2	98994.	89	-6.8	3.25	-0.25	95.8	97.4	99.3	103.0	109.5	113.7	111.1	186.0
310	297.2	98816.	64	-6.6	3.28	-0.27	99.3	100.5	101.1	103.3	108.0	111.1	109.3	184.0
313	299.7	98964	89	-6.9	3.30	-0.13	96.9	98.3	100.0	103.6	110.1	114.0	111.7	186.6
314	297.3	98812.	64	-6.9	3.33	-0.12	100.5	101.6	102.3	103.6	108.1	110.8	110.1	184.6
315	299.7	98819.	89	-7.0	3.33	-0.06	98.3	99.7	101.6	104.8	110.0	114.5	111.5	186.8
316	297.5	98863.	64	-7.0	3.34	-0.04	103.0	104.0	104.4	105.2	109.2	111.6	110.3	185.5
321	299.7	98765.	89	-7.3	3.39	0.12	100.2	101.3	103.3	106.4	110.6	115.2	111.7	187.8
322	299.5	98910.	64	-7.4	3.39	0.16	103.8	104.1	104.8	106.6	109.4	112.8	110.7	188.6
349	300.2	98889.	89	-5.2	2.58	-1.97	92.3	93.6	95.0	98.0	103.7	106.6	107.7	180.5
1301	299.8	98913.	89	-9.8	1.65	-0.41	99.4	100.2	101.6	103.0	101.4	101.3	101.2	180.9
1302	301.4	98920.	64	-9.8	1.67	-0.40	103.8	103.9	103.8	103.5	102.0	99.9	97.3	181.4
1313	300.1	98886	89	-10.4	1.80	-0.01	99.2	100.1	101.7	103.6	97.3	103.0	103.0	182.8
1314	301.3	98950.	64	-10.4	1.80	-0.00	104.8	105.6	106.1	104.8	102.2	102.8	98.9	185.8
1323	300.4	98802	66	-10.7	1.89	0.23	102.2	103.5	104.9	106.6	105.2	104.7	104.7	187.9
1324	300.8	98876	66	-10.8	1.90	0.25	105.1	106.1	107.9	105.7	103.6	103.0	100.8	185.3
4303	298.3	99152	68	-6.3	3.16	-0.57	94.7	97.0	98.7	102.3	107.7	111.0	109.7	184.5

Table I- 5 (Concluded)

***** S.I.UNITS *****

NOZZLE - MODEL 03 CONTINUED

TEST POINT	V _{ac}	V _j	T _T	T _J	P _r	Ḡ	F	PNL (FULL SIZE 2400 FT SIDE LINE) dB							OAPWL	
	m/s	m/s	o K	o K		kg/s	N	ANGLE RELATIVE TO INLET, DEGREES							dB	
			DEG K	Pascal	%	dB	LVM	LBM	50	60	70	90	120	130	140	dB
361 4313	0.	738.5	962.2	714.2	3.1330	360.0	16616									
4321	0.	752.2	953.3	694.9	3.3414	385.8	18140									
5301	0.	507.8	480.6	352.0	2.9675	490.2	15555									
5313	0.	523.6	480.0	343.6	3.2257	532.9	17442									
5323	0	534.6	481.1	338.9	3.4081	561.8	18764									
4313			298.6	99145.	68	-6.9	3.29	-0.16	97.6	99.2	100.9	104.3	109.1	112.8	110.1	186.1
4321			298.3	99152.	68	-7.4	3.37	0.12	98.7	100.6	102.1	105.5	109.9	113.8	110.8	187.3
5301			299.4	99179.	69	-9.8	1.65	-0.42	97.7	98.6	100.1	101.7	100.9	100.6	100.0	178.4
5313			298.9	99152.	69	-10.4	1.79	-0.03	99.0	100.0	101.5	103.3	102.4	102.4	102.1	180.7
5323			298.9	99038.	68	-10.7	1.88	0.20	100.2	101.2	102.6	104.8	103.9	103.3	103.3	182.0

Table I-6. Aerodynamic and Acoustic Test Data - Model 4.

NOZZLE - MODEL 04 AREA [MODEL SIZE = 25.28 ; FULL SIZE = 1400.00] SQ.IN.

TEST POINT	V _{ac} FT/SEC	P _r	T _T DEG R	V _J FT/SEC	Ẇ LB/SEC	F LB
401	0	2.72	1725	2284	693.5	49232
402	400	2.72	1730	2289	693.5	49348
403	0	2.84	1736	2335	722.9	52469
404	400	2.87	1737	2345	728.7	53107
405	0	2.97	1739	2379	755.0	55822
406	400	2.97	1736	2377	755.2	55790
407	0	3.02	1728	2387	770.0	57133
408	400	3.04	1735	2397	772.1	57510
411	0	3.07	1734	2407	781.7	58474
412	400	3.09	1732	2410	785.6	58848
413	0	3.12	1731	2418	793.6	59643
414	400	3.11	1741	2423	795.5	59911
415	0	3.16	1737	2435	803.5	60806
416	400	3.18	1742	2443	806.4	61236
419	0	3.23	1729	2447	821.9	62514
420	400	3.23	1750	2463	817.6	62597
421	0	3.33	1738	2481	846.0	65233
422	400	3.34	1739	2484	846.6	65357
423	0	3.53	1739	2533	897.5	70652
424	400	3.54	1744	2537	895.8	70644

TEST POINT	T _{amb} DEG R	P _{amb} PSIA	RH %	NF dB	LVM	LBM	PNL (FULL SIZE, 2400 FT SIDE LINE), dB ANGLE RELATIVE TO INLET, DEGREES							OAPWL dB
							50	60	70	90	120	130	140	
401	527.3	14.46	58	-5.8	3.07	-0.93	95.0	95.9	97.8	102.0	108.5	112.4	111.3	185.2
402	537.7	14.45	47	-5.9	3.04	-0.91	97.3	97.4	98.3	100.3	105.0	108.3	108.5	181.2
403	526.8	14.46	58	-6.1	3.17	-0.66	94.8	95.7	97.8	102.5	109.1	114.1	112.2	186.0
404	538.1	14.45	47	-6.3	3.14	-0.61	97.1	97.6	98.8	100.8	106.1	109.8	109.5	182.6
405	529.7	14.46	58	-6.4	3.24	-0.42	96.1	97.0	98.9	103.3	110.0	114.7	112.3	186.4
406	537.1	14.45	47	-6.5	3.21	-0.42	99.5	99.8	100.7	102.4	107.3	110.6	110.2	183.5
407	530.2	14.45	58	-6.6	3.25	-0.33	96.3	97.2	99.1	103.4	110.1	114.9	111.4	186.3
408	539.7	14.45	47	-6.7	3.23	-0.31	100.0	100.1	101.2	102.8	107.7	111.3	110.4	184.3
411	530.2	14.45	58	-6.7	3.29	-0.25	96.3	97.4	99.2	103.6	110.3	115.0	111.1	186.4
412	539.7	14.44	45	-6.8	3.26	-0.23	100.0	100.3	101.0	102.8	107.9	111.7	110.7	184.2
413	530.5	14.46	58	-6.8	3.31	-0.18	96.5	97.6	99.4	103.6	110.4	115.2	111.6	186.5
414	537.6	14.56	44	-6.9	3.29	-0.19	100.5	100.6	101.4	103.3	108.4	111.9	110.9	184.7
415	530.4	14.45	58	-6.9	3.34	-0.12	96.8	98.0	99.9	104.1	110.6	115.3	111.9	186.7
416	537.7	14.45	45	-7.0	3.32	-0.10	100.8	101.0	101.7	103.5	108.6	112.2	111.0	185.3
419	531.7	14.45	55	-7.1	3.35	-0.03	97.8	99.0	100.6	104.9	110.4	115.5	112.0	187.4
420	538.6	14.45	45	-7.1	3.35	-0.02	102.0	101.4	102.3	104.2	108.9	112.6	111.3	185.5
421	532.7	14.45	55	-7.3	3.41	0.11	99.6	100.6	102.0	106.3	111.1	115.8	112.3	187.9
422	538.5	14.43	45	-7.3	3.39	0.12	103.5	103.3	104.0	105.8	109.6	113.1	111.8	186.3
423	533.1	14.45	55	-7.7	3.50	0.34	100.1	101.1	102.9	107.1	112.3	116.9	112.7	188.7
424	539.5	14.43	45	-7.7	3.48	0.35	105.0	104.8	105.4	106.5	110.8	114.4	112.1	187.5

Table I-6. (Cont'd)

NOZZLE - MODEL 04 CONTINUED

TEST POINT	V _{ac} FT/SEC	P _r	T _T DEG R	V _J FT/SEC	W LB/SEC	F LB
449	0	2.36	1590	2048	628.0	39975
451	0	2.41	1716	2155	618.0	41394
452	400	2.42	1720	2160	617.5	41448
453	0	3.92	1731	2610	997.0	80877
454	400	3.91	1746	2620	990.2	80643
1405	0	3.07	873	1696	1116.7	58863
1406	400	3.05	874	1691	1111.5	58426
1411	0	3.18	872	1716	1156.7	61683
1412	400	3.18	868	1714	1165.7	62098
1413	0	3.23	865	1720	1182.6	63237
1414	400	3.23	861	1716	1188.8	63417
1415	0	3.22	859	1713	1185.4	63095
1416	400	3.26	866	1727	1196.1	64201
1419	0	3.31	851	1721	1224.2	65490
1420	400	3.32	861	1733	1221.8	65802
1421	0	3.37	851	1731	1244.4	66968
1422	400	3.37	854	1734	1243.7	67038
1466	400	3.02	999	1802	1026.6	57502
1468	400	3.04	1254	2029	913.1	57579
1470	400	3.02	1487	2208	831.5	57071

TEST POINT	T _{amb} DEG R	P _{amb} PSIA	RH %	NF dB	LVM	LBM	PNL (FULL SIZE, 2400 FT SIDE LINE), dB						OAPWL dB	
							ANGLE RELATIVE TO INLET, DEGREES							
							50	60	70	90	120	130	140	
449	535.5	14.44	51	-5.2	2.57	-2.05	93.3	94.2	96.0	99.6	104.7	107.3	108.1	187.3
451	536.0	14.46	55	-5.0	2.78	-1.82	93.3	93.9	95.8	100.4	105.7	108.9	109.1	182.7
452	537.7	14.45	51	-5.0	2.79	-1.81	94.0	94.6	95.6	98.1	102.5	104.2	104.5	177.7
453	532.8	14.45	55	-8.4	3.63	0.71	99.0	100.2	101.9	106.9	113.3	117.8	113.5	189.5
454	539.0	14.44	45	-8.4	3.62	0.70	102.7	103.0	104.0	106.3	111.9	115.7	113.0	188.6
1405	525.1	14.43	61	-9.9	1.79	-0.25	97.5	98.7	99.5	102.2	101.6	103.4	104.3	180.4
1406	542.9	14.49	42	-10.0	1.70	-0.29	100.1	101.0	101.4	100.1	99.0	98.7	97.6	176.0
1411	527.0	14.44	61	-10.1	1.83	-0.10	97.3	98.5	99.5	101.9	101.8	103.8	104.8	180.6
1412	542.6	14.50	42	-10.3	1.76	-0.09	100.3	101.1	101.6	100.4	99.6	99.4	98.5	176.4
1413	527.3	14.44	61	-10.3	1.84	-0.02	97.3	98.8	100.0	103.6	102.2	104.3	104.9	181.2
1414	543.5	14.50	42	-10.5	1.77	-0.02	101.1	101.6	102.1	101.1	100.0	99.7	99.0	176.9
1415	536.9	14.49	58	-10.4	1.78	-0.03	97.6	99.2	100.6	103.9	102.7	104.2	105.1	181.4
1416	543.0	14.49	42	-10.5	1.80	0.02	101.8	102.5	103.6	101.8	100.5	100.4	99.4	177.8
1419	536.8	14.48	58	-10.6	1.81	0.09	98.7	99.9	101.1	106.1	103.4	104.6	106.0	182.4
1420	542.4	14.50	42	-10.6	1.81	0.10	102.4	103.7	104.8	103.3	101.3	101.1	100.2	178.9
1421	539.0	14.47	58	-10.7	1.82	0.16	98.9	100.5	102.3	106.9	104.0	105.4	106.4	182.8
1422	542.8	14.49	42	-10.8	1.81	0.16	105.0	110.6	105.7	104.0	102.1	101.9	101.0	180.9
1466	539.3	14.48	44	-9.3	2.00	-0.34	100.3	100.3	100.4	100.7	100.2	100.2	99.6	176.9
1468	540.6	14.40	45	-8.2	2.50	-0.31	100.3	99.7	100.3	100.9	102.5	104.4	105.4	179.4
1470	539.3	14.44	45	-7.4	2.88	-0.34	100.3	99.7	100.4	101.5	105.2	108.1	109.2	181.9

Table I-6. (Cont'd)

364

NOZZLE - MODEL CONTINUED

TEST POINT	V _{ac} FT/SEC	P _r	T _T DEG R	V _j FT/SEC	W LB/SEC	F LB
7401	0	1.50	1745	1519	366.7	17314
9405	0	3.03	1360	2112	877.3	57580
9406	400	2.99	1347	2092	886.2	57619
9411	0	3.14	1341	2126	916.8	60577
9412	400	3.14	1345	2130	917.0	60707
9413	0	3.17	1340	2132	924.8	61271
9414	400	3.15	1352	2136	915.7	60797
9415	0	3.27	1346	2161	953.0	64018
9416	400	3.28	1351	2167	953.3	64208
9421	0	3.36	1384	2214	966.0	66480
9422	400	3.35	1371	2201	966.9	66145

TEST POINT	T _{amb} DEG R	P _{amb} PSIA	RH %	NF dB	LVM	LBM	PNL (FULL SIZE 2400 FT SIDE LINE), dB						OAPWL dB	
							ANGLE RELATIVE TO INLET, DEGREES							
							50	60	70	90	120	130	140	
7401	541.3	14.50	44	-2.6	1.25	-10.00	79.4	80.8	83.0	87.5	91.6	92.2	90.2	167.6
9405	542.2	14.50	44	-7.8	2.67	-0.33	96.3	97.6	98.8	101.7	106.0	109.5	111.3	184.3
9406	543.3	14.74	42	-7.9	2.63	-0.38	100.1	100.3	100.9	101.0	103.3	105.9	107.3	180.5
9411	541.2	14.49	44	-8.1	2.71	-0.15	96.5	97.7	98.9	101.9	106.8	110.4	112.0	184.9
9412	543.3	14.51	42	-8.2	2.71	-0.15	99.6	100.1	100.7	100.8	104.0	106.5	108.0	181.1
9413	541.7	14.49	44	-8.2	2.72	-0.11	96.6	98.0	99.2	102.1	106.5	110.3	112.0	184.9
9414	543.2	14.50	42	-8.1	2.72	-0.14	100.2	100.5	100.7	101.5	104.4	106.9	108.5	181.4
9415	540.0	14.48	58	-8.4	2.78	0.03	98.6	100.0	101.2	103.8	107.3	110.8	112.7	185.7
9416	542.9	14.50	42	-8.4	2.78	0.04	102.7	103.1	103.0	103.0	105.3	108.2	109.4	183.0
9421	539.5	14.49	58	-8.5	2.89	0.15	100.0	101.6	102.6	105.2	108.3	112.4	112.6	186.4
9422	543.8	14.48	42	-8.5	2.84	0.13	105.4	105.6	104.9	104.2	106.1	108.6	110.1	183.8

Table I-6. (Cont'd)

***** S.I.UNITS *****

NOZZLE - MODEL 04 AREA [MODEL SIZE] 0 0163 FULL SIZE = 0 9031] sq.m.

TEST POINT	V ac	V j	T T	T j	P r	W	F
	m/s	m/s	o K	o K		kg/s	N
401	0.	696.2	958.3	739.9	2.7176	314.6	13687
402	122.	697.7	961.1	741.6	2.7236	314.6	13719
403	0.	711.7	964.4	735.9	2.8421	327.9	14587
404	122.	714.8	965.0	734.5	2.8677	330.5	14764
405	0.	725.1	966.1	727.9	2.9706	342.5	15519
406	122.	724.5	964.4	726.6	2.9704	342.6	15510
407	0	727.6	960.0	719.9	3.0213	349.3	15883
408	122.	730.6	963.9	722.1	3.0353	350.2	15988
411	0.	733.7	963.3	718.9	3.0730	354.6	16256
412	122	734.6	962.2	717.3	3.0885	356.3	16360
413	0.	737.0	961.7	715.2	3.1163	360.0	16581
414	122.	738.5	967.2	719.7	3.1109	360.8	16656
415	0.	742.2	965.0	714.8	3.1613	364.5	16904
416	122	744.6	967.8	716.0	3.1777	365.8	17024
419	0.	745.8	960.6	707.4	3.2259	372.8	17379
420	122.	750.7	972.2	716.2	3.2300	370.9	17402
421	0.	756.2	965.6	705.1	3.3285	383.7	18135
422	122.	757.1	966.1	704.9	3.3367	384.0	18170
423	0	772.1	966.1	693.9	3.5338	407.1	19642
424	122.	773.3	968.9	695.9	3.5360	406.3	19640

365

TEST POINT	T amb DEG K	P amb Pascal	RH %	NF dB	LVM	LBM	PNL (FULL SIZE 2400 FT SIDE LINE) dB						OAPWL dB	
							ANGLE RELATIVE TO INLET DEGREES							
							50	60	70	90	120	130		140
401	292.9	99684.	58	-5.8	3.07	-0.93	95.0	95.9	97.8	102.0	108.5	112.4	111.3	185.2
402	298.7	99610.	47	-5.9	3.04	-0.91	97.3	97.4	98.3	100.3	105.0	108.3	108.5	181.2
403	292.7	99681.	58	-6.1	3.17	-0.66	94.8	95.7	97.8	102.5	109.1	114.1	112.2	186.0
404	298.9	99627.	47	-6.3	3.14	-0.61	97.1	97.6	98.8	100.8	106.1	109.8	109.5	182.6
405	294.3	99671.	58	-6.4	3.24	-0.42	96.1	97.0	98.9	103.3	110.0	114.7	112.3	186.4
406	298.4	99620	47	-6.5	3.21	-0.42	99.5	99.8	100.7	102.4	107.3	110.6	110.2	183.5
407	294.5	99633.	58	-6.6	3.25	-0.33	96.3	97.2	99.1	103.4	110.1	114.9	111.4	186.3
408	299.8	99658.	47	-6.7	3.23	-0.31	100.0	100.1	101.2	102.8	107.7	111.3	110.4	184.3
411	294.5	99610	58	-6.7	3.29	-0.25	96.3	97.4	99.2	103.6	110.3	115.0	111.1	186.4
412	299.8	99556.	45	-6.8	3.26	-0.23	100.0	100.3	101.0	102.8	107.9	111.7	110.7	184.2
413	294.7	99664.	58	-6.8	3.31	-0.18	96.5	97.6	99.4	103.6	110.4	115.2	111.6	186.5
414	298.7	100357	44	-6.9	3.29	-0.19	100.5	100.6	101.4	103.3	108.4	111.9	110.9	184.7
415	294.7	99633	58	-6.9	3.34	-0.12	96.8	98.0	99.9	104.1	110.6	115.3	111.9	186.7
416	298.7	99633	45	-7.0	3.32	-0.10	100.8	101.0	101.7	103.5	108.6	112.2	111.0	185.3
419	295.4	99637	55	-7.1	3.35	-0.03	97.8	99.0	100.6	104.9	110.4	115.5	112.0	187.4
420	299.2	99606	45	-7.1	3.35	-0.02	102.0	101.4	102.3	104.2	108.9	112.6	111.3	185.5
421	295.9	99654	55	-7.3	3.41	0.11	99.6	100.6	102.0	106.3	111.1	115.8	112.3	187.9
422	299.2	99516.	45	-7.3	3.39	0.12	103.5	103.3	104.0	105.8	109.6	113.1	111.8	186.3
423	296.2	99620.	55	-7.7	3.50	0.34	100.1	101.1	102.9	107.1	112.3	116.9	112.7	188.7
424	299.7	99526.	45	-7.7	3.48	0.35	105.0	104.8	105.4	106.5	110.8	114.4	112.1	187.5

Table I-6. (Cont'd)

NOZZLE - MODEL 04 CONTINUED

***** S.I.UNITS *****

366

TEST POINT	V ac	V j	T T	T j	P r	W kg/s	F N
449	0.	624.2	883.3	705.6	2.3592	284.9	11113
451	0.	656.8	953.3	759.8	2.4140	280.3	11508
452	122.	658.4	955.6	761.4	2.4181	280.1	11523
453	0	795.5	961.7	670.8	3.9159	452.2	22484
454	122	798.6	970.0	677.2	3.9106	449.1	22419
1405	0.	516.9	485.0	351.8	3.0718	506.5	16364
1406	122	515.4	485.6	353.1	3.0453	504.2	16243
1411	0.	523.0	484.4	348.0	3.1757	524.7	17148
1412	122	522.4	482.2	346.5	3.1826	528.8	17264
1413	0.	524.3	480.6	343.4	3.2346	536.4	17580
1414	122.	523.0	478.3	342.1	3.2319	539.2	17630
1415	0	522.1	477.2	341.7	3.2219	537.7	17541
1416	122	526.4	481.1	343.1	3.2632	542.5	17848
1419	0	524.6	472.8	335.8	3.3122	555.3	18207
1420	122	528.2	478.3	339.4	3.3216	554.2	18293
1421	0.	527.6	472.8	334.1	3.3696	564.5	18618
1422	122	528.5	474.4	335.3	3.3687	564.1	18637
1466	122	549.2	555.0	405.1	3.0157	465.7	15986
1468	122.	618.4	696.7	511.8	3.0377	414.2	16007
1470	122.	673.0	826.1	613.9	3.0174	377.2	15866

TEST POINT	T amb DEG.K	P amb Pascal	RH %	NF dB	LVM	LBM	PNL (FULL SIZE 2400 FT SIDE LINE), dB							OAPWL dB
							ANGLE RELATIVE TO INLET DEGREES							
							50	60	70	90	120	130	140	
449	297.5	99590.	51	-5.2	2.57	-2.05	93.3	94.2	96.0	99.6	104.7	107.3	108.1	187.3
451	297.8	99715.	55	-5.0	2.78	-1.82	93.3	93.9	95.8	100.4	105.7	108.9	109.1	182.7
452	298.7	99600.	51	-5.0	2.79	-1.81	94.0	94.6	95.6	98.1	102.5	104.2	104.5	177.7
453	296.0	99637.	55	-8.4	3.63	0.71	99.0	100.2	101.9	106.9	113.3	117.8	113.5	189.5
454	299.4	99533.	45	-8.4	3.62	0.70	102.7	103.0	104.0	106.3	111.9	115.7	113.0	188.6
1405	291.7	99462.	61	-9.9	1.79	-0.25	97.5	98.7	99.5	102.2	101.6	103.4	104.3	180.4
1406	301.6	99910.	42	-10.0	1.70	-0.29	100.1	101.0	101.4	100.1	99.0	98.7	97.6	176.0
1411	292.8	99580.	61	-10.1	1.83	-0.10	97.3	98.5	99.5	101.9	101.8	103.8	104.8	180.6
1412	301.4	99953.	42	-10.3	1.76	-0.09	100.3	101.1	101.6	100.4	99.6	99.4	98.5	176.4
1413	292.9	99563.	61	-10.3	1.84	-0.02	97.3	98.8	100.0	103.6	102.2	104.3	104.9	181.2
1414	301.9	99960.	42	-10.5	1.77	-0.02	101.1	101.6	102.1	101.1	100.0	99.7	99.0	176.9
1415	298.3	99873.	58	-10.4	1.78	-0.03	97.6	99.2	100.6	103.9	102.7	104.2	105.1	181.4
1416	301.7	99883.	42	-10.5	1.80	0.02	101.8	102.5	103.6	101.8	100.5	100.4	99.4	177.8
1419	298.2	99856	58	-10.6	1.81	0.09	98.7	99.9	101.1	106.1	103.4	104.6	106.0	182.4
1420	301.3	99947.	42	-10.6	1.81	0.10	102.4	103.7	104.8	103.3	101.3	101.1	100.2	178.9
1421	299.4	99772.	58	-10.7	1.82	0.16	98.9	100.5	102.3	106.9	104.0	105.4	106.4	182.8
1422	301.5	99910.	42	-10.8	1.81	0.16	105.0	110.6	105.7	104.0	102.1	101.9	101.0	180.9
1466	299.6	99809.	44	-9.3	2.00	-0.34	100.3	100.3	100.4	100.7	100.2	100.2	99.6	176.9
1468	300.3	99307.	45	-8.2	2.50	-0.31	100.3	99.7	100.3	100.9	102.5	104.4	105.4	179.4
1470	299.6	99540.	45	-7.4	2.88	-0.34	100.3	99.7	100.4	101.5	105.2	108.1	109.2	181.9

Table I-6. (Concluded)

***** S I.UNITS *****

NOZZLE - MODEL CONTINUED

TEST POINT	V _{ac}	V _j	T _T	T _j	P _r	Ẇ	F
	m/s	m/s	°K	°K		kg/s	N
7401	0.	463.0	969.4	876.3	1.4995	166.3	4813
9405	0.	643.7	755.6	558.3	3.0254	397.9	16008
9406	122	637.6	748.3	554.3	2.9910	402.0	16018
9411	0.	648.0	745.0	544.1	3.1398	415.9	16841
9412	122	649.2	747.2	545.8	3.1422	415.9	16877
9413	0.	649.8	744.4	542.3	3.1662	419.5	17034
9414	122.	651.1	751.1	548.3	3.1469	415.4	16902
9415	0.	658.7	747.8	539.5	3.2719	432.3	17797
9416	122	660.5	750.6	541.7	3.2761	432.4	17850
9421	0.	674.8	768.9	551.4	3.3642	438.2	18482
9422	122.	670.9	761.7	546.6	3.3518	438.6	18389

367

TEST POINT	T _{amb} DEG.K	P _{amb} Pascal	RH %	NF dB	LVM	LBM	PNL (FULL SIZE 2400 FT SIDE LINE), dB							OAPWL dB
							ANGLE RELATIVE TO INLET, DEGREES							
							50	60	70	90	120	130	140	
7401	300.7	99997	44	-2.6	1.25	-10.00	79.4	80.8	83.0	87.5	91.6	92.2	90.2	167.6
9405	301.2	99960	44	-7.8	2.67	-0.33	96.3	97.6	98.8	101.7	106.0	109.5	111.3	184.3
9406	301.8	101614.	42	-7.9	2.63	-0.38	100.1	100.3	100.9	101.0	103.3	105.9	107.3	180.5
9411	300.7	99913	44	-8.1	2.71	-0.15	96.5	97.7	98.9	101.9	106.8	110.4	112.0	184.9
9412	301.8	100024	42	-8.2	2.71	-0.15	99.6	100.1	100.7	100.8	104.0	106.5	108.0	181.1
9413	300.9	99906	44	-8.2	2.72	-0.11	96.6	98.0	99.2	102.1	106.5	110.3	112.0	184.9
9414	301.8	99977.	42	-8.1	2.72	-0.14	100.2	100.5	100.7	101.5	104.4	106.9	108.5	181.4
9415	300.0	99835	58	-8.4	2.78	0.03	98.6	100.0	101.2	103.8	107.3	110.8	112.7	185.7
9416	301.6	99964	42	-8.4	2.78	0.04	102.7	103.1	103.0	103.0	105.3	108.2	109.4	183.0
9421	299.7	99886.	58	-8.5	2.89	0.15	100.0	101.6	102.6	105.2	108.3	112.4	112.6	186.4
9422	302.1	99869.	42	-8.5	2.84	0.13	105.4	105.6	104.9	104.2	106.1	108.6	110.1	183.8

Table I-7. Aerodynamic and Acoustic Test Data - Model 5.

NOZZLE - MODEL 05		AREA [MODEL SIZE				= 19.89 ; FULL SIZE		= 1400.00] SQ.IN.						
TEST POINT	V _{ac} FT/SEC	P _r	T _T DEG R	V _J FT/SEC	Ẇ LB/SEC	F LB	PNL (FULL SIZE, 2400 FT SIDE LINE), dB						OAPWL	
							ANGLE RELATIVE TO INLET, DEGREES							
							50	60	70	90	120	130	140	
507	0	3.02	1713	2378	771.3	57002								
508	400	3.01	1712	2373	770.6	56844								
513	0	3.13	1718	2412	795.6	59631								
514	400	3.12	1706	2401	800.6	59746								
519	0	3.23	1707	2432	824.2	62315								
520	400	3.20	1701	2420	821.1	61760								
541	0	2.40	1696	2137	615.6	40889								
542	400	2.41	1712	2152	616.7	41252								
543	0	2.70	1703	2264	692.2	48699								
544	400	2.69	1727	2275	684.3	48385								
545	0	3.62	1718	2537	921.9	72694								
546	400	3.61	1696	2518	928.9	72703								
1505	0	3.07	853	1677	1125.8	58675								
1507	0	3.12	857	1690	1139.0	59824								
1511	0	3.18	853	1698	1164.8	61476								
1513	0	3.22	851	1704	1182.4	62619								
1515	0	3.27	851	1713	1201.1	63960								
1519	0	3.32	852	1725	1219.3	65358								
1521	0	3.37	853	1734	1234.1	66495								
507	528.3	14.39	69	-6.6	3.24	-0.33	96.7	100.4	102.9	104.0	99.0	104.3	102.8	181.7
508	532.8	14.43	82	-6.6	3.22	-0.35	101.3	103.9	106.2	105.0	99.1	104.0	99.9	181.2
513	528.4	14.38	69	-6.8	3.30	-0.17	96.9	100.5	103.4	104.2	99.2	104.8	102.4	181.7
514	531.6	14.44	82	-6.9	3.27	-0.18	103.8	105.1	106.9	105.3	99.9	104.8	101.1	182.0
519	528.3	14.37	69	-7.1	3.34	-0.02	97.2	100.9	103.4	104.6	99.6	104.7	103.4	182.5
520	531.3	14.43	82	-7.1	3.31	-0.06	102.2	105.3	107.3	105.4	100.7	104.8	101.4	182.5
541	527.9	14.39	69	-4.9	2.78	-1.87	91.6	94.7	99.4	99.5	95.4	101.3	99.5	177.8
542	535.3	14.42	82	-5.0	2.78	-1.83	95.7	97.6	102.2	99.8	94.9	99.2	95.8	175.6
543	528.6	14.40	69	-5.8	3.03	-0.96	94.3	98.2	101.4	102.1	97.3	103.0	100.2	179.8
544	534.6	14.42	82	-5.8	3.03	-0.99	97.8	100.7	103.8	102.4	97.0	101.2	98.0	178.3
545	528.1	14.39	69	-7.9	3.53	0.43	98.2	101.6	104.4	105.6	100.5	106.2	105.6	183.7
546	534.5	14.43	82	-8.0	3.47	0.43	103.2	105.9	108.1	106.6	101.5	106.0	102.9	183.4
1505	526.4	14.37	77	-10.0	1.73	-0.25	95.8	99.0	99.0	102.4	94.9	96.5	96.2	178.5
1507	525.8	14.36	77	-10.1	1.77	-0.18	95.9	99.8	99.2	102.6	95.0	98.1	96.3	178.9
1511	527.4	14.38	77	-10.2	1.78	-0.09	96.1	99.8	99.3	103.1	95.2	97.8	96.7	179.0
1513	527.4	14.40	77	-10.3	1.80	-0.04	96.1	100.0	99.4	103.0	95.4	98.5	96.9	178.9
1515	527.6	14.39	77	-10.4	1.82	0.03	96.5	100.2	99.6	103.3	95.5	98.5	97.3	179.4
1519	527.5	14.39	77	-10.5	1.85	0.10	96.6	100.2	99.6	103.4	95.3	98.6	97.3	179.4
1521	527.5	14.37	77	-10.6	1.88	0.16	96.8	100.2	99.9	103.5	95.7	99.1	97.4	179.6

Table I-7. (Concluded)

***** S.I.UNITS *****

NOZZLE - MODEL 05 AREA [MODEL SIZE] = 0.0128 ; FULL SIZE = 0 9031] sq.m.

TEST POINT	V ac	V j	T T	T j	P r	W	F
	m/s	m/s	o K	o K		kg/s	N
507	0.	724.8	951.7	713.2	3.0247	349.9	15847
508	122.	723.3	951.1	713.2	3.0138	349.5	15803
513	0.	735.2	954.4	708.8	3.1268	360.9	16578
514	122.	731.8	947.8	703.5	3.1226	363.1	16610
519	0	741.3	948.3	697.6	3.2307	373.9	17324
520	122.	737.6	945.0	696.8	3.2010	372.4	17170
541	0.	651.4	942.2	751.5	2.4026	279.2	11367
542	122.	655.9	951.1	758.1	2.4128	279.7	11468
543	0.	690.1	946.1	730.7	2.7042	314.0	13538
544	122.	693.4	959.4	742.7	2.6903	310.4	13451
545	0.	773.3	954.4	680.3	3.6206	418.2	20209
546	122.	767.5	942.2	671.1	3.6138	421.3	20212
1505	0	511.1	473.9	343.8	3.0729	510.7	16312
1507	0	515.1	476.1	344.0	3.1180	516.6	16631
1511	0.	517.6	473.9	340.6	3.1787	528.3	17091
1513	0.	519.4	472.8	338.7	3.2183	536.3	17408
1515	0.	522.1	472.8	336.9	3.2707	544.8	17781
1519	0	525.8	473.3	336.0	3.3235	553.1	18170
1521	0.	528.5	473.9	335.0	3.3690	559.8	18486

369

TEST POINT	T amb DEG.K	P amb Pascal	RH %	NF dB	LVM	LBM	PNL (FULL SIZE 2400 FT SIDE LINE) dB							OAPWL dB
							ANGLE RELATIVE TO INLET DEGREES							
							50	60	70	90	120	130	140	
507	293.5	99240.	69	-6.6	3.24	-0.33	96.7	100.4	102.9	104.0	99.0	104.3	102.8	181.7
508	296.0	99459	82	-6.6	3.22	-0.35	101.3	103.9	106.2	105.0	99.1	104.0	99.9	181.2
513	293.6	99172.	69	-6.8	3.30	-0.17	96.9	100.5	103.4	104.2	99.2	104.8	102.4	181.7
514	295.3	99540.	82	-6.9	3.27	-0.18	103.8	105.1	106.9	105.3	99.9	104.8	101.1	182.0
519	293.5	99103.	69	-7.1	3.34	-0.02	97.2	100.9	103.4	104.6	99.6	104.7	103.4	182.5
520	295.2	99459	82	-7.1	3.31	-0.06	102.2	105.3	107.3	105.4	100.7	104.8	101.4	182.5
541	293.3	99182.	69	-4.9	2.78	-1.87	91.6	94.7	99.4	99.5	95.4	101.3	99.5	177.8
542	297.4	99442.	82	-5.0	2.78	-1.83	95.7	97.6	102.2	99.8	94.9	99.2	95.8	175.6
543	293.7	99290.	69	-5.8	3.03	-0.96	94.3	98.2	101.4	102.1	97.3	103.0	100.2	179.8
544	297.0	99398.	82	-5.8	3.03	-0.99	97.8	100.7	103.8	102.4	97.0	101.2	98.0	178.3
545	293.4	99240	69	-7.9	3.53	0.43	98.2	101.6	104.4	105.6	100.5	106.2	105.6	183.7
546	296.9	99486.	82	-8.0	3.47	0.43	103.2	105.9	108.1	106.6	101.5	106.0	102.9	183.4
1505	292.5	99095.	77	-10.0	1.73	-0.25	95.8	99.0	99.0	102.4	94.9	96.5	96.2	178.5
1507	292.1	99028	77	-10.1	1.77	-0.18	95.9	99.8	99.2	102.6	95.0	98.1	96.3	178.9
1511	293.0	99112.	77	-10.2	1.78	-0.09	96.1	99.8	99.3	103.1	95.2	97.8	96.7	179.0
1513	293.0	99267.	77	-10.3	1.80	-0.04	96.1	100.0	99.4	103.0	95.4	98.5	96.9	178.9
1515	293.1	99196.	77	-10.4	1.82	0.03	96.5	100.2	99.6	103.3	95.5	98.5	97.3	179.4
1519	293.1	99193.	77	-10.5	1.85	0.10	96.6	100.2	99.6	103.4	95.3	98.6	97.3	179.4
1521	293.1	99085.	77	-10.6	1.88	0.16	96.8	100.2	99.9	103.5	95.7	99.1	97.4	179.6

Table I-8. Aerodynamic and Acoustic Test Data - Model 6.

NOZZLE - MODEL 06		AREA [MODEL SIZE				= 19.65 , FULL SIZE		= 1400.00] SQ.IN				
TEST POINT	V _{ac}	P _r	T _T	V _J	W	F						
	FT/SEC		DEG R	FT/SEC	LB/SEC	LB						
601	0	2.71	1711	2273	697.6	49286						
602	400	2.72	1710	2274	696.7	49242						
603	0	2.87	1715	2331	736.6	53367						
604	400	2.87	1721	2333	733.2	53165						
605	0	2.96	1712	2356	757.9	55502						
606	400	2.95	1710	2353	756.7	55350						
607	0	3.03	1705	2373	778.7	57423						
608	400	3.02	1727	2387	771.2	57216						
611	0	3.08	1711	2394	790.1	58781						
612	400	3.07	1718	2395	784.2	58376						
613	0	3.13	1714	2410	802.2	60082						
614	400	3.13	1720	2414	796.8	59779						
615	0	3.18	1712	2423	814.8	61356						
616	400	3.18	1732	2438	806.3	61096						
619	0	3.23	1707	2433	824.4	62334						
620	400	3.23	1727	2447	824.1	62686						
621	0	3.32	1714	2462	851.2	65135						
622	400	3.33	1709	2461	848.3	64879						
623	0	3.51	1715	2509	898.4	70064						
624	400	3.52	1718	2513	895.2	69916						

TEST POINT	T _{amb}	P _{amb}	RH	NF	LVM	LBM	PNL (FULL SIZE, 2400 FT SIDE LINE), dB						OAPWL	
	DEG R	PSIA	%	dB			ANGLE RELATIVE TO INLET, DEGREES							
							50	60	70	90	120	130	140	dB
601	535.0	14.50	47	-5.9	3.02	-0.93	93.6	97.7	98.8	101.3	103.4	105.2	106.2	181.5
602	536.2	14.45	42	-5.9	3.02	-0.92	101.9	103.6	102.7	103.5	103.6	98.6	101.8	179.7
603	536.0	14.48	47	-6.3	3.13	-0.60	94.1	97.4	98.3	101.5	103.7	105.9	107.6	182.0
604	541.8	14.46	42	-6.3	3.11	-0.61	99.2	102.5	102.1	103.4	105.1	101.6	103.4	180.4
605	535.6	14.47	47	-6.5	3.17	-0.44	93.9	97.2	98.1	101.6	104.4	106.8	108.3	182.4
606	536.7	14.45	83	-6.5	3.16	-0.45	99.0	101.9	102.5	102.7	104.3	101.6	103.7	179.9
607	536.3	14.48	47	-6.7	3.20	-0.32	93.8	97.2	99.0	101.4	104.6	107.4	108.7	182.7
608	537.4	14.45	83	-6.7	3.22	-0.33	98.9	101.8	102.3	102.7	104.8	103.3	104.6	180.3
611	537.2	14.46	47	-6.8	3.24	-0.24	94.1	97.6	99.3	101.9	104.9	107.6	109.4	183.0
612	540.8	14.43	66	-6.8	3.22	-0.25	99.2	102.2	102.6	102.8	105.1	103.5	104.8	180.9
613	537.2	14.46	47	-6.9	3.26	-0.16	94.1	97.9	99.6	102.1	105.2	107.9	109.6	183.2
614	540.7	14.39	66	-6.9	3.26	-0.16	100.2	102.6	102.9	103.4	105.3	105.0	105.3	181.3
615	537.0	14.45	47	-7.1	3.29	-0.09	94.5	98.2	99.7	102.3	105.2	108.3	109.7	183.8
616	542.6	14.38	63	-7.0	3.29	-0.09	100.3	102.7	102.9	103.4	105.6	105.3	105.7	181.6
619	537.3	14.37	47	-7.2	3.31	-0.02	94.6	98.4	100.0	102.6	105.6	109.0	110.2	183.8
620	542.3	14.45	63	-7.2	3.31	-0.02	100.2	102.8	103.3	103.8	105.8	105.7	106.3	182.0
621	536.9	14.45	41	-7.4	3.36	0.10	95.5	99.3	101.0	103.3	106.0	109.3	110.8	184.3
622	541.0	14.35	59	-7.4	3.34	0.11	100.4	104.0	103.9	104.1	105.6	106.1	107.4	182.6
623	537.3	14.45	42	-7.8	3.44	0.32	95.4	99.1	101.0	103.6	107.2	111.3	111.7	185.5
624	544.3	14.39	59	-7.8	3.42	0.33	100.5	103.4	104.0	105.3	107.0	107.6	108.7	183.7

Table I-8. (Cont'd)

NOZZLE - MODEL 06 CONTINUED

TEST POINT	V _{ac} FT/SEC	P _r	T _T DEG R	V _j FT/SEC	W LB/SEC	F LB
1605	0	3.07	878	1701	1116.8	59042
1607	0	3.12	865	1699	1145.3	60494
1611	0	3.17	866	1709	1161.0	61674
1613	0	3.21	863	1714	1179.6	62851
1615	0	3.27	866	1729	1197.6	64348
1619	0	3.33	864	1738	1222.1	66017
1621	0	3.37	864	1745	1236.6	67059

TEST POINT	T _{amb} DEG R	P _{amb} PSIA	RH %	NF dB	LVM	LBM	PNL (FULL SIZE, 2400 FT SIDE LINE), dB						OAPWL dB	
							ANGLE RELATIVE TO INLET, DEGREES							
							50	60	70	90	120	130	140	
1605	528.8	14.49	47	-9.9	1.79	-0.26	94.0	97.2	98.6	100.1	98.4	98.8	98.5	177.5
1607	530.5	14.49	47	-10.1	1.78	-0.17	94.2	97.6	98.8	100.3	98.4	98.6	98.0	177.3
1611	530.6	14.48	47	-10.2	1.80	-0.11	95.1	98.3	99.5	100.8	98.8	99.0	98.2	177.7
1613	531.9	14.49	47	-10.3	1.81	-0.05	95.0	98.5	99.6	100.8	98.7	99.0	98.4	177.9
1615	532.2	14.47	47	-10.4	1.84	0.03	95.1	98.4	99.7	101.0	98.8	99.0	98.7	178.3
1619	532.5	14.47	47	-10.5	1.86	0.11	96.1	99.3	100.6	101.8	99.2	99.5	99.1	178.7
1621	533.0	14.48	47	-10.6	1.88	0.16	96.0	98.2	99.9	101.9	99.7	99.9	99.5	178.8

Table I-8. (Cont'd)

***** S.I.UNITS *****

NOZZLE - MODEL 06 AREA [MODEL SIZE] = 0.0127 FULL SIZE = 0.9031] sq m.

TEST POINT	V _{ac}	V _j	T _T	T _J	P _r	W	F
	m/s	m/s	°K	°K		kg/s	N
601	0.	692.8	950.6	733.7	2.7146	316.4	13702
602	122.	693.1	950.0	732.9	2.7186	316.0	13689
603	0	710.5	952.8	724.3	2.8725	334.1	14836
604	122.	711.1	956.1	726.9	2.8678	332.6	14780
605	0.	718.1	951.1	717.3	2.9563	343.8	15430
606	122	717.2	950.0	716.6	2.9528	343.2	15388
607	0	723.3	947.2	709.1	3.0282	353.2	15964
608	122	727.6	959.4	719.1	3.0242	349.8	15906
611	0.	729.7	950.6	708.5	3.0830	358.4	16341
612	122.	730.0	954.4	712.1	3.0716	355.7	16229
613	0.	734.6	952.2	706.4	3.1321	363.9	16703
614	122	735.8	955.6	709.1	3.1319	361.4	16619
615	0.	738.5	951.1	702.9	3.1814	369.6	17057
616	122.	743.1	962.2	711.4	3.1840	365.7	16985
619	0.	741.6	948.3	697.6	3.2315	373.9	17329
620	122	745.8	959.4	706.1	3.2323	373.8	17427
621	0.	750.4	952.2	694.8	3.3245	386.1	18108
622	122	750.1	949.4	692.4	3.3325	384.8	18037
623	0.	764.7	952.8	684.7	3.5117	407.5	19478
624	122.	766.0	954.4	685.8	3.5171	406.1	19437

372

TEST POINT	T _{amb} DEG K	P _{amb} Pascal	RH %	NF dB	LVM	LBM	PNL (FULL SIZE 2400 FT SIDE LINE), dB					OAPWL dB		
							ANGLE RELATIVE TO INLET DEGREES							
							50	60	70	90	120		130	140
601	297.2	99940.	47	-5.9	3.02	-0.93	93.6	97.7	98.8	101.3	103.4	105.2	106.2	181.5
602	297.9	99640.	42	-5.9	3.02	-0.92	101.9	103.6	102.7	103.5	103.6	98.6	101.8	179.7
603	297.8	99860	47	-6.3	3.13	-0.60	94.1	97.4	98.3	101.5	103.7	105.9	107.6	182.0
604	301.0	99717.	42	-6.3	3.11	-0.61	99.2	102.5	102.1	103.4	105.1	101.6	103.4	180.4
605	297.5	99748.	47	-6.5	3.17	-0.44	93.9	97.2	98.1	101.6	104.4	106.8	108.3	182.4
606	298.2	99640.	83	-6.5	3.16	-0.45	99.0	101.9	102.5	102.7	104.3	101.6	103.7	179.9
607	297.9	99805.	47	-6.7	3.20	-0.32	93.8	97.2	99.0	101.4	104.6	107.4	108.7	182.7
608	298.5	99644	83	-6.7	3.22	-0.33	98.9	101.8	102.3	102.7	104.8	103.3	104.6	180.3
611	298.4	99671.	47	-6.8	3.24	-0.24	94.1	97.6	99.3	101.9	104.9	107.6	109.4	183.0
612	300.4	99495.	66	-6.8	3.22	-0.25	99.2	102.2	102.6	102.8	105.1	103.5	104.8	180.9
613	298.4	99691.	47	-6.9	3.26	-0.16	94.1	97.9	99.6	102.1	105.2	107.9	109.6	183.2
614	300.4	99196.	66	-6.9	3.26	-0.16	100.2	102.6	102.9	103.4	105.3	105.0	105.3	181.3
615	298.3	99647	47	-7.1	3.29	-0.09	94.5	98.2	99.7	102.3	105.2	108.3	109.7	183.8
616	301.4	99125.	63	-7.0	3.29	-0.09	100.3	102.7	102.9	103.4	105.6	105.3	105.7	181.6
619	298.5	99102.	47	-7.2	3.31	-0.02	94.6	98.4	100.0	102.6	105.6	109.0	110.2	183.8
620	301.3	99637.	63	-7.2	3.31	-0.02	100.2	102.8	103.3	103.8	105.8	105.7	106.3	182.0
621	298.3	99651.	41	-7.4	3.36	0.10	95.5	99.3	101.0	103.3	106.0	109.3	110.8	184.3
622	300.5	98937	59	-7.4	3.34	0.11	100.4	104.0	103.9	104.1	105.6	106.1	107.4	182.6
623	298.5	99600.	42	-7.8	3.44	0.32	95.4	99.1	101.0	103.6	107.2	111.3	111.7	185.5
624	302.4	99189	59	-7.8	3.42	0.33	100.5	103.4	104.0	105.3	107.0	107.6	108.7	183.7

Table I-8. (Concluded)

***** S.I.UNITS *****

NOZZLE - MODEL 06 CONTINUED

TEST POINT	V ac	V j	T T	T j	P r	W	F	PNL (FULL SIZE 2400 FT SIDE LINE) dB							OAPWL
	m/s	m/s	o K	o K		kg/s	N	ANGLE RELATIVE TO INLET DEGREES							dB
			DEG.K	Pascal	%	dB		50	60	70	90	120	130	140	
373 1605	0.	518.5	487.8	354.2	3.0690	506.6	1641	94.0	97.2	98.6	100.1	98.4	98.8	98.5	177.5
1607	0.	517.9	480.6	347.2	3.1237	519.5	1681	94.2	97.6	98.8	100.3	98.4	98.6	98.0	177.3
1611	0	520.9	481.1	345.9	3.1698	526.6	1714	95.1	98.3	99.5	100.8	98.8	99.0	98.2	177.7
1613	0.	522.4	479.4	343.4	3.2126	535.1	1747	95.0	98.5	99.6	100.8	98.7	99.0	98.4	177.9
1615	0.	527.0	481.1	342.8	3.2718	543.2	1788	95.1	98.4	99.7	101.0	98.8	99.0	98.7	178.3
1619	0	529.7	480.0	340.2	3.3342	554.3	1835	96.1	99.3	100.6	101.8	99.2	99.5	99.1	178.7
1621	0.	531.9	480.0	339.1	3.3711	560.9	1864	96.0	98.2	99.9	101.9	99.7	99.9	99.5	178.8

TABLE II-1. AERODYNAMIC CONDITIONS OF LV TEST POINTS OF MODEL 1, CONVERGENT CIRCULAR NOZZLE

TEST POINT	P_r	T_T	T_s	V_j	$V_{a/c}$	REMARKS
		$^{\circ}K$ ($^{\circ}R$)	$^{\circ}K$ ($^{\circ}R$)	m/s (ft/s)	m/s (ft/s)	
113	3.128	946 (1703)	702 (1264)	732 (2402)	0	STATIC CONDITION, CORRESPONDS TO C-D DESIGN POINT
114	3.128	963 (1734)	716 (1288)	739 (2425)	122 (400)	FLIGHT SIMILATED, CORRESPONDS TO C-D DESIGN POINT
121	3.316	949 (1708)	693 (1247)	749 (2457)	0	STATIC CONDITION, UNDEREXPANDED FLOW
122	3.323	953 (1715)	696 (1252)	751 (2464)	122 (400)	FLIGHT SIMILATED, UNDEREXPANDED FLOW

P_r = PRESSURE RATIO
 T_T = TOTAL TEMPERATURE
 T_s = STATIC TEMPERATURE

V_j = FULLY EXPANDED JET EXIT VELOCITY
 $V_{a/c}$ = FREE JET VELOCITY

TABLE II-2. AERODYNAMIC CONDITIONS OF LV TEST POINTS OF MODEL 2, CONVERGENT-DIVERGENT CIRCULAR NOZZLE FOR DESIGN AT $M_j \approx 1.4$

TEST POINT	P_r	T_T	T_S	V_j	$V_{a/c}$	REMARKS
		$^{\circ}K$ ($^{\circ}R$)	$^{\circ}K$ ($^{\circ}R$)	m/s (ft/s)	m/s (ft/s)	
213	3.121	949 (1708)	704 (1268)	732 (2403)	0	STATIC CONDITION, C-D DESIGN POINT
214	3.121	953 (1716)	708 (1275)	734 (2409)	122 (400)	FLIGHT SIMULATED, C-D DESIGN POINT
221	3.309	943 (1697)	688 (1239)	746 (2447)	0	STATIC CONDITION, UNDEREXPANDED FLOW
222	3.312	948 (1707)	693 (1247)	748 (2455)	122 (400)	FLIGHT SIMULATED, UNDEREXPANDED FLOW
207	3.018	948 (1707)	711 (1280)	723 (2372)	0	STATIC CONDITION, OVEREXPANDED FLOW
211	3.074	949 (1709)	708 (1274)	728 (2390)	0	STATIC CONDITION, OVEREXPANDED FLOW

P_r = PRESSURE RATIO
 T_T = TOTAL TEMPERATURE
 T_S = STATIC TEMPERATURE

V_j = FULLY EXPANDED JET EXIT VELOCITY
 $V_{a/c}$ = FREE JET VELOCITY

TABLE II-3. AERODYNAMIC CONDITIONS OF LV TEST POINTS OF MODEL 3
CONTOURED CONVERGENT ANNULAR PLUG NOZZLE

TEST POINT	P_r	T_T	T_s	V_j	$V_{a/c}$	REMARKS
		$^{\circ}K$ ($^{\circ}R$)	$^{\circ}K$ ($^{\circ}R$)	m/s (ft/s)	m/s (ft/s)	
313	3.146	971 (1747)	721 (1297)	743 (2439)	0	STATIC CONDITION, CORRESPONDS TO C-D DESIGN POINT
314	3.136	952 (1713)	706 (1271)	735 (2411)	122 (400)	FLIGHT SIMULATED, CORRESPONDS TO C-D DESIGN POINT
321	3.320	963 (1733)	703 (1266)	755 (2476)	0	STATIC CONDITION, UNDEREXPANDED FLOW
322	3.353	955 (1719)	696 (1252)	754 (2474)	122 (400)	FLIGHT SIMULATED, UNDEREXPANDED FLOW
309	3.061	955 (1719)	713 (1284)	730 (2394)	0	STATIC CONDITION, OVEREXPANDED FLOW
1313	3.239	487 (877)	348 (627)	528 (1734)	0	STATIC CONDITION, LOW TEMP. CORRESPONDS TO C-D DESIGN PT.

P_r = PRESSURE RATIO
 T_T = TOTAL TEMPERATURE
 T_s = STATIC TEMPERATURE

V_j = FULLY EXPANDED JET EXIT VELOCITY
 $V_{a/c}$ = FREE JET VELOCITY

TABLE II-4.

AERODYNAMIC CONDITIONS OF LV TEST POINTS OF MODEL 4
CONVERGENT-DIVERGENT ANNULAR PLUG NOZZLE FOR DESIGN
AT $M_j \approx 1.4$

TEST POINT	P_r	T_T	T_s	V_j	$V_{a/c}$	REMARKS
		$^{\circ}K$ ($^{\circ}R$)	$^{\circ}K$ ($^{\circ}R$)	m/s (ft/s)	m/s (ft/s)	
413	3.108	957 (1723)	712 (1282)	735 (2411)	0	STATIC CONDITION, C-D DESIGN POINT
414	3.122	966 (1739)	718 (1293)	739 (2426)	122 (400)	FLIGHT SIMULATED, C-D DESIGN POINT
421	3.299	966 (1738)	707 (1272)	754 (2474)	0	STATIC CONDITION, UNDEREXPANDED FLOW
422	3.329	963 (1733)	703 (1265)	756 (2479)	122 (400)	FLIGHT SIMULATED, UNDEREXPANDED FLOW
407	3.025	962 (1732)	722 (1299)	729 (2392)	0	STATIC CONDITION, OVEREXPANDED FLOW
411	3.069	962 (1732)	718 (1293)	733 (2405)	0	STATIC CONDITION, OVEREXPANDED FLOW
419	3.214	938 (1689)	691 (1243)	736 (2416)	0	STATIC CONDITION, UNDEREXPANDED FLOW

P_r = PRESSURE RATIO
 T_T = TOTAL TEMPERATURE
 T_s = STATIC TEMPERATURE

V_j = FULLY EXPANDED JET EXIT VELOCITY
 $V_{a/c}$ = FREE JET VELOCITY

TABLE II-5. AERODYNAMIC CONDITIONS OF LV TEST POINTS OF MODEL 5, CONVERGENT 20-ELEMENT ANNULAR SUPPRESSOR NOZZLE

TEST POINT	P_r	T_T	T_s	V_j	$V_{a/c}$	REMARKS
		$^{\circ}K$ ($^{\circ}R$)	$^{\circ}K$ ($^{\circ}R$)	m/s (ft/s)	m/s (ft/s)	
513	3.123	962 (1732)	715 (1287)	738 (2421)	0	STATIC CONDITION, CORRESPONDS TO C-D DESIGN POINT
514	3.128	957 (1722)	711 (1279)	736 (2415)	122 (400)	FLIGHT SIMULATED, CORRESPONDS TO C-D DESIGN POINT
1513	3.209	472 (850)	338 (609)	518 (1701)	0	STATIC CONDITION, LOW TEMP. CORRESPONDS TO C-D DESIGN PT.
1514	3.214	472 (850)	338 (609)	519 (1702)	122 (400)	FLIGHT SIMULATED, LOW TEMP. CORRESPONDS TO C-D DESIGN PT.

378

P_r = PRESSURE RATIO
 T_T = TOTAL TEMPERATURE
 T_s = STATIC TEMPERATURE

V_j = FULLY EXPANDED JET EXIT VELOCITY
 $V_{a/c}$ = FREE JET VELOCITY

TABLE II-6. AERODYNAMIC CONDITIONS OF LV TEST POINTS OF MODEL 6, CONVERGENT-DIVERGENT 20-ELEMENT ANNULAR SUPPRESSOR NOZZLE FOR DESIGN
AT $M_j \approx 1.4$

TEST POINT	P_r	T_T	T_s	V_j	$V_{a/c}$	REMARKS
		$^{\circ}K$ ($^{\circ}R$)	$^{\circ}K$ ($^{\circ}R$)	m/s (ft/s)	m/s (ft/s)	
613	3.128	960 (1728)	713 (1283)	738 (2420)	0	STATIC CONDITION, C-D DESIGN POINT
614	3.125	961 (1729)	713 (1284)	737 (2419)	122 (400)	FLIGHT SIMULATED, C-D DESIGN POINT
1613	3.216	473 (852)	339 (610)	519 (1704)	0	STATIC CONDITION, LOW TEMP. C-D DESIGN POINT
1614	3.215	474 (853)	339 (611)	520 (1706)	122 (400)	FLIGHT SIMULATED, LOW TEMP. C-D DESIGN POINT

379

P_r = PRESSURE RATIO
 T_T = TOTAL TEMPERATURE
 T_s = STATIC TEMPERATURE

V_j = FULLY EXPANDED JET EXIT VELOCITY
 $V_{a/c}$ = FREE JET VELOCITY

TABLE III-1. Test Details of Shadowgraph Photographs with Convergent Circular Nozzle (Model 1).

Test Point	Shadowgraph Test Flow Conditions				Photograph Details		Matching Acoustic Test Point	Matching LV Test Point	
	$V_{a/c}$, fps	P_r	T_T , $^{\circ}R$	V_j , fps	No.	Shadowgraph Center Location X(In.) Along Centerline			Pictorial Representation
113	0	3.12	1718	2411	2	3.33		113	113
					3	10.50			
					4	17.67			
					5	24.42			
					6	31.45			
114	400	3.13	1721	2414	10	3.19		114	114
					11	10.50			
					12	17.67			
					13	24.42			
					14	31.45			
5114	400	3.23	834	1689	15	3.38		-	-
					16	10.20			
					17	18.08			
					18	24.96			
					19	31.85			

380

APPENDIX III. AERODYNAMIC TEST MATRIX FOR SHADOWGRAPH PHOTO TESTS
(Summarized from Reference 2-1)

Table III-1. (Concluded)

Test Point	Shadowgraph Test Flow Conditions				Photograph Details			Matching Acoustic Test Point	Matching LV Test Point
	$V_{a/c}$, fps	P_r	T_T , $^{\circ}R$	V_j , fps	No.	Shadowgraph Center Location X(In.) Along Centerline	Pictorial Representation		
5113	0	3.22	839	1693	20	3.00		-	-
					21	10.74			
					22	17.77			
					23	24.66			
					24	31.19			
7113	0	3.24	537	1358	30	3.51		-	-
					31	10.26			
					32	16.50			
					33	23.39			
					34	30.92			

TABLE III-2. Test Details of Shadowgraph Photographs with Convergent-Divergent Circular Nozzle (Model 2).

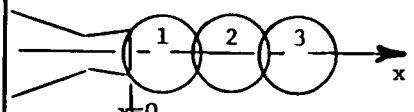
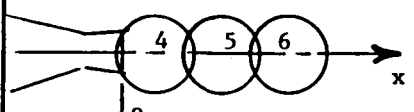
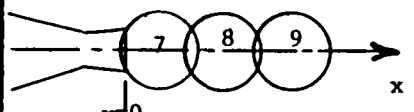
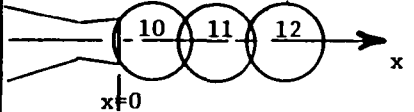
Test Point	Shadowgraph Test Flow Conditions				Photograph Details			Matching Acoustic Test Point	Matching LV Test Point
	$V_{a/c}$, fps	P_r	T_T , $^{\circ}R$	V_j , fps	No.	Shadowgraph Center Location X(In.) Along Centerline	Pictorial Representation,		
213	0	3.12	1716	2408	1	3.16		213	213
					2	9.91			
					3	16.65			
221	0	3.31	1710	2458	4	3.20		221	221
					5	9.95			
					6	16.69			
222	400	3.31	1706	2454	7	3.18		222	222
					8	9.93			
					9	16.67			
214	400	3.11	1707	2400	10	3.18		214	214
					11	10.14			
					12	16.67			

Table III-2. (Concluded).

383

Test Point	Shadowgraph Test Flow Conditions				Photograph Details			Matching Acoustic Test Point	Matching LV Test Point
	$V_{a/c}$, fps	P_r	T_{T^*} , $^{\circ}R$	V_{j^*} , fps	No.	Shadowgraph Center Location X(In.) Along Centerline	Pictorial Representation		
7214	400	3.24	559	1384	13	3.32		-	-
					14	10.07			
					15	16.81			
					16	23.56			
7213	0	3.24	517	1332	18	3.16		-	-
					19	10.62			
					20	17.36			
					21	24.11			
7211	0	3.21	514	1323	22	3.20		-	-
					23	9.95			
					24	16.69			
					25	23.44			
211	0	3.16	866	1708	27	3.16		1211	-
					28	9.91			
					29	16.65			

TABLE III-3. Test Details of Shadowgraph Photographs with Convergent Annular Nozzle (Model 3).

Test Point	Shadowgraph Test Flow Conditions				Photograph Details				Matching Acoustic Test Point	Matching LV Test Point
	V _{a/c} , fps	P _r	T _T , °R	V _j , fps	No.	Shadowgraph Center Location		Pictorial Representation		
						X (In)	Y (In)			
4313 (With Tabs)	0	3.11	1726	2413	4	-9.9	4.02		4313	-
					5	2.67	0.0			
					6	9.77	0.0			
4321 (With Tabs)	0	3.33	1688	2444	9	-9.68	4.02		4321	-
					10	2.82	0.0			
					11	9.92	0.0			
5323 (With Tabs)	0	3.39	856	1740	12	-9.39	4.02		5323	-
					13	2.82	0.0			
					14	9.92	0.0			
1313	0	3.22	866	1720	16	-9.31	3.69		1313	1313
					17	2.97	0.0			
					18	10.07	0.0			

Table III-3. (Concluded).

Test Point	Shadowgraph Test Flow Conditions				Photograph Details			Matching Acoustic Test Point	Matching LV Test Point	
	$V_{a/c}$, fps	P_r	T_T , $^{\circ}R$	V_j , fps	No.	Shadowgraph Center Location				Pictorial Representation
						X (In)	Y (In)			
313	0	3.14	1731	2424	20	-9.35	4.03		313	313
					21	-2.40	4.03			
					22	2.43	0.0			
					23	9.53	0.0			
314	400	3.14	1709	2410	25	-9.73	4.05		314	314
					26	-2.63	4.05			
					27	2.20	0.0			
					28	9.30	0.0			
322	400	3.31	1715	2460	30	-9.42	4.03		322	322
					31	2.51	0.0			

TABLE III-4. Test Details of Shadowgraph Photographs with Convergent-Divergent Annular Nozzle (Model 4).

Test Point	Shadowgraph Test Flow Conditions				Photograph Details				Matching Acoustic Test Point	Matching LV Test Point
	$V_{a/c}$, fps	P_r	T_T , $^{\circ}R$	V_j , fps	No.	Shadowgraph Center Location		Pictorial Representation		
						X (In)	Y (In)			
413	0	3.10	1687	2382	3	-6.94	3.1		413	413
					4	0.23	3.1			
					7	2.08	0.0			
					5	9.18	0.0			
411	0	3.07	1704	2387	8	-6.85	3.1		411	411
					9	0.32	3.1			
					10	2.17	0.0			
					11	9.27	0.0			
421	0	3.32	1687	2442	14	-6.85	3.1		421	421
					15	0.32	3.1			
					16	2.17	0.0			
					17	9.27	0.0			

Table III-4. (Concluded).

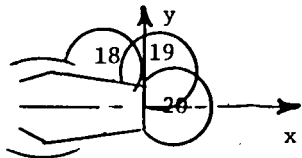
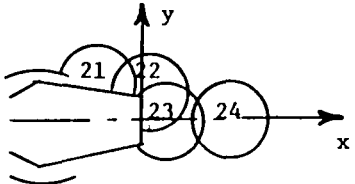
Test Point	Shadowgraph Test Flow Conditions				Photograph Details				Matching Acoustic Test Point	Matching LV Test Point
	$V_{a/c}$, fps	P_r	T_T , $^{\circ}R$	V_j , fps	No.	Shadowgraph Center Location		Pictorial Representation		
						X (In)	Y (In)			
422	400	3.34	1693	2451	18	-7.09	3.1		422	422
					19	0.08	3.1			
					20	1.93	0.0			
414	400	3.09	1700	2389	21	-7.09	3.1		414	414
					22	0.08	3.1			
					23	1.93	0.0			
					24	9.03	0.0			

Table III-5. Test Details of Shadowgraph Photographs with Convergent Suppressor Nozzle (Model 5).

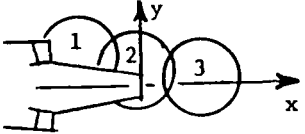
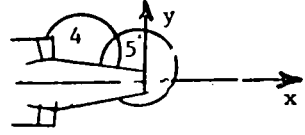
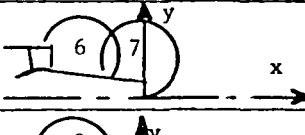

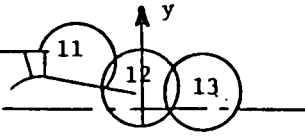
Test Point	Shadowgraph Test Flow Conditions				Photograph Details				Matching Acoustic Test Point	Matching LV Test Point
	$V_{a/c}$, fps	P_r	T_T , $^{\circ}R$	V_j , fps	No.	Shadowgraph Center Location		Pictorial Representation		
						X (In)	Y (In)			
1513	0	3.21	849	1701	1				1513	1513
					2					
					3					
1521	0	3.37	852	1733	4				1521	-
					5					
513	0	3.12	1717	2411	6				513	513
					7					
514	400	3.13	1725	2420	8				514	514
1514	400	3.22	849	1702	11				-	1514
					12					
					13					

Table III-5. (Concluded).

Test Point	Shadowgraph Test Flow Conditions				Photograph Details				Matching Acoustic Test Point	Matching LV Test Point
	$V_{a/c}$, fps	P_r	T_T , $^{\circ}R$	V_j , fps	No.	Shadowgraph Center Location		Pictorial Representation		
						X (In)	Y (In)			
1522	400	3.37	859	1740	14				-	-
					15					
					16					
7513	0	3.27	542	1368	20				-	-
					21					
					22					
					23					
					24					

Table III-6. Test Details of Shadowgraph Photographs with Convergent-Divergent Suppressor Nozzle (Model 6)

Test Point	Shadowgraph Test Flow Conditions				Photograph Details				Matching Acoustic Test Point	Matching LV Test Point
	$V_{a/c}$, fps	P_r	T_T , $^{\circ}R$	V_j , fps	No.	Shadowgraph Center Location		Pictorial Representation		
						X (In)	Y (In)			
613	0	3.13	1715	2412	1	-6.57	4.28		613	613
					2	0.53	2.73			
					3	7.63	0.0			
					4	14.73	0.0			
					5	21.83	0.0			
614	400	3.13	1712	2410	6	-6.57	4.28		614	614
					7	0.53	2.73			
					8	7.63	0.0			
					9	14.73	0.0			
					10	21.83	0.0			
4614	400	3.72	1726	2566	11	-6.57	4.28		-	-
4612	400	3.42	1730	2499	12	-6.57	4.28		-	-

Table III-6. (Continued).

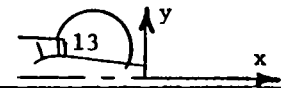

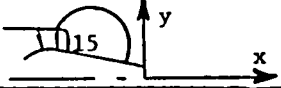

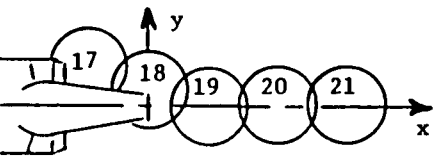
Test Point	Shadowgraph Test Flow Conditions				Photograph Details				Matching Acoustic Test Point	Matching LV Test Point
	$V_{a/c}$, fps	P_r	T_T , $^{\circ}R$	V_j , fps	No.	Shadowgraph Center Location		Pictorial Representation		
						X (In)	Y (In)			
4610	400	3.21	1740	2451	13	-6.57	4.28		-	-
4606	400	3.02	1733	2390	14	-6.57	4.28		-	-
4604	400	2.72	1732	2290	15	-6.57	4.28		-	-
4602	400	2.37	1591	2055	16	-6.57	4.28		-	-
7614	400	3.26	609	1448	17	-5.52	3.52		-	-
					18	1.58	0.99			
					19	8.68	0.0			
					20	15.78	0.0			
					21	22.88	0.0			

Table III-6. (Concluded).

Test Point	Shadowgraph Test Flow Conditions				Photograph Details				Matching Acoustic Test Point	Matching LV Test Point
	$V_{a/c}$, fps	P_r	T_T , $^{\circ}R$	V_j , fps	No.	Shadowgraph Center Location		Pictorial Representation		
						X (In)	Y (In)			
7613	0	3.26	560	1389	22	-6.3	3.52		-	-
					23	0.8	0.67			
					24	7.9	0.0			
					25	15.0	0.0			
					26	22.1	0.0			

392

E-2282

0-

1. Report No. NASA CR-3845		2. Government Accession No.		3. Recipient's Catalog No.	
4. Title and Subtitle Experimental Investigation of Shock-Cell Noise Reduction for Single Stream Nozzles in Simulated Flight				5. Report Date December 1984	
				6. Performing Organization Code	
7. Author(s) K. Yamamoto, J. F. Brausch, T. F. Balsa, B. A. Janardan, and P. R. Knott				8. Performing Organization Report No. R82AEB492	
				10. Work Unit No.	
9. Performing Organization Name and Address General Electric Company Aircraft Engine Business Group Cincinnati, Ohio 45215				11. Contract or Grant No. NAS3-22514	
				13. Type of Report and Period Covered Contractor Report	
12. Sponsoring Agency Name and Address National Aeronautics and Space Administration Washington, D.C. 20546				14. Sponsoring Agency Code 505-31-3B (E-2282)	
15. Supplementary Notes Final report. Project Manager, James R. Stone, Fluid Mechanics and Instrumentation Division, NASA Lewis Research Center, Cleveland, Ohio 44135.					
16. Abstract Seven single stream model nozzles were tested in Anechoic Free-jet Acoustic Test Facility for a total of one hundred forty acoustic test points so as to evaluate the effectiveness of Convergent-Divergent (C-D) flowpaths in the reduction of shock-cell noise under both static and simulated flight conditions. The test nozzles included a baseline convergent circular nozzle, a C-D circular nozzle, a convergent annular plug nozzle, a C-D annular plug nozzle, a convergent multi-element suppressor plug nozzle and a C-D multi-element suppressor plug nozzle. In addition, diagnostic flow visualization with shadowgraph and aerodynamic plume measurements with laser velocimeter were performed with the test nozzles. Most of the tests were conducted at elevated exhaust nozzle total temperatures (~ 1730°R) and nozzle pressure ratios that are typical of mixed conditions of a variable cycle engine applicable for advanced supersonic transport. Also, a theory of shock-cell noise for annular plug nozzles with shock-cells in the vicinity of the plug was developed based on recent theories of shock-turbulence interaction. Major results of this investigation include: (a) At the C-D design condition, the static and simulated flight PNL at an angle of 50 deg. to the inlet relative to the baseline convergent circular nozzle, respectively, indicate (1) 7.5 and 11 dB reduction with the C-D circular nozzle, (2) 6 and 8 dB for the C-D annular nozzle and (3) 9.5 and 10 dB for the C-D multi-element suppressor nozzle. The benefit of these C-D nozzles is observed over a broad range of pressure ratios in the vicinity of their design conditions. (b) At the C-D design condition, the C-D annular nozzle was found to be free of shock-cells on the plug. However, shock-cells downstream of the plug were noted indicating complete shock-cell noise reduction has not been achieved by the C-D termination on the annular plug nozzle.					
17. Key Words (Suggested by Author(s)) Shock-cell noise Supersonic jet noise Convergent-divergent nozzles Acoustic flight noise simulation Laser velocimeter measurements			18. Distribution Statement Unclassified - unlimited STAR Category 71		
19. Security Classif. (of this report) Unclassified		20. Security Classif. (of this page) Unclassified		21. No. of pages 396	22. Price* A17

*For sale by the National Technical Information Service, Springfield, Virginia 22161